TEL AVIV UNIVERSITY

THE IBY AND ALADAR FLEISCHMAN FACULTY OF ENGINEERING

The Zandman-Slaner Graduate School of Engineering

MIXED MODE FRACTURE BEHAVIOR OF A MULTI-DIRECTIONAL LAMINATE COMPOSITE PRODUCED BY A WET LAYUP

By

Mor Mega

THESIS SUBMITTED TO THE SENATE OF TEL-AVIV UNIVERSITY

in partial fulfillment of the requirements for the degree of

"DOCTOR OF PHILOSOPHY"

ISBN: 9788831482141

April 2021

THE IBY AND ALADAR FLEISCHMAN FACULTY OF ENGINEERING
The Zandman-Slaner Graduate School of Engineering

MIXED MODE FRACTURE BEHAVIOR OF A MULTI-DIRECTIONAL LAMINATE COMPOSITE PRODUCED BY A WET LAYUP

By
Mor Mega

THESIS SUBMITTED TO THE SENATE OF TEL-AVIV UNIVERSITY
in partial fulfillment of the requirements for the degree of
"DOCTOR OF PHILOSOPHY"

Under The Supervision of Prof. Leslie Banks-Sills
April 2021

THE IBY AND ALADAR FLEISCHMAN FACULTY OF ENGINEERING

The Zandman-Slaner Graduate School of Engineering

This work was carried out under the supervision of

Research Supervisor: Leslie Banks-Sills

Prof. Leslie Banks-Sills

To my loving family
Thank you for the endless love and happiness you bring into my life every day

Acknowledgement

The journey to completing this Ph.D. thesis was challenging and thrilling, with many ups and downs along the way. First, I would like to thank my supervisor who has become my mentor throughout this journey, Prof. Leslie Banks-Sills. It must be said that our relationship was always interesting and that thanks to the conflicts and challenges, I have grown, matured and became a better person. Prof. Banks-Sills, is a dominant figure in the field of fracture and fatigue mechanics, she is creative and dedicated to research, as well as to her students. I can honestly say that she has become my role model for excellency. Prof. Banks-Sills has guided me to a modus operandi of self-criticism which has enabled me to doubt everything and take nothing for granted, qualities which are a necessity for every researcher. I cant find the words to express my gratitude for the time and effort that she has dedicated to the accomplishment of this research. Her devotion, dedication, uncompromising care to details, assistance and support through every step of the way are truly acknowledged.

I would also like to thank my good friend Ido Meshi, although Ido was in the laboratory for a short period of time, his assistance with binding the numerical code used for the M-integral into one piece was not obvious and greatly appreciated. Moreover, his friendship was valuable to me. Also, I wish to acknowledge Rami Eliasi and Dr. Victor Fourman for their assistance, advise, support, patience and most of all encouragement throughout this journey. Dr. Fourman took a role in carrying out all tests. His technical knowledge has assisted in improving the experimental set-up, as well as solving problems along the way. Mr. Eliasi has vast knowledge with numerical analyses which contributed to the numerical part of this investigation. Moreover, his daily encouragement, advise and smile made the hard parts of this journey easier. I deeply thank my friends and colleagues from the fracture mechanics laboratory. The weekly meetings, discussions, assistance and friendship contributed to the accomplishment of this research. Special thanks to Karin Lavon, my dear friend, for all the talks, coffee breaks and lunches. Finally, a huge thanks to my beloved family, my husband Oded, our two beautiful children Yasmin and Ariel, as well as to my dear parents Frida and Yossi Pelleg. This journey was not possible without you!!! Thank you for being by my side throughout the whole way. Thank you for the support, advise, understanding and unconditional love. This research was supported by the Israel Ministry of Science, Technology and Space, Grant number: 00040436000.

Abstract

Carbon fiber reinforced polymers are used for improving performance and lowering operational costs of structures, particularly in the aerospace industry. However, lack of knowledge of the fracture behavior of these composites may result in catastrophic disasters. Understanding delamination initiation and propagation of carbon fiber reinforced polymer laminates (CFRPs) may assist in preventing catastrophic failures of structures such as airplanes. Precise engineering tools may lead to safer design, improved performance, as well as lowered operational costs of structures constructed from these materials. This study focuses on a delamination between two fiber reinforced composite plies. The upper ply is a UD fabric with fibers oriented in the 0°- direction and the lower ply is a plain balanced weave with tows oriented in the $+45°/-45°$ - directions. The composite is manufactured by a wet-layup process.

Twenty-seven successful mixed mode fracture toughness tests were carried out using Brazilian disk specimens to determine the fracture toughness properties of this composite and interface. During each test, a load P was applied at an angle ω with respect to an artificial delamination located between the investigated plies. Seven loading angles were used to achieve different mixed mode combinations. Based on the results, using finite element analyses in conjunction with the three-dimensional conservative interaction energy integral or M-integral and the displacement extrapolation method, the stress intensity factors resulting from mechanical loads, as well as residual curing stresses were obtained along the delamination front for each specimen. The stress intensity factors were superposed and used to calculate the interface initiation energy release rate and mode mixities or phase angles. Finally, two and three-dimensional failure criteria were proposed for this material and interface and a statistical analysis with a 10% probability of unexpected failure in the safe zone with a confidence of 95% was performed. The failure curves and surfaces may be used to predict catastrophic failure for this material and interface, as well as to lead to a better understanding of interlaminar delamination.

Initiation and propagation properties were determined based on nearly mode I, nearly mode II and mixed mode fracture toughness and fracture resistance tests. For mode I, DCB tests, which were performed and described in Chocron and Banks-Sills (2019), were reanalyzed. For the nearly mode II and mixed mode initiation and resistance properties, C-ELS and MMELS fracture tests were performed, respectively, and analyzed. These

tests were quasi-static and consisted of two stages. In the first test stage, an artificial delamination was extended and in the second test stage, propagation from a natural precrack was observed. The experimental and numerical results obtained from the tests were employed to determine the fracture resistance $\mathcal{G}_{iR}$-curves for nearly mode I, nearly mode II and for one mixed mode I/II deformation ratio. The $\mathcal{G}_{iR}$-curves were generated by means of a local M-integral approach, as well as by means of the global experimental compliance method (ECM) and included determination of the initiation $\mathcal{G}_{ic}$ and steady-state propagation $\mathcal{G}_{iss}$ values. The $\mathcal{G}_{iR}$-curves obtained using both methods were compared for each tested specimen. In addition, the phase angles $\hat{\psi}$ and ϕ which define the mode mixities, were calculated for each specimen and test. The R-curves found may be used to account for the fracture resistance energy release rate required for propagation and to assist in improving the design and safety of a structure made of this laminate with this interface.

Contents

List of Symbols

Latin letters - upper case

A area of a body or integration area

A^* statistically reduced average value of some parameter

A_1 integration area

A_1, B fitting parameters in eq. 5.6)

$A_i, B_i, C_i (i = 1, 2)$ constants used to define the crack displacement jump

A_i $(i = 0, 1, 2)$ fitting parameters in eq. (5.13) relating the energy release rate J to the load P

A_k sub-area of a body or sub integration area of material k

A_{0k} sub-area or sub integration area of material k between the inner ring and the delamination tip as shown in Fig. 1.9

$\overline{A}$ average value of some parameter

$\mathbf{A}$ complex 3×3 matrix composed of the Stroh eigenvectors

$\mathbf{A}_k (k = 1, 2)$ complex 3×3 matrix composed of the Stroh eigenvectors for material k

B thickness of BD specimen or thickness of cylindrical FEM used for the benchmark problems in Section 3.3

$B_j^{(i)}$ $(j = 0, 1)$ fitting parameters for specimen i in eq. (5.15) relating the energy release rate J to the delamination length a and the related load P

${}_kB_s$ $(s = 1, 2, 3)$ elements in the asymptotic displacement and stress fields

$\mathbf{B}$ complex 3×3 matrix composed of the Stroh eigenvectors

$\mathbf{B}_k (k = 1, 2)$ complex 3×3 matrix composed of the Stroh eigenvectors for material k

C compliance

C parameter used to define K_m^* in eq. (3.10)

C_0 intercept of the line relating the compliance C and the cubed delamination length a^3

$C_j^{(i)}$ $(j = 0, 1, 2)$ fitting parameters for specimen i in eq. (5.16) relating the stress intensity factor $K_m^{(i)}$ $(m = 1, 2)$ to the delamination length a and the related load P

C_v vertical offset distance between the arrest hole diameter and the delamination, shown in Fig. 4.5b

C_{cal} compliance of the calibration specimen for the MMB test (calculated)

C_{FE} compliance measured from an FEA

$C_{ijks}(i, j, k, s = 1, 2, 3$ stiffness tensor coefficients

C_{sys} compliance of the MMB loading system

$D_{ii}(i = 1, 2, 3)$ diagonal components of matrix $\boldsymbol{D}$, no summation implied

$\boldsymbol{D}$ 3×3 matrix related to $\boldsymbol{L}_k$

$\tilde{D}$ constant related to the first two diagonal members of matrix $\boldsymbol{D}$

$E, \overline{E}$ Young's moduli

E_A Young's moduli in the axial direction in a transversely isotropic material

E_T Young's moduli in the transverse direction in a transversely isotropic material

E_{1f} flexural modulus

E_{cal} Young's modulus of the MMB compliance calibration specimen

$E_{ii}(i = 1, 2, 3)$ Young's moduli in the x_i-direction, no summation implied

F correction for large displacements

F represents a force unit

$F(z)$ arbitrary function of z

G_A axial shear modulus in a transversely isotropic material

$G_{ij}(i, j = 1, 2, 3)$ shear moduli

G_T transverse shear modulus in a transversely isotropic material

$\mathcal{G}$ energy release rate

$\mathcal{G}^{(f)}$ energy release rate related to mechanical applied load

$\mathcal{G}^{(r)}$ energy release rate related to residual curing thermal stresses

$\mathcal{G}^{(T)}$ total energy release rate resulting from mechanical applied load, as well as residual curing thermal stresses

$\mathcal{G}_i$ interface energy release rate

$\mathcal{G}_m (m = I, II, III)$ energy release rate related to deformation to mode m

$\mathcal{G}_T$ total energy release rate

$\mathcal{G}_1^{(i)}$ $(i = N, P)$ critical mode 1 energy release rate for $\hat{\psi} = 0$ for negative $(i = N)$/positive $(i = P)$ loading angles

$\mathcal{G}_{1c}$ critical mode 1 energy release rate for $\hat{\psi} = 0$

$\mathcal{G}_{1c}^{*}$ critical statistically reduced mode 1 energy release rate for $\hat{\psi} = 0$

$\mathcal{G}_{ic}$ initiation critical interface energy release rate or fracture toughness

$\mathcal{G}_{ic}^{*}$ statistically reduced initiation critical interface energy release rate or fracture toughness

$\mathcal{G}_{iR}$ resistance energy release rate

$\mathcal{G}_{iss}$ interface steady state resistance energy release rate

$\mathcal{G}_{mR}$ $(m = I, II)$ nearly mode m resistance energy release rate

$\mathcal{G}_{mss}$ $(m = I, II)$ interface mode m steady state resistance energy release rate

$\mathcal{G}_{os}$ in-plane interface energy release rate

$\mathcal{G}_c$ initiation critical energy release rate or fracture toughness

$\mathcal{G}_R$ resistance energy release rate

$\mathcal{G}_s$ out-of-plane interface energy release rate

$\mathcal{G}_{Tc}$ total critical energy release rate

$\overline{\mathcal{G}}_{1c}$ average mode 1 energy release rate

$\overline{\mathcal{G}}_i$ average interface energy release rate through the beam specimen width b for a specific delamination length a

H parameter related to the mechanical properties of the isotropic materials above and below the interface

H_1, H_2 parameters related to the mechanical properties of the anisotropic materials above and below the interface

H_T, H_B vertical top and bottom heights between the composite strip edge and the delamination, shown in Fig. 4.8a

I intercept of branch 2 or branch 3 in the '3 branch' or '5 branch' two dimensional failure criteria, respectively, in the $(\hat{K}_1 - \hat{K}_2)$-plane

I^* reduced value of I

$\Im$ imaginary part of a complex expression

$\boldsymbol{I}$ the identity matrix

J_{FE} J-integral result calculated using Abaqus (2017) from an FEA with a specific displacement d

J_{VIS} J-integral related to P_{VIS}

$\hat{K}^{(P)}_{2(max)}$ $(i = N, P)$ normalized maximum value of the mode 2 stress intensity factor from all $\hat{K}_2$ values observed at failure for the BD specimens related to the calculation of $\hat{K}^{(P)}_1$ for positive loading angles.

$\hat{K}^{(N)}_{2(min)}$ $(i = N, P)$ normalized minimum value of the mode 2 stress intensity factor from all $\hat{K}_2$ values observed at failure for the BD specimens related to the calculation of $\hat{K}^{(N)}_1$ for negative loading angles.

K a statistical reduction factor

K in-plane stress intensity factor

K stiffness of the springs in Section 5.3

K_{III} out-of-plane stress intensity factor

$K_{mc} (m = I, II, III \text{ or } 1, 2, 3)$ critical stress intensity factor corresponding to mode m

K_{AC-FE} stiffness of each C-ELS specimen in the AC (first) test stage obtained from the related FEA

K_{AC} stiffness of each C-ELS specimen in the AC (first) test stage

$K^{(1)}_{m_N} (m = I, II, III \text{ or } 1, 2, III)$ average value along the segment L_N of the stress intensity factor corresponding to mode m of the problem sought

$K_{m_N}^{(2\alpha)}(m = I, II, III \text{ or } 1, 2, III; \alpha = a, b, c)$ average value along the segment L_N of the stress intensity factor corresponding to mode m of the auxiliary solution

$K_m(m = I, II, III \text{ or } 1, 2, 3)$ stress intensity factor corresponding to mode m

$K_m^{(1)}(m = I, II, III \text{ or } 1, 2, III)$ stress intensity factor corresponding to mode m of the problem sought

$K_m^{(2\alpha)}(m = I, II, III \text{ or } 1, 2, III; \alpha = a, b, c)$ stress intensity factor corresponding to mode m of the auxiliary solution

$K_m^{(f)}(m = 1, 2, 3)$ stress intensity factor resulting from mechanical loads corresponding to mode m

$K_m^{(r)}(m = 1, 2, 3)$ stress intensity factor resulting from thermal curing stresses corresponding to mode m

$K_m^{(T)}(m = 1, 2, 3)$ total stress intensity factor corresponding to mode m

$K_m^*(m = I, II, III \text{ or } 1, 2, 3)$ local stress intensity factors related to mode m

$K_m^{DE}(m = 1, 2, III)$ stress intensity factor obtained by means of the DE method

$K_m^{M-integral}(m = 1, 2, III)$ stress intensity factor obtained by means of the M-integral

K_{PC-FE} stiffness of each C-ELS specimen in the PC (second) test stage obtained from the related FEA

K_{PC} stiffness of each C-ELS specimen in the PC (second) test stage

$\hat{K}$ in-plane stress intensity factor with regular units

$\hat{K}_1^{(i)}$ $(i = N, P)$ normalized mode 1 stress intensity factor for negative $(i = N)$/ positive $(i = P)$ loading angles

$\hat{K}_1^{*(i)}$ $(i = N, P)$ reduced value of $\hat{K}_1^{(i)}$ obtained by means of statistical analysis

$\hat{K}_{2(avg)}^{(i)}$ $(i = N, P)$ normalized average value of the mode 2 stress intensity factor from all $\hat{K}_2$ values observed at failure for the BD specimens related to the calculation of $\hat{K}_1^{(i)}$ for negative $(i = N)$/ positive $(i = P)$ loading angles.

$\hat{K}_{2c}^{(i)}$ $(i = N, P)$ normalized mode 2 stress intensity factor for negative $(i = N)$/ positive $(i = P)$ loading angles for $\hat{K}_1 = 0$

$\hat{K}_{2c}^{*(i)}$ $(i = N, P)$ intersection between the statistical branch and the $\hat{K}_2$ axis

$\hat{K}_{1c}$ critical statistically reduced $\hat{K}_{1c}$

$\hat{K}_{mc}$ $(m = 1, 2)$ critical normalized in-plane stress intensity factor corresponding to mode m

$\hat{K}_{mFE}$ $(m = 1, 2)$ normalized stress intensity factors corresponding to mode m obtained from the FEAs with $d = 10$ mm and $a = 50, 60, 70, 80$ mm

$\hat{K}'_m$ $(m = 1, 2)$ rotated axes in the direction of one of the branches in the 3 branch or 5 branch criterion

$\hat{K}_m$ $(m = 1, 2)$ normalized in-plane stress intensity factor corresponding to mode m

$\hat{K}_m^{(f)}(m = 1, 2, 3)$ normalized stress intensity factor with regular units resulting from mechanical loads corresponding to mode m

$\hat{K}_m^{(r)}(m = 1, 2, 3)$ normalized stress intensity factor with regular units resulting from thermal curing stresses corresponding to mode m

$\hat{K}_m^{(T)}(m = 1, 2, 3)$ normalized total stress intensity factor with regular units corresponding to mode m

$\hat{K}_1^{\prime(i)}$ $(i = N, P, S)$ average value in the rotated space of all $\hat{K}'_1$ values related to branch i in the 3 branch or 5 branch failure criterion

$\hat{K}_1^{\prime *(i)}$ $(i = N, P)$ statistically reduced average value in the rotated coordinate system of all $\hat{K}'_1$ values related to a specific branch in the 3 branch or 5 branch failure criterion

$\tilde{K}$ in-plane non-dimensional complex stress intensity factor

$\tilde{K}_m^{(f)}(a/R)(m = 1, 2)$ mechanical non-dimensional stress intensity factor corresponding to mode m

$\tilde{K}_m^{(r)}(a/R)(m = 1, 2)$ residual thermal non-dimensional stress intensity factor corresponding to mode m

$\hat{L}$ arbitrary length parameter

L represents a length unit

L span length from the load-line in the MMB and ENF test apparatus

L_f free length between the load-line and the clamp in the C-ELS and MMELS specimens

L_I invariant value related to $\hat{L}$

$L_j(j = 2, 3, 4)$ differential operators of order j, functions of the reduced elastic compliance coefficients

L_{fAC} free length between the load-line and the clamp in the AC (first) test stage of the C-ELS and MMELS tests

L_{fPC} free length between the load-line and the clamp in the PC (second) test stage of the C-ELS and MMELS tests

$\boldsymbol{L}_k (k = 1, 2)$ one of the three real Barnett-Lothe tensors for material k

$M, M^{(1,2\alpha)} (\alpha = a, b, c)$ M-integral

$M_N^{(1,2\alpha)} (\alpha = a, b, c)$ average value of M-integral within element N

${}_kM_{st}^* \ (s, t = 1, 2$ elements in the asymptotic displacement and stress fields

${}_kM_{st} \ (s = 1, 2 \ \ t = 1, .., 4)$ elements in the asymptotic displacement and stress fields

$N_m(\xi, \eta, \zeta)$ shape functions of a twenty node, isoparametric element

${}_kN_{st}; \ {}_kN_{st}^*; \ {}_k\tilde{N}_{st} \ (s, t = 1, 2)$ elements in the asymptotic displacement and stress fields

P applied load

P_g weight of the lever and attached apparatus of the MMB specimen

P_i selected load along the linear fit to the linear portion of the load-displacement curve, corresponding to d_i

$P_{5\%/max}$ maximum value between $P_{5\%}$ and P_{max}

$P_{5\%}$ intersection between the original load-displacement curve obtained from the test and a 5% offset curve from the calculated compliance.

P_{cr} critical fracture load

P_{FE} load obtained from an FEA related to a specific displacement d

$P_{i0}, P_{j1} \ (i = 0, 1, .., 5; j = 0, 1, .., 4)$ fitting parameters used to describe the surfaces relating $K_m^{(f)}$ to the delamination length a and the location x_3 along the specimen width

P_{max} maximum load in the load-displacement curve obtained from the test for $d < d_{(5\%)}$

P_{NL} load measured at the point where non-linearity began in th load-displacement curve

P_{VIS} load measured visually at the point where delamination propagation is initiated

${}_kQ_s; \ {}_kQ_{s+2} \ (s = 1, 2)$ elements in the asymptotic displacement and stress fields

$\mathbf{Q}$ 3×3 matrix composed of components of the stiffness matrix

R radius of a BD specimen or of the cylindrical body used in the benchmark problems in Section 3.3

R_i $(i = R, L)$ R=right and L=left horizontal distance between the delamination tip and the BD diameter, shown in Fig. 4.8a

$R_{i(calc)}$ $(i = R, L)$ calculated (scaled) R=right and L=left horizontal distance between the delamination tip and the BD diameter, shown in Fig. 4.8a

$R_{i(m)}$ $(i = R, L)$ measured R=right and L=left horizontal distance between the delamination tip and the BD diameter, shown in Fig. 4.8a

$2R$ diameter of a BD specimen

$\mathbf{R}$ 3×3 matrix composed of components of the stiffness matrix

$\Re$ real part of a complex expression

$S'^{(k)}_{\alpha,\beta}(\alpha, \beta = 1, ..., 6; k = 1, 2)$ components of the reduced compliance matrix for material k

$S^{(k)}(k = 1, 2)$ compliance matrix for material k

$S^{(k)}_{\alpha,\beta}(\alpha, \beta = 1, ..., 6; k = 1, 2)$ components of the compliance matrix for material k

S_T perimeter of a body

$\boldsymbol{S}_k(k = 1, 2)$ one of the three real Barnett-Lothe tensors for material k

$\breve{S}$ 3×3 matrix related to $\boldsymbol{D}$ and $\boldsymbol{W}$

$\mathbf{T}$ 3×3 matrix composed of components of the stiffness matrix

$T_i(i = 1, 2)$ traction component in the i direction

${}_kU^{(m)}_\alpha(\theta)(k = 1, 2; \alpha = 1, 2; m = 1, 2)$ in-plane displacement functions for material k, related to mode m

${}_kU^{(m)}_{III}(\theta)(k = 1, 2; \alpha = 1, 2)$ out-of-plane displacement functions for material k, related to mode III

V_f volume fraction

$V_k(k = 1, 2)$ integration volume

$V_m(m = yarn, RUC)$ volume of the yarn or of the RUC

$V_{f(m)}(m = 41, UD_E, UD_C, W_E, W_C)$ volume fraction of 41 = plies 29 through 69 in th BD plate, UD_E=expanded unidirectional plies, UD_C=compressed unidirectional plies, W_E=expanded woven plies, W_C=compressed woven plies

$V_{f(m)}(m = e, g, e+g, T300)$ volume fraction of e = epoxy, g=glass fibers, $e+g$=epoxy and glass fibers, T300=carbon fibers

$V_{f(m)}(m = f/w, y/w, f/y)$ volume fraction of f/w=fibers in the weave, y/w= yarn in weave or RUC, f/y=fibers in yarn

W strain energy density

$W_{i,j}(i, j = 1, 2, 3)$ components of $\mathbf{W}$

${}_kW^{(1,2\alpha)}(\alpha = a, b, c; k = 1, 2)$ interaction or mutual strain energy density in material k

$\boldsymbol{W}$ 3×3 matrix related to $\boldsymbol{L}_k$ and $\boldsymbol{S}_k$

${}_kW_F^{(1,2\alpha)}(\alpha = a, b, c; k = 1, 2)$ interaction or mutual strain energy density in material k resulting from mechanical loads

Latin letters - lower case

a crack or delamination length measured from the load line for beam type specimens or crack or delamination length of the FEM used for the benchmark problems in Section 3.3

a delamination length measured visually from images captured during the test, as the delamination extends

a yarn width in a woven ply used to determine material properties

a_0 artificial insert length, measured from the load-line in beam type specimens, equal to the average of a_{0f} and a_{0b}

$a_\alpha(\alpha = 1, ..., 6)$ eigenvectors of Stroh formalism

a_f final delamination length at the end of a beam type specimen test

$a_i(i = 1, 2, 3)$ arbitrary complex constants used with the Stroh formalism

a_i total artificial insert length for beam type specimens

a_p natural precrack delamination length for beam type specimens

a_{0AC} average artificial delamination length from the load-line calculated as the average of a_{0f} and a_{0b} measured from the front and back sides of a beam type specimen, respectively

a_{0b} artificial insert length, measured from the front side of the beam type specimens, from the load-line

a_{0f} artificial insert length, measured from the front side of the beam type specimens, from the load-line

$a_{0PC-VIS}$ average precrack length, measured from front and back using Imagej software from the load-line

a_{0PC} average precrack length, measured from front and back using the Confocal microscope from the load-line

a_{bPC} precrack length, measured from the back side of the beam type specimens, from the load-line

a_{fPC} precrack length, measured from the front side of the beam type specimens, from the load-line

a_{ib} total artificial insert length, measured from the back side of the beam type specimens

a_{if} total artificial insert length, measured from the front side of the beam type specimens

a_{cr} half BD delamination length at fracture

$\boldsymbol{a}$ eigenvector of Stroh formalism

Δa virtual delamination extension shown in Fig. 3.1

Δa_0 the difference between a_{0f} and a_{0b}

Δa_{iss} initial Δa value related to the steady state energy release rate $\mathcal{G}_{iss}$

$\tilde{a}$ corrected delamination length

$\boldsymbol{b}$ eigenvector of Stroh formalism related to $\boldsymbol{a}$

$\overline{b}$ average of all width measurements b of each beam type specimen

$2a$ BD specimen initial central artificial delamination length

$2a_c$ BD specimen critical central delamination length before failure

b width of beam type specimen

b_{cal} width of specimen used for compliance calibration for the MMB test

$b_i (i = 0, 1, .., 14)$ fitting parameters used to describe the curves relating $K_m^{(r)}$ to the location x_3 along the specimen width

$b_i (i = 1, 2, 3)$ arbitrary complex constants related to a_i

c lever length of the MMB test apparatus

c_g lever length to the center of gravity

d actuator displacement

d_2, d_3 unknown constant within d_m, related to the oscillatory part and the regular square-root singularity part of the solution, respectively

d_h, d_v horizontal and vertical diameters of the arrest hole in the BD specimen, shown in Fig. 4.5b

d_i $(i = 1, 2)$ selected displacement along the linear fit to the linear portion of the load-displacement curve, corresponding to P_i

$\boldsymbol{d}$ arbitrary complex vector

$\boldsymbol{d}, \overline{\boldsymbol{d}}, \boldsymbol{d}_m (m = 1, 2)$ arbitrary vectors corresponding to stress singularity δ_m, related to oscillatory part of the solution

$\boldsymbol{d}^*, \boldsymbol{d}_3$ arbitrary vector corresponding to stress singularity δ_3, related to regular square-root singularity part of solution

$f^{(k)}(z_\alpha^{(k)})(\alpha = 1, 2, 3; k = 1, 2)$ arbitrary functions in the Stroh formalism for material k

$f_\alpha(z_\alpha)(\alpha = 1..., 6)$ arbitrary functions in the Stroh formalism

g distance between yarns in a woven ply used to determine material properties

$\boldsymbol{g}_k (k = 1, 2)$ arbitrary complex vector of material k

$2h$ thickness of beam-type specimen

h woven ply thickness or height, used to determine material properties, also this parameter is the thickness or height of each ply in the BD specimen

$h_0^{(1)}$ height of the UD ply, above the delamination, in the BD specimen, shown in Fig. 4.18

$h_{45}^{(1)}$ height of the woven ply, below the delamination, in the BD specimen, shown in Fig. 4.18

$\overline{2h}$ average of all thickness measurements $2h$ of each beam type specimen

$k = 1, 2$ upper (1) or lower (2) plies along an interface

$k_i^{(k)} (i = 1, 2, 3 \;\; k = 1, 2$ normalization factors in Stroh formalism for material k

l total length of beam type specimens

$l_1^{(N)}(x3)$ parabolic normalized virtual crack extension along the crack front within element N in the x_1-direction

l_1 distance from the center of the load block to the mid-plane of the specimen

$l_j(p)(j = 2, 3, 4)$ polynomials in p of degree j

m slope of the load-displacement curve of a tested MMB specimen or the slope from the plot of the compliance C versus the cubed delamination length a^3 measured from the MMELS test

m, n fitting parameters in the criterion in eq. (1.105)

m_{cal} slope of the load-displacement curve related to the compliance calibration of the MMB system

n number of experimental data points used to determine the average value to be reduced with the statistical analysis

n slope of a plot of the cube-root of the compliance versus free length L_f

${}_k m_s$ $(s = 1, 2)$ elements in the asymptotic displacement and stress fields

$n_j(j = 1, 2)$ unit normal vector in the j direction to the perimeter of the body

p complex constant

$p_\alpha^{(k)}(\alpha = 1, 2, 3; k = 1, 2)$ eigenvalues obtained by Lekhnitskii and Stroh formalisms for material k

$p_\alpha(\alpha = 1, 2, 3)$ eigenvalues obtained by Lekhnitskii and Stroh formalisms

${}_k n_{st}$, ${}_k n^*_{st}$ $(s = 1, 2, 3;\ \ t = 1, 2)$ elements in the asymptotic displacement and stress fields

q_{1m} components of a vector which determines the virtual displacement at the element nodal points

q_1 normalized virtual crack extension function

$\boldsymbol{q}_\alpha, \tilde{\boldsymbol{q}}_\alpha$ arbitrary 3×1 constant vector for material k

r distance from crack or delamination front; radius in a polar coordinate system

s standard deviation

t thickness of BD specimen

$\Delta \boldsymbol{u}_{os}$ oscillatory singularity crack face displacement jump vector

$\Delta \boldsymbol{u}_s$ regular square-root singularity crack face displacement jump vector

Δu_i displacement "jump" of the crack faces in the i-direction

$\mathbf{u}$ vector form of the displacement field

$u^{(k)}(k=1,2)$ displacement vector for material k

$u_3^{(k)}$ out-of-plane displacement component for material k

$u_\alpha^{(k)}(k=1,2)$ in-plane displacement component for material k

$u_i(i=1,2,3)$ displacement components in the i direction

$u_\alpha(\alpha=1,2)$ displacement component in the α direction

$\boldsymbol{u}_s^{(k)}(k=1,2)$ regular square-root singular part of $u^{(k)}$

$\boldsymbol{u}_{os}^{(k)}(k=1,2)$ oscillatory singular part of $u^{(k)}$

$u_i^{(1)}(i=1,2,3)$ components of displacement field of the problem sought for a homogeneous material

$u_i^{(2\alpha)}(i=1,2,3;\alpha=a,b,c)$ components of displacement field of the auxiliary solution for a homogeneous material

$u_i^{(k)}(i=1,2,3\ :k=1,2)$ displacement components in the i direction for material k

${}_k u_i^{(1)}(i=1,2,3;k=1,2)$ components of displacement field of the problem sought for material k

${}_k u_i^{(2\alpha)}(i=1,2,3;\alpha=a,b,c;k=1,2)$ components of displacement field of the auxiliary solution for material k

$x_i(i=1,2,3)$ x,y,z axes in cartesian coordinate system

z complex variable

$z_i\ (i=P,\gamma)$ z-variate model P=probability and γ=confidence level

$z_*^{(k)}(\alpha=1,..,6;k=1,2)$ complex variable related to p_α of material k

$z_\alpha^{(k)}(\alpha=1,..,6;k=1,2)$ complex variable related to p_α of material k

Greek letters - upper case

$\Delta\vartheta_i$ temperature change related to specimen i

Δ_I delamination length corrections for the mode I using CBT

Δ_{II} delamination length corrections for the mode II using CBT

${}_k\Delta\vartheta (k = 1, 2)$ total temperature change in material k

${}_k\Delta\vartheta^{(1)} (k = 1, 2)$ total temperature change for material k of the problem sought

${}_k\Delta\vartheta^{(2\alpha)} (\alpha = a, b, c; k = 1, 2)$ total temperature change of the auxiliary solution for material k, taken to be zero

$\mathbf{\Phi}$ stress function vector related to the Stroh formalism

Γ transverse modulus correction parameter

$\Phi_i (i = 1, 2, 3)$ components of the stress function related to the Stroh formalism

Π potential energy

${}_k\Sigma_{3,\beta}^{(III)}(\theta) (k = 1, 2; \beta = 1, 2, 3)$ out-of-plane stress functions for material k, related to mode III

${}_k\Sigma_{\alpha,\beta}^{(m)}(\theta) (k = 1, 2; \alpha = 1, 2; \beta = 1, 2; m = 1, 2)$ in-plane stress functions for material k, related to mode m

Greek letters - lower case

α loading angle for the Arcan specimen

α_A coefficients of thermal expansion (CTEs) in the axial direction in a transversly isotropic material

$\alpha_k (k = 1, 2)$ coefficients of thermal expansion (CTEs) of material k

α_T coefficients of thermal expansion (CTEs) in the transverse direction in a transversly isotropic material

β angle of the yarn in the RUC shown in Fig. 4.7

β defined in eq. (2.70) and related to the oscillatory parameter ε

$\beta^{(i)}$ $(i = N, P)$ slope of the oblique line obtained for negative $(i = N)$/positive $(i = P)$ loading angles

$\beta^{(S)}$ slope of branch 2 or branch 3 in the '3 branch' or '5 branch' criteria' respectively, in the $(\hat{K}_1 - \hat{K}_2)$-plane

$\beta_\alpha (\alpha = 1, 2, 3)$ real constants related to imaginary part of p_α

$\beta_\alpha^{(k)} (\alpha = 1, 2, 3; k = 1, 2)$ real constants related to imaginary part of $p_\alpha^{(k)}$ for material k

δ order of stress singularity

δ_m stress singularity components

δ_{ij} Kronecker delta

γ parameter used to define K_m^* in eq. (3.10)

${}_k\alpha_{rs}(r,s=1,2,3\,;k=1,2)$ components of the coefficients of thermal expansion (CTE) for material$k$

${}_k\beta_s^*\ (s=1,2)$ elements in the asymptotic displacement and stress fields

${}_k\beta_{ij}$ componebnts of the tensor given in eq. (3.25) for an unisotropic material

ε oscillatory parameter (positive)

$\varepsilon_\alpha(\alpha=1,...,6)$ contracted strain components

ε_{ij} components of the strain tensor

${}_k\varepsilon_{rs}$ total strain components of the strain tensor related to material k

$\varepsilon_{ij}^{(1)}(i,j=1,2,3)$ strain components of the problem sought for a homogeneous material

$\varepsilon_{ij}^{(2\alpha)}(i,j=1,2,3;\alpha=a,b,c)$ strain components of the auxiliary solution for a homogeneous material

${}_k\varepsilon_{ij}^{(1)}(i,j=1,2,3;k=1,2)$ strain components of the problem sought for material k

${}_k\varepsilon_{ij}^{(2\alpha)}(i,j=1,2,3;\alpha=a,b,c;k=1,2)$ strain components of the auxiliary solution for material k

${}_k\varepsilon_{ij}^{m(2\alpha)}(i,j=1,2,3;\alpha=a,b,c;k=1,2)$ mechanical strain components of the auxiliary solution for material k

${}_k\varepsilon_{ij}^{T(2\alpha)}(i,j=1,2,3;\alpha=a,b,c;k=1,2)$ total strain components of the auxiliary solution for material k

θ angle in a polar coordinate system

$\theta^{(N)}$ rotation angle for branch 1 in the 3 branch or 5 branch criterion

$\theta^{(P)}$ rotation angle for branch 2 and 3 in the 3 branch criterion or branches 3 and 5 in the 5 branch criterion

θ_1 first correction factor used to calculate correction for large diplacements F used with CBT

θ_2 second correction factor used to calculate correction for large diplacements F used with CBT

ϑ_i temprature measured at the begining of each BD test.

κ Kosolov parameter in a homogeneous, linear elastic, isotropic material

κ_k Kosolov parameter of the upper ($k = 1$) or lower ($k = 2$) plies in the interface

$\lambda_k (k = 1, 2)$ Lam*é* constant

μ shear modulus in a homogeneous, linear elastic, isotropic material

μ_k shear moduli of the upper ($k = 1$) or lower ($k = 2$) plies in the interface

$\overline{\mu}$ average shear modulus for an interface

ν Poisson's ratio in a homogeneous, linear elastic, isotropic material

ν_A Poisson's ratio in the axial direction in a transversly isotropic material

ν_k Poisson's ratio of the upper ($k = 1$)nor lower ($k = 2$) plies in the interface

ν_T Poisson's ratio in the transverse direction in a transversly isotropic material

$\nu_{ij} (i, j = 1, 2, 3)$ Poisson's ratio

$\boldsymbol{\sigma}$ vector form of the stress field

σ normal stress

$\sigma_{\alpha\beta} (\alpha, \beta = 1, 2, 3)$ components of the stress tensor in polar or cartesian coordinates

$\sigma_{ij} (i, j = 1, 2, 3)$ components of the stress tensor in polar coordinates

$\sigma_\beta (\beta = 1, ..., 6)$ contracted stress components

$\sigma_{ij}^{(1)} (i, j = 1, 2, 3)$ stress components of the problem sought for a homogeneous material

$\sigma_{ij}^{(2\alpha)} (i, j = 1, 2, 3; \alpha = a, b, c)$ stress components of the auxiliary solution for a homogeneous material

${}_k\sigma_{ij}^{(1)} (i, j = 1, 2, 3; k = 1, 2)$ stress components of the problem sought for material k

${}_k\sigma_{ij}^{(2\alpha)} (i, j = 1, 2, 3; \alpha = a, b, c; k = 1, 2)$ stress components of the auxiliary solution for material k

τ_i in-plane shear

τ_o out-of-plane shear

${}_k\varphi_s$ $(s = 1, 2, 3)$ elements in the asymptotic displacement and stress fields

$\boldsymbol{\phi}^{(k)} (k = 1, 2)$ stress function vector of material k

$\boldsymbol{\phi}_{os}^{(k)} (k = 1, 2)$ oscillatory singular part of $\boldsymbol{\phi}^{(k)}$

$\boldsymbol{\phi}_s^{(k)} (k = 1, 2)$ regular square-root singular part of $\boldsymbol{\phi}^{(k)}$

χ delamination length correction parameter or one of the two Airy potential functions

ϕ out-of-plane to in-plane phase angle

ψ one of the two Airy potential functions

$\hat{\psi}$ in-plane phase angle

$\hat{\psi}^{(i)}$ $(i = N, P)$ value of the in-plane phase angle $\hat{\psi}$ at the intersection of two adjacent branches for negative $(i = N)$/positive $(i = P)$ loading angles

$\hat{\psi}^{(i)*}$ $(i = N, P)$ reduced value of $\hat{\psi}^{(i)}$ obtained after a statistical analysis was performed

ω BD specimen loading angle or arbitrary constant associated with torsion about the x_3-axis

$\zeta (k = 1, 2)$ a parameter which depends on the eigenvalues of material k and the polar angle θ

Abbreviations

J J-integral results for the energy release rate obtained from Abaqus (2017)

4ENF four-point bending, end notch flexure

AC artificial crack

ADCB asymmetric double cantilever beam

ASTM American Society for Testing and Materials

B-K Benzeggagh and Kenane (1996)

BC boundary condition

BD Brazilian disk

C-ELS calibrated end loaded split

CAL calibration procedure

CBT corrected beam theory

CBTE corrected beam theory using using the effective crack length

CFRP carbon fiber reinforced polymer

CLS crack lap shear

CT computed tomography

CV coefficient of variation

DCB double cantilever beam

DE displacement extrapolation

DIC digital image correlation

ECM experimental compliance method

ELS end loaded split

ENF end notch flexure

EPH hardener Epikure

EPR Epikote resin

ESIS European Structural Integrity Society

FE finite element

FEA finite element analysis

FEM finite element model

FRMM fixed ratio mixed mode

GFRP glass fiber reinforced polymer

GUI geometrical user interface

HFGMC High Fidelity Generalized Method of Cells

ISO International Organization for Standardization

LRD largest relative difference

MCC modified compliance calibration

MD multidirectional

MMB mixed mode bending

MMELS mixed mode end loaded split

MMF mixed mode flexure

NDT non-destructive testing

NL non-linear

PC precrack

PMMA polymethyl methacrylate

PTFE polytetrafluoroethylene

PTU programable timing unit

RD relative difference

RH relative humidity

RMSE round mean square error

RUC repetitive unit cell

SBT simple beam theory

SD standard deviation

SE standard error

SEM scanning electron microscopy

SLB single leg bending

SLFPB single leg four point bend

UD unidirectional

VAMAS Versailles Project on Advanced Materials and Standards

VIS visual

List of Figures

List of Tables

Chapter 1

Introduction

Throughout history, structural cracks have caused many catastrophical failures in aircraft, space shuttles, ships, trains, etc. Some well known examples of such failures are the de Havilland D.H.106 Comet, the Columbia space shuttle, the Liberty ships, the Versailles train and more. Each of these disasters concluded with deaths and injuries of many people. Investigation of each of these disasters showed that the cause was high stresses resulting from loads lower than the loads the structure was designed to sustain. The high stresses generally occurred at stress raisers in the structure leading to cracks and eventual failure. Understanding crack formation may prevent many catastrophic failures in the future.

Fracture mechanics enables the definition of conditions under which a crack may propagate; this may be helpful in preventing failure. The first milestone in investigating cracks was achieved by Griffith (1920, 1924), who determined the maximum stress applied before a crack propagates. His investigation was based on energy concepts, deriving an energy based criterion for failure. It was not until World War II that fracture mechanics became of significant interest and received renewed attention. The main reason for this was the massive production of Liberty ships which suffered from hull and deck cracks. Nearly 1,500 instances of significant brittle fractures were found in the ships. About 1,200 ships suffered from cracks during the war (about 30% of all Liberty-class ships), and 3 were lost when the ship suddenly split in two. Investigation of cracks began by Irwin (1948) and his group at the U.S Naval Research Laboratory (NRL) with research regarding the kinetic energy of a crack and its propagation rate. Irwin had much influence on the progress of fracture mechanics as a new science and a powerful engineering tool used today for numerous problems in determining material failure (Yarema, 1996).

This thesis deals with a delamination in a composite laminate. Composite materials are materials composed of two or more materials whose properties are different from those of the original properties of each individual constituent. Since composites have properties which may be tailored to a specific application, use of composite materials has grown in recent times. The properties of a fiber reinforced composite are strongly influenced by fiber orientation and fiber volume fraction (Mallick, 2007). Different properties such as

flexibility, stiffness, strength, weight, fatigue life, thermal insulation and thermal conductivity, may be determined based on specified needs (Jones, 1998). As a result of their high stiffness and low weight (Taylor, 2008), carbon fiber reinforced polymers (CFRP) are widely used in many fields, especially in the aircraft industry. For this reason, these composites may be helpful in improving performance and lowering operational costs of aircraft.

A laminate composite material is formed from plies which are thin layers with a fiber orientation required to produce the desired properties (Jones, 1998). The plies are stacked to a determined thickness; the sequence of plies influences the thermal and mechanical properties of the composite. Interlaminar stresses in conjunction with the low through thickness strength caused by the fibers lying in the laminate plane without providing reinforcement through the composite thickness, may result in delamination (Wisnom, 2012). Impact, material and structural discontinuities, as well as in-service loads may cause the appearance of delaminations at different locations. Continued loading may lead to structural failure.

This study focuses on a delamination between two carbon fiber reinforced polymer (CFRP) composite plies, where each ply has a different fiber orientation and different properties. Emphasis will be placed on determining the critical interface initiation and resistance energy release rate properties of the specific composite, consisting of a specific layup. In this chapter, basic concepts in fracture mechanics, as well as methods for investigating a delamination within a laminate will be presented. In Section 1.1, the behavior of a crack in an isotropic body and along the interface between two isotropic materials will be presented. Methods which allow calculation of the stress intensity factors are described in Section 1.2. These methods include displacement extrapolation (DE) and two conservative integrals: the J-integral and the M-integral, for thermal and mechanical loading. A review of fracture toughness testing methods will be presented in Section 1.3. First, a discussion of the different composite types, unidirectional (UD), multi-directional (MD) and woven fabric composites, will be made. Then different fracture toughness testing methods for modes I and II will be explained. Finally, different mixed mode test methods and specimens used for UD, MD and woven composites will be presented including the mixed mode bending (MMB) specimen, the mixed mode end loaded split (MMELS) specimen, the Arcan specimen and the Brazilian disk (BD) specimen. Research objectives are discussed in Section 1.4.

1.1 Introduction to fracture mechanics

The term fracture mechanics refers to a specialized field of solid mechanics where quantitative geometrical and mechanical relations are found to describe causes for structural failure in a body with an assumed crack. Consider a semi-infinite crack within a linear

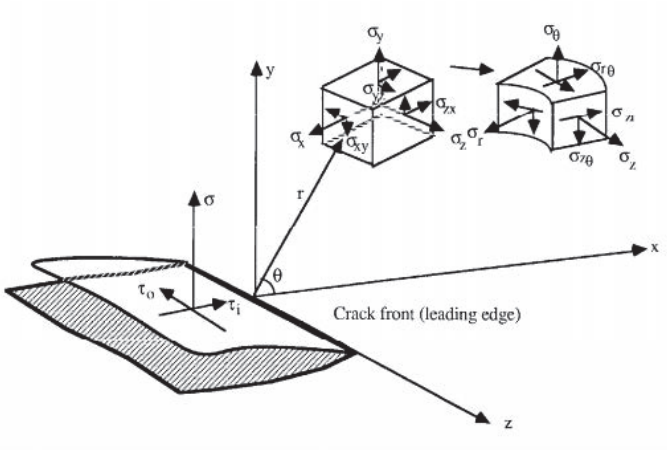

Figure 1.1: Stress state in Cartesian and polar coordinate systems at the crack tip. (Whittaker et al. 1996).

elastic, homogenous, isotropic infinite body. The body may be subjected to any combination of three basic stresses: normal stress σ, in-plane shear stress τ_i and out-of-plane shear stress τ_o, as illustrated in Fig 1.1. These stresses result in three basic deformation configurations known in the literature as mode I, mode II and mode III, as illustrated in Fig 1.2. Mode I is a normal-opening mode, mode II is the in-plane sliding mode and mode III is the out-of-plane tearing mode. Mixed mode deformation is a combination of any of the three modes.

The pioneer of fracture studies was A.A. Griffith (1893 –1963); his energy balance approach was the basis for the stress intensity factor approach presented by Irwin (1957, 1958) and widely used today. The stress intensity factor K, is a calculated parameter, related to geometry and applied force of a particular problem. This parameter characterizes the stress and displacement field in the neighborhood of a crack tip. For each deformation mode described in Fig 1.2, a corresponding stress intensity factor (K_I, K_{II}, K_{III}) exists.

The stress field near the crack tip may be described by means of an asymptotic solution

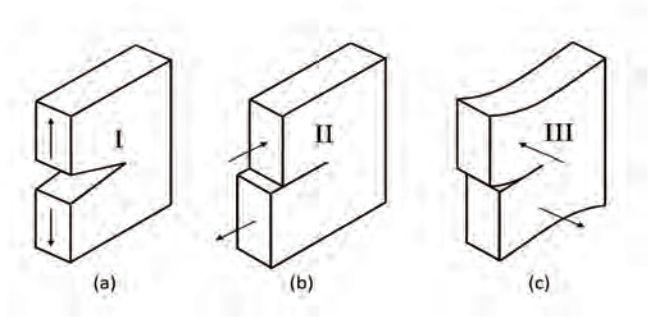

Figure 1.2: Deformation modes: (a) mode I, (b) mode II, (c) mode III.

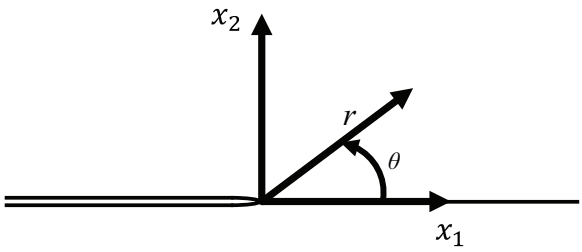

Figure 1.3: Crack tip coordinates

as was determined by Williams (1957) and Irwin (1957, 1958), namely

$$\sigma_{ij} = \sum_{m=I}^{III} \frac{K_m}{\sqrt{2\pi r}} f_{ij}^{(m)}(\theta) + O(r^0) \,, \tag{1.1}$$

where $m = I, II, III$ is the deformation mode, r and θ are the polar coordinates at the crack tip, as illustrated in Fig 1.3, and $f_{ij}^{(m)}(\theta)$ are known functions for each mode. The indices i and j correspond to each stress component in the stress tensor, represented in an orthogonal coordinate system (polar or Cartesian). The stress intensity factor for each mode, K_m, uniquely governs the intensity of the stresses in the neighborhood of a crack tip. It may be noted from eq. (1.1) that a square-root singularity appears in the first term of the asymptotic stress solution near the crack tip. In other words, the stresses vary as $\sigma_{ij} \simeq r^{-\frac{1}{2}}$ in the vicinity of the crack tip; as r goes to zero, the stresses go to infinity. This is not physically realizable since no material can bear infinite stresses. For a metal, for example, near the tip of the crack, the effective stress exceeds the yield strength σ_Y, so that a plastic zone results. In this small region, bounded by the radius r_p, the asymptotic solution is not valid since it was developed based on linear elastic fracture mechanics (LEFM). In order to justify the asymptotic solution in the elastic region, the plastic region must be sufficiently small, much smaller than the crack length and other body dimensions. The higher order terms of the asymptotic solution are negligible in comparison to the first term of the solution in the vicinity of the crack tip. These are necessary to describe the deformation and stresses far away from the crack tip. As r increases, the first term goes to zero.

Explicit expressions for the stresses in the neighborhood of a crack tip in a homogeneous, isotropic material subjected to deformation modes I, II and III are given by

$$\left\{ \begin{array}{c} \sigma_{11} \\ \sigma_{12} \\ \sigma_{22} \end{array} \right\} = \frac{K_I}{\sqrt{2\pi r}} \cos\frac{\theta}{2} \left\{ \begin{array}{c} 1 - \sin\frac{\theta}{2}\sin\frac{3\theta}{2} \\ \sin\frac{\theta}{2}\cos\frac{3\theta}{2} \\ 1 + \sin\frac{\theta}{2}\sin\frac{3\theta}{2} \end{array} \right\} \,, \tag{1.2}$$

$$\left\{ \begin{array}{c} \sigma_{11} \\ \sigma_{12} \\ \sigma_{22} \end{array} \right\} = \frac{K_{II}}{\sqrt{2\pi r}} \left\{ \begin{array}{c} -\sin\frac{\theta}{2}\left(2+\cos\frac{\theta}{2}\cos\frac{3\theta}{2}\right) \\ \cos\frac{\theta}{2}\left(1-\sin\frac{\theta}{2}\sin\frac{3\theta}{2}\right) \\ \sin\frac{\theta}{2}\cos\frac{\theta}{2}\cos\frac{3\theta}{2} \end{array} \right\} , \tag{1.3}$$

$$\left\{ \begin{array}{c} \sigma_{13} \\ \\ \sigma_{23} \end{array} \right\} = \frac{K_{III}}{\sqrt{2\pi r}} \left\{ \begin{array}{c} -\sin\frac{\theta}{2} \\ \\ \cos\frac{\theta}{2} \end{array} \right\} . \tag{1.4}$$

The corresponding displacement field is

$$\left\{ \begin{array}{c} u_1 \\ u_2 \end{array} \right\} = \frac{K_I}{2\mu}\sqrt{\frac{r}{2\pi}} \left\{ \begin{array}{c} \cos\frac{\theta}{2}\left(\kappa-1+2\sin^2\frac{\theta}{2}\right) \\ \sin\frac{\theta}{2}\left(\kappa+1-2\cos^2\frac{\theta}{2}\right) \end{array} \right\} , \tag{1.5}$$

$$\left\{ \begin{array}{c} u_1 \\ u_2 \end{array} \right\} = \frac{K_{II}}{2\mu}\sqrt{\frac{r}{2\pi}} \left\{ \begin{array}{c} \sin\frac{\theta}{2}\left(\kappa+1+2\cos^2\frac{\theta}{2}\right) \\ -\cos\frac{\theta}{2}\left(\kappa-1-2\sin^2\frac{\theta}{2}\right) \end{array} \right\} , \tag{1.6}$$

$$u_3 = 2\frac{K_{III}}{\mu}\sqrt{\frac{r}{2\pi}}\sin\frac{\theta}{2} , \tag{1.7}$$

where σ_{ij} $(i,j=1,2,3)$ are stresses in the i direction applied on a surface defined with a normal in the j-direction and u_i $(i=1,2,3)$ are the displacements in the x_1, x_2 and x_3-directions, presented in Fig. 1.3. In eqs. (1.5) to (1.7), μ is the shear modulus and κ is determined by

$$\kappa = \begin{cases} 3-4\nu , & \text{plane strain} \\ \dfrac{3-\nu}{1+\nu} , & \text{generalized plane stress} \end{cases} \tag{1.8}$$

where ν is Poisson's ratio.

The stress intensity factors describe the magnitude of the stresses near the crack tip based on the geometry and loading conditions. When a single mode is applied, crack propagation may occur once the corresponding stress intensity factor reaches a critical value. For example, if mode I is applied, the crack will propagate once $K_I = K_{Ic}$. This critical value is the fracture toughness, a material property introduced in a special report (ASTM Committee, 1960). This material property, K_{mc}, $(m = I, II, III)$, allows prediction of catastrophic crack propagation for a particular mode. In the case of mixed modes, different fracture criteria exist.

Another important parameter related to the stress intensity factors (Irwin, 1957, 1958) is the energy release rate or Griffith's energy, denoted by $\mathcal{G}$. This parameter represents

the energy release rate or decrease of potential energy per unit crack advance per unit thickness. It is given by

$$\mathcal{G} = -\frac{d\pi}{da} \tag{1.9}$$

where a is the crack length and π is the potential energy given in two dimensions as

$$\pi = \int_A W dA - \int_{S_T} T_i u_i dS \ . \tag{1.10}$$

In eq. (1.10), A is the area of the body, S_T is the perimeter of the body on which tractions are applied, and

$$W = \frac{1}{2}\,\sigma_{ij}\varepsilon_{ij} \tag{1.11}$$

is the strain energy density for a linear elastic material where σ_{ij} and ε_{ij} are the stress and strain components in the direction denoted by $i, j = 1, 2$, respectively. In eq. (1.10), the traction components are given as

$$T_i = \sigma_{ij} n_j \tag{1.12}$$

where n_j are the components of the unit normal vector to S_T. In eq. (1.10), u_i are the displacement components in the corresponding direction. The overall energy release rate, $\mathcal{G}_T$, is the sum of energy release rates for each mode, namely,

$$\mathcal{G}_T = \mathcal{G}_I + \mathcal{G}_{II} + \mathcal{G}_{III} \ . \tag{1.13}$$

In many cases, the out-of-plane energy release rate component may be neglected from eq. (1.13) and the in-plane energy release rate becomes

$$\mathcal{G}_T = \mathcal{G}_I + \mathcal{G}_{II} \ . \tag{1.14}$$

Using the asymptotic stress expansion and the crack closure integral, it is possible to obtain a relation between the energy release rate and the stress intensity factors as (Irwin, 1958)

$$\mathcal{G} = \begin{cases} \dfrac{1}{\overline{\overline{E}}}\left(K_I^2 + K_{II}^2\right) + \dfrac{K_{III}^2}{2\mu} \ , & \text{plane strain} \\ \dfrac{1}{\overline{\overline{E}}}\left(K_I^2 + K_{II}^2\right) \ , & \text{generalized plane stress} \end{cases} \tag{1.15}$$

where K_I, K_{II}, and K_{III} are the stress intensity factors in modes I, II, and III, respectively, and $\overline{E}$ is given by

$$\frac{1}{\overline{\overline{E}}} = \begin{cases} \dfrac{1-\nu^2}{E} \ , & \text{plane strain} \\ \dfrac{1}{E} \ , & \text{generalized plane stress} \end{cases} \tag{1.16}$$

where E is Young's modulus. The relations, described in eq. (1.15), between $\mathcal{G}$ and K_m are correct only in the case of self-similar crack extension meaning a crack propagating in its own plane.

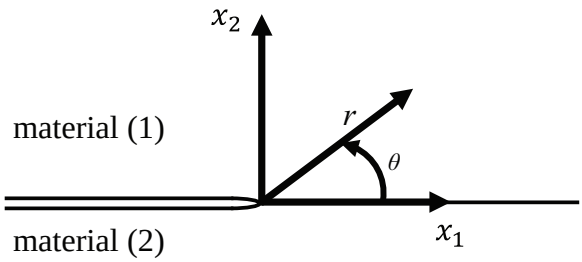

Figure 1.4: An interface crack between two dissimilar materials.

In Fig. 1.4, a crack along the interface between two materials is presented. Each material is denoted by k $(k = 1, 2)$, where $k = 1$ represents the upper material and $k = 2$ represents the lower material. For the case of two linear, elastic, homogenous and isotropic materials, the stress and displacement fields were derived by Williams (1959) and showed strong oscillations near the crack tip. Their behavior was first obtained as

$$\sigma \sim r^{-\frac{1}{2}} \left\{ \begin{array}{c} \sin\left(\varepsilon \ln r\right) \\ \cos\left(\varepsilon \ln r\right) \end{array} \right\} , \tag{1.17}$$

$$u \sim r^{\frac{1}{2}} \left\{ \begin{array}{c} \sin\left(\varepsilon \ln r\right) \\ \cos\left(\varepsilon \ln r\right) \end{array} \right\} , \tag{1.18}$$

where, σ and u are the stresses and displacements, respectively, r is the distance from the crack tip, shown in Fig. 1.4 and ε is the oscillatory parameter. This parameter is related to the mechanical properties of both materials and given by

$$\varepsilon = \frac{1}{2\pi} \ln\left(\frac{\kappa_1 \mu_2 + \mu_1}{\kappa_2 \mu_1 + \mu_2}\right) , \tag{1.19}$$

where μ_k $(k = 1, 2)$ are the shear moduli of the upper and lower materials, respectively. The Kosolov parameter, κ_k, is given by

$$\kappa_k = \left\{ \begin{array}{ll} 3 - 4\nu_k \ , & \text{plane strain} \\ \dfrac{3 - \nu_k}{1 + \nu_k} \ , & \text{generalized plane stress} \end{array} \right. \tag{1.20}$$

where ν_k $(k = 1, 2)$ are the Poisson's ratios of each material. The singular oscillations found in the displacement field show interpenetration of the crack faces which is physically unrealistic.

To employ the asymptotic oscillatory solution, the interpenetration zone is required to be sufficiently small compared to the crack length and other specimen dimensions (Rice, 1988). The first term of the asymptotic solution for the in-plane stresses of an interface crack are given by

$$\sigma_{\alpha\beta}^{(k)} = \frac{1}{\sqrt{2\pi r}} \left[\Re\left(K r^{i\varepsilon}\right) \, {}_k\Sigma_{\alpha\beta}^{(1)}(\theta, \varepsilon) + \Im\left(K r^{i\varepsilon}\right) \, {}_k\Sigma_{\alpha\beta}^{(2)}(\theta, \varepsilon) \right] . \tag{1.21}$$

The subscripts $\alpha, \beta = 1, 2$ denote the stress components in either polar or Cartesian coordinates. The subscript $k = 1, 2$ denotes the upper and lower materials respectively, and r and θ are the crack tip polar coordinates shown in Fig. 1.4. The symbols $\Re$ and $\Im$ denote the real and imaginary parts of the quantity in parentheses. The known functions of θ, ${}_k\Sigma^{(1)}_{\alpha\beta}$, ${}_k\Sigma^{(2)}_{\alpha\beta}$, in eq. (1.21), correspond to modes 1 and 2, respectively, they may be found in Rice et al. (1990) and Deng (1993) for polar and Cartesian coordinate systems, respectively. The complex stress intensity factor, K, is defined as

$$K = K_1 + iK_2 \ , \tag{1.22}$$

where $i = \sqrt{-1}$, K_1 and K_2 are the real stress intensity factors for modes 1 and 2, respectively. Unlike the case of a homogeneous material where K_I and K_{II} are the stress intensity factors associated with tension and in-plane shear deformations, respectively, it may be shown that for an interface crack in a tensile field, both K_1 and K_2 exist and do not relate to one specific deformation mode. These modes are coupled.

The out-of-plane stress components are given by

$$\sigma^{(k)}_{\alpha 3} = \frac{K_{III}}{\sqrt{2\pi r}} \, {}_k\Sigma^{(III)}_{\alpha 3}(\theta) \tag{1.23}$$

where K_{III} is the mode III stress intensity factor and the function ${}_k\Sigma^{(III)}_{\alpha 3}(\theta)$ may be found in Deng (1993). The out-of-plane mode is decoupled from the two in-plane modes which are inherently coupled.

The in-plane displacement components are also coupled and given by

$$u^{(k)}_{\alpha} = \sqrt{\frac{1}{2\pi r}} \left[\Re \left(K r^{i\varepsilon} \right) \, {}_kU^{(1)}_{\alpha}(\theta) + \Im \left(K r^{i\varepsilon} \right) \, {}_kU^{(2)}_{\alpha}(\theta) \right] \ , \tag{1.24}$$

where $\alpha = 1, 2$ and the expressions ${}_kU^{(1)}_{\alpha}(\theta)$ and ${}_kU^{(2)}_{\alpha}(\theta)$ may be found in Deng (1993). The out-of plane displacement component is decoupled and may be written as

$$u^{(k)}_{3} = \sqrt{\frac{r}{2\pi}} K_{III} \, {}_kU^{(III)}_{3}(\theta) \ , \tag{1.25}$$

where ${}_kU^{(III)}_{\alpha}(\theta)$ is also found in Deng (1993).

The stress intensity factor K has unconventional units. It may be normalized as

$$\hat{K} = K \hat{L}^{i\varepsilon} \ , \tag{1.26}$$

where $\hat{K}$ is the normalized stress intensity factor and $\hat{L}$ is an arbitrary length. A phase angle may be defined as

$$\hat{\psi} = \arctan \left\{ \frac{\Im(K \hat{L}^{i\varepsilon})}{\Re(K \hat{L}^{i\varepsilon})} \right\} = \arctan \left\{ \frac{\sigma_{12}}{\sigma_{22}} \right\} \Bigg|_{\theta=0, r=\hat{L}} \ . \tag{1.27}$$

The phase angle $\hat{\psi}$ represents the in-plane mode mixity; it may also be expressed as the ratio of the in-plane shear stress to the tensile stress along the interface ($\theta = 0$) at a distance $r = \hat{L}$ from the crack tip. A second phase angle may also be defined as

$$\phi = \arctan\left\{\sqrt{\frac{H}{2\overline{\mu}}}\frac{K_{III}}{\sqrt{K_1^2+K_2^2}}\right\} = \arctan\left(\sqrt{\frac{H}{2\overline{\mu}}}\frac{\sigma_{32}}{\sqrt{\sigma_{22}^2+\sigma_{12}^2}}\right)\Bigg|_{\theta=0,r=\hat{L}}, \tag{1.28}$$

where H and $\overline{\mu}$ are related to the interface and given by

$$\frac{1}{H} = \frac{1}{2\cosh^2\pi\varepsilon}\left(\frac{1}{\overline{E}_1}+\frac{1}{\overline{E}_2}\right), \tag{1.29}$$

$$\frac{1}{\overline{\mu}} = \frac{1}{4}\left(\frac{1}{\mu_1}+\frac{1}{\mu_2}\right). \tag{1.30}$$

The parameters $\overline{E}_k$ are defined in eq. (1.16) and the subscripts $k = 1, 2$ represent the upper and lower materials, respectively. The phase angle ϕ represents the ratio of the out-of-plane mode to the in-plane modes. It may also be expressed as an out-of-plane shear stress to the magnitude of the in-plane stresses along the interface ($\theta = 0$) at a distance $r = \hat{L}$ from the crack tip. The phase angles $\hat{\psi}$ and ϕ may be considered as mode mixity parameters.

The energy release rate for an interface crack is given by (Malyshev and Saganik, 1965)

$$\mathcal{G}_i = \frac{1}{H}(K_1^2+K_2^2)+\frac{1}{\overline{\mu}}K_{III}^2, \tag{1.31}$$

where i represents the interface. By manipulating eq. (1.31), it is possible to show that $\mathcal{G}_i$ may be written as

$$\mathcal{G}_i = \frac{\hat{K}_1{}^2}{H}\left(1+\tan^2\hat{\psi}\right)\left(1+\tan^2\phi\right), \tag{1.32}$$

where $\hat{\psi}$ and ϕ are the phase angles and $\hat{K}_1$ is the real part of the normalized stress intensity factor given in eq. (1.26).

As in the case of a crack in a homogeneous solid, once $\mathcal{G}_i$ reaches a critical value $\mathcal{G}_{ic}$, the crack may propagate. This critical value, $\mathcal{G}_{ic}$, is a function of $\hat{\psi}$ and ϕ and may be used to describe a failure surface for crack propagation between two isotropic materials, namely

$$\mathcal{G}_{ic} = \overline{\mathcal{G}}_{1c}\left(1+\tan^2\hat{\psi}\right)\left(1+\tan^2\phi\right), \tag{1.33}$$

where $\overline{\mathcal{G}}_{1c}$ is defined as

$$\overline{\mathcal{G}}_{1c} = \text{avg}\left(\frac{\hat{K}_1^2}{H}\right). \tag{1.34}$$

The value of $\overline{\mathcal{G}}_{1c}$ may be obtained from the average of $\hat{K}_1^2/H$, calculated separately for each test. In Banks-Sills and Ashkenazi (2000), the two-dimensional curve from eq. (1.33) was presented.

1.2 Methods for extracting stress intensity factors

The stress intensity factors K_I, K_{II} and K_{III} in a linear elastic, homogeneous, isotropic material may be numerically calculated using several methods. Two will be presented here. Both methods make use of a finite element analysis (FEA) and of the first term of the asymptotic solution. First, the displacement extrapolation method will be presented in Section 1.2.1. This method was first introduced by Chan et al. (1970) for isotropic materials. It is a direct method in which the crack opening, sliding and tearing displacements are used to calculate the stress intensity factors. The second method is the interaction energy M-integral which is an indirect method. It is based on energy considerations; it was first derived by Chen and Sheild (1977) and implemented in Yau et al. (1980) for a linear elastic, homogeneous, isotropic material. By means of this integral, with use of auxiliary solutions, a sufficient number of equations to determine the stress intensity factors are obtained. In section 1.2.2, the two-dimensional mechanical and thermal M-integrals will be discussed and extended for three-dimensions.

1.2.1 Displacement extrapolation

In this section the displacement extrapolation method will be presented for a crack within a linear elastic, homogenous, isotropic material. With this method, the crack opening, sliding and tearing displacements are used to calculate the stress intensity factors.

Considering a semi-infinite crack in a body of infinite extent, the first term of the asymptotic displacement field, given in eqs. (1.5) through (1.7), may be used to describe the relative displacements of the crack faces in a small region near the crack front. By substituting $\theta = \pm\pi$ in these equations, the displacements in different directions, relative to the crack faces become

$$\begin{aligned}
\Delta u_1 &\equiv u_1(r,\theta=\pi) - u_1(r,\theta=-\pi) &&= \frac{\kappa+1}{\mu}\sqrt{\frac{r}{2\pi}}K_{II} \quad , \\
\Delta u_2 &\equiv u_2(r,\theta=\pi) - u_2(r,\theta=-\pi) &&= \frac{\kappa+1}{\mu}\sqrt{\frac{r}{2\pi}}K_{I} \quad , \\
\Delta u_3 &\equiv u_3(r,\theta=\pi) - u_3(r,\theta=-\pi) &&= \frac{4}{\mu}\sqrt{\frac{r}{2\pi}}K_{III}
\end{aligned} \tag{1.35}$$

where u_1, u_2 and u_3 are the displacements in the x_1, x_2 and x_3 - directions, respectively, and the parameters r and θ are the crack tip polar coordinates shown in Fig. 1.3. The mechanical property μ in eqs. (1.35) is the shear modulus and κ is given in eq. (1.8). By manipulating eqs. (1.35), an expression for the local stress intensity factors at a distance r along the crack faces may be obtained. These local stress intensity factors are denoted

as K_I^*, K_{II}^* and K_{III}^* and are given explicitly as

$$\begin{aligned} K_I^* &= \frac{\mu\sqrt{2\pi}}{\kappa+1}\frac{\Delta u_2}{\sqrt{r}} \ , \\ K_{II}^* &= \frac{\mu\sqrt{2\pi}}{\kappa+1}\frac{\Delta u_1}{\sqrt{r}} \ , \\ K_{III}^* &= \frac{\mu\sqrt{2\pi}}{4}\frac{\Delta u_3}{\sqrt{r}} \ . \end{aligned} \tag{1.36}$$

Only the first term of the asymptotic displacement field is used to obtain the expressions in eqs. (1.35) and (1.36). It was shown that with use of higher order terms, the crack displacement jumps may be written as (Williams, 1957)

$$\begin{aligned} \Delta u_1 &= A_1 r^{1/2} + A_2 r^{3/2} + O(r^{5/2}) \ , \\ \Delta u_2 &= B_1 r^{1/2} + B_2 r^{3/2} + O(r^{5/2}) \ , \\ \Delta u_3 &= C_1 r^{1/2} + C_2 r^{3/2} + O(r^{5/2}) \end{aligned} \tag{1.37}$$

where A_i,B_i and C_i $(i = 1, 2)$ are constants and r is the distance from the crack front. For terms r^n $(n = 1, 2, ...)$ in the series in eqs. (1.37), the coefficients are zero on the crack faces. By dividing eqs. (1.37) by $\sqrt{r}$ these equations take the form

$$\begin{aligned} \frac{\Delta u_1}{\sqrt{r}} &= A_1 + A_2 r + O(r^2) \ , \\ \frac{\Delta u_2}{\sqrt{r}} &= B_1 + B_2 r + O(r^2) \ , \\ \frac{\Delta u_3}{\sqrt{r}} &= C_1 + C_2 r + O(r^2) \ . \end{aligned} \tag{1.38}$$

By substituting eqs. (1.38) into eqs. (1.36), local stress intensity factors may be written as

$$\begin{aligned} K_I^* &= \frac{\mu\sqrt{2\pi}}{\kappa+1}\left[B_1 + B_2 r + O(r^2)\right] \ , \\ K_{II}^* &= \frac{\mu\sqrt{2\pi}}{\kappa+1}\left[A_1 + A_2 r + O(r^2)\right] \ , \\ K_{III}^* &= \frac{\mu\sqrt{2\pi}}{4}\left[C_1 + C_2 r + O(r^2)\right] \ . \end{aligned} \tag{1.39}$$

A linear relation between the local stress intensity factors and r is observed in eqs. (1.39). On the other hand, division of eqs. (1.35) by $\sqrt{r}$ yields

$$\begin{aligned} \frac{\Delta u_1}{\sqrt{r}} &= \frac{\kappa+1}{\mu\sqrt{2\pi}} K_{II} \ , \\ \frac{\Delta u_2}{\sqrt{r}} &= \frac{\kappa+1}{\mu\sqrt{2\pi}} K_I \ , \\ \frac{\Delta u_3}{\sqrt{r}} &= \frac{4}{\mu\sqrt{2\pi}} K_{III} \ . \end{aligned} \tag{1.40}$$

It is apparent that by comparing eqs. (1.38) with eqs. (1.40) as $r \to 0$, the stress intensity factors K_I, K_{II} and K_{III} are proportional to the constants B_1, A_1 and C_1, respectively.

As $r \to 0$, the local stress intensity factors K_m^* $(m = I, II, III)$ are equal to the stress intensity factors K_m $(m = I, II, III)$. Hence, it may be concluded that the stress intensity factors may be calculated from the values of the local stress intensity factors for $r \to 0$. In other words,

$$\begin{aligned} K_I &= \lim_{r\to 0} \quad K_I^* \quad , \\ K_{II} &= \lim_{r\to 0} \quad K_{II}^* \quad , \\ K_{III} &= \lim_{r\to 0} \quad K_{III}^* \quad . \end{aligned} \tag{1.41}$$

The displacement extrapolation method may be used to obtain the stress intensity factors of a given problem. In such a case, the displacement field is obtained numerically by means of a finite element analysis. The results are substituted into eqs. (1.36) to determine the local stress intensity factors K_m^* $(m = I, II, III)$ versus the distance from the crack front normalized by the delamination length r/a. Graphs of this relation are plotted and based on eqs. (1.39) they are expected to be linear. It may be noted that in a small region near the crack front, the asymptotic solution is not valid, as well as far from the crack front where the linear representation of the displacement jump is not valid. Hence, the points near the crack front, as well as points far from the crack front are excluded from the calculations. Linear behavior of the local K_m^*-values $(m = I, II, III)$ occurs for some distance along the crack faces. The most accurate value for the stress intensity factors K_m $(m = I, II, III)$ may be chosen by fitting a line through various groups of three points. A correlation coefficient is then calculated for each fit. The line with the correlation coefficient closest to 1 is used to obtain the stress intensity factors K_m $(m = I, II, III)$ from linear extrapolation of that line to $r = 0$.

The displacement extrapolation method has many advantages. In addition to being a simple, straight forward approach to obtain the stress intensity factors, this method is suitable for all fracture modes and enables evaluation of all stress intensity factors. However, this method is not as accurate as an energy based method. Moreover, the main flaw of this method is that there are several options for the linear extrapolation which may produce a range of results for the stress intensity factors. In the case of an interface crack, the displacement extrapolation method may be extended. In Section 3.1, the particular case of a delamination along an interface between a transversely isotropic material and a tetragonal material will be described.

1.2.2 Conservative M-integrals

The interaction energy conservative integral or M-integral is known to be an accurate method for extracting stress intensity factors based on energy considerations (Banks-Sills,

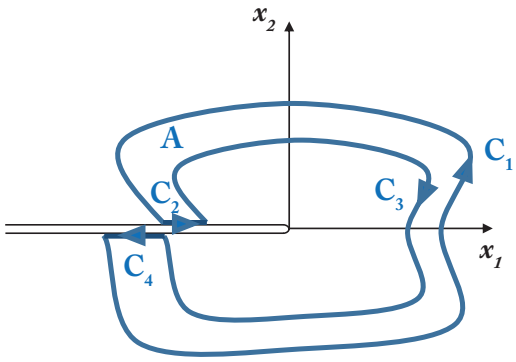

Figure 1.5: Integration area A for a crack in a homogeneous body.

1991). By means of this integral, with use of auxiliary solutions, a sufficient number of equations are obtained to determine the stress intensity factors occurring under mixed mode conditions. In this investigation, an M-integral for determination of the stress intensity factors resulting from mechanical loading, as well as from residual thermal curing stresses will be used. In Section 1.2.2.1, a short review of the two and three-dimensional mechanical M-integrals for homogeneous materials and for an interface between two homogeneous materials will be presented. The two and three-dimensional thermal M-integrals for these materials will be described in Section 1.2.2.2.

1.2.2.1 Mechanical M-integral

The mechanical M-integral was first derived by Chen and Sheild (1977) from the conservative J-integral (Rice, 1968). It was then implemented in Yau et al. (1980) for a homogeneous, isotropic material and extended by Yau and Wang (1984) for an interface crack between two homogeneous, isotropic materials. A three-dimensional mechanical M-integral was first presented for a homogeneous isotropic material by Nakamura and Parks (1989) and extended for dissimilar monoclinic materials by Freed and Banks-Sills (2005).

The M-integral is a conservative integral which may be used to separate the stress intensity factors for different modes. It was first presented as a line integral in Chen and Sheild (1977). Since it is path independent, it may be transformed to an area integral and given for a crack in a homogeneous isotropic body as

$$M^{(1,2\alpha)} = \int_A \left[\left(\sigma_{ij}^{(1)} \frac{\partial u_i^{(2\alpha)}}{\partial x_1} + \sigma_{ij}^{(2\alpha)} \frac{\partial u_i^{(1)}}{\partial x_1} \right) - W^{(1,2\alpha)} \delta_{1j} \right] \frac{\partial q_1}{\partial x_j} \, dA \ . \tag{1.42}$$

In eq. (1.42), indicial notation is used where summation is implied over repeated indices. The subscripts $i, j = 1, 2$, A is the integration area shown in Fig. 1.5, the superscript (1) represents the numerical solution for the problem which is being solved; (2α) represents

Table 1.1: Stress intensity factors for the two-dimensional auxiliary solutions used for a homogeneous crack problem.

solution	K_I	K_{II}
2a	1	0
2b	0	1

two auxiliary solutions, $2a$ and $2b$. In addition, the parameter δ_{1j} is the Kronecker delta and the interaction strain energy density is given by

$$W^{(1,2\alpha)} = \sigma_{ij}^{(1)} \varepsilon_{ij}^{(2\alpha)} = \sigma_{ij}^{(2\alpha)} \varepsilon_{ij}^{(1)} . \tag{1.43}$$

The function q_1 is defined as

$$q_1 = \begin{cases} 1 & \text{on} \quad C_3 \\ 0 & \text{on} \quad C_1 \end{cases} , \tag{1.44}$$

and is sufficiently continuous and differentiable within A.

In order to obtain the stress intensity factors for a two-dimensional problem of a crack in a homogeneous material, the two solutions are superposed, so that

$$u_i = u_i^{(1)} + u_i^{(2\alpha)} , \tag{1.45}$$

$$\sigma_{ij} = \sigma_{ij}^{(1)} + \sigma_{ij}^{(2\alpha)} , \tag{1.46}$$

$$\varepsilon_{ij} = \varepsilon_{ij}^{(1)} + \varepsilon_{ij}^{(2\alpha)} , \tag{1.47}$$

$$K_I = K_I^{(1)} + K_I^{(2\alpha)} , \tag{1.48}$$

$$K_{II} = K_{II}^{(1)} + K_{II}^{(2\alpha)} \quad . \tag{1.49}$$

The first term of the asymptotic expansion is used as the auxiliary solution with two sets of stress intensity factors, denoted by $2a$ and $2b$ and shown in Table 1.1. For a homogeneous, isotropic material the explicit expressions for the first term of the asymptotic expansion of the displacement field are given in eqs. (1.5) and (1.6). The stress and strain components $\sigma_{ij}^{(2\alpha)}$ and $\epsilon_{ij}^{(2\alpha)}$ $(i, j = 1, 2)$, respectively, are developed by means of a finite element formulation through the derivatives of the shape functions.

On the other hand, it is possible to write the relation between $M^{(1,2\alpha)}$ and the stress intensity factors of a homogeneous, isotropic material as

$$M^{(1,2\alpha)} = \frac{2}{\overline{E}} \left\{ K_I^{(1)} K_I^{(2\alpha)} + K_{II}^{(1)} K_{II}^{(2\alpha)} \right\} \tag{1.50}$$

where $\overline{E}$ is defined in eq. (1.16). For the auxiliary solution $2a$, found using Table 1.1, eq. (1.50) reduces to

$$M^{(1,2a)} = \frac{2}{\overline{E}} K_I^{(1)} . \tag{1.51}$$

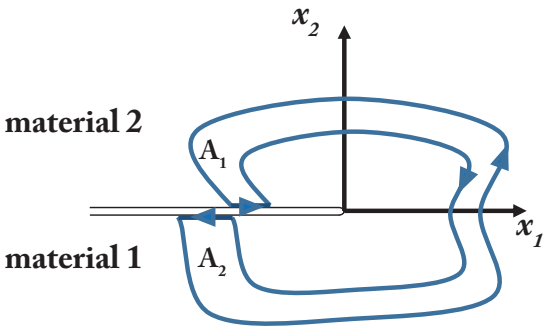

Figure 1.6: Integration areas A_k for a crack along an interface between two materials.

By equating eqs. (1.42) and (1.51), the mode I stress intensity factor is obtained as

$$K_I^{(1)} = \frac{\overline{E}}{2} \int_A \left[\left(\sigma_{ij}^{(1)} \frac{\partial u_i^{(2a)}}{\partial x_1} + \sigma_{ij}^{(2a)} \frac{\partial u_i^{(1)}}{\partial x_1} \right) - W^{(1,2a)} \delta_{1j} \right] \frac{\partial q_1}{\partial x_j} \, dA \ . \tag{1.52}$$

In the same manner, for auxiliary solution $2b$, found using Table 1.1, eq. (1.50) reduces to

$$M^{(1,2b)} = \frac{2}{\overline{E}} K_{II}^{(1)} \ ; \tag{1.53}$$

so that,

$$K_{II}^{(1)} = \frac{\overline{E}}{2} \int_A \left[\left(\sigma_{ij}^{(1)} \frac{\partial u_i^{(2b)}}{\partial x_1} + \sigma_{ij}^{(2b)} \frac{\partial u_i^{(1)}}{\partial x_1} \right) - W^{(1,2b)} \delta_{1j} \right] \frac{\partial q_1}{\partial x_j} \, dA \ . \tag{1.54}$$

For an interface crack between two isotropic materials, several modifications may be made. The upper and lower materials are denoted by $k = 1, 2$, respectively, and the integration area A is divided into two sub-areas A_k, as shown in Fig. 1.6. As a result, the two-dimensional M-integral from eq. (1.42) takes the form

$$M^{(1,2\alpha)} = \int_{A_k} \left[\left({}_k\sigma_{ij}^{(1)} \frac{\partial \ {}_k u_i^{(2\alpha)}}{\partial x_1} + \ {}_k\sigma_{ij}^{(2\alpha)} \frac{\partial \ {}_k u_i^{(1)}}{\partial x_1} \right) - \ {}_k W^{(1,2\alpha)} \delta_{1j} \right] \frac{\partial q_1}{\partial x_j} \, dA \ . \tag{1.55}$$

Moreover, instead of K_I and K_{II} for modes one and two, respectively, the in-plane stress intensity factors are coupled and referred to as K_1 and K_2, as shown in eq. (1.22). As a result, eq. (1.50) takes the form

$$M^{(1,2\alpha)} = \frac{2}{H} \left\{ K_1^{(1)} K_1^{(2\alpha)} + K_2^{(1)} K_2^{(2\alpha)} \right\} \ , \tag{1.56}$$

where H is defined in eq. (1.29). Moreover, the first term of the asymptotic solution for an interface crack is different than that of a crack in a homogeneous body, and is given in eq. (1.24) for the displacement field. In the same manner used for a crack in a homogeneous material, the auxiliary solutions make use of the first term of the asymptotic expansion. Two specific stress intensity factor pairs are used. These pairs are presented in Table 1.2 where $2a$ and $2b$ represent the two cases considered, respectively.

Table 1.2: Stress intensity factors for the two-dimensional auxiliary solutions for an interface crack problem.

solution	K_1	K_2
2a	1	0
2b	0	1

A three-dimensional M-integral for a straight through crack in a homogeneous material was extended from the three-dimensional J-integral (Li et al., 1985). A review of this method for two- and three-dimensional mixed mode problems for isotropic and anisotropic materials was given in Banks-Sills (2010). In that paper, the three-dimensional M-integral used for a crack in a homogeneous isotropic material was given by

$$M_N^{(1,2\alpha)} = \frac{1}{A_1}\int_V \left\{ \sigma_{ij}^{(1)} \frac{\partial u_i^{(2\alpha)}}{\partial x_1} + \sigma_{ij}^{(2\alpha)} \frac{\partial u_i^{(1)}}{\partial x_1} - W^{(1,2\alpha)}\delta_{1j} \right\} \frac{\partial q_1}{\partial x_j}\, dV \ , \tag{1.57}$$

where $i, j = 1, 2, 3$ and

$$A_1 = \int_0^{L_N} \ell_1^{(N)}(x_3) dx_3 \ . \tag{1.58}$$

In eq. (1.57), $M_N^{(1,2\alpha)}$ is the average value of $M^{(1,2\alpha)}$ along the crack front for element N. The parameter $\ell_1^{(N)}(x_3)$ in eq. (1.58), is the normalized virtual crack extension of element N in the x_1-direction. This extension is assumed to be parabolic as shown in Fig. 1.7 for element N. Local coordinates are considered for each element N used in the calculation. The integration on the right hand side of eq. (1.57) takes place in volume V of finite elements which is one element thick through the specimen thickness. The cross-section of the volumes in which integration takes place is shown in Fig. 1.8. It may be noted that the elements adjacent to the crack front generally produce inaccurate results. In eq. (1.57), the displacement components $u_i^{(1)}$ and stress components $\sigma_{ij}^{(1)}$ are obtained

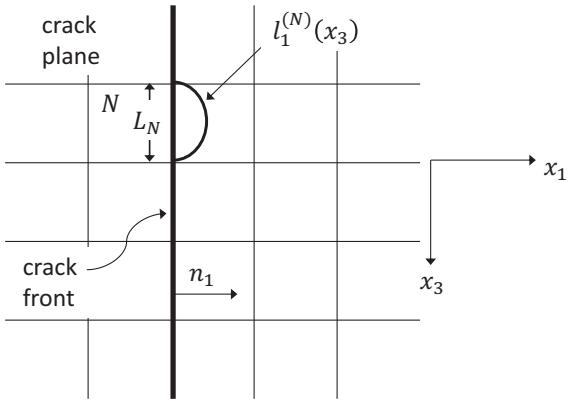

Figure 1.7: Virtual crack extension along the crack front, denoted in the finite element mesh.

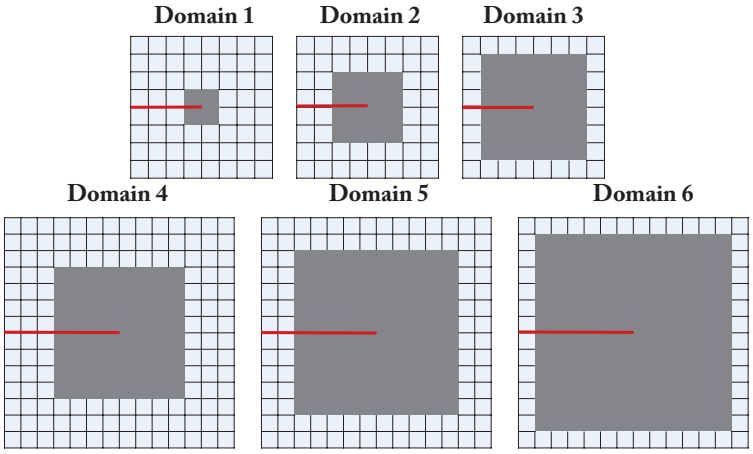

Figure 1.8: Cross-section of integration domains which are one element thick.

from the FE solution of the problem at hand. The auxiliary solution components $u_i^{(2\alpha)}$ are obtained from the first term of the asymptotic solution. The auxiliary stress and strain components $\sigma_{ij}^{(2\alpha)}$ and $\epsilon_{ij}^{(2\alpha)}$, respectively, are determined by means of a finite element formulation through the derivatives of the shape functions. The auxiliary solutions are calculated using specific values for the stress intensity factors, given in Table 1.3. The mutual strain energy density $W^{(1,2\alpha)}$ is defined in eq. (1.43). The parameter q_1 is defined as

$$q_1 = \sum_{m=1}^{20} N_m\left(\xi,\eta,\zeta\right) q_{1m} \ , \tag{1.59}$$

where $N_m\left(\xi,\eta,\zeta\right)$ are the shape functions of a twenty noded, isoparametric element and q_{1m} is a component of the vector which determines the virtual displacement at the element nodal points.

On the other hand, the value of $M_N^{(1,2\alpha)}$ is related to the stress intensity factors as

$$M_N^{(1,2\alpha)} = \frac{2}{\overline{E}}\left\{K_{I_N}^{(1)}K_{I_N}^{(2\alpha)} + K_{II_N}^{(1)}K_{II_N}^{(2\alpha)}\right\} + \frac{1}{\mu}K_{III_N}^{(1)}K_{III_N}^{(2\alpha)} \ , \tag{1.60}$$

where the parameter $\overline{E}$ is defined in eq. (1.16) and μ is the shear modulus. For a three-dimensional homogeneous material with the use of the auxiliary solution for each case

Table 1.3: Stress intensity factors for the three-dimensional auxiliary solutions.

solution	K_I	K_{II}	K_{III}
2a	1	0	0
2b	0	1	0
2c	0	0	1 .

Table 1.4: Stress intensity factors for the three-dimensional auxiliary solutions.

solution	K_1	K_2	K_{III}
2a	1	0	0
2b	0	1	0
2c	0	0	1 .

($2a$, $2b$ and $2c$) in eqs. (1.57) and (1.60) with the aid of Table 1.3, it may be shown that

$$K_{I_N}^{(1)} = \frac{\overline{E}}{2A_1}\int_V \left\{\sigma_{ij}^{(1)}\frac{\partial u_i^{(2a)}}{\partial x_1} + \sigma_{ij}^{(2a)}\frac{\partial u_i^{(1)}}{\partial x_1} - W^{(1,2a)}\delta_{1j}\right\}\frac{\partial q_1}{\partial x_j}\,dV\ , \tag{1.61}$$

$$K_{II_N}^{(1)} = \frac{\overline{E}}{2A_1}\int_V \left\{\sigma_{ij}^{(1)}\frac{\partial u_i^{(2b)}}{\partial x_1} + \sigma_{ij}^{(2b)}\frac{\partial u_i^{(1)}}{\partial x_1} - W^{(1,2b)}\delta_{1j}\right\}\frac{\partial q_1}{\partial x_j}\,dV\ , \tag{1.62}$$

$$K_{III_N}^{(1)} = \frac{\mu}{A_1}\int_V \left\{\sigma_{ij}^{(1)}\frac{\partial u_i^{(2c)}}{\partial x_1} + \sigma_{ij}^{(2c)}\frac{\partial u_i^{(1)}}{\partial x_1} - W^{(1,2c)}\delta_{1j}\right\}\frac{\partial q_1}{\partial x_j}\,dV\ . \tag{1.63}$$

The calculated stress intensity factors are an average value along the segment L_N, shown in Fig. 1.7.

For a three-dimensional interface crack, several modifications are required. First, the in-plane stress intensity factors are coupled. Nonetheless, eq. (1.60) becomes

$$M_N^{(1,2\alpha)} = \frac{2}{H}\left\{K_{1_N}^{(1)}K_{1_N}^{(2\alpha)} + K_{2_N}^{(1)}K_{2_N}^{(2\alpha)}\right\} + \frac{2}{\overline{\mu}}K_{III_N}^{(1)}K_{III_N}^{(2\alpha)} \tag{1.64}$$

where H and $\overline{\mu}$ are defined for an interface between two isotropic materials in eqs. (1.29) and (1.30), respectively. Moreover, for an interface crack, the first two terms of the asymptotic solution of the displacement field are given in eqs. (1.24) and (1.25). In the same manner used for a crack in a homogenous material, the auxiliary solutions are obtained from these terms for three specific cases presented in Table 1.4. In addition, the integral in eq. (1.57) is replaced with

$$M_N^{(1,2\alpha)} = \frac{1}{A_1}\sum_{k=1}^{2}\int_{V_k}\left\{{}_k\sigma_{ij}^{(1)}\frac{\partial\ {}_ku_i^{(2\alpha)}}{\partial x_1} + {}_k\sigma_{ij}^{(2\alpha)}\frac{\partial\ {}_ku_i^{(1)}}{\partial x_1} - {}_kW^{(1,2\alpha)}\delta_{1j}\right\}\frac{\partial q_1}{\partial x_j}\,dV\ , \tag{1.65}$$

where $i,j = 1,2,3$ and $k = 1,2$ represents the upper and lower materials, respectively. The volume V_k consists of a slice of elements orthogonal to the delamination front. A cross-section of the domains of integration are illustrated in Fig. 1.8. Using eqs. (1.64) and (1.65), it is possible to determine the mechanical stress intensity factors $K_1^{(1)}$, $K_2^{(1)}$ and $K_{III}^{(1)}$ as

$$K_1^{(1)} = \frac{H}{2A_1}\sum_{k=1}^{2}\int_{V_k}\left[{}_k\sigma_{ij}^{(1)}\frac{\partial\ {}_ku_i^{(2a)}}{\partial x_1} + {}_k\sigma_{ij}^{(2a)}\frac{\partial\ {}_ku_i^{(1)}}{\partial x_1} - {}_kW^{(1,2a)}\delta_{1j}\right]\frac{\partial q_1}{\partial x_j}\,dV\ ; \tag{1.66}$$

$$K_2^{(1)} = \frac{H}{2A_1}\sum_{k=1}^{2}\int_{V_k}\left[{}_k\sigma_{ij}^{(1)}\,\frac{\partial\,{}_k u_i^{(2b)}}{\partial x_1} + {}_k\sigma_{ij}^{(2b)}\,\frac{\partial\,{}_k u_i^{(1)}}{\partial x_1} - {}_k W^{(1,2b)}\delta_{1j}\right]\frac{\partial q_1}{\partial x_j}\,dV\;; \quad (1.67)$$

$$K_{III}^{(1)} = \frac{\overline{\mu}}{2A_1}\sum_{k=1}^{2}\int_{V_k}\left[{}_k\sigma_{ij}^{(1)}\,\frac{\partial\,{}_k u_i^{(2c)}}{\partial x_1} + {}_k\sigma_{ij}^{(2c)}\,\frac{\partial\,{}_k u_i^{(1)}}{\partial x_1} - {}_k W^{(1,2c)}\delta_{1j}\right]\frac{\partial q_1}{\partial x_j}\,dV \quad (1.68)$$

where the superscript (1) denotes the numerical solution for the problem which is being solved. In eqs. (1.66) through (1.68), the parameters H and $\overline{\mu}$ are defined for an interface between two isotropic materials in eqs. (1.29) and (1.30), respectively.

1.2.2.2 Thermal M-integral

The conservative thermal J-integral for homogeneous isotropic materials (Wilson and Yu, 1979) was extended for interface crack problems by Banks-Sills and Dolev (2004). In that paper, the M-integral for two-dimensional thermal-elastic bimaterial problems was also derived. A three-dimensional thermal J-integral was first presented for a homogeneous isotropic material by Shih et al. (1986) and extended for dissimilar anisotropic materials by Banks-Sills et al. (2006). In the latter paper, the three-dimensional thermal M-integral for dissimilar anisotropic materials was also derived.

With the thermal M-integral, the thermal stress intensity factors, resulting from residual curing stresses, may be calculated. The two-dimensional M-integral for a crack along an interface between two isotropic materials may be written as (Banks-Sills and Dolev, 2004)

$$\begin{aligned} M^{(1,2\alpha)} = &\sum_{k=1}^{2}\int_{A_k}\left({}_k\sigma_{ij}^{(1)}\frac{\partial_k u_i^{(2\alpha)}}{\partial x_1} + {}_k\sigma_{ij}^{(2\alpha)}\frac{\partial_k u_i^{(1)}}{\partial x_1} - {}_k W_F^{(1,2\alpha)}\delta_{1j}\right)\frac{\partial q_1}{\partial x_j}\,dA + \\ &\sum_{k=1}^{2}{}_k\beta_{ij}\int_{A_k}{}_k\varepsilon_{ij}^{m(2\alpha)}\frac{\partial_k\Delta\vartheta^{(1)}}{\partial x_1}q_1 dA + \sum_{k=1}^{2}{}_k\beta_{ij}\int_{A_{0k}}{}_k\varepsilon_{ij}^{m(2\alpha)}\frac{\partial_k\Delta\vartheta^{(1)}}{\partial x_1}q_1 dA \end{aligned} \quad (1.69)$$

where $k = 1, 2$ denotes the upper and lower materials, respectively. In the case of a crack along an interface between two isotropic materials, ${}_k\beta_{ij}$ is defined as

$${}_k\beta_{ij} = {}_k\overline{\beta}\delta_{ij} \quad (1.70)$$

where ${}_k\overline{\beta}$ is given for plane strain as

$${}_k\overline{\beta} = \frac{E_k\alpha_k}{1-2\nu_k}\;. \quad (1.71)$$

In eq. (1.71), E_k, ν_k and α_k are the Young's moduli, Poisson's ratios, and coefficients of thermal expansion (CTE) of the upper and lower materials, respectively. In eq. (1.69), the integration area A_k is the area between the two rings surrounding the delamination tip as shown in Fig. 1.9. This area is the same as that for the mechanical integral. The

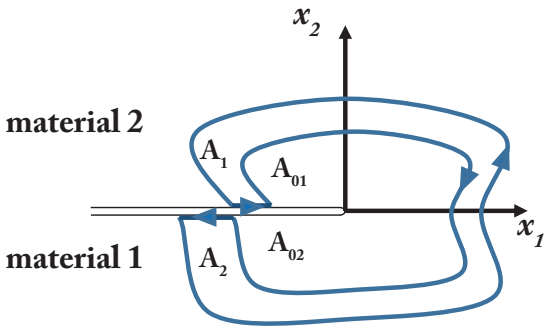

Figure 1.9: Integration areas A_k and A_{0k} $(k = 1, 2)$ for a crack along an interface between two materials.

integration area A_{0k} is the area between the inner ring and the delamination tip (see Fig. 1.9). The parameter ${}_kW_F^{(1,2)}$ is the interaction strain energy density, given by

$$ {}_kW_F^{(1,2\alpha)} = {}_k\sigma_{ij}^{(1)}\ {}_k\varepsilon_{ij}^{m(2\alpha)} = {}_k\sigma_{ij}^{(2\alpha)}\ {}_k\varepsilon_{ij}^{T(1)} - {}_k\beta_{ij}\ {}_k\Delta\vartheta^{(1)}\ {}_k\varepsilon_{ij}^{m(2\alpha)} \ . \tag{1.72} $$

In eq. (1.72), the superscript m represents the mechanical strains. The total strains resulting from both thermal and mechanical loads are represented using the superscript T. For an interface between two isotropic materials the stress-strain relation may be written as

$$ {}_k\sigma_{ij} = 2\mu_k\ {}_k\varepsilon_{ij} + \lambda_k\ {}_k\varepsilon_{ss}\delta ij - {}_k\overline{\beta}\ {}_k\Delta\vartheta\delta_{ij} \tag{1.73} $$

where μ_k and λ_k $(k = 1, 2)$ are Lamé constants and the parameter ${}_k\Delta\vartheta$ is the temperature change in material k. The temperature change for the auxiliary solution ${}_k\Delta\vartheta^{(2\alpha)}$ is taken to be zero. Hence, the total temperature change ${}_k\Delta\vartheta$ in each material k is equal to the temperature change in the problem which is being solved, namely ${}_k\Delta\vartheta^{(1)}$.

If the temperature change considered is constant everywhere, then eq. (1.69) becomes

$$ M^{(1,2\alpha)} = \sum_{k=1}^{2}\int_{A_k}\left({}_k\sigma_{ij}^{(1)}\frac{\partial\ {}_ku_i^{(2\alpha)}}{\partial x_1} + {}_k\sigma_{ij}^{(2\alpha)}\frac{\partial\ {}_ku_i^{(1)}}{\partial x_1} - {}_kW_F^{(1,2\alpha)}\delta_{1j}\right)\frac{\partial q_1}{\partial x_j}\,dA \ . \tag{1.74} $$

This integral is identical to the M-integral for applied loads, given in eq. (1.42), except for the interaction strain energy density ${}_kW_F$ given in eq. (1.72), as well as, the constitutive equation presented in eq. (1.73), both used in the thermal case.

The superscript 2α, $(\alpha = a, b)$ denotes the auxiliary solution. This solution is calculated from the first term of the asymptotic solution for the cases presented in Table 1.2. The desired thermal stress intensity factors $K_1^{(r)}$ and $K_2^{(r)}$ may be obtained by equating eq. (1.56) with eq. (1.74) as

$$ K_1^{(r)} = \frac{H}{2}\sum_{k=1}^{2}\int_{A_k}\left({}_k\sigma_{ij}^{(1)}\frac{\partial\ {}_ku_i^{(2a)}}{\partial x_1} + {}_k\sigma_{ij}^{(2a)}\frac{\partial\ {}_ku_i^{(1)}}{\partial x_1} - {}_kW_F^{(1,2a)}\delta_{1j}\right)\frac{\partial q_1}{\partial x_j}\,dA\ ; \tag{1.75} $$

$$ K_2^{(r)} = \frac{H}{2}\sum_{k=1}^{2}\int_{A_k}\left({}_k\sigma_{ij}^{(1)}\frac{\partial\ {}_ku_i^{(2b)}}{\partial x_1} + {}_k\sigma_{ij}^{(2b)}\frac{\partial\ {}_ku_i^{(1)}}{\partial x_1} - {}_kW_F^{(1,2b)}\delta_{1j}\right)\frac{\partial q_1}{\partial x_j}\,dA \ . \tag{1.76} $$

In eq. (1.75) and (1.76), the superscript (r) indicates the residual stresses of the sought after solution.

In three dimensions, the thermal M-integral becomes

$$M_N^{(1,2\alpha)} = \frac{1}{A_1}\sum_{k=1}^{2}\int_{V_k}\left\{\left[{}_k\sigma_{ij}^{(1)}\frac{\partial\,{}_k u_i^{(2\alpha)}}{\partial x_1} + {}_k\sigma_{ij}^{(2\alpha)}\frac{\partial\,{}_k u_i^{(1)}}{\partial x_1} - {}_kW_F^{(1,2\alpha)}\delta_{1j}\right]\frac{\partial q_1}{\partial x_j} + {}_k\beta_{ij}\;{}_k\varepsilon_{ij}^{m(2)}\;\frac{\partial\,{}_k\Delta\vartheta^{(1)}}{\partial x_1}q_1\right\}dV \quad (1.77)$$

where A_1 is given in eq. (1.58). If the temperature change considered is constant everywhere, then eq. (1.77) becomes

$$M_N^{(1,2\alpha)} = \frac{1}{A_1}\sum_{k=1}^{2}\int_{V_k}\left[{}_k\sigma_{ij}^{(1)}\frac{\partial\,{}_k u_i^{(2\alpha)}}{\partial x_1} + {}_k\sigma_{ij}^{(2\alpha)}\frac{\partial\,{}_k u_i^{(1)}}{\partial x_1} - {}_kW_F^{(1,2\alpha)}\delta_{1j}\right]\frac{\partial q_1}{\partial x_j}\;. \quad (1.78)$$

On the other hand, the thermal three-dimensional M-integral may also be defined using stress intensity factors as shown in eq. (1.64). By equating eq. (1.78) with eq. (1.64), the thermal stress intensity factors in the three-dimensional case of a delamination along an interface between two isotropic materials may be found as

$$K_1^{(r)} = \frac{H}{2A_1}\sum_{k=1}^{2}\int_{V_k}\left[{}_k\sigma_{ij}^{(1)}\frac{\partial_k\,u_i^{(2a)}}{\partial x_1} + {}_k\sigma_{ij}^{(2a)}\frac{\partial_k\,u_i^{(1)}}{\partial x_1} - {}_kW_F^{(1,2a)}\delta_{1j}\right]\frac{\partial q_1}{\partial x_j}\;; \quad (1.79)$$

$$K_2^{(r)} = \frac{H}{2A_1}\sum_{k=1}^{2}\int_{V_k}\left[{}_k\sigma_{ij}^{(1)}\frac{\partial_k\,u_i^{(2b)}}{\partial x_1} + {}_k\sigma_{ij}^{(2b)}\frac{\partial_k\,u_i^{(1)}}{\partial x_1} - {}_kW_F^{(1,2b)}\delta_{1j}\right]\frac{\partial q_1}{\partial x_j}\;; \quad (1.80)$$

$$K_{III}^{(r)} = \frac{\overline{\mu}}{2A_1}\sum_{k=1}^{2}\int_{V_k}\left[{}_k\sigma_{ij}^{(1)}\frac{\partial_k\,u_i^{(2c)}}{\partial x_1} + {}_k\sigma_{ij}^{(2c)}\frac{\partial_k\,u_i^{(1)}}{\partial x_1} - {}_kW_F^{(1,2c)}\delta_{1j}\right]\frac{\partial q_1}{\partial x_j} \quad (1.81)$$

where H and $\overline{\mu}$ are defined for an interface between two isotropic materials in eqs. (1.29) and (1.30), respectively.

The obtained mechanical and thermal stress intensity factors given in eqs. (1.66) through (1.68) and in eqs. (3.28) through (3.30), respectively, are superposed to obtain the total stress intensity factors, namely

$$K_1^T = K_1^{(f)} + K_1^{(r)}\;; \quad (1.82)$$

$$K_2^T = K_2^{(f)} + K_2^{(r)}\;; \quad (1.83)$$

$$K_{III}^T = K_{III}^{(f)} + K_{III}^{(r)}\;. \quad (1.84)$$

The superscript f represents the solution for the applied force. Using the total stress intensity factors, the interface energy release rate and phase angles given in eqs. (1.31), (1.27) and (1.28), respectively, may be calculated.

1.3 Fracture toughness testing methods of laminate composites

Fiber reinforced polymer composites have emerged as important structural engineering materials because of their high stiffness to weight ratio or high strength to weight ratio. However, it has been observed that composites have poor resistance to delamination. Premature delamination may arise from various internal defects formed during manufacturing or as a result of in-service loading such as fatigue or impact events. These defects may result in delamination initiation and propagation. The delamination may reduce the strength and stiffness of the composite significantly. Fracture toughness characterization of composites is necessary in order to determine load-bearing capacity of a structure, which is important for design considerations.

A number of different test specimens have been developed for pure mode I, pure mode II and mixed mode I/II testing. All standards known today are limited to unidirectional (UD) composite, but have been used for multi-directional (MD) and woven fabric composite testing, as well.

In Section 1.3.1, the structure and differences between UD, MD and woven fabric composites will be discussed. The different fracture test methods used for pure mode I and pure mode II will be presented in Section 1.3.2. Mixed mode tests may be carried out on different specimen types. In Section 1.3.3, some of the most commonly used specimens for mixed mode testing will be discussed. Each specimen group will be presented in a different sub-section. Beam specimens will be mentioned in Section 1.3.3.1 where the MMB and MMELS specimens will be considered. The Arcan specimen will be discussed in Section 1.3.3.2. Finally, in Section 1.3.3.3, the BD specimen will be presented.

1.3.1 Material types: UD, MD and woven fabric composites

Different test methods exist for measurement of interlaminar fracture toughness of UD, MD and woven composites. In a UD laminate, all fibers are oriented in the same direction resulting in high strength and stiffness in that direction and relatively low strength and stiffness in the transverse direction. The majority of fracture toughness composite research has focused on UD laminates. Two ASTM standards (ASTM D5528-13, 2014; ASTM D6671M-13, 2014; ASTM D7905/D7905M-14,2014) , two ISO standards (ISO 15024:2001(E), 2011; ISO 15114:2014(E), 2014) and additional test methods (which have not yet been standardized) may be found in the literature for determination of interlaminar fracture toughness for mode I, mode II and mixed mode I/II conditions. All five existing standards are limited to UD composites, but have been used for UD, MD and woven fabric composites.

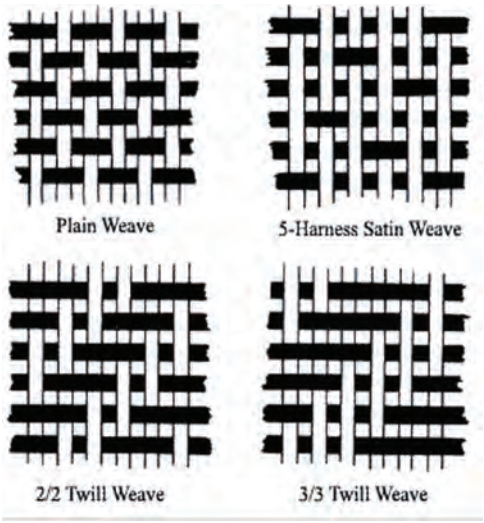

Figure 1.10: Several two-dimensional woven fabric structures (http://33.media.tumblr. com/tumblr_mch438Tl8m1qb86xo.gif, April, 2015).

In an MD laminate, the fibers in each lamina are in an optimized direction. Delamination growth occurs between plies and in both UD and MD composites, the propagation direction may not coincide with a fiber direction. Woven fabric composites are known to have higher impact resistance, fatigue resistance, fracture toughness and damage tolerance than UD laminates (Naik, 2003). These are commonly used for manufacturing composite structures. It has been shown in the literature that for woven fabrics the difference between initiation and propagation energy release rate is larger than in UD laminates. Moreover, the delamination is expected to be more tortuous, with a longer, less stable crack path (Feret et al., 2013).

Woven materials are fabricated on a loom from an interlacing yarn by means of an effective machine process with large areas of material fabricated at low cost (Dexter, 1998). The yarn is composed of bundled or twisted fibers and resin and considered transversely isotropic. The textile may be in the form of one of many patterns including plain, satin or twill weaves as shown in Fig. 1.10. A woven fabric is made from interlacing a yarn over and under an orthogonal yarn in a regular pattern, forming warp and weft. Warp indicates the longitudinal direction and weft indicates the transverse direction. Such a woven fabric may either have balanced or unbalanced properties. In a balanced fabric, both warp and weft directions contain the same fiber volume fraction. In an unbalanced woven fabric, the number of fibers per area, used for the warp and weft directions, is unequal. In the current investigation, one of the materials used is a balanced plain weave with tows in the warp oriented in the $+45°$-direction and those in the weft in the $-45°$-direction. This plain weave is referred to in this thesis as $+45°/-45°$.

The interlaced yarn of the woven fabric causes complicated fracture mechanisms. Fracture toughness values of woven composites may be influenced by many parameters such as deformation type, weave pattern, fabric geometry, manufacturing process, volume fraction

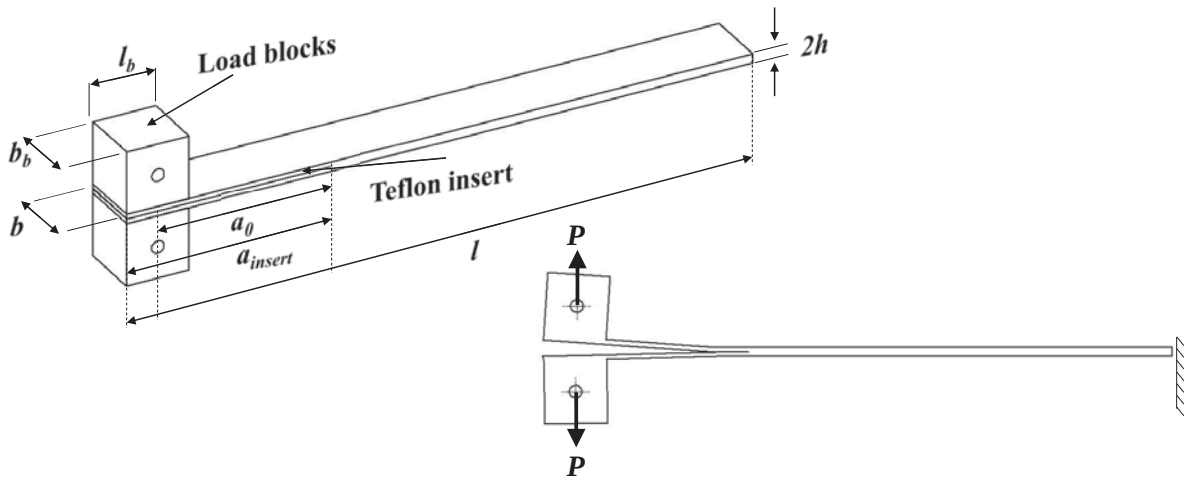

Figure 1.11: Double cantilever beam DCB specimen with piano hinges (ASTM D5528-13, 2014).

of the fibers in the yarn, volume fraction of the fibers in the fabric and the delamination propagation direction. These aspects have been of great interest to industry and research. Fracture toughness values for mode I, mode II and mixed mode may be obtained from tests. Currently, there are no standardized tests available for woven composites. However, modifications of the test methods known for UD composites have been used in the literature to investigate the behavior of these materials.

1.3.2 Modes I and II fracture toughness testing

Two standards are known today for fracture toughness delamination testing under mode I conditions, namely, the ASTM D 5528-13 (2014) and ISO 15024:2001 (2011) standards. Both make use of the double cantilever beam (DCB) specimen shown in Fig. 1.11. Use of the DCB specimen under displacement control, results in stable crack growth in starts and arrests as the displacement increases. Both standards are appropriate for determining the mode I fracture toughness $\mathcal{G}_{Ic}$ of CFRP and GFRP thermosets and thermoplastics. However, they are both limited to UD fiber reinforced composites. Regardless of these limitations, both methods have been used in numerous studies for UD composites (Kusaka et al., 1998; Tamuzs et al., 2001; Pereira and de Morais, 2004; Szekrényes and Uj, 2004) , MD composites (Choi et al., 1999; De Morais et al., 2003; Gong et al., 2010; Chocron and Banks-Sills, 2019) and woven fabric composites (Naik et al., 2002; Pereira et al., 2004; Banks-Sills et al., 2013; Simon et al., 2017).

For determining interlaminar mode II fracture toughness $\mathcal{G}_{IIc}$, many test specimens have been proposed in the literature. Two standardized specimens and two which have not been standardized will be considered here. The two standard mode II test methods are the ASTM D7905/D7905M-14 (2014) using an End Notched Flexure (ENF) specimen shown in Fig. 1.12a and the ISO 15114:2014(E) (2014) standard using a calibrated-end

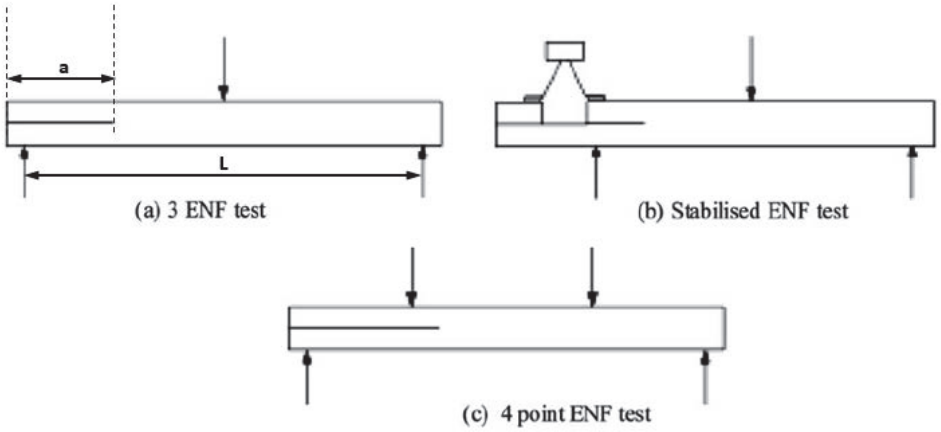

Figure 1.12: Mode II test specimens. (a) ENF (b) SENF and (c) 4ENF (Blackman et al., 2006).

loaded split (C-ELS) specimen shown in Fig. 1.13a. Two additional specimens discussed in this section are the stabilized ENF (SENF) specimen and the four point bending ENF (4ENF) specimen shown in Figs. 1.12b and 1.12c, respectively; both are variations of the ENF specimen.

The ENF specimen (Fig. 1.12a) has the same geometry as the DCB specimen. It is mentioned in the standard that tests may be carried out using the same specimen for both non-precracked and precracked toughness testing or by means of different specimens for only non-precracked toughness testing and for only precracked toughness testing. In the former case, the recommended specimen length is $a_i + l \geq 160$ mm, where $a_i + l$ is the total specimen length and a_i indicates the total insert length. In the latter case (different specimens for the precracked and non-precracked tests), the recommended specimen length is $a_i + l \geq 130$ mm. In both cases, the total insert length a_i shall be approximately 50 mm and greater than 45 mm so that $a_0 = 30$ mm, measured from the left loading roller to the insert tip. The recommended specimen width is 19 mm $\leq b \leq$ 26 mm; this should be measured at the three points of contact with the loading rollers and

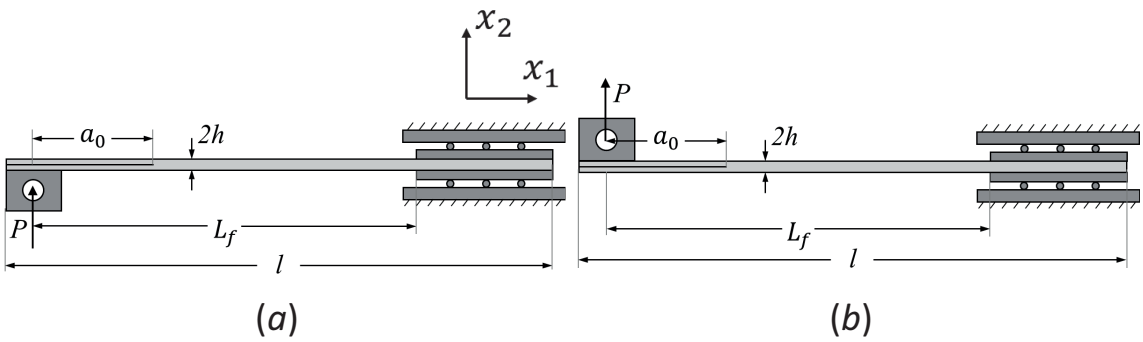

Figure 1.13: (a) Mode II calibrated-end loaded split (C-ELS) specimen (ISO standard 15114:2014(E), 2014) and (b) mixed mode end loaded split (MMELS) specimen.

the variations of these measurements shall not exceed 0.5 mm. Specimen recommended thickness is approximately 3.4mm $\leq 2h \leq$ 4.7mm and shall be measured six times, twice at each location the width is measured; the variations in specimen thickness shall not exceed 5% of the mean value. The three point bend loading device is utilized for this test. Use of the ENF specimen under displacement control results in non-stable delamination growth (ASTM D7905/D7905M-14, 2014). Many investigations related to specimen design and test analysis methods were carried out to improve the proposed ENF test design and procedure (Carlsson et al., 1986a; Davidson et al., 1995). Mode II fracture toughness tests using this method have been carried out on UD composites (Carlsson et al., 1986b; Aksoy and Carlsson, 1992; Davidson et al., 1995) and MD composites (Davidson et al., 1995; Ozdil et al., 1998; Pereira et al., 2004).

The SENF test (Fig. 1.12b) includes a feedback control procedure based on the delamination shear displacement. A Round Robin organized by the Versailles Project on Advanced Materials and Standards (VAMAS) concluded that this test procedure was too complex for an international standard.

The 4ENF test (Fig. 1.12c) is a modified version of the ENF specimen using four point flexure rather than three point. This procedure appears to resolve some problems found in the ENF test and offered three significant advantages: stable delamination propagation, a simple test fixture and a straightforward data analysis (Davies et al., 1998). Two main disadvantages of this test procedure are higher friction between delamination faces than was obtained in the ENF test and difficulties in measuring the delamination length (Blackman et al., 2006). Results from different 4ENF tests carried out at different laboratories were consistent and stable delamination propagation was achieved. From these tests significantly higher $\mathcal{G}_{IIc}$ values compared with results from ENF tests were obtained. These differences were examined in more detail by considering the influence of the loading roller diameter, specimen geometry and fixture compliance. The tested parameters were found to have minor effect (less than 5%) and a sufficient explanation for the measured differences was not provided from the investigation of these considered parameters (Davies et al., 1998).

The ELS and C-ELS specimens (Fig. 1.13a) are the same. The C-ELS procedure, presented in the ISO standard 15114:2014(E) (2014), uses the ELS test apparatus and specifies an experimental procedure to calibrate the clamping fixture and simultaneously determine the flexural modulus of the specimen. The ELS and C-ELS tests were used previously and improved before the latter was standardized (Wang and Williams, 1992; Blackman et al., 2006).

The C-ELS specimen is similar to the DCB specimen with a recommended total length $l = 190$ mm or $l \geq a_0 + 110$ mm, where a_0 is the starter delamination length, measured from the load-line as shown in Fig. 1.13a. The starter delamination length should satisfy the requirement that $a_0 \geq 50$ mm. This artificial delamination is then extended at

least 2 mm and no more than 5 mm in a mode I or mode II procedure, prior to testing. Delamination growth is unstable in mode II; hence, using this procedure for inducing a natural delamination is more complex and a detailed recommended procedure is specified in the standard. The recommended specimen width is $b = 20$ mm and may vary between 15 mm and 30 mm. Three width measurements shall be made and recorded at evenly spaced points along the specimen length. Specimen thickness is measured three times along the center line of the specimen and the maximum difference between measurements is prescribed to be lower than 0.1 mm where the required thickness shall be $2h \approx 3$ mm for a 0.6 fiber volume fraction of a CFRP specimen and $2h \approx 5$ mm for a 0.6 fiber volume fraction of GFRP specimen. Note that the specimens are prescribed to be UD. The test is carried out in displacement control and the load is transferred to the specimen through a load block which is loaded vertically and includes a pin to allow rotation of the bottom end of the specimen at the delamination end. A clamping arrangement creates free horizontal sliding of the specimen in the bearings but restricts vertical motion and rotation (see Fig. 1.13a). It is noted in the standard that an energy analysis predicted that the test is stable for approximately $0.75 > a_p/L_f > 0.55$, where a_p is the natural delamination length between the load-line and the tip of the natural delamination. Hence, stability may be improved by using larger values of a_p/L_f, but this will result in delamination propagation length reduction.

1.3.3 Mixed mode fracture toughness testing

Only one standard exists for mixed mode fracture tests of UD fiber reinforced laminate composites (ASTM D6671M-13, 2014). This standard utilizes the MMB specimen. Its main advantage is that various mode mixities may be achieved. Many other beam type specimens have been suggested for this type of testing, among them is the MMELS specimen. A test protocol based on Round Robins has been proposed for the MMELS specimen. All beam type specimens suitable for mixed mode testing which have not been standardized, including the MMELS, have a small number of mixed mode ratios which limits their usefulness. The MMB and MMELS will be discussed in Section 1.3.3.1. Other beam type specimens presented in the literature will be mentioned in that section, as well.

Other test methods and specimen configurations (not beam types) have been developed to achieve a wide range of mode mixities. Among these test methods, two will be described here: the Arcan specimen and the BD specimen. Both specimens enable a wide mode mixity range using one specimen and test setup. The Arcan specimen will be presented in Section 1.3.3.2 and the BD specimen will be discussed in Section 1.3.3.3.

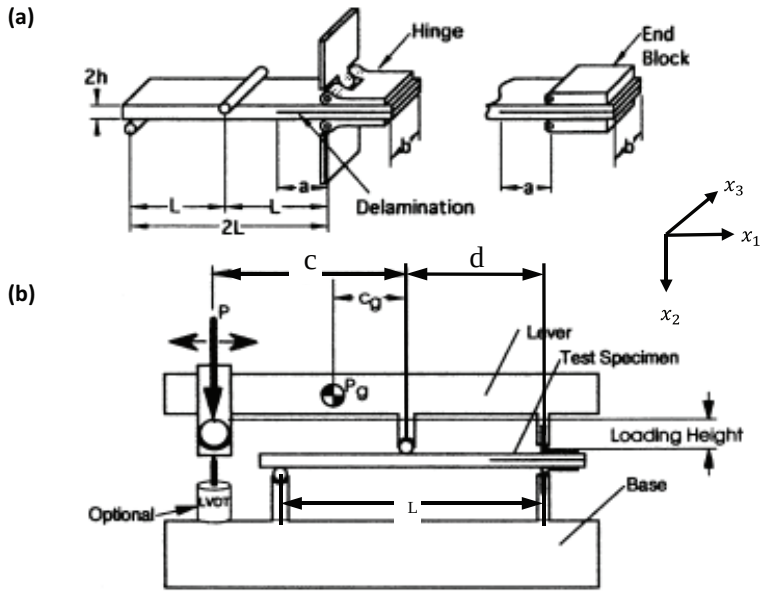

Figure 1.14: MMB test setup: (a) MMB specimen (b) MMB aparatus (ASTM D6671M-13, 2014)

1.3.3.1 Beam specimens: MMB and MMELS

The ASTM D6671M-13 (2014) standard, based on an MMB specimen and apparatus, is the only standardized test method for determining fracture toughness of CFRP and GFRP UD composites under mixed mode conditions. The main advantage of this test method is that it enables a wide range of mixed mode ratios using a single apparatus. The MMELS specimen, also known as the asymmetric double cantilever beam (ADCB) or the fixed ratio mixed mode (FRMM) test (Hashemi et al., 1990; Xiao et al., 1993; Choi et al., 1999; Blackman et al., 2001; Szekrényes and Uj, 2004) was utilized by ESIS and was part of a few Round Robin activities. Although this specimen may be used to obtain only a single mixed mode ratio, it utilizes the DCB specimen and the same apparatus used for the pure mode II ELS test. This may be useful for performing parallel DCB, ELS tests for pure modes I and II, and MMELS tests for a specific mixed mode ratio.

Many other beam type specimens have also been proposed and used for mixed mode delamination fracture toughness determination. Among these specimens are the single leg bending (SLB) (Davidson and Sundararaman, 1996, Szekrényes and Uj, 2004) and the single leg four point bend (SLFPB) test (Tracy et al., 2003), the crack lap shear (CLS) test (Ramkumar and Whitcomb, 1985, Lai et al., 1996), and the mixed mode flexure (MMF) test (Yoon and Hong, 1990a).

The MMB test specimen was first introduced by Reeder and Crews (1990) and after some modifications to reduce non-linearities, the method was standardized (ASTM D6671M-13 (2014)). The test specimen and apparatus are presented in Fig. 1.14a and

1.14b, respectively. In Fig. 1.14a, a is the delamination length measured from the load-line, b is the width of the specimen, L is the span length from the load-line and $2h$ is the thickness of the specimen. The test shall be conducted under displacement control with a constant displacement rate in the range of 0.5 mm/min and 5 mm/min. The load is applied through piano hinges or alternative tabs shown in Fig. 1.14a. In Fig. 1.14b, P is the applied load, c is the lever length of the MMB test apparatus, c_g and P_g are the length to center of gravity and the weight of the lever and attached loading apparatus, respectively. The overall specimen length is not critical, but should be about 137 mm; the width b is recommended to be between 20 mm and 25 mm and the thickness $2h$ is between 3 mm and 5 mm. The tested specimen contains an initial artificial delamination specified to be of length $2a$, approximately 50 mm long which is about 25 mm from the loading tabs. The initial delamination is obtained by inserting a non-adhesive insert during the layup stage of specimen manufacture.

The MMB test produces various mode mixities by varying the length of the lever arm c in Fig. 1.14b. The lever arm length c for a specific mode mixity in the range $0.15 \leq \mathcal{G}_{II}/\mathcal{G}_T \leq 0.95$ is obtained from an iterative solution using the energy release rates $\mathcal{G}_I$ and $\mathcal{G}_{II}$ and may be calculated as

$$\begin{aligned} c = \Big[& 0.167 + 0.000137\tilde{a}^2 - 0.108\sqrt{\ln(\tilde{a})}\,(\mathcal{G}_{II}/\mathcal{G}_T)^4 \\ & + \frac{-1400 + 0.725\tilde{a}^2 - 141\ln(\tilde{a}) - 302\ln(\mathcal{G}_{II}/\mathcal{G}_T)}{219 - 5000\,(\mathcal{G}_{II}/\mathcal{G}_T) + 55\ln(\tilde{a})} \Big] L \end{aligned} \tag{1.85}$$

where $\mathcal{G}_T$ is the total energy release rate given in eq. (1.14). and $\tilde{a}$ is defined as

$$\tilde{a} = \frac{a}{h\chi}\,. \tag{1.86}$$

The parameter χ is the delamination length correction parameter and is defined as

$$\chi \equiv \sqrt{\frac{E_{11}}{G_{13}}\left[3 - 2\left(\frac{\Gamma}{1+\Gamma}\right)^2\right]}\,. \tag{1.87}$$

In eq. (1.87), E_{11} is the longitudinal modulus of elasticity measured in tension, G_{13} is the out-of-plane or axial shear modulus which may be assumed equal to the in-plane shear modulus G_{12} and Γ is the transverse modulus correction parameter given as

$$\Gamma \equiv 1.18\frac{\sqrt{E_{11}E_{22}}}{G_{13}}\,, \tag{1.88}$$

where E_{22} is the transverse modulus of elasticity.

A specific mode mixity determines the ratio between the mode I energy release rate $\mathcal{G}_I$ and the mode II energy release rate $\mathcal{G}_{II}$. Linear elastic behavior is assumed in calculating the total mixed mode fracture toughness $\mathcal{G}_c$. This assumption is only valid when the

damage and non-linear deformation zones in front of the delamination are small compared to the specimen thickness. Three fracture toughness values may be obtained by this method. The first is for delamination initiation from an artificial delamination; the second is for delamination propagation. A third toughness value may be obtained by precracking the specimen which is not recommended. This value should be lower than the value of the fracture toughness measured with the artificial delamination. Depending on the mode mixity tested, the delamination will grow from the insert in either a stable or unstable manner where toughness values are attainable only when stable propagation takes place (ASTM D6671M-13, 2014).

The displacement is measured from the cross-head separation of the load frame or from an external gage attached to the MMB apparatus. If the load point displacement is measured from the cross-head separation, a load system compliance correction must be made to include the load frame and the MMB apparatus. Compliance calibration of the MMB testing system must be determined for each lever length c. The system compliance is determined using a calibration specimen which is a rectangular homogeneous bar at least as stiff as steel, with a known Young's modulus. The calibration specimen is loaded in the MMB apparatus and the slope of the load-displacement curve m_{cal} is measured. The compliance of the calibration specimen may be calculated by

$$C_{cal} = \frac{2L\left(c+L\right)^2}{E_{cal}b_{cal}^3} \ , \tag{1.89}$$

where E_{cal} and b_{cal} are the Young's modulus and the width of the calibration bar, respectively. The compliance of the MMB loading system is then given as

$$C_{sys} = \frac{1}{m_{cal}} - C_{cal} \ . \tag{1.90}$$

If the load point displacement is measured using an external gage or transducer, calibration correction is not necessary and $C_{sys} = 0$. Various equations are presented in the standard for different parameters, among them are the flexural modulus E_{1f}, the fracture toughness $\mathcal{G}_c$ and mode mixity $\mathcal{G}_{II}/\mathcal{G}_T$. The flexural modulus is given as

$$E_{1f} = \frac{8\left(a_0+\chi h\right)^3\left(3c+L\right)^2 + \left[6\left(a_0+0.42\chi h\right)^3 + 4L^3\right]\left(3c+L\right)^2}{16L^2bh^3\left(\dfrac{1}{m} - C_{sys}\right)} \ , \tag{1.91}$$

where a_0 is the initial delamination length, c is the lever length of the MMB test apparatus given in eq. (1.85), m is the slope of the load-displacement record of a tested specimen. The energy release rate for mode I may be calculated as

$$\mathcal{G}_I = \frac{12P^2\left(3c-L\right)^2}{16b^2h^3L^2E_{1f}}\left(a+\chi h\right)^2 \ , \tag{1.92}$$

where P is the critical load and a is the delamination length. The energy release rate for mode II may be calculated as

$$\mathcal{G}_{II} = \frac{9P^2\left(c+L\right)^2}{16b^2h^3L^2E_{1f}}\left(a+0.42\chi h\right)^2 \ . \tag{1.93}$$

The total mixed mode energy release rate $\mathcal{G}_T$ is a superposition of the two modes as shown in eq. (1.14). The energy release rate expressions presented in eqs. (1.92) and (1.93) were developed based on classical beam theory (Williams, 1988) with delamination length corrections of χh (Williams, 1989; Wang and Williams, 1992; Kinloch et al., 1993). The corrected equations were compared with FE results and good agreement was found (Bhashyan and Davidson, 1997). For critical conditions which will cause delamination growth, the total energy release rate in eq. (1.14) is equal to the fracture toughness value $\mathcal{G}_{Tc}$ for a specific ratio $\mathcal{G}_{II}/\mathcal{G}_{Tc}$. In some cases, the lever weight may cause significant loading of the MMB specimen and affect the measured toughness value. Corrections for such cases are available in the standard.

Interlaminar fracture tests under mixed mode loading conditions using the MMB specimen have been conducted for UD composites (Benzeggagh and Kenane, 1996; Pereira and de Morais, 2008), MD composites (Ozdil and Carlsson, 1999; Dharmawan et al., 2006; de Morais and Pereira, 2007; Pereira and de Morais, 2008) and woven fabrics (Gill et al., 2009; Feret et al., 2013). The study performed by Pereira and de Morais (2008) and the study performed by Feret et al. (2013) will be described here. In the study of Pereira and de Morais (2008), carbon fibers (T300) within a toughened epoxy manufactured from a prepreg (reference HS 160 REM) formed into laminates were investigated. DCB, ENF and MMB tests were conducted on unidirectional $(0_{34}//0_{34})$ and multi-directional laminates with the following layups: $[(0_2/90)_6/0_2//(0_2/90)_6/0_2]$, $[(0_2/90)_6/0_2//45/(0_2/90)_6/0_2]$,$[(0_2/90)_6/0_2//90/(0_2/90)_6/0_2]$, $[0_{10}// \pm 45/0_{10}/ \pm 45/0_{10}]$ and $[0_{10}//90/0_{12}/90/0_{10}]$. Note that two slashes indicate the position of the delamination. The tested specimens were obtained from laminate plates manufactured by hot plate pressing and cut with a water jet. All specimens had width $b = 20$ mm. The total specimen length l for the DCB specimen or the span length L between the load-lines for the ENF and MMB specimens, shown in Figs. 1.11, 1.14 and 1.12a, respectively, were $l, L = 160$ mm for UD specimens and $l, L = 200$ mm for MD specimens. In addition, the delamination length $a = 55$ mm and $a = 70$ mm were used for UD and MD specimens, respectively. Note that a_0 in Fig. 1.11 equals a. A delamination was formed using a 13 μm thick polytetrafluoroethylene (PTFE) film. A minimum of five specimens was tested for each method, mode mixity and layup. All tests were carried out in displacement control under a 2 mm/min loading rate which is in the loading rate range recommended in the ASTM DCB, ENF and MMB standards (ASTM D5528-13,2014; ASTM D7905/D7905M-14, 2014; and ASTM D6671M-13, 2014, respectively).

A beam model was developed for predicting the compliance and total energy release rate $\mathcal{G}_T$ for the MMB test. It consisted of superposition of both compliances and energy release rates calculated from the DCB and the ENF models and presented in Pereira and de Morais (2008). It could not be shown that these expressions coincided with those in the ASTM 6671M-13 standard (2014). The compliance of the beam model was compared with experimental data from the DCB, ENF and MMB tests. The comparison showed that

the beam model produced results with a 5% maximum difference from the experimental results.

DCB and ENF tests were carried out in previous studies (Pereira and de Morais, 2004; Pereira et al., 2004, respectively) and conducted again in Pereira and de Morais (2008) for various reasons such as verification of the $\mathcal{G}_{Ic}$ and $\mathcal{G}_{IIc}$ results. In the previous studies, specimens with a fiber volume fraction of $V_f = 58\%$ were tested in displacement control, under a displacement rate of 1 mm/min; whereas, in Pereira and de Morais (2008), the specimens tested had a fiber volume fraction of $V_f = 62\%$ and a loading rate of 2 mm/min was used. The results for the fracture toughness were found to be lower for the specimens with the higher fiber volume fraction. In the study carried out by Pereira and de Morais (2008), the $\mathcal{G}_{Ic}$ values found from DCB tests for UD [0°//0°] and MD [0°//45°] and [0°//90°] interfaces were 242, 264 and 245 N/m, respectively. These results are 14-20% lower than the 302, 323 and 284 N/m, respectively, found in Pereira and de Morais (2004). For the ENF tests, the $\mathcal{G}_{IIc}$ results were also lower for the higher volume fraction specimens. In the study made by Pereira and de Morais (2008), the $\mathcal{G}_{IIc}$ values for [0°//0°], [0°//45°] and [0°//90°] interfaces were found to be $847, 881$ and 909 N/m, respectively; whereas, in Pereira et al. (2004), the results were found to be $1115, 1082$ and 1621 N/m. The results found in 2008 are $19 - 24\%$ lower than the ones found in 2004 for the first two interfaces. The authors suggested that a possible reason for the difference in the results was the difference in the fiber volume fraction of the tested specimens.

In the MMB tests, the lever arm lengths c used (see Fig. 1.14) were between 40 mm and 280 mm for UD specimens and between 50 mm and 350 mm for MD specimens with a range of $\mathcal{G}_{II}/\mathcal{G}_T \approx 0.12 - 0.85$, where $\mathcal{G}_T$ is given in eq. (1.14). Misalignment of the loading axis and the center of mass of the lever and attachments may result in unwanted initial loading of the specimen. Therefore, the MMB fixture employed included a balancing weight at the end of the lever arm to avoid any initial loading. The delamination of the mode II dominated tests initiated in an unstable manner, as expected, with no intraply damage observed. Mode I dominated tests showed an unexpected minor instability causing an unclear initiation point in the load-displacement curve. Fiber bridging was observed in all layups and caused load increase after delamination initiation in the mode I dominant tests. Intraply damage was observed in the MD [0°//45°] and [0°//90°] layups.

An investigation of the effect of fiber volume fraction on mixed mode interlaminar fracture toughness was made by Feret et al. (2013). The material tested was a 5 harness satin (5HS) woven (as seen in Fig. 1.10) carbon/epoxy composite manufactured by resin transfer moulding (RTM). Mode I, mode II and mixed mode tests with mode ratios I/II of 3 : 1, 1 : 1, and 1 : 3 were carried out using the DCB, ENF and MMB methods, respectively. Each loading condition was repeated six times with a total of 60 specimens with fiber volume fractions of 57% and 66%. All specimens used in the investigation had a width of approximately 20 mm, average thickness of 4.4 ± 0.03 mm and total length

of 140 mm for the DCB and MMB specimens and 170 mm for the ENF specimens. The initial delamination was created in all specimens using a 10 μm thick Teflon film placed at the mid-plane. The length of the delamination from the load-line in the DCB and MMB specimens was 50 mm and 30 mm, respectively. Three different initial delamination lengths of 20 mm, 30 mm and 40 mm from the load-line were used for the ENF specimen. In all testing methods, the specimens were loaded in displacement control. The displacement rate for the DCB and MMB tests was 0.5 mm/min during loading and 25 mm/min during unloading. These loading rates are the slowest recommended in both the DCB and MMB standards (ASTM D5528-13, 2014; ASTM D6671M-13, 2014). The displacement rate used for the ENF test was 0.8 mm/min during loading and 1.6 mm/min during unloading. The recommended constant displacement rate mentioned in the ENF ASTM D7905/D7905M-14 (2014) standard is between 0.1 mm/min and 0.8 mm/min for loading and 0.1 mm/min and 1.6 mm/min for unloading.

Resistance to delamination R-curves were obtained for each specific mixed mode ratio and fiber volume fraction. During delamination propagation in both modes I and II dominated tests, the toughness values increased before reaching a stabilized propagation toughness plateau. Initiation and steady state propagation fracture toughness values were obtained from these R-curves. The steady state values were determined from the plateau part of each R-curve. The same R-curve behavior was also observed in an investigation made by Gill et al. (2009). In the investigation carried out by Feret et al. (2013), for all specimens and tested modes, regardless of the mixed mode ratio, the initial fracture toughness $\mathcal{G}_{Ic}$, $\mathcal{G}_{IIc}$ and $\mathcal{G}_{Tc}$ were found to be lower for the material with a higher fiber volume fraction. These results coincide with the findings for UD composites found for the critical energy release rates in Pereira et al. (2004) and Pereira and de Morais (2004, 2008). In a separate investigation of the same material, made by Gill et al. (2009), different results were found. Minimal variations in the initial fracture toughness values were obtained from mode I tests for specimens with different fiber volume fractions and inconsistent results were obtained from mixed mode tests with a higher mode II component.

A consistent trend for the plateau propagation toughness values was not found from the results. The explanation for this was that the plateau propagation values were affected by both fiber volume fraction and mode ratio. For the material with a higher fiber volume fraction, with a high mode I component, the propagation toughness values were found to be higher and for a high mode II component, lower than the values obtained for the lower fiber volume fraction material. It may be noted that fewer results were obtained for the high mode II component tests because the plateau region was not reached as a result of increased delamination instability.

A fractographic analysis was made and three toughening mechanisms were discussed which included non-planar fiber architecture, fiber bridging and shear hackles. The non-planer fiber architecture caused a tortuous, longer delamination path, resulting in a higher

energy requirement for additional fracture surfaces. An intraply toughening mechanism called fiber bridging caused the propagating delamination to arrest. This resulted with the need of additional energy for the delamination to grow and overcome the tensile strength of the bridging fibers. For all mixed mode ratios, as the mode II contribution increased, fiber bridging complexity increased and shear hackles in the resin, between weft fibers, perpendicular to the direction of the delamination growth, were observed. The latter was believed to be the major energy dissipating mechanism at high mode II. These toughening mechanisms provide an explanation for the results obtained and described above for the propagation toughness values for a higher mode I contribution versus a higher mode II contribution. For a high mode I contribution, fiber bridging is the most dominant mechanism; hence, a higher fiber volume fraction results with higher propagation toughness values. For a high mode II contribution, the shear hackle mechanism is dominant and the resin becomes dominant. This leads to a lower propagation toughness in the case of a higher fiber volume fraction. It was also mentioned that fiber volume fraction has a negligible effect on the propagation toughness when these two mechanisms are balanced. For this material, a balance was reached at an approximately 75% mode II contribution.

The main advantage of the MMB test is that it enables testing of a wide range of mixed mode ratios by simply relocating the lever arm of the apparatus (see Fig. 1.14b). However, the MMB test does not include pure modes I and II testing; hence, both DCB and ENF specimens and test setups are necessary for obtaining all in-plane mode combinations. The advantage of the MMELS specimen is that testing requires the same fixture as that used for the C-ELS geometry (Fig. 1.13a). The only difference is that in a C-ELS test, the load is applied to the lower specimen leg causing both legs to move together (see Fig. 1.13a) and in the MMELS test the load is applied only to the upper leg allowing the bottom leg to deform freely (see Fig. 1.13b).

The MMELS test protocol (Blackman et al., 2001) prescribes a test procedure for determination of the fracture toughness resistance curve of UD CFRP or GFRP composites under a fixed mixed mode I/II deformation ratio of 4/3 (for the case of a delamination located at mid-plane). The protocol includes the recommended specimen dimensions presented in the ISO standard 15114:2014(E) (2014) for the C-ELS specimen and is summarized in Section 1.3.2, here. It is noted in the protocol that the free length of the specimen L_f (see Fig. 1.13b) is generally 100 mm but may be shorter for promoting delamination propagation in some materials. An initial delamination is created using a starter film insert as thin as possible with maximum thickness of 13 μm and at least 50 mm long from the load-line, placed at mid-plane during moulding. A natural delamination may be obtained in mode I by either a DCB rig or by a wedge opening procedure. Alternatively, mode II deformation or a mixed mode I/II test procedure may be used to obtain the natural delamination.

The test is conducted under displacement control at a constant rate between 1 mm/min

for specimens in which the specimen length $l = 170$ mm (see Fig. 1.13b) and 5 mm/min for longer specimens. The load and displacement signals are recorded. The delamination length is to be measured visually using a traveling microscope in increments of 1 mm or less in the first 5 mm of delamination propagation. After that, it should be measured in 5 mm increments. For the last 5 mm of delamination propagation, the delamination length should be measured in increments of 1 mm. The ideal maximum delamination growth should be 40 mm with a minimum distance of 10 mm from the clamped end. Once the maximum delamination length is reached, the specimen is completely unloaded at a constant rate of 25 mm/min (or less). A minimum of five specimens should be tested and stable delamination growth is expected. Analysis of the test results may be carried out using two different methods, the corrected beam theory (CBT) or the experimental compliance method (ECM).

Using CBT, the total energy release rate $\mathcal{G}_T$ is given as the sum of the $\mathcal{G}_I$ and the $\mathcal{G}_{II}$ components where

$$\mathcal{G}_I = \frac{3P^2\left(a + \Delta_I\right)^2}{b^2 E_{1f} h^3} F \ , \tag{1.94}$$

$$\mathcal{G}_{II} = \frac{9P^2\left(a + \Delta_{II}\right)^2}{4b^2 E_{1f} h^3} F \ . \tag{1.95}$$

In eqs. (1.94) and (1.95), P is the load, a is the delamination length measured from the load-line and Δ_I and Δ_{II} are the delamination length corrections for the mode I and II components, respectively. A detailed explanation for obtaining the delamination length correction for mode I may be found in the ISO 15024:2001(E) (2011) standard. The correction for mode II is determined from $\Delta_{II} = 0.42\Delta_I$. The width and thickness of the specimen are b and $2h$, respectively, and E_{1f} is the flexure modulus, parallel to the fiber direction. The flexural modulus may be determined from an independent measurement with a separate three-point bend test or from a clamp calibration test (Blackman et al., 2006) and calculated as

$$E = \frac{1}{2b(hn)^3} \tag{1.96}$$

where n is the slope of a plot of the cube-root of the compliance versus free length L_f. The compliance is calculated as

$$C = \frac{d}{P} \tag{1.97}$$

where both the machine load P and the corresponding machine displacement d are recorded during the test. In eqs. (1.94) and (1.95), F is a correction for large displacements, given by

$$F = \left[1 - \theta_1 \left(\frac{d}{L_f}\right)^2 - \theta_2 \left(\frac{dl_1}{L_f^2}\right)\right] \tag{1.98}$$

where d is the machine displacement, l_1 is the distance from the center of the load block to the mid-plane of the specimen and L_f is the free length of the specimen (see dimensions

in Fig. 1.13b). The factors θ_1 and θ_2 are calculated as

$$\theta_1 = \frac{3}{20} \frac{\left[15 + 150\left(\frac{a}{L_f}\right)^2 + 367\left(\frac{a}{L_f}\right)^4\right]}{\left[1 + 7\left(\frac{a}{L_f}\right)^3\right]^2} \tag{1.99}$$

$$\theta_2 = 3\left(\frac{L_f}{a}\right) \frac{\left[1 + 7\left(\frac{a}{L_f}\right)^2\right]}{\left[1 + 7\left(\frac{a}{L_f}\right)^3\right]} \, . \tag{1.100}$$

Analysis of the test results by means of ECM is based on experimental results for the delamination length a and the compliance C shown in eq. (1.97). The mixed mode energy release rate $\mathcal{G}_T$ may be calculated as

$$\mathcal{G}_T = \frac{3P^2 m a^3}{2b} F \tag{1.101}$$

where the load and specimen width are defined as P and b, respectively, and m is the slope from the plot of the compliance C versus the cubed delamination length a^3. The delamination length a is measured visually by means of a traveling microscope from the load-line and F is the correction factor defined in eq. (1.98). The separate modes I and II energy release rates may be found based on the fact that $\mathcal{G}_I/\mathcal{G}_{II} = 4/3$, hence

$$\mathcal{G}_I = 0.57\mathcal{G}_T \tag{1.102}$$

$$\mathcal{G}_{II} = 0.43\mathcal{G}_T \, . \tag{1.103}$$

Resistance curves or R-curves of $\mathcal{G}_I$ and $\mathcal{G}_{II}$ versus the delamination length are obtained. It is noted that a minimum of 15 points shall be recorded for each specimen.

For specimens with different arm thickness

$$\frac{\mathcal{G}_I}{\mathcal{G}_{II}} = \frac{1}{3}\left[\frac{h_1}{h_2}\left(1 + \frac{h_1}{h_2}\right)\right]^2 \tag{1.104}$$

where h_1 and h_2 are the distance between the top of the specimen and the film insert and between the film insert and the bottom of the specimen, respectively (see Fig. 1.13b). Another problem is friction and potential micro-cracking ahead of the delamination front. It may be noted that high mode II MMB tests suffer from the same problem but to a greater extent. The results of the test may be analyzed using CBT which requires additional tests (DCB for obtaining the delamination correction length Δ_I and a method for obtaining the flexure modulus E_{1f}). If the results are analyzed using ECM, then insufficient delamination propagation or unstable delamination growth may cause inaccurate results (Blackman et al., 2001).

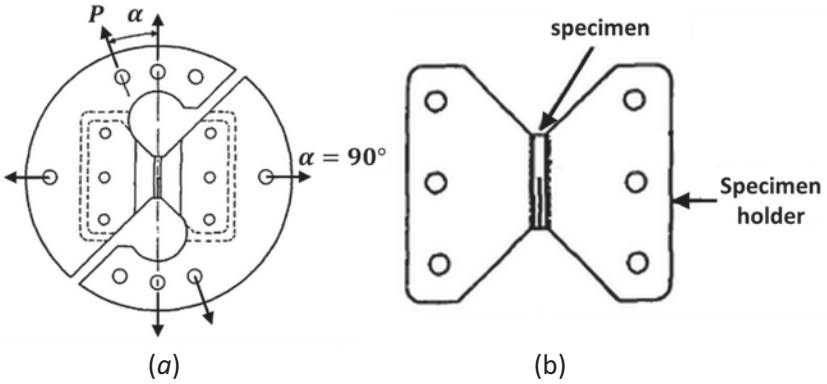

Figure 1.15: Arcan specimen: (a) loading fixture for pure shear and mixed mode interlaminar fracture testing and (b) specimen and holder (Arcan et al., 1987).

1.3.3.2 Arcan specimen

Although the MMELS method is simple there are some problems with the test procedure and analysis method. The most significant problem is that only one mixed mode ratio may be obtained. This ratio is independent of the delamination length and is nearly constant for UD composites. The ratio may be found from the relation of the mixed mode ratio and film location.

The Arcan specimen holder and loading fixture presented in Fig. 1.15 are one of many configurations appearing in the literature for mode II and mixed mode testing of laminate composites. Specimen shapes and arrangements are presented in Fig. 1.16, where specimens shown in Figs 1.16a–1.16c are used for shear modulus testing and specimens shown in Figs. 1.16d–1.16g are used for mode II and mixed mode fracture testing. It

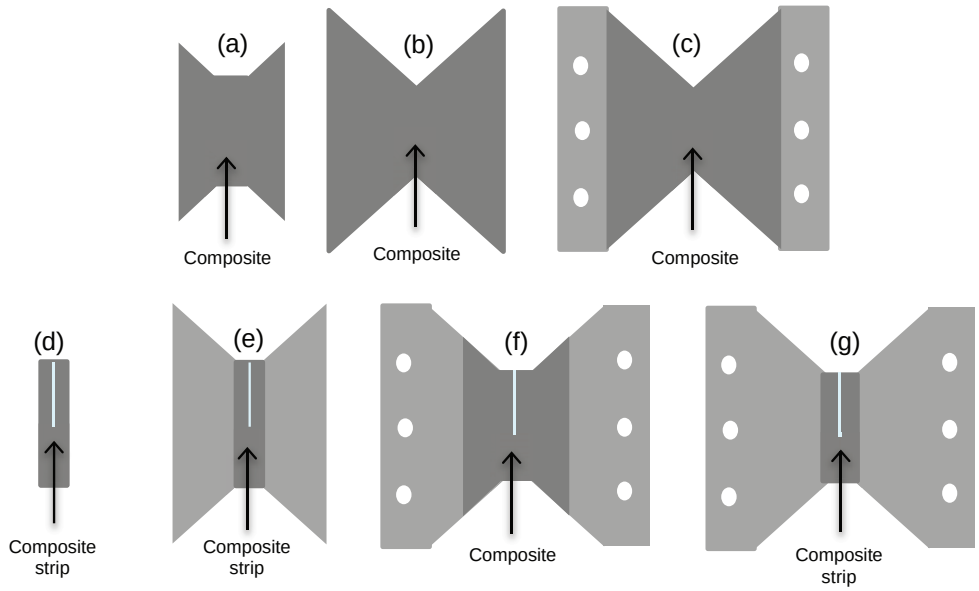

Figure 1.16: Arcan specimen configurations: (a-c) for shear modulus determination and (d-g) for mode II and mixed mode testing.

should be noted that the specimen and fixture described here are not the original one proposed by Arcan. The Arcan specimen was originally designed to measure the shear modulus of composite materials (Arcan et al., 1978). A modified specimen was later proposed for mode II and mixed mode fracture testing (Banks-Sills et al., 1984). The Arcan test was designed based on the existence of a uniform two-dimensional stress field. This region was investigated using a homogeneous photoelastic specimen without a crack. The stress field was obtained by means of FE and photoelastic analyses. Although a dominant shear region in an uncracked specimen was found for the range of loading angles between $0^\circ \leq \alpha \leq 20^\circ$ (see Fig. 1.15a)(Banks-Sills et al., 1984), the Arcan specimen has been used in many fracture toughness investigations (Yoon and Hong, 1990b; Nikbakht and Choupani, 2008; Choupani, 2008; Nikbakht and Choupani, 2009 and Heydari et al., 2011) for all loading angles α, with and without angular limitations.

The Arcan test specimen may be attached to the fixture in different ways. The original design tested by Banks-Sills et al. (1984) included a butterfly shaped specimen glued to the fixture (see Fig. 1.16a). Later, a common configuration, used in many investigations, included a specimen holder with two or three pins at each end as shown in Figs. 1.16c, 1.16f, and 1.16g. In each case, the composite specimen was designed differently to reduce local stress raisers and make use of a smaller composite body. The fixture to fit this design is presented in Fig. 1.15a. Loading is applied through a pair of holes located on opposite sides of a diameter. The shape of the loading fixture and holder create deformation between pure mode I and pure mode II. Various combinations of modes I and II deformation are obtained by rotating the fixture. Each loading angle, α in Fig. 1.15a, creates a different combination of mixed mode conditions.

Many variations of the Arcan fixture and specimen have been proposed in the literature. Another specimen type used included a rectangular specimen and holder together with a circular Arcan fixture (Rikards, 2000). It may be noted that this specimen does not have the desired uniform field in an uncracked specimen. The results obtained from tests using this specimen are less reliable than those obtained with the Arcan specimen (Banks-Sills, 2015).

Mixed mode fracture delamination tests using the Arcan specimen were made for different interfaces. Choupani (2008) investigated the fracture toughness of adhesive/adherent joints. Different types of composites have also been characterized using this test method, for example, Yoon and Hong (1990b) investigated UD composites and Nikbakht and Choupani (2008), tested MD composites. Woven fabric composites were also tested using the Arcan specimen by Nikbakht and Choupani (2009) and Heydari et al. (2011). The investigations made by Yoon and Hong (1990b), Choupani (2008) and Heydari et al. (2011) will be summarized here.

Interlaminar fracture behavior characteristics of a unidirectional graphite/epoxy composite laminate were evaluated experimentally with the Arcan test by Yoon and Hong

(1990b). The specimen configuration used is presented in Fig. 1.16d and was glued to the fixture without the holder. Seven different loading angles were tested with between three to six specimens for each loading angle. Results showed that the mode I stress intensity factor remained almost constant for loading angles larger than 15° while the mode II stress intensity factor decreased monotonically with an increase in the loading angle from 0° (pure mode II) to 90° (pure mode I). The energy release rate values obtained were 60.0 N/m for $\mathcal{G}_{Ic}$ and 312.0 N/m for $\mathcal{G}_{IIc}$. The fracture toughness in terms of K_{Ic} and K_{IIc} were not explicitly given but may be obtained from analytical expressions given in the article. An empirical mixed mode fracture criterion in the form of

$$\left(\frac{K_I}{K_{Ic}}\right)^m + \left(\frac{K_{II}}{K_{IIc}}\right)^n = 1 \tag{1.105}$$

was used to model the fracture behavior under mixed mode deformation. Yoon and Hong (1990b) found that their experimental results showed a good fit for $m = 2$ and $n = 3$. In their investigation, it was noted that the Arcan test produced unstable delamination growth.

Fracture of adhesive joints constructed from several combinations of adherends (composite and metal) was considered by Choupani (2008). Experiments were carried out using the Arcan specimen presented in Fig. 1.16g. In the middle of the adhesive layer, a starter crack was introduced using a non-adhering film. For each loading angle, at least three tests were carried out with a total of 63 specimens with different adherends tested. Results showed that the relationship between mode I, mode II, and mixed mode fracture toughness of all adherends was $\mathcal{G}_{Ic} \leq \mathcal{G}_{Tc} \leq \mathcal{G}_{IIc}$, where $\mathcal{G}_{Tc}$ is given in eq. (1.14) and is the critical value at fracture for the specific mixed mode ratio $\mathcal{G}_{II}/\mathcal{G}_{Tc}$. Crack growth between the aluminum adherend tested was predominately cohesive, mostly in the middle of the adhesive layer. In the steel adherends, the crack growth was almost cohesive with no distinct pattern of the movement between the adhesive/adherend upper and lower interfaces. For the woven carbon fiber/polyetherimide (CF/PEI) composite adherends, the crack initiated in the adhesive, running into the adhesive/adherend interface. Results showed that the mode I stress intensity factor increased and the mode II stress intensity factor decreased with an increase in the loading angle from 0° (pure mode II) to 90° (pure mode I) for all adherends tested. The fracture toughness values obtained for K_{Ic} were 0.76 MPa$\sqrt{\text{m}}$, 0.65 MPa$\sqrt{\text{m}}$ and 0.47 MPa$\sqrt{\text{m}}$ for the aluminum, CF/PEI composite and steel adherends, respectively. The fracture toughness values obtained for K_{IIc} were 1.24 MPa$\sqrt{\text{m}}$, 0.81 MPa$\sqrt{\text{m}}$ and 0.88 MPa$\sqrt{\text{m}}$ for the aluminum, CF/PEI composite and steel adherends, respectively. It was also noted that the results obtained with specimens fabricated from composite adherends fit well with the criterion presented in eq. (1.105) for values of $m = 2$ and $n = 3$.

Heydari et al. (2011) carried out an experimental and numerical investigation of a carbon/polyester woven composite. The tested specimens were composed of 130 woven

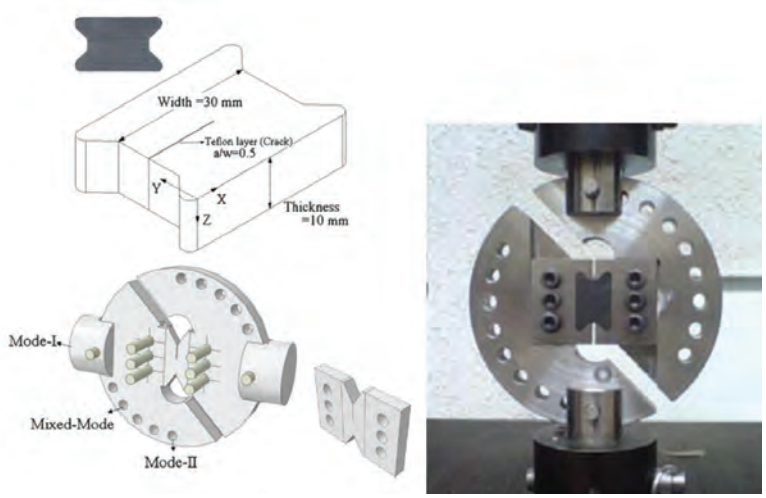

Figure 1.17: Modified Arcan specimen and fixture (Heydari et al., 2011).

plies, with the direction of the fibers and the edge delamination coinciding. Each ply was approximately 0.2 mm thick. The starter delamination was obtained using a 0.1 mm thick Teflon film inserted in the middle of the laminate. Tests were carried out using a modified version of the Arcan specimen (see Fig. 1.17) under a full range of mode mixities which were produced by varying the loading angle α ($\alpha = 0°, 15°, 30°, 45°, 60°, 75°$ and $90°$, see Fig. 1.15), from pure mode II to pure mode I. The modified Arcan specimen was attached to the fixture by three pins on each side (see Fig. 1.17). The grips of the fixture were loaded in tension. Tests were conducted in displacement control with a displacement rate of 0.5 mm/min and repeated at least three times for each loading angle.

Using a finite element, linear elastic analysis of the entire apparatus and specimen, under plane strain conditions, a relation between the non-dimensional stress intensity factors and crack length was obtained. The mechanical properties used in the analysis are presented in Table 1.5. Using a conservative two-dimensional M-integral, non-dimensional stress intensity factors were determined for non-dimensional delamination lengths a/W between 0.1 and 0.8, where a is the delamination length and W, the specimen width (see Fig. 1.17). It must be noted that in the article, the equations for the auxiliary stress field in the vicinity of the delamination front were given for an isotropic material rather than for the tetragonal material tested. Yet, it appears that the stress calculation was made using Abaqus software auxiliary functions and that the given equations were not used. Therefore, it may be assumed that the calculations are correct. Using fourth order

Table 1.5: Elastic properties of carbon-polyester laminated composite.

$E_1 = E_2$ (GPa)	E_3 (GPa)	$G_{13} = G_{23}$ (GPa)	G_{12} (GPa)	$\nu_{13} = \nu_{23}$	ν_{12}
43.7	8.2	2.6	6.4	0.31	0.037

polynomial expressions, the geometrical factors necessary for calculating the critical stress intensity factors for the modified Arcan specimen, were derived. From the obtained results, it was observed that both the mode I and mode II non-dimensional stress intensity factors increased with increasing delamination length. Large changes were observed in the former and minor changes in the latter. A graph of non-dimensional stress intensity factors versus loading angle revealed that the non-dimensional mode II stress intensity factors decreased but remained dominant for increasing loading angles from 0° (pure mode II) to 15° and that the mode I stress intensity factor increased and remained dominant for loading angles between 30° and 90° (pure mode I).

For each loading angle, using the fracture loads, together with the calibration equations, the interlaminar fracture toughness and critical energy release rates for mode I and II were obtained. The interlaminar mode I fracture toughness, K_{Ic} was found from pure mode I tests ($\alpha = 90°$) as 1.08 MPa$\sqrt{\text{m}}$. This value was lower than the interlaminar mode II fracture toughness, K_{IIc} which was found from pure mode II tests ($\alpha = 0°$) as 1.20 MPa$\sqrt{\text{m}}$, meaning that the material is tougher in in-plane shear deformation than in opening deformation.

Critical energy release rates were calculated based on the stress intensity factor failure values, apparently, using relations given by Sih et al. (1965) and Banks-Sills et al. (2005a) for an orthotropic material. They were plotted as a function of the ratio $\mathcal{G}_{II}/\mathcal{G}_T$ where $\mathcal{G}_T$ is given in eq. (1.14). It was observed from the graph that for $\mathcal{G}_{II}/\mathcal{G}_T \leq 0.53$, $\mathcal{G}_I$ decreased as $\mathcal{G}_{II}/\mathcal{G}_T$ increased and remained dominant; above this value, the increasing $\mathcal{G}_{II}$ value became dominant.

1.3.3.3 Brazilian disk specimen

In order to obtain a wide range of mode mixities, using a simple test set up and only one specimen type and fixture, it has been decided to carry out mixed mode fracture tests, in the current investigation, using the Brazilian disk (BD) specimen. The BD specimen has been used in mixed mode fracture tests of many types of interfaces. In this section, investigations including isotropic and interface cracks between two isotropic materials will be presented, as well as investigations of UD and MD composite laminates.

Isotropic and interface cracks between two isotropic materials have been tested using the BD specimen. There are different methods, described in the literature, for measuring fracture properties of a linear elastic, homogeneous, isotropic material and of a crack along the interface between two linear elastic, homogeneous, isotropic materials. In order to carry out mixed mode tests, one method makes use of a BD specimen.

A BD specimen composed of homogeneous material is presented in Fig. 1.18a. The load P is applied at an angle ω with respect to the crack which may be varied to achieve different mixed mode combinations. A central crack of length $2a$ is located in the middle

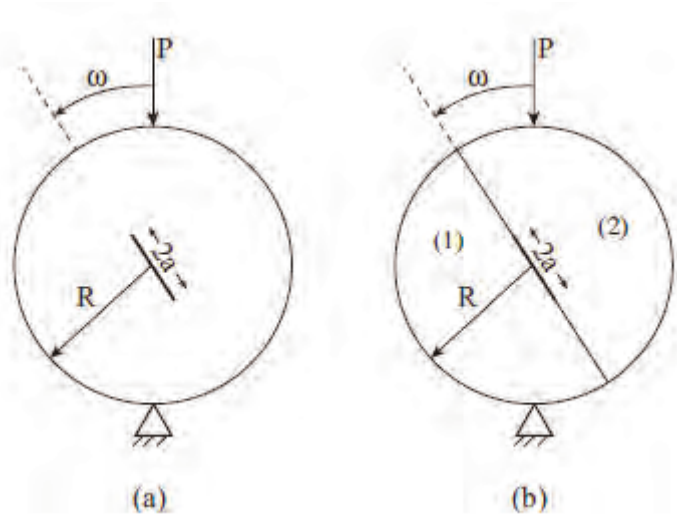

Figure 1.18: Brazilian disk specimen ($\omega > 0$): (a) homogeneous material (b) interface crack between two isotropic, homogeneous materials.

of the specimen and the specimen diameter is $2R$. Atkinson et al. (1982) presented an explicit series solution for the stress intensity factors valid for any orientation ω of the BD specimen. It was noted that the crack closed for angles between $21.3° - 27.2°$ for a normalized crack length of $0.3 \leq \ a/R \leq 0.6$. The stress intensity factors from this derivation were compared for different loading angles and crack lengths with previous numerical results. The comparison showed differences of less than 10% for a two term solution and no discernible differences for a five term solution. Another solution based on a small crack approximation was obtained and compared with results from both the series solution and finite element (FE) analyses. This comparison showed that the small crack approximation was quite good. Finally, the feasibility of using the BD specimen as a reliable method to investigate the problem of combined mode fracture was demonstrated by conducting tests on a homogeneous polymethyl methacrylate (PMMA) BD specimen with a diameter of 1.5 in. and an approximate thickness of 0.125 in. Test results were obtained for both modes I and II.

This specimen was then utilized to determine the interface toughness for two perfectly bonded homogeneous, isotropic materials (Banks-Sills et al., 1999 and Banks-Sills et al., 2000). Unlike the case of a homogeneous material, each time a different material pair is tested, a new set of calibration equations is required. A calibration equation relates the stress intensity factors to the loading and geometric parameters. In those studies, a normalized complex stress intensity factor was given in terms of the non-dimensional crack length a/R for different values of the loading angle ω. A methodology including analysis of experimental results for two different material pairs was presented. The dimensions of the BD specimen used had a nominal radius $R = 20$ mm, a nominal thickness $t = 8$ mm and a varying central crack of length $2a$ along the interface (see Fig. 1.18b). The load P was applied at an angle ω which was varied to achieve different mixed mode combinations.

In both investigations, the methodology for obtaining the total complex stress intensity factor $K^{(T)}$ was described. The superscript T indicates total which is the superposition of the stress intensity factors resulting from applied loading (f) and residual curing stresses (r). The stress intensity factors caused by applied loading were calculated using two-dimensional FE analyses together with the interaction energy or M-integral which was previously described in Section 1.2.2. For a unit load and a unit specimen thickness, $K_1^{(f)}$ and $K_2^{(f)}$ were obtained for a set of specific loading angles ω and a set of non-dimensional crack lengths a/R. The set of non-dimensional stress intensity factors $\tilde{K}_1^{(f)}$ and $\tilde{K}_2^{(f)}$ were calculated from the results, using

$$\tilde{K}^{(f)} = \frac{2\pi R t a^{i\varepsilon}}{P\sqrt{\pi a}} K^{(f)} \,, \tag{1.106}$$

where R and t are the radius and thickness of the specimen, respectively, a is the half-crack length, P is applied load as seen in Fig. 1.18b and ε is the oscillatory parameter given in eq. (1.19). The stress intensity factors $\tilde{K}$ and K are complex, see eq. (1.22). Curve fitting of the calculated $\tilde{K}_1^{(f)}$ and $\tilde{K}_2^{(f)}$ produced the calibration equations. After the tests were completed, for specific values a_{cr}/R and ω, $\tilde{K}_1^{(f)}$ and $\tilde{K}_2^{(f)}$ were calculated from the corresponding calibration equations. The stress intensity factors $K_1^{(f)}$ and $K_2^{(f)}$ were then determined from eq. (1.106) with the measured values of P_{cr}, a_{cr}, R and t from the tests.

The stress intensity factors caused by residual stresses were calculated using calibration equations, as well. The temperature change experienced by the specimens during curing caused residual stresses in the specimens. The stress intensity factors were determined by use of a weight function method, presented by Banks-Sills (1993), and two-dimensional FE analyses. For a set of non-dimensional crack lengths and a $\Delta\vartheta = 5°\text{C}$ temperature decrease, $K_1^{(r)}$ and $K_2^{(r)}$ were obtained. Non-dimensional stress intensity factors were calculated from

$$\tilde{K}^{(r)} = \frac{K^{(r)} \hat{a}^{i\varepsilon}}{\sigma\sqrt{\pi a}} \,, \tag{1.107}$$

where

$$\sigma = \frac{\left[(1-\nu_1)\,\alpha_1 - (1-\nu_2)\,\alpha_2\right]\Delta\vartheta}{\dfrac{1}{\overline{E}_2} - \dfrac{1}{\overline{E}_1}} \,, \tag{1.108}$$

for given values of $\nu_k, \overline{E}_k$ and α_k $(k = 1, 2)$. In eq. (1.108), the parameters α_k are the thermal expansion coefficients of each material and the parameters $\overline{E}_k$ are defined in eq. (1.16); the subscripts $k = 1, 2$ represent the upper and lower materials, respectively. Curve fitting of the calculated values of $\tilde{K}_1^{(r)}$ and $\tilde{K}_2^{(r)}$ produced calibration equations for the normalized residual stress intensity factors $\tilde{K}_1^{(r)}$ and $\tilde{K}_2^{(r)}$ in terms of a/R. Use of these equations was made for each fracture test to calculate the values of $\tilde{K}_1^{(r)}$ and $\tilde{K}_2^{(r)}$ for a critical normalized crack length a_{cr}/R. Finally, the stress intensity factors $K_1^{(r)}$ and $K_2^{(r)}$ were determined from eq. (1.107), for test values of $\Delta\vartheta$, σ and a_{cr}.

Superposition of the stress intensity factors, $K_1^{(f)}$ and $K_2^{(f)}$, resulting from applied load, and $K_1^{(r)}$ and $K_2^{(r)}$, resulting from specimen curing, yielded the values of $K_1^{(T)}$ and $K_2^{(T)}$. In turn, the critical energy release rate $\mathcal{G}_{ic}$ for each test was computed from eq. (1.31). It may be noted that a two-dimensional analysis was considered here, so that K_{III} was omitted. The phase angles $\hat{\psi}$ were obtained from eq. (1.27) for $\hat{L} = 600$ μm for the glass/epoxy specimens and $\hat{L} = 100$ μm for the ceramic pair of materials. The oscillatory parameter was found from eq. (1.19) to be $\varepsilon = -0.088$ for the glass/epoxy interface and $\varepsilon = -0.00563$ for the interface between the ceramic pair of materials. In each case, the $\mathcal{G}_{ic}$ values were plotted as a function of $\hat{\psi}$.

In Banks-Sills et al. (1999), results for the interface between glass and epoxy were presented. The specimens were composed of two semi-circles: the first made of glass and the second epoxy with an aluminum arc about the epoxy. The specimens were cured in an oven at 25°C. An initial notch was fabricated along the interface by means of Teflon strips. Natural cracks with 9.01 mm$\leq a_c \leq$ 11.32 mm were developed with a loading angle of 5° and a maximum pre-load $P \leq 1500$ N. The specimens were tested at room temperature so that $\Delta\vartheta$ varied between -4.5°C and $+2.3$°C. Twenty-five tests were carried out with a range of loading angles between $-10° \leq \omega \leq 13°$ (see Fig. 1.18b). The test results were presented and discussed in Banks-Sills and Ashkenazi (2000). To obtain the failure curve in eq. (1.33) with $\phi = 0$, the value of $\overline{\mathcal{G}}_{1c}$ was calculated to be 5.12 N/m.

In Banks-Sills et al. (2000), the interface between two ceramic clays, K-142 and K-144 was considered. The fabrication process included heating and cooling with temperature holding steps. The range of critical crack lengths was measured as 5.4 mm $\leq a_c \leq$ 6.4 mm. Thirty-one tests were carried out with a range of loading angles between $-15° \leq \omega \leq 15°$. The value of $\overline{\mathcal{G}}_{1c}$ was found to be 3.7 N/m and a criterion was then found from eq. (1.33) with $\phi = 0$. In both investigations, the test results fit the trend of the failure curve well, with observed scatter.

In Banks-Sills et al. (2010), the necessity of using a three-dimensional approach to predict interface fracture, when in-plane loading is applied, was investigated. The two material pairs of glass/epoxy and the ceramic clays were reconsidered using two and three-dimensional analyses. Stress intensity factors resulting from applied load and residual stresses were obtained by means of the FE method with an interaction energy integral. Stress intensity factors for the applied force $K_1^{(f)}$ and $K_2^{(f)}$ were obtained by means of the two-dimensional M-integral with the appropriate crack length and applied force. There was a maximum difference of 0.9% and -1.2% in the results obtained here as compared to those obtained in Banks-Sills et al (1999) for the glass/epoxy specimens and Banks-Sills et al. (2000) for the two ceramic clay specimens, respectively. Stress intensity factors resulting from residual stresses, $K_1^{(r)}$ and $K_2^{(r)}$, were determined by means of a two-dimensional thermal M-integral. There was a maximum difference of -2.6% and 5.6% in the results obtained here as compared to those obtained in Banks-Sills et al. (1999) for

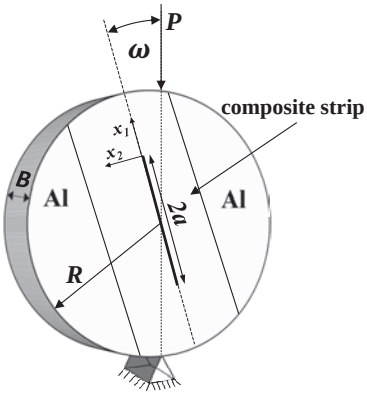

Figure 1.19: Illustration of a BD specimen with a delamination between two fiber reinforced composite plies ($\omega > 0$).

the glass/epoxy specimens and Banks-Sills et al. (2000) for the ceramic clay specimens, respectively. It is thought that the M-integral used in this investigation produced more accurate results than the weight function.

In addition, the specimens were reanalyzed by means of a three-dimensional FEA. Stress intensity factors $K_1^{(f)}$, $K_2^{(f)}$ and $K_{III}^{(f)}$, as well as $K_1^{(r)}$, $K_2^{(r)}$ and $K_{III}^{(r)}$, were obtained. Normalized stress intensity factors resulting from applied load and from residual stresses were calculated using eq. (1.26) and presented as a function of the normalized x_3-coordinate (see Fig. 1.3). The results, as expected, were symmetric with respect to the center plane of the specimens for $\hat{K}_1^{(f)}$, $\hat{K}_1^{(r)}$, $\hat{K}_2^{(f)}$ and $\hat{K}_2^{(r)}$ and antisymmetric for $\hat{K}_{III}^{(f)}$ and $\hat{K}_{III}^{(r)}$.

Based on these analyses, two and three-dimensional fracture criteria were presented and compared. For the two-dimensional failure curves, ϕ was omitted in eq. (1.33). It was concluded that for these cases of an isotropic body containing an interface crack, subjected to in-plane loading, two-dimensional analysis and fracture criteria were sufficient and three-dimensional analyses were unnecessary and did not provide new information.

The BD specimen presented in Fig. 1.19 is a modification of the homogeneous and bimaterial specimens presented in Fig. 1.18. The modified specimen includes a composite strip with a specific layup and a delamination along an interface between two plies. The composite strip is glued to two aluminium partial disks, creating a circular specimen. Loading and geometric description of the specimen may be found earlier in this section.

A methodology for measuring delamination toughness of MD fiber reinforced laminates using the BD specimen was first introduced by Banks-Sills et al. (2005b). In their investigation a CFRP (AS4/3502) composite prepreg was considered. Two different layups were fabricated. The first layup was composed of three layers, [0°//90°/0°], where each layer was approximately 4.2 mm thick. The second layup was composed of five layers, [±45°/0°//90°/0°/ ± 45°]. Each of the outer layers was approximately 4.4 mm thick and the three inner layers were about 0.54 mm thick. Note that two slashes indicate the

position of the delamination which was the same in both layups; that is between 0° and 90° plies. The delamination was obtained using a 25.4 μm thick Teflon strip. The oscillatory parameter which is a function of the mechanical properties was found to be $\varepsilon = -0.0363$. After the curing process, residual stresses and a series of transverse cracks which were observed within the 90° layer were assumed to affect the values of the modes 1 and 2 stress intensity factors, as well as the interface delamination toughness. Therefore, these two phenomena were taken into account in the calculation of the stress intensity factors. Tests were carried out to obtain the critical load, P_c and the delamination length, $2a_c$ at failure. The problem was treated in two dimensions with modes 1 and 2 present. The shear mode III component was neglected although it may increase in regions in which the delamination front intersects with the free surfaces of the specimen. Expressions for in-plane stresses and crack face displacements in the vicinity of the delamination front for two homogenized transversely isotropic materials were given in an earlier paper (Banks-Sills and Boniface, 2000). Matrices and parameters for this specific 0°//90° interface were found following Ting (1996). These expressions are derived in the current investigation for the materials considered here and further described in Chapter 2. Mechanical stress intensity factors, resulting from loading, were calculated using the FE method and a mechanical M-integral. Thermal stress intensity factors were determined using a thermal M-integral developed in Banks-Sills and Dolev (2004). It was also concluded that the transverse cracks acted to lower the stress intensity factors and their presence and location affected the mode mixity. The total stress intensity factors, namely, $K_1^{(T)}$ and $K_2^{(T)}$, were computed by superposition of the mechanical and thermal stress intensity factors obtained.

Results of the thermal, mechanical and superposed stress intensity factors K_1 and K_2 were presented for each of the layups tested, for each loading angle ω, load P_c and crack length at fracture $2a$. Interface toughness values $\mathcal{G}_{ic}$ were also presented as a function of the phase angle $\hat{\psi}$, defined in eq. (1.27). The toughness data $\mathcal{G}_{ic}$ were centered about $\hat{\psi} = 0$ using the length parameter $\hat{L} = 100$ μm. Use of this parameter is presented in eq. (1.26). Interface toughness results measured with both layups correlated well with each other. The mode 1 delamination toughness $\overline{\mathcal{G}}_{1c}$, was found as 26.5 N/m from eq. (1.34). In addition, an energy based two-dimensional fracture criterion was applied as shown in eq. (1.33), with $\phi = 0$. It was observed that the test values fit well with the failure criterion; hence, a reliable delamination failure prediction for the tested 0°//90° interface was found.

The methodology developed in Banks-Sills et al. (2005b) was extended to a +45°//−45° interface in Banks-Sills et al. (2006). Mixed mode fracture tests were conducted on the same CFRP (AS4/3502) composite material, using the BD specimen. The interface fracture toughness $\mathcal{G}_{ic}$ was determined as a function of the two phase angles $\hat{\psi}$ and ϕ described in eqs. (1.27) and (1.28), respectively. Basic expressions related to interface fracture for this specific pair were given. Unlike the case studied by Banks-Sills et al. (2005b), where the problem was treated in two dimensions, the problem discussed in this

case was three-dimensional. The complex stress intensity factor which is the amplitude of the square-root, oscillatory singularity was given as $K = K_1 + iK_3$ and the mode II stress intensity factor K_{II}, which is the amplitude of the square-root singularity, represented the in-plane shear deformation. The stress intensity factors resulting from the applied load were determined using a mechanical three-dimensional M-integral (Freed and Banks-Sills, 2005). A thermal three-dimensional M-integral was presented for calculation of the stress intensity factors resulting from residual curing stresses and used to find the thermal stress intensity factors.

Composite strips for the BD specimen in Fig. 1.19 were cut from an approximately 12.4 mm thick plate with an inner layup of $[0°/-45°//+45°/0°]_s$. Each layer had a nominal thickness of 0.54 mm. To prevent plate bending, $\pm 45°$ outer layers, approximately 4.05 mm thick, were included in the layup. The delamination was placed between one of the $+45°$ and the $-45°$ inner layers. The delamination was obtained using a 25.4 μm thick Teflon strip. The length of the Teflon strip of 15.4 mm determined the length of the delamination $2a$. The oscillatory parameter was found to be $\varepsilon = 0.000615$. Tests were carried out and the load P_c and the delamination length $2a_c$ at fracture were obtained.

Finite element analyses were carried out to obtain the stress intensity factors resulting from the applied load and residual stresses; these were superposed to determine $K_1^{(T)}$, $K_{II}^{(T)}$ and $K_3^{(T)}$. Interface toughness values $\mathcal{G}_{ic}$ and the corresponding phase angles $\hat{\psi}$ in eq. (1.27) and ϕ in eq. (1.28) were obtained. The length parameter $\hat{L}$ was chosen to be 200 μm. The mode 1 delamination toughness $\overline{\mathcal{G}}_{1c}$ was found as 90.3 N/m from eq. (1.34). In addition, an energy based three-dimensional fracture criterion was determined as shown in eq. (1.33). The failure surface may be used to predict failure.

In the current investigation, mixed mode fracture experiments will be carried out on a UD/woven fabric composite with a delamination between a UD ply and a woven ply. Tests will be carried out using a BD specimen. With this specimen, a wide range of mode mixities may be achieved using a single specimen type and fixture.

1.4 Research objectives

The aim of this research investigation is to predict the delamination failure of a fiber reinforced composite laminate with a delamination between a UD ply with fibers oriented in the 0°-direction and a plain balanced weave ply with fibers oriented in the $+45°/-45°$-directions. The laminate is fabricated by means of a wet-layup. This material is composed of carbon T300 fibers and an epoxy matrix; the epoxy is Epikote resin L20 with the hardener Epikure 960 (EPR-L20/EPH960). Both critical initiation energy release rates, as well as resistance energy release rates required for propagation are considered.

The main goals of this investigation include: (1) development of the first term of the asymptotic solution to be used for the displacement extrapolation method and mechanical and thermal M-integrals for this material and interface, as well as development of software based upon these tools to be used in analyses of the tests; (2) carrying out fracture toughness tests by means of several specimen types, namely, the Brazilian disk (BD), calibrated-end loaded split (C-ELS) and mixed mode end loaded split (MMELS) specimens under various mixed mode ratios; (3) obtaining stress intensity factors, the interface energy release rate and phase angles by means of the analytical-numerical tools developed for the tested specimens when subjected to mechanical loading, as well as residual thermal curing stresses; (4) developing two and three-dimensional initiation failure criteria for the investigated interface and material; (5) comparing results obtained by means of the different specimen types and several analyses methods; (6) determining fracture resistance curves or R-curves for the investigated material and interface. Realizing these objectives should lead to a better understanding of interlaminar delamination for this composite and interface. This understanding may improve the design and safety of such structures.

In Chapter 2, the composite type and properties of the materials used in this investigation will be described. The eigenvalues and eigenvectors found for the specific interface considered will be presented and used to develop the first term of the asymptotic stress and displacement fields. Two methods for extracting stress intensity factors will be presented in Chapter 3. Use of the first term of the asymptotic displacement field is made for both methods. First, the displacement extrapolation (DE) method will be presented. Then, the interaction energy conservative integral or M-integral for mechanical loading and residual thermal curing stresses, will be described. Both methods are used in conjunction with a finite element solution of the body in order to determine and separate the stress intensity factors.

The mixed mode fracture toughness test procedure using the BD specimen, together with test results and analysis of the specimens will be presented in Chapter 4. The critical interface energy release rate $\mathcal{G}_{ic}$ and phase angles found based on the tests carried out will also be shown. Finally in this chapter, two and three-dimensional failure criteria are proposed and statistical analyses are performed to account for scatter in the test results.

In Chapter 5, resistance curves were determined based upon results from nearly mode I, nearly mode II and mixed mode fracture tests. Initiation, propagation and steady state energy release rate values, were determined. For mode I, results from DCB tests which were performed and described in Chocron and Banks-Sills (2019) were reanalyzed using the ECM. For nearly mode II and mixed mode deformations, tests were performed with C-ELS and MMELS specimens, respectively. The results were analyzed by means of the post-processors described in Chapter 3, as well as by means of ECM. The obtained resistance curves were compared. In addition, the phase angles $\hat{\psi}$ and ϕ were calculated.

Finally, a discussion and conclusions of the results are made in Chapter 6 where comparison of the initiation fracture toughness values $\mathcal{G}_{ic}$ obtained from all specimen types is presented.

Chapter 2

The asymptotic stress and displacement fields

In this chapter, the analytic expressions for the first term of the asymptotic stress and displacement fields of a delamination along the interface between two composite plies is developed. The upper ply is a unidirectional (UD) fabric composite with 97% carbon fibers oriented in the 0°-direction (the x_1-direction in Fig. 2.1), and 3% glass fibers oriented in the transverse direction. The lower ply is a plain balanced weave with fibers oriented in the $+45°/-45°$-directions. The former is referred to as material (1) in Fig. 2.1, and the latter is material (2). The mechanical properties of each material will be described in Section 2.1. The stress function and the displacement fields were derived based on Stroh (1958) and Lekhnitskii (1963) formalisms as described by Ting (1996). Since both methods are equivalent, as has been shown by Barnett and Kirchner (1997), they were used interchangeably in the development. In Section 2.2, the sextic differential equation developed by Lekhnitskii (1963) is presented and the eigenvalues and eigenvectors for both materials are obtained. The eigenvalues may be arranged into two matrices **A** and **B**. These matrices are employed to calculate the oscillating parameter ε. In Section 2.3, the displacement and stress fields in the neighborhood of a general delamination front are presented (see Ting, 1996, for details). Using appropriate boundary conditions, the first

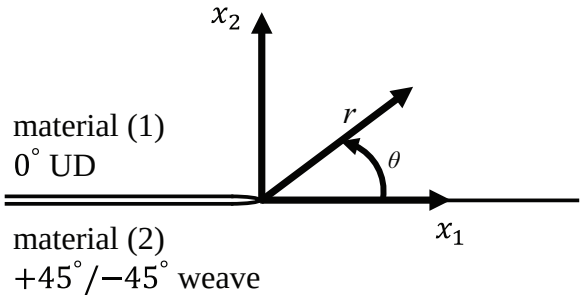

Figure 2.1: An interface crack between a UD composite with fibers in the 0°-direction and a $+45°/-45°$ weave.

Table 2.1: Properties of the epoxy and hardner EPR-L20/EPH-960 (provided by IAI).

material	E (GPa)	ν	α (10^{-6}/C°)
EPR-L20/EPH-960	2.8	0.36	70

term of the asymptotic expansion for the stress and displacement fields of the delamination along the interface between the two specific materials shown in Fig. 2.1 are developed. These are based on the effective mechanical properties of each material as described in Section 2.1, as well as matrices **A** and **B**, defined in Section 2.2.

2.1 Mechanical structure and properties

In this study, a delamination between two composite plies is investigated. The upper material is a UD fabric and contains mainly carbon fibers in the 0°-direction (the x_1-direction in Fig. 2.1), as well as some glass fibers directed in the transverse direction. The lower ply is a $+45°/-45°$ plain weave. Each material is denoted by k, where $k = 1$ is used for the upper material, while $k = 2$ for the lower material, as shown in Fig. 2.1. Both materials are composed of carbon T300 fibers embedded in an epoxy matrix. The epoxy EPR-L20/EPH-960 is isotropic and may be fully described by two independent elastic constants and one thermal constant: Young's modulus E, Poisson's ratio ν and the coefficient of thermal expansion (CTE) α. The mechanical and thermal properties of the epoxy are presented in Table 2.1. These were provided by the manufacturer of the material. A range of properties may be found in the literature for carbon T300. The mechanical properties used in this investigation are given in Miyagawa et al. (2005). The axial CTE of the T300 carbon may be found in a Torayca T300 data sheet (2015); its transverse component was taken from Bowles and Tompkins (1989). Properties of the graphite T300 fibers are presented in Table 2.2. The upper material is a UD fabric and contains some glass fibers directed in the transverse direction. In the modeling, Young's modulus, Poisson's ratio and the coefficient of thermal expansion (CTE) of the glass were

Table 2.2: Mechanical (Miyagawa et al., 2005) and thermal (Torayca T300 data sheet, 2015, Bowles and Tompkins, 1989) properties of graphite T300 fibers.

material	E_A (GPa)	E_T (GPa)	G_A (GPa)	G_T (GPa)	ν_A	ν_T	α_A (10^{-6}/C°)	α_T (10^{-6}/C°)
T300	230.0	8.0	27.3	3.1	0.26	0.30	-0.41	10.08

Table 2.3: Mechanical and thermal properties of the glass fibers (Matweb, 2015).

material	E (Gpa)	ν	α (10^{-6}/C°)
Glass	69	0.22	7.2

also used. These properties are given in Table 2.3. The upper material may be considered transversely isotropic with $x_1 = 0$ a plane of symmetry (see Fig. 2.1). A transversely isotropic material may be described by five independent mechanical properties E_A, E_T, ν_A, ν_T and G_A; E_A and E_T are the axial and transverse Young's moduli, respectively, ν_A and ν_T are the axial and transverse Poisson's ratios, respectively, and G_A is the axial shear modulus. The transverse shear modulus, G_T, may be calculated as

$$G_T = \frac{E_T}{2\,(1+\nu_T)} \quad . \tag{2.1}$$

The axial and transverse CTEs are respectively, α_A and α_T.

Four out of five necessary properties (E_A, E_T, G_A and ν_A) of the UD fabric, used in the current investigation, were obtained experimentally and are presented in the first line of Table 2.4. The missing properties G_T and ν_T were obtained by means of the High-Fidelity Generalized Method of Cells (HFGMC) (Aboudi, 2004) and from the relation between G_T and ν_T, given in eq. (2.1).

The structure of this UD fabric includes T300 carbon and glass fibers embedded in an epoxy matrix, as shown in Fig. 2.2. The total fiber volume fraction (including both fiber types) was determined using a weight fraction test. The volume fraction was then

Table 2.4: UD fabric mechanical properties obtained from experiments and from three HFGMC models: model 1: $V_{f(T300)} = 0.58$, $V_{f(e)} = 0.42$, $E_{(e)} = 2.8$ GPa; model 2: $V_{f(T300)} = 0.58$, $V_{f(e+g)} = 0.42$, $E_{(e+g)} = 5.9$ GPa; and model 3: $V_{f(T300)} = 0.485$, $V_{f(e+g)} = 0.42$, $E_{(e+g)} = 5.9$ GPa and the final properties used in this investigation for numerical verification.

method	V_f	E_A (GPa)	E_T (GPa)	G_A (GPa)	G_T (GPa)	ν_A	ν_T
experiments	0.58	114.6	7.2	2.8	-	0.39	-
HFGMC model 1	0.58	134.6	5.3	3.7	1.8	0.30	0.43
HFGMC model 2	0.58	135.9	7.5	6.7	2.6	0.30	0.41
HFGMC model 3	0.485	114.6	7.4	5.3	2.6	0.31	0.44
final properties		**114.6**	**7.2**	**2.8**	**2.5**	**0.39**	**0.44**

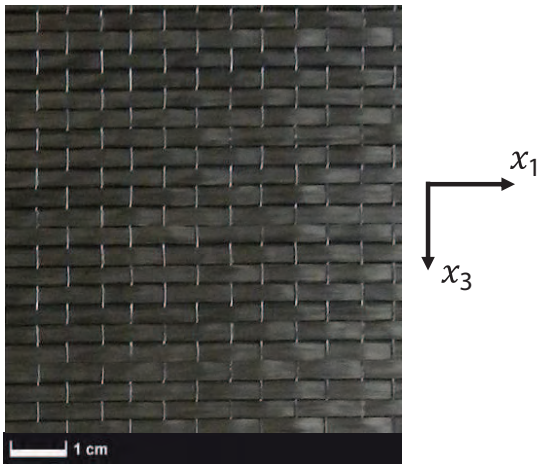

Figure 2.2: UD fabric structure; carbon fibers are in the x_1-direction; glass fibers are in the x_3-direction.

calculated and determined as 0.6. This value includes 97% carbon fibers in the axial direction and 3% glass fibers in the transverse direction. Hence, the material is composed of approximately $V_{f(T300)} = 0.58$ (carbon fibers), $V_{f(g)} = 0.02$ (glass fibers) and the volume fraction of the remaining epoxy matrix which is $V_{f(e)} = 0.4$; the subscripts $T300$, e and g represent the T300 fibers, the epoxy matrix and the glass fibers, respectively.

Three different HFGMC models were used to obtain the mechanical properties. First, a model composed of carbon fibers with $V_{f(T300)} = 0.58$ was used, as was determined based on a calculation of the weight fraction experimental results. In this model, the glass fibers are neglected and the epoxy is assumed to have a volume fraction of $V_{f(e)} = 0.42$. The results from this model are presented in the second row of Table 2.4 (model 1). The obtained properties were found to be higher than expected in the axial direction and lower than expected in the transverse direction.

The second model was composed of $V_{f(T300)} = 0.58$ and a combination of the glass fibers and the epoxy matrix, namely, $V_{f(e+g)} = 0.42$; the subscript $e + g$ represents the combination of the glass fibers and the epoxy matrix. Young's modulus for the epoxy and glass was calculated by means of the rule of mixtures. This new modulus was used to model the matrix of the composite as if the matrix were isotropic. Hence, the glass fibers stiffen the material not only in the direction transverse to the carbon fibers, but also in their axial direction. This approximation was implemented in order to simplify the design of the HFGMC model, leading to an increase in the composite properties in the transverse direction of the composite. The matrix is composed of 40% EPR-L20/EPH-960 epoxy and 2% glass fibers. Hence, 95.3% of the matrix is the epoxy and 4.7% is fiberglass. For the rule of mixtures

$$E_{(e+g)} = V_{(f(e))}E_{(e)} + V_{(f(g))}E_{(g)} \quad . \tag{2.2}$$

The Young's modulus of the EPR-L20/EPH-960 epoxy matrix including the glass fibers

was found to be $E_{(e+g)} = 5.9$ GPa and used in the micromechanical model. The UD fabric mechanical properties obtained from this model are presented in the third row of Table 2.4 (model 2). It may be observed from the results that the glass fibers had a negligible contribution to the axial Young's modulus E_A of the UD fabric of less than 1%. On the other hand, the result for the transverse Young's modulus increased by 41.5% and the new value of 7.5 GPa was found to be closer to the experimental result of 7.2 GPa. It may also be noted that the value of G_A is overestimated.

To better understand the obtained results, a simple calculation, using the rule of mixtures, was made

$$E_A = V_{f(T300)}E_{A(T300)} + V_{f(e)}E_{(e)} + V_{f(g)}E_{(g)} \quad . \tag{2.3}$$

The axial Young's modulus was calculated to be 134.6 GPa. This result is much higher than the experimental result and shows exact agreement with the HFGMC model. The actual volume fraction of the carbon fibers may be lower than that measured, causing the significantly lower experimental results in the axial direction.

In the third HFGMC model, the volume fraction of the T300 carbon fibers was chosen to produce the axial Young's modulus obtained by means of the tests, namely 0.485. In this model, the Young's modulus of glass fibers was again included in the modulus of the matrix as calculated with model 2. The results for the mechanical properties obtained from this model are presented in the fourth row of Table 2.4 (model 3). The axial and transverse Young's moduli, as obtained from this model, agree well with the experimental results. It was observed further that the maximum change in ν_T was -6.8% between model 2 and 3 and was only -2.3% between model 1 and 3. As a result of this relatively small change compared with the changes of the other properties, the value obtained for ν_T from model 3 was chosen for modeling this material. The final properties were chosen from the experiments, together with $\nu_T = 0.44$ from the HFGMC model. The value of G_T was calculated using eq. (2.1). These properties are presented in the fifth row of Table 2.4 (final properties). The final chosen fiber volume fraction value is the one used to obtain the missing property of ν_T using HFGMC. This volume fraction was only used to obtain properties which resemble the experimental results, but will not be further used in this study. Based on the methodology described here for the UD fabric ply properties, the properties of the tested specimens will be obtained using the fiber volume fractions measured for those specimens.

The lower material ($k = 2$ in Fig 2.1) is a plain woven composite with fibers in the $+45°/-45°$-direction. The weave with fibers in the $0°/90°$-direction is rotated by $45°$ about the x_2-axis in Fig 2.3a, resulting in the fibers rotated in the $\pm 45°$-direction. This material is tetragonal, defined by six independent mechanical properties. Some of the effective mechanical properties, used in this investigation, were determined by means of the two-step HFGMC (for details see Aboudi, 2004 and Decad, 2008); others were

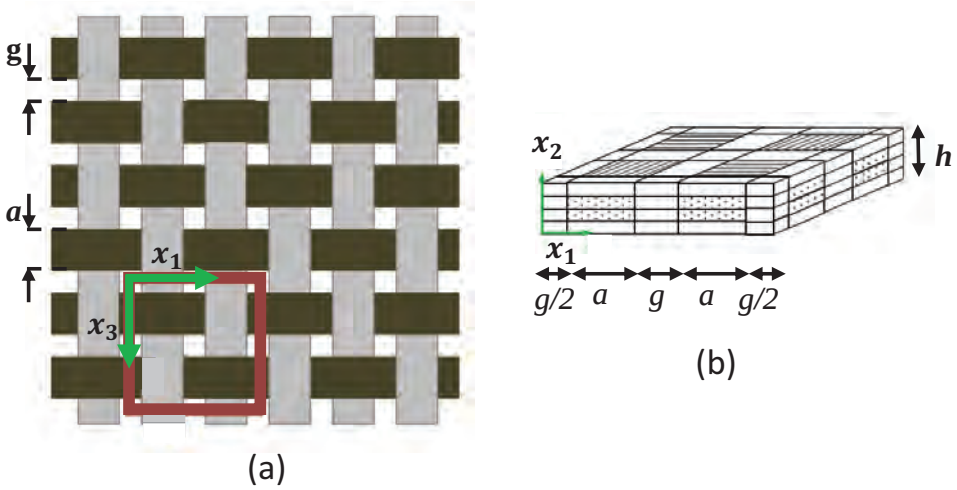

Figure 2.3: Repeating unit cell (RUC): (a) a plain weave with a representative unit cell shown in red. (b) Schematic drawing of the RUC model.

obtained from experiments. All properties were found for a plain weave with fibers in the 0°/90°-direction as shown in Fig. 2.3a and transformed by a 45° rotation.

The experimental results, as well as the measured volume fraction $V_{f(f/w)}$, are presented in Table 2.5, in the first row. Note that the subscripts f and w, in parenthesis, represent the fibers in the weave, respectively. In Table 2.5, $E_{11} = E_{33}$ are the Young's moduli in the x_1 and x_3-directions, respectively, that is, the in-plane elastic moduli (see Fig 2.3a); E_{22} is the out-of-plane Young's modulus; G_{13} is the in-plane shear modulus and $G_{23} = G_{21}$ are the out-of-plane shear moduli; ν_{13} is the in-plane Poisson's ratio and $\nu_{23} = \nu_{21}$ are the out-of-plane Poisson's ratios. Note that

$$\frac{\nu_{ij}}{E_{ii}} = \frac{\nu_{ji}}{E_{jj}} \quad . \tag{2.4}$$

To use the HFGMC micromechanical model, a repeating unit cell (RUC) shown in Fig. 2.3 is defined. In Fig. 2.3a, a plain weave is shown, with the chosen RUC marked

Table 2.5: Woven fabric mechanical properties obtained from experiments and from HFGMC models for a 0°/90° weave, and the final properties chosen for this investigation for numerical verification.

method	$V_{f(f/w)}$	$E_{11} = E_{33}$ (GPa)	E_{22} (GPa)	G_{13} (GPa)	$G_{21} = G_{23}$ (GPa)	ν_{13}	$\nu_{21} = \nu_{23}$
experiments	0.45	57.8	-	3.1	-	0.1	-
HFGMC model 1	0.45	46.7	5.6	2.7	2	0.038	0.051
HFGMC model 2	0.55	57.4	6.2	3.7	2.4	0.032	0.045
final properties		**57.8**	**6.2**	**3.1**	**2.4**	**0.1**	**0.045**

in red. This RUC is repetitive and maintains the symmetry of the model. The RUC is composed of yarn and epoxy where the yarn is a UD composite bundle of fibers and epoxy. In Fig. 2.3b, a schematic drawing of the chosen RUC is presented. The drawing includes sub-cells with either epoxy or yarn, oriented in a defined direction. The geometrical dimensions of the yarn and the epoxy in the RUC may be measured, as shown in Fig. 2.3a, where a is the yarn width, g is the distance between yarns and h is the thickness of each ply. These properties are then used in the micro-mechanical model as shown in Fig. 2.3b. The geometrical measurements were obtained from a cross-section of the weave using a digital microscope with a magnification of 10× (DinoLite AM311ST, AnMo Electronics, Hsinchu,Taiwan); the averaged results were $a = 1.73$ mm and $g = 0.27$ mm obtained from 77 and 79 measurements, respectively. The average thickness of each ply $h = 0.24$ mm was obtained by dividing the specimen thickness by the number of plies, namely 10.

The volume fraction of the yarn in the RUC was calculated. The calculation was carried out using the geometrical measurements of a and g, as shown in Fig. 2.3. The total yarn volume in the RUC was calculated as

$$V_{yarn} = h\left[\left(16a^2\right) + (16ag)\right] \ ; \tag{2.5}$$

the total volume of the RUC, was calculated as

$$V_{RUC} = 4h(2a + 2g)^2. \tag{2.6}$$

The volume fraction $V_{f(y/w)}$ of the yarn (y) in the weave (w) or the RUC is obtained from

$$V_{f(y/w)} = \frac{V_{yarn}}{V_{RUC}} \ . \tag{2.7}$$

This value was found to be 0.87.

The weight fraction of the fibers within the composite were measured by the plate manufacturer and the volume fraction was calculated to be $V_{f(f/w)} = 0.45$. Using this value, the volume fraction of the fibers within the yarn $V_{f(f/y)}$ where the subscripts f and y, in parenthesis, represent the fibers in the yarn, respectively, was found from

$$V_{f(f/y)} = \frac{V_{f(f/w)}}{V_{f(y/w)}} = \frac{0.45}{0.87} \ . \tag{2.8}$$

The result is a fiber volume fraction of $V_{f(f/y)} = 0.52$ within the yarn. This volume fraction was used in the HFGMC Geometrical User Interface (GUI) to calculate the yarn properties.

The yarn is a UD material, effectively transversely isotropic, composed of a volume fraction of 0.52 of T300 carbon fibers and 0.48 EPR-L20/EPH-960 epoxy. The desired properties E_A, E_T, ν_A, ν_T and G_A were obtained by means of HFGMC. The transverse shear modulus G_T, was calculated by means of eq. (2.1). The yarn properties found are

Table 2.6: Fiber volume fractions and yarn properties used to obtain weave properties.

$\frac{\text{fibers}}{\text{weave}}$	$\frac{\text{yarn}}{\text{weave}}$	$\frac{\text{fibers}}{\text{yarn}}$	E_A	E_T	G_A	G_T	ν_A	ν_T
(measured)	(geometry a, g)	(calculated)	(GPa)	(GPa)	(GPa)	(GPa)		
0.45	0.87	0.52	121.0	5.0	3.1	1.8	0.31	0.40
0.55	0.87	0.63	147.1	5.5	4.5	1.9	0.29	0.42

presented in the first row in Table 2.6. Also presented, are the volume fractions described previously.

The mechanical properties presented in Table 2.6 and the geometrically measured parameters a, g and h, were used as input for an HFGMC two-step calculation to obtain the weave properties. The model produced the mechanical properties shown in the second row and denoted as 'HFGMC model 1' in Table 2.5. It may be observed that there is a great difference between the experimentally obtained result for the in-plane Young's modulus and that obtained using HFGMC.

To better understand the results obtained from the model and the experiments, a simplified rule of mixtures was used to determine an upper bound for the Young's modulus within the weave, namely

$$E_{33(weave)} = E_{11(weave)} = \frac{V_{f(f/w)}}{2} E_{A(T300)} + \frac{V_{f(f/w)}}{2} E_{T(T300)} + \left(1 - V_{f(f/w)}\right) E_{(e)} \quad . \quad (2.9)$$

Although the result was expected to produce an upper bound for the in-plane Young's moduli $E_{11} = E_{33}$, it was found to be 55.1 GPa, which is lower than the obtained experimental result. Another method was then used to check the upper bound of the in-plane Young's moduli. An HFGMC cross-ply model was considered; the results were expected to be higher in the in-plane directions than were obtained for the weave. The in-plane Young's moduli calculated from this model were also 55.1 GPa, again lower than the obtained experimental result. Perhaps there was an error in the measured weight fraction.

In order to obtain values for the in-plane Young's moduli $E_{11} = E_{33}$ similar to those from the tests, HFGMC was used with the volume fraction of the fibers in the weave incremented from the experimentally obtained value of 0.45 to 0.55. The volume fraction of the fibers in the yarn was then calculated from the first two terms of eq. (2.8) to be 0.63 (see Table 2.6). This value was obtained by dividing the volume fraction of the fibers in the weave (0.55) by the volume fraction of the yarn in the weave (0.87). The mechanical properties of the yarn E_A, E_T, ν_A, ν_T and G_A were calculated for the case of $V_{f(f/y)} = 0.63$ by means of HFGMC for a transversely isotropic material. The transverse shear modulus G_T, was calculated by means of eq. (2.1). The results for the calculated mechanical properties of the yarn are presented in the second row in Table 2.6.

Table 2.7: Final transformed woven fabric mechanical properties with fibers in the $+45°/-45°$-directions.

material	$E_{11}^{(2)} = E_{33}^{(2)}$ (GPa)	$E_{22}^{(2)}$ (GPa)	$G_{13}^{(2)}$ (GPa)	$G_{21}^{(2)} = G_{23}^{(2)}$ (GPa)	$\nu_{13}^{(2)}$	$\nu_{21}^{(2)} = \nu_{23}^{(2)}$
$+45°/-45°$	**11.3**	**6.2**	**26.2**	**2.4**	**0.8**	**0.040**

The yarn properties, as well as the geometrically measured parameters a, g and h, were again used as input for an HFGMC two-step calculation (Aboudi, 2004; Decad, 2008) to obtain the weave properties. The results are presented in the third row of Table 2.5 denoted as 'model 2'. The final properties for a plain weave with fibers oriented in the $0°/90°$-direction were taken from the tests. The missing properties were taken from the HFGMC two-step model results, namely E_{22}, G_{21} and ν_{21}. The experimental and calculated results show good agreement for the in-plane Young's moduli. The final properties are shown in the fourth row in Table 2.5.

The properties obtained for the $0°/90°$ weave were rotated by $45°$ about the x_2-axis in Fig. 2.3a. The transformed final properties, to be used in further calculations, are presented in Table 2.7. The transformation is described in Ting (1996, pp. 53-56). Note that these properties will be recalculated for specimens that will be tested in this investigation based on the volume fractions measured for these specimens. These calculations will be made using the same methodology that has been described in this section. In addition, it may be noted that a superscript (2) appears on the mechanical properties presented in Table 2.7 to indicate that these results are used for material (2) in Fig. 2.1 with fibers oriented in the $+45°$ and $-45°$-directions.

The effective thermal properties for each material were not calculated at this point because no experimental data was found for comparison with the properties obtained from HFGMC. The coefficients of thermal expansion (CTEs) will be calculated by means of HFGMC for the volume fractions obtained for the tested specimens.

The compliance matrix for the upper material, $k = 1$, is given by

$$\boldsymbol{S}^{(1)} = \begin{bmatrix} \frac{1}{E_A} & -\frac{\nu_A}{E_A} & -\frac{\nu_A}{E_A} & 0 & 0 & 0 \\ & \frac{1}{E_T} & -\frac{\nu_T}{E_T} & 0 & 0 & 0 \\ & & \frac{1}{E_T} & 0 & 0 & 0 \\ & & & \frac{1}{G_T} & 0 & 0 \\ & & \text{sym} & & \frac{1}{G_A} & 0 \\ & & & & & \frac{1}{G_A} \end{bmatrix} . \tag{2.10}$$

The compliance matrix may be written with reduced compliance components, $S'_{\alpha\beta}$ ($\alpha, \beta = 1, ..., 6$), where

$$S'_{\alpha\beta} = S_{\alpha\beta} - \frac{S_{\alpha 3} S_{3\beta}}{S_{33}} \ . \tag{2.11}$$

Note that

$$S'_{3\alpha} = S'_{\alpha 3} = 0 \ , \tag{2.12}$$

where $\alpha = 1, ..., 6$. The reduced compliance coefficients for $k = 1$ are found as

$$S'^{(1)}_{11} = \frac{1}{E_A} \left(1 - \nu_A^2 \frac{E_T}{E_A} \right) \tag{2.13}$$

$$S'^{(1)}_{12} = -\frac{\nu_A}{E_A} \left(1 + \nu_T \right) \tag{2.14}$$

$$S'^{(1)}_{22} = \frac{1}{E_T} \left(1 - \nu_T^2 \right) \tag{2.15}$$

$$S'^{(1)}_{44} = \frac{2 \left(1 + \nu_T \right)}{E_T} \tag{2.16}$$

$$S'^{(1)}_{55} = S'^{(1)}_{66} = \frac{1}{G_A} \tag{2.17}$$

$$S'^{(1)}_{14} = S'^{(1)}_{15} = S'^{(1)}_{16} = 0 \tag{2.18}$$

$$S'^{(1)}_{24} = S'^{(1)}_{25} = S'^{(1)}_{26} = 0 \tag{2.19}$$

$$S'^{(1)}_{45} = S'^{(1)}_{46} = S'^{(1)}_{56} = 0 \ . \tag{2.20}$$

The reduced compliance components are symmetric.

The lower woven material with tows in the $+45°/-45°$-directions, referred to as $k = 2$ in Fig. 2.1, is tetragonal with $x_2 = 0$ a symmetry plane. This material may be described

with six independent mechanical properties E_{11}, E_{22}, ν_{21}, ν_{13}, G_{23} and G_{13} (for the axes, see Fig. 2.1) where $E_{11} = E_{33}$ and E_{22} are the Young's moduli; $\nu_{21} = \nu_{23}$ and ν_{13} are the Poisson's ratio's; $G_{21} = G_{23}$ and G_{13} are the shear moduli. For this material, the properties used in the numerical verification made in this investigation and given in Table 2.7. Note that the mechanical properties obey the relation presented in eq. (2.4). The compliance matrix for a tetragonal material with $x_2 = 0$ a symmetry plane is of the form

$$\boldsymbol{S}^{(2)} = \begin{bmatrix} \frac{1}{E_{11}^{(2)}} & -\frac{\nu_{12}^{(2)}}{E_{11}^{(2)}} & -\frac{\nu_{13}^{(2)}}{E_{11}^{(2)}} & 0 & 0 & 0 \\ & \frac{1}{E_{22}^{(2)}} & -\frac{\nu_{23}^{(2)}}{E_{22}^{(2)}} & 0 & 0 & 0 \\ & & \frac{1}{E_{11}^{(2)}} & 0 & 0 & 0 \\ & \text{sym} & & \frac{1}{G_{23}^{(2)}} & 0 & 0 \\ & & & & \frac{1}{G_{13}^{(2)}} & 0 \\ & & & & & \frac{1}{G_{23}^{(2)}} \end{bmatrix} . \tag{2.21}$$

The reduced compliance components are

$$S_{11}'^{(2)} = \frac{1 - \nu_{13}^{(2)\,2}}{E_{11}^{(2)}} \tag{2.22}$$

$$S_{12}'^{(2)} = -\frac{\nu_{21}^{(2)}\left(1 + \nu_{13}^{(2)}\right)}{E_{22}^{(2)}} \tag{2.23}$$

$$S_{22}'^{(2)} = \frac{1}{E_{22}^{(2)}}\left(1 - [\nu_{21}^{(2)}]^2 \frac{E_{11}^{(2)}}{E_{22}^{(2)}}\right) \tag{2.24}$$

$$S_{44}'^{(2)} = S_{66}'^{(2)} = \frac{1}{G_{23}^{(2)}} \tag{2.25}$$

$$S_{55}'^{(2)} = \frac{1}{G_{13}^{(2)}} \tag{2.26}$$

$$S_{14}'^{(2)} = S_{15}'^{(2)} = S_{16}'^{(2)} = 0 \tag{2.27}$$

$$S_{24}'^{(2)} = S_{25}'^{(2)} = S_{26}'^{(2)} = 0 \tag{2.28}$$

$$S_{45}'^{(2)} = S_{46}'^{(2)} = S_{56}'^{(2)} = 0 \ . \tag{2.29}$$

2.2 Eigenvalues and eigenvectors

Using the Lekhnitskii (1963) formalism as described in Appendix A, a sextic differential equation is produced, shown in eq. (A.11). For the two materials described in Section 2.1, $L_3 = 0$ so that

$$(L_2 L_4)\,\chi = 0 \tag{2.30}$$

where L_2 and L_4 are defined in eqs. (A.12). A general solution is chosen to be

$$\chi \;=\; F(z) \tag{2.31}$$

where the definition of z appears in eq. (A.14) and for completeness is given here as

$$z = x_1 + p x_2. \tag{2.32}$$

The parameter p in eq. (2.32) is a complex constant. As a result, the sextic equation from eq. (A.15) becomes

$$l_2(p) l_4(p) = 0 \tag{2.33}$$

where

$$l_2 = S'_{55} p^2 + S'_{44} \tag{2.34}$$

and

$$l_4 = S'_{11} p^4 + (2S'_{12} + S'_{66})\, p^2 + S'_{22} \quad . \tag{2.35}$$

The solution of eq. (2.33) provides three pairs of complex conjugate roots p, where

$$p_{\alpha+3} = \overline{p}_\alpha, \qquad \Im(p_\alpha) > 0, \qquad (\alpha = 1, 2, 3) \quad . \tag{2.36}$$

The obtained roots are

$$p_{1,2}^{(k)} = \sqrt{\frac{-(2S_{12}'^{(k)} + S_{66}'^{(k)}) \pm \sqrt{\left(2S_{12}'^{(k)} + S_{66}'^{(k)}\right)^2 - 4 S_{11}'^{(k)} S_{22}'^{(k)}}}{2 S_{11}'^{(k)}}}\,, \tag{2.37}$$

and

$$p_3^{(k)} = i\sqrt{\frac{S_{44}'^{(k)}}{S_{55}'^{(k)}}}. \tag{2.38}$$

The upper material is transversely isotropic and so the expression in the inner square-root of eq. (2.37) is always positive. For that reason the eigenvalues are given by

$$p_1^{(1)} = i\beta_1^{(1)}, \;\; p_2 = i\beta_2^{(1)} \;\; p_3^{(1)} = i\beta_3^{(1)} \quad . \tag{2.39}$$

where

$$\beta_{1,2}^{(1)} = \sqrt{\frac{(2S_{12}'^{(1)} + S_{66}'^{(1)}) \mp \sqrt{\left(2S_{12}'^{(1)} + S_{66}'^{(1)}\right)^2 - 4 S_{11}'^{(1)} S_{22}'^{(1)}}}{2 S_{11}'^{(1)}}}\,, \tag{2.40}$$

and

$$\beta_3^{(1)} = \sqrt{\frac{S'^{(1)}_{44}}{S'^{(1)}_{55}}} \quad . \tag{2.41}$$

In the case of the lower material, which is tetragonal, the inner square-root expression may be positive or negative. If the inner square-root expression is positive, the obtained eigenvalues are of the form shown in eq. (2.39), if the expression is negative then the obtained eigenvalues are given by

$$p_1^{(2)} = \alpha^{(2)} + i\beta^{(2)}, \quad p_2^{(2)} = -\alpha^{(2)} + i\beta^{(2)}, \quad p_3^{(2)} = i\beta_3^{(2)}. \tag{2.42}$$

In this study, substituting the properties given in Table 2.7 into the reduced compliance components given in eqs. (2.22)-(2.29), the eigenvalues are found to be of the former form presented in eq. (2.39) namely,

$$p_1^{(2)} = i\beta_1^{(2)}, \quad p_2 = i\beta_2^{(2)} \quad p_3^{(2)} = i\beta_3^{(2)} \quad . \tag{2.43}$$

2.3 The displacement and stress fields for an interface delamination

In this section, the first term of the asymptotic solution for a delamination along an interface between two anisotropic materials is presented. The solution will then be developed for the specific interface with a delamination between a transversely isotropic and a tetragonal material shown in Fig. 2.1 and described in Section 2.1.

The displacement field and stress function for a delamination along an interface between two anisotropic materials is derived from the sextic formalism due to Stroh (1958), presented in eqs. (A.24) and (A.29), respectively. The first term of the asymptotic solution is obtained by using eq. (A.30) and defining a general solution of the form

$$f^{(k)}\left(z_\alpha^{(k)}\right) = {z_\alpha^{(k)}}^{\delta+1} \tag{2.44}$$

where δ is the order of the stress singularity and $z_\alpha^{(k)}$ $(\alpha = 1, 2, 3)$ from eq. (2.32) is given as

$$z_\alpha^{(k)} = x_1 + p_\alpha^{(k)} x_2 \quad . \tag{2.45}$$

In eqs. (2.44) and (2.45), $k = 1, 2$ represents the upper and lower materials, respectively. The parameter $z_\alpha^{(k)}$ may be written in polar coordinates, as

$${z_\alpha}^{(k)} = r{\zeta_\alpha}^{(k)}, \qquad {\zeta_\alpha}^{(k)} = \cos\theta + {p_\alpha}^{(k)} \sin\theta \tag{2.46}$$

where r is the distance from the crack tip and θ is the polar angle shown in Fig. 2.1. Following Ting (1996, p. 341) it is possible to write

$$\mathbf{u}^{(k)} = \left\{ \mathbf{A}_k \left\langle \, z_\alpha^{(k)\,\delta+1} \, \right\rangle \mathbf{q}_k + \overline{\mathbf{A}}_k \left\langle \, \overline{z}_\alpha^{(k)\,\delta+1} \, \right\rangle \widetilde{\mathbf{q}}_k \right\} \tag{2.47}$$

$$\boldsymbol{\phi}^{(k)} = \left\{ \mathbf{B}_k \left\langle \, z_\alpha^{(k)\,\delta+1} \, \right\rangle \mathbf{q}_k + \overline{\mathbf{B}}_k \left\langle \, \overline{z}_\alpha^{(k)\,\delta+1} \, \right\rangle \widetilde{\mathbf{q}}_k \right\} \quad . \tag{2.48}$$

where, the matrices $\mathbf{A}_k$ and $\mathbf{B}_k$ are 3×3 matrices related to the mechanical properties of the two materials. The bar over a parameter, a vector or a matrix represents the complex conjugate. The diagonal matrix $\left\langle \, z_\alpha^{(k)\,\delta+1} \, \right\rangle$ is defined as

$$\left\langle \, z_\alpha^{(k)\,\delta+1} \, \right\rangle = \text{diag} \left[\, z_1^{(k)\,\delta+1}, \; z_2^{(k)\,\delta+1}, \; z_3^{(k)\,\delta+1} \, \right] . \tag{2.49}$$

The complex constant δ and vectors $\mathbf{q}_k$ and $\widetilde{\mathbf{q}}_k$ are unknown and may be found by using boundary and continuity conditions.

The matrices $\mathbf{A}_k$ and $\mathbf{B}_k$ are obtained by comparing Stroh's general solutions with Lekhnitskii's general solutions. For further explanation see Ting (1996, pp. 170-172). For the materials studied here, and the components of the effective compliance matrix of each material presented in Section 2.1, these matrices become

$$\mathbf{A}_k = - \begin{bmatrix} k_1^{(k)} \left(S_{11}'^{(k)} \, \beta_1^{(k)\,2} - S_{12}'^{(k)} \right) & k_2^{(k)} \left(S_{11}'^{(k)} \, \beta_2^{(k)\,2} - S_{12}'^{(k)} \right) & 0 \\ \dfrac{i k_1^{(k)}}{\beta_1^{(k)}} \left(S_{22}'^{(k)} - S_{12}'^{(k)} \, \beta_1^{(k)\,2} \right) & \dfrac{i k_2^{(k)}}{\beta_2^{(k)}} \left(S_{22}'^{(k)} - S_{12}'^{(k)} \, \beta_2^{(k)\,2} \right) & 0 \\ 0 & 0 & -\dfrac{i k_3^{(k)} \, S_{44}'^{(k)}}{\beta_3^{(k)}} \end{bmatrix} , \tag{2.50}$$

and

$$\mathbf{B}_k = \begin{bmatrix} -i k_1^{(k)} \beta_1^{(k)} & -i k_2^{(k)} \beta_2^{(k)} & 0 \\ k_1^{(k)} & k_2^{(k)} & 0 \\ 0 & 0 & -k_3^{(k)} \end{bmatrix} . \tag{2.51}$$

In eqs. (2.50) and (2.51), $k_\alpha^{(k)}$, $\alpha = 1, 2, 3$, are normalizing parameters. For further calculations, $\mathbf{B}_k^{-1}$ and $-\mathbf{A}_k \mathbf{B}_k^{-1}$ are found as

$$\mathbf{B}_k^{-1} = \frac{1}{\beta_2^{(k)} - \beta_1^{(k)}} \begin{bmatrix} -\dfrac{i}{k_1^{(k)}} & \dfrac{\beta_2^{(k)}}{k_1^{(k)}} & 0 \\ \dfrac{i}{k_2^{(k)}} & -\dfrac{\beta_1^{(k)}}{k_2^{(1)}} & 0 \\ 0 & 0 & \dfrac{\beta_1^{(k)} - \beta_2^{(k)}}{k_3^{(k)}} \end{bmatrix} \tag{2.52}$$

$$-\mathbf{A}_k \mathbf{B}_k^{-1} = \begin{bmatrix} i S_{11}'^{(k)} \left(\beta_1^{(k)} + \beta_2^{(k)} \right) & -S_{12}'^{(k)} - \sqrt{S_{11}'^{(k)} \, S_{22}'^{(k)}} & 0 \\ S_{12}'^{(k)} + \sqrt{S_{11}'^{(k)} \, S_{22}'^{(k)}} & i \sqrt{S_{11}'^{(k)} \, S_{22}'^{(k)}} \left(\beta_1^{(k)} + \beta_2^{(k)} \right) & 0 \\ 0 & 0 & i \sqrt{S_{44}'^{(k)} \, S_{55}'^{(k)}} \end{bmatrix} . \tag{2.53}$$

The boundary conditions used to determine δ, $\mathbf{q}_k$ and $\widetilde{\mathbf{q}}_k$, $k = 1, 2$, include two main requirements. First, the delamination faces are traction free, so that

$$\boldsymbol{\phi}^{(1)}(\pi) = \boldsymbol{\phi}^{(2)}(-\pi) = 0 \ . \tag{2.54}$$

The second requirement is that the two materials are perfectly bonded along the interface ahead of the delamination. Thus, traction and displacement continuity along the bonded part of the interface implies that

$$\begin{array}{rcl} \boldsymbol{\phi}^{(1)}\big|_{\theta=0} & = & \boldsymbol{\phi}^{(2)}\big|_{\theta=0} \\ \mathbf{u}^{(1)}\big|_{\theta=0} & = & \mathbf{u}^{(2)}\big|_{\theta=0} \end{array} \ . \tag{2.55}$$

By setting the vectors $\mathbf{q}_k$ and $\widetilde{\mathbf{q}}_k$ in eq. (2.48) to be

$$\begin{array}{rcl} \mathbf{q}_k & = & (-1)^k \ \dfrac{i}{2} \ \mathbf{B}_k^{-1} \ e^{(-1)^k i\delta\pi} \ \mathbf{g}_k \ , \\ \widetilde{\mathbf{q}}_k & = & (-1)^{(k+1)} \ \dfrac{i}{2} \ \overline{\mathbf{B}}_k{}^{-1} \ e^{(-1)^{k+1} i\delta\pi} \ \mathbf{g}_k \ , \end{array} \tag{2.56}$$

the boundary condition in eq. (2.54) is satisfied. In eq. (2.56), $\mathbf{g}_k$ are two, arbitrary, 3×1 complex vectors. Traction continuity in eq. $(2.55)_1$ leads to the relation

$$\mathbf{g}_1 = \mathbf{g}_2 \equiv \mathbf{g} \ . \tag{2.57}$$

The order of the stress singularities δ may be determined by using the displacement continuity condition in eq. $(2.55)_2$. This requirement leads to the relation

$$\left\{ \breve{\mathbf{S}} - \cot(\delta\pi)\mathbf{I} \right\} \mathbf{g} = 0 \ , \tag{2.58}$$

where

$$\begin{array}{rcl} \breve{\mathbf{S}} & = & \mathbf{D}^{-1}\mathbf{W} \\ \mathbf{D} & = & \mathbf{L}_1{}^{-1} + \mathbf{L}_2{}^{-1} \\ \mathbf{W} & = & \mathbf{S}_1\mathbf{L}_1{}^{-1} - \mathbf{S}_2\mathbf{L}_2{}^{-1} \end{array} \ . \tag{2.59}$$

The tensors $\mathbf{S}_k$ and $\mathbf{L}_k$, $(k = 1, 2)$, known as the Barnett-Lothe tensors, are real. These tensors may be determined using

$$-\mathbf{A}_k\mathbf{B}_k^{-1} = \mathbf{S}_k\mathbf{L}_k^{-1} + i\mathbf{L}_k^{-1} \ . \tag{2.60}$$

In eq. (2.58), $\mathbf{I}$ is a unit 3×3 matrix. Using the relation in eq. (2.60) with the explicit expressions given in eq. (2.53), it is possible to write

$$\mathbf{S_k L_k}^{-1} = \begin{bmatrix} 0 & -S_{12}'^{(k)} - \sqrt{S_{11}'^{(k)} S_{22}'^{(k)}} & 0 \\ S_{12}'^{(k)} + \sqrt{S_{11}'^{(k)} S_{22}'^{(k)}} & 0 & 0 \\ 0 & 0 & 0 \end{bmatrix} \tag{2.61}$$

and

$$\mathbf{L}_k^{-1} = \begin{bmatrix} S_{11}'^{(k)} \left(\beta_1^{(k)} + \beta_2^{(k)}\right) & 0 & 0 \\ 0 & \sqrt{S_{11}'^{(k)} S_{22}'^{(k)}} \left(\beta_1^{(k)} + \beta_2^{(k)}\right) & 0 \\ 0 & 0 & \sqrt{S_{44}'^{(k)} S_{55}'^{(k)}} \end{bmatrix} . \tag{2.62}$$

The matrices $\mathbf{D}$ and $\mathbf{W}$ in eq. $(2.59)_2$ and eq. $(2.59)_3$, respectively, are functions of the Barnettt-Lothe tensors and may be written explicitly as

$$\mathbf{D} = \begin{bmatrix} \sum_{k=1}^{2} S_{11}'^{(k)} \left(\beta_1^{(k)} + \beta_2^{(k)}\right) & 0 & 0 \\ 0 & \sum_{k=1}^{2} \sqrt{S_{11}'^{(k)} S_{22}'^{(k)}} \left(\beta_1^{(k)} + \beta_2^{(k)}\right) & 0 \\ 0 & 0 & \sum_{k=1}^{2} \sqrt{S_{44}'^{(k)} S_{55}'^{(k)}} \end{bmatrix} \tag{2.63}$$

and

$$\mathbf{W} = \begin{bmatrix} 0 & \sum_{k=1}^{2} (-1)^k \left(S_{12}'^{(k)} + \sqrt{S_{11}'^{(k)} S_{22}'^{(k)}}\right) & 0 \\ \sum_{k=1}^{2} (-1)^{k-1} \left(S_{12}'^{(k)} + \sqrt{S_{11}'^{(k)} S_{22}'^{(k)}}\right) & 0 & 0 \\ 0 & 0 & 0 \end{bmatrix} . \tag{2.64}$$

It should be noted that the members of the matrix $\mathbf{W}$ have the same value with opposite signs, namely

$$W_{12} = -W_{21} \ . \tag{2.65}$$

In the case of the material properties presented in Section 2.1 and used in this study, the value of W_{12} is positive. The matrix $\breve{\mathbf{S}}$ is calculated from eq. $(2.59)_1$ as

$$\breve{\mathbf{S}} = \begin{bmatrix} 0 & \dfrac{W_{12}}{D_{11}} & 0 \\ \dfrac{W_{21}}{D_{22}} & 0 & 0 \\ 0 & 0 & 0 \end{bmatrix} . \tag{2.66}$$

The explicit expressions are

$$\begin{aligned} \breve{S}_{12} &= \frac{\sum_{k=1}^{2} (-1)^k \left(S_{12}'^{(k)} + \sqrt{S_{11}'^{(k)} S_{22}'^{(k)}}\right)}{\sum_{k=1}^{2} S_{11}'^{(k)} \left(\beta_1^{(k)} + \beta_2^{(k)}\right)} \\ \breve{S}_{21} &= \frac{\sum_{k=1}^{2} (-1)^{k-1} \left(S_{12}'^{(k)} + \sqrt{S_{11}'^{(k)} S_{22}'^{(k)}}\right)}{\sum_{k=1}^{2} \sqrt{S_{11}'^{(k)} S_{22}'^{(k)}} \left(\beta_1^{(k)} + \beta_2^{(k)}\right)} \ . \end{aligned} \tag{2.67}$$

All parameters in eq. (2.58), which is an eigenvalue equation, have been defined. The order of the stress singularities δ may be calculated using this equation. The parameter $\cot \delta\pi$ are the eigenvalues and $\mathbf{g}$ are the eigenvectors in eq. (2.58). The eigenvalues may be obtained from a non-trivial solution, namely

$$\det \left[\breve{\mathbf{S}} - \cot(\delta\pi)\mathbf{I} \right] = 0 \quad . \tag{2.68}$$

The eigenvalues obtained are

$$\cot(\delta\pi) = \mp \frac{iW_{12}}{\sqrt{D_{11}D_{22}}} \ , \quad 0 \tag{2.69}$$

recalling that $W_{12} > 0$. Note that, D_{11} and D_{22} have the same sign for a delamination along the interface between the two materials investigated in this study. A parameter β may be defined as

$$\beta \equiv \frac{W_{12}}{\sqrt{D_{11}D_{22}}} \tag{2.70}$$

where β is taken to be positive (Ting, 1996, p. 426). Finally, the order of the stress singularities δ_m, $m = 1, 2, 3$, may be calculated from eq. (2.69) as

$$\delta_1 = -\frac{1}{2} + i\varepsilon, \quad \delta_2 = -\frac{1}{2} - i\varepsilon, \quad \delta_3 = -\frac{1}{2} \tag{2.71}$$

where the oscillatory parameter ε is given by

$$\varepsilon = \frac{1}{2\pi} \ln \left(\frac{1+\beta}{1-\beta} \right) \tag{2.72}$$

and $\varepsilon > 0$, since β is positive.

The eigenvectors $\mathbf{g}_m$ may be found by substituting the eigenvalues δ_m into eq. (2.58), so that

$$\mathbf{g}_1 = \mathbf{d}, \quad \mathbf{g}_2 = \overline{\mathbf{d}} \quad \mathbf{g}_3 = \mathbf{d}^* \tag{2.73}$$

for which

$$\mathbf{d} = \left\{ \begin{array}{c} i\sqrt{\dfrac{D_{22}}{D_{11}}} \\ 1 \\ 0 \end{array} \right\} d_2, \quad \mathbf{d}^* = \left\{ \begin{array}{c} 0 \\ 0 \\ 1 \end{array} \right\} d_3 \quad . \tag{2.74}$$

In eq. (2.74), d_2 is an unknown complex constant and the constant d_3 is real. Furthermore, d_2 may be uniquely related to the complex stress intensity factor K which is defined in eq. (1.22) and d_3 may be uniquely related to the mode III stress intensity factor K_{III}. These relations will be found later in this section.

The displacement field $\mathbf{u}^{(k)}$ and the stress function $\boldsymbol{\phi}^{(k)}$ may be separated into two superposed parts, the oscillatory, square-root singular and the square-root singular part. The oscillatory, square-root singular solution is composed of two superposed solutions

corresponding to δ_1 and δ_2. The square-root singular solution corresponds to δ_3. These vectors may be written as

$$\begin{aligned} \mathbf{u}^{(k)} &= \mathbf{u}_{os}^{(k)} + \mathbf{u}_{s}^{(k)} \\ \boldsymbol{\phi}^{(k)} &= \boldsymbol{\phi}_{os}^{(k)} + \boldsymbol{\phi}_{s}^{(k)} \end{aligned} \tag{2.75}$$

where the subscripts os and s represent the oscillatory, square-root singular and the square-root singular parts of the solution, respectively. By substituting $\delta_1 = \delta$ and $\delta_2 = \overline{\delta}$ with their corresponding related eigenvectors $\mathbf{d}$ and $\overline{\mathbf{d}}$, respectively, into eqs. (2.56), (2.57), (2.74) and then into eqs. (2.47) and (2.48), the oscillatory, square-root singular solution takes the form

$$\begin{aligned} \mathbf{u}_{os}^{(k)} &= \Re\left\{e^{(-1)^{k-1}\pi\varepsilon}\mathbf{A}_k \left\langle z_*^{(k)\,(\frac{1}{2}+i\varepsilon)}\right\rangle \mathbf{B}_k{}^{-1}\,\mathbf{d} + e^{(-1)^{k}\pi\varepsilon}\mathbf{A}_k \left\langle z_*^{(k)\,(\frac{1}{2}-i\varepsilon)}\right\rangle \mathbf{B}_k^{-1}\,\overline{\mathbf{d}}\right\} \\ \boldsymbol{\phi}_{os}^{(k)} &= \Re\left\{e^{(-1)^{k-1}\pi\varepsilon}\mathbf{B}_k \left\langle z_*^{(k)}\ (\tfrac{1}{2}+i\varepsilon)\right\rangle \mathbf{B}_k{}^{-1}\,\mathbf{d} + e^{(-1)^{k}\pi\varepsilon}\mathbf{B}_k \left\langle z_*^{(k)\,(\frac{1}{2}-i\varepsilon)}\right\rangle \mathbf{B}_k{}^{-1}\,\overline{\mathbf{d}}\right\} . \end{aligned} \tag{2.76}$$

It may be mentioned that much mathematical manipulation is required to arrive at eqs. (2.76). In the same way, by substituting $\delta_3 = -\frac{1}{2}$ with the corresponding eigenvector $\mathbf{d}^*$ into the same equations, namely, eqs. (2.56), (2.57), (2.74) and then into eqs. (2.47) and (2.48), the square-root singular solution becomes

$$\begin{aligned} \mathbf{u}_{s}^{(k)} &= \Re\left\{\mathbf{A}_k \left\langle z_*^{(k)\,\frac{1}{2}}\right\rangle \mathbf{B}_k{}^{-1}\right\}\mathbf{d}^* \\ \boldsymbol{\phi}_{s}^{(k)} &= \Re\left\{\mathbf{B}_k \left\langle z_*^{(k)\,\frac{1}{2}}\right\rangle \mathbf{B}_k{}^{-1}\right\}\mathbf{d}^* . \end{aligned} \tag{2.77}$$

In order to relate the eigenvector constants d_2 and d_3, in eqs. (2.74), to the stress intensity factors, K and K_{III}, respectively, the traction components on the interface $\sigma_{i2}(\theta = 0)$, $i = 1, 2, 3$, are needed. The traction components are related to the stress function through eq. $(A.28)_2$. By differentiating eq. $(2.76)_2$ and eq. $(2.77)_2$ by x_1 and substituting the results into eq. $(A.28)_2$, with $\theta = 0$, the oscillatory, square-root singular and square-root singular parts of the traction components along the interface may be found. The tractions obtained may be written as

$$\begin{aligned} \boldsymbol{\phi}_{os,1}^{(k)}|_{\theta=0} &= r^{-\frac{1}{2}}\cosh(\pi\varepsilon)\Re\left\{(1+2i\varepsilon)r^{i\varepsilon}\,\mathbf{d}\right\} \\ \boldsymbol{\phi}_{s,1}^{(k)}|_{\theta=0} &= \frac{1}{2}r^{-\frac{1}{2}}\mathbf{d}^* \end{aligned} \tag{2.78}$$

for the oscillatory, square-root singular and the square-root singular parts, respectively. An explicit expression for the oscillatory component may be written as

$$\left\{\begin{array}{c} \sigma_{12os} \\ \sigma_{22os} \\ \sigma_{32os} \end{array}\right\}\Bigg|_{\theta=0} = r^{-\frac{1}{2}}\cosh\pi\varepsilon \left\{\begin{array}{c} -\sqrt{\dfrac{D_{22}}{D_{11}}}\,\Im\left[(1+2i\varepsilon)r^{i\varepsilon}d_2\right] \\ \Re\left[(1+2i\varepsilon)r^{i\varepsilon}d_2\right] \\ 0 \end{array}\right\} \tag{2.79}$$

and the square-root singular component may be written as

$$\left\{ \begin{array}{c} \sigma_{12_s} \\ \sigma_{22_s} \\ \sigma_{32_s} \end{array} \right\} \Bigg|_{\theta=0} = \frac{1}{2} d_3 r^{-\frac{1}{2}} \left\{ \begin{array}{c} 0 \\ 0 \\ 1 \end{array} \right\} \quad . \tag{2.80}$$

It may be observed that $\sigma_{12} = \sigma_{12os}$, $\sigma_{22} = \sigma_{22os}$ and $\sigma_{32} = \sigma_{32s}$.

In order to fully define all parameters in the displacement field and stress function, d_2 and d_3 must be obtained. First, d_2 will be determined as a function of the complex stress intensity factor K, given in eq. (1.22). This complex stress intensity factor may be defined as

$$K \equiv \lim_{r \to 0} \sqrt{2\pi r}\, r^{-i\varepsilon} \left(\sigma_{22} - i \sqrt{\frac{D_{11}}{D_{22}}} \sigma_{21} \right) \Bigg|_{\theta=0} . \tag{2.81}$$

For plane deformation conditions, along the interface ahead of the delamination tip, the in-plane stress components from eq. (2.81) may be written as

$$\sigma_{22}(r) - i \sqrt{\frac{D_{11}}{D_{22}}} \sigma_{21}(r) \Bigg|_{\theta=0} = \frac{K r^{i\varepsilon}}{\sqrt{2\pi r}} \quad . \tag{2.82}$$

By substituting eq. (2.79) into eq. (2.82), d_2 may be obtained as

$$d_2 = \frac{K}{\sqrt{2\pi}(1 + 2i\varepsilon) \cosh \pi\varepsilon} \quad . \tag{2.83}$$

In a similar manner, K_{III} is defined as

$$K_{III} \equiv \lim_{r \to 0} \sqrt{2\pi r}\, \sigma_{23} \Big|_{\theta=0} \quad . \tag{2.84}$$

For plane deformation conditions, along the interface ahead of the delamination tip, the out-of-plane stress component from eq. (2.84) may be written as

$$\sigma_{23}(r)|_{\theta=0} = \frac{K_{III}}{\sqrt{2\pi r}} \quad . \tag{2.85}$$

By substituting eq. (2.80) into eq. (2.85), d_3 may be obtained as

$$d_3 = \frac{2 K_{III}}{\sqrt{2\pi}} \quad . \tag{2.86}$$

The displacement field and stress function vectors $\mathbf{u}^{(k)}$, $\boldsymbol{\phi}^{(k)}$ $(k = 1, 2)$ may now be written explicitly using definitions presented in this section. For the displacement field, matrix multiplications in eq. $(2.76)_1$ were carried out. The first term of the asymptotic expansion of the in-plane displacement components may be written as

$$u_\alpha^{(k)} = \sqrt{\frac{r}{2\pi}} \left[\Re \left(K r^{i\varepsilon} \right) \, {}_kU_\alpha^{(1)}(\theta) + \Im \left(K r^{i\varepsilon} \right) \, {}_kU_\alpha^{(2)}(\theta) \right] \tag{2.87}$$

with $\alpha = 1, 2$, representing the directions x_1 and x_2 (see Fig. 2.1), respectively, and the superscripts 1 and 2 representing the functions related to the real and imaginary parts of $Kr^{i\varepsilon}$, respectively. In the same manner, matrix multiplications in eq. $(2.77)_1$ were carried out and the explicit expression for the out-of-plane displacement may be written as

$$u_3^{(k)} = \sqrt{\frac{r}{2\pi}} K_{III}\ {}_kU_3^{(III)}(\theta) \quad . \tag{2.88}$$

In eqs. (2.87) and (2.88), the displacement functions ${}_kU_\alpha^{(1)}(\theta)$, ${}_kU_\alpha^{(2)}(\theta)$ and ${}_kU_3^{(III)}(\theta)$ are given below. These functions depend upon θ, and the mechanical properties, all given previously in this section and in Sections 2.1 and 2.2 of this chapter. These properties will be recalculated with respect to the fiber volume factions measured in the specimens which will be tested. It may be noted that these functions have units of L^2/F where L is a length unit and F is force. The in-plane displacement functions for both the upper and lower materials are given by

$$\begin{aligned}
{}_kU_1^{(1)} &= {}_kc_1^* \sum_{s=1}^{2}\sum_{t=1}^{2} (-1)^{s+t}\ {}_k\widetilde{N}_{st}\ {}_kQ_s \left({}_kN_{st}^*\widetilde{D} + {}_k\beta_s^*\right) \\
{}_kU_1^{(2)} &= {}_kc_1^* \sum_{s=1}^{2}\sum_{t=1}^{2} (-1)^{s}\ {}_k\widetilde{N}_{st}\ {}_kQ_s \left({}_kn_{st}^*\widetilde{D} + {}_kM_{st}^*\ {}_k\beta_s^*\right) \\
{}_kU_2^{(1)} &= {}_kc_1^* \sum_{s=1}^{2}\sum_{t=1}^{2} (-1)^{s}\ {}_k\widetilde{N}_{st}\ {}_kQ_{s+2} \left(\beta_s^{(k)}\right)^{-1} \left({}_kM_{st}^*\widetilde{D} + {}_kn_{st}^*\ {}_k\beta_s^*\right) \\
{}_kU_2^{(2)} &= -{}_kc_1^* \sum_{s=1}^{2}\sum_{t=1}^{2} (-1)^{s+t}\ {}_k\widetilde{N}_{st}\ {}_kQ_{s+2} \left(\beta_s^{(k)}\right)^{-1} \left(\widetilde{D} + {}_kN_{st}^*\ {}_k\beta_s^*\right)
\end{aligned} \tag{2.89}$$

.

In eqs. (2.89) for $s, t = 1, 2$, ${}_kc_s^*$, ${}_k\widetilde{N}_{st}$, ${}_kN_{st}^*$, ${}_kn_{st}^*$, ${}_kM_{st}^*$ and ${}_k\beta_s^*$ are given as

$$\begin{aligned}
{}_kc_s^* &= \frac{2\left[\frac{1}{2}\left(1+4\varepsilon^2\right)\right]^{s-1}}{\left(\beta_1^{(k)} - \beta_2^{(k)}\right)\left(1+4\varepsilon^2\right)\cosh \pi\varepsilon}, & {}_k\widetilde{N}_{st} &= {}_kn_{st}\ {}_kN_{st}\ {}_kM_{st}\ {}_kB_s{}^{1/4} \ , \\
{}_kN_{st}^* &= {}_kN_{s1}\ {}_kN_{s2}\ {}_kN_{st}{}^{-2}, & {}_kn_{st}^* &= {}_kn_{s1}\ {}_kn_{s2}\ {}_kn_{st}{}^{-2} \ , \\
{}_kM_{st}^* &= {}_kM_{s1}\ {}_kM_{s2}\ {}_kM_{st}^{-2} \ , & {}_k\beta_s^* &= \beta_1^{(k)}\ \beta_2^{(k)} \left(\beta_s^{(k)}\right)^{-1}
\end{aligned} \tag{2.90}$$

where ε is given in eq. (2.72) and the parameters $\beta_s^{(k)}$ may be found in eq. (2.40). In eqs. (2.90), ${}_k\widetilde{N}_{st}$, ${}_kN_{st}^*$, ${}_kn_{st}^*$ and ${}_kM_{st}^*$ are defined with ${}_kN_{st}$ and ${}_kM_{st}$, where $s = 1, 2$, and with ${}_kn_{st}$, where $s = 1, 2, 3$, namely

$$\begin{aligned}
{}_kn_{s1} &= \cos\left(\frac{{}_k\varphi_s}{2}\right) , & {}_kn_{s2} &= \sin\left(\frac{{}_k\varphi_s}{2}\right) , \\
{}_kN_{s1} &= \cosh\left[\varepsilon(\pi + (-1)^k\ {}_k\varphi_s)\right] , & {}_kN_{s2} &= (-1)^{(k-1)} \sinh\left[\varepsilon(\pi + (-1)^k\ {}_k\varphi_s)\right] \\
{}_kM_{s1} &= {}_kM_{s3} + 2\varepsilon\ {}_kM_{s4} , & {}_kM_{s2} &= {}_kM_{s4} - 2\varepsilon\ {}_kM_{s3} , \\
{}_kM_{s3} &= \cos\left({}_km_s\right) , & {}_kM_{s4} &= \sin\left({}_km_s\right) .
\end{aligned} \tag{2.91}$$

In eqs. (2.91), the parameters ${}_kM_{st}$ are defined with ${}_km_s$ and the parameters ${}_kN_{st}$ and ${}_kn_{st}$ are defined using ${}_k\varphi_s$. The parameters ${}_km_s$ $(s = 1, 2)$ and ${}_k\varphi_s$ $(s = 1, 2, 3)$ are given

as

$$\begin{aligned} {}_k m_s &= \frac{\varepsilon}{2} \ln \left({}_k B_s \right) , \\ {}_k \varphi_s &= \arg \left(\cos\theta + i \beta_s^{(k)} \sin\theta \right) , \end{aligned} \tag{2.92}$$

where ${}_k B_s$ $(s = 1, 2, 3)$ is defined as

$${}_k B_s = \cos^2\theta + \left(\beta_s^{(k)} \right)^2 \sin^2\theta \ . \tag{2.93}$$

In eq. (2.89), the parameters ${}_k Q_s$ and ${}_k Q_{s+2}$ where $s = 1, 2$ are given by

$${}_k Q_s = -S_{12}^{\prime(k)} + \left(\beta_s{}^{(k)} \right)^2 S_{11}^{\prime(k)} , \qquad {}_k Q_{s+2} = S_{22}^{\prime(k)} - \left(\beta_s^{(k)} \right)^2 S_{12}^{\prime(k)} . \tag{2.94}$$

The parameter $\widetilde{D}$ is defined as

$$\widetilde{D} = \sqrt{\frac{D_{22}}{D_{11}}} , \tag{2.95}$$

using two diagonal members of the matrix $\mathbf{D}$ given in eq. (2.63). The out-of-plane displacement functions in eq. (2.88) are written as

$${}_k U_3^{(III)} = 2 \left({}_k B_3 \right)^{\frac{1}{4}} {}_k n_{32} \sqrt{S_{44}^{\prime(k)} S_{55}^{\prime(k)}} \tag{2.96}$$

Explicit expressions for the stress components were obtained using eqs. (A.28). By differentiation of the vector $\boldsymbol{\phi}$, given in eq. $(2.76)_2$, and substituting parameters described in this section, the first term of the asymptotic expansion for the in-plane stress components was obtained. This expression may be written as

$$\sigma_{\alpha\beta}^{(k)} = \frac{1}{\sqrt{2\pi r}} \left[\Re \left(K r^{i\varepsilon} \right) \ {}_k \Sigma_{\alpha\beta}^{(1)}(\theta) + \Im \left(K r^{i\varepsilon} \right) \ {}_k \Sigma_{\alpha\beta}^{(2)}(\theta) \right] , \tag{2.97}$$

with α, $\beta = 1, 2$, representing the directions x_1 and x_2, respectively, and the superscripts 1 and 2 representing the functions related to the real and imaginary parts of $K r^{i\varepsilon}$, respectively. Explicit expressions for the functions ${}_k \Sigma_{\alpha\beta}^{(1)}(\theta)$ and ${}_k \Sigma_{\alpha\beta}^{(2)}(\theta)$ are given below. The expression for the out-of-plane stress components is found in a similar manner by differentiating eq. $(2.77)_2$, so that

$$\sigma_{\alpha 3}^{(k)} = \frac{K_{III}}{\sqrt{2\pi r}} \, {}_k \Sigma_{\alpha 3}^{(III)}(\theta) \ . \tag{2.98}$$

Explicit expressions for the functions ${}_k \Sigma_{\alpha 3}^{(III)}(\theta)$ are also given below.

With the representation shown in eq. (2.97), the in-plane stress functions ${}_k \Sigma_{\alpha\beta}^{(1)}(\theta)$ and

${}_k\Sigma^{(2)}_{\alpha\beta}(\theta)$ may be written as

$$
\begin{aligned}
{}_k\Sigma^{(1)}_{11} &= -{}_kc^*_2 \sum_{s=1}^{2}\sum_{t=1}^{2} (-1)^s {}_k\widetilde{N}_{st}\, ({}_kB_s)^{-\frac{1}{2}} \left(\beta_s^{(k)}\right)^2 \left({}_kN^*_{st}\,\widetilde{D} + {}_k\beta^*_s\right) \\
{}_k\Sigma^{(2)}_{11} &= {}_kc^*_2 \sum_{s=1}^{2}\sum_{t=1}^{2} (-1)^{s+t} {}_k\widetilde{N}^{(k)}_{st}\, ({}_kB_s)^{-\frac{1}{2}} \left(\beta_s^{(k)}\right)^2 \left({}_kn^*_{st}\,\widetilde{D} - {}_kM^*_{st}\,{}_k\beta^*_s\right) \\
{}_k\Sigma^{(1)}_{12} &= -{}_kc^*_2 \sum_{s=1}^{2}\sum_{t=1}^{2} (-1)^{s+t} {}_k\widetilde{N}_{st}\, ({}_kB_s)^{-\frac{1}{2}}\, \beta_s^{(k)} \left({}_kM^*_{st}\,\widetilde{D} - {}_kn^*_{st}\,{}_k\beta^*_s\right) \\
{}_k\Sigma^{(2)}_{12} &= {}_kc^*_2 \sum_{s=1}^{2}\sum_{t=1}^{2} (-1)^{s} {}_k\widetilde{N}_{st}\, ({}_kB_s)^{-\frac{1}{2}}\, \beta_s^{(k)} \left(\widetilde{D} + {}_kN^*_{st}\,{}_k\beta^*_s\right) \\
{}_k\Sigma^{(1)}_{22} &= {}_kc^*_2 \sum_{s=1}^{2}\sum_{t=1}^{2} (-1)^{s} {}_k\widetilde{N}_{st}\, ({}_kB_s)^{-\frac{1}{2}} \left({}_kN^*_{st}\,\widetilde{D} + {}_k\beta^*_s\right) \\
{}_k\Sigma^{(2)}_{22} &= -{}_kc^*_2 \sum_{s=1}^{2}\sum_{t=1}^{2} (-1)^{s+t} {}_k\widetilde{N}_{st}\, ({}_kB_s)^{-\frac{1}{2}} \left({}_kn^*_{st}\,\widetilde{D} - {}_kM^*_{st}\,{}_k\beta^*_s\right) \quad .
\end{aligned}
\tag{2.99}
$$

where all functions used are given in eqs. (2.90), (2.94),(2.95), (2.91), (2.92) and (2.93). The out-of-plane functions ${}_k\Sigma^{(III)}_{\alpha 3}$ are given by

$$
\begin{aligned}
{}_k\Sigma^{(III)}_{13} &= -\beta_3^{(k)}\, ({}_kB_3)^{-\frac{1}{4}}\, {}_kn_{32} \\
{}_k\Sigma^{(III)}_{23} &= ({}_kB_3)^{-\frac{1}{4}}\, {}_kn_{31}
\end{aligned}
\tag{2.100}
$$

where the parameters ${}_kB_3$ and ${}_kn_{32}$ are given in eqs. (2.93) and $(2.91)_2$, respectively.

Chapter 3

Methods for extracting stress intensity factors

Stress intensity factors for a given problem may be calculated numerically using various methods. In this investigation, the displacement extrapolation method and the conservative, interaction energy M-integral are used. In the first chapter, in Sections 1.2.1 and 1.2.2, both methods were introduced, respectively, for linear elastic, homogeneous, isotropic materials.

In this chapter, both methods will be extended for a delamination along an interface between a transversely isotropic UD fabric and a tetragonal weave. Both methods make use of the first term of the asymptotic expansion for the displacements, presented in Section 2.3, along with a finite element analysis. First, the displacement extrapolation method will be presented in Section 3.1. This direct method is considered to be less accurate than the energy based M-integral and is used for validation of the results (Banks-Sills, 2010). The conservative, interaction energy integral or M-integral is an energy based method and will be presented in Section 3.2. This integral was derived from the conservative J-integral; therefore, the J-integral will be considered first. In eq. (1.31), an expression relating the energy release rate $\mathcal{G}$ and a combination of the stress intensity factors is presented. Since $J = \mathcal{G}$ this expression relates J to the stress intensity factors. However, from this equation the stress intensity factors for the different modes cannot be separated. In order to separate the different stress intensity factors in a mixed mode problem, the M-integral, with use of auxiliary solutions, is employed. This integral provides a sufficient number of equations allowing determination of the stress intensity factors K_1, K_2 and K_{III}. Both extended methods and software were validated with three mechanical benchmark problems and one thermal problem. Comparison made for this purpose are described in Section 3.3.

3.1 Displacement extrapolation method

One of the methods used to extract the stress intensity factors K_1, K_2 and K_{III} is the displacement extrapolation (DE) method. In this section, the DE method will be presented and extended for the particular case of a delamination along an interface of a transversely isotropic material and a tetragonal material. In particular, the interface between a UD fabric with fibers mainly in the 0°- direction and a $+45°/-45°$ balanced plain weave as shown in Fig. 2.1 is considered. The first term of the displacement field in the vicinity of the delamination front which was developed in Section 2.3 may be employed to extract the stress intensity factors using the DE method.

The delamination displacement jump within the neighborhood of the delamination front is defined by

$$\Delta u_i \equiv u_i^{(1)}(r, \theta = \pi) - u_i^{(2)}(r, \theta = -\pi) \tag{3.1}$$

where the coordinate system is shown in Fig. 2.1. Here the superscripts (1) and (2) represent the upper and lower materials, respectively, and u_i is the displacement in the x_i-direction for $i = 1, 2, 3$. Substitution of $\theta = \pi$ and $\theta = -\pi$ for the upper and lower materials, respectively, into the oscillatory, square-root singular and the square-root singular displacement expressions in eqs. (2.87) and (2.88) will result in

$$\begin{aligned} \mathbf{u}_{os}^{(1)}\Big|_{\theta=\pi} &= 2\sqrt{r}\,\mathbf{L}_1^{-1}\Re\left\{r^{i\varepsilon}\mathbf{d}\right\}\ , \\ \mathbf{u}_{os}^{(2)}\Big|_{\theta=-\pi} &= -2\sqrt{r}\,\mathbf{L}_2^{-1}\Re\left\{r^{i\varepsilon}\mathbf{d}\right\}\ , \end{aligned} \tag{3.2}$$

and

$$\begin{aligned} \mathbf{u}_{s}^{(1)}\Big|_{\theta=\pi} &= \sqrt{r}\,\mathbf{L}_1^{-1}\mathbf{d}^*\ , \\ \mathbf{u}_{s}^{(2)}\Big|_{\theta=-\pi} &= -\sqrt{r}\,\mathbf{L}_2^{-1}\mathbf{d}^*\ , \end{aligned} \tag{3.3}$$

respectively. In eqs. (3.2), and (3.3), $\mathbf{L}_k^{-1}$ is defined in eq. (2.62). The jump in the oscillatory, square-root singular displacement may be obtained by substituting eqs. $(3.2)_1$ and $(3.2)_2$ into eq. (3.1) as

$$\Delta\mathbf{u}_{os} = 2\sqrt{r}\,\mathbf{D}\,\Re\left\{r^{i\varepsilon}\mathbf{d}\right\} \tag{3.4}$$

where $\mathbf{D}$ is the 3×3 matrix given in eq. (2.63). For the jump in the square-root singular, displacement, eqs. $(3.3)_1$ and $(3.3)_2$ are substituted into eq. (3.1) leading to

$$\Delta\mathbf{u}_{s} = \sqrt{r}\,\mathbf{D}\,\mathbf{d}^*\ . \tag{3.5}$$

Using $\mathbf{D}$ and $\mathbf{d}$ given in eqs. (2.63), $(2.74)_1$ and (2.83) in eq. (3.4), the oscillatory,

square-root singular part of the delamination face displacement jump vector may be obtained as

$$\left\{ \begin{array}{c} \Delta u_{1os} \\ \Delta u_{2os} \\ \Delta u_{3os} \end{array} \right\} = \sqrt{\frac{2r}{\pi}} \frac{D_{22}}{\cosh \pi\varepsilon} \left\{ \begin{array}{c} -\sqrt{\frac{D_{11}}{D_{22}}} \Im \left[\frac{K r^{i\varepsilon}}{1+2i\varepsilon} \right] \\ \Re \left[\frac{K r^{i\varepsilon}}{1+2i\varepsilon} \right] \\ 0 \end{array} \right\} \tag{3.6}$$

where D_{11} and D_{22} are diagonal elements of the matrix $\mathbf{D}$. In the same manner, by substituting $\mathbf{D}$ and $\mathbf{d}^*$ given in eqs. (2.63), $(2.74)_2$ and (2.86) into eq. (3.5), the square-root singular part of the delamination face displacement jump vector may be obtained as

$$\left\{ \begin{array}{c} \Delta u_{1s} \\ \Delta u_{2s} \\ \Delta u_{3s} \end{array} \right\} = \sqrt{\frac{2r}{\pi}} D_{33} K_{III} \left\{ \begin{array}{c} 0 \\ 0 \\ 1 \end{array} \right\} \quad . \tag{3.7}$$

From the obtained delamination face displacement jump components given in eqs. (3.6) and (3.7) , it may be observed that the square-root singular part of Δu_1 and Δu_2 is zero, therefore they have only oscillatory, square-root singular components; whereas, Δu_3 is solely square-root singular ($\Delta u_{3os} = 0$).

In the same manner that the traction components along the interface ahead of the delamination front are related to the stress intensity factors, as given in eqs. (2.81) and (2.84), it is possible to obtain a relation between the delamination face displacement jump components and the local stress intensity factors K_1^*, K_2^* and K_{III}^* as

$$\Delta u_2 - i\widetilde{D}\Delta u_1 = \frac{2D_{22}}{(1+2i\varepsilon)\cosh \pi\varepsilon} \sqrt{\frac{r}{2\pi}} K r^{i\varepsilon} \tag{3.8}$$

and

$$\Delta u_3 = 2D_{33} \sqrt{\frac{r}{2\pi}} K_{III} \quad . \tag{3.9}$$

These expressions are separated for the in-plane stress intensity factor K, given in eq. (1.22), and the out-of-plane stress intensity factor K_{III}, respectively. The parameter $\widetilde{D}$ in eq. (3.8) is given in eq. (2.95) and the parameter D_{22} is a diagonal member of the matrix $\mathbf{D}$ given in eq. (2.63). In eq. (3.9), D_{33} is a diagonal member of the matrix $\mathbf{D}$, as well. By manipulating eq. (3.8), explicit expressions for the local stress intensity factors may be written as

$$\begin{aligned} K_1^*(r) &= C\sqrt{\frac{2\pi}{r}} \cos\left[\gamma(r,\varepsilon)\right] \\ K_2^*(r) &= C\sqrt{\frac{2\pi}{r}} \sin\left[\gamma(r,\varepsilon)\right] \end{aligned} \tag{3.10}$$

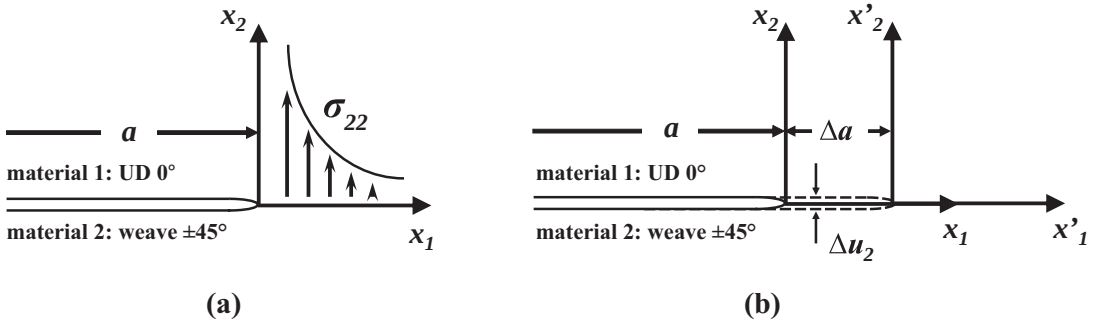

Figure 3.1: Delamination tip (a) before virtual delamination opening Δa; (b) after virtual delamination opening Δa.

where

$$C = \frac{\sqrt{1+4\varepsilon^2}\cosh \pi\varepsilon}{2D_{22}} \sqrt{(\Delta u_2)^2 + \left(\widetilde{D}\Delta u_1\right)^2} \tag{3.11}$$

and

$$\gamma = \left[\tan^{-1}\left(\frac{-\widetilde{D}\Delta u_1}{\Delta u_2}\right) + \tan^{-1}(2\varepsilon) - \varepsilon \ln r\right] \quad . \tag{3.12}$$

From eq. (3.9), the out-of-plane local stress intensity factor K^*_{III} is obtained as

$$K^*_{III}(r) = \frac{\sqrt{2\pi}}{2D_{33}} \frac{\Delta u_3}{\sqrt{r}} \quad . \tag{3.13}$$

3.2 Interaction energy integral

The stress intensity factors K_1, K_2 and K_{III} may be extracted using the interaction energy or M-integral. In this section, the three-dimensional M-integral will be extended for the particular case of a delamination along an interface of a transversely isotropic material and a tetragonal material. In particular, the interface between a UD fabric with fibers mainly in the 0°-direction and a $+45°/-45°$ balanced plain weave as shown in Fig. 2.1 is considered.

Based on the Irwin crack closure integral (Irwin, 1958), an explicit expression for the in-plane interface energy release rate for a delamination along an interface between a transversely isotropic material and a tetragonal material may be developed beginning with

$$\mathcal{G}_{os} = \lim_{\Delta a \to 0} \frac{1}{2\Delta a} \int_0^{\Delta a} \Re \left\{ \left[\sigma_{22}(x_1) - i\sqrt{\frac{D_{11}}{D_{22}}}\sigma_{21}(x_1)\right] \times \left[\Delta u_2(\Delta a - x_1) + i\sqrt{\frac{D_{22}}{D_{11}}}\Delta u_1(\Delta a - x_1)\right] \right\} dx_1 \quad . \tag{3.14}$$

In eq. (3.14), the subscript *os* represents the oscillatory, square-root singular solution which contributes to the in-plane part of the energy release rate, Δa is the virtual delamination extension shown in Fig. 3.1b, $\Re$ represents the real part of the quantity in parentheses and $i = \sqrt{-1}$. The parameters D_{11} and D_{22} are diagonal members of the matrix $\mathbf{D}$ given in eq. (2.63) and related to the mechanical properties of the upper and lower materials. In eq. (3.14), σ_{22} and σ_{21} are the traction components calculated ahead of the delamination front on the interface before the delamination has been extended. In Fig. 3.1a, the normal stress is shown schematically. It is known that the stresses oscillate near the delamination front. The displacement jumps Δu_2 and Δu_1 are calculated along the delamination faces after it has been extended. The jump Δu_2 is shown in Fig. 3.1b. For the out-of-plane interface energy release rate, an explicit expression may also be developed beginning with

$$\mathcal{G}_s = \lim_{\Delta a \to 0} \frac{1}{2\Delta a} \int_0^{\Delta a} \sigma_{23}(x) \Delta u_3(\Delta a - x) dx \tag{3.15}$$

where the subscript s represents the square-root singular solution which contributes to the out-of-plane part of the energy release rate.

The in-plane interface energy release rate given in eq. (3.14) and the out-of-plane interface energy release rate given in eq. (3.15) are also related to the in-plane stress intensity factor K, given in eq. (1.22) and to the out-of-plane stress intensity factor K_{III}, respectively. By substituting eqs. (2.82), with $r = x_1$, and the complex conjugate of (3.8), with $r = \Delta a - x_1$, into eq. (3.14) and carrying out the integration, a relation between the in-plane interface energy release rate, given in eq. (3.14) and the in-plane stress intensity factors may be obtained. In the same manner, the out-of-plane relation between the mode *III* interface energy release rate and the out-of-plane stress intensity factor K_{III} may be obtained by substituting eq. (2.85), with $r = x_1$, and eq. (3.9), with $r = \Delta a - x_1$, into eq. (3.15) and carrying out the integration.

As was previously shown in eq. (1.13) for a homogeneous material, the overall energy release rate, $\mathcal{G}_T$, is the sum of the in-plane and out-of-plane energy release rates. For an interface between two isotropic or anisotropic materials, this expression becomes

$$\mathcal{G}_i = \mathcal{G}_{os} + \mathcal{G}_s \tag{3.16}$$

where the subscript i represents interface. Thus, the interface energy release rate becomes

$$\mathcal{G}_i = \frac{1}{H_1}\left(K_1^2 + K_2^2\right) + \frac{1}{H_2} K_{III}^2 \quad . \tag{3.17}$$

where

$$\begin{aligned} \frac{1}{H_1} &= \frac{D_{22}}{4\cosh^2 \pi\varepsilon} \\ \frac{1}{H_2} &= \frac{D_{33}}{4} \quad . \end{aligned} \tag{3.18}$$

In eqs. (3.18), D_{22} and D_{33} are diagonal members of the matrix $\mathbf{D}$ given in eq. (2.63) and the oscillating parameter ε is found from the mechanical properties of the two materials and given in eq. (2.72).

For a delamination along an interface between a transversely isotropic material and a tetragonal material, the two phase angles $\hat{\psi}$ and ϕ are given by

$$\hat{\psi} = \arctan\left\{\frac{\Im(K\hat{L}^{i\varepsilon})}{\Re(K\hat{L}^{i\varepsilon})}\right\} = \arctan\left\{\sqrt{\frac{D_{11}}{D_{22}}}\frac{\sigma_{12}}{\sigma_{22}}\right\}\Bigg|_{\theta=0,r=\hat{L}} \tag{3.19}$$

and

$$\phi = \arctan\left\{\sqrt{\frac{H_1}{H_2}}\frac{K_{III}}{\sqrt{K_1^2+K_2^2}}\right\} = \arctan\left(\sqrt{\frac{H_1}{H_2}}\frac{\sigma_{32}}{\sqrt{\sigma_{22}^2+\sigma_{12}^2}}\right)\Bigg|_{\theta=0,r=\hat{L}}, \tag{3.20}$$

respectively. It should be recalled that the parameter $\hat{L}$ in eqs. (3.19) and (3.20) is an arbitrary length.

The three-dimensional mechanical M-integral was presented in eq. (1.65) for a delamination along an interface between two isotropic materials. By equating this expression with the expression given in eq. (1.64), the mechanical stress intensity factors were obtained. For the material combination studied here eq. (1.64) is replaced by

$$M_N^{(1,2\alpha)} = \frac{2}{H_1}\left\{K_{1_N}^{(1)}K_{1_N}^{(2\alpha)} + K_{2_N}^{(1)}K_{2_N}^{(2\alpha)}\right\} + \frac{2}{H_2}K_{III_N}^{(1)}K_{III_N}^{(2\alpha)} \ . \tag{3.21}$$

In eq. (3.21), the parameters H_1 and H_2 are given in eq. (3.18). The auxiliary solutions 2α ($\alpha = a, b, c$) are calculated from the first term of the asymptotic solution of the displacement components. The first term of the asymptotic solution for the specific interface studied here was developed and is given in eqs. (2.87) and (2.88). The stress intensity factors related to cases $2\alpha = 2a, 2b$ and $2c$ are given in Table 1.4. By equating eq. (1.65) with eq. (3.21), the mechanical stress intensity factors are obtained as

$$K_1^{(1)} = \frac{H_1}{2A_1}\sum_{k=1}^{2}\int_{V_k}\left[{}_k\sigma_{ij}^{(1)}\frac{\partial\,{}_ku_i^{(2a)}}{\partial x_1} + {}_k\sigma_{ij}^{(2a)}\frac{\partial\,{}_ku_i^{(1)}}{\partial x_1} - {}_kW^{(1,2a)}\delta_{1j}\right]\frac{\partial q_1}{\partial x_j}\,dV\ ; \tag{3.22}$$

$$K_2^{(1)} = \frac{H_1}{2A_1}\sum_{k=1}^{2}\int_{V_k}\left[{}_k\sigma_{ij}^{(1)}\frac{\partial\,{}_ku_i^{(2b)}}{\partial x_1} + {}_k\sigma_{ij}^{(2b)}\frac{\partial\,{}_ku_i^{(1)}}{\partial x_1} - {}_kW^{(1,2b)}\delta_{1j}\right]\frac{\partial q_1}{\partial x_j}\,dV\ ; \tag{3.23}$$

$$K_{III}^{(1)} = \frac{H_2}{2A_1}\sum_{k=1}^{2}\int_{V_k}\left[{}_k\sigma_{ij}^{(1)}\frac{\partial\,{}_ku_i^{(2c)}}{\partial x_1} + {}_k\sigma_{ij}^{(2c)}\frac{\partial\,{}_ku_i^{(1)}}{\partial x_1} - {}_kW^{(1,2c)}\delta_{1j}\right]\frac{\partial q_1}{\partial x_j}\,dV \tag{3.24}$$

The thermal three-dimensional M-integral was presented in eq. (1.78) for a constant temperature change. For a delamination along an interface between two anisotropic materials ${}_k\beta_{ij}$ is given as

$${}_k\beta_{ij} = {}_kC_{ijrs}\,{}_k\alpha_{rs} \ . \tag{3.25}$$

where the upper and lower materials are denoted by $k = 1, 2$, respectively, with no summation on k. In eq. (3.25), C_{ijrs} $(i, j, r, s = 1, 2, 3)$ are the stiffness components for each material. Both compliance matrices, in contracted form, for the materials on each side of the interface were presented in eqs. (2.10) and (2.21), for the upper and lower materials, respectively. The stiffness matrices for both materials are equal to the inverse of these compliance matrices. In eq. (3.25), ${}_k\alpha_{rs}$ are the components of the coefficients of thermal expansion (CTE) for each material. The stress-strain-thermal constitutive relation is given by

$$ {}_k\sigma_{ij} \;=\; {}_kC_{ijrs}\;{}_k\varepsilon_{rs} \;-\; {}_k\beta_{ij}\;{}_k\Delta\vartheta \tag{3.26} $$

where ${}_k\Delta\vartheta$ represents the temperature change in each material and ${}_k\varepsilon_{rs}$ are the total strain components of each material. In the same manner as that for a delamination along an interface between two isotropic materials, the auxiliary temperature change ${}_k\Delta\vartheta^{(2\alpha)}$ is taken to be zero so that the auxiliary solution is the same as that for mechanical loading. The temperature change in each material k is then equal to the temperature change in the problem at hand, namely

$$ {}_k\Delta\vartheta = \;{}_k\Delta\vartheta^{(1)}. \tag{3.27} $$

By equating eq. (1.78) with eq. (3.21), the thermal stress intensity factors in the three-dimensional case of the delamination studied here may be found as

$$ K_1^{(r)} \;=\; \frac{H_1}{2A_1}\sum_{k=1}^{2}\int_{V_k}\left[{}_k\sigma_{ij}^{(1)}\,\frac{\partial\;{}_ku_i^{(2a)}}{\partial x_1} \;+\; {}_k\sigma_{ij}^{(2a)}\,\frac{\partial\;{}_ku_i^{(1)}}{\partial x_1} \;-\; {}_kW_F^{(1,2a)}\delta_{1j}\right]\frac{\partial q_1}{\partial x_j} \tag{3.28} $$

$$ K_2^{(r)} \;=\; \frac{H_1}{2A_1}\sum_{k=1}^{2}\int_{V_k}\left[{}_k\sigma_{ij}^{(1)}\,\frac{\partial\;{}_ku_i^{(2b)}}{\partial x_1} \;+\; {}_k\sigma_{ij}^{(2b)}\,\frac{\partial\;{}_ku_i^{(1)}}{\partial x_1} \;-\; {}_kW_F^{(1,2b)}\delta_{1j}\right]\frac{\partial q_1}{\partial x_j} \tag{3.29} $$

$$ K_{III}^{(r)} \;=\; \frac{H_2}{2A_1}\sum_{k=1}^{2}\int_{V_k}\left[{}_k\sigma_{ij}^{(1)}\,\frac{\partial\;{}_ku_i^{(2c)}}{\partial x_1} \;+\; {}_k\sigma_{ij}^{(2c)}\,\frac{\partial\;{}_ku_i^{(1)}}{\partial x_1} \;-\; {}_kW_F^{(1,2c)}\delta_{1j}\right]\frac{\partial q_1}{\partial x_j} \tag{3.30} $$

where H_1 and H_2 are given in eq. (3.18), and the interaction strain energy density is given in eq. (1.72).

3.3 Benchmark problems

The methodology for determining the mechanical and thermal stress intensity factors includes development of the first term of the asymptotic expansion of the displacement components, as presented in Section 2.3, as well as development of expressions and software for the DE method and the mechanical and thermal M-integrals, as described in Sections 3.1 and 3.2, respectively. In order to demonstrate the validity of the developed expressions and post processors, as well as to assess their accuracy, three benchmark problems were solved to validate the mechanical M-integral and DE method. In addition, a thermal problem with an applied temperature change was carried out. The mechanical

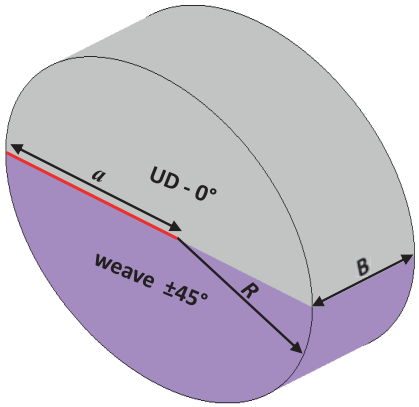

Figure 3.2: Three-dimensional cylindrical model containing an edge delamination used for the benchmark problems and for the thermal problem. The upper and lower materials are colored in gray and purple, respectively.

properties of both the upper and lower materials were homogenized to obtain effective properties which were presented in Section 2.1. These properties will be recalculated for the specimens used in the fracture tests. Some recalculations were carried out, although not final; they were used in the benchmark problems. The thermal properties, used in the thermal problem, were calculated for the upper and lower materials using HFGMC. These properties will be recalculated by means of HFGMC for the fiber volume fractions of the specimens used in the fracture tests. The effective properties are used to determine the stress intensity factors.

The solved benchmark problems, as well as the thermal problem are for a cylindrical body composed of two materials, in grey and purple, respectively, shown in Fig. 3.2; between them is an edge delamination. In Fig. 3.2, a is the delamination length, R is the radius of the cylindrical body and B is its thickness. The specific sizes of the model used were $R = 30$ mm, $a = 30$ mm and $B = 20$ mm. In the benchmark problems, the first term of the asymptotic solution for the displacement components in eqs. (2.87) and (2.88) were applied to the outer boundary of the body except for the delamination faces, which were assumed to be traction free. Three sets of stress intensity factors were imposed to obtain the desired displacement components for each problem. These are shown in Table 1.4 as $2a$, $2b$ and $2c$. In the thermal problem, a coupled thermal-stress analysis was carried out. Two steps were used in the calculation. The initial step consists of application of a uniform temperature, 0° C; the final step consists of application of a uniform temperature, $-60°$ C.

In Fig. 3.3, the mesh used, is shown. The mesh contains 83,200 twenty-noded isoparametric elements of type C3D20 and C3D20T in the mechanical benchmark and thermal problem, respectively, with 352,513 nodal points. Quarter-point elements were used surrounding the delamination front to model the dominant square-root singularity. The elements near the delamination front had a size of $0.15 \times 0.15 \times 1$ mm^3, where element

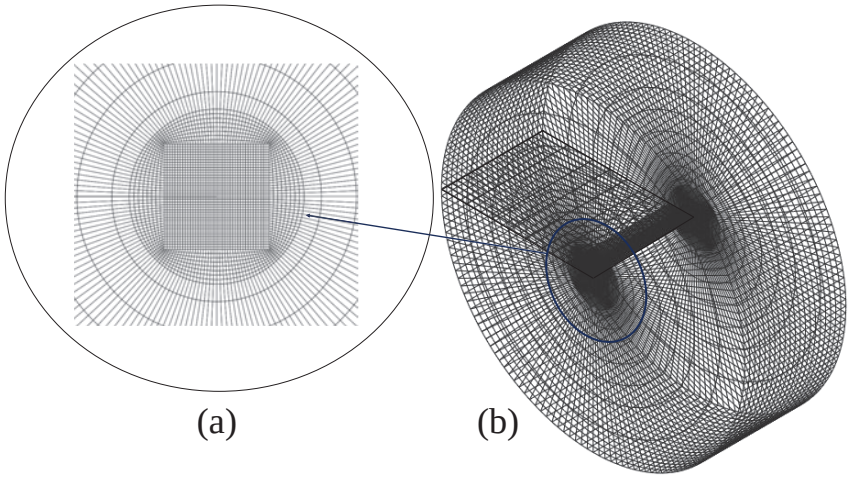

Figure 3.3: Finite element mesh for benchmark problem (a) focused view of the delamination region; (b) entire model.

density was increased, as shown in Fig. 3.3a. An in-plane aspect ratio of 1×1 was fulfilled in this region in order to enhance modeling of the singular stresses; through the thickness, this ratio was not maintained.

Finite element analyses were performed using the FE program Abaqus (2017) to obtain the displacement fields of each problem. The deformed models for the three sets of stress intensity factors used, are presented in Fig. 3.4. The displacement field was used for calculating the stress intensity factors by means of the DE method and the mechanical and thermal M-integrals. With the M-integral, strain and stress components were determined from the displacement components by means of a finite element scheme for both the FE results and the auxiliary solutions. In the three benchmark problems, for both methods, the stress intensity factors obtained were compared with the expected imposed stress intensity factors shown in Table 1.4. The stress intensity factors for the thermal problem were obtained using the DE method and compared with those obtained using the thermal

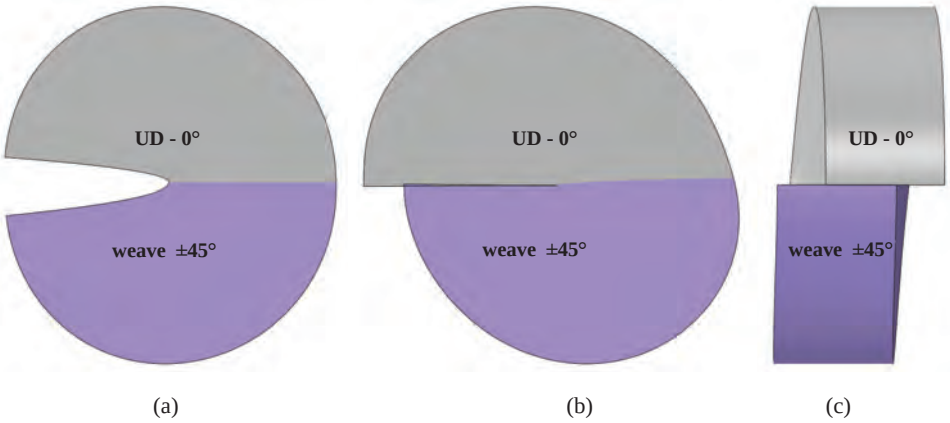

Figure 3.4: Three benchmark deformed models (a) $K_1^{(f)} = 1$, $K_2^{(f)} = 0$, $K_{III}^{(f)} = 0$; (b) $K_1^{(f)} = 0$, $K_2^{(f)} = 1$, $K_{III}^{(f)} = 0$; (c) $K_1^{(f)} = 0$, $K_2^{(f)} = 0$, $K_{III}^{(f)} = 1$.

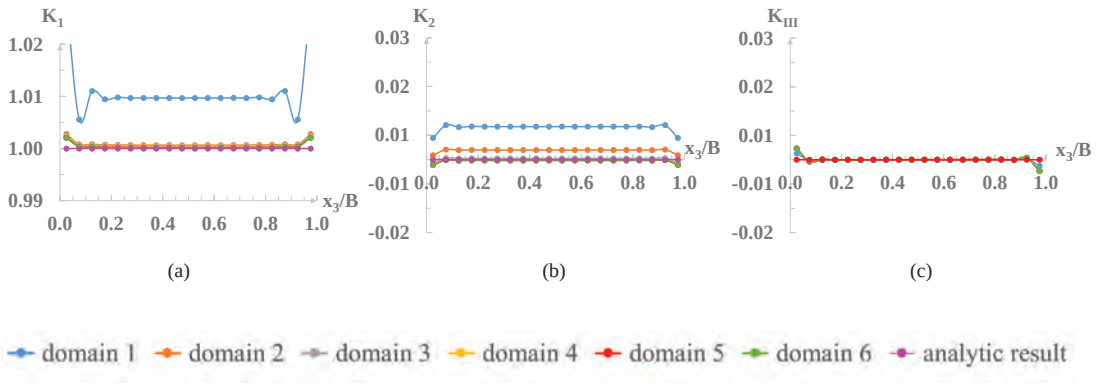

Figure 3.5: Stress intensity factors for the first benchmark problem: $K_1^{(f)} = 1$, $K_2^{(f)} = 0$ and $K_{III}^{(f)} = 0$; (a) $K_1^{(f)}$, (b) $K_2^{(f)}$ and (c) $K_{III}^{(f)}$.

M-integral. With this comparison the quality of the mechanical M-integral and DE methods was evaluated. Results for the three benchmark problems will be described first, then results from the thermal problem will be presented.

In the mechanical case, DE was carried out. It has been observed in other cases that the local stress intensity factors $K_1^{*(f)}$, $K_2^{*(f)}$ and $K_{III}^{*(f)}$ in eqs. (3.10) and (3.13), respectively, produced the exact imposed solutions. Extrapolation led to the exact result. The results give confidence to the accuracy of the solution. In general, results obtained with the DE method are less accurate than those found by means of the M-integral.

The M-integral was calculated and the stress intensity factors were obtained for each volume containing a layer of elements along the delamination front from eqs. (3.22) - (3.24). The calculated stress intensity factors along the delamination front for the three benchmark problems are plotted in Figs. 3.5, 3.6 and 3.7 as a function of the normalized coordinate x_3/B (see Fig. 1.7). The parameter B is the model thickness shown in Fig 3.2. Six domains were used in the calculations, as shown in Fig. 1.8. For each stress intensity

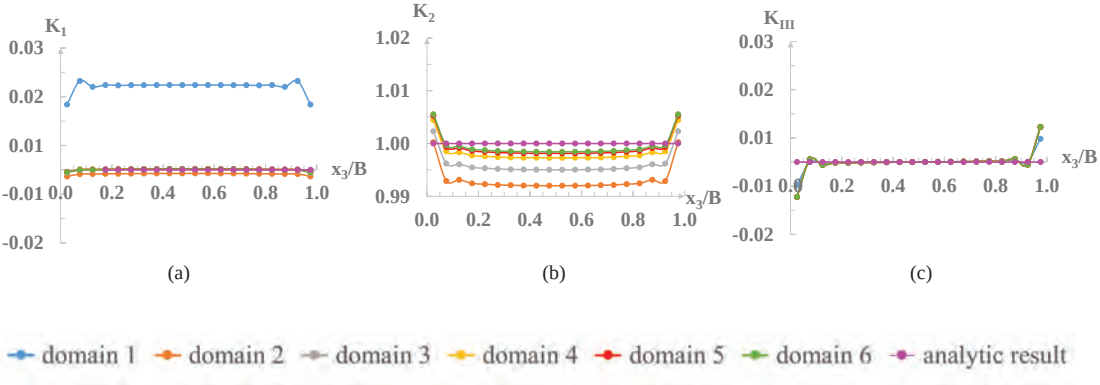

Figure 3.6: Stress intensity factors for the second benchmark problem: $K_1^{(f)} = 0$, $K_2^{(f)} = 1$ and $K_{III}^{(f)} = 0$; (a) $K_1^{(f)}$, (b) $K_2^{(f)}$ and (c) $K_{III}^{(f)}$.

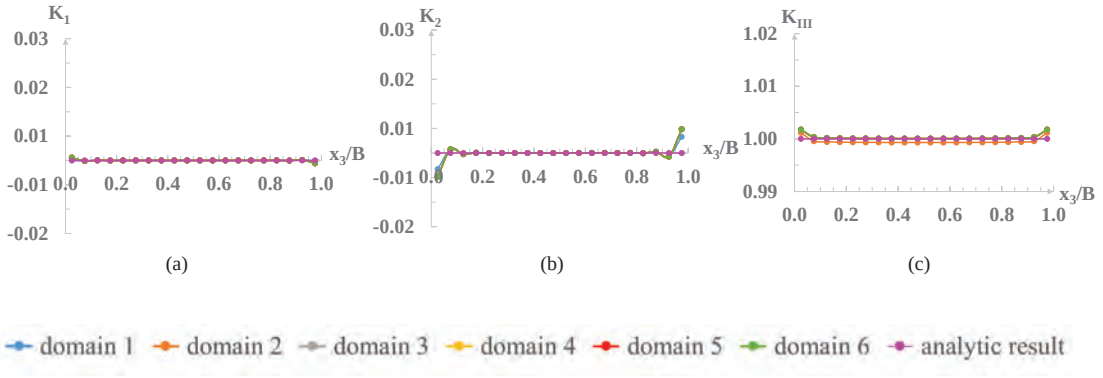

Figure 3.7: Stress intensity factors for the third benchmark problem: $K_1^{(f)} = 0$, $K_2^{(f)} = 0$ and $K_{III}^{(f)} = 1$; (a) $K_1^{(f)}$, (b) $K_2^{(f)}$ and (c) $K_{III}^{(f)}$.

factor, a percent difference was calculated as

$$\% \text{ difference} = \frac{\left(K_m^{(1)} - K_m^{(2)}\right)}{K_m^{(2)}} \times 100 \tag{3.31}$$

where $K_m^{(1)}$, $m = 1, 2, III$, is the stress intensity factor obtained from the M-integral and $K_m^{(2)}$ represents the the exact value of K_m. In the denominator, the analytic result for the dominant stress intensity factor was used meaning $K_m^{(2)}$ in the denominator is unity in all cases.

In the three solved benchmark problems, it is observed as expected, that the results for domain 1, the smallest domain, closest to the delamination front, are less accurate than all other domains. This error is a result of the stress singularity near the delamination front which is not accurately represented in the FEA. In addition, relatively large errors are observed for the calculated stress intensity factors, adjacent to the outer surfaces of the body, namely $x_3/B \to 0$ and $x_3/B \to 1$. It may be noted that, as expected, the results from the first and second benchmark problems in Figs. 3.5 and 3.6, respectively, show $K_1^{(f)}$ and $K_2^{(f)}$ to be symmetric about the mid-surface ($x_3/B = 0.5$) and $K_{III}^{(f)}$ is anti-symmetric. For the third benchmark problem in Fig. 3.7, the opposite trend occurs, $K_1^{(f)}$ and $K_2^{(f)}$ are anti-symmetric about the mid-surface ($x_3/B = 0.5$) and $K_{III}^{(f)}$ is symmetric.

The results of the first benchmark problem (case 2a in Table 1.4) are presented in Fig. 3.5. The errors calculated using eq. (3.31) in domain 1, neglecting the results obtained near the outer specimen surfaces, were found to be approximately 1%, 0.7% and 0% for $K_1^{(f)}$, $K_2^{(f)}$ and $K_{III}^{(f)}$, respectively. For the stress intensity factors calculated in domains 2 to 6, these errors decreased and converged to 0.01%, 0.02% and 0% for $K_1^{(f)}$, $K_2^{(f)}$ and $K_{III}^{(f)}$, respectively. Tabulated results of the first benchmark problem are presented in Appendix B in Tables B.1 and B.2.

The results for the second benchmark problem (case 2b in Table 1.4) are presented in Fig. 3.6. The error in $K_2^{(f)}$ calculated in domain 1, neglecting the results obtained near

the outer surfaces, was found to be approximately 26% which is very high compared to all other calculated errors. Hence, the curve for $K_2^{(f)}$ in domain 1, is off the scale and is not shown in Fig. 3.6b. A clear decrease of this error was observed in the other domains. In domain 2, the error was approximately 0.8% and in domains 3 through 6, the results converge and the error is reduced to less than 0.16%. For $K_1^{(f)}$ and $K_{III}^{(f)}$, the errors found in domain 1 were 1.8%, and 0.01%, respectively. These errors decreased in the other domains and reached the values of 0.01% and 0%, respectively, in the sixth domain. Tabulated results for the second benchmark problem are presented in Appendix B in Tables B.3 and B.4.

The results for the third benchmark problem (case 2*c* in Table 1.4) are presented in Fig. 3.7. The errors calculated for this problem were lower than those for the other two benchmark problems. This occurs since there is only a square-root singularity along the delamination front and the quarter-point elements model this well. In domain 1, neglecting the results obtained near the outer surfaces, the errors were found to be approximately 0%, 0% and 3.2% for $K_1^{(f)}$, $K_2^{(f)}$ and $K_{III}^{(f)}$, respectively. The results remain constant for $K_1^{(f)}$ and $K_2^{(f)}$ in the other domains and the error in domain 6 for $K_{III}^{(f)}$ decreases to approximately 0.01%. Tabulated results of the third benchmark problem are presented in Appendix B in Tables B.5 and B.6.

With the obtained stress intensity factors from the three solved benchmark problems, the DE method and the mechanical M-integral were seen to be valid. Neglecting the results obtained from domain 1, excellent results were obtained from both methods. Hence, it may be concluded that the software used for both methods is both correct and accurate. This software will be used to analyze the experimental data.

For the thermal problem, both the DE method and the M-integral were used to obtain the stress intensity factors. Twenty elements, through the thickness, were used in the model. With the DE method, the displacement at each nodal point is obtained from the FE model at the upper and lower faces of the delamination and used in eqs. (3.10) and (3.13) to determine twenty-one values of the local stress intensity factors $K_1^*(r)$, $K_2^*(r)$ and $K_{III}^*(r)$ for each distance r from the delamination front, along the delamination faces. Linear regression was applied to every three sequential points at a distance of $0.025 \leq r/R \leq 0.3$, where R is the radius of the disk and r/R represents the normalized distance from the delamination front in which the DE produced valid values. Goodness of fit was assessed for every set of results using the coefficient of determination. The points taken from the best fit were extrapolated to determine K_m^{DE}, $m = 1, 2, III$. Tabulated results from the thermal problem obtained by means of the DE method are presented in Appendix B in Table B.7. With the M-integral, the stress intensity factors are obtained for each volume containing a layer of elements along the delamination front from eqs. (3.28) - (3.30). A value is obtained for each stress intensity factor for each element along the delamination front, resulting with twenty values through the model thickness. In addition,

in the same manner as that for the mechanical M-integral, six domains were used in the calculations, as shown in Fig. 1.8. Tabulated results from the thermal problem obtained by means of the thermal M-integral are presented in Appendix B in Tables B.8 and B.9. Path independence is achieved in paths 4 through 6.

In order to validate the results obtained with the thermal M-integral, for each stress intensity factor, a percent difference between the results obtained by the M-integral, for each domain, and the results obtained using the DE method was calculated using eq. (3.31) where $K_m^{(1)}$, $m = 1, 2, III$, is the stress intensity factor obtained by means of the DE method and $K_m^{(2)}$ is the stress intensity factor obtained from the thermal M-integral. It may be noted that in order to compare the results, the values obtained from the DE method for two adjacent nodes were averaged so as to give a result in the middle of the element. Note that, the quantities obtained by this comparison are not exact.

As observed with the mechanical M-integral, the results for domain 1 were less accurate than those obtained for all other domains. In order to evaluate the differences between the first and sixth domains, a comparison of the thermal stress intensity factors $K_1^{(r)}$, $K_2^{(r)}$ and $K_{III}^{(r)}$ obtained for these domains was made and differences of $0.7-12.7\%, 15.9-28.0\%$ and $1.9-3.2\%$ were observed, respectively. These large differences are a result of the square-root, oscillatory stress singularity at the delamination front causing the results for domain 1 to be less accurate than those obtained for all other domains. In addition, it should be noted that convergence was observed for the results obtained from the M-integral in domains four, five and six.

Tabulated results of the averaged values obtained from the DE method and used in the comparison, as well as the results obtained from the sixth domain with the M-integral are presented in Appendix B in Table B.10. The percent differences between the values obtained using both methods, as calculated with eq. (3.31), are also shown in that table. Differences of $0.2-3.6\%, 3.1-7.2\%$ and $0.0-0.1\%$ were observed for the thermal stress intensity factors $K_1^{(r)}$, $K_2^{(r)}$ and $K_{III}^{(r)}$, respectively. Note that, the stress intensity factors obtained by the DE method, adjacent to the outer surfaces of the body, namely $x_3/B \to 0$ and $x_3/B \to 1$, were neglected. It was observed that at these locations, the values of $K_m^*(r)$, $m = 1, 2, III$, were not linear as a function of r, as expected. Since linearity is necessary for the use of this method, these results were not used. Hence, two values on each outer surface were omitted for $K_1^{(r)}$ and $K_2^{(r)}$ and one value on each outer surface was omitted for $K_{III}^{(r)}$. The differences between the values of the stress intensity factors obtained by means of the M-integral and DE method which were omitted, show that the DE method is not sufficiently reliable to use in predicting failure.

In a previous investigation by Rogel (2009), two sets of material pairs, namely, two UD plies with fibers oriented in the $+30°/-60°$ and $-30°/+60°$-directions were investigated. A similar comparison of the stress intensity factors obtained with the M-integral, as well as with the DE method for a thermal problem was made. The comparison in that study

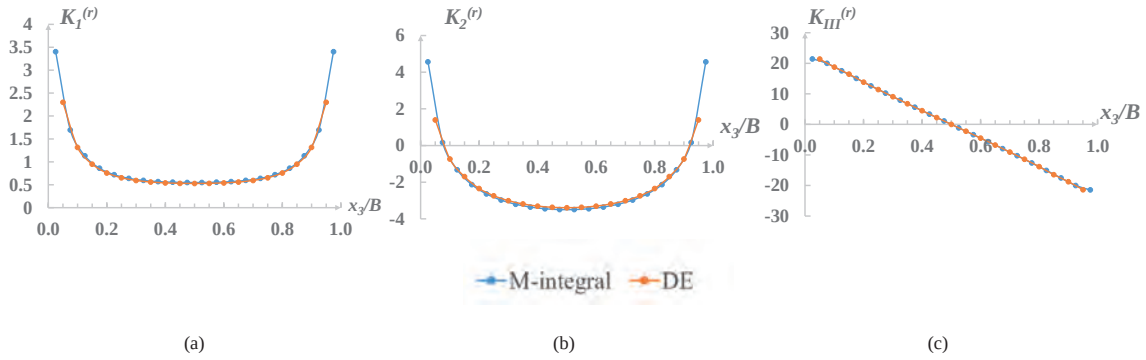

Figure 3.8: Stress intensity factors for the thermal problem; (a) $K_1^{(r)}$, (b) $K_2^{(r)}$ and (c) $K_{III}^{(r)}$.

provided larger differences than observed in the current investigation. Differences of up to 34%, 9% and 10% were obtained for $K_1^{(r)}$, $K_2^{(r)}$ and $K_{III}^{(r)}$, respectively, using the finest mesh and the largest calculation domain, domain four. Similarly to what was done here, the results obtained from the outer surfaces of the model were neglected in the comparison. The differences observed here are less than those found in that study with the same two methods. It may be noted that the mesh used here is much finer than that used in Rogel (2009). Perhaps a finer mesh would lead to smaller differences.

The calculated stress intensity factors along the delamination front, obtained from the DE method and from the M-integral in the sixth domain for the thermal problem are plotted in Fig. 3.8 as a function of the normalized delamination front coordinate x_3/B (see Fig. 1.7). The parameter B is the model thickness shown in Fig 3.2. It may be observed from Fig. 3.8 that the results from the thermal problem for $K_1^{(r)}$ and $K_2^{(r)}$ are symmetric about the mid-surface ($x_3/B = 0.5$) and $K_{III}^{(r)}$ is anti-symmetric.

The interface energy release rate $\mathcal{G}_i^{(r)}$ $(i = 1, 2, III)$ along the delamination front was computed using eq. (3.17) for the results obtained from the M-integral in the sixth domain and for the results obtained from DE. In addition, comparisons were made between results for $\mathcal{G}_i^{(r)}$ obtained by means of the M-integral, DE and J-integral computed by Abaqus (2017). The results obtained from all three methods are presented in Fig. 3.9. Small differences of approximately $0-1.3\%$ were observed for the comparison of J from Abaqus (2017) and $\mathcal{G}_i^{(M-\text{integral})}$ computed with the M-integral in the sixth domain. Larger differences of up to 15.5% were observed when comparing $\mathcal{G}_i^{(M-\text{integral})}$ versus $\mathcal{G}_i^{(DE)}$. Note that the largest differences were found in the mid-thickness of the model, where vary small values of $\mathcal{G}_i^{(r)}$ were obtained. If only results larger than 10 N/m are taken into account in the comparisons, these differences become approximately $0-0.3\%$ and $0.2-6.6\%$ for $\mathcal{G}_i^{(M-\text{integral})}$ compared with the results from Abaqus (2017) for J and for the comparison of $\mathcal{G}_i^{(M-\text{integral})}$ versus $\mathcal{G}_i^{(DE)}$, respectively. Note that in all comparisons discussed here, the results obtained from DE on the outer surfaces of the model, were neglected.

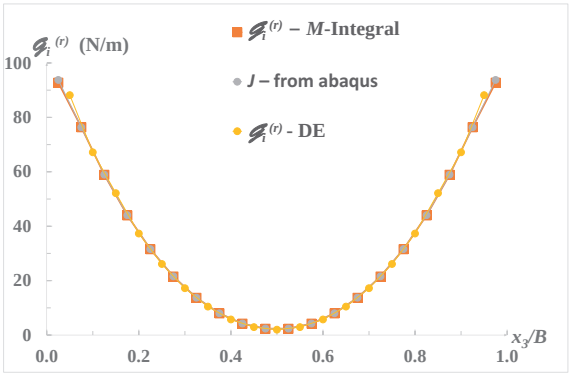

Figure 3.9: Comparison of the thermal $\mathcal{G}_i^{(r)}$ calculated by means of DE, the M-integral in the sixth domain and the J-integral computed by Abaqus (2017) at the sixth domain.

It may be concluded that the software used for both methods is correct. This software will be used to analyze the experimental data. It may be pointed out that the DE method leads to higher errors and is not recommended as a stand alone method. It may be used to validate results obtained with the more accurate M-integral.

Chapter 4

Fracture tests using the Brazilian disk specimens

In this investigation, mixed mode fracture tests were carried out in order to produce a failure criterion for the material pair studied. Various specimen types may be used for mixed mode fracture toughness testing. Some were discussed in Section 1.3. The Brazilian disk (BD) specimen, described in Section 1.3.3.3, was chosen to be used here.

A plate was designed for the BD specimens and manufactured by means of a wet-layup process. This process involved impregnation of dry reinforcement with a low viscosity thermosetting epoxy resin using hand lamination. The dry reinforcement was impregnated on a flat surface. Specimens were cut from the plate using a water jet and then glued to aluminum partial disks, as shown in Fig. 1.19. In Section 4.1, the plate design is presented. The mechanical and thermal properties of the UD and the woven plies in the plate were recalculated for the measured volume fractions based on the methodology described in Section 2.1. Details regarding these calculations, as well as the resulting properties which will be used in the analyses are discussed in Section 4.2. As described in Section 1.3.3.3, the Brazilian disk specimen has been used for mixed mode fracture tests for different interfaces. Based on the mixed mode protocol presented in Banks-Sills et al. (1999), Banks-Sills et al. (2000), Banks-Sills et al. (2005b) and Banks-Sills et al. (2006), a detailed protocol has been developed to be used for the tests carried out here. This protocol is described in Section 4.3.

Twenty-seven successful tests were carried out with different loading angles ω, shown in Fig. 1.19, to obtain results for various mixed mode combinations. The specimen dimensions and test results are presented in Section 4.4. In Section 4.5 a convergence study for the FE model mesh for both mechanical and thermal loading is presented. In addition, in this section domain independence is examined for both the mechanical and thermal M-integrals. The FEAs used to analyze each BD specimen, as well as the results obtained from the analyses are presented in Section 4.6. Based on the results and analyses, several two and three-dimensional mixed mode interface failure criteria are proposed for

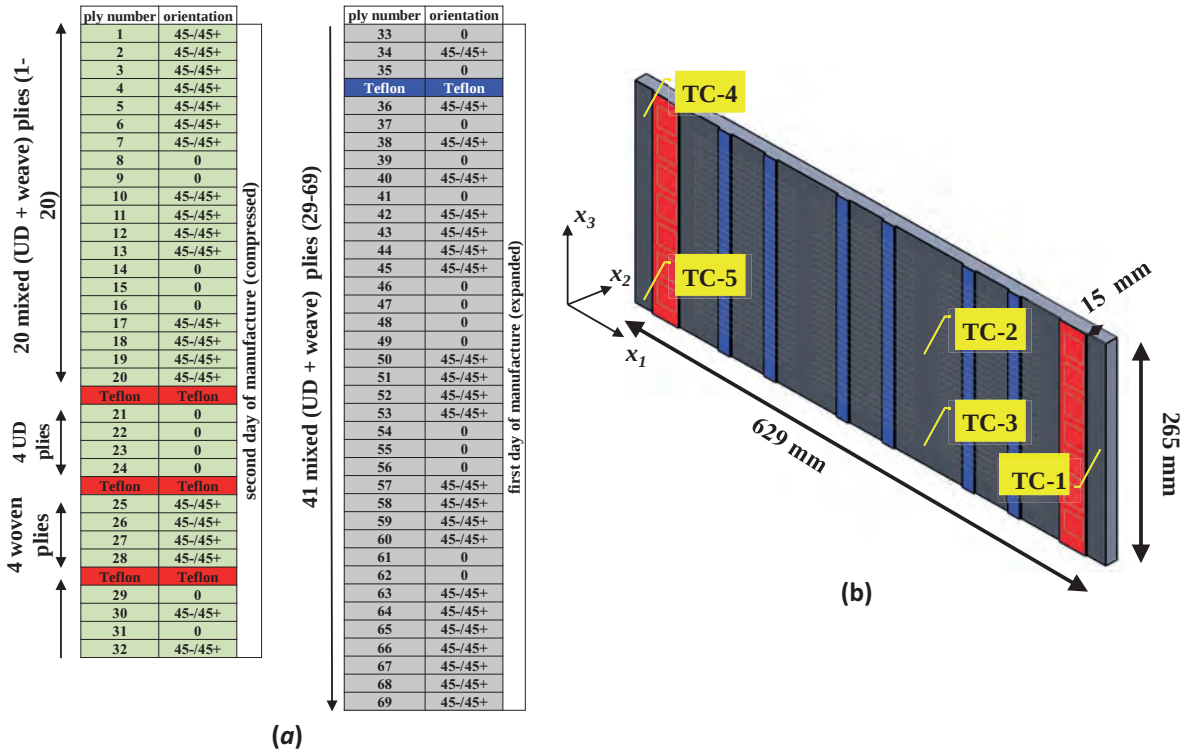

Figure 4.1: Schematic view of the composite Brazilian disk plate design: ; (a) layup; (b) thermo-couples and Teflon film locations, blue - delamination and red - separation.

predicting delamination failure of the multi-directional, laminate composite studied. The curves and surfaces obtained are described in Section 4.7. Also in this section, a statistical analysis is carried out to obtain failure curves or surfaces with a 10% probability of unexpected failure in the safe zone with a 95% confidence. These curves or surfaces may be used to predict failure of structures fabricated from the investigated material and interface, as well as to assist in composite design.

4.1 Plate for fracture tests and Brazilian disk specimen design

A laminate composite carbon/epoxy plate containing 69 plies was designed. Each woven ply thickness may range from 0.21 mm to 0.27 mm and each UD fabric ply is approximately 0.2 mm thick. The composite plate layup was designed to create a nominal thickness of approximately 15 mm. This layup is presented in Fig. 4.1a. The layup of the plies was chosen based on previous experience to be both symmetric and balanced about the mid UD-fabric ply, with a stacking sequence of $[(45/-45)_7, 0_2, (45/-45)_4, 0_3, (45/-45)_4, 0_4\ , (45/-45)_4, (0/(45/-45))_2, 0, (45/-45), 0// (45/-45), 0, ((45/-45)/0)_2, (45/-45)_4, 0_4, (45/-45)_4, 0_3, (45/-45)_4, 0_2, (45/-45)_7]$. The layup listed here begins with ply

1 which is the uppermost ply in the plate and ends with ply 69 which is located at the bottom of the plate.

Before the plate was manufactured, FE analyses were carried out using the finite element program Abaqus (2017) to determine the possible loading angles ω, for which the delamination near its front is open. The dimensions of the BD FE model used were $R = 20$ mm, $2a = 16$ mm and $B = 8$ mm, where R represents the specimen radius, $2a$ represents the delamination length and B represents the specimen thickness (see Fig. 1.19). The FE mesh of the specimen contained 406,080 C3D20 quadratic hexahedral elements with 1,683,565 nodes. The mechanical properties used in the analyses are given in the last row in Table 2.4 and Table 2.7, for the UD and woven fabrics, respectively. These properties are not those of the plate which was used in the BD tests. For the BD specimens tested, new material properties were obtained after the plate was manufactured. These are presented in Section 4.2. It may be noted that the thermal residual curing stresses were neglected in the predesign analyses. The numerical results from the predesign analyses showed that the delamination faces are open for loading angles in the range $-13° \leq \omega \leq 5°$. For loading angles in the range of $8° \leq \omega \leq 13°$, the delamination faces remained open on one side of the delamination and closed on the other side. On this basis, the designed layup of the composite plate was approved for fabrication.

Five thermo-couples (TC) were inserted during plate fabrication at different locations, as shown in Fig. 4.1b, to verify a uniform degree of cure during the curing process. As a result of the temperature changes applied during the curing process, residual stresses were induced within the laminate. Polytetrafluoroethylene (PTFE) strips, 15 μm thick, were positioned at different locations in the plate, as shown schematically in red and blue in Fig. 4.1. The PTFE film used to create the artificial delamination, shown in blue, was placed periodically between the UD-fabric ply (ply 35), and a plain woven ply (ply 36), shown as the double slash in the layup description. The PTFE films shown in red were used for ply separation, to provide samples used to measure the carbon fiber weight fraction W_f. The separation of four UD-fabric plies and four woven plies was enabled using these PTFE strips. Plies 1 through 20, as well as plies 36 through 69 were also separated which included both UD fabric and woven fabric plies. These plies are denoted in Fig. 4.1a as "mixed".

The composite plate was fabricated in two stages by means of a wet-layup. The first stage included plies 69 to 33 shown in gray in Fig. 4.1a. The plies were held in a vacuum bag for 12 hours and then cured in an oven at 40° C for two hours. The second stage included plies 32 to 1 arranged on top of plies 69 to 33 shown in green in Fig. 4.1a. The plate was then held in a vacuum bag for 24 hours and a full curing procedure was carried out. During curing, the vacuum bag was placed in an oven for 30 minutes at 60° C, 30 minutes at 70° C and finally 5 hours at 80° C. The temperature was decreased 3° C/min. The plate was then held in the vacuum bag for an additional 24 hours.

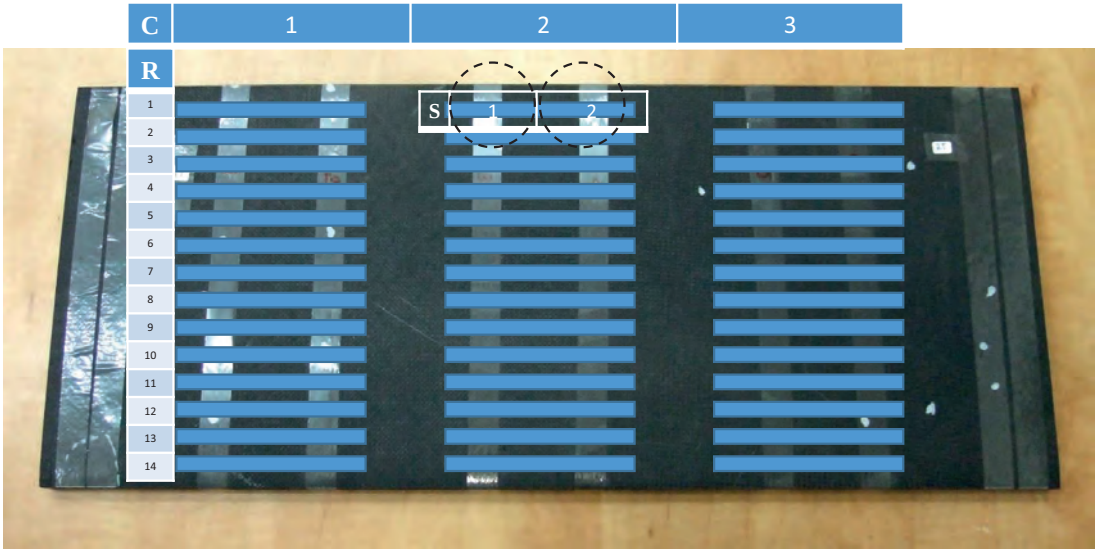

Figure 4.2: The manufactured plate for the Brazilian disk specimens, each specimen in the plate is numbered as C.R.S.

The manufactured plate is presented in Fig. 4.2, a schematic view of the specimens cut from the plate and their numbering as Column, Row, Side (C.R.S.) are denoted. The plate size was approximately 16.56 mm thick, 265 mm wide and 629 mm long. After the manufacturing process was complete, a non-destructive test (NDT) was performed to identify voids, as well as the location of the Teflon strips. From the NDT results, the Teflon was identified. In addition, ply separation was observed (for example, see red arrows in Fig. 4.3), as well as many voids.

The temperature measured by the TCs increased monotonically to a maximum of 85° C in all five locations measured. It was concluded that a uniform degree of cure was obtained within the composite plate. However, after the plate was completed, it was observed that plies 33 to 69 were thicker than plies 1 to 32. In Fig. 4.4, two parts of the plate are shown. It may be noted that the upper part consists of 34 plies and the lower part, 35. The lower part is formed by plies 36 to 69 which measures approximately 9.8 mm

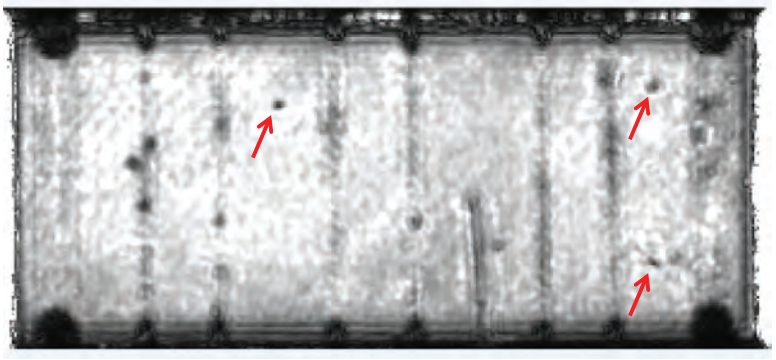

Figure 4.3: Non-destructive testing result; red arrows indicate ply separation locations.

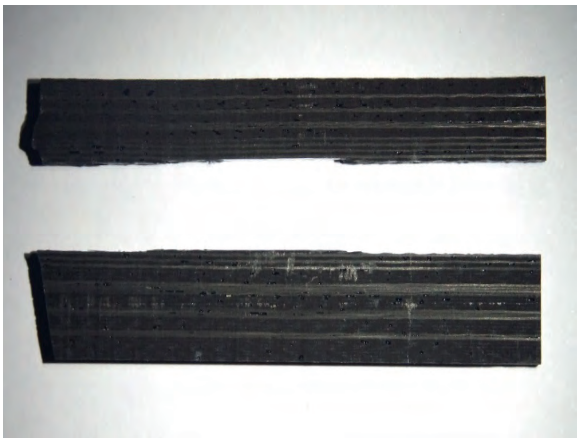

Figure 4.4: Two parts of the plate. The lower part includes expanded plies 69 to 36 (approximate thickness 9.8 mm); the upper part includes compressed plies 32 to 1 and expanded plies 35 to 33 (approximate thickness 7.2 mm).

using a micrometer; this is the expanded part of the plate. Plies 1 to 35 form the upper part of the plate shown in Fig. 4.4. Plies 1 to 32 are compressed and plies 33 to 35 are expanded. This part of the plate measured approximately 7.2 mm using a micrometer. It may be noted that the average plate thickness, measured with a micrometer was found to be 16.56 mm. Hence, the sum of the thicknesses of both parts shown in Fig. 4.4 was found to be greater than this average measurement. It may be observed that the measurement of the two parts in Fig. 4.4 varies at different locations. Nonetheless, the differences in thickness of the two parts of the specimen appear to be a result of a stronger vacuum used during the second manufacturing stage. Thus, unfortunately, the two parts of the plate have different fiber volume fractions, resulting in different mechanical and thermal properties.

Strips were formed from the plate using a water-jet cutter. Aluminum blocks were glued to each strip on the bottom and top sides of the laminate and cut again using the same water-jet cutter, creating circular BD specimens with an approximate thickness $B \approx 8$ mm, diameter $2R \approx 40$ mm and an artificial delamination of length $2a \approx 16$ mm, as illustrated in Fig. 1.19. During each test, a specific loading angle ω between the delamination line and the load line as shown in Fig. 1.19 is chosen. For each value of ω, the mixed mode ratio between the opening and shear deformation changes. Both negative ($\omega < 0°$) and positive ($\omega > 0°$) loading angles were used in the tests. For the latter, the delamination will propagate from the lower delamination front. To prevent this occurrence, an arrest hole was introduced with the water-jet cutter, as shown in Fig. 4.5a. The horizontal and vertical diameters d_h and d_v, of $\sim$2 mm, respectively, are illustrated in Fig. 4.5b, together with the offset distance from the delamination c_v. The hole was induced only for specimens tested with a positive loading angle. It may be noted that the aluminum partial disks in Fig. 4.5a were covered with black tape in order to prevent light reflection during the test.

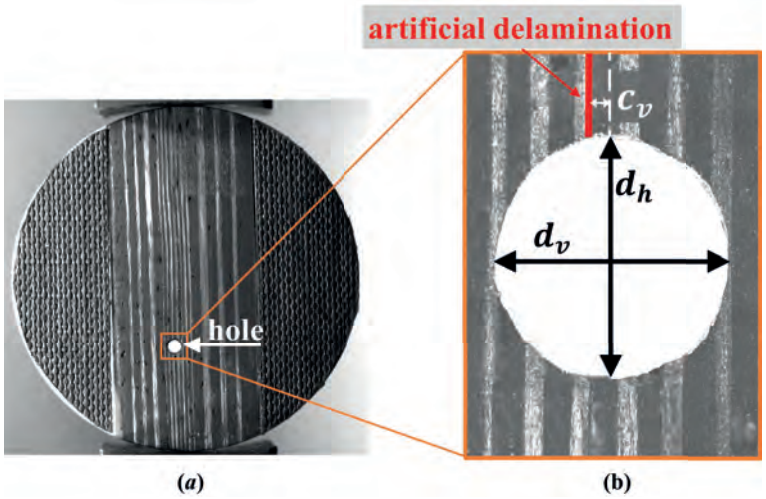

Figure 4.5: (a) Brazilian disk specimen with a hole at the lower delamination front; (b) enlarged view of the hole.

Fiber weight fraction measurements were carried out on four parts of the layup, shown in Fig. 4.1a. These included three parts from the compressed section and one part from both the compressed and expanded sections of the plate. Each group of plies is presented in columns one through five of Table 4.1, where the number of plies of each type in each group is given, indicating whether the plies are in the compressed or expanded part of the plate. Five specimens were measured from each group of plies. The obtained weight fractions were converted into fiber volume fractions. These were calculated using the density of the weight fraction specimens, as well as that of the epoxy and the carbon. It may be noted that there is about 3% glass fibers within the total percentage of fibers in the UD fabric. These were included as carbon fibers in calculating the fiber volume fraction V_f. In Table 4.1, the average volume fractions obtained for each group of plies and the related standard deviations (SDs) are shown in columns six and seven, respectively. Based upon the fiber volume fractions, the mechanical properties and CTEs of each material in the upper and lower parts of the plate were determined.

Table 4.1: Fiber volume fraction V_f of three compressed parts of the plate and one mixed (compressed and expanded) part calculated from weight fraction measurements.

ply number	UD 0°		weave $+45°/-45°$		V_f - average	SD
	compressed	expanded	compressed	expanded		
1-20	5	0	15	0	0.54	±0.004
21-24	4	0	0	0	0.58	±0.013
25-28	0	0	4	0	0.52	±0.003
29-69	2	14	2	23	0.39	±0.018

4.2 Effective mechanical and thermal properties of the UD and woven plies of the BD specimens

In this section, effective mechanical and thermal properties of the materials in the fabricated plate for the BD specimens are presented. The materials on either side of the interface are a UD fabric and a woven composite as shown in Fig. 2.1. The upper material is the UD fabric with carbon fibers in the 0°- direction (the x_1- direction in Fig. 2.1), with a small percentage of glass fibers in the x_3- direction to hold the carbon fibers together. The lower material is a plain weave with tows oriented in the $+45°/-45°$- directions. In Section 2.1, effective mechanical properties were found for these materials using HFGMC (Aboudi, 2004). Those calculations were carried out in order to verify tested values of the mechanical properties. Those tests were performed for specimens with different volume fractions than those in the plate used for the BD specimens. Hence, the properties are recalculated using the volume fractions which are appropriate here.

In order to calculate the properties in the expanded part of the plate, V_f of the glass and carbon fibers in the UD fabric and the volume fraction of the carbon fibers in the woven fabric composite plies were calculated as

$$V_{f(41)} = \frac{1}{41}\left[2V_{f(UD_C)} + 2V_{f(W_C)} + 14V_{f(UD_E)} + 23V_{f(W_E)}\right] \tag{4.1}$$

where $V_{f(41)}$ is the total fiber volume fraction of plies 29 to 69 (41 plies), given in Table 4.1, the subscripts UD_E and W_E represent the UD fabric and the woven fabric in the expanded part of the plate, respectively. In the same manner, the subscripts UD_C and W_C refer to the UD and woven fabrics in the compressed part of the plate, respectively. The latter fiber volume fractions $V_{f(UD_C)}$ and $V_{f(W_C)}$ are given in Table 4.1, where the volume fractions $V_{f(UD_E)}$ and $V_{f(W_E)}$, for plies in the expanded part of the plate are unknown. In order to calculate these fiber volume fractions, it was assumed that the ratio between the measured volume fractions in the compressed part of the plate remain constant in the expanded part of the plate as well, namely

$$\frac{V_{f(UD_C)}}{V_{f(W_C)}} = \frac{0.58}{0.52} = 1.12\ ; \tag{4.2}$$

so that,

$$\frac{V_{f(UD_E)}}{V_{f(W_E)}} = 1.12\ . \tag{4.3}$$

By substituting eq. (4.3) into eq. (4.1), the desired fiber volume fractions were obtained for the expanded part of the plate as $V_{f(UD_E)} = 0.40$ which includes the carbon and the glass fibers and $V_{f(W_E)} = 0.36$. Summarized values of the total fiber volume fractions obtained for each material in the compressed and expanded parts of the plate are given in Table 4.2. For all plies, the carbon fiber volume fraction was used to obtain the mechanical properties and CTEs in the expanded and compressed parts of the plate.

Table 4.2: Volume fractions of the fibers (both glass and carbon) in the UD fabric and the carbon fibers in the woven fabric in the compressed and expanded parts of the plate.

	material	V_f
compressed	$+45°/-45°$	0.52
	UD 0°	0.58
expanded	$+45°/-45°$	0.36
	UD 0°	0.40

The UD-fabric is treated as transversely isotropic. The properties E_A, E_T, ν_A and G_A were calculated according to experimentally obtained properties as related to the proportion of the carbon fiber volume fractions in the current plate verses those in the experiment. These are presented in the second column in Table 4.3. These were calculated as 97% of the total fiber volume fractions shown in Table 4.2. The ratios between each of these carbon fiber volume fractions, in Table 4.3, to that related to the plate which was used to determine mechanical properties, namely $V_f = 0.58$, was calculated. The required properties were determined in proportion to the obtained ratio with respect to the experimental properties in the second line in Table 2.4. The resulting values of E_A, E_T, ν_A and G_A are presented in Table 4.3. Since there was no experimental data for ν_T, α_A and α_T, these were calculated using the High-Fidelity Generalized Method of Cells (HFGMC) (Aboudi, 2004). Using the values of V_f in Table 4.3, the stiffnesses calculated by HFGMC were too high. To obtain values corresponding to those of the tests, in the same manner as that described in Section 2.1, the carbon fiber volume fractions were reduced to 0.47 and 0.33, for the compressed and expanded parts of the plate, respectively. The resulting values of ν_T, α_A and α_T are also shown in Table 4.3. Moreover, for properties in the transverse direction, namely ν_T and α_T, the effect of the glass fibers was taken into consideration by the rule of mixtures, raising $E = 2.8$ GPa for the epoxy in Table 2.1 to $E = 5.9$ GPa. The value of G_T was obtained using eq. (2.1).

The lower ply along the interface is a plain, balanced weave which is effectively tetragonal with $x_2 = 0$ a symmetry plane. This material is described by six independent mechanical properties and two CTEs. The Young's moduli are $E_{11} = E_{33}$ and E_{22}; $\nu_{21} = \nu_{23}$ and ν_{13} are the Poisson's ratios; $G_{21} = G_{23}$ and G_{13} are the shear moduli; and $\alpha_{11} = \alpha_{33}$ and α_{22} are the CTEs (see Figs. 2.3a and 2.3b for coordinate directions). The effective

Table 4.3: Compressed and expanded UD-fabric mechanical properties and CTEs.

	V_f	E_A (GPa)	E_T (GPa)	G_A (GPa)	G_T (GPa)	ν_A	ν_T	α_A $(\times 10^{-6}/°\text{C})$	α_T $(\times 10^{-6}/°\text{C})$
compressed	0.56	110.6	7.0	2.7	2.5	0.38	0.42	53.2	0.62
expanded	0.39	77.1	4.8	1.9	1.6	0.26	0.48	65.1	1.46

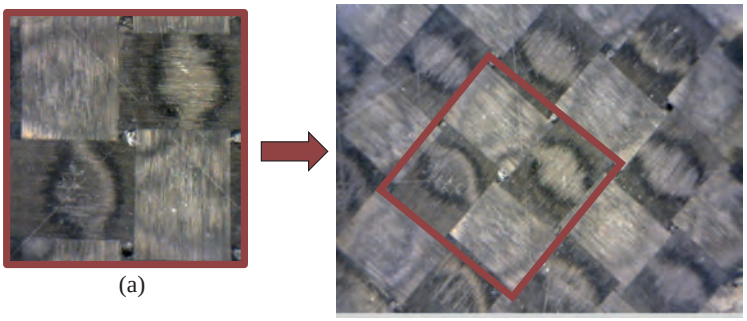

(a) (b)

Figure 4.6: (a) A plain weave with fibers oriented in the 0°/90°- directions similar to the RUC shown in red in Fig. 2.3; (b) a plain weave with fibers oriented in the +45°/−45°- directions with the RUC shown in red

mechanical properties and CTEs of the woven fabric were determined by means of the two-step HFGMC (Aboudi, 2004; Decad, 2008). All properties were found for a plain weave with fibers oriented in the 0°/90°- directions as shown in Fig. 4.6a and transformed by a 45° rotation about the x_2 - axis as shown in Fig. 4.6b.

The measured and calculated carbon fiber volume fractions of 0.52 and 0.36, given in Table 4.2, respectively, for the compressed and expanded parts of the plate were used in the calculation. In addition, a repeating unit cell (RUC) shown in Fig. 2.3a in two dimensions and Fig. 2.3b in three dimensions, was used in the calculation. The parameters required for an HFGMC calculation are the width of the yarn a, the length and width of the epoxy between the yarn g, and the ply thickness h shown in Figs. 2.3a and. 2.3b. A digital microscope with a magnification of 10× (DinoLite AM311ST, AnMo Electronics, Hsinchu, Taiwan) was used to measure the parameters a and g. Measurements were carried out at 98 and 86 locations, respectively, on the outer upper and lower plies of the plate to obtain these parameters for the compressed and expanded woven fabric, respectively. The thickness of each ply h was obtained using the optical mode of an Olympus Confocal Microscope (model number OLS4100; Tokyo, Japan) by measuring the thickness of several groups of woven plies and dividing by the number of plies in that group. For this measurement 10 specimens were used. The average results for a, g and h, as well as standard deviations are presented in the columns 2 through 4 in Table 4.4. The angle β of the yarn in the RUC is shown in Fig. 4.7. This angle is also considered in the HFGMC calculation and may be determined using the parameters g and h as

Table 4.4: Geometric measurements of the compressed and expanded weave.

	a (mm)	g (mm)	h (mm)	β (°)
compressed	1.80 ±0.007	0.20 ±0.006	0.22 ±0.007	15.4
expanded	1.70 ±0.012	0.26 ±0.009	0.30 ±0.004	16.1

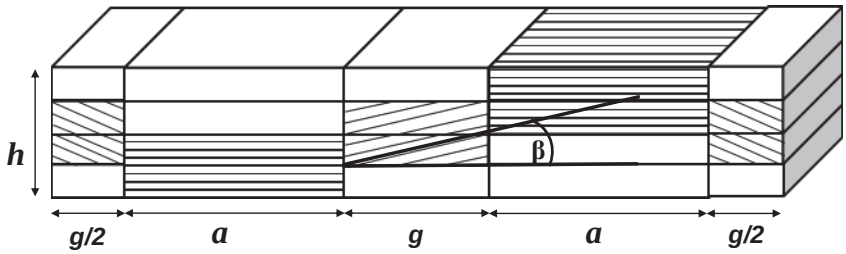

Figure 4.7: Schematic view of part of the RUC in Fig. 2.3b, showing the angle β of the yarn in the RUC.

$$\beta = \tan^{-1}\left(\frac{h}{4g}\right) \ . \tag{4.4}$$

Results of this angle are given in the last column in Table 4.4.

Using the geometric parameters a, g and h given in Table 4.4, the volume of the yarn in the RUC, volume of the RUC and the volume of yarn in the weave (Decad, 2008) were calculated by means of eqs. (2.5) to (2.7), respectively. The volume fraction of the fibers in the weave $V_{f(f/w)}$, where the f in parenthesis denotes fiber, were given in Table 4.2. These values for the expanded and compressed woven fabrics are shown again in the second column of Table 4.5. The results for the volume fractions of the yarn in the weave are presented in the third column of Table 4.5. Using

$$V_{f(f/y)} = \frac{V_{f(f/w)}}{V_{f(y/w)}} \ , \tag{4.5}$$

the volume fraction of the fibers in the yarn $V_{f(f/y)}$ were obtained. These values are presented in the fourth column of Table 4.5 and were used in the calculation of the yarn properties.

The mechanical properties and CTEs of the yarn were obtained by means of HFGMC for the carbon fiber volume fractions $V_{f(f/y)}$ in Table 4.5 and are presented in Table 4.6. The Young's moduli in the axial and transverse directions are E_A and E_T, respectively; the shear modulus in the axial direction is G_A; the Poisson's ratios in the axial and transverse directions are ν_A and ν_T, respectively; the shear modulus G_T was obtained from eq. (2.1).

The mechanical properties presented in Table 4.6 for the yarn and the geometric parameters a, g and h in Table 4.4, were used as input to an HFGMC two-step calculation to obtain the weave mechanical properties. These are presented in Table 4.7. The subscripts

Table 4.5: Volume fraction of the carbon fibers in the weave, yarn in the weave, and carbon fibers in the yarn for the compressed and expanded parts of the plate.

	$V_{f(f/w)}$	$V_{f(y/w)}$	$V_{f(f/y)}$
compressed	0.52	0.90	0.58
expanded	0.36	0.87	0.41

Table 4.6: Yarn properties of the compressed and expanded parts of the plate, used to obtain weave properties.

	$V_{f(f/y)}$	E_A (GPa)	E_T (GPa)	G_A (GPa)	G_T (GPa)	ν_A	ν_T	α_A $(\times 10^{-6}/°\text{C})$	α_T $(\times 10^{-6}/°\text{C})$
compressed	0.58	134.6	5.5	3.7	2.0	0.30	0.40	0.26	43.9
expanded	0.41	96.0	4.7	2.3	1.6	0.32	0.45	0.87	58.3

on the properties refer to the axes in Figs. 2.3a and 2.3b. The properties obtained for the 0°/90° weave, shown in Fig. 4.6a, were transformed by a 45° rotation about the x_2 - axis (Ting pp. 53-56, 1996) to the form shown in Fig 4.6b. The transformed mechanical properties which were used in all further calculations are presented in Table 4.8.

In the same manner as that for the mechanical properties, the CTEs for the compressed and expanded woven fabrics were obtained using a two step HFGMC calculation. The CTEs of the yarn are presented in Table 4.6. These together with the geometric measurements for a, g and h, given in Table 4.4, were used as input for HFGMC to obtain the CTEs for the expanded and compressed woven fabrics with fibers oriented in the 0°/90°-directions. The obtained CTEs remain the same for fibers oriented in the $+45°/-45°$- directions and are shown in Table 4.8. These values were used in the finite element analyses (FEAs) of the tested specimens. It may be noted that the effective CTEs obtained for the expanded woven fabric in the x_2 - direction is higher than that of both constituents. This phenomenon may occur for composites with low fiber volume fractions and is discussed in (Aboudi pp. 66-71, 1991).

Using the mechanical properties given in Tables. 4.3 and 4.8 for the expanded UD and woven plies, respectively, parameters which are required for the first term of the asymptotic expansion, as well as for the DE method and for the mechanical and thermal M-integrals were computed and are presented in Table 4.9. Among these are ε defined in eq. (2.72), D_{11}, D_{22} and D_{33} which are the diagonal members of the matrix $\mathbf{D}$, given in eq. (2.63), W_{12} given in eq. (2.64) and H_1 and H_2 defined in eqs. (3.18). These parameters are related to the mechanical properties of the two materials along the investigated interface.

Table 4.7: Compressed and expanded woven fabric mechanical properties obtained from HFGMC models for a 0°/90° weave.

	$V_{f(f/w)}$	$E_{11} = E_{33}$ (GPa)	E_{22} (GPa)	G_{13} (GPa)	$G_{21} = G_{23}$ (GPa)	ν_{13}	$\nu_{21} = \nu_{23}$
compressed	0.52	52.8	6.2	3.2	2.2	0.036	0.049
expanded	0.36	34.2	5.4	2.1	1.7	0.052	0.073

Table 4.8: Mechanical properties and CTEs of the compressed and expanded woven fabric with fibers in the $+45°/-45°$- directions.

	V_f	$E_{11} = E_{33}$ (GPa)	E_{22} (GPa)	G_{13} (GPa)	$G_{21} = G_{23}$ (GPa)	ν_{13}	$\nu_{21} = \nu_{23}$	$\alpha_{11} = \alpha_{33}$ $(\times 10^{-6}/°\text{C})$	α_{22} $(\times 10^{-6}/°\text{C})$
compressed	0.52	11.5	6.2	25.5	2.2	0.84	0.049	4.1	65.7
expanded	0.36	7.5	5.4	16.3	1.7	0.79	0.073	7.3	85.8

4.3 BD test protocol

A fracture test protocol was developed to be used for the Brazilian disk specimens tested here. The protocol is based upon the mixed mode methods used in Banks-Sills et al. (1999, 2000, 2005b, 2006) and will be described here in detail. Prior to each test, geometrical parameters of each specimen were measured. Then, test preparation was performed and finally the test procedure was carried out.

Specimen preparation included geometric measurements of each specimen. The composite strip thickness B and the specimen diameter $2R$ were measured using a digital micrometer with a resolution of 0.001 mm and a digital caliper with a resolution of 0.01 mm, respectively. The thickness B was measured at six locations in front of the delamination, three times on each side as marked with white stars in Fig. 4.8a. The specimen diameter $2R$ shown in purple in that figure was measured three times in the composite part of the specimen. These dimensions were averaged and used in the FEA of each specimen.

Additional measurements, shown in Fig 4.8a, were performed. Among these are the insert or critical delamination length at fracture $2a_c$, and the horizontal distance between each side of the delamination front and the specimen diameter, R_R and R_L where the subscripts R and L represent right and left, respectively. These were measured using an Olympus Confocal Microscope (model number OLS4100; Tokyo, Japan) using its optical mode. The resolution of the measurement is 0.16 $(\text{pixel}/\mu\text{m})^2$. The center of the artificial delamination was found from these measured dimensions and used to place the specimen accurately in the loading frame during the test.

In addition, before testing, each specimen was photographed with the Olympus confocal microscope using its optical mode. The images were stitched together using ImageJ

Table 4.9: Parameters related to the mechanical properties of the expanded UD and woven plies in Tables 4.3 and 4.8, respectively.

ε	D_{11}	D_{22}	D_{33}	W_{12}	H_1	H_2
	(1/GPa)	(1/GPa)	(1/GPa)	(1/GPa)	(GPa)	(GPa)
$2.257{\cdot}10^{-2}$	$2.791{\cdot}10^{-1}$	$6.786{\cdot}10^{-1}$	$7.599{\cdot}10^{-1}$	$3.081{\cdot}10^{-2}$	5.924	5.264

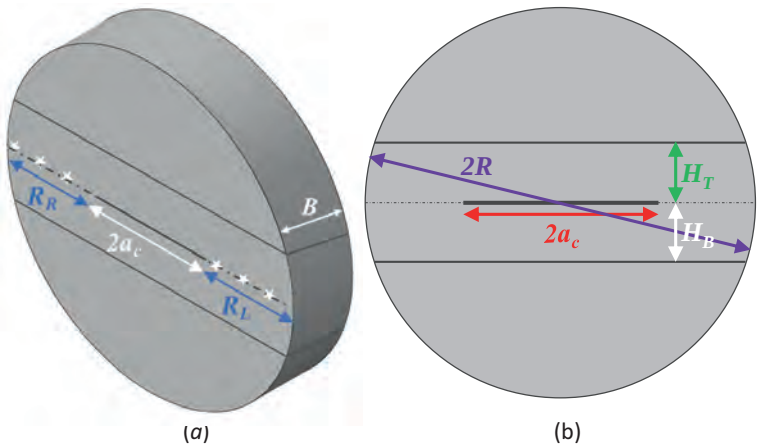

Figure 4.8: Illustration of a BD specimen with some dimensions and their measurement location: (a) three-dimensional view, and (b) two-dimensional view.

software (2015) to create a high resolution photograph of the composite strip. An example of such a photograph is presented in Fig. 4.9. Recall that there are twenty-seven ply groups for each specimen, fourteen above the delamination and thirteen below it. Using the same ImageJ software, the stitched photograph of each specimen was used to measure, the height of each stack of plies with fibers oriented in the same direction. These measurements were also used in the FE model. In addition, by summing up the heights of the stacked plies above and below the delamination, values of H_T and H_B, respectively, shown in Fig. 4.8b in green and white, respectively, were obtained. These parameters represent the vertical location of the delamination within the composite strip and were also used to place the specimen accurately in the loading frame during the test.

Using the same stitched photograph, for specimens containing a hole, additional measurements were carried out. The horizontal and vertical hole diameter d_h and d_v, respectively, as well as the vertical offset distance between the hole center and the delamination

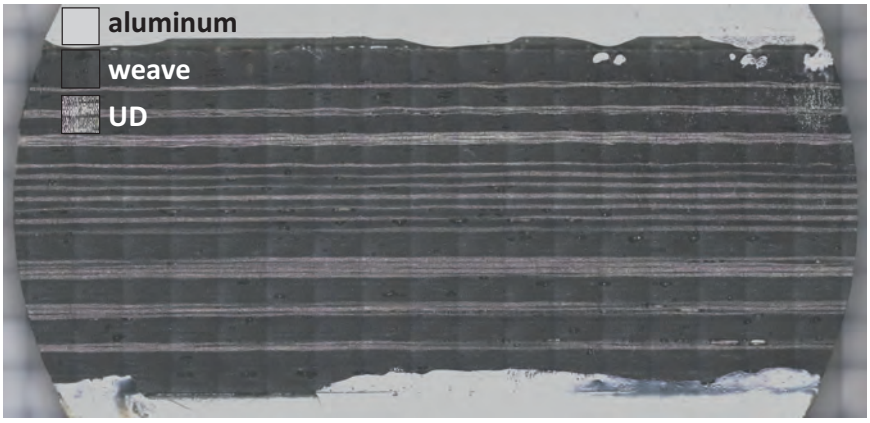

Figure 4.9: Example of a high resolution photograph of specimen BD1.6.2 stitched using ImageJ software (ImageJ, 2015) from 19 × 9 photographs obtained by the optical mode of the confocal microscope.

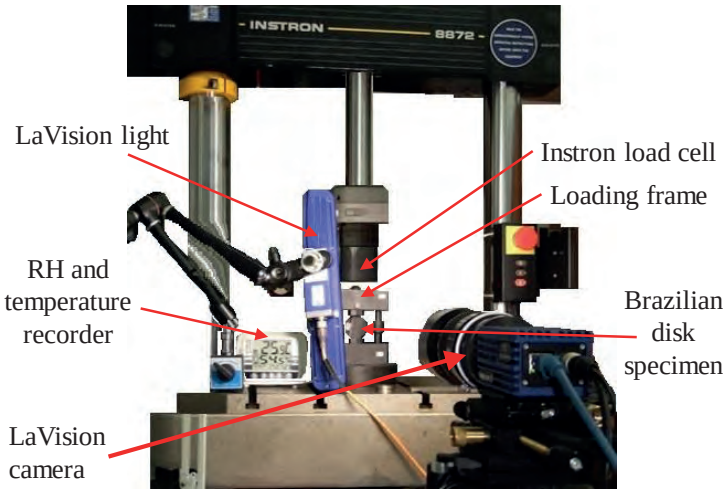

Figure 4.10: Experimental setup of the BD mixed mode fracture toughness test.

c_v, shown in Fig. 4.5b, were measured to be modeled in the FEA.

After specimen preparation was completed, black tape was placed on the aluminum to prevent light reflection. Then, specimens were conditioned at a temperature of $23° \pm 1°$ C and a relative humidity (RH) of $50\% \pm 3\%$ for at least one week in a conditioning chamber (M.R.C. BTH80/-20, Holon, Israel) which is well within the tolerance of the ASTM Standard D5229/D5229M (2011).

After the specimens were prepared, the test was setup. A LaVision system composed of one camera, a programmable timing unit (PTU) and computer software were employed during the test. The camera used is a monochrome CCD of LaVision (model no. 1101396; Göttingen, Germany) with a 5 MP Imager Pro SX, resolution 2456×2058 pixels, and a Nikon Micro-Nikkor 105 mm f/2.8 lens. The camera was connected to a LaVision external PTU and controlled by DaVis (2015) computer software. The test setup is presented in Fig. 4.10. Note that the PTU and the computer controlling the LaVision DaVis software are not shown in the figure.

Before testing, the camera was straightened using a level and scaled by photographing the specimen with millimetric paper taped to it. Then, the specimen was placed in the loading frame as shown in Fig. 4.11. The required loading angle ω, in the $x_1 - x_2$ - plane (see Fig. 1.19), specified for each test, was measured from an image of the specimen and loading frame obtained by the LaVision system. Using Vision Assistant software (2005), the angle between the load line and the delamination line was measured with respect to the delamination center. In addition, the specimen location in the loading frame was examined so that the load line and the delamination center approximately intersect. This was verified using an image of the specimen and frame, obtained by the Lavision system.

The delamination location was marked on the specimen image, based on the measured values of R_R, R_L, $2a_c$, H_T and H_B, shown in Figs. 4.8. The load line is marked on an

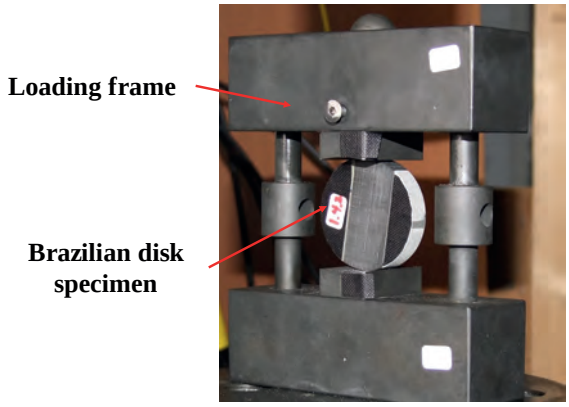

Figure 4.11: Brazilian disk specimen and loading frame.

image of the specimen as a vertical line between the two contact points of the loading frame and the specimen as shown in Fig. 4.12. Then, the intersection of the two lines is examined; ideally, they intersect at the delamination center. In some cases, especially for smaller loading angles, namely $-2 < \omega < 2°$, the intersection obtained was not ideal, but it always took place within a quarter of the total delamination length. This positioning was accounted for in the FEAs. The loading angle was measured using Vision Assistant (2005) software. Continuous measurements of the temperature and relative humidity, respectively, were recorded in the Instron working area.

During a test, the loading frame in Fig. 4.11 was loaded by the Instron loading machine (model number 8872; High Wycombe, England), with a load cell of maximum load 25,000 N and an accuracy of $\pm 0.25\%$ of the reading for loads greater than 250 N. The cross-head displacement of the Instron was increased quasi-statically at a rate of 0.5 mm/min. During the test, the applied load and the cross-head displacement were monitored by the Instron system. The applied load and images were synchronized by the LaVision system. Images of the specimen were acquired at a rate of 5 Hz as the load increased until fracture.

After each test, it was verified that failure occurred as a result of propagation from the artificial delamination at the upper delamination front. Verification was made from

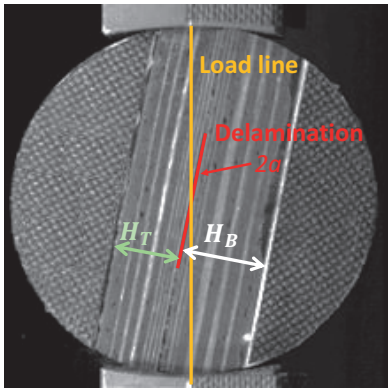

Figure 4.12: Brazilian disk specimen image marked with the delamination location and the load line before testing.

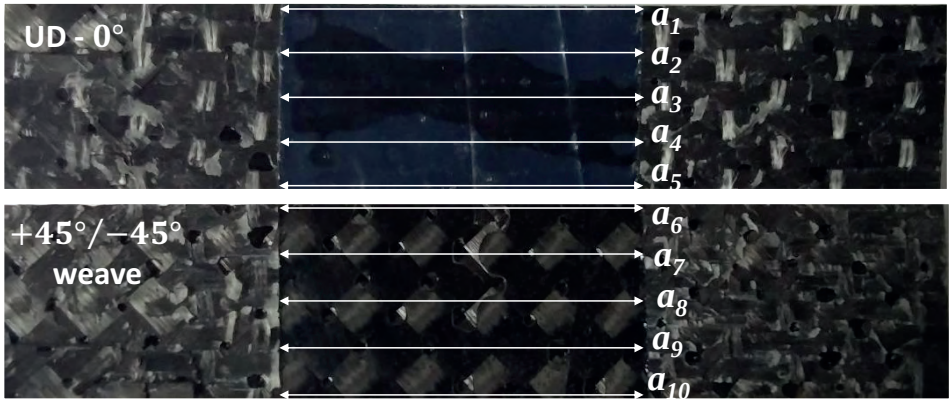

Figure 4.13: Fracture surface of specimen BD1.3.2.

images obtained by the LaVision system during each test. The critical load at fracture P_c, for each specimen, was obtained from the load-displacement curve. In addition, the temperature difference $\Delta\vartheta_i$ between the highest temperature measured during curing (85°C) and the temperature measured during the test was calculated as

$$\Delta\vartheta_i = \vartheta_i - 85^\circ \tag{4.6}$$

where ϑ_i is the temperature measured at the beginning of each test. In addition, for two specimens, digital image correlation (DIC) was performed for comparison of the displacement field obtained during the test and the displacement field obtained using an FEA.

The parameters $2a_c$, R_R and R_L shown in Fig 4.8a were remeasured after a test from the fracture surface of each specimen which was split into two parts. The measurements were made using the optical mode of the confocal microscope with a resolution of 0.16 (pixel/μm)^2. An image of the fracture surface used for this measurement is presented in Fig. 4.13. The critical delamination length $2a_c$ was measured after each test as the length of the smooth part on the fracture surface at ten locations through the specimen thickness. These are marked in Fig. 4.13, on each side of the split specimen. From the ten measurements obtained, the inner six, three from each of the lower and upper parts of the specimen, were averaged. In the same manner, the distances $R_{L(m)}$ and $R_{R(m)}$, respectively, shown in Fig. 1.19, were measured. Note that the subscript m represents measured values and the subscript c is the critical length at fracture. The specimen diameter was calculated as

$$D = R_{R(m)} + 2a_c + R_{L(m)} \quad . \tag{4.7}$$

Since there were slight differences between the diameter D and the measured diameter $2R$, the dimensions $R_{L(m)}$ and $R_{R(m)}$ where scaled so that $2R = D$. Recall that the diameter of the composite strip was measured before the test. The new dimensions $R_{L(calc)}$ and $R_{R(calc)}$, where the subscript *calc* represents the calculated (scaled) values, were obtained

using the ratio between $2R - 2a_c$ and the computed diameter $D - 2a_c$ as

$$R_{i(calc)} = \frac{2(R - a_c)R_{i(m)}}{D - 2a_c} \tag{4.8}$$

where $i = L, R$.

4.4 BD test results

In order to determine the mixed mode fracture toughness of the specific material and interface illustrated in Fig. 2.1, twenty-seven successful mixed mode fracture toughness tests were carried out. These included twenty tests with negative loading angles of $\omega \approx -2°, -5°, -10°$ and $-13°$ and seven tests with positive loading angles of $\omega \approx 2°, 5°$ and $10°$ (see Fig. 1.19a for the definition of positive and negative loading angles). For $\omega > 0°$, the BD specimens contained a hole at the lower delamination front, as shown in Fig. 4.5a.

The geometric parameters described in Section 4.3 were measured for each specimen to be used in the FE models. The average delamination length $2a_c$, average thickness B and average composite diameter $2R$ of each specimen, as well as the standard error of each, were calculated and are presented in the second, third and fourth columns of Table 4.10. These dimensions were used in the FEA of each specimen. In addition, $R_{R(m)}$ and $R_{L(m)}$, illustrated in Fig. 4.8a, where (m) represents the measured values, are presented in the fifth and sixth columns of that table, respectively. The diameter D was calculated for each specimen using eq. (4.7) and the results are presented in the seventh column of that table. Note that the calculation included more significant figures than shown in Table 4.10. The values $R_{R(calc)}$ and $R_{L(calc)}$ which were calculated by means of eq. (4.8) and used in the FEAs are shown in the eighth and ninth columns of Table 4.10, respectively. Note that the maximum difference between the measured $R_{L(m)}$ and $R_{R(m)}$ and calculated $R_{L(calc)}$ and $R_{R(calc)}$ values is approximately 0.3 mm.

Additional measurements were performed which included measuring the height of each stack of plies shown in Fig 4.9. The results were used in the FEAs. From these measurements, the average height of a single ply was found as 0.15 ± 0.02 mm and 0.27 ± 0.01 mm for the compressed UD and woven plies, respectively. For the expanded part of the composite, the ply heights were found to be 0.23 ± 0.02 mm and 0.35 ± 0.04 mm for the UD and woven plies, respectively. All heights of the stacked plies above and below the delamination were added together and referred to as H_T and H_B, respectively, as illustrated in Figs. 4.8b and 4.12. The obtained results are presented in Table 4.11. These dimensions were used to place the specimen in the frame before each test, as was described in Section 4.3.

Table 4.10: Dimensions of each BD specimen.

specimen number	$2a_c$ (mm)	B (mm)	$2R$ (mm)	$R_{R(m)}$ (mm)	$R_{L(m)}$ (mm)	D (mm)	$R_{R(calc)}$ (mm)	$R_{L(calc)}$ (mm)
BD1.6.1	15.0 ±0.093	8.5 ±0.022	40.7 ±0.040	40.7	13.5	12.2	12.2	13.5
BD1.14.2	13.6 ±0.076	7.9 ±0.022	40.3 ±0.031	40.0	13.2	13.4	13.3	13.3
BD1.8.2	14.3 ±0.157	7.9 ±0.028	40.2 ±0.023	39.9	12.6	13.2	13.1	12.7
BD1.8.1	15.7 ±0.055	8.0 ±0.014	40.2 ±0.023	39.9	11.4	13.0	12.8	11.6
BD1.12.2	14.6 ±0.190	7.8 ±0.005	40.3 ±0.032	40.1	11.9	13.7	13.6	12.0
BD1.2.2	15.6 ±0.092	8.4 ±0.053	40.5 ±0.026	40.3	13.2	11.7	11.6	13.3
BD1.3.1	15.3 ±0.078	8.5 ±0.083	40.6 ±0.050	40.1	11.9	13.3	13.0	12.1
BD1.1.2	14.9 ±0.102	8.4 ±0.053	40.8 ±0.046	40.5	12.5	13.2	13.0	12.7
BD1.2.1	14.9 ±0.057	8.4 ±0.061	40.3 ±0.062	39.9	13.4	11.8	11.7	13.6
BD1.1.1	15.1 ±0.102	8.3 ±0.015	40.6 ±0.035	40.5	12.7	12.7	12.7	12.7
BD1.3.2	15.2 ±0.039	8.3 ±0.063	40.2 ±0.052	40.3	11.9	13.2	13.2	11.8
BD1.4.2	15.5 ±0.063	8.4 ±0.051	40.9 ±0.047	40.7	13.0	12.3	12.2	13.1
BD1.6.2	15.3 ±0.057	8.4 ±0.033	40.5 ±0.153	40.4	12.5	12.7	12.7	12.5
BD1.5.1	15.3 ±0.233	8.2 ±0.070	40.6 ±0.032	40.6	12.4	12.9	12.9	12.4
BD1.4.1	15.7 ±0.090	8.4 ±0.032	40.6 ±0.025	40.5	13.4	11.4	11.4	13.5
BD1.7.1	15.0 ±0.046	8.3 ±0.037	40.6 ±0.040	40.4	11.6	13.9	13.8	11.7
BD1.11.2	15.7 ±0.060	7.8 ±0.051	40.3 ±0.047	40.1	12.0	12.5	12.4	12.1
BD1.7.2	15.2 ±0.047	8.3 ±0.058	40.6 ±0.066	40.4	13.0	12.3	12.2	13.1
BD1.13.2	16.0 ±0.040	7.9 ±0.023	40.2 ±0.026	40.1	11.4	12.8	12.7	11.5
BD1.5.2	15.0 ±0.135	8.3 ±0.010	40.8 ±0.047	40.4	12.8	12.7	12.5	13.1
BD2.8.1	16.9 ±0.103	7.8 ±0.074	40.3 ±0.020	39.9	11.6	11.7	11.5	11.7
BD2.7.1	15.5 ±0.092	7.7 ±0.013	40.3 ±0.015	40.0	11.5	13.1	12.9	11.7
BD2.7.2	17.5 ±0.089	7.8 ±0.014	40.3 ±0.026	39.9	10.2	12.4	12.2	10.4
BD1.13.1	12.2 ±0.036	7.8 ±0.014	40.3 ±0.042	40.2	12.6	15.5	15.5	12.6
BD2.8.2	15.4 ±0.126	7.7 ±0.006	40.3 ±0.031	39.9	12.9	11.8	11.6	13.1
BD2.1.1	16.0 ±0.128	7.8 ±0.045	40.4 ±0.025	40.2	12.1	12.2	12.1	12.2
BD2.4.2	16.3 ±0.235	7.7 ±0.006	40.2 ±0.006	40.2	11.7	12.2	12.2	11.7

For the specimens with a hole which were tested with $\omega > 0°$, the measured horizontal and vertical hole diameters d_h, d_v, respectively, as well as the vertical offset distances between the hole center and the delamination c_v, illustrated in Fig. 4.5b, were also measured and are shown in Table 4.12. These values were also used in the FEA models.

Results from all twenty seven tests are reported here. In Table 4.13, the temperature ϑ_i and relative humidity (RH), measured at the beginning of each test, are presented. Note that except for specimens BD1.2.2 and BD1.4.2, all temperatures measured were within the tolerance recommended in the ASTM Standard D5229/D5229M (2011) of $23° \pm 3°$C. In addition, for seven specimens, the RH was not in the range of $50 \pm 10\%$ defined in that standard. In Table 4.13, the loading angle ω, the critical delamination length $2a_c$ and the critical load at fracture P_c, are also presented for each specimen.

Load-displacement curves from the tests are shown in Figs. 4.14 and 4.15 for specimens loaded with negative and positive loading angles, respectively. It may be observed from the curves and from Table 4.13 that the critical loads P_c measured for specimens loaded with negative loading angles, were larger than those loaded with positive loading angles. In addition, it may be observed from the plots that for specimens loaded with $\omega \approx -2°, 2°$

Table 4.11: Composite heights above and below the delamination.

specimen number	H_T (mm)	H_B (mm)
BD1.6.1	7.19	9.62
BD1.14.2	7.75	10.00
BD1.8.2	7.61	10.12
BD1.8.1	7.02	9.99
BD1.12.2	7.04	9.16
BD1.2.2	7.41	10.21
BD1.3.1	7.28	10.21
BD1.1.2	7.42	10.22
BD1.2.1	7.11	9.92
BD1.1.1	7.07	10.22
BD1.3.2	7.20	10.56
BD1.4.2	7.03	10.18
BD1.6.2	7.15	9.39
BD1.5.1	7.30	9.77
BD1.4.1	7.15	9.99
BD1.7.1	7.18	9.20
BD1.11.2	7.58	10.39
BD1.7.2	7.22	9.63
BD1.13.2	7.48	9.87
BD1.5.2	7.23	9.58
BD2.8.1	7.45	9.79
BD2.7.1	7.54	9.49
BD2.7.2	7.56	9.61
BD1.13.1	7.54	9.84
BD2.8.2	7.51	9.33
BD2.1.1	7.23	9.12
BD2.4.2	7.54	9.40

and 5°, the compliance was not linear throughout the entire test. Whereas, for all other loading angles, the load increased in a nonlinear manner until approximately 3 kN, where it became linear as the displacement grew. It may be pointed out that for specimens loaded with a negative loading angle, as the loading angle increased in absolute value, the critical load before failure generally decreased. As for specimens loaded with positive loading angles, except for specimen BD2.4.2, as the loading angle increased, the load generally increased, as well.

Table 4.12: Dimensions of the hole in each BD specimen tested with loading angle $\omega > 0°$.

specimen number	d_h (mm)	d_v (mm)	c_v (mm)
BD2.8.1	1.77	1.76	0.12
BD2.7.1	1.71	1.69	0.40
BD2.7.2	1.81	1.97	0.00
BD1.13.1	1.09	1.09	-0.17
BD2.8.2	1.69	1.85	0.00
BD2.1.1	1.68	1.61	0.13
BD2.4.2	1.65	1.71	-0.57

Table 4.13: Parameters from each BD test including the temperature measured during each test ϑ_i, relative humidity (RH), loading angle ω, critical delamination length $2a_c$ and critical load at fracture P_c.

specimen no.	ϑ_i (°C)	RH (%)	ω (°)	$2a_c$ (mm)	P_c (kN)
BD1.6.1	25.6	59.8	-1.9	15.0	10.6
BD1.14.2	24.1	39.0	-2.0	13.6	11.0
BD1.8.2	23.3	58.2	-2.2	14.3	11.8
BD1.8.1	23.4	58.3	-2.5	15.7	10.8
BD1.12.2	23.1	57.9	-2.6	14.6	10.8
BD1.2.2	26.3	58.4	-4.4	15.6	10.8
BD1.3.1	25.9	57.6	-4.7	15.3	10.9
BD1.1.2	24.0	37.0	-4.9	15.3	10.5
BD1.2.1	25.8	57.8	-5.3	14.9	9.4
BD1.1.1	25.8	38.6	-5.3	15.1	10.3
BD1.3.2	25.6	54.9	-9.9	15.2	7.5
BD1.4.2	26.2	53.0	-10.1	15.5	8.5
BD1.6.2	22.4	60.1	-10.3	15.3	8.0
BD1.5.1	25.9	53.1	-10.3	15.3	7.5
BD1.4.1	24.3	63.0	-10.5	15.7	7.5
BD1.7.1	21.9	58.4	-12.7	15.0	8.1
BD1.11.2	20.7	54.7	-12.9	15.7	7.7
BD1.7.2	23.4	61.3	-12.9	15.2	7.8
BD1.13.2	22.9	56.3	-12.9	16.0	7.1
BD1.5.2	22.4	60.1	-13.0	15.0	8.1
BD2.8.1	23.7	50.0	2.1	16.9	5.1
BD2.7.1	22.6	54.0	2.3	15.5	6.5
BD2.7.2	21.9	51.8	1.9	17.5	6.0
BD1.13.1	24.2	45.8	4.9	12.2	7.5
BD2.8.2	23.7	50.9	5.1	15.4	6.5
BD2.1.1	23.5	44.4	5.4	16.0	8.9
BD2.4.2	22.4	50.9	9.5	16.3	5.8

In Fig. 4.14a, results for specimens loaded at an approximate loading angle of $-2°$, are presented. Some scatter may be observed between the slopes of the different specimens, as well as in the critical load P_c measured before the delamination propagated which was found to range between 10.6 kN and 11.8 kN. It shall be noted that it is difficult to position the specimen accurately in the frame when smaller loading angles are considered. The setup of the specimen in the frame was discussed in Section 4.3 and presented in Fig. 4.12. In Fig. 4.14b, results for specimens loaded at an approximate loading angle of $-5°$, are presented. From the plot, it may be observed that specimens BD1.2.1, BD1.2.2 and BD1.3.1 suffered from some damage at a loading value of approximately 2.2-2.5 kN. In the images obtained from the tests, this damage is visible in the region near the applied load. It may be noted, that these three tests were held on the same day and that this damage might be a result of something different in the setup that day. However, the critical load P_c, before the delamination propagated, does not appear to be affected by this damage. The critical load was found to be in the range of 10.3 kN and 10.9 kN for four out of five specimens tested at this loading angle. For the fifth specimen, the critical load was measured to be lower than the others with a value of $P_c = 9.4$ kN. Since the

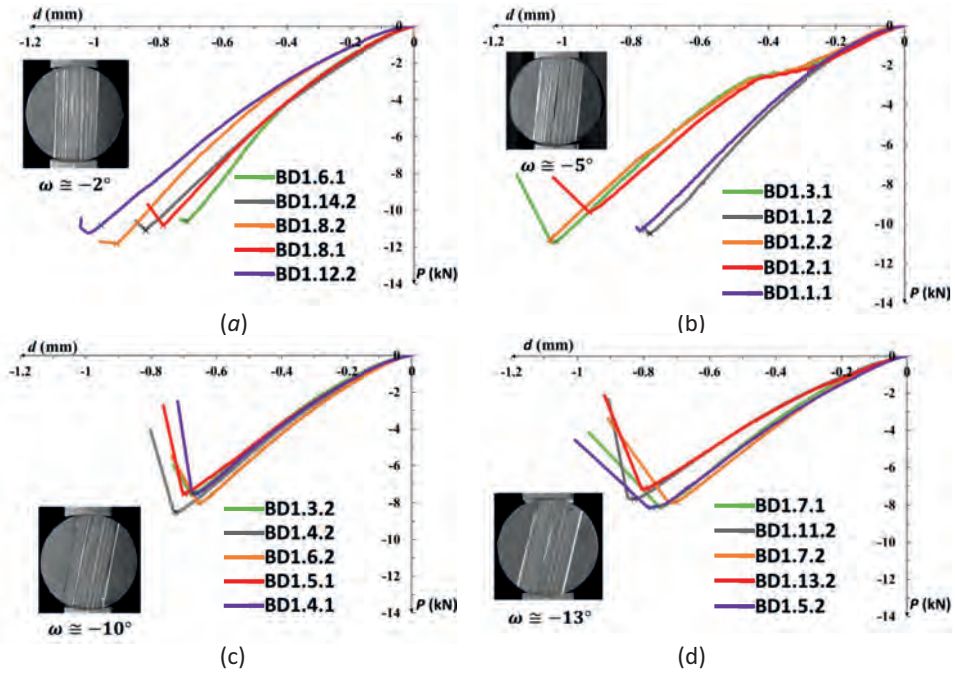

Figure 4.14: Brazilian disk specimen load-displacement curves ($\omega < 0$): (a) five specimens with $\omega \approx -2°$; (b) five specimens with $\omega \approx -5°$; (c) five specimens with $\omega \approx -10°$; (d) five specimens with $\omega \approx -13°$.

critical load was found to be similar in all tests, these specimens were used in the analyses. In Fig. 4.14c, results for specimens loaded with $\omega \approx -10°$ are presented. For this loading angle, the critical load was found to be 7.5 kN $\leq P_c \leq$ 8.5 kN. It may be observed from the figure that for specimens BD1.3.2, BD1.5.1 and BD1.4.1, the delamination propagated at a

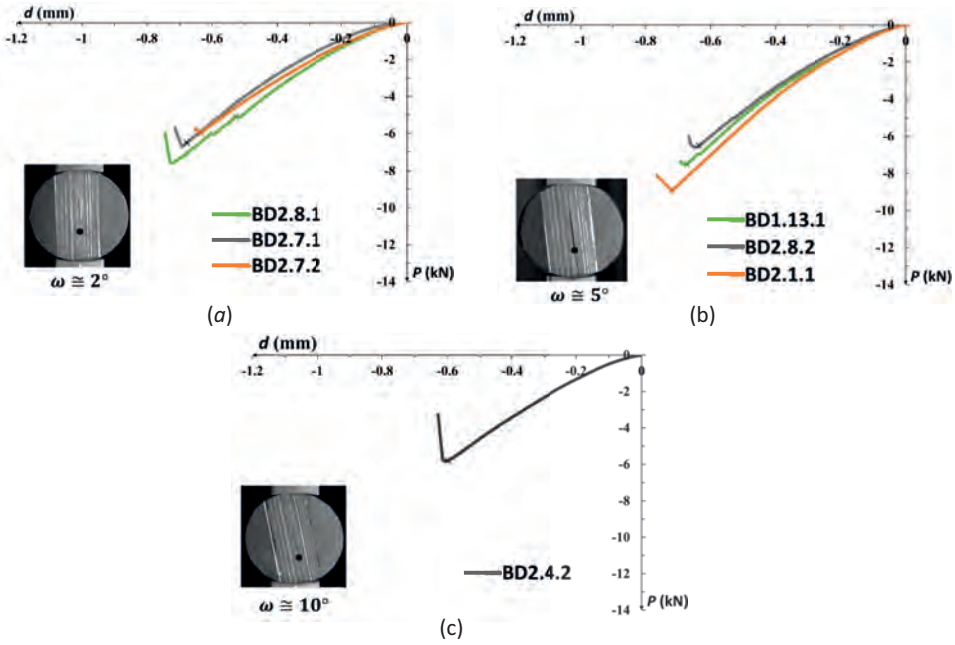

Figure 4.15: Brazilian disk specimen load-displacement curves ($\omega > 0$): (a) three specimens with $\omega \approx 2°$; (b) three specimens with $\omega \approx 5°$; (c) one specimen with $\omega \approx 10°$.

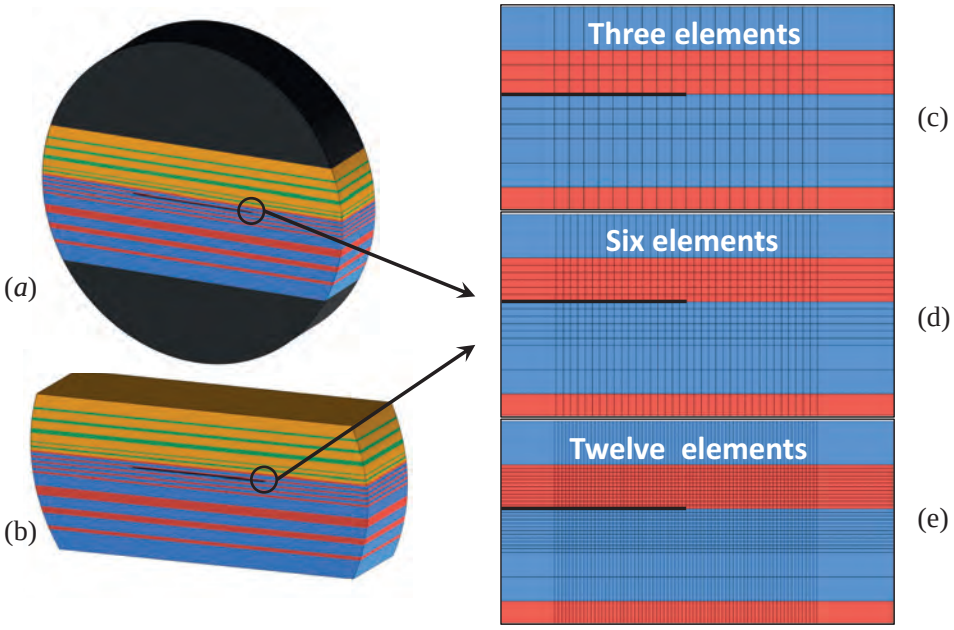

Figure 4.16: Mesh of BD specimen: (a) mechanical model and (b) thermal model. (c) Coarse mesh; (d) fine mesh and (e) finest mesh in the neighborhood of the delamination front.

similar value of approximately 7.5 N where for the other two specimens, P_c was measured to be somewhat higher. During the tests, the behavior of all five specimens loaded at this angle was similar. Results for specimens loaded with $\omega \approx -13°$, are presented in Fig. 4.14d. For this loading angle, the critical load was found to be 7.1 kN $\leq P_c \leq$ 8.1 kN. It may be observed that specimens BD1.13.2 and BD1.11.2 resulted with similar behavior throughout the test. In addition, specimens BD1.7.1, BD 1.7.2 and BD1.5.2 also resulted with similar behavior.

In Fig. 4.15a, 4.15b and 4.15c, load-displacement curves for specimens with a hole which were tested with a loading angle of approximately $\omega \approx 2°$, $5°$ and $9°$ are shown, respectively. It may be observed that the curves are similar for each set of specimens. For these specimens the critical load was found to be 5.1 kN $\leq P_c \leq$ 8.9 kN which is generally lower than the critical loads obtained for specimens loaded with negative loading angles .

4.5 Convergence and domain independence

In this section, mesh convergence and domain independence for the M-integral are presented. The FE program Abaqus (2017) was used to obtain the stress and displacement fields. The FEA results were used with the DE method and the M-integrals, presented in Sections 3.1 and 3.2, respectively, to determine stress intensity factors resulting from mechanical loading, as well as from residual curing stresses. Two types of problems were considered, mechanical and thermal, shown in Figs. 4.16a and 4.16b, respectively. Three

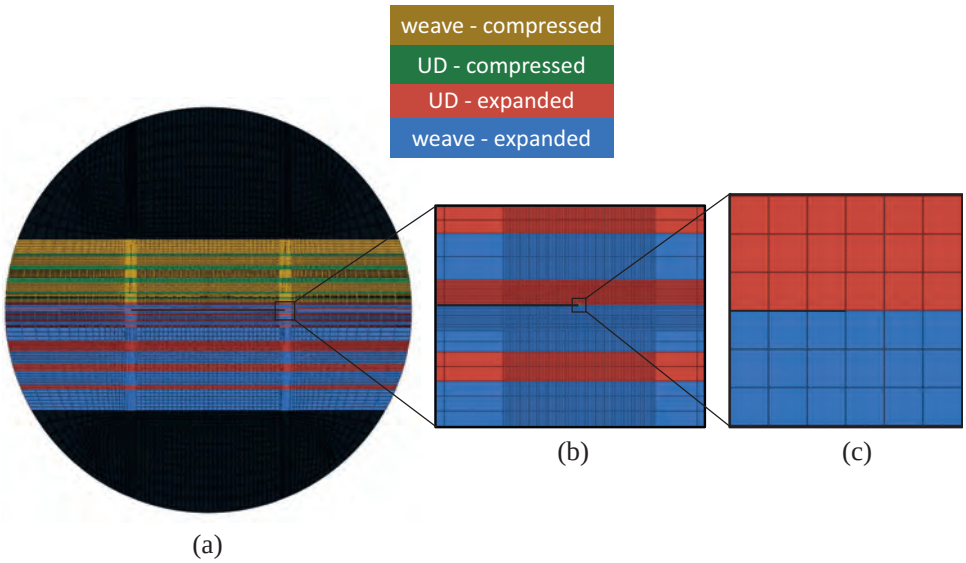

Figure 4.17: (a) In-plane finest mesh of a Brazilian disk specimen; (b) enlarged view of six plies near the delamination front; (c) enlarged view of elements at the delamination front.

meshes were created using the dimensions of specimen BD1.1.1 given in Table 4.10. The loading angle used in the FEAs was $\omega = -5.32°$. An example for a positive loading angle is shown in Fig. 1.19. Also used were the composite stack heights, critical applied load $P_c = 10.3$ kN and the test temperature difference from eq. (4.6), $\Delta\vartheta_i = -59.2°$ C $i = BD1.1.1$.

In Fig. 4.17a, a two-dimensional view of the finest mesh of the BD specimen is presented. The model is composed of the composite strip with two aluminum partial disks colored in black in Fig. 4.17a. In the thermal analyses the aluminum disks were omitted with the mesh of the composite strip remaining the same. The composite strip is composed of twenty-seven ply groups including 6 woven compressed, 5 UD compressed, 8 woven expanded and 8 UD expanded plies. These plies are represented in yellow, green, blue and pink, respectively, in Figs. 4.16a, 4.16b and 4.17. The mechanical properties and CTEs for each material used in the composite strip are given in Tables 4.3 and 4.8 for the UD fabric and the woven fabric plies, respectively. The mechanical properties used for the aluminum were Young's modulus $E = 69$ MPa and Poisson's ratio $\nu = 0.33$.

Twenty-noded, isoparametric, quadratic brick elements were used in solving both problems. For the mechanical problem, element type C3D20 was used; for the thermal problem, use was made of element type C3D20T. The plies above and below the delamination are from the expanded part of the plate, as may be seen in Fig. 4.17b. A denser mesh was used near the delamination front, to model the square-root, oscillatory singularity. In addition, along the delamination front, quarter-point elements with an in-plane aspect ratio of 1×1 were used as shown for the finest mesh in Figs. 4.17c and 4.18. Since the upper UD ply is thinner than the lower woven ply, in order to obtain such elements, the woven

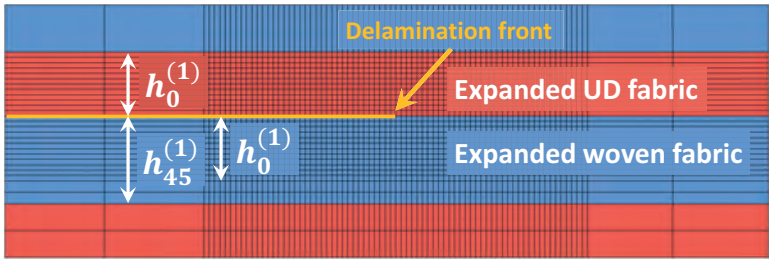

Figure 4.18: Brazilian disk specimen model - partitioning in the delamination front region.

ply was partitioned into two layers with the same properties from Table 4.8 used for each. The height of the upper layer was determined to be equal to the height of the upper UD ply, namely $h_0^{(1)}$ in Fig. 4.18. The total height of the two lower layers was determined to be equal to the measured woven ply thickness, namely $h_{45}^{(1)}$ in Fig. 4.18. In this way, the upper UD ply and the upper layer of the lower woven ply near the delamination are composed of the same thickness and are meshed with elements of the same size.

The total number of elements in each mesh was determined by the mesh refinement near the delamination front. In order to examine convergence, each element in the ply above and below the delamination was divided into four elements for each mesh refinement. That is, three, six and twelve layers of elements were used in the coarse, fine and finest meshes, respectively, as shown in Figs. 4.16c, 4.16d and 4.16e. The number of elements and nodal points used in each mesh for each of the models are specified in Table 4.14. Note that in the corresponding thermal model, the aluminum partial disks were omitted, resulting in fewer elements in those meshes as compared to the mechanical model.

The load and displacement boundary conditions (BCs) used are illustrated in Fig. 4.19 where the loads are represented using yellow arrows and the displacement BCs using orange triangles and circles. In Fig. 4.19a, an isometric view of the BD specimen is presented and in Fig. 4.19b a two-dimensional view is shown. Two coordinate systems were used to model the directions of the load and displacement BCs. The first is the global coordinate system (x_1, x_2, x_3), defined in Fig. 1.19, and oriented parallel to the delamination surface. The second coordinate system (x_1', x_2', x_3) is rotated according to the loading angle ω, about the x_3-axis, so that it is oriented in the direction of the load.

Table 4.14: Number of nodal points, elements and element size near the delamination front (ESNDF) in the mechanical and thermal models for coarse, fine and finest meshes.

	mechanical model		thermal model		ESNDF
mesh type	nodes	elements	nodes	elements	mm × mm × mm
coarse	943,840	224,040	755,804	178,760	0.060 × 0.060 × 0.415
fine	1,451,224	345,360	1,173,548	278,480	0.030 × 0.030 × 0.415
finest	2,579,848	615,480	2,122,892	505,900	0.015 × 0.015 × 0.415

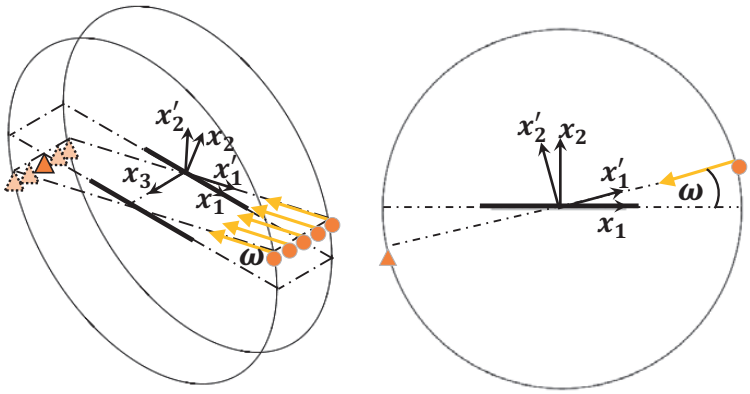

(a) (b)

Figure 4.19: Illustration of the applied loads and displacement boundary conditions applied to a BD specimen; (a) isometric view and (b) two-dimensional view of specimen center plane.

A fine mesh was used in the region in which the load is applied in order to properly model the loading angle which was used in the test. The critical load obtained from the test was applied as a line load in the radial direction as shown in Fig. 4.19. The nodes to which the load is applied are prevented from moving in the tangential direction perpendicular to it. Directly opposite the load line, on the other specimen side, nodes along the specimen thickness are restrained from moving in both the in-plane radial direction corresponding to the direction of the applied load, and to the tangential direction that is orthogonal to it. One point at the center of this line is restrained for movement in the out-of-plane direction.

The DE method described in Section 3.1 and the mechanical and thermal M-integrals described in Section 3.2 were used to determine the stress intensity factors for each problem. For the DE method, eqs. (3.10) and (3.13) were used to calculate the local stress intensity factors related to the different modes. The results were extrapolated for $r \to 0$ to obtain global stress intensity factors. The stress intensity factors obtained by means of the mechanical M-integral were calculated using eqs. (3.22) through (3.24). The stress intensity factors resulting from residual thermal stresses are given in eqs. (3.28) through (3.30). Six domains, shown in Fig. 1.8, were used in the analyses of the fine and finest meshes. For the coarse mesh, since the UD fabric ply above the delamination contained only three elements through its height, only three domains could be used for the M-integral. The differences between the results obtained using the different models were computed using eq. (3.31) where the superscript (1) represents the coarser mesh used in the comparison and the superscript (2), the finer mesh. The subscript $i = 1, 2, III$, represents the mode of the stress intensity factor. The largest relative differences (LRDs) between the results obtained for the coarse and fine, as well as, the fine and finest meshes are presented in Tables 4.15 and 4.16, for the mechanical and thermal stress intensity factors, respectively.

For the mechanical case, it is observed that the differences in the values of $K_1^{(f)}$ and

Table 4.15: Comparison of the mechanical stress intensity factors obtained from the different meshes. Largest relative differences (LRD) through the model thickness were calculated using eq. (3.31).

	M-integral			DE		
	$K_1^{(f)}$	$K_2^{(f)}$	$K_{III}^{(f)}$	$K_1^{(f)}$	$K_2^{(f)}$	$K_{III}^{(f)}$
LRD - coarse vs fine	0.15%	-0.30%	0.34%	-1.06%	-2.40%	1.63%
LRD - fine vs finest	0.04%	-0.03%	-0.40%	1.15%	-0.24%	-0.31%

$K_2^{(f)}$ calculated using the M-integral in the sixth domain for the fine and finest meshes were reduced to 0.04% and 0.03%, respectively. For $K_{III}^{(f)}$, the calculated difference changed slightly, but there is no decrease. The differences between the stress intensity factors obtained using the DE method were sometimes above 1%, leading to the conclusion that the DE method is less accurate than the M-integral. But the results corroborate each other. For the thermal case, it is observed that the differences between the results obtained from the different meshes using the M-integral in the sixth domain reduced when the fine and finest meshes were compared. For the results obtained using the DE method, the differences also decreased for the finer meshes. Again, it is seen that it is more difficult to obtain accurate results with the DE method. Moreover, the thermal problem is more difficult than the mechanical problem.

It may be concluded that the results obtained from the different meshes have converged using the finest mesh for both mechanical and thermal loading. Since the difference in computer time between the fine and finest meshes was not significant, the finest mesh was used for all analyses of the BD specimens.

For the chosen finest BD mesh and model, shown in Figs. 4.16e and 4.17, domain independence was examined. The mechanical and thermal stress intensity factors which were calculated by means of the mechanical and thermal M-integrals, respectively, in six domains shown in Fig. 1.8, were compared. The results obtained from all domains for each stress intensity factor are plotted in Figs. 4.20a through 4.20f as a function of the normalized specimen thickness x_3/B. For all calculated stress intensity factors, the results

Table 4.16: Comparison of the thermal stress intensity factors obtained from the different meshes. Largest relative differences (LRD) through the model thickness were calculated using eq. (3.31).

	M-integral			DE		
	$K_1^{(r)}$	$K_2^{(r)}$	$K_{III}^{(r)}$	$K_1^{(r)}$	$K_2^{(r)}$	$K_{III}^{(r)}$
LRD - coarse vs fine	0.81%	3.91%	0.82%	0.92%	5.24%	2.3%
LRD - fine vs finest	-0.36%	0.90%	0.24%	0.81%	-2.17%	1.81%

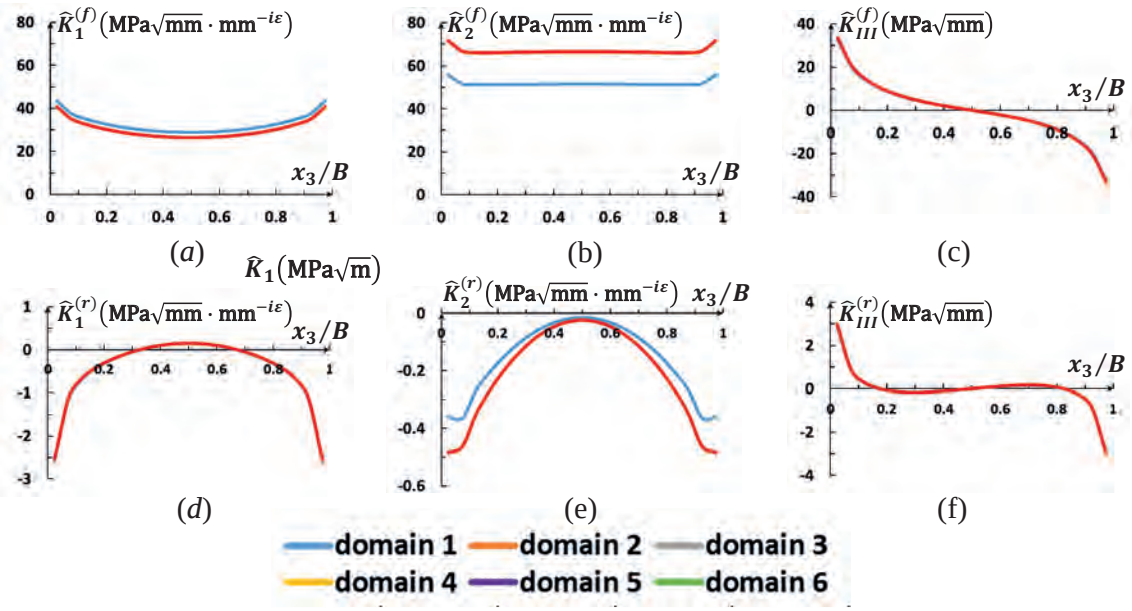

Figure 4.20: Stress intensity factors in six domains (a) $K_1^{(f)}$; (b) $K_2^{(f)}$; (c) $K_{III}^{(f)}$; (d) $K_1^{(r)}$; (e) $K_2^{(r)}$; (f) $K_{III}^{(r)}$

for domain 1, the smallest domain, closest to the delamination front, differ from all other domains. This is a result of the stress singularity near the delamination front which is not accurately represented in the FE analysis. This difference is visible in Figs. 4.20a, 4.20b and 4.20e, for $K_1^{(f)}$, $K_2^{(f)}$ and $K_2^{(r)}$, respectively. For all plots in Fig. 4.20 similar results are presented for domains 2 through 6.

In Table 4.17, the largest relative difference (LRD) between every two adjacent domains, is presented. These were calculated by means of eq. (3.31) where the superscript (1) represents the smaller domain used in the comparison and the superscript (2), the larger domain. The subscript $i = 1, 2, III$, refer to the stress intensity factor mode. The LRDs calculated for the differences between the results obtained from domains 1 and 2

Table 4.17: Comparison of the mechanical and thermal stress intensity factors obtained in six different domains (see Fig. 1.8 for the finest mesh). Largest relative differences (LRD) through the model thickness were calculated using eq. (3.31).

LRD	$K_1^{(f)}$	$K_2^{(f)}$	$K_{III}^{(f)}$	$K_1^{(r)}$	$K_2^{(r)}$	$K_{III}^{(r)}$
		(%)			(%)	
domain 1 and domain 2	9.17	22.46	3.07	62.41	37.03	3.22
domain 2 and domain 3	0.20	0.27	0.12	8.91	3.79	0.22
domain 3 and domain 4	0.05	0.17	0.04	1.26	0.57	0.50
domain 4 and domain 5	0.01	0.06	0.01	1.47	0.72	0.47
domain 5 and domain 6	0.01	0.02	0.01	0.90	0.39	0.17

are shown in the third row in Table 4.17. These LRDs are respectively large for all stress intensity factors. Recall that this is a result of the stress singularity near the delamination front. As expected, for larger domains, these LRDs decrease. It should be noted that the largest LRD value was calculated for $K_1^{(r)}$ to be 62.41%. This value is large since the two compared $K_1^{(r)}$ values tend to zero. A decrease in the LRD values calculated for all stress intensity factors obtained in domains 2 and 3 is clearly observed in the fourth row in Table 4.17. Mesh independence is found for domains 3 through 6 for all mechanical and thermal stress intensity factors.

4.6 BD test analysis

Twenty-seven BD specimens were analyzed by means of the finest FE model, described in Section 4.5 and presented in Fig. 4.17. Mechanical and thermal stress intensity factors were calculated for each specimen by means of the DE method, as well as the mechanical and thermal M-integrals, presented in Sections 3.1 and 3.2, respectively. In this section, details regarding the models used, as well as results from the analyses are presented.

A parametric representation was used to create a three-dimensional FE mesh for each BD specimen, so that it could be changed according to the actual measured geometry. The parameters in this representation include the specimen diameter $2R$, specimen thickness B, critical delamination length $2a_c$ and the location of the delamination defined by $R_{R(calc)}$ and $R_{L(calc)}$. These parameters are shown in Fig 4.8 and given for each specimen in Table 4.10. In addition, the height of each group of plies, shown in Fig. 4.9, was modeled specifically for each specimen, using the parametric definitions.

For each specimen, two problems were considered, mechanical and thermal. In the former, the failure load P_c determined from the test and given in the last column of Table 4.13 was applied to the FE model. In the latter, the FE model was subjected to a uniform decrease in temperature. The temperature difference $\Delta\vartheta_i$ was applied to the model. This value was calculated by means of eq. (4.6) where ϑ_i is the temperature measured at the beginning of each test (i) and given in the second column of Table 4.13. The curing temperature was $\vartheta = 85°$. The mechanical and residual curing stress intensity factors $K_i^{(f)}$ and $K_i^{(r)}$, $i = 1, 2, III$, respectively, were calculated at twenty elements along the delamination front, through the specimen thickness using the mechanical and thermal M-integrals, respectively. The results obtained in the fourth, fifth and sixth domains (see Fig. 1.8) were averaged and superposed to obtain the in-plane and out-of-plane total stress intensity factors for every element along the delamination front using eqs. (1.82), (1.83) and (1.84). The DE method was used for corroboration; the results obtained using this method are not presented here.

For specimens BD2.8.2 and BD1.2.1, loaded with similar positive and negative loading angles of $\omega \approx \pm 5°$, the stress intensity factors from domains 4, 5 and 6 (see Fig. 1.8) were

Table 4.18: Averaged stress intensity factors from the fourth, fifth and sixth domains of the mechanical and thermal M- integrals for specimen BD2.8.2 with $\omega = 5.1°$.

x_3/B	$K_1^{(f)}$ $\left(\text{MPa}\sqrt{\text{mm}}\,(\text{mm})^{-i\varepsilon}\right)$	$K_2^{(f)}$	$K_{III}^{(f)}$ $(\text{MPa}\sqrt{\text{mm}})$	$K_1^{(r)}$ $\left(\text{MPa}\sqrt{\text{mm}}\,(\text{mm})^{-i\varepsilon}\right)$	$K_2^{(r)}$	$K_{III}^{(r)}$ $(\text{MPa}\sqrt{\text{mm}})$
0.025	13.07	-56.33	-22.23	-3.68	-0.68	3.52
0.075	18.11	-53.38	-15.01	-1.73	-0.63	1.04
0.125	18.68	-52.88	-11.11	-0.98	-0.45	0.26
0.175	18.51	-52.75	-8.46	-0.57	-0.34	-0.04
0.225	18.20	-52.72	-6.48	-0.30	-0.26	-0.17
0.275	17.89	-52.72	-4.91	-0.11	-0.20	-0.21
0.325	17.61	-52.72	-3.61	0.04	-0.15	-0.20
0.375	17.40	-52.72	-2.47	0.14	-0.12	-0.16
0.425	17.26	-52.73	-1.44	0.21	-0.09	-0.10
0.475	17.19	-52.73	-0.48	0.24	-0.08	-0.04
0.525	17.19	-52.73	0.48	0.24	-0.08	0.04
0.575	17.26	-52.73	1.44	0.21	-0.09	0.10
0.625	17.40	-52.72	2.47	0.14	-0.12	0.16
0.675	17.61	-52.72	3.61	0.04	-0.15	0.20
0.725	17.89	-52.72	4.91	-0.11	-0.20	0.21
0.775	18.20	-52.72	6.48	-0.30	-0.26	0.17
0.825	18.51	-52.75	8.46	-0.57	-0.34	0.04
0.875	18.68	-52.88	11.11	-0.98	-0.45	-0.26
0.925	18.11	-53.38	15.01	-1.73	-0.63	-1.04
0.975	13.07	-56.33	22.23	-3.68	-0.68	-3.52

averaged and are presented in Tables 4.18 and 4.19, respectively. Note that the values presented possess units. It may be noted that K_1 and K_2 are symmetric with respect to the specimen center plane and K_{III} is anti-symmetric. From these tables it may be observed that the residual curing stress intensity factors are relatively small compared to the mechanical ones. The residual curing stress intensity factors are largest near the specimen free surfaces and decrease towards the mid-thickness, where they approach zero for $K_2^{(r)}$ and $K_{III}^{(r)}$.

In a previous study for a crack along an interface between two linear, elastic ceramic clays (Banks-Sills et al., 2000), the results for positive and negative loading angles were found to be similar in absolute values. For the interface studied here, smaller mechanical stress intensity factors $K_i^{(f)}$, $i = 1, 2, III$, in absolute value, were observed for specimens loaded with positive loading angles in comparison to those obtained for nearly the same negative loading angles. Examples of these results are presented in Tables 4.18 and 4.19 for $\omega = 5.1°$ and $\omega = -5.3°$, respectively. In addition, for the case studied here, larger mixed mode ratios $K_2^{(f)}/K_1^{(f)}$, in absolute values were found at mid-thickness for $\omega > 0°$ as compared to that for $\omega < 0°$. For example, the in-plane mixed mode ratio at mid-plane for specimens BD2.8.2 and BD1.2.1 with loading angles $\omega = 5.1°$ and $\omega = -5.3°$, respectively, were found to be -3.07 and 2.56, respectively. Thus, it is possible to conclude that the stress intensity factors, mode mixity and critical energy release rate are not symmetric for positive and negative loading angles for the material and interface studied here.

Table 4.19: Averaged stress intensity factors from the fourth, fifth and sixth domains of the mechanical and thermal M- integrals for specimen BD1.2.1 with $\omega = -5.3°$.

x_3/B	$K_1^{(f)}$ $\left(\text{MPa}\sqrt{\text{mm}}\,(\text{mm})^{-i\varepsilon}\right)$	$K_2^{(f)}$	$K_{III}^{(f)}$ $(\text{MPa}\sqrt{\text{mm}})$	$K_1^{(r)}$ $\left(\text{MPa}\sqrt{\text{mm}}\,(\text{mm})^{-i\varepsilon}\right)$	$K_2^{(r)}$	$K_{III}^{(r)}$ $(\text{MPa}\sqrt{\text{mm}})$
0.025	39.12	69.15	32.27	-2.82	-0.52	3.39
0.075	33.49	64.57	19.59	-1.30	-0.54	1.08
0.125	31.10	64.05	13.69	-0.72	-0.41	0.36
0.175	29.45	64.10	9.98	-0.39	-0.31	0.06
0.225	28.18	64.27	7.37	-0.15	-0.24	-0.08
0.275	27.18	64.43	5.42	0.02	-0.18	-0.14
0.325	26.41	64.56	3.88	0.16	-0.13	-0.14
0.375	25.86	64.65	2.61	0.25	-0.09	-0.12
0.425	25.51	64.71	1.51	0.31	-0.07	-0.08
0.475	25.33	64.74	0.49	0.35	-0.06	-0.03
0.525	25.33	64.74	-0.49	0.35	-0.06	0.03
0.575	25.51	64.71	-1.51	0.31	-0.07	0.08
0.625	25.86	64.65	-2.61	0.25	-0.09	0.12
0.675	26.41	64.56	-3.88	0.16	-0.13	0.14
0.725	27.18	64.43	-5.42	0.02	-0.18	0.14
0.775	28.18	64.27	-7.37	-0.15	-0.24	0.08
0.825	29.45	64.10	-9.98	-0.39	-0.31	-0.06
0.875	31.10	64.05	-13.69	-0.72	-0.41	-0.36
0.925	33.49	64.57	-19.59	-1.30	-0.54	-1.08
0.975	39.12	69.15	-32.27	-2.82	-0.52	-3.39

In Fig. 4.21, an example of the displacement field found from DIC and from the FE mechanical analysis is presented for specimen BD1.2.1 with a loading angle of $\omega = -5.3°$. The displacement in the x_2 and x_1 - directions which are the delamination opening and in-plane sliding directions, respectively, are shown in Figs. 4.21a and 4.21b, respectively. Since the residual curing stresses have a relatively small contribution to the displacement field which is taken into account in the DIC, a good correlation between the physical deformation measured with DIC and those obtained by means of FEA is observed. These results give confidence that the numerical analyses, as well as the mechanical properties

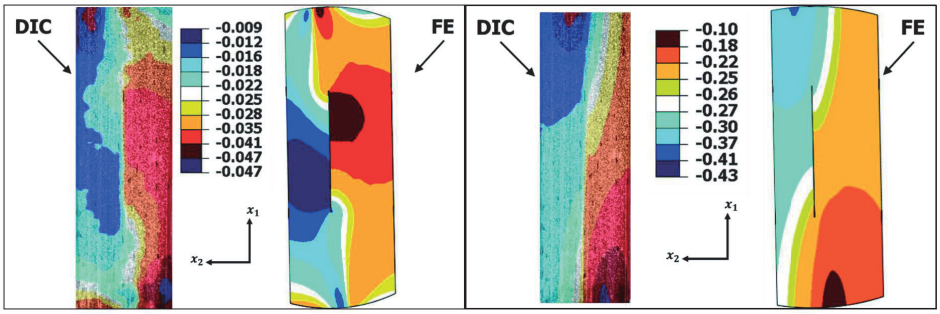

(a) (b)

Figure 4.21: Comparison of the displacement field obtained from DIC versus FEA for specimen BD1.2.1 with $\omega = -5.3°$, the scale of the color bar is in mm; displacement in the (a) x_2-direction or (opening) and (b) x_1-direction (shear).

used are correct.

It may be noted that for specimen BD2.4.2 which was loaded with $\omega = 9.5°$, interpenetration or contact of the upper and lower plies near the delamination front was observed. For $x_3/B < 0.2$ and $x_3/B > 0.8$, the contact length is greater than 5% of half the delamination length a, reaching 40% at the specimen outer surfaces. For $0.2 < x_3/B < 0.8$ this contact region was less than 5% of half the delamination length a. Although contact occurred, results are reported for this specimen. For values of $\omega > 9.5°$, significant contact was observed throughout the delamination thickness; results from these specimens were not used. For specimens loaded with $\omega \approx 5°$, a contact length of approximately 3% of half the delamination length a was observed on the outer surfaces of the specimen. For all other specimens, no interpenetration or contact were found.

The phase angles, $\hat{\psi}$ and ϕ which represent the in-plane and out-of-plane to in-plane mode mixities, respectively, as well as the critical interface energy release rate $\mathcal{G}_{ic}$ were calculated for each element along the delamination front through the thickness of each specimen. The calculation was performed using the total stress intensity factors by means of eqs. (3.19), (3.20) and (3.17), respectively, where $\mathcal{G}_{ic} = \mathcal{G}_i$. The values of ε, H_1 and H_2 which were used in the calculations are presented in Table 4.9.

The phase angles $\hat{\psi}$ and ϕ, as well as the critical interface energy release rate $\mathcal{G}_{ic}$ values obtained at $x_3/B = 0.475$ and $x_3/B = 0.525$ for each specimen are the same and presented in Table 4.20. The results obtained for each specimen at $x_3/B = 0.175$ and $x_3/B = 0.825$ are also the same and are presented in Table 4.21. Also in those tables are the parameters $\hat{K}_i$ $(i = 1, 2)$ which are the normalized in-plane stress intensity factors calculated by means of eq. (1.26) with an arbitrary length parameter $\hat{L}$. The length scale $\hat{L}$ may be used as a fitting parameter in a failure criterion and was chosen here to be $\hat{L} = 100$ μm. The normalization was used to regularize the units. The resulting units are the same as those of the out-of-plane stress intensity factor, namely, $FL^{-3/2}$, where L and F represent length and force, respectively.

It may be observed in Tables 4.20 and 4.21 that generally, as the absolute value of ω increases, the values of $\hat{K}_1^{(T)}$ decrease, whereas, the absolute values of $\hat{K}_2^{(T)}$ increase. This results in an increasing phase angle $\hat{\psi}$, in absolute value, for larger loading angles ω, in absolute value. In addition, it may be observed that the values of the out-of-plane stress intensity factors are small compared to the in-plane stress intensity factors, especially for smaller absolute values of the loading angle ω. In Table 4.20, along the specimen centerline, values of $K_{III}^{(T)}$ are nearly zero, resulting in negligible values of ϕ. In Table 4.21, values of $K_{III}^{(T)}$ and ϕ are larger than those at the specimen mid-thickness. Yet, in both cases ϕ is small compared to $\hat{\psi}$, indicating that the out-of-plane mode mixity remains smaller than the in-plane mode mixity through the specimen thickness. Finally, it may be observed that the critical interface energy release rate $\mathcal{G}_{ic}$, found for each specimen, generally increases as mode 2 becomes dominant for larger loading angles, in absolute

Table 4.20: The loading angle ω, critical interface energy release rate $\mathcal{G}_{ic}$, phase angles $\hat{\psi}$ and ϕ, and normalized total stress intensity factors $\hat{K}_1^{(T)}$, $\hat{K}_2^{(T)}$ and $K_{III}^{(T)}$ calculated for $\hat{L} = 100$ μm for the $0°//(+45°/-45°)$ interface at specimen $x_3/B = 0.475$ and $x_3/B = 0.525$.

specimen	ω (°)	$\mathcal{G}_{ic}$ (N/m)	$\hat{\psi}$ (rad)	ϕ (rad)	$\hat{K}_1^{(T)}$ (MPa$\sqrt{\text{m}}$)	$\hat{K}_2^{(T)}$ (MPa$\sqrt{\text{m}}$)	$K_{III}^{(T)}$ (MPa$\sqrt{\text{m}}$)
BD1.6.1	-1.9	262.7	0.656	0.003	0.99	0.76	0.00
BD1.14.2	-2.0	331.4	0.689	0.002	1.08	0.89	0.00
BD1.8.2	-2.2	378.0	0.744	0.004	1.10	1.01	0.01
BD1.8.1	-2.5	471.0	0.800	0.003	1.16	1.20	0.00
BD1.12.2	-2.6	472.8	0.850	0.003	1.10	1.26	0.00
BD1.2.2	-4.4	685.6	1.076	0.006	0.96	1.77	0.01
BD1.3.1	-4.7	788.9	1.128	0.005	0.93	1.95	0.01
BD1.1.2	-4.9	703.4	1.088	0.007	0.95	1.81	0.01
BD1.2.1	-5.3	817.5	1.141	0.007	0.92	2.00	0.01
BD1.1.1	-5.3	864.8	1.135	0.007	0.96	2.05	0.02
BD1.3.2	-9.9	819.0	1.361	0.010	0.46	2.15	0.02
BD1.4.2	-10.1	986.5	1.365	0.009	0.49	2.37	0.02
BD1.6.2	-10.3	909.2	1.386	0.009	0.43	2.28	0.02
BD1.5.1	-10.3	864.7	1.376	0.010	0.44	2.22	0.02
BD1.4.1	-10.5	820.8	1.368	0.011	0.44	2.16	0.02
BD1.7.1	-12.7	1033.6	1.455	0.009	0.29	2.46	0.02
BD1.11.2	-12.9	1256.9	1.458	0.012	0.31	2.71	0.03
BD1.7.2	-12.9	984.8	1.441	0.009	0.31	2.40	0.02
BD1.13.2	-12.9	1036.8	1.450	0.011	0.30	2.46	0.03
BD1.5.2	-13.0	1024.3	1.435	0.010	0.33	2.44	0.02
BD2.8.1	2.1	101.7	-0.741	-0.008	0.57	-0.52	-0.01
BD2.7.1	2.3	167.2	-0.933	0.000	0.59	-0.80	0.00
BD2.7.2	1.9	539.6	-1.237	-0.008	0.59	-1.69	-0.01
BD1.13.1	4.9	598.3	-1.310	-0.010	0.49	-1.82	-0.02
BD2.8.2	5.1	520.2	-1.304	-0.010	0.46	-1.70	-0.02
BD2.1.1	5.4	985.8	-1.330	-0.009	0.58	-2.35	-0.02
BD2.4.2	9.5	1013.8	-1.543	-0.012	0.07	-2.45	-0.03

value. For each tested BD specimen, results from the analyses are presented in Tables C.1 through C.27.

4.7 Two and three-dimensional failure criteria

In this section, two and three-dimensional failure criteria are proposed and examined using results obtained from the testing and analyses of the mixed mode fracture toughness BD tests. These results are presented for each specimen in Tables C.1 through C.27. The criteria may be used for predicting delamination failure for the multi-directional laminate composite investigated here.

Table 4.21: The loading angle ω, interface energy release rate $\mathcal{G}_{ic}$, phase angles $\hat{\psi}$ and ϕ, and normalized total stress intensity factors $\hat{K}_1^{(T)}$, $\hat{K}_2^{(T)}$ and $K_{III}^{(T)}$ calculated for $\hat{L} = 100$ μm for the $0°//(+45°/-45°)$ interface for each specimen at $x_3/B = 0.175$ and $x_3/B = 0.825$.

specimen	ω (°)	$\mathcal{G}_{ic}$ (N/m)	$\hat{\psi}$ (rad)	ϕ (rad)	$\hat{K}_1^{(T)}$ (MPa$\sqrt{\text{m}}$)	$\hat{K}_2^{(T)}$ (MPa$\sqrt{\text{m}}$)	$K_{III}^{(T)}$ (MPa$\sqrt{\text{m}}$)
BD1.6.1	-1.9	291.8	0.601	0.055	1.08	0.74	0.07
BD1.14.2	-2.0	363.8	0.634	0.051	1.18	0.87	0.07
BD1.8.2	-2.2	416.5	0.687	0.071	1.21	0.99	0.11
BD1.8.1	-2.5	514.7	0.743	0.060	1.28	1.18	0.10
BD1.12.2	-2.6	512.2	0.792	0.057	1.22	1.24	0.09
BD1.2.2	-4.4	709.3	1.036	0.097	1.04	1.76	0.19
BD1.3.1	-4.7	807.6	1.089	0.085	1.01	1.93	0.18
BD1.1.2	-4.9	731.7	1.044	0.111	1.04	1.79	0.22
BD1.2.1	-5.3	834.9	1.106	0.110	0.99	1.98	0.23
BD1.1.1	-5.3	892.2	1.098	0.110	1.04	2.03	0.24
BD1.3.2	-9.9	823.1	1.349	0.149	0.48	2.13	0.31
BD1.4.2	-10.1	985.8	1.354	0.135	0.51	2.34	0.31
BD1.6.2	-10.3	908.3	1.378	0.131	0.44	2.26	0.29
BD1.5.1	-10.3	868.8	1.364	0.149	0.46	2.20	0.32
BD1.4.1	-10.5	827.2	1.357	0.154	0.46	2.14	0.32
BD1.7.1	-12.7	1026.0	1.460	0.134	0.27	2.43	0.31
BD1.11.2	-12.9	1267.8	1.457	0.169	0.31	2.68	0.44
BD1.7.2	-12.9	980.3	1.443	0.135	0.30	2.37	0.31
BD1.13.2	-12.9	1038.1	1.452	0.153	0.29	2.43	0.36
BD1.5.2	-13.0	1021.3	1.437	0.137	0.32	2.42	0.32
BD2.8.1	2.1	114.2	-0.725	-0.088	0.60	-0.53	-0.07
BD2.7.1	2.3	177.6	-0.911	-0.008	0.62	-0.80	-0.01
BD2.7.2	1.9	561.8	-1.217	-0.106	0.63	-1.70	-0.18
BD1.13.1	4.9	618.7	-1.299	-0.131	0.51	-1.83	-0.24
BD2.8.2	5.1	536.5	-1.297	-0.125	0.48	-1.70	-0.21
BD2.1.1	5.4	1008.4	-1.319	-0.119	0.60	-2.35	-0.27
BD2.4.2	9.5	1038.2	-1.552	-0.157	0.05	-2.45	-0.37

First, a description of various failure criteria from the literature is presented in Section 4.7.1. In Section 4.7.2, two-dimensional criteria, based upon the in-plane stress intensity factors $K_1^{(T)}$ and $K_2^{(T)}$ given in eqs. (1.82) and (1.83), respectively, as well as criteria based upon the interface energy release rate $\mathcal{G}_{ic}$ and the in-plane phase angle calculated in eqs. (3.17) and (3.19), respectively, are proposed. In addition, the influence of the length scale $\hat{L}$ is discussed. A statistical analysis for the proposed two-dimensional criteria is presented in Section 4.7.3. The two-dimensional criteria are extended to three-dimensions and examined again using the BD test results in Section 4.7.4. The three-dimensional criteria account for the results of $K_{III}^{(T)}$ and the phase angle ϕ, calculated in eqs. (1.84) and (3.20), respectively. Finally in this section, the statistical analysis described in Section 4.7.3 is extended to the three-dimensional failure criteria.

4.7.1 Introduction to failure criteria

In realistic situations, composite structures are exposed to axial or multiaxial service loads. Therefore, when a composite structure contains a delamination, regardless of its source, the delamination is subjected to opening, in-plane sliding and out-of-plane tearing deformations which may cause propagation and possibly result in catastrophic failure. Since the fracture toughness changes significantly as a function of the mode mixity, failure envelopes, which provide critical fracture toughness values for each mode mixity, are necessary for better structural design and should ensure safety. It has been shown that for different materials, various failure responses occur (Reeder, 1993). Hence, in order to model mixed mode delamination failure, a single criterion may be used only if it includes parameters which are fit to test data for each material system.

A review of two and three-dimensional mixed mode failure criteria based on the critical energy release rate for a delamination between UD plies may be found in Reeder (1993, 2013). Some criteria were initially written in terms of stress intensity factors and rewritten based on energy release rates. An early linear criterion was generalized to become a power law, given as (Wu, 1967)

$$\left(\frac{\mathcal{G}_I}{\mathcal{G}_{Ic}}\right)^{\alpha} + \left(\frac{\mathcal{G}_{II}}{\mathcal{G}_{IIc}}\right)^{\beta} = 1 \ . \tag{4.9}$$

In eq. (4.9), the parameters $\mathcal{G}_I$ and $\mathcal{G}_{II}$ are the modes I and II energy release rates, and $\mathcal{G}_{Ic}$ and $\mathcal{G}_{IIc}$ are their critical values or fracture toughness, respectively. The fitting parameters α and β are used to obtain a best fit to experimental data for various materials. This criterion has been used in the literature (Reeder, 1993; Donaldson, 1985; Mall and Kochhar, 1986; Chow and Atluri, 1997) and was found to fit data well for several UD composites. Another two-dimensional criterion referred to as the B-K criterion was introduced in Benzeggagh and Kenane (1996) and reviewed in Reeder (2013). This criterion is given as

$$\mathcal{G}_{Tc} = \mathcal{G}_{Ic} + (\mathcal{G}_{IIc} - \mathcal{G}_{Ic}) \left(\frac{\mathcal{G}_{II}}{\mathcal{G}_T}\right)^{\eta} \tag{4.10}$$

where

$$\mathcal{G}_T = \mathcal{G}_I + \mathcal{G}_{II} \tag{4.11}$$

is the total energy release rate, $\mathcal{G}_{Tc}$ is the total critical energy release rate or fracture toughness and η is a fitting parameter.

The criteria described above were fit to experimental data obtained from double cantilever beam (DCB), end notch flexure (ENF) and mixed mode bending (MMB) specimens (Reeder, 1993). Three different UD carbon fiber reinforced polymers (CFRPs) were tested, namely AS4/3501-6, IM7/977-2 and AS4/PEEK. These criteria modeled the failure response quite well for UD materials but were not examined for the case of a delamination along an interface between two dissimilar plies.

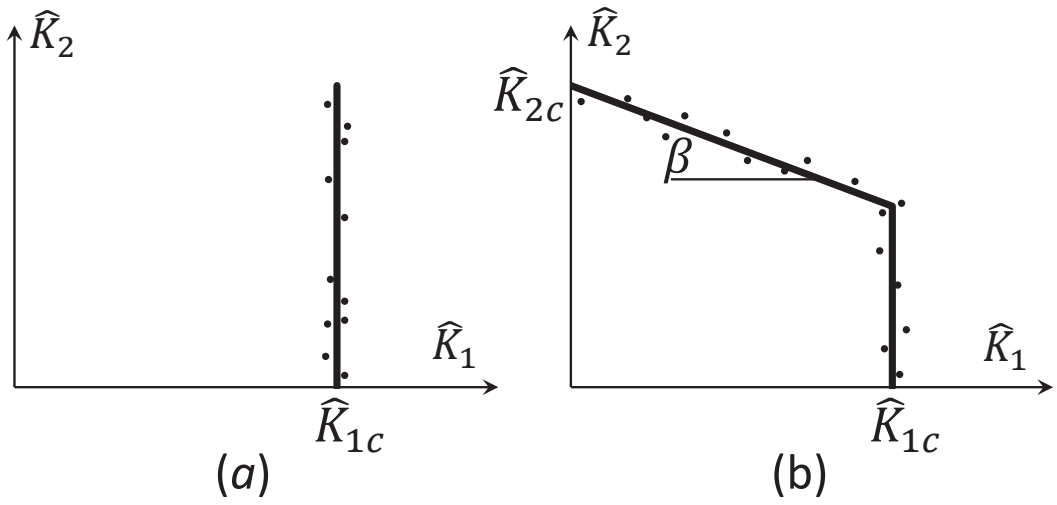

Figure 4.22: Schematic representation of two-dimensional criteria proposed for a crack between two dissimilar materials (Wang, 1997): (a) eq. (4.12) and (b) eq. (4.14).

In Wang (1997), additional criteria which were previously used for homogeneous materials were examined for mixed mode experimental results obtained from a steel/epoxy bimaterial with an interface crack. It was found that classical criteria such as the maximum tangential stress criterion (Erdogan and Sih, 1963), the maximum critical stress intensity factors criterion (Hussain et al., 1974) and the minimum strain energy density criterion (Sih, 1973) do not fit the experimental data.

For an interface crack between two dissimilar materials a different criterion is required. In Wang (1997), two-dimensional mixed mode failure criteria were proposed. The first is governed by

$$\hat{K}_1 = \hat{K}_{1c} \tag{4.12}$$

where

$$\hat{K}_{1c} = \text{avg}\left(\hat{K}_1\right) \tag{4.13}$$

for all values of $\hat{K}_2$, as shown schematically in Fig. 4.22a. The second criterion may be written as

$$\hat{K}_1 = \min\left(\hat{K}_{1c}, \frac{\hat{K}_2 - \hat{K}_{2c}}{\beta}\right) \tag{4.14}$$

where $\hat{K}_{2c}$ is the normalized mode 2 critical stress intensity factor when $\hat{K}_1 = 0$, as shown schematically in Fig. 4.22b, and β is the slope of the oblique line. Data is illustrated as scatter about the criteria.

In Wang (1997), the criteria in eqs. (4.12) and (4.14) were fit to data obtained from mixed mode fracture tests for two dissimilar linear elastic, homogeneous and isotropic materials. Results for a brittle epoxy layer (Ciba Geigy type F922), sandwiched between aluminium alloy substrates were presented in Akisanya and Fleck (1992) and examined in

Wang (1997). These showed good correlation with the criterion in eq. (4.12). Results for aluminum/epoxy, brass/epoxy, plexiglass/epoxy and steel/epoxy (Wang and Suo, 1990; Wang, 1997) showed correlation with the criterion in eq. (4.14). Note that only positive $\hat{K}_2$ values were examined.

Criteria for additional materials were examined in Banks-Sills and Ashkenazi (2000), as well as in Banks-Sills et al. (2000, 2005b and 2006). In Banks-Sills et al. (1999, 2000), BD specimens containing a crack along the interface between glass/epoxy and two ceramic clays were tested, respectively, under various mixed mode deformations. It was shown in Banks-Sills and Ashkenazi (2000) and Banks-Sills et al. (2000) that the criterion in eqs. (4.12) and (4.13) correlated well with the results. In Banks-Sills et al. (2005b, 2006), a delamination along an interface between two UD plies with fibers oriented in different directions, namely, $0°//90°$ and $+45°//-45°$, respectively, was examined and all test data also fit eq. (4.12) well.

The criteria in eqs. (4.12) and (4.14) may be rewritten in terms of the interface energy release rate. The two-dimensional relation between the interface energy release rate $\mathcal{G}_i$ and the in-plane stress intensity factors is given as

$$\mathcal{G}_i = \frac{1}{H_1}\left(K_1^2 + K_2^2\right) \quad , \tag{4.15}$$

where the parameter H_1 is defined in eq. $(3.18)_1$. By manipulating eq. (4.15), a criterion may be written in the $(\mathcal{G}_{ic}, \hat{\psi})$-plane as (Banks-Sills and Ashkenazi, 2000; Banks-Sills et al., 2000, 2005b)

$$\mathcal{G}_{ic} = \overline{\mathcal{G}}_{1c}\left(1 + \tan^2\hat{\psi}\right) \tag{4.16}$$

where $\mathcal{G}_{ic}$ is the critical interface energy release rate or fracture toughness and $\hat{\psi}$ is the in-plane mode mixity phase angle in eq. (3.19). In eq. (4.16), $\overline{\mathcal{G}}_{1c}$ was defined as (Banks-Sills and Ashkenazi, 2000; Banks-Sills et al., 2000; Banks-Sills et al., 2005b)

$$\overline{\mathcal{G}}_{1c} \equiv \frac{\hat{K}_{1c}^2}{H_1} \tag{4.17}$$

and $\hat{K}_{1c}$ is given in eq. (4.13). The criterion in eq. (4.16) is shown schematically in Fig. 4.23a. Another criterion may be derived from eq. (4.15) and written as (Wang, 1997)

$$\mathcal{G}_{ic} = \mathcal{G}_1\left(1 + \tan^2\hat{\psi}\right) \tag{4.18}$$

where

$$\mathcal{G}_1 \equiv \frac{\hat{K}_1^2}{H_1} \tag{4.19}$$

and $\hat{K}_1$ is derived from eq. (4.14) to be

$$\hat{K}_1 = \min\left(\hat{K}_{1c}, \frac{\hat{K}_{2c}}{\tan\hat{\psi} - \beta}\right) \quad . \tag{4.20}$$

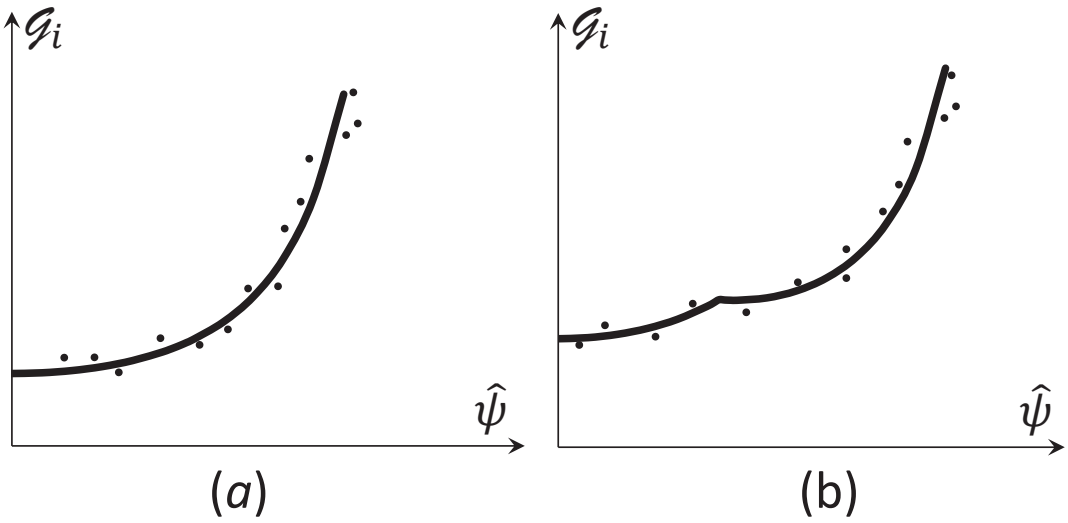

Figure 4.23: Schematic representation of two-dimensional criteria in the $(\mathcal{G}_{ic}, \hat{\psi})$-plane, proposed for a crack between two dissimilar materials. The criterion in (a) eq. (4.16) (Banks-Sills and Ashkenazi, 2000; Banks-Sills et al., 2000; Banks-Sills et al. 2005) and (b) eq. (4.18) (Wang, 1997).

The criterion in eq. (4.18) is shown schematically in Fig. 4.23b.

For three-dimensions and the interfaces considered here, the energy release rate is given as

$$\mathcal{G}_i = \frac{1}{H_1}\left(K_1^2 + K_2^2\right) + \frac{1}{H_2}K_{III}^2 \tag{4.21}$$

where H_2 is also a function of the mechanical properties of both materials on either side of the interface and given in eq. $(3.18)_2$. From here, a three-dimensional failure criterion may be obtained as (Banks-Sills, 2010)

$$\mathcal{G}_{ic} = \overline{\mathcal{G}}_{1c}\left(1 + \tan^2\hat{\psi}\right)\left(1 + \tan^2\phi\right) \tag{4.22}$$

where ϕ is calculated in eq. (3.20). Note that in Banks-Sills et al. (2006), the three-dimensional criterion in eq. (4.22) was proposed in which the out-of-plane stress intensity factor was related to the square-root, oscillatory singularity and the in-plane sliding stress intensity factor K_{II} was the amplitude of the square-root singularity. In this investigation, two and three-dimensional failure criteria are proposed and examined using the results obtained from mixed mode BD fracture toughness tests.

4.7.2 Two-dimensional failure criteria

In this section, the criteria given in eqs. (4.14) and (4.18) are extended to include both positive and negative $\hat{K}_2$ values. The proposed criteria are developed here using the results from the twenty-seven mixed mode fracture toughness BD tests described in Sections 4.3,

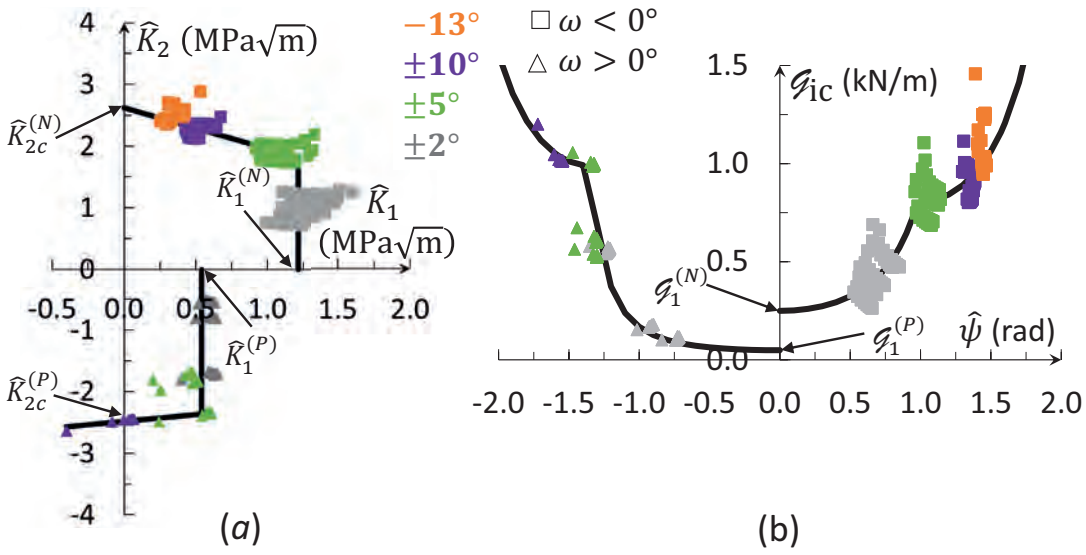

Figure 4.24: Two-dimensional 'separated' criterion ($\hat{L} = 100$ μm): (a) in the $(\hat{K}_1 - \hat{K}_2)$-plane using eq. (4.23); (b) in the $(\mathcal{G}_{ic}, \hat{\psi})$-plane using eq. (4.27) substituted into eq. (4.19) and then into eq. (4.18).

4.4 and 4.6 with the superposed total stress intensity factors $K_i^{(T)}$ $(i = 1, 2)$ given in the second and third columns of Tables C.1 through C.27. From these total values, the normalized stress intensity factors $\hat{K}_i^{(T)}$ $(i = 1, 2)$ were calculated by means of eq. (1.26) with a fitting length scale parameter $\hat{L} = 100$ μm. In addition, the in-plane phase angle $\hat{\psi}$, as well as the in-plane critical energy release rates at failure $\mathcal{G}_{ic}$ were obtained using eqs. (3.19) and (4.15), respectively. Note that $\mathcal{G}_i = \mathcal{G}_{ic}$ in eq. (4.15) when $\hat{K}_1$, and $\hat{K}_2$ are critical values.

Since the tests were performed for both positive and negative loading angles, both negative and positive $\hat{K}_2$ values, respectively, were obtained. Guided by the criterion in eq. (4.14), four ranges were obtained for $\hat{K}_1$, namely,

$$\hat{K}_1 = \begin{cases} \min\left(\hat{K}_1^{(N)}, \dfrac{\hat{K}_2 - \hat{K}_{2c}^{(N)}}{\beta^{(N)}}\right) & \text{for} \quad \hat{K}_2 > 0 \\ \min\left(\hat{K}_1^{(P)}, \dfrac{\hat{K}_2 - \hat{K}_{2c}^{(P)}}{\beta^{(P)}}\right) & \text{for} \quad \hat{K}_2 < 0 \end{cases} \tag{4.23}$$

where (N) and (P) represent negative or positive loading angles, respectively. The proposed criterion was examined using the stress intensity factors $\hat{K}_1, \hat{K}_2$ and K_{III}, given in the fifth through seventh columns in Tables C.1 through C.27 which were calculated with $\hat{L} = 100$ μm. The stress intensity factor values were projected onto the $(\hat{K}_1, \hat{K}_2)$-plane as shown in Fig. 4.24a with $K_{III} = 0$. Note that for a different choice of the value of $\hat{L}$, the parameters governing the criterion, namely, $\hat{K}_1^{(i)}$, $\hat{K}_{2c}^{(i)}$ and $\beta^{(i)}$ $(i = N, P)$, result in different values. The values of $\hat{K}_{2c}^{(i)}$ and $\beta^{(i)}$, for each material system, were obtained

Table 4.22: Values of $\hat{K}_{2c}^{(i)}$ and $\beta^{(i)}$ $(i = N, P)$ for the 'separated', '3 branch' and '5 branch' criteria in eqs. (4.23), (4.24) and (4.25) for $\hat{L} = 100$ μm.

$\hat{K}_{2c}^{(N)}$ (MPa$\sqrt{\text{m}}$)	$\beta^{(N)}$	$\hat{K}_{2c}^{(P)}$ (MPa$\sqrt{\text{m}}$)	$\beta^{(P)}$
2.62	-0.67	-2.48	0.22

as the intercept and slope, as shown in Fig. 4.24a, respectively, of the oblique lines which were fit to the $\hat{K}_2$ verses $\hat{K}_1$ values at failure from tested specimens at 20 locations along the delamination front through the specimen thickness. Results from specimens loaded with $\omega < -3°$ were used to calculate $\hat{K}_{2c}^{(N)}$ and $\beta^{(N)}$; specimens loaded with $\omega \geq 5.4°$ were used to determine $\hat{K}_{2c}^{(P)}$ and $\beta^{(P)}$. The obtained values are presented in Table 4.22.

The value of $\hat{K}_1^{(N)}$ shown in Fig. 4.24a was calculated as the average of all $\hat{K}_1$ values, along the delamination front, which were obtained at failure for specimens loaded with $\omega \approx -2°$. In the same manner, $\hat{K}_1^{(P)}$ was obtained from specimens which were loaded with $1.9° < \omega < 5.4°$. The obtained values are presented in Table 4.23. Other important values related to $\hat{K}_2$ are shown in Table 4.23; these will be discussed in the sequel.

It may be observed that using the criterion in eq. (4.23) with $\hat{L} = 100$ μm, $\hat{K}_{2c}^{(N)} \neq \left|\hat{K}_{2c}^{(P)}\right|$. Since the investigated interface is not symmetric, this result is not surprising. On the other hand, as may be seen in Fig. 4.24a, $\hat{K}_1^{(N)} \neq \hat{K}_1^{(P)}$, resulting in two different values for $\hat{K}_{1c}$. This result is problematic since it would have been expected that one $\hat{K}_{1c}$ value would be found. This motivates consideration of another value of $\hat{L}$ for which $\hat{K}_1^{(N)} = \hat{K}_1^{(P)}$. It was found that for $\hat{L} = 26.8$ m, $\hat{K}_{1c} = 0.89$ MPa$\sqrt{\text{m}}$, as shown in Fig. 4.25a. Indeed, this value of $\hat{L}$ is a physically unrealistic length scale. Hence, a different solution was proposed. It may be noted that for the interface studied here, the experimental data in Fig. 4.25a fit the failure curve quite well. From a practical point of view, it may have been simpler to proceed with this curve.

In order to obtain one value of $\hat{K}_{1c}$ with $\hat{L} = 100$ μm, the criterion in eq. (4.23) was modified and the '3 branch' criterion shown in Fig. 4.26a was proposed. This criterion is composed of three branches, as shown in the figure where also data from the tests is

Table 4.23: Values of $\hat{K}_1^{(i)}$ and the corresponding minimum and average $\hat{K}_2^{(i)}$ $(i = N, P)$ for $\hat{L} = 100$ μm. All parameters have units of MPa$\sqrt{\text{m}}$.

$\hat{K}_1^{(N)}$	$\hat{K}_{2(min)}^{(N)}$	$\hat{K}_{2(avg)}^{(N)}$	$\hat{K}_1^{(P)}$	$\hat{K}_{2(max)}^{(P)}$	$\hat{K}_{2(avg)}^{(P)}$
1.22	0.72	1.01	0.54	-0.52	-1.32

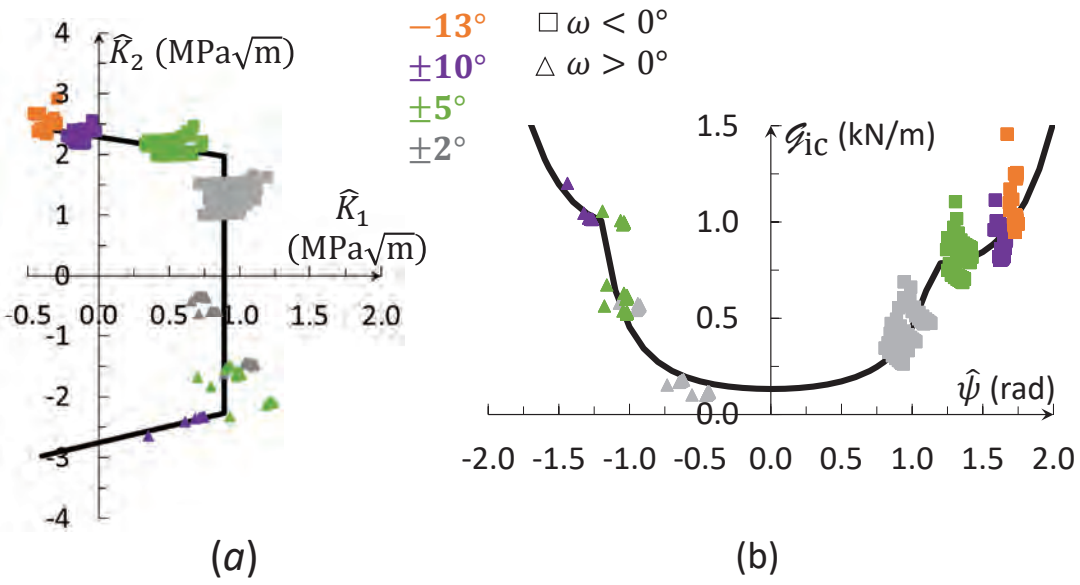

Figure 4.25: Two-dimensional criterion ($\hat{L} = 26.8$ m): (a) in the $(\hat{K}_1 - \hat{K}_2)$-plane using eq. (4.23), $\hat{K}_{1c} = 0.89$ MPa$\sqrt{\text{m}}$; (b) in the $(\mathcal{G}_{ic}, \hat{\psi})$-plane using eq. (4.27) substituted into eq. (4.19) and then into eq. (4.18).

presented. The '3 branch' failure criterion is calculated by means of

$$\hat{K}_1 = \begin{cases} \min\left(\dfrac{\hat{K}_2 - I}{\beta^{(S)}}, \dfrac{\hat{K}_2 - \hat{K}_{2c}^{(N)}}{\beta^{(N)}}\right) & \text{for} \quad \hat{K}_2 > 0 \\ \min\left(\dfrac{\hat{K}_2 - I}{\beta^{(S)}}, \dfrac{\hat{K}_2 - \hat{K}_{2c}^{(P)}}{\beta^{(P)}}\right) & \text{for} \quad \hat{K}_2 < 0 \end{cases} \tag{4.24}$$

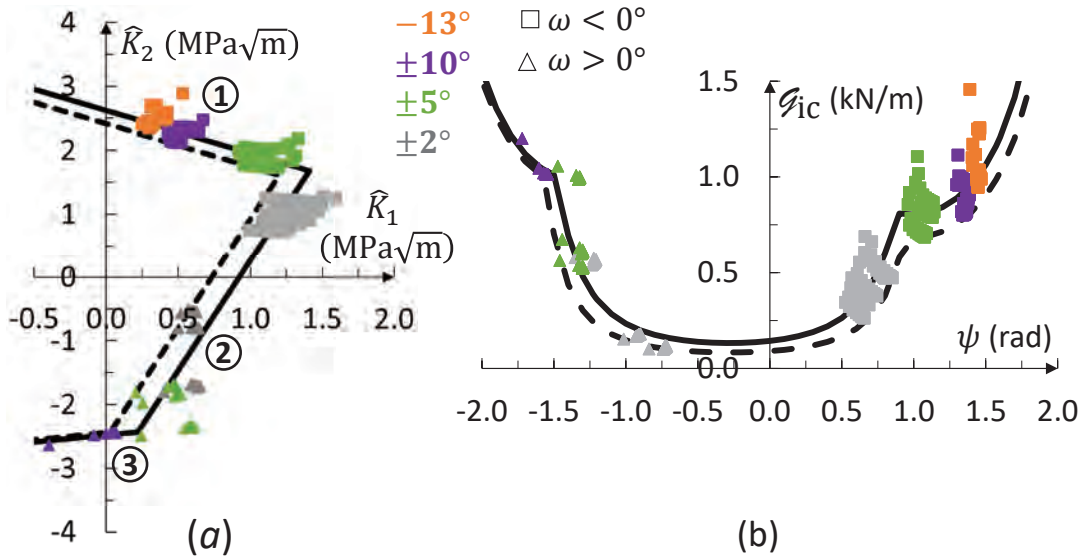

Figure 4.26: Two-dimensional three branch criterion ($\hat{L} = 100$ μm) (a) in the $(\hat{K}_1 - \hat{K}_2)$-plane using eq. (4.24) (b) in the $(\mathcal{G}_{ic}, \hat{\psi})$-plane using eq. (4.28) substituted into eq. (4.19) and then into eq. (4.18)

.

Table 4.24: The intercept I and slope $\beta^{(S)}$ of the line joining the points $(\hat{K}_1^{(N)},\hat{K}_2^{(N)})$ and $(\hat{K}_1^{(P)},\hat{K}_2^{(P)})$, for $\hat{L} = 100$ μm, for the '3 branch' and '5 branch' criteria.

'3 branch' criterion			'5 branch' criterion		
I (MPa$\sqrt{\text{m}}$)	$\beta^{(S)}$	$\hat{K}_{1c}$ (MPa$\sqrt{\text{m}}$)	I (MPa$\sqrt{\text{m}}$)	$\beta^{(S)}$	$\hat{K}_{1c}$ (MPa$\sqrt{\text{m}}$)
-3.19	3.45	0.92	-1.51	1.83	0.82

where I and $\beta^{(S)}$ are the intercept and slope, respectively, of branch 2 in Fig 4.26a. This line is obtained by joining $(\hat{K}_1^{(N)},\hat{K}_{2(avg)}^{(N)})$ and $(\hat{K}_1^{(P)},\hat{K}_{2(avg)}^{(P)})$. Values for $\hat{K}_1^{(i)}$ $(i = N, P)$ for $\hat{L} = 100$ μm are shown in the first and fourth columns of Table 4.23, respectively. Values of $\hat{K}_{2(avg)}^{(i)}$ with $\hat{L} = 100$ μm , are presented in the third and sixth columns, respectively, of that table. Recall that $\hat{K}_1^{(i)}$ are shown in Fig. 4.24a and are calculated as the average of all $\hat{K}_1$ values, along the delamination front, which are obtained at failure for specimens with a dominant mode 1 deformation. The values of $\hat{K}_{2(avg)}^{(i)}$ are obtained as the average value from all $\hat{K}_2$ values observed at failure for the specimens related to the calculation of $K_1^{(i)}$. The values obtained for I and $\beta^{(S)}$ are shown in the first and second columns of Table 4.24 and referred to as the '3 branch' criterion.

To propose another option for a failure criterion, the criterion in eq. (4.24) is further modified as

$$\hat{K}_1 = \begin{cases} \min\left[\min\left(\hat{K}_1^{(N)}, \dfrac{\hat{K}_2 - I}{\beta^{(S)}}\right), \dfrac{\hat{K}_2 - \hat{K}_{2c}^{(N)}}{\beta^{(N)}}\right] & \text{for} \quad \hat{K}_2 > 0 \\ \min\left[\max\left(\hat{K}_1^{(P)}, \dfrac{\hat{K}_2 - I}{\beta^{(S)}}\right), \dfrac{\hat{K}_2 - \hat{K}_{2c}^{(P)}}{\beta^{(P)}}\right] & \text{for} \quad \hat{K}_2 < 0 \end{cases} \tag{4.25}$$

to obtain a five branch criterion. In Fig. 4.27a, data from the tests, as well as the failure curve obtained using eq. (4.25), with $\hat{L} = 100$ μm, is presented. It may be observed that this criterion includes five branches, marked in Fig. 4.27a, where branches 1 and 5 are the same as branches 1 and 3 of the '3 branch' criterion in Fig. 4.26a with intercept $\hat{K}_{2c}^{(i)}$ and slope $\beta^{(i)}$ $(i = N, P)$, given in Table 4.22. Branch 3 is determined as a line with a different intercept I and slope $\beta^{(S)}$ than those used for the '3 branch' criterion. Here, the intercept and slope were determined from joining $(\hat{K}_1^{(N)},\hat{K}_{2(min)}^{(N)})$ and $(\hat{K}_1^{(P)},\hat{K}_{2(max)}^{(P)})$ shown in the first, second, fourth and fifth columns of Table 4.23 for $\hat{L} = 100$ μm. The values of $\hat{K}_{2(min)}^{(N)}$ and $\hat{K}_{2(max)}^{(P)}$ are the minimum and maximum values, respectively, from all $\hat{K}_2$ values observed at failure for the specimens related to the calculation of $K_1^{(i)}$ $(i = N, P)$. The values obtained for I and $\beta^{(S)}$ are shown in the fourth and fifth columns of Table 4.24, respectively, and referred to as the '5 branch' criterion. Branches 2 and 4 of this criterion are constant values equal to $\hat{K}_1^{(i)}$ $(i = N, P)$ which are given in Table 4.23. The values of $\hat{K}_{1c}$ obtained for $\hat{K}_2 = 0$ using the '3 branch' and '5 branch' criteria in eqs. (4.24)

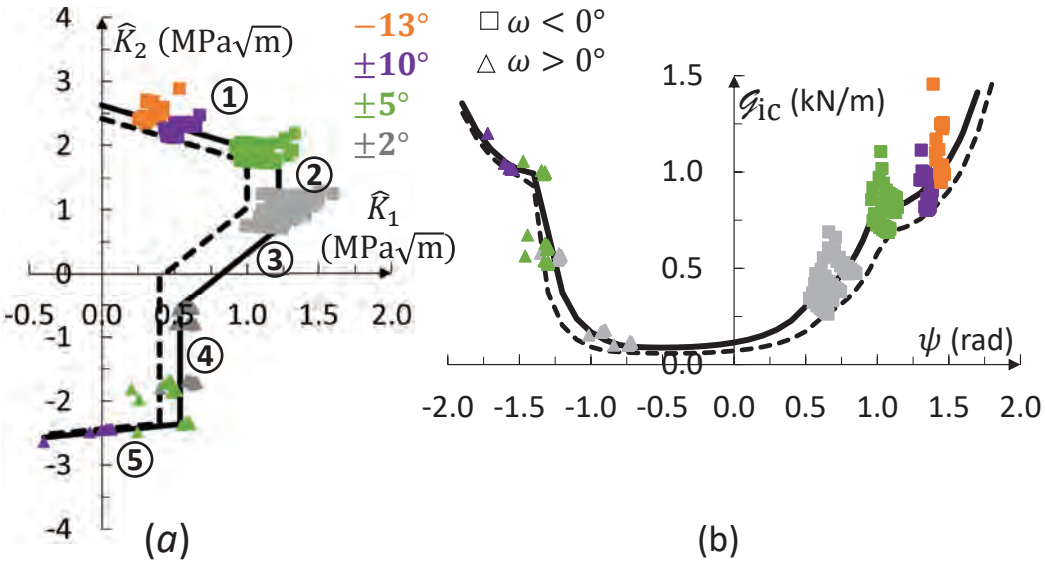

Figure 4.27: Two-dimensional five branch criterion ($\hat{L} = 100$ μm) (a) in the $(\hat{K}_1 - \hat{K}_2)$-plane using eq. (4.25) (b) in the $(\mathcal{G}_{ic}, \hat{\psi})$-plane using eq. (4.30) substituted into eq. (4.19) and then into eq. (4.18).

and (4.25), respectively, may be calculated as

$$\hat{K}_{1c} = -\frac{I}{\beta^{(S)}} \tag{4.26}$$

and are presented in the third and sixth columns of Table 4.24, respectively.

It is common to describe two-dimensional failure criteria in the $(\mathcal{G}_{ic}, \hat{\psi})$-plane where $\mathcal{G}_{ic}$ is the critical in-plane interface energy release rate at fracture, calculated in eq. (4.15), and $\hat{\psi}$ is the in-plane mode mixity phase angle, given in eq. (3.19). In order to do so, an expression for $\hat{K}_1$ in terms of $\hat{\psi}$ is required. For the 'separated' criterion in eq. (4.23) and Fig. 4.24, this relation may be written as

$$\hat{K}_1 = \left\{ \begin{array}{ll} \min\left(\hat{K}_1^{(N)}, \dfrac{\hat{K}_{2c}^{(N)}}{\tan\hat{\psi} - \beta^{(N)}}\right) & \text{for} \quad \hat{\psi} > 0 \\ \\ \min\left(\hat{K}_1^{(P)}, \dfrac{\hat{K}_{2c}^{(P)}}{\tan\hat{\psi} - \beta^{(P)}}\right) & \text{for} \quad \hat{\psi} < 0 \end{array} \right\} \tag{4.27}$$

where $i = N, P$ and (N) and (P) represent negative or positive loading angles, respectively. The values of $\hat{K}_1^{(i)}$ are presented in the first and fourth columns in Table 4.23 and $\hat{K}_{2c}^{(i)}$ and $\beta^{(i)}$ may be found in Table 4.22.

For the '3 branch' criterion in eq. (4.24) and Fig. 4.26a, the relation between $\hat{K}_1$ and

Table 4.25: Values of $\hat{\psi}^{(i)}$ and $\hat{\psi}^{*(i)}$ obtained from eq. (4.29) for the '3 branch' criterion and from eq. (4.31) for the '5 branch' criterion. The starred quantities are from the statistical analysis.

criterion	'3 branch'		'5 branch'	
i	N	P	N	P
$\hat{\psi}^{(i)}$	0.87	-1.48	0.54	-0.77
$\hat{\psi}^{*(i)}$	0.93	-1.56	0.62	-0.92

$\hat{\psi}$ may be derived as

$$\hat{K}_1 = \begin{cases} \dfrac{\hat{K}_{2c}^{(N)}}{\tan\hat{\psi} - \beta^{(N)}} & \text{for} \quad \hat{\psi} \geq \hat{\psi}^{(N)} \\ \dfrac{I}{\tan\hat{\psi} - \beta^{(S)}} & \text{for} \quad \hat{\psi}^{(P)} \leq \hat{\psi} \leq \hat{\psi}^{(N)} \\ \dfrac{\hat{K}_{2c}^{(P)}}{\tan\hat{\psi} - \beta^{(P)}} & \text{for} \quad \hat{\psi} \leq \hat{\psi}^{(P)} \end{cases} \tag{4.28}$$

where the values of $\hat{K}_{2c}^{(i)}$ and $\beta^{(i)}$ $(i = N, P)$ are given in Table 4.22 and the values of I and $\beta^{(S)}$ are given in Table 4.24, under the '3 branch' criterion. The boundary of each function, $\hat{\psi}^{(i)}$ $(i = N, P)$, is defined as the value of $\hat{\psi}$ at the intersection of two adjacent branches, and given in the second and third columns in Table 4.25. These values may be calculated as

$$\hat{\psi}^{(i)} = \tan^{-1}\left(\frac{I\beta^{(i)} - \hat{K}_{2c}^{(i)}\beta^{(S)}}{I - \hat{K}_{2c}^{(i)}}\right) \tag{4.29}$$

where $i = N, P$.

Similarly, for the '5 branch' criterion in eq. (4.25) and Fig. 4.27a, the relation between $\hat{K}_1$ and $\hat{\psi}$ is obtained as

$$\hat{K}_1 = \begin{cases} \min\left(\hat{K}_1^{(N)}, \dfrac{\hat{K}_{2c}^{(N)}}{\tan\hat{\psi} - \beta^{(N)}}\right) & \text{for} \quad \hat{\psi} \geq \hat{\psi}^{(N)} \\ \dfrac{I}{\tan\hat{\psi} - \beta^{(S)}} & \text{for} \quad \hat{\psi}^{(P)} \leq \hat{\psi} \leq \hat{\psi}^{(N)} \\ \min\left(\hat{K}_1^{(P)}, \dfrac{\hat{K}_{2c}^{(P)}}{\tan\hat{\psi} - \beta^{(P)}}\right) & \text{for} \quad \hat{\psi} \leq \hat{\psi}^{(P)} \end{cases} \tag{4.30}$$

where $\hat{K}_{2c}^{(i)}$ and $\beta^{(i)}$ $(i = N, P)$ are the same as those used for the '3 branch' criterion and given in Table 4.22; I and $\beta^{(S)}$ are presented in Table 4.24 for the '5 branch' criterion; values of $\hat{K}_1^{(i)}$ are presented in the first and fourth columns in Table 4.23 and $\hat{\psi}^{(i)}$ are the values of $\hat{\psi}$ at the intersection of branches 2 and 3 for $i = N$, and branches 3 and

Table 4.26: Values of $\mathcal{G}_{1c}$ for $\psi = 0$ for the '3 branch' and '5 branch' criteria in eqs. (4.28) and (4.30) for $\hat{\psi}^{(P)} < \hat{\psi} < \hat{\psi}^{(N)}$ substituted into eq. (4.19) with $\hat{L} = 100$ μm.

$\mathcal{G}_{1c}$ (N/m)	
'3 branch'	'5 branch'
143.7	114.4

4 for $i = P$. The $\hat{\psi}^{(i)}$ values obtained are presented in the fourth and fifth columns in Table 4.25, and were calculated as

$$\hat{\psi}^{(i)} = \tan^{-1}\left(\frac{I}{\hat{K}_1^{(i)}} + \beta^{(S)}\right) \tag{4.31}$$

where $i = N, P$.

In order to obtain two-dimensional failure criteria in the $(\mathcal{G}_{ic}, \hat{\psi})$-plane, the expressions in eqs. (4.27), (4.28) and (4.30) were substituted into eq. (4.19) to define expressions for $\mathcal{G}_1$ in terms of $\hat{\psi}$. The parameter H_1 in eq. (4.19) is given in Table 4.9. Note that the parameter $\mathcal{G}_{1c}$ is the energy release rate for $\hat{\psi} = 0$. These relations are then substituted into eq. (4.18) to obtain the two-dimensional 'separated', '3 branch', and '5 branch' criteria, shown in Figs. 4.24b, 4.26b and 4.27b, respectively, all calculated for $\hat{L} = 100$ μm. In those figures, data obtained from the BD tests, as well as the failure curve determined in the $(\mathcal{G}_{ic}, \hat{\psi})$-plane are presented.

It may be observed in Fig. 4.24b that the curve is not continuous for $\hat{L} = 100$ μm since $\mathcal{G}_1^{(N)} \neq \mathcal{G}_1^{(P)}$. This result is problematic since two values are obtained for the critical mode 1 interface energy release rate $\mathcal{G}_{1c}$. This problem is the same as that found in Fig. 4.24a from eq. (4.23) in the $(\hat{K}_1, \hat{K}_2)$-plane, where two values of $\hat{K}_{1c}$ were observed since $\hat{K}_1^{(N)} \neq \left|\hat{K}_1^{(P)}\right|$. This was solved by choosing $\hat{L} = 26.8$ m, as was done for eq. (4.23) in order to obtain $\hat{K}_1^{(N)} = \hat{K}_1^{(P)}$. With this value of $\hat{L}$, $\mathcal{G}_{1c} = 132.6$ N/m. Data from the tests, as well as the failure curve obtained for $\hat{L} = 26.8$ m are presented in Fig. 4.25b. Of course, as mentioned earlier, this value of $\hat{L}$ is not physically appropriate.

For the '3 branch' and '5 branch' criteria in the $(\mathcal{G}_{ic}, \hat{\psi})$-plane, values of $\mathcal{G}_{1c}$ are obtained for $\hat{\psi} = 0$ from eqs. (4.19) and (4.26), with $\hat{L} = 100$ μm. The results are presented in Table 4.26. It may be noted that in Banks-Sills and Ashkenazi (2000), Banks-Sills et al. (2000, 2005b) for values of $\hat{\psi} = \pm\pi/2$, the value of $\mathcal{G}_{ic}$ obtained from the criterion in eq. (4.16) approaches infinity; whereas, for the '3 branch' and '5 branch' criteria in eqs. (4.28) and (4.30), respectively, substituted into eq. (4.19) and then into eq. (4.18), this is not the case. The expressions for branches 1 and 3 shown in Fig. 4.26b for the '3 branch' criterion and branches 1 and 5 shown in Fig. 4.27b for the '5 branch' criterion, may be written as

$$\mathcal{G}_{ic} = \frac{1}{H_1}\left[\frac{\hat{K}_{2c}^{(i)}}{\tan\hat{\psi} - \beta^{(i)}}\right]^2 \left(1 + \tan^2\hat{\psi}\right) \tag{4.32}$$

where $i = N, P$. In eq. (4.32), the parameter H_1 is given in Table 4.9 and $\hat{K}_{2c}^{(i)}$ and $\beta^{(i)}$ $(i = N, P)$ are given in Table 4.22. In the limit as $\hat{\psi} \to \pm\pi/2$, values of $\mathcal{G}_{ic}$ from eq. (4.32) are found to be constant and are given by

$$\lim_{\hat{\psi}\to\pm\pi/2} \mathcal{G}_{ic} = \frac{\hat{K}_{2c}^{(i)^2}}{H_1} \quad . \tag{4.33}$$

This implies that the values of $\hat{\psi}$ using these criteria are not limited to $-\pi/2 < \hat{\psi} < \pi/2$.

For each of the proposed criteria, considering each specimen individually, three types of predictions occur, namely, complete failure, initiation, and no failure. To employ these failure curves, a structure containing a through the thickness delamination, between the two plies studied here is analyzed to determine the stress intensity factors $\hat{K}_1$ and $\hat{K}_2$ or the interface energy release rate $\mathcal{G}_i$ and phase angle $\hat{\psi}$ with $\hat{L} = 100$ μm. For the criteria in the $(\hat{K}_1, \hat{K}_2)$-plane, the points $(\hat{K}_1, \hat{K}_2)$ are plotted and compared to either, the '3 branch' or the '5 branch' criterion from eqs. (4.24) or (4.25), respectively, shown in Figs. 4.26a and 4.27a, respectively. If all of the points along the delamination front are outside the criterion, failure is expected. If some points are within and some are outside the curve, it is expected that those points which have failed will induce the remainder of the points along the delamination front to propagate. For a specific specimen, if all points are within the curve, then failure is not expected. In the same manner, for the criteria in the $(\mathcal{G}_{ic}, \hat{\psi})$-plane, the points $(\mathcal{G}_{ic}, \hat{\psi})$ are plotted in Figs. 4.26b and 4.27b, respectively, for either the '3 branch' or the '5 branch' criteria where the failure curves in the figures were obtained by means of eqs. (4.28) or (4.30), respectively, with eqs. (4.18) and (4.19). If all of the points along the delamination front are above the curve, failure is expected. If some points are above and some are below the curve, it is expected that those points which have failed will induce the remainder of the points along the delamination front to propagate. If all points are below the curve, then failure is not expected.

For each criterion proposed here, there is scatter about the predicted failure curves, as may be seen in Figs. 4.26 and 4.27 in both the $(\hat{K}_1, \hat{K}_2)$-plane and in the $(\mathcal{G}_{ic}, \hat{\psi})$-plane. Note that for other composite laminates scatter was also observed (Banks-Sills et al., 2005b; 2006). In those cases, a statistical analysis was carried out to predict failure (Banks-Sills, 2015). For the material system studied here, it was found that all points through the thickness of four specimens are outside or above the failure curves obtained from the '3 branch' and '5 branch' criteria in the $(\hat{K}_1, \hat{K}_2)$-plane and in the $(\mathcal{G}_{ic}, \hat{\psi})$-plane, as may be observed in Figs. 4.26 and 4.27. This implies that complete failure is expected through the thickness of these specimens. In addition, for both the '3 branch' and '5 branch' criteria, all points through the thickness of two specimens were found to

be within the safe zone as predicted by the failure curves. This implies that failure is not expected for these specimens. Yet, since it is known that these specimens failed, the prediction is considered as scatter in the results. This will be taken into account using a statistical analysis in Section 4.7.3.

It may be noted that in Zhao et al. (2017), a somewhat different approach was taken to present the test data. The ordinate in Figs. 4.26b and 4.27b remain the same, but the abscissa is taken to be an invariant length parameter

$$L_I = \hat{L} \exp\left(-\frac{\hat{\psi}}{\varepsilon}\right) \quad . \tag{4.34}$$

It might appear at first sight that L_I is a function of $\hat{L}$. But the combination of the quantities in eq. (4.34) result in an invariant value for L_I. However, Banks-Sills (2020) has shown that the invariant length parameter L_I has values which are unrealistically large and small, whereas $\hat{L}$ is a physical length scale. Moreover, in that paper it was shown that the choice of $\hat{L}$ used to determine L_I affects the quality of the fit of the failure curve to the tested data in the $(\mathcal{G}_{ic}, L_I)$-plane.

4.7.3 Statistical analysis

In this section, a statistical analysis is performed for the two-dimensional criteria proposed in Section 4.7.2. In Banks-Sills (2015), a statistical analysis for 10% probability of unexpected failure in the safe zone was applied to the two-dimensional criterion in eq. (4.16) and the three-dimensional criterion in eq. (4.22). Two statistical models were used, the z-variate for determination of probability with a confidence interval (Natrella, 1963) and the t-distribution for statistical intervals (Whitmore, 1986; Luko and Neubauer, 2011). Since the z-variate model allowed for a confidence interval, it is used here for the two-dimensional criteria in eqs. (4.24) and (4.25) in the $(\hat{K}_1, \hat{K}_2)$-plane and for eqs. (4.28) and (4.30) in the $(\mathcal{G}_{ic}, \hat{\psi})$-plane. The statistical analysis is performed in the $(\hat{K}_1, \hat{K}_2)$-plane to obtain statistical values for the constant parameters $\hat{K}_1^{(i)}$, $\hat{K}_{2c}^{(i)}$ $(i = N, P)$ and I. These statistical values are then used in eqs. (4.24) and (4.25) in the $(\hat{K}_1, \hat{K}_2)$-plane and in eqs. (4.28) and (4.30) and then into eq. (4.19) and into eq. (4.18) in the $(\mathcal{G}_{ic}, \hat{\psi})$-plane to obtain the reduced statistical failure criteria shown as dashed curves in Figs. 4.26 and 4.27.

For the z-variate approach, an average value of some parameter $\overline{A}$ is reduced by a statistical factor K in a manner proportional to the standard deviation s of the data which was used to calculate that average value, namely

$$A^* = \overline{A} - K \cdot s \quad . \tag{4.35}$$

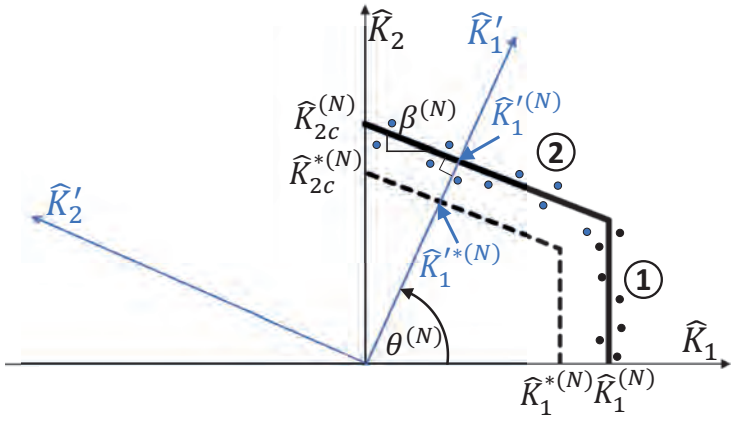

Figure 4.28: An illustration of the rotated coordinate system $(\hat{K}_1' - \hat{K}_2')$ for the criterion in eq. (4.14).

The value of K is determined using the z-variate (Natrella, 1963) as

$$K = \frac{|z_P| + \sqrt{z_P^2 - a \cdot b}}{a} \quad . \tag{4.36}$$

In eq. (4.36),

$$a = 1 - \frac{z_\gamma^2}{2(n-1)} \qquad \text{and} \qquad b = z_P^2 - \frac{z_\gamma^2}{n} \tag{4.37}$$

where n is the number of data points used to obtain the average value $\overline{A}$, and z_P and z_γ are the z-variate probability and confidence, respectively. Finally, A^* in eq. (4.35) is the statistically reduced value. For the case of a 10% probability of unexpected failure with a confidence of 95%, $P = 0.1$ and $\gamma = 0.95$. Consequently, $z_P = z_{0.1} = -1.2816$ and $z_\gamma = z_{0.95} = 1.6449$. Then, there is only a 10% probability with a 95% confidence that a new data point will be smaller than A^*.

Unlike in Banks-Sills (2015) where the statistically reduced criteria for eqs. (4.16) and (4.22) were obtained by applying the statistical model to $\overline{\mathcal{G}}_{1c}$ in eq. (1.34), here, the criteria include several branches. As a result, the statistical approach used in Banks-Sills (2015) is modified. The '3 branch' criterion in eq. (4.24) is composed of functions relating $\hat{K}_1$ and $\hat{K}_2$. The '5 branch' criterion in eq. (4.25) is composed of the same functions, as well as branches 2 and 4 in Fig. 4.27a which have constant values. For these branches the statistical approach is similar to that in Banks-Sills (2015). Although there, the reduction was performed for the averaged critical energy release rate $\overline{\mathcal{G}}_{1c}$ in eq. (1.34) in the $(\mathcal{G}_{ic}, \hat{\psi})$-plane, whereas here the reduction is applied to the values $\hat{K}_1^{(i)}$ $(i = N, P)$ in the $(\hat{K}_1, \hat{K}_2)$-plane.

In Fig. 4.28, examples of two branch types are presented for $\hat{K}_2 > 0$ and $i = N$. Branch 1 is governed by the average value of $\hat{K}_1^{(N)}$, whereas, branch 2 is an example of a relation between $\hat{K}_1$ and $\hat{K}_2$ involving the constants $\hat{K}_{2c}^{(N)}$ and $\beta^{(N)}$. For branch 1, the statistical analysis is performed in the same manner as that in Banks-Sills (2015) using

eq. (4.35) with $A^* = \hat{K}_1^{*(N)}$, $\overline{A} = \hat{K}_1^{(N)}$, and K calculated using eq. (4.36). The statistical value $K_1^{*(N)}$ is obtained from this analysis and used in the required criteria.

In the case where $\hat{K}_2$ is a function of $\hat{K}_1$ as for branch 2 in Fig. 4.28, a rotated coordinate system, $(\hat{K}_1', \hat{K}_2')$, is used. In Fig. 4.28 this coordinate system, in blue, has been found by a counterclockwise rotation of $\theta^{(N)}$ where the slope

$$\beta^{(N)} = -\cot\theta^{(N)} \quad . \tag{4.38}$$

The required rotated coordinate system $(\hat{K}_1', \hat{K}_2')$ is obtained from

$$\left\{ \begin{array}{c} \hat{K}_1' \\ \hat{K}_2' \end{array} \right\} = \left[\begin{array}{cc} \cos\theta^{(N)} & \sin\theta^{(N)} \\ -\sin\theta^{(N)} & \cos\theta^{(N)} \end{array} \right] \left\{ \begin{array}{c} \hat{K}_1 \\ \hat{K}_2 \end{array} \right\} \quad . \tag{4.39}$$

Using the relation in eq. (4.38), the rotation in eq. (4.39) may be rewritten in terms of $\beta^{(N)}$ as

$$\left\{ \begin{array}{c} \hat{K}_1' \\ \hat{K}_2' \end{array} \right\} = \frac{1}{\sqrt{1+\beta^{(N)2}}} \left[\begin{array}{cc} -\beta^{(N)} & 1 \\ -1 & -\beta^{(N)} \end{array} \right] \left\{ \begin{array}{c} \hat{K}_1 \\ \hat{K}_2 \end{array} \right\} \quad . \tag{4.40}$$

For branch 2, the statistical analysis is carried out in the rotated space. By means of eq. (4.40), all data points $(\hat{K}_1, \hat{K}_2)$ related to branch 2 in Fig. 4.28 are defined in the $(\hat{K}_1', \hat{K}_2')$ coordinate system. The average of all $\hat{K}_1'$ values is calculated as $\hat{K}_1'^{(N)}$, as illustrated in blue in Fig. 4.28. The statistical reduction is then performed in the rotated space using eq. (4.35) with $A^* = \hat{K}_1'^{*(N)}$, $\overline{A} = \hat{K}_1'^{(N)}$, and the statistical factor K is obtained from eq. (4.36). The resulting statistical value $\hat{K}_1'^{*(N)}$ is illustrated in blue in Fig. 4.28. Once this statistical value is found in the rotated $(\hat{K}_1', \hat{K}_2')$-space, the obtained dashed line in Fig. 4.28, is rotated to the original $(\hat{K}_1, \hat{K}_2)$-space. Finally, the required statistical value of $\hat{K}_{2c}^{*(N)}$, illustrated in Fig. 4.28, is obtained as the intersection of the dashed line and the $\hat{K}_2$-axis. This value is used to describe the statistical relation between $\hat{K}_1$ and $\hat{K}_2$ in the original coordinate system. It may be noted that the slope of branch 2 remains the same.

The statistical procedure described here was applied to the criteria presented in Section 4.7.2. Recall that all of the statistical values found are based on the original results in Tables 4.22 through 4.24 which were obtained for the case $\hat{L} = 100$ μm.

For the '3 branch' criterion in eq. (4.24) and in Fig. 4.26a, all three branches include a relation between $\hat{K}_1$ and $\hat{K}_2$ which is similar to that discussed for the case of branch 2 in Fig. 4.28. However, for branches 2 and 3 of this criterion in Fig. 4.26a, the slopes $\beta^{(S)}$ and $\beta^{(P)}$, respectively, are positive and the coordinate rotation is clockwise. For these branches, the transformation equations between the $(\hat{K}_1, \hat{K}_2)$ and $(\hat{K}_1', \hat{K}_2')$-axes are given by

$$\left\{ \begin{array}{c} \hat{K}_1' \\ \hat{K}_2' \end{array} \right\} = \frac{1}{\sqrt{1+\beta^{(i)2}}} \left[\begin{array}{cc} \beta^{(i)} & -1 \\ 1 & \beta^{(i)} \end{array} \right] \left\{ \begin{array}{c} \hat{K}_1 \\ \hat{K}_2 \end{array} \right\} \tag{4.41}$$

Table 4.27: Statistical parameters related to branches 1, 2 and 3 of the '3 branch' criterion and 1 and 5 of the '5 branch' criterion in Figs. 4.26a and 4.27a, respectively, including the average $\hat{K}_1^{'(i)}$ value, number of data points n used, statistical parameter K, standard deviation s, statistically reduced $\hat{K}_1^{'*(i)}$ value in the rotated coordinate system, and the intersection $\hat{K}_{2c}^{*(i)}$ between the statistically obtained branch and the $\hat{K}_2$-axis in the original coordinate system.

i	$\hat{K}_1^{'(i)}$ (MPa$\sqrt{\text{m}}$)	n	K	s (MPa$\sqrt{\text{m}}$)	$\hat{K}_1^{'*(i)}$	$\hat{K}_{2c}^{*(i)}$ / I^* (MPa$\sqrt{\text{m}}$)
N	2.18	300	1.42	0.12	2.01	2.42
P	2.42	40	1.69	0.02	2.38	-2.44
S ('3 branch')	0.89	200	1.45	0.13	0.70	-2.53

where $i = P, S$ and

$$\beta^{(P)} = \cot\theta^{(P)} \qquad \beta^{(S)} = \cot\theta^{(S)} \quad . \tag{4.42}$$

Recall that the values of $\beta^{(i)}$ for the '3 branch' criterion are given in Table 4.22 for $i = N, P$ and in Table 4.24 for $i = S$.

In the same manner as that for branch 2 in Fig. 4.28, the statistical model is applied in the rotated space and then the statistical curves are transformed back to the original $(\hat{K}_1, \hat{K}_2)$-space. The average values of the data related to each branch in the '3 branch' criterion were obtained in the rotated $(\hat{K}_1', \hat{K}_2')$ coordinate system and referred to as $\hat{K}_1^{'(i)}$ $(i = N, P, S)$. In Table 4.27, the obtained $\hat{K}_1^{'(i)}$ values are presented in the second column, along with the number of data points used n, the statistical factor K and standard deviation s, given in columns three through five, respectively. These results were used in eq. (4.35) to calculate the statistically reduced values of $\hat{K}_1^{'*(i)}$ $(i = N, P, S)$, in the rotated space which are presented in the sixth column in Table 4.27. Finally, the required statistical intercepts $\hat{K}_{2c}^{*(i)}$ $(i = N, P)$ and I^* are obtained and presented in the seventh column of Table 4.27. These parameters are defined as the intersection of the statistically obtained branches, shown as dashed lines in Fig. 4.26a with the $\hat{K}_2$-axis. Their values are used to describe the statistical relation between $\hat{K}_1$ and $\hat{K}_2$ in the original coordinate system. It may be noted that since most of the data points related to branch 3 were in the failure zone of the original branch, the statistical analysis had a negligible effect on the statistical branch, namely $\hat{K}_{2c}^{(P)} = -2.48$ MPa$\sqrt{\text{m}}$ was calculated to be $\hat{K}_{2c}^{*(P)} = -2.44$ MPa$\sqrt{\text{m}}$.

The statistical '3 branch' failure criterion was obtained with a 10% probability and a 95% confidence that all $(\hat{K}_1, \hat{K}_2)$ data points from a new specimen will be in the safe zone but will fail. In the $(\hat{K}_1, \hat{K}_2)$-plane, the statistical '3 branch' criterion was determined using eq. (4.24) with the statistical parameters $\hat{K}_{2c}^{*(i)}$ $(i = N, P)$ and I^* in Table 4.27 in place of $\hat{K}_{2c}^{(i)}$ and I, respectively. Note that the values for $\beta^{(i)}$ $(i = N, P, S)$ used for the statistical criterion are the same as those used for the original criterion and given

Table 4.28: Statistical parameters K and s, used in eq. (4.35) to obtain $\hat{K}_1^{*(i)}$ $(i = N, P)$ for branches 2 and 4 of the '5 branch' criterion in eqs. (4.25) and (4.30), with $\hat{L} = 100$ μm.

i	$\hat{K}_1^{*(i)}$ (MPa$\sqrt{\text{m}}$)	n	K	s (MPa$\sqrt{\text{m}}$)
N	1.00	100	1.52	0.14
P	0.40	100	1.52	0.09

in Tables 4.22 and 4.24 for $i = N, P$ and $i = S$, respectively. The statistical '3 branch' criterion is presented as the dashed curve in Fig. 4.26a.

In order to obtain the '3 branch' statistical criterion in the $(\mathcal{G}_{ic}, \hat{\psi})$-plane, the statistical parameters $\hat{K}_{2c}^{*(i)}$ $(i = N, P)$ and I^* in Table 4.27 replace $\hat{K}_{2c}^{(i)}$ and I, respectively, in eq. (4.28) with $\beta^{(i)}$ $(i = N, P, S)$ given in Table 4.22. The boundaries $\hat{\psi}^{*(i)}$ $(i = N, P)$ presented in Table 4.25 were used in the equation. These boundaries were determined by means of eq. (4.29) with $\hat{K}_{2c}^{*(i)}$ $(i = N, P)$ and I^* replacing $\hat{K}_{2c}^{(i)}$ and I, respectively, together with $\beta^{(i)}$ $(i = N, P, S)$. This substitution is performed in order to obtain statistical relations between $\hat{K}_1$ and $\hat{\psi}$. These relations are substituted into eq. (4.19) to obtain expressions for $\mathcal{G}_1$ in terms of $\hat{\psi}$ which are then substituted into eq. (4.18) to obtain the statistical criteria in the $(\mathcal{G}_{ic}, \hat{\psi})$-plane. This statistical '3 branch' criterion is shown as the dashed curve in Fig. 4.26b.

For the statistical analysis of the '5 branch' criterion in eq. (4.25), branches 1 and 5 in Fig. 4.27a are the same as branches 1 and 3 for the '3 branch' criterion in Fig. 4.26a and, therefore, make use of the same statistical parameters $\hat{K}_{2c}^{*(i)}$ $(i = N, P)$ presented in Table 4.27. For branches 2 and 4 of this criterion, values of $K_1^{*(i)}$ $(i = N, P)$ were obtained in the same manner as that described for branch 1 in Fig. 4.28. The statistical factor K in eq. (4.36), and the standard deviation s related to $\hat{K}_1^{(i)}$ and used in eq. (4.35), are given in the fourth and fifth columns in Table 4.28. The statistical $\hat{K}_1^{*(i)}$ values $(i = N, P)$ obtained are presented in the second column of Table 4.28. Since there is no data along branch 3 of the '5 branch' criterion in Fig. 4.27a and only statistics on $\hat{K}_1^{(i)}$ $(i = N, P)$ could be carried out, the statistical values related to this branch, namely, the intercept I^* and slope $\beta^{*(S)}$, were obtained by means of linear interpolation between the two points $(\hat{K}_1^{*(N)}, \hat{K}_{2(min)}^{(N)})$ and $(\hat{K}_1^{*(P)}, \hat{K}_{2(max)}^{(P)})$. Values of $\hat{K}_{2(min)}^{(N)}$ and $\hat{K}_{2(max)}^{(P)}$ are presented in Table 4.23. The intercept I^* which defines the intersection between the statistically obtained branch and the $\hat{K}_2$-axis, as well as the slope $\beta^{*(S)}$ of this statistical branch are given in Table 4.29.

Table 4.29: Statistical values for branch 3 of the '5 branch' criterion in Fig. 4.27a including the intercept I^* and the slope $\beta^{*(S)}$.

I^* (MPa$\sqrt{\text{m}}$)	$\beta^{*(S)}$
-1.34	2.06

Note that I^* and $\beta^{*(S)}$ were obtained differently from those of the '3 branch' criterion.

Finally, the statistical '5 branch' failure criterion was obtained with a 10% probability and a 95% confidence that all ($\hat{K}_1$, $\hat{K}_2$) data points from a new specimen will be in the safe zone but will fail. In the $(\hat{K}_1, \hat{K}_2)$-plane, the statistical criterion was determined using eq. (4.25) with the statistical parameters $\hat{K}_{2c}^{*(i)}$ and $\hat{K}_1^{*(i)}$ $(i = N, P)$ in Tables 4.27 and 4.28, respectively, as well as I^* and $\beta^{*(S)}$ from Table 4.29, replacing the original values of $\hat{K}_{2c}^{(i)}$, $\hat{K}_1^{(i)}$, I and $\beta^{(S)}$, respectively. Note that the slopes $\beta^{(i)}$ $(i = N, P)$ in Table 4.22 from the original criterion, were used in branches 1 and 5 of the statistical criterion. The statistical '5 branch' criterion in the $(\hat{K}_1, \hat{K}_2)$-plane is presented as the dashed curve in Fig. 4.27a.

In order to obtain the statistical '5 branch' criterion in the $(\mathcal{G}_{ic}, \hat{\psi})$-plane, I^* and $\beta^{*(S)}$ from Table 4.29 along with $\hat{K}_{2c}^{*(i)}$ and $\hat{K}_1^{*(i)}$ $(i = N, P)$ in Tables 4.27 and 4.28, respectively, are used in eq. (4.30) replacing I and $\beta^{(S)}$, as well as $\hat{K}_{2c}^{(i)}$ and $\hat{K}_1^{(i)}$ $(i = N, P)$. The boundary points $\hat{\psi}^{*(i)}$ $(i = N, P)$, presented in Table 4.25 for the '5-branch' criterion, were used in the equation and calculated using eq. (4.31) with the statistical parameters $\hat{K}_1^{*(i)}$, I^* and $\beta^{*(S)}$ in Tables 4.28 and 4.29, respectively, replacing $\hat{K}_1^{(i)}$, I and $\beta^{(S)}$, respectively. The resulting relation was then substituted into eqs. (4.18) and (4.19). The statistical '5 branch' criterion in the $(\mathcal{G}_{ic}, \hat{\psi})$-plane is shown as the dashed curve in Fig. 4.27b.

The same predictions for complete failure or failure initiation obtained using the '3 branch' and '5 branch' statistical criteria in the $(\hat{K}_1, \hat{K}_2)$-plane were observed in the $(\mathcal{G}_{ic}, \hat{\psi})$-plane. Using the statistical criteria, two types of predictions were observed, namely, complete failure or failure initiation. By means of the '3 branch' criterion in eq. (4.24) with the statistical parameters, all data points through the thickness of twenty-four specimens were outside the curve, hence, complete failure would have been predicted by the statistical curve for these specimens. For the remaining three specimens, some points were within and some outside the dashed curve meaning that failure initiation would have been predicted. With the '5 branch' criterion in eq. (4.25), using the statistical parameters, complete failure was observed for twenty-five specimens; whereas, failure initiation would have been predicted for the remaining two specimens, respectively. These results demonstrate the confidence level in using the proposed statistical criteria for failure predictions.

The statistical $\hat{K}_{1c}^*$ values, found when $\hat{K}_2 = 0$, were obtained for each criterion and material system, using eq. (4.26). For the '3 branch' criterion, the statistical value I^* in the seventh column of Table 4.27 and the original slope $\beta^{(S)}$ in Table 4.24, were used. For the '5 branch' criterion, the statistical values I^* and $\beta^{*(S)}$ in Table 4.29, were used. The results are given in the first and third columns in Table 4.30. The statistical $\mathcal{G}_{1c}^*$ values obtained for $\hat{\psi} = 0$ from eqs. (4.19) and (4.26), are given in the second and fourth columns in that table for the '3 branch' and '5 branch' criteria.

Table 4.30: Critical values of $\mathcal{G}_{ic}^{*}$ for $\hat{\psi} = 0$ obtained from eq. (4.19) with $\hat{K}_1$ calculated with eq. (4.28) and (4.30), for the '3-branch' and '5-branch' criteria, respectively. Critical values of $\hat{K}_{1c}^{*}$ for $\hat{K}_2 = 0$ from eq. (4.26) with $\beta^{(S)}$ and I^* from Tables 4.24 and 4.27, respectively, for the '3 branch' criterion and with $\beta^{*(S)}$ and I^* in Table 4.29 for the '5 branch' criterion using $\hat{L} = 100$ μm.

'3 branch' criterion		'5 branch' criterion	
$\hat{K}_{1c}^{*}$ (MPa$\sqrt{\text{m}}$)	$\mathcal{G}_{1c}^{*}$ (N/m)	$\hat{K}_{1c}^{*}$ (MPa$\sqrt{\text{m}}$)	$\mathcal{G}_{1c}^{*}$ (N/m)
0.73	90.6	0.65	71.5

4.7.4 Three-dimensional failure criteria

In this section, the two-dimensional criteria proposed in Section 4.7.2 are extended to three dimensions. In Banks-Sills et al. (2006, 2010), the three-dimensional criterion in eq. (4.22) was used. A similar criterion may be proposed here by extending the criterion in eq. (4.18) to three dimensions as

$$\mathcal{G}_{ic} = \mathcal{G}_1 \left(1 + \tan^2 \psi\right) \left(1 + \tan^2 \phi\right) \quad . \tag{4.43}$$

In eq. (4.43), ϕ is the phase angle, defined in eq. (3.20), and $\mathcal{G}_1$ is defined in eq. (4.19) where $\hat{K}_1$ may be obtained using the '3 branch' or '5 branch' criteria in eqs. (4.28) and (4.30), respectively. The parameters H_1 and H_2 used in these equations are presented in Table 4.9. With the three-dimensional criterion, mode *III* deformation is accounted for. For the BD specimens, it was observed that K_{III} was more significant at the free edges of the specimen.

In Figs. 4.29, four views of the '3 branch' surface, are presented. In Figs. 4.30, four views of the '5 branch' surface, are presented. Videos of these surfaces may be viewed by links of the '3 branch', '5 branch', respectively. It may be observed that the surfaces in Figs. 4.29 and Figs. 4.30 are very similar. Both appear to show a clear separation between three different surfaces. For the '3 branch' criterion, these are a result of the three separate branches in eq. (4.28) in two dimensions. For the '5 branch' criterion, branches 1 and 5 create the external surfaces observed. Branches 2 to 4 are difficult to distinguish but produced a lower value of $\mathcal{G}_{1c}$ than branch 2 of the '3-branch' criterion, as shown in Table 4.26. The data points obtained from the BD tests are also shown in each of these figures. It may be observed that some of the data points are above the surface, in the failure zone, and some are below it, in the safe zone.

Similar to the two-dimensional criteria proposed in Section 4.7.2, for the three-dimensional criteria, considering each specimen individually, the same three types of predictions occurred, namely, complete failure, initiation, and no failure. The scatter of the results found in the three-dimensional criteria is similar to that observed with the two-dimensional criteria in Section 4.7.2. Using eqs. (4.19) and (4.43) for the '3 branch' or the '5 branch' three-dimensional criterion, all points along the delamination front for two specimens are

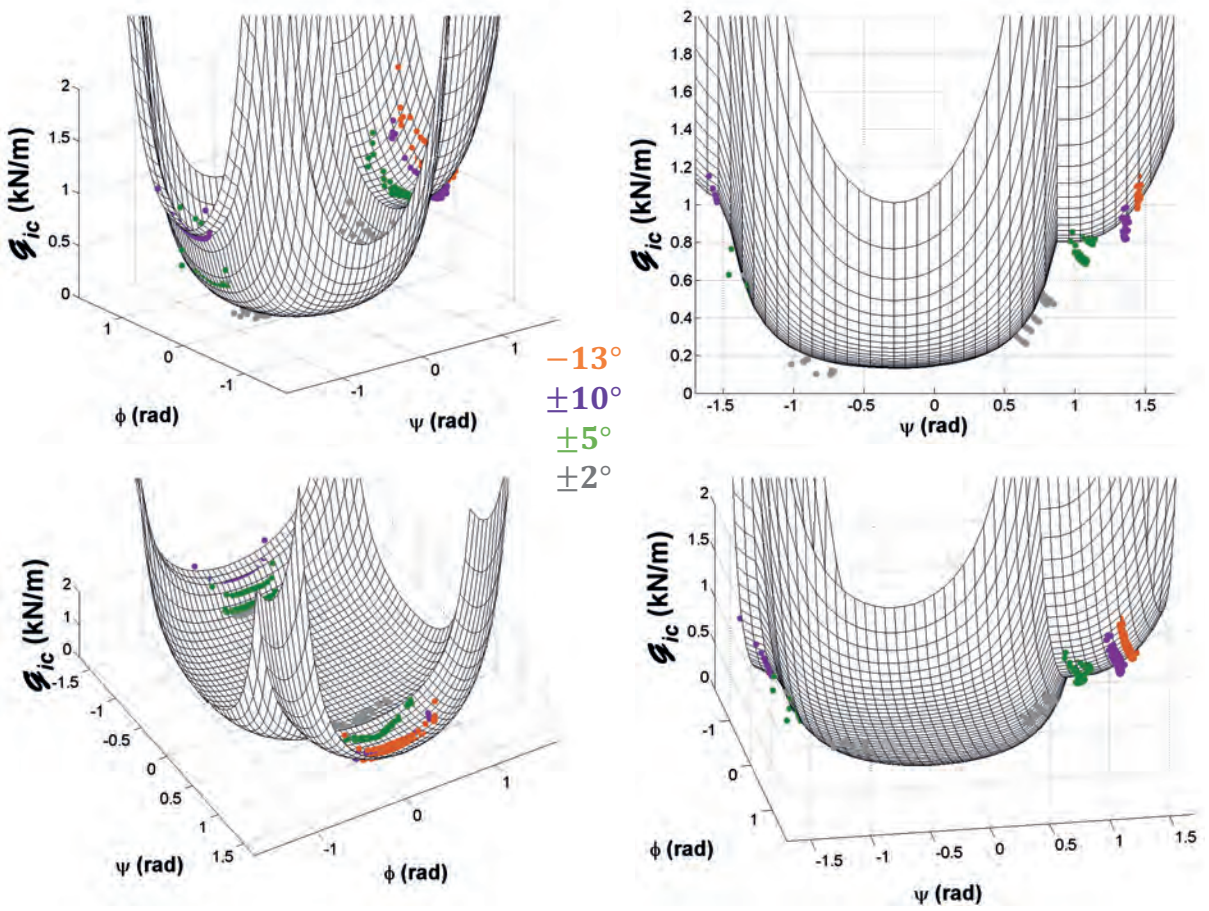

Figure 4.29: Four views of the three-dimensional '3 branch' failure surface from eqs. (4.19), (4.28) and (4.43) with $\hat{L} = 100$ μm using the parameters $\hat{K}_{2c}^{(i)}$, $\beta^{(i)}$ $(i = N, P)$, I and $\beta^{(S)}$ in Tables 4.22 and 4.24 with the boundaries $\psi^{(i)}$ in Table 4.25. '3 branch'.

in the safe zone. Since these specimens failed, the statistical approach described in Section 4.7.3 was applied to the three-dimensional criteria. The statistical parameters $\hat{K}_{2c}^{*(i)}$ and I^* in Table 4.27, and $\beta^{(i)}$ $(i = N, P, S)$ in Tables 4.22 and 4.24, respectively, were used in place of $\hat{K}_{2c}^{(i)}$ and I, for the '3 branch' criterion in eq. (4.28). For the '5 branch' criterion in eq. (4.30), I^* and $\beta^{*(S)}$ in Table 4.29, were used in place of I and $\beta^{(S)}$, respectively, and $\hat{K}_{2c}^{*(i)}$ and $\hat{K}_{1}^{*(i)}$ $(i = N, P)$ in Tables 4.27 and 4.28, respectively, were used in place of $\hat{K}_{2c}^{(i)}$ and $\hat{K}_{1}^{(i)}$ $(i = N, P)$. In addition, the parameters $\beta^{(i)}$ $(i = N, P)$ in Table 4.22, were used. The '3 branch' and '5 branch' three-dimensional statistical criteria and failure surfaces were obtained by substituting eqs. (4.28) and (4.30), respectively, with the related statistical parameters into eq. (4.19), and then into eq. (4.43).

Several views of the obtained statistical surfaces are presented in Figs. 4.31 and Figs. 4.32 for the '3 branch' and '5 branch' criteria, respectively. Videos of these surfaces may be viewed by links of the statistical '3 branch' and statistical '5 branch'. It may be observed in the figures that the obtained statistical surfaces are similar to those

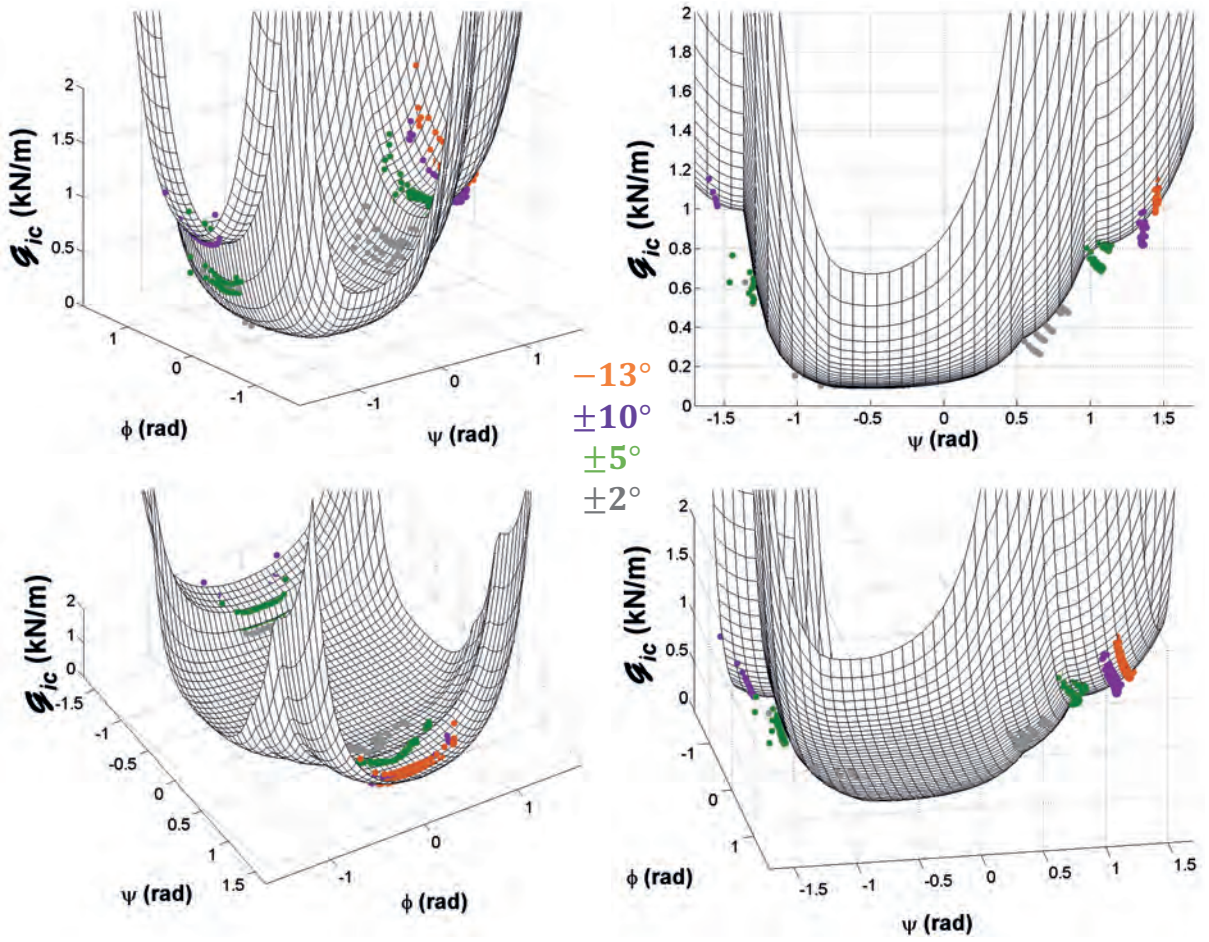

Figure 4.30: Four views of the three-dimensional '5 branch' failure surface from eqs. (4.19), (4.30) and (4.43) with $\hat{L} = 100$ μm using the parameters $\hat{K}_{2c}^{(i)}$, $\beta^{(i)}$, $\hat{K}_{1}^{(i)}$ $(i = N, P)$, I and $\beta^{(S)}$ in Tables 4.22 through 4.24 with the boundaries $\psi^{(i)}$ in Table 4.25. '5 branch'.

in Figs. 4.29 and Figs. 4.30, respectively, but with lowered surfaces. Since they are statistically reduced, the statistical $\mathcal{G}_{ic}^{*}$ values are lower than those of the original criteria. In addition, the statistical $\mathcal{G}_{1c}^{*}$ values, which are the same as those calculated using the statistical two-dimensional '3 branch' and '5 branch' criteria and given in Table 4.30 are also lower than the original $\mathcal{G}_{1c}$ values in Table 4.26. It may be observed that for both criteria, most of the data points are in the failure zone above the surface, whereas only a few data points remain in the safe zone. As observed in the two-dimensional case, both statistical surfaces predict complete failure or failure initiation for all specimens. There are no specimens for which failure was not predicted. Hence, the three-dimensional statistical failure surfaces may be used for failure prediction of these material systems and interface.

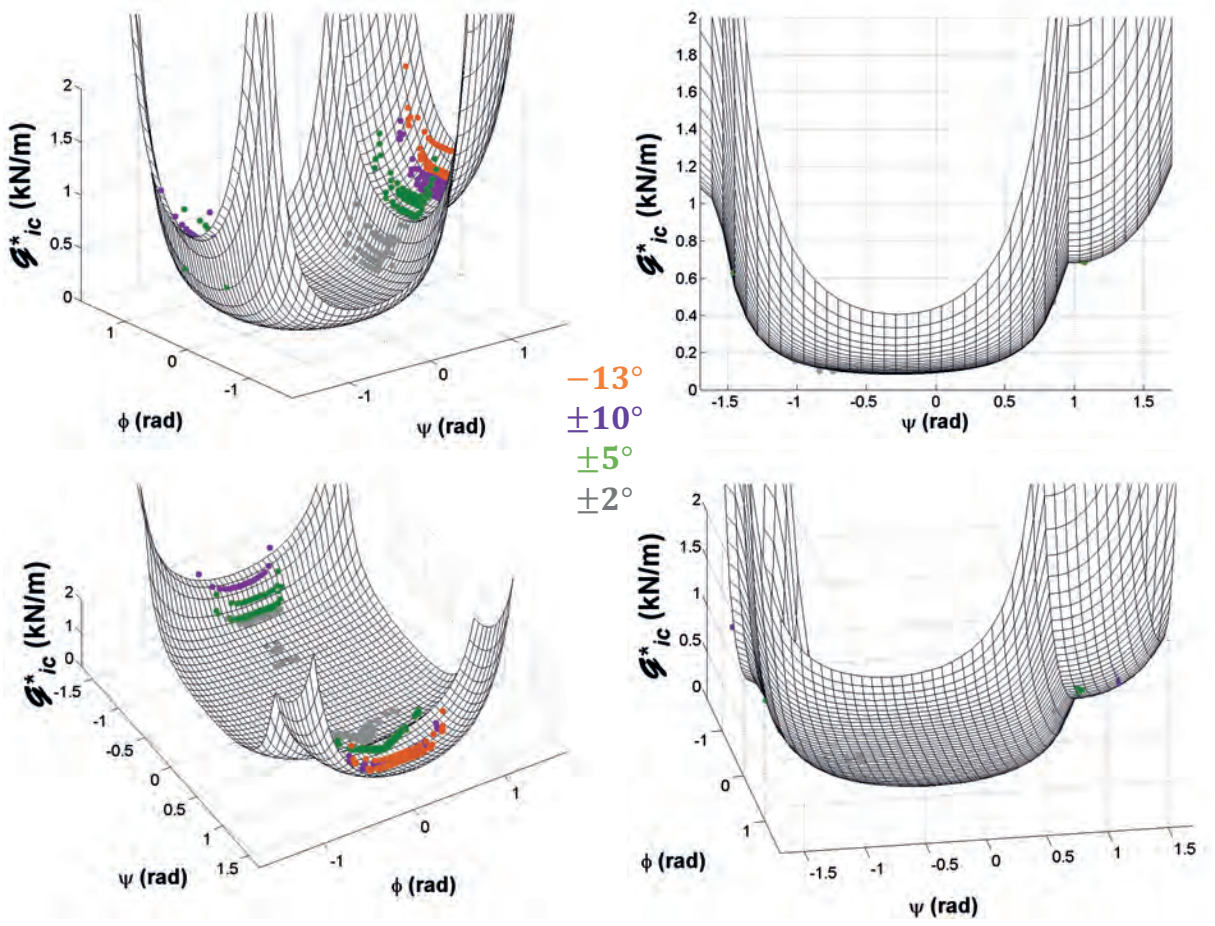

Figure 4.31: Four views of the three-dimensional '3 branch' statistical failure surface for the wet-layup material system from eqs. (4.19), (4.28) and (4.43) with the boundaries $\psi^{*(i)}$ $(i = N, P)$ in Table 4.25 and $\hat{L} = 100$ μm using the statistical parameters $\hat{K}^{*(i)}_{2c}$ $(i = N, P)$ and I^* in Table 4.27, as well as $\beta^{(i)}$ $(i = N, P, S)$ in Tables 4.22 and 4.24 for $i = N, P$ and $i = S$, respectively. statistical '3 branch'.

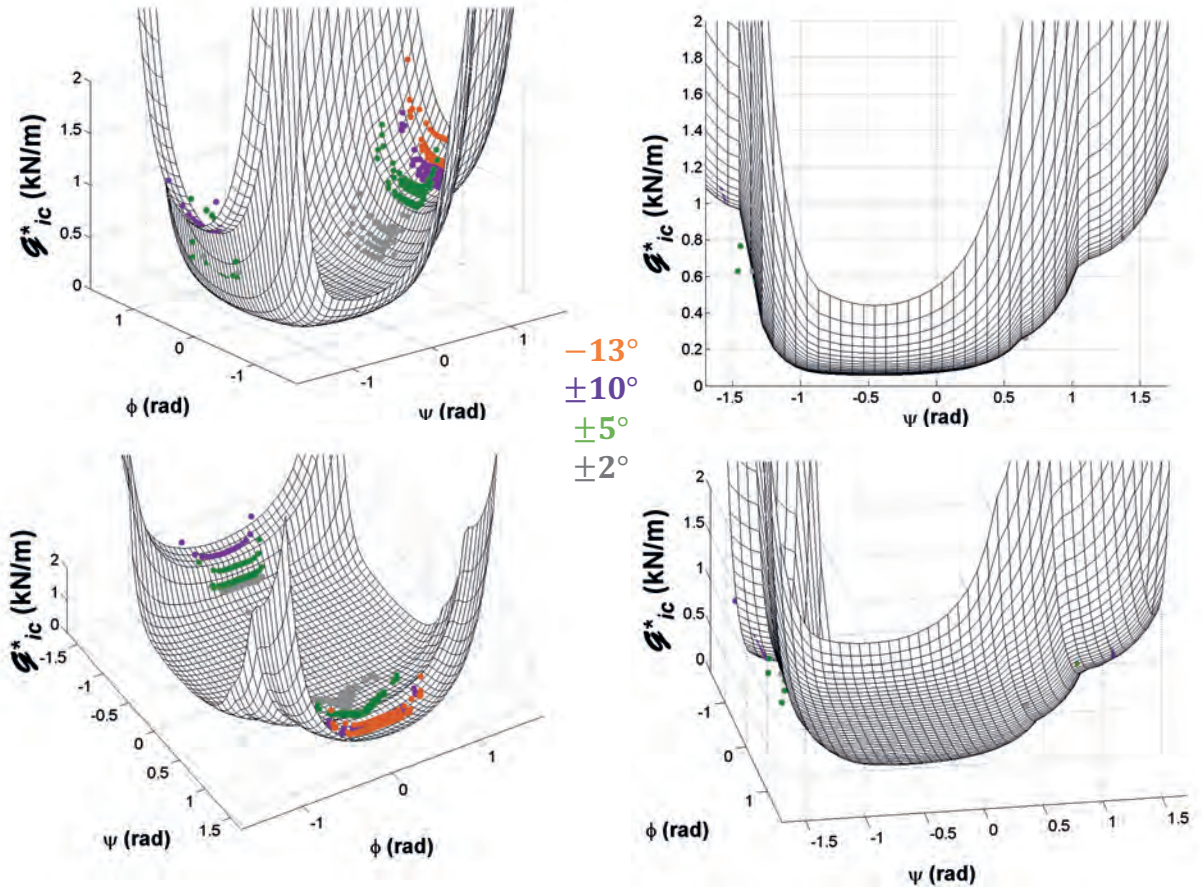

Figure 4.32: Four views of the three-dimensional '5 branch' statistical failure surface for the wet-layup material system from eqs. (4.19), (4.30) and (4.43) with the boundaries $\psi^{*(i)}$ $(i = N, P)$ in Table 4.25 and $\hat{L} = 100$ μm using the statistical parameters $\hat{K}_{2c}^{*(i)}$ and $\hat{K}_{1}^{*(i)}$ $(i = N, P)$ in Tables 4.27 and 4.28, respectively, I^* and $\beta^{*(S)}$ from Table 4.29 and $\beta^{(i)}$ $(i = N, P)$ in Table 4.22. statistical '5 branch'.

Chapter 5

Fracture toughness tests using beam type specimens

In this investigation, beam type tests including the calibrated-end loaded split (C-ELS) and mixed mode end loaded split (MMELS) specimens which may provide for stable delamination propagation when tested in displacement control were tested quasi-statically. In addition, results from Chocron and Banks-Sills (2019) for double cantilever beam (DCB) tests, with nearly mode I deformation, were reanalyzed. From the three test types, fracture resistance curves or R-curves were determined where the amount of energy required for the delamination to propagate $\mathcal{G}_R$ as a function of the delamination extension Δa is presented.

The same material and interface tested in Section 4 was tested again here and in Chocron and Banks-Sills (2019) using beam type specimens. A new plate was designed for these specimens with a different layup than that described in Section 4.1 for the BD specimens. The plate was manufactured by means of a wet-layup process. The design, layup, specimen dimensions, and mechanical properties of each ply in the plate are described in Section 5.1. In Section 5.2, the results obtained in Chocron and Banks-Sills (2019) from nearly mode I DCB tests are presented. These results were used in Chocron and Banks-Sills (2019) to calculate $\mathcal{G}_{IR}$ values as a function of the delamination extension Δa by means of FEAs in conjunction with the three dimensional M-integral described in Section 3.2. The analyses performed in that study are summarized in Section 5.2. The results from the quasi-static DCB tests in Chocron and Banks-Sills (2019) were used again here to calculate the $\mathcal{G}_{IR}$ values as a function of the delamination extension Δa by means of an additional method, namely, the experimental compliance method (ECM) presented in the ISO-15114 Standard (2014) for the C-ELS test and adapted here for the DCB test results. The R-curves obtained by means of the two methods, ECM here and the M-integral in Chocron and Banks-Sills (2019), are presented and compared in Section 5.2.

Six C-ELS and five MMELS specimens were tested and analyzed to obtain stress intensity factors $K_m^{(f)}$ and $K_m^{(r)}$ $(m = 1, 2, III)$ resulting from mechanical loading and

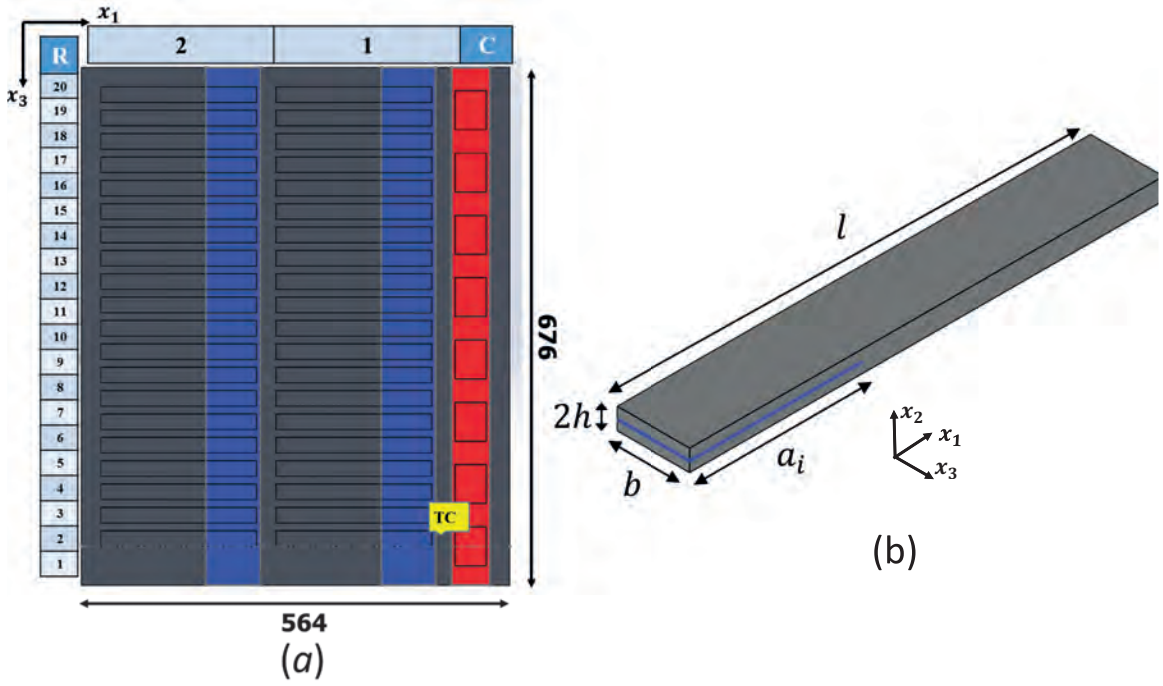

Figure 5.1: (a) Schematic view of the designed plate for DCB, C-ELS and MMELS specimens (each specimen in the plate is numbered as R.C.). Teflon film locations in the plate are colored, blue - delamination and red - weight fraction; (b) specimen dimensions.

curing stresses, respectively, as well as the mode mixity phase angles $\hat{\psi}$ and ϕ. Moreover, the resistance energy release rates $\mathcal{G}_{iR}$ as a function of the delamination extension Δa were determined. In Sections 5.3.1 and 5.4.1, test protocols for the C-ELS nearly mode II tests and for the MMELS mixed mode tests, respectively, are presented. The analyses and results from each test are presented in Sections 5.3 and 5.4, for the C-ELS and MMELS tests, respectively.

5.1 Materials

In this study, six C-ELS and five MMELS specimens were tested quasi-statically. The specimens were fabricated by means of a water-jet process from a MD carbon fiber reinforced (CFRP) laminate composed of the same material used for the BD tests in Section 4, but with a different layup. Note that the specimens used in Chocron and Banks-Sills (2019) for quasi-static and fatigue DCB tests were also fabricated from the same MD CFRP plate. The geometry of the plate was designed for forty specimens as shown in Fig. 5.1a. In Fig. 5.1b, an example of one beam specimen is presented. Dimensions of this specimen were determined based on previous knowledge from the literature for DCB, C-ELS and MMELS tests (ISO 15024:2001(E), 2001; ASTM D5528-13, 2014 ; ISO-15114:2014(E),2014; Blackman et al., 2001). These dimensions are presented in Table. 5.1

Table 5.1: Dimensions for DCB, C-ELS and MMELS tests (chosen based on recommendations in ISO 15024:2001(E) (2001), ASTM D5528-13 (2014), ISO-15114:2014(E) (2014), Blackman et al. (2001))

l (mm)	b (mm)	$2h$ (mm)	a_i (mm)
200	20	≈ 5	60-65

where l is the total specimen length, b is the specimen width, $2h$ is the specimen thickness and a_i is the total insert length.

The laminate was composed of 19 plies to create a maximum thickness of approximately 5 mm. The stacking sequence used was $\{[(+45°/-45°),(0°/90°)]_4,(+45°/-45°),0°//(+45°/-45°),[(0°/90°),(+45°/-45°)]_4\}$. Note that the double slash indicates the initial delamination location which was introduced using a 13 μm thick PTFE film along the interface investigated in this study. For a description of the materials see Section 2.1. Note that the material properties in the plate are calculated based on the measured fiber weight fraction of each ply. These properties differ from those in Section 2.1.

In Fig. 5.1a three PTFE film strips are shown. The PTFE film indicated in blue was used to create the initial delamination. The red PTFE strip in Fig. 5.1a was used to separate the nine woven lower plies so that weight fraction tests could be performed on nine plies. The volume fraction of the carbon fibers in the woven fabric was then calculated from the results of these tests. In addition, an accompanying specimen containing 10 UD plies was fabricated together with the plate. This was done to measure the weight fraction of the carbon fibers in the UD composite, as well as to measure the average thickness of a ply.

The plate was manufactured by means of a wet-layup process. One thermo-couple (TC) was inserted during plate fabrication as shown in Fig 5.1a to verify a uniform degree of cure during the curing process. From the TC, a monotonically increasing temperature was observed with a maximum of 90° C. Since no exothermic reactions were measured by the thermocouple and the plate is relatively thin, it was concluded that a uniform degree of cure was obtained within the composite plate. As a result of the temperature changes applied during the curing process, residual stresses were induced within the laminate. The fabricated plate thickness, width and length were measured to be approximately 4.8 mm by 564 mm by 676 mm, respectively. The UD fabric ply thickness was measured from the accompanying specimen to be approximately 0.145 mm thick. Hence, it may be concluded that each woven ply is approximately 0.27 mm thick.

After the manufacturing process was completed, NDT was performed on the composite plate to identify voids. Low porosity was observed from these results. Void content in each ply was measured. The fiber and epoxy volume fractions, as well as the void content of each ply were presented in Chocron and Banks-Sills (2019) and are shown here in

Table 5.2: Volume fractions of the material contents in the UD and woven plies.

material	T300 fibers (%)	EPR-L20/EPH-960 (%)	glass fibers (%)	voids (%)
UD	51.8	40	4.3	3.9
weave	42.7	53.8	-	3.5

Table 5.2. Mechanical properties and CTEs of each ply were calculated by means of HFGMC (Aboudi, 2004) and may also be found in Chocron and Banks-Sills (2019). These properties are presented here in Table 5.3 for the UD fabric ply, and in Table 5.4 for the woven plies with fibers oriented in the $+45°/-45°$ and $0°/90°$- directions.

5.2 Nearly mode I fracture toughness tests - DCB specimens

In this section, DCB fracture toughness tests which were performed and described in Chocron and Banks-Sills (2019) are presented. In that study, mechanical and thermal FEAs were preformed for each tested specimen. The obtained displacement fields were used with the mechanical and thermal M-integrals presented in Section 3.2 to obtain stress intensity factors resulting from mechanical and residual curing stresses, respectively. These were superposed to obtain the total stress intensity factors. In addition, $\mathcal{G}_{IR}$ values as a function of the delamination extension Δa were obtained. These analyses are described in detail in Chocron and Banks-Sills (2019). For completeness, a short summary of these analyses, as well as the resulting R-curve are presented here.

Also in this section, the DCB test results obtained in Chocron and Banks-Sills (2019) were used to obtain $\mathcal{G}_{IR}$ values as a function of the delamination extension Δa by means of ECM (ISO-15114, 2014). Note that although the ECM was suggested in the standard for mode II testing by means of the C-ELS specimen, it was chosen here to analyze the DCB results. Finally, in this section, the R-curve obtained here by means of ECM is compared to that obtained in Chocron and Banks-Sills (2019) by means of the M-integral.

In Chocron and Banks-Sills (2019), five DCB specimens were tested quasi-statically. During each test, images of the specimen were obtained every 5 s by means of the LaVision digital camera described in Section 4.3. In addition, the load P and actuator displacement d were recorded throughout the test. These values were synchronized with the images by means of the LaVision system. Load-displacement curves from each test may be found in

Table 5.3: UD fabric mechanical properties and CTEs.

E_A (GPa)	E_T (GPa)	G_A (GPa)	G_T (GPa)	ν_A	ν_T (10^{-6}/°C)	α_A (10^{-6}/°C)	α_T
104.4	8.7	6.6	3.2	0.30	0.36	2.3	49.7

Table 5.4: Woven fabric mechanical properties and CTEs obtained from HFGMC models for the $0°/90°$ and $+45°/-45°$ woven fabrics.

fiber orientation	$E_{11}=E_{33}$ (GPa)	E_{22} (GPa)	G_{13} (GPa)	$G_{21}=G_{23}$ (GPa)	ν_{13}	$\nu_{21}=\nu_{23}$	$\alpha_{11}=\alpha_{33}$ (10^{-6}/°C)	α_{22} (10^{-6}/°C)
$0°/90°$	43.9	4.9	2.3	1.8	0.034	0.046	4.3	72.1
$+45°/-45°$	8.4	4.9	21.2	1.8	0.82	0.046	4.3	72.1

Chocron and Banks-Sills (2019). After each test was completed, delamination lengths a, as the delamination propagated, were measured from the images. For each measured value of a, the load P which caused delamination propagation, as well as the associated actuator displacement d were noted to be used in the analyses. In addition, the temperature at the beginning of each test ϑ_i was recorded and may also be found in Chocron and Banks-Sills (2019).

For each specimen, six mechanical FEAs and one thermal FEA were performed. In the six mechanical FEAs, a different delamination length was modeled for every analysis, namely, $a = 50$ mm, 65 mm, 80 mm, 95 mm, 110 mm and 120 mm. For all analyses, the applied load was set to $P = 1$ N. The displacement fields obtained from these analyses were used with the three-dimensional mechanical M-integral described in Section 3.2 to obtain six data sets of $K_m^{(f)}$ $(m = 1, 2, III)$ each related to a specific value of a. Each data set is composed of forty $K_m^{(f)}$ values along the delamination front. Hence, for each specimen, data points in the three-dimensional space $(K_m^{(f)}, a, x_3)$ were obtained. Surfaces were fit through these data sets for $m = 1, 2, III$. These fitting surfaces, are described mathematically as

$$K_m^{(f)}(a, x_3) = \sum_{i=0}^{5} p_{i0} x_3^i + \sum_{j=0}^{4} p_{j1} x_3^j a \quad . \tag{5.1}$$

In eq. (5.1), p_{i0} and p_{j1} $(i = 0, 1, .., 5$ and $j = 0, 1, .., 4)$ are the surface fitting constants. Specific values for these constants for each specimen may be found in Chocron and Banks-Sills (2019).

One thermal analysis was performed for each specimen with an applied temperature $\Delta\vartheta_i$ calculated as

$$\Delta\vartheta_i = \vartheta_i - 90° \tag{5.2}$$

where ϑ_i was the temperature recorded at the beginning of each test and 90° the highest temperature measured by means of the thermocouple during curing. Since the effect of the delamination length on the thermal stress intensity factors was found to be negligible, as was shown in Chocron and Banks-Sills (2019), only one delamination length $a = 85$ mm was used for all thermal analyses. By means of the thermal M-integral, described in Section 3.2, with the displacement field obtained from each thermal FEA, one set of stress intensity factors $K_m^{(r)}$ $(m = 1, 2, III)$, resulting from residual curing stresses, along

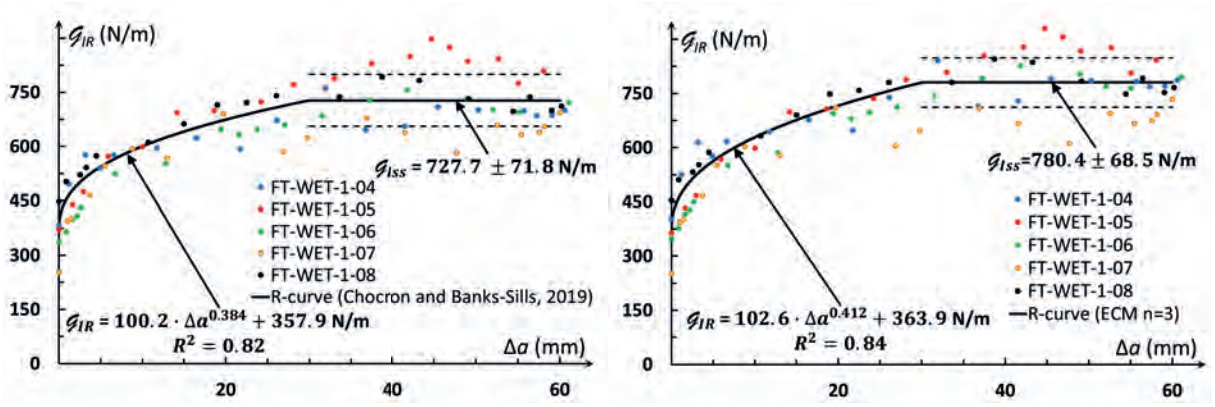

Figure 5.2: Resistance curves: $\mathcal{G}_{IR}$ versus $\Delta a = a - a_0$ obtained by means of the (a) M-integral (Chocron and Banks-Sills, 2019) and (b) ECM with $n = 3$, and m and C_0 from Table 5.5.

the delamination front were obtained. A fourteenth order polynomial curve fit between $K_m^{(r)}$ and x_3 was obtained as

$$K_m^{(r)}(x_3) = \sum_{i=0}^{14} b_i x_3^i \quad . \tag{5.3}$$

where b_i are fifteen fitting parameters given specifically in Chocron and Banks-Sills (2019) for each specimen.

Recall that the delamination lengths a, as the delamination extended, were measured after each test from the images which were acquired throughout the test. For every measured a, expressions of $K_m^{(f)}$ and $K_m^{(r)}$ were obtained as a function of x_3 by means of eqs. (5.1) and (5.3), respectively. These expressions were superposed to determine an expression for the total stress intensity factors $K_m^{(T)}$ as a function of x_3, namely,

$$K_m^{(T)}(a, x_3) = P K_m^{(f)}(a, x_3) + K_m^{(r)}(x_3) \quad . \tag{5.4}$$

In eq. (5.4), the load P, associated with each measured delamination length a, as the delamination extended, was used. For each measured delamination length a, the critical energy release rate $\mathcal{G}_i$ as a function of x_3 was expressed by means of eq. (3.17) with use of eq. (5.4). Finally, these expressions were integrated as

$$\overline{\mathcal{G}}_i = \frac{1}{b} \int_0^b \mathcal{G}_i(a, x_3) dx_3 \tag{5.5}$$

to obtain the average $\overline{\mathcal{G}}_i$ value for each delamination length a.

In Chocron and Banks-Sills (2019), $\mathcal{G}_i$ and $\overline{\mathcal{G}}_i$ in eqs. (3.17) and (5.5), respectively, were identified as $\mathcal{G}_I$ and $\overline{\mathcal{G}}_I$, respectively. This was done since the contributions of K_2 and K_{III} were small compared to the contribution of K_1. Hence, K_2 and K_{III} were neglected for the phase angle calculations in eqs. (3.19) and (3.20); whereas for the energy release rate calculation in eq. (3.17), they were included. In Fig. 5.2a, the obtained $\mathcal{G}_{IR}$ values are

Table 5.5: Fitting parameters related to the relation between the compliance C and delamination length a in eq. (5.8) with $n = 3$.

specimen	m $(10^{-6}/(N \cdot \text{mm}^2))$	C_0 (mm/N)
FT-WET-1-04	0.98	0.058
FT-WET-1-05	0.90	0.045
FT-WET-1-06	0.98	0.035
FT-WET-1-07	0.97	0.033
FT-WET-1-08	1.00	0.022

plotted as points for each specimen as a function of the delamination extension $\Delta a = a - a_0$ where a_0 is the initial delamination length of each specimen, measured from the load-line. Note that the overbar in eq. (5.5), representing the average through the width $\mathcal{G}_{IR}$ value, is omitted. An R-curve is shown as the black curve in Fig. 5.2a. The fracture toughness $\mathcal{G}_{ic}$, identified as $\mathcal{G}_{Ic}$, was determined as the average of the five $\mathcal{G}_{Ic}$ values found for each tested specimen by means of eq. (5.5) at $\Delta a = 0$ mm. Recall that the overbar in the equation is omitted. The $\mathcal{G}_{Ic}$ value with its standard deviation is presented in the second column of the second row in Table 5.6.

For the data points between $0 \leq \Delta a \leq 30$ mm, increasing $\mathcal{G}_{IR}$ values are observed in Fig. 5.2a as Δa increases. These values were described by means of a power law of the form

$$\mathcal{G}_{iR} = A_1(\Delta a)^B + \mathcal{G}_{ic} \quad . \tag{5.6}$$

Recall that $\mathcal{G}_{iR}$ and $\mathcal{G}_{ic}$ were identified in Chocron and Banks-Sills (2019) as $\mathcal{G}_{IR}$ and $\mathcal{G}_{Ic}$. The fitting parameters A_1 and B, obtained from Chocron and Banks-Sills (2019), are given in the fourth and fifth columns in the second row of Table 5.6. It may be noted that in eq. (5.6), $\mathcal{G}_{iR}$ and $\mathcal{G}_{ic}$ have units of N/m, Δa has units of mm and A_1 has units which are consistent with these. At $\Delta a = 30$ mm, a steady state $\mathcal{G}_{Iss}$ value is reached. This value was calculated as the average of all $\mathcal{G}_{IR}$ values obtained from eq. (5.5) for the different specimens for $\Delta a \geq 30$ mm. The resulting $\mathcal{G}_{Iss}$ value with its standard deviation is presented in the third column in the second row of Table 5.6.

Several LEFM data reduction schemes may be found in the literature to obtain the initial critical interface energy release rate $\mathcal{G}_{ic}$, as well as the resistance energy $\mathcal{G}_{iR}$ for

Table 5.6: The parameters $\mathcal{G}_{Ic}$, $\mathcal{G}_{Iss}$, A_1 and B in the nearly pure mode I R-curves obtained by means of the M-integral (Chocron and Banks-Sills, 2019) and by means of ECM in eq. (5.9) for DCB specimens.

Method for calculation	$\mathcal{G}_{Ic}$ (N/m)	$\mathcal{G}_{Iss}$ (N/m)	A_1 (N/m·mm^B)	B
M-integral	357.9 ± 71.1	727.7 ± 71.8	100.2	0.384
ECM	363.9 ± 75.1	780.4 ± 68.5	102.6	0.412

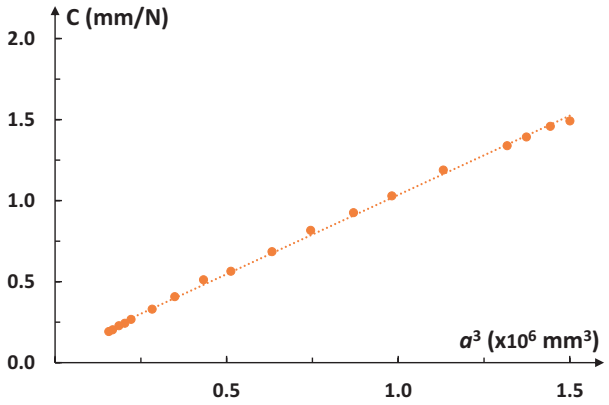

Figure 5.3: Compliance versus delamination length to the power $n = 3$ for specimen FT-WET-1-04.

mode I DCB tests (ASTM D 5528-13, 2014; ISO 15024:2001, 2001), for mode II C-ELS tests (ISO-15114, 2014) or for mixed mode MMELS tests (Williams, 1988; Hashemi et al., 1990; Blackman et al., 2001). Among these methods are corrected beam theory (CBT), corrected beam theory using the effective crack length (CBTE), modified compliance calibration (MCC), experimental compliance method (ECM) and simple beam theory (SBT) which are all derived from the Irwin-Kies equation (Irwin and Kies, 1954) given as

$$\mathcal{G}_{ic} = \frac{P^2}{2b} \cdot \frac{dC}{da} \quad . \tag{5.7}$$

In eq. (5.7), P is the load, b is the specimen width, C is the compliance given in eq. (1.97) and a is the delamination length. Values for these parameters may be found in Chocron and Banks-Sills (2019) for each specimen. It may be noted that since the delamination considered here is along an interface between two dissimilar plies in an MD laminate, where the two specimen arms have different thicknesses and mechanical properties, some of these methods are not applicable.

The ECM method described in the ISO-15114 (2014) standard for mode II, and in Blackman et al. (2001) for mixed modes, is recommended for both initiation and propagation tests to obtain $\mathcal{G}_c$ and $\mathcal{G}_R$ values, respectively. It was chosen to be applied here to the DCB specimens tested in Chocron and Banks-Sills (2019) in order compare local and global methods for obtaining a resistance curve for nearly mode I deformation.

Calculations by means of this method begin with a relation between the compliance C and the delamination length a, throughout the test. This relation is assumed to behave as (ISO-15114, 2014)

$$C = C_0 + ma^3 \tag{5.8}$$

where C_0 and m represent the intercept and slope, respectively, of the line relating the compliance C measured from the test versus a^3. An example of C verses a^3 for specimen FT-WET-1-04 is shown as orange points in Fig. 5.3. The orange dotted line in the figure represents the linear fit to the data points from which C_0 and m are obtained. The

obtained values are presented for each specimen in Table 5.5. In order to calculate the energy release rate $\mathcal{G}_i$, an expression of the derivative of eq. (5.8) is substituted into eq. (5.7) to obtain

$$\mathcal{G}_i = \frac{3P^2a^2m}{2b} \quad . \tag{5.9}$$

Note that in the C-ELS ISO (2014) standard eq. (5.9) included multiplication with F/N where F and N are correction factors which account for large displacements and the loading blocks, respectively. Here these parameters were taken as unity. The values of P, a and b for each specimen may be found in Chocron and Banks-Sills (2019) and m is taken from Table 5.5.

In Fig. 5.2b, the $\mathcal{G}_{IR}$ values obtained by means of eq. (5.9), with m in Table 5.5, are plotted as points for each specimen as a function of the delamination extension Δa. An R-curve is shown as the black curve in the figure. The fracture toughness $\mathcal{G}_{Ic}$ was calculated as the average of all $\mathcal{G}_{Ic}$ values obtained for the different specimens by means of eq. (5.9). The resulting value with its standard deviation is presented in the second column in the third row of Table 5.6. In addition, for $\Delta a \geq 30$ mm, the value of $\mathcal{G}_{Iss}$ is found from the average of those data points. The resulting value with its standard deviation is presented in the third column in the third row of Table 5.6.

A power law of the form in eq. (5.6) was fit to the points between $0 \leq \Delta a \leq 30$ mm. To this end, A_1 in eq. (5.6) is taken to be a fitting parameter. By means of the nonlinear Generalized Reduced Gradient (GRG) method in Excel (2016), the best fit was found. The calculation was made so that for the linear relation between the individual data points of $\mathcal{G}_{IR}$ for each specimen, shown in Fig. 5.2b, and Δa^B where B is related to A_1, the coefficient of determination R^2 closest to unity is obtained. During the fitting process, values of A_1 are incremented, so that the value of R^2 changes. Once the value of R^2 ceases to increase, the solver stops and produces the best fit for A_1. Note that this method produces a local maximum for R^2 which is not necessarily the global maximum. Hence, for different initial values of A_1, a different fit may be obtained. The solver was run multiple times with several initial values for A_1. The parameter B was expressed in the fitting as

$$B = \frac{\log\left(\dfrac{\mathcal{G}_{iss} - \mathcal{G}_{ic}}{A_1}\right)}{\log\left(\Delta a_{iss}\right)} \quad . \tag{5.10}$$

Note that this relation was obtained by manipulation of eq. (5.6). In eq. (5.10), for the results from the DCB tests used here, $\mathcal{G}_{iss} \approx \mathcal{G}_{Iss}$ is shown in Table 5.6. The parameter Δa_{ss} in eq. (5.10), is the initial delamination extension value related to steady state $\mathcal{G}_{Iss}$; here, $\Delta a_{ss} = 30$ mm. The parameters A_1 and B obtained for eq. (5.6) are given in the fourth and fifth columns of the third row of Table 5.6. The initial value used in the GRG method to obtain these parameters was $A_1 = 100$.

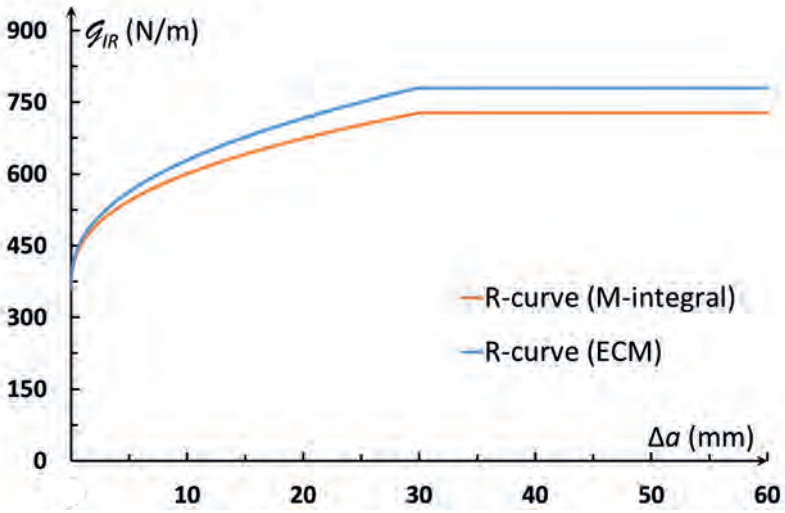

Figure 5.4: Comparison of the nearly mode I resistance curves obtained by means of the M-integral (Chocron and Banks-Sills, 2019) and by means of ECM in eq. (5.9).

The R-curves obtained by means of the M-integral in Chocron and Banks-Sills (2019), as well as by means of ECM in eq. (5.9) are compared in Fig. 5.4. Although these R-curves are similar, it is important to note that the R-curve obtained in Chocron and Banks-Sills (2019) by means of the M-integral was found to be more conservative. Results for $\mathcal{G}_{Ic}$ and $\mathcal{G}_{Iss}$ obtained by means of both methods are presented in Table 5.6. Relative differences (RDs) in these results were calculated by means of eq. (3.31) where the superscript (1) represents the value obtained with ECM, the superscript (2) is the value obtained in Chocron and Banks-Sills (2019) by means of the M-integral, and $i = I$. From this comparison, a small difference of 1.7% was obtained for $\mathcal{G}_{Ic}$. For $\mathcal{G}_{Iss}$, a larger difference of 7.2% was calculated. From these results, it is possible to conclude that the M-integral local approach provides results which correspond well with the global ECM method. It may be noted that an approach using the relation in eq. (5.8) was applied, but with 3 replaced by the best fit for the power to the data from the test. Larger differences were observed from these results with respect to those obtained in Chocron and Banks-Sills (2019). Hence, they are not presented here.

5.3 Nearly mode II fracture toughness tests - C-ELS specimens

In this investigation, six C-ELS specimens, with nearly mode II deformations, were tested quasi-statically. In Section 5.3.1, the protocol for the C-ELS tests is presented. Results from these tests are delineated in Section 5.3.2. Two-dimensional FEAs were performed for each specimen and are described in Section 5.3.3. Stress intensity factors $K_m^{(f)}$ $(m = 1, 2)$ resulting from mechanical loading were calculated by means of the displacement extrapolation (DE) method presented in Section 3.1, as well as with the virtual crack

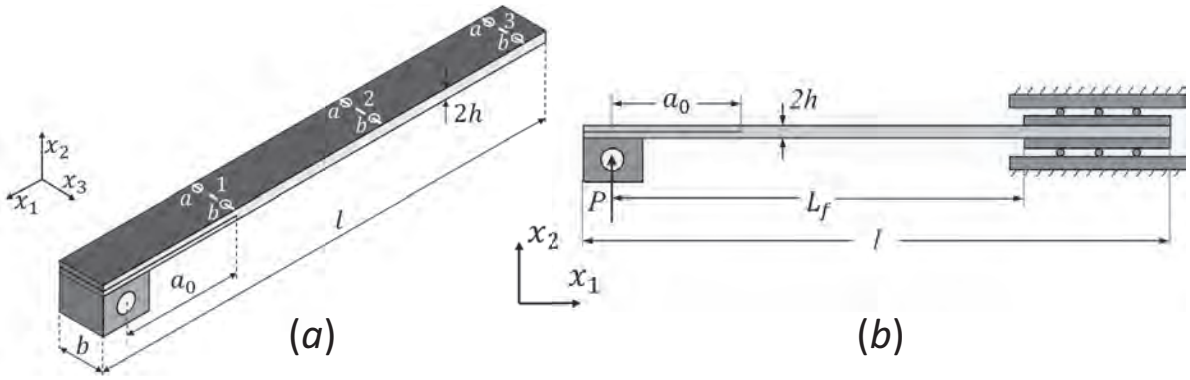

Figure 5.5: Illustration of the C-ELS specimen: (a) isometric view with measurement locations; (b) two-dimensional view of the C-ELS specimen, apparatus and applied load.

closure technique (VCCT) (Farkash and Banks-Sills, 2017). These were normalized using the length scale $\hat{L} = 100$ μm and the mixed mode phase angle $\hat{\psi}$ in eq. (3.19) was determined, so that the in-plane mode mixity was calculated for each test. Results from these calculations are presented in Section 5.3.4. Critical initiation energy release rate values $\mathcal{G}_{IIc}$ were obtained for each specimen by means of an area J-integral, DE and VCCT. Also, the fracture resistance energy values $\mathcal{G}_{IIR}$ were obtained as a function of the delamination extension Δa by means of ECM (ISO-15114:2014(E), 2014), as well as the FE method with appropriate post-processors. These calculations, as well as the resulting two R-curves are presented and compared in Section 5.3.4.

5.3.1 C-ELS test protocol

In this study, six quasi-static mode II dominant fracture toughness tests were carried out guided by the ISO-15114 standard (2014) for determination of the mode II fracture resistance for unidirectionally reinforced materials using the C-ELS specimen. In addition, one calibration test was performed following the protocol described in the ISO-15114 standard (2014). The results were used for verification of the global FEA response by means of a comparison between the test and the FEA compliances. In this section, a protocol for the calibration test, as well as for the C-ELS fracture tests are presented.

The same specimen, shown in Fig. 5.5a, was used for both the calibration test, as well as for the fracture tests. The specimen thickness $2h$ and width b were measured at six and three locations, respectively, shown as white circles and dashed lines, respectively, in Fig. 5.5a. These measurements were performed by means of a micrometer with a resolution of 0.001 mm and by means of a caliper with a resolution of 0.01 mm, respectively. The thickness $2h$ was measured on each side of the specimen at a distance of approximately 3 mm from the outer specimen edge. It is required in the ISO-15114 (2014) standard that the maximum variation in the thickness $2h$ would not exceed 0.1 mm. No specific

requirement is mentioned in the standard for a maximum variation in the width b. It may be noted that the ISO-15114 (2014) standard requires only three measurements of the thickness and width, at evenly spaced locations along the specimen length. Here, two measurements of $2h$ were acquired, one on each side of the specimen. This was done in order to insure that there is no significant tapering, as a result of possible misalignment in the bonding procedure. The insert length a_i shown in Fig. 5.1b was measured on the front and back sides of the specimen, a_{if} and a_{ib}, respectively, using the optical mode of the confocal microscope described in Section 4.3. Note that it is recommended in the ISO-15114 (2014) standard that the initial delamination length a_0, measured from the load-line to the edge of the PTFE film, shall be greater than 50 mm so that the influence of the load block may be neglected. This requirement implies that the measured a_i values shall be greater than 60 mm. It is also required in the standard that the differences in length between the two sides a_{if} and a_{ib} would be less than 2 mm. The length of the specimen l in Figs. 5.5, was measured with a ruler. According to the ISO-15114 (2014) standard, it is required that $l \geq a_i + 110$ mm.

After all measurements were completed, both edges of each specimen were coated with a thin layer of white water based acrylic paint. Before the paint was applied, in order to create a borderline for the paint at the insert tip, the end of the insert was determined by means of the optical mode of the confocal microscope. Clear tape was then attached on both sides of the specimen at the insert tip. After the coating layer was dry, straight vertical lines across the specimen edge were marked at regular increments of 2 mm, starting at the insert tip and extending to approximately $a = 100$ mm, measured from the load-line.

For the C-ELS fracture specimens, as recommended in the ISO-15114 (2014) standard, the free length was calculated as

$$L_f = \frac{4a_{0f}}{3} \tag{5.11}$$

where a_{0f} is the insert length on the front side of the specimen, measured from the load-line to the delamination tip as illustrated with the parameter a_0 in Figs. 5.5. For each specimen, the calculated L_f value was marked. For the calibration specimen, the free length L_f shown in Fig. 5.5b was marked at $L_f = 50, 60, 70, 80, 90, 100$ and 110 mm. Finally, each specimen was conditioned at a temperature of $23° \pm 1°$ C and a relative humidity (RH) of $50\% \pm 3\%$ for at least one week in a conditioning chamber (M.R.C. BTH80/-20, Holon, Israel) which is well within the tolerance of the ASTM Standard D5229/D5229M (2011).

A schematic illustration of the test apparatus used in the fracture tests, as well as for the calibration procedure is shown in Fig. 5.5b. There was a difference between the setup for the fracture test and calibration procedure. For the former, the load block was attached as shown in Fig. 5.5b so that the applied displacement is expected to result with $K_2 \geq 0$ for the case of the investigated interface. Note that the upper ply is the UD

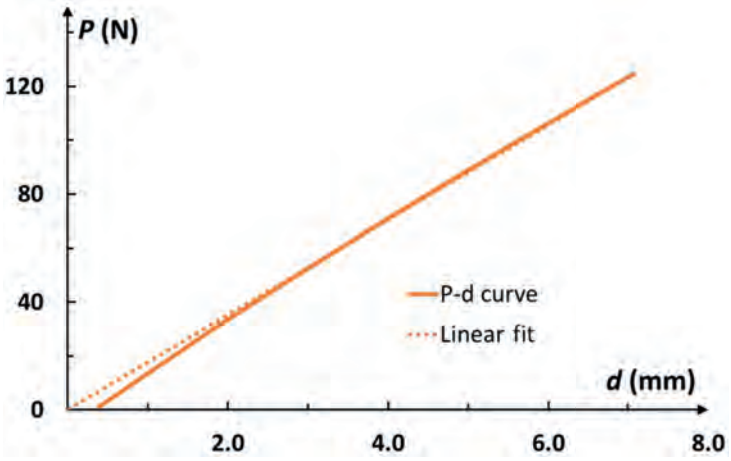

Figure 5.6: Illustration of a load-displacement curve and the fit to a linear portion of the curve.

fabric as shown in Fig. 2.1. For the latter, the load block was attached to the side of the specimen which does not contain the delamination. In this way, the specimen was attached to the fixture so that the side of the specimen with the initial delamination was clamped, opposite to the configuration shown in Fig. 5.5b. Thus, the specimen behaved as one cantilever beam. The load was applied to the specimen through a load block by means of the same Instron loading machine described in Section 4.3, with a 250 N load cell. The load block was pulled vertically through a pin, as shown in Fig. 5.5b. The clamping fixture creates free horizontal sliding of the specimen by means of bearings, but restricts vertical motion and rotation as may be observed in Fig. 5.5b. A LaVision system composed of one monochrome camera, described in Section 4.3, was employed during the test. Also, a programmable timing unit (PTU) controlled by DaVis (2015) computer software was used. During each test, images of the specimen were acquired at a rate of 2 Hz. Both fracture and calibration tests were conducted in displacement control.

The calibration procedure was carried out following the protocol given in the C-ELS ISO-15114 (2014) standard. The specimen was initially fixed so that $L_f = 110$ mm. When mounting a specimen, a torque wrench was used to tighten the retaining bolts to 8 Nm. This torque was chosen according to the suggestion of the ISO-15114 (2014) standard. The displacement was increased with a constant rate of 1 mm/min up to 250 N. At this point, the displacement was decreased at a rate of 5 mm/min. The same procedure was repeated for six additional free lengths of $50 \leq L_f \leq 100$ with L_f in decreasing increments. Load-displacement curves were obtained for each free length. The curve was translated so that the extrapolated linear loading portion would emanate from the origin as presented in Fig. 5.6 with the dotted line. Each specimen compliance C was calculated as

$$C = \frac{d_2 - d_1}{P_2 - P_1} \tag{5.12}$$

where (d_i, P_i) $(i = 1, 2)$ are two selected points along the linear part of the dotted curve

shown in Fig. 5.6. Two-dimensional FEAs were carried out for each L_f. The differences between the global response of the calibration specimen and that of the FEA was examined by comparing the compliance calculated by means of eq. (5.12) with that obtained from each FEA.

The fracture resistance tests were performed in two stages. In the first stage, the delamination propagates from the insert, referred to as the artificial crack or AC stage. In the second stage, the delamination propagates from the precrack (PC) which was achieved during the first stage. For the AC stage, the specimen was positioned in the clamping fixture, as shown in Fig. 5.5b at the L_f which was calculated using eq. (5.11). During this stage, the specimen was loaded in displacement control with a constant displacement rate of 1 mm/min until delamination propagation of between 2 and 5 mm was observed. At this point, the test was interrupted and the specimen was fully unloaded at a displacement rate of 5 mm/min.

For each specimen, load-displacement curves for the AC stage were plotted. The initiation load at failure P was determined in three ways: non-linear (NL), visual (VIS), and 5% offset or maximum load, as recommended in the C-ELS-15114 (2014) standard. With the NL method, P_{NL} was obtained from the load-displacement curve at the point in which non-linearity began. Visually, the value of P_{VIS} was found from an image captured by the LaVision system during the test for which delamination propagation was first observed. For the 5% offset or maximum load, a line was drawn at a 5% offset from the calculated compliance. The value of $P_{(5\%)}$ was determined at the intersection between the original load-displacement curve and the offset line. This value was compared with the maximum load P_{max} obtained for $d \leq d_{5\%}$. The maximum value of these two was chosen as $P_{(5\%/max)}$. For all three values of P, the corresponding actuator displacement d, and delamination length a were obtained from the synchronized images.

Two-dimensional FE mechanical analyses were performed for each specimen for the AC test stage. Two analyses were carried out for each specimen. The first, with the load $P_{(5\%/max)}$ applied, and the second with the load P_{VIS} applied. The results from each analysis were used to calculate the stress intensity factors by means of the DE method described in Section 3.1 and by means of VCCT (Farkash and Banks-Sills, 2017). Normalized $\hat{K}_1$ and $\hat{K}_2$ values were then calculated by means eq. (1.26) with the length parameter $\hat{L} = 100$ μm. From the results, the in-plane phase angle $\hat{\psi}$ was calculated for each specimen using eq. (3.19). Note that for a C-ELS test, dominant $\hat{K}_2$ values were expected. Hence, for an interface delamination with dominant in-plane shear deformation, it was assumed here that $\mathcal{G}_i \approx \mathcal{G}_{II}$.

The initiation energy release rate $\mathcal{G}_{IIc}$ values for $\Delta a = 0$ for each specimen were determined using eq. (3.17) with the calculated values of $\hat{K}_1$ and $\hat{K}_2$ instead of K_1 and K_2, respectively, and $K_{III} = 0$. In addition, from the FEAs with the load $P_{(5\%/max)}$ applied, values of J at $\Delta a = 0$ were obtained by means of the FEA results by means of

the area J-integral of Abaqus (2017). The integral was calculated for increasing applied loads up to the final applied load $P_{(5\%/max)}$. The resulting values of J were plotted verses the load P and a polynomial parabolic fit of the form

$$J^{(i)}(P) = A_0^{(i)} + A_1^{(i)} P + A_2^{(i)} P^2 \tag{5.13}$$

was used to describe the behavior of J for each specimen i as a function of the load P. In eq. (5.13), $A_0^{(i)}$, $A_1^{(i)}$ and $A_2^{(i)}$ are fitting parameters. The values of J related to the final displacement and corresponding load applied in each analysis were calculated using eq. (5.13) and compared with the $\mathcal{G}_{IIc}$ values which were determined with eq. (3.17) based on the VCCT results. Note that these results are expected to be approximately the same in order to validate the calculated energy release rate values obtained. Values of J which corresponded to the NL, visual and 5% offset or maximum initiation loads were calculated by means of eq. (5.13) to obtain three initial energy release rate values. Also, a thermal FEA was carried out, to obtain the stress intensity factors resulting from residual curing stresses.

At the end of the AC stage, after the specimen was completely unloaded, the specimen was dismounted. By means of the optical mode of the confocal microscope, the precracked delamination lengths a_{fPC} and a_{bPC}, front and back, respectively, were measured from the load-line to the delamination tip. A range of values for L_f was calculated as (ISO-15114, 2014)

$$a_{fPC}/0.75 \leq L_f \leq a_{fPC}/0.55 \ . \tag{5.14}$$

A new L_f value within the calculated range was chosen and marked on the specimen. Note that increasing the value of L_f causes less stable propagation. The specimen was remounted in the C-ELS apparatus and loaded at a displacement rate of 0.5 mm/min until the delamination tip was within 10 mm of the clamp. At this point, the test was stopped and the specimen was fully unloaded at a displacement rate of 5 mm/min.

Load-displacement curves were plotted for the PC stage for all specimens. The delamination lengths a, as the delamination extended, were measured after each test from the images which were acquired throughout the test. For every measured value of a, the corresponding P and d values were obtained from the synchronized images. These values were used to obtain R-curves for each specimen using two methods: ECM and the J-integral.

The ECM, described in Section 5.2, is recommended to be used for both AC and PC stages in the C-ELS tests. However, since for the AC stage, only a small number of visual data points exist, a value of m in eqs. (5.8) and (5.9), could not be accurately determined. Hence, this method was only used for the PC stage. Moreover, it is important to note that with the ECM, the delamination length, which is known to be difficult to measure for mode II testing (Blackman, et al, 2005; Blackman, et al, 2006; Pérez-Galmés, et al, 2018), was used and may result in some inaccuracies. By means of eq. (5.9), $\mathcal{G}_{IIR}$ values were calculated as a function of the delamination extension Δa. The value m was obtained

from eq. (5.8) with the compliance C calculated using eq. (5.12). The resulting $\mathcal{G}_{IIR}$ values were plotted verses the delamination extension Δa and a fracture resistance curve was obtained for each specimen.

The second method used was based on FEAs along with the J-integral, VCCT and the DE method. For each specimen, four two-dimensional analyses were carried out with $a = 50, 60, 70$ and 80 mm. For all analyses and each specimen, the relevant measured specimen thickness $2h$ was used, as well as the value of L_f from the PC stage of the test. The same arbitrary actuator displacement value $d = 10$ mm was applied in all analyses. Values of $J_{FE}/(bP_{FE})^2$ at $d = 10$ mm were obtained for each delamination length a. Note that P_{FE} in the denominator has units of force per unit width. Hence, in order to use the total load applied to the specimen, it was multiplied by the specimen width b. A parabolic fit between these points was then used to obtain a relation of the form

$$J^{(i)}(P, a) = P^2 \left(C_0^{(i)} + C_1^{(i)} a + C_2^{(i)} a^2 \right) \tag{5.15}$$

where P is the load associated with the delamination lengths a, measured for the PC stage of each test as the delamination propagated, and $C_0^{(i)}$, $C_1^{(i)}$, and $C_2^{(i)}$ are the obtained fitting parameters for specimen (i). By means of this relation and the measured values of a and P obtained from the images of the test, a fracture resistance curve was determined.

In addition, values of K_1 and K_2 were obtained by means of the VCCT (Farkash and Banks-Sills, 2017) and the DE method described in Section 3.1. In order to avoid complex units, the results were normalized using eq. (1.26) with the length parameter $\hat{L} = 100$ μm. Since the DE method is considered less accurate than VCCT, it was only used for validation of the results obtained by means of the VCCT. A relation between $\hat{K}_m$ and a was found as

$$\hat{K}_m^{(i)}(a) = P(B_0^{(i)} + B_1^{(i)} a) \tag{5.16}$$

where $m = 1, 2$, P is the load associated with each delamination length a, measured from the test, and $B_0^{(i)}$ and $B_1^{(i)}$ are fitting parameters for specimen (i). These parameters were obtained from a linear fit to $\hat{K}_{mFE}/(bP_{FE})$ obtained from the VCCT at $d = 10$ mm verses $a = 50, 60, 70$ and 80 mm. The measured values of a and P obtained from the images of each test were used in eq. (5.16) to calculate $\hat{K}_m$ as a function of the delamination extension a. With these results, the phase angle $\hat{\psi}$ was also calculated by means of eq. (3.19) as a function of the delamination extension a.

5.3.2 C-ELS test results

Six C-ELS specimens were tested quasi-statically and one calibration test was performed, both guided by the protocol described in Section 5.3.1. Each specimen is denoted as Test type-R-C where 'Test type' represents the C-ELS fracture test (CELS) or the calibration

Table 5.7: C-ELS and calibration specimens measurements: thickness $2h$ and width b shown in Fig. 5.5a. Delamination lengths for C-ELS specimens for AC stage of the fracture test.

specimen no.	$2h_{1a}$ (mm)	$2h_{1b}$ (mm)	$2h_{2a}$ (mm)	$2h_{2b}$ (mm)	$2h_{3a}$ (mm)	$2h_{3b}$ (mm)	$\overline{2h}$ (mm)	SD (mm)
CELS-2-2	4.78	4.81	4.79	4.76	4.58	4.53	4.71	0.123
CELS-2-3	4.89	4.88	4.90	4.87	4.70	4.66	4.81	0.107
CELS-2-4	4.88	4.87	4.92	4.86	4.80	4.81	4.85	0.046
CELS-2-5	4.80	4.75	4.82	4.85	4.78	4.77	4.80	0.036
CELS-2-6	4.83	4.87	4.90	4.92	4.76	4.79	4.84	0.063
CELS-2-7	4.77	4.76	4.80	4.84	4.71	4.70	4.76	0.051
CAL-2-9	4.79	4.96	4.97	4.86	4.92	4.80	4.88	0.078

specimen no.	b_1 (mm)	b_2 (mm)	b_3 (mm)	$\overline{b}$ (mm)	SD
CELS-2-2	19.82	19.86	19.71	19.80	0.062
CELS-2-3	19.85	19.89	19.75	19.83	0.061
CELS-2-4	19.78	19.83	19.78	19.80	0.024
CELS-2-5	19.81	19.88	20.03	19.91	0.092
CELS-2-6	19.89	19.87	19.85	19.87	0.016
CELS-2-7	19.86	19.79	20.00	19.88	0.087
CAL-2-9	19.71	19.72	19.80	19.74	0.040

specimen no.	a_{0f} (mm)	a_{0b} (mm)	Δa_0 (mm)	a_0 (mm)
CELS-2-2	51.81	52.46	-0.65	52.13
CELS-2-3	52.64	53.52	-0.88	53.08
CELS-2-4	52.64	52.73	-0.09	52.69
CELS-2-5	53.10	52.44	0.67	52.77
CELS-2-6	52.93	53.46	-0.52	53.19
CELS-2-7	52.89	52.80	0.08	52.85

procedure (CAL). The parameters R and C, shown in Fig. 5.1, denote the row and column location of the specimen in the plate, respectively.

As described in Section 5.3.1, prior to testing, each specimen width b and thickness $2h$ were measured at the locations marked in Fig. 5.5a. Results from these measurements, as well as the average values and standard deviations (SDs) are presented in Table 5.7. Specimen CELS-2-5 fulfills the ISO-15114 (2014) standard requirement. For the remainder of the specimens, it may be observed that the maximum variation in the thickness measurements are in the range 0.12 mm to 0.28 mm which may be a result of the wet-layup manufacturing process. These variations do not fulfill the ISO-15114 (2014) standard requirements. In addition, it may be observed that the variations in the width b are rather small.

In addition, for each specimen, the delamination length a_{if} and a_{ib} were measured as described in Section 5.3.1 from the specimen edge to the end of the delamination front,

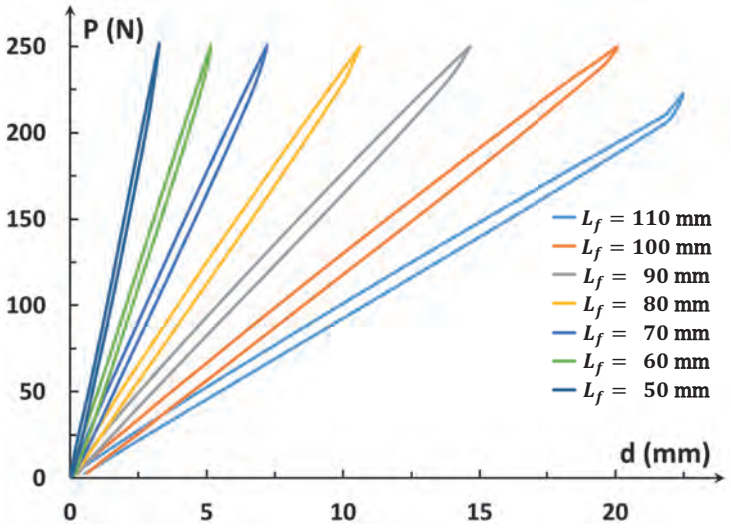

Figure 5.7: Load-displacement curves for the calibration procedure of specimen CAL-2-9.

on both sides of the specimen. The length of each load block, between the load block edge and the load-line was also measured. The obtained value was subtracted from a_{if} and a_{ib} to obtain a_{0f} and a_{0b}, respectively. The resulting a_{0f} and a_{0b} values are presented in Table 5.7. The difference Δa_0 between a_{0f} and a_{0b}, as well as the average of the two values a_0, are also presented in this table. It may be observed that the differences between the two sides for all specimens are less than 2 mm which meets the recommendations in the C-ELS ISO-15114 standard (2014). In addition, the length of the specimens l shown in Fig. 5.5 was measured as 200 mm for all specimens which also meets the ISO-15114 (2014) standard requirements.

The load-displacement curves obtained for the calibration specimen CAL-2-9 are presented in Fig. 5.7. It may be observed from the figure that for $L_f = 110$ mm, the specimen compliance suddenly changed at $P \approx 222$ N. This was caused by large bending deformation which resulted in contact between the specimen and the load block hinge. At this point, before reaching $P = 250$ N, the test was interrupted. In addition, the last part of the curve was omitted in the analyses.

The compliance C for each value of L_f was calculated from the linear loading part of each curve by means of eq. (5.12). The obtained results are presented in the second column of Table 5.8, as well as with blue points in Fig. 5.8 as a function of L_f. For every value of L_f used in the calibration test, an FEA was performed . The compliance of each FEA was calculated as

$$C_{FE} = \frac{d}{P} \tag{5.17}$$

where P is the maximum load applied in each analysis and d is the displacement obtained for this load. The obtained C_{FE} values are presented in the third column of Table 5.8. These values are plotted with orange triangles as a function of L_f in Fig. 5.8. It may be observed from the figure that for increasing values of L_f, the specimen compliance

Table 5.8: Calibration test for specimen CAL-2-9: compliance from eq. (5.12) verses that from the FEA results.

L_f (mm)	C ($\times 10^{-3}$ mm/N)	C_{FE} ($\times 10^{-3}$ mm/N)	RD(C) (%)
110	106.57	100.69	-5.5
100	79.92	77.51	-3.0
90	59.80	58.21	-2.7
80	43.79	42.44	-3.1
70	29.38	29.83	1.5
60	20.59	20.03	-2.7
50	12.60	12.69	0.7

C, as well as the FEA compliance C_{FE} increase. Relative differences (RDs) between the obtained C and C_{FE} values were calculated by means of eq. (3.31) where the superscript (1) represents C_{FE} obtained from the FEA results with eq. (5.17) and (2) is C obtained from the test results using eq. (5.12). Since the RDs for all L_f values used in the tests were found to be $\Delta C \leq 6\%$, it may be concluded that the global response obtained by means of the numerical analysis is well correlated with the test results and that the fixture and mechanical properties in the analyses are modeled correctly. However, from Table 5.8 it may be observed that $\Delta C \leq 0$ for five specimens implying that the FEAs are stiffer than the tested specimens. This could have been resolved by adding springs to the fixture in the FEAs and calibrating the compliance of the fixture to the global results obtained from the tests.

Load-displacement curves for the AC stage of all six C-ELS specimens tested are presented in Fig. 5.9a. In addition, in the second column in Table 5.9, the stiffness K_{AC} of each specimen which was calculated as the slope of the loading portion of each curve in Fig. 5.9a, is presented. It may be observed from Fig. 5.9a, as well as from the calculated

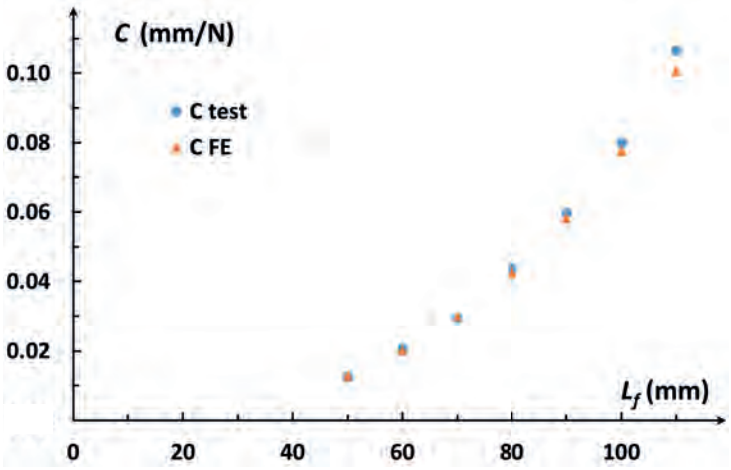

Figure 5.8: For specimen CAL-2-9, compliance from the calibration test C verses that from the FEA results C_{FE} as a function of L_f.

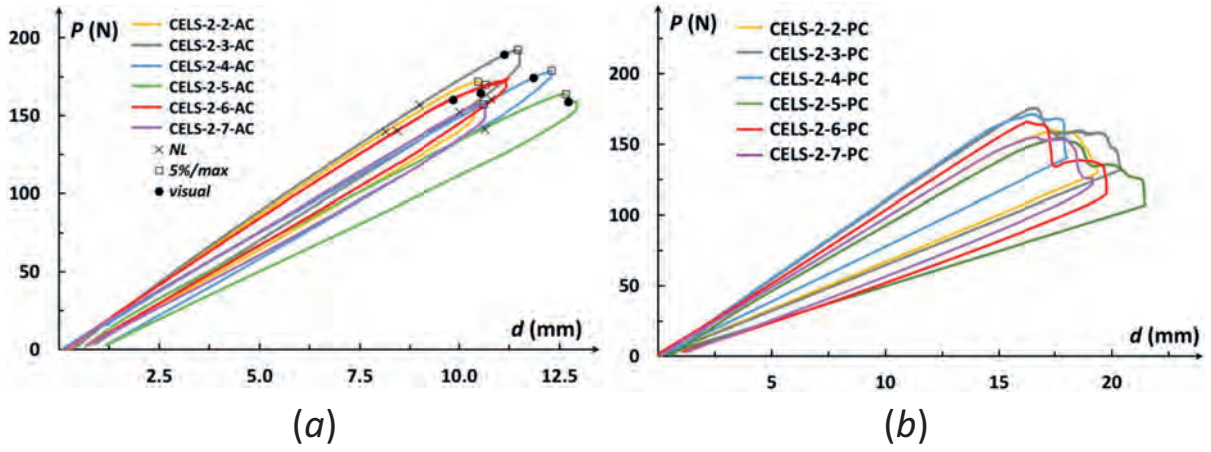

Figure 5.9: Load-displacement curves for the C-ELS tests: (a) AC stage and (b) PC stage.

stiffnesses K_{AC} in Table 5.9 that specimens CELS-2-4-AC and CELS-2-5-AC are less stiff than the other specimens. Since the investigated material was manufactured by means of a wet-layup process, perhaps differences in the stiffness occurred. In the third column in Table 5.9, the initial delamination length a_{0AC} which is the average a_0 in the last column in Table 5.7, is presented. The free length L_{fAC}, obtained from eq. (5.11) for the AC stage of each test, and measured in the test with a ruler is shown in the fourth column of this table. Values of P_{NL}, P_{VIS} and $P_{5\%/max}$, as well as the related d_{NL}, d_{VIS} and $d_{5\%/max}$ are presented in the fifth through tenth columns in Table 5.9, respectively. These are also indicated on each curve in Fig. 5.9a. Average values, standard errors (SEs) and the coefficient of variation (CV) are presented at the last three rows in this table.

In Fig 5.9b, load-displacement curves for the PC (second) stage of all six C-ELS specimens tested are presented. In the third column of Table 5.10, average values of a_{0PC}, which were measured by means of the optical mode of the confocal microscope

Table 5.9: The stiffness of the loading portion K_{AC}, the delamination length a_{0AC} and free length L_{fAC} of the AC stage of each C-ELS test, as well as, the loads and displacements obtained for each specimen before the initial artificial delamination propagated, along with average values, SEs and CVs.

specimen no.	K_{AC} (N/mm)	a_{0AC} (mm)	L_{fAC} (mm)	P_{NL} (N)	P_{VIS} (N)	$P_{5\%/max}$ (N)	d_{NL} (mm)	d_{VIS} (mm)	$d_{5\%/max}$ (mm)
CELS-2-2	17.2	52.1	69	139.6	164.6	171.6	8.1	10.5	10.5
CELS-2-3	17.6	53.1	70	156.9	189.4	192.5	9.0	11.1	11.5
CELS-2-4	14.9	52.7	70	160.3	174.5	179.1	10.9	11.8	12.4
CELS-2-5	13.5	52.8	71	141.4	158.8	164.0	10.7	12.7	12.7
CELS-2-6	16.8	53.2	71	140.2	160.3	169.9	8.4	9.8	10.7
CELS-2-7	15.2	52.9	71	152.3		157.4	10.1		10.6
Average				148.5	169.5	172.4	9.5	11.2	11.4
SE				3.8	5.7	5.0	0.5	0.5	0.4
CV(%)				6.2	7.5	7.1	12.2	10.0	8.4

Table 5.10: The stiffness of the loading portion of the PC stage K_{PC}, the delamination length a_{0PC} measured before the PC stage of the test by means of the confocal microscope and the delamination length $a_{0PC-VIS}$ measured after the test from the images acquired by the LaVision system by means of ImageJ (2015) software, as well as the free length L_{PC} used in the PC stage of each C-ELS test.

specimen no.	K_{PC} (N/mm)	a_{0PC} (mm)	$a_{0PC-VIS}$ (mm)	L_{fPC} (mm)
CELS-2-2	9.8	58.5	59.2	92
CELS-2-3	10.9	55.9	58.0	90
CELS-2-4	11.1	55.2	57.0	88
CELS-2-5	9.3	56.4	58.1	93
CELS-2-6	10.4	55.7	57.7	90
CELS-2-7	9.8	56.0	57.9	89

after the AC test stage ended and before the PC stage began, are presented. In addition, in the fourth column of this table, $a_{0PC-VIS}$, are shown. These values were measured from the images obtained by means of the LaVision system during the PC stage of the test and measured with ImageJ software (2015), just before the delamination propagated. Values of a_{0PC} and $a_{0PC-VIS}$ should be the same, however, since the measurement of a_{0PC} was performed when the specimen arms are closed and the specimen is dismounted, this measurement resulted in less accurate values which differed from $a_{0PC-VIS}$ which were obtained by means of the LaVision system. In the fifth column of Table 5.10, the L_{fPC} values which were measured with a ruler for each test are presented. It may be observed that generally, as the value of L_{fPC} increases, the stiffness K_{PC} of the specimen, measured as the slope of the linear loading portion of each curve and presented in the second column in Table 5.10, decreases. In Table 5.11, values of P_{NL}, P_{VIS} and $P_{5\%/max}$ measured from the PC stage of each test, as well as the related d_{NL}, d_{VIS} and $d_{5\%/max}$ values, are shown.

Table 5.11: The loads and displacements obtained for each specimen from the PC stage of each test, at initiation, along with average values, SEs and CVs.

specimen no.	P_{NL} (N)	P_{VIS} (N)	$P_{5\%/max}$ (N)	d_{NL} (mm)	d_{VIS} (mm)	$d_{5\%/max}$ (mm)
CELS-2-2	144.0	150.8	158.4	14.8	15.7	17.0
CELS-2-3	157.1	175.3	175.8	14.5	16.5	16.7
CELS-2-4	158.6	165.5	169.9	14.3	15.3	16.0
CELS-2-5	144.4	149.4	154.7	15.7	16.6	17.6
CELS-2-6	162.1	164.5	166.0	15.7	16.0	16.3
CELS-2-7	143.9	154.5	154.8	14.7	16.5	16.6
Average	151.7	160.0	163.3	16.7	16.1	14.9
SE	3.5	4.1	3.5	0.5	0.5	0.6
CV (%)	2.5	3.4	2.9	5.0	4.4	3.4

Table 5.12: Values of m and C_0 used in eq. (5.8) and (5.9) for each C-ELS test based on a linear fit to the data of a^3 verses C in Tables D.1 through D.6.

specimen no.	C_0 ($\times 10^{-2}$ mm/N)	m ($\times 10^{-7}$/(mm^{2}N))
CELS-2-2	7.47	1.44
CELS-2-3	6.73	1.48
CELS-2-4	6.52	1.53
CELS-2-5	7.89	1.67
CELS-2-6	6.84	1.53
CELS-2-7	8.04	1.34

It may be noted that the choice of $L_f = L_{fPC}$ in the PC stage was made arbitrarily in the range given in eq. (5.14). Perhaps, choosing a constant relation between L_f and a in the required range and using it for all tested specimens in the PC stage would have resulted with less variations in the stiffnesses of the specimens.

It may be observed from Figs. 5.9 that the loading portion of the load-displacement curves of the PC stage appear to be linear; whereas, those of the AC stage exhibit a small curvature. This may indicate that during the first loading stage (AC), a process zone was evolving near the insert front which was fully evolved once the delamination initiated. Thus, when the specimen was reloaded in the PC stage, the process zone was already present and the specimen behaved linearly. It is also interesting to note that the average values of P_{VIS} and $P_{5\%/max}$ in Table 5.9 for the AC stage are higher than those in Table 5.11 for the PC stage. Whereas, the P_{NL} average value obtained in the AC stage is lower than that of the PC stage. This may be a result of the non-linearity of the AC loading curves which made it difficult to determine a clear point at which non-linearity began. Moreover, it may be observed from Tables 5.9 and 5.11 that smaller values of CV were obtained for the PC stage as compared to those of the AC stage.

Values of a were measured from the load-line to the delamination tip as the delamination propagated by means of ImageJ (2015) software from the images captured using the LaVision system during the PC stage of each test. From each measured image, the related synchronized load P and actuator displacement d were also obtained. In Tables D.1 through D.6, the measured values of a, P and d are presented for each specimen. In addition, for each specimen, for every measured delamination length, the compliance values C were calculated using eq. (5.12). These C values are also presented in Tables D.1 through D.6. Using the data points (C, a^3), the slope and intercept m and C_0, respectively, in eq. (5.8), were obtained for each specimen as described in Section 5.3.1. The obtained values for each specimen are presented in Table 5.12.

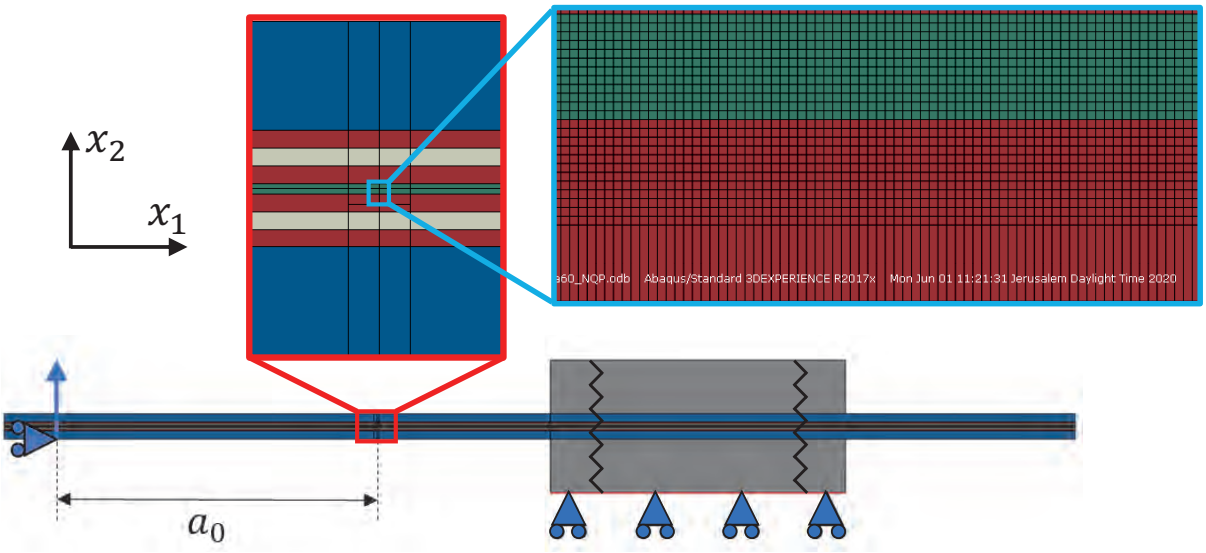

Figure 5.10: Illustration of the C-ELS fine FE model including boundary conditions and a focused view of the ply distribution.

5.3.3 C-ELS FE model convergence

In this section, mesh convergence for the C-ELS mechanical FEA is presented. The chosen mesh is then used for specimen CELS-2-2 with several delamination length values from Table D.1 to evaluate the accuracy of the results from the analyses compared to those obtained from the test. A displacement d was applied to the specimen. The load P_{FE} obtained for each delamination length is compared with the load P measured from the test. In addition, a thermal analysis was performed to account for the residual curing stresses. Since the results from the thermal analysis were negligible with respect to those obtained from the mechanical models, they were not included in the specimen analyses. This will be shown in the sequel.

Two-dimensional mechanical FEAs were performed with Abaqus (2017). Convergence was examined by means of three meshes. The dimensions $\overline{b}$ and $\overline{2h}$ of specimen CELS-2-2, given in Table 5.7, were used in the model with $a_0 = 50$ mm and $L_f = 92$ mm. From these analyses, stress and displacement fields were obtained and used in the VCCT (Farkash and Banks-Sills, 2017) and in the DE method presented in Section 3.1, to determine stress intensity factors. Convergence of these results for the three meshes was examined.

In Fig. 5.10, the two-dimensional finite element model (FEM) of the C-ELS specimen is presented. Recall that the laminate is composed of 19 plies with the stacking sequence $\{[(+45°/-45°),(0°/90°)]_4,(+45°/-45°),0°//(+45°/-45°),[(0°/90°),(+45°/-45°)]_4\}$. Four plies above the interface and three plies below it were modeled using the effective material properties in Tables 5.3 and 5.4 for the UD fabric and the $+45°/-45°$ and $0°/90°$ woven fabrics, respectively. A focused view of the modeled plies is presented in a

Table 5.13: Effective mechanical properties of alternating $+45°/-45°$ and $0°/90°$ woven fabrics.

$E_{11} = E_{33}$ (GPa)	E_{22} (GPa)	G_{13} (GPa)	$G_{21} = G_{23}$ (GPa)	ν_{13}	$\nu_{21} = \nu_{23}$
30.9	4.9	11.7	1.8	0.32	0.046

red frame in Fig. 5.10 with the UD fabric illustrated in green and the $+45°/-45°$ and $0°/90°$ woven fabrics illustrated in red and white, respectively. The six outer upper and outer lower plies were modeled as one effective homogenous, anisotropic material, shown in blue in Fig. 5.10. Since these plies are relatively far from the delamination/interface, it was assumed that it was not necessary to model each ply individually. Material properties for this effective material were obtained by means of HFGMC (Aboudi, 2004) and given in Table 5.13.

Three different meshes were used in the convergence study, namely, coarse, fine and finest. A description of each mesh is presented in Table 5.14. Eight-noded, quadratic, quadrilateral, plane strain elements of type CPE8 were used. For each mesh, two analyses were performed, with and without quarter-point elements near the delamination tip. Results from the analyses without quarter-point elements were used for VCCT; whereas the results from the analyses with quarter-point elements were used for the DE method and the J-integral of Abaqus (2017). A denser mesh was used near the delamination front, to model the square-root, oscillatory singularity. In addition, along the delamination front, elements with an in-plane aspect ratio of 1×1 were used for each mesh. In order to obtain such elements, the woven ply was partitioned into two layers, as shown in the focused view in the blue frame in Fig. 5.10, with the same properties from Table 5.4 used for both. The thickness of the upper layer was determined to be $h_{45}^{(1)} = h_0^{(1)}$ and equal to 0.145 mm, the thickness of the UD fabric. In this way, the upper UD ply and the upper layer of the lower woven ply near the delamination are composed of the same thickness and are meshed with elements of the same size.

As shown in Fig. 5.10, two steel plates were added to the model, acting as the clamp of the C-ELS apparatus. The top and bottom edges of the steel plates were constrained so that all nodes along the two edges have the same displacement in the x_1- direction. Two spring elements were added, as shown in Fig 5.10, to compensate for the apparatus compliance. Each one connects the top and bottom steel plates. For the convergence study, the stiffness of the springs K was chosen to be 100 N/mm. Surface-to-surface

Table 5.14: Three meshes which were used in a convergence study of the C-ELS specimen.

	no. of elements	no. of nodes	element size near delamination tip (mm^2)
coarse	6,394	19,993	0.024×0.024
fine	17,672	54,611	0.012×0.012
finest	63,986	195,117	0.006×0.006

Table 5.15: The normalized in-plane stress intensity factors $\hat{K}_1$ and $\hat{K}_2$ with $\hat{L} = 100$ μm, as well as the phase angle $\hat{\psi}$, $\mathcal{G}_i$ from eq. (3.17) with $K_{III} = 0$ and J from the area J-integral in Abaqus (2017) for each C-ELS mesh.

	$\hat{K}_1$ (MPa$\sqrt{\text{m}}$)	$\hat{K}_2$ (MPa$\sqrt{\text{m}}$)	$\hat{\psi}$ (rad) ($\hat{L} = 100$ μm)	$\mathcal{G}_i$ (N/m)	J (N/m)
coarse	0.223	1.742	1.444	391.9	391.9
fine	0.220	1.744	1.445	392.6	392.6
finest	0.216	1.745	1.448	392.6	392.6

contact interaction was implemented along approximately half of the delamination line, far from the delamination tip, to prevent interpenetration. Note that, near the delamination tip, delamination face opening was obtained. Also, between the specimen edges and the steel plates, contact interaction was used. A specific displacement $d = 10$ mm was applied in the model and at the deflection point, the degree of freedom in the x_1- direction was fixed, as illustrated in Fig 5.10.

By means of VCCT (Farkash and Banks-Sills, 2017) mechanical stress intensity factors were obtained for the three meshes. In addition, the DE method described in Section 3.1 was used for verification of the obtained values. The stress intensity factors found by means of VCCT were normalized using eq. (1.26) with $\hat{L} = 100$ μm. The obtained values are presented in Table 5.15. In the fourth column of Table 5.15, values of the phase angle $\hat{\psi}$, calculated by means of eq. (3.19) with $\hat{L} = 100$ μm, are presented for each mesh. It may be observed that the obtained values of $\hat{\psi}$ are rather close. In addition, the in-plane energy release rate values $\mathcal{G}_i$ were calculated by means of eq. (3.17) with K_1 and K_2 replaced with the normalized $\hat{K}_1$ and $\hat{K}_2$ values, and $K_{III} = 0$. Also, values of J were obtained for each mesh from the FEAs using the area J-integral of Abaqus (2017). In the fifth and sixth columns in Table 5.15, the results obtained for $\mathcal{G}_i$ and J for each mesh are presented, respectively. It may be observed that $\mathcal{G}_i \approx J$.

For all meshes, relative differences (RDs) between the normalized $\hat{K}_m$ ($m = 1, 2$) values obtained by means of VCCT and those obtained with the DE method were calculated using eq. (3.31) with the superscript (1) representing $\hat{K}_m$ obtained from the DE method and (2) representing the $\hat{K}_m$ values obtained with VCCT. For $\hat{K}_1$ and $\hat{K}_2$, the RDs were found to be lower than 5% and 1%, respectively. Recall that the value of $\hat{K}_1$ is small with respect to the value of $\hat{K}_2$ so that the differences in these values are less substantial for the calculation of $\hat{\psi}$ or $\mathcal{G}_i$. In addition, the in-plane phase angle $\hat{\psi}$ and the energy release rate $\mathcal{G}_i$ were calculated using the $\hat{K}_m$ values obtained from both methods. The obtained normalized stress intensity factors were used in eqs. (3.19) and (3.17) to obtain $\hat{\psi}$ and $\mathcal{G}_i$, respectively. Note that in eq. (3.17), the parameters K_1 and K_2 were replaced with $\hat{K}_1$ and $\hat{K}_2$, and $K_{III} = 0$. The obtained RDs for both parameters were found to be less than 0.5%. The small RD values for the results obtained with the VCCT and those obtained by means of the DE method give confidence that the obtained stress intensity factors are reliable.

Table 5.16: Relative differences (RDs) calculated using eq. (3.31) between different C-ELS meshes of the mechanical stress intensity factors, as well as $\mathcal{G}_i$ from eq. (3.17) with $K_{III} = 0$ and the calculated J.

	RD(K_1)	RD(K_2)	RD($\hat{\psi}$)	RD($\mathcal{G}_i$)	RD(J)
coarse vs fine	1.4%	-0.1%	-0.1%	-0.2%	-0.2%
fine vs finest	1.7%	0.0%	-0.1%	0.0%	0.0%

Relative differences for the parameters in Table 5.15 between each pair of meshes were calculated using eq. (3.31) where the superscript (1) represents the coarser mesh used in the comparison and the superscript (2), the finer mesh. The subscript $m = 1, 2$, represents the mode of the stress intensity factor. The obtained differences for the coarse and fine, as well as, the fine and finest meshes are presented in Table 5.16. Note that the RDs were obtained for a higher precision than that presented in Table 5.15. It may be observed that convergence was achieved for $\hat{K}_2$, $\hat{\psi}$, $\mathcal{G}_i$ and J. However, for $\hat{K}_1$ the obtained RDs increase as the mesh becomes finer. Based on this result it may seem that this parameter has not fully converged. But, it is important to note that since $\hat{K}_1$ is rather small, the RDs are highly influenced by small differences in the calculated values obtained for this parameter. Despite the small increase in RD for $\hat{K}_1$, the fine mesh was chosen to be used for the analyses of the tested C-ELS specimens.

After the convergence study was completed, the FEA for applied loads with the fine mesh, described in Table 5.14, was examined using five of the measured delamination lengths a in Table D.1. The chosen a values, measured between the load-line and the delamination tip, are presented in the first column in Table 5.17. The related synchronized actuator displacement d and load P are also presented in this table. In Fig. 5.11, the load-displacement curve obtained from the PC stage of the test for specimen CELS-2-2 is presented with a black curve. Also in this figure, the displacements d and loads P related to the five values of the visual delamination lengths measured for this specimen and given in Table 5.17 are marked with red crosses. For each delamination length a in Table 5.17, the related actuator displacement d was applied in the FEA. The load-displacement curve obtained from each FEA is displayed in Fig. 5.11, with a different

Table 5.17: Delamination length a, actuator displacement d and load P obtained from the PC stage of the C-ELS test for specimen C-ELS-2-2, as well as the resulting P_{FE} values obtained from the analyses and RDs between the measured and calculated loads.

a (mm)	d (mm)	P (N)	P_{FE} (N)	ΔP (%)
59.2	15.7	150.8	151.1	0.31
65.0	17.9	158.8	158.2	-0.79
70.3	18.7	150.1	150.2	0.15
74.6	19.1	138.9	141.0	2.06
78.6	19.3	129.0	132.1	3.11

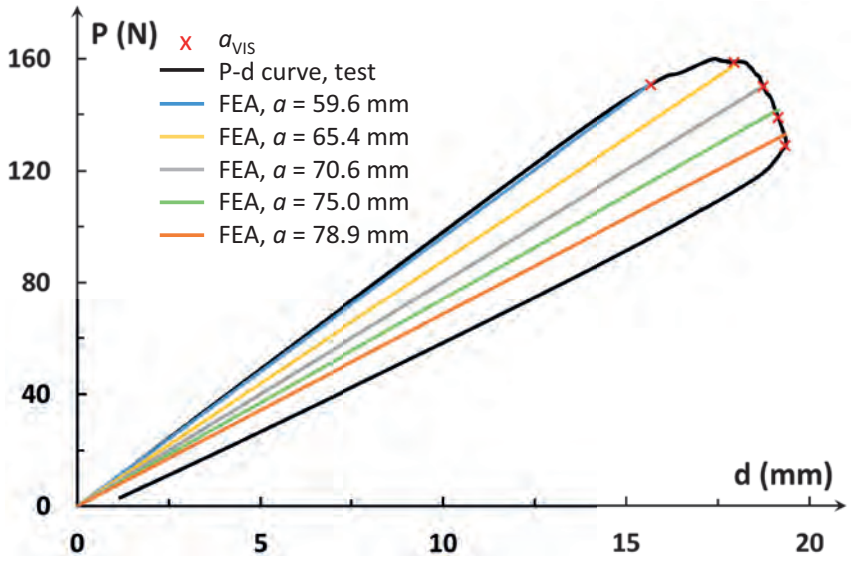

Figure 5.11: Load-displacement curves from the PC stage of the C-ELS test, as well as from the FEAs for the delamination lengths in Table 5.17 for specimen CELS-2-2.

color used for each delamination length a. Since the end point of the load-displacement curves obtained from the FEAs is rather close to the red crosses which represent the values measured from the test, it may be concluded that the global response obtained by means of the FEAs is similar to that obtained from the PC stage of the test. In addition, the load P_{FE}, obtained from each FEA for the applied displacement d is presented in the fourth column of Table 5.17. Relative differences between the loads P measured in the test and those obtained from the FEAs were calculated by means of eq. (3.31) where the parameter with the superscript (1) represents P_{FE} and the parameter with superscript (2) represents P. The results are presented in the fifth column of Table 5.17. From the results shown in Fig. 5.11 and in Table 5.17, it may be concluded that the test configuration and specimen are well modeled in the FEA.

In addition to the mechanical FEAs, three thermal two-dimensional analyses were performed for three chosen values of a from the first column of Table 5.17. These chosen values are presented in the first column in Table 5.18. In the thermal models, the total delamination length, $a + 10$ mm between the specimen edge and the delamination tip,

Table 5.18: Comparison between the in-plane thermal and total stress intensity factors and energy release rate.

a (mm)	$\Delta\vartheta_i$ (°C)	$K_1^{(r)}$ $\left(\text{MPa}\sqrt{\text{mm}}\,(\text{mm})^{-i\varepsilon}\right)$	$K_2^{(r)}$	$K_1^{(f)}$	$K_2^{(f)}$	$K_1^{(T)}$	$K_2^{(T)}$	$\mathcal{G}^{(r)}$ (N/m)	$\mathcal{G}^{(T)}$ (N/m)	$K_1^{(r)}/K_1^{(T)}$	$K_2^{(r)}/K_2^{(T)}$	$\mathcal{G}^{(r)}/\mathcal{G}^{(T)}$ $\times 10^{-4}$
59.57	-64	0.11	0.56	2.14	85.09	2.25	85.65	0.04	932.7	0.048	0.007	0.4
70.61		0.11	0.56	2.87	99.86	2.98	100.42	0.04	1282.3	0.036	0.006	0.3
78.92		0.11	0.56	3.07	98.59	3.18	99.15	0.04	1250.4	0.034	0.006	0.3

was modeled. The mesh in Fig. 5.10 was employed in the analyses without the fixture. The dimensions $\overline{b}$ and $\overline{2h}$ of specimen C-ELS-2-2, given in Table 5.1, were used in the models. The fine mesh with the smallest element size presented in Table 5.14 was chosen. This mesh consisted of 44,817 nodes and 14,544 quadratic quadrilateral elements of type CPE8. Recall that the same specimen mesh with modeling of the steel plates consisted of 54,607 nodes and 17,672 elements. A temperature difference was imposed with eq. (5.2).

$$\Delta\vartheta_i = \vartheta_i - 90^\circ \tag{5.18}$$

where ϑ_i is the temperature measured at the beginning of each test and 90° is the maximum temperature measured during curing. In the thermal FEAs, $\vartheta_i = 26^\circ$ C, resulting with an applied temperature change of $\Delta\vartheta_i = -64^\circ$ C.

By means of VCCT (Farkash and Banks-Sills, 2017) mechanical and thermal stress intensity factors were obtained for the three delamination length values a in Table 5.18 for both the mechanical and thermal FEAs, respectively. In addition, the DE method described in Section 3.1 was used to verify the obtained values. The thermal stress intensity factors, resulting from residual curing stresses and found by means of VCCT, are presented in the third and fourth columns in Table 5.18. It may be observed that these stress intensity factors are not a function of the delamination length. The mechanical stress intensity factors resulting from the applied load for the same delamination lengths are presented in columns five and six of this table. Note that these values are functions of the delamination length a, applied in each analysis, as well as the load P_{FE} obtained from each analysis, both presented in Table 5.17. It may be observed that for $a = 78.92$, the value of P_{FE} is lower than that obtained for $a = 70.61$. As a result, a slight decrease in the calculated $K_2^{(f)}$ value, in Table 5.18, was obtained. Superposition of the thermal and mechanical values was performed to obtain the total stress intensity factors which are presented in the seventh and eighth columns of Table 5.18. In columns eleven and twelve, $K_m^{(r)}/K_m^{(T)}$ $(m = 1, 2)$ are presented. It may be observed that the contributions of the thermal $K_1^{(r)}$ and $K_2^{(r)}$ values are rather small, respectively, and may be considered negligible.

The energy release rates resulting from both mechanical and thermal residual curing stresses $\mathcal{G}^{(T)}$, as well as those obtained only from thermal residual curing stresses $\mathcal{G}^{(r)}$, were calculated by means of eq. (3.17) with $K_{III} = 0$. The results are presented in the ninth and tenth columns of Table 5.18. In the last column of this table, the contribution of $\mathcal{G}^{(r)}$ to $\mathcal{G}^{(T)}$, is examined. From the results, it may be observed that the influence of the thermal residual curing energy release rate is negligible. It may be pointed out that the analyses shown in Fig. 5.11 also demonstrate that the thermal residual curing stresses are negligible in the global behavior of the specimen. It may be concluded that the results obtained by means of the thermal analyses may be neglected with respect to the mechanical results. Hence, thermal analyses were not carried out in the analyses of the tested specimens.

5.3.4 C-ELS test analyses and $\mathcal{G}_{IIR}$-curve

For each C-ELS specimen tested, six mechanical FEAs were performed using the fine mesh presented in Table 5.16. In all C-ELS FEAs, the model presented in Fig. 5.10 was used with $\overline{2h}$ and $\overline{b}$ given for each specimen in Table 5.7. In this section, the dimensions in Tables 5.7, 5.9 and 5.10, as well as the boundary conditions applied to each FEA are described. For each specimen, the VCCT and the DE method were employed with the FEAs to obtain the in-plane stress intensity factors which are also presented here. The obtained values were normalized according to eq. (1.26) with $\hat{L} = 100$ μm and used to calculate the in-plane phase angle $\hat{\psi}$ in eq. (3.19). The resulting values are shown in this section as a function of the delamination extension. From the resulting values it was possible to conclude that nearly mode II deformation is obtained during the entire C-ELS test implying that the contribution of K_1 is rather small compared to that of K_2. Hence, $\mathcal{G}_i \approx \mathcal{G}_{II}$.

For each specimen, the J values obtained with the area J-integral of Abaqus (2017) for each FEA were used to obtain an expression for J in terms of the load P and the delamination length a. The relation obtained for each specimen is presented in this section. This relation was used with the results from each test to determine the fracture resistance energy release rate $\mathcal{G}_{IIR}$ as a function of the delamination extension Δa. By means of the data points obtained for all specimens, an R-curve for nearly mode II deformation was determined and is presented here. An additional R-curve was calculated by means of the global ECM and is also presented here. Finally, the two R-curves are compared.

First, analyses for the PC (second) stage of each test were carried out in order to calibrate the stiffness K of the springs in the C-ELS fixture, shown in Fig. 5.10. Values of $a_{0PC-VIS}$, the visually detected delamination length at initiation, and L_{fPC} shown in Fig. 5.5b, which were modeled in the PC stage FEA of each specimen, are presented in the fourth and fifth columns in Table 5.10. The displacement d_{VIS} related to the visual load P_{VIS} in Table 5.11, obtained from the PC stage of the test, was applied to each model.

In order to calibrate the spring stiffness K, the stiffnesses K_{PC} and K_{FE-PC} obtained from the linear loading portion of the load-displacement curve of the PC stage of each test and from the related FEA, respectively, were compared. For each specimen, the relative difference (RD) between the two stiffnesses was calculated by means of eq. (3.31) with the superscript (1) representing K_{FE-PC} and (2) representing K_{PC}. The value of K was chosen so that $\text{RD}(K_{PC}) \leq |2|$ %. The chosen spring stiffness values are presented in the second column of Table 5.19. For each specimen, each of these K values was used in each FEA related to a specific specimen. In Table 5.19, K_{PC} and K_{FE-PC} are presented in columns six and seven, respectively, for each specimen. The value of K_{FE-PC} was obtained from the FEAs with the chosen spring stiffness K. It may be observed in column eight

Table 5.19: Comparison between the stiffness obtained from the AC and PC stages of each C-ELS test and that obtained from the FEA.

stage		AC			PC		
specimen no.	K (N/mm)	K_{AC} (N/mm)	K_{FE-AC} (N/mm)	RD(K_{AC}) (%)	K_{PC} (N/mm)	K_{FE-PC} (N/mm)	RD(K_{PC}) (%)
CELS-2-2	100	17.2	17.6	1.9	9.8	9.6	-1.6
CELS-2-3	100	17.6	17.5	-0.5	10.9	10.9	-0.4
CELS-2-4	50	14.9	16.5	10.2	11.1	10.9	-1.9
CELS-2-5	30	13.5	16.5	22.4	9.3	9.3	0.6
CELS-2-6	50	16.8	16.4	-2.0	10.4	10.3	-0.5
CELS-2-7	50	15.2	15.6	2.4	9.8	9.9	0.5

of this table that all calculated RDs related to the PC stage satisfy the requirement that $\text{RD}(K_{PC}) \leq |2|\,\%$. Note that the RDs related to the FEAs of the (first) AC stage are also presented in this table and will be discussed next.

In order to obtain the initial critical energy release rate values $\mathcal{G}_{ic} \approx \mathcal{G}_{IIc}$, FEAs of the AC stage of each test were carried out. The values of a_{0AC} and L_{fAC}, measured for each specimen and presented in the third and fourth columns in Table 5.9 were used in each FEA. The 5%/max load $P_{5\%/max}$, obtained from the AC stage, also presented in this table, was calculated per unit width and applied to the FEAs as $P_{FE} = P_{5\%/max}/\overline{b}$. The stiffness obtained from each FEA was compared to that obtained from the test. The stiffnesses K_{AC} and K_{FE-AC}, as well as the calculated RDs are presented in the third through fifth columns in Table 5.19. It may be noted that except for specimens CELS-2-4 and CELS-2-5, the RDs between the stiffness values obtained from the FEAs verses those from the tests were found to be $\text{RD}(K_{AC}) \leq |2.5|\,\%$. Recall that lower stiffnesses, with respect to the other tested specimens, were observed for specimens CELS-2-4 and CELS-2-5 and presented in Fig 5.9a. As a result, the differences between K_{AC} and K_{FE-AC} are rather large for these two specimens and may cause inaccuracies of the results related to the AC stage FEAs for these specimens. It was thought that it is better to incur this inaccuracy than to adjust the stiffness of the spring constants K in Table 5.19 to obtain a better correlation between the slopes of the load-displacement curves.

For each analysis in the AC (first) test stage, for increasing incremental applied loads per unit width, P_{FE}, up to the final applied load $P_{FE} = P_{5\%/max}/\overline{b}$ where $P_{5\%/max}$ is given in Table 5.9, the area J-integral of Abaqus (2017) was calculated. The resulting J values in the fourth, fifth and sixth domains, shown in Fig. 1.8, were averaged. The loads per unit width, P_{FE} (N/mm), which were applied in each analysis were multiplied by the width of the specimen $\overline{b}$, given in Table 5.7 for each specimen, to determine the total load P for a specimen of width $\overline{b}$. In Fig. 5.12, the obtained J values for specimen CELS-2-2 are plotted verses these $P = \overline{b}P_{FE}$ values, resulting from the FEAs, with blue points. As described in Section 5.3.1, a parabolic curve of the form in eq. (5.13) was fit to the obtained data points. By means of the obtained relation, values of J may be

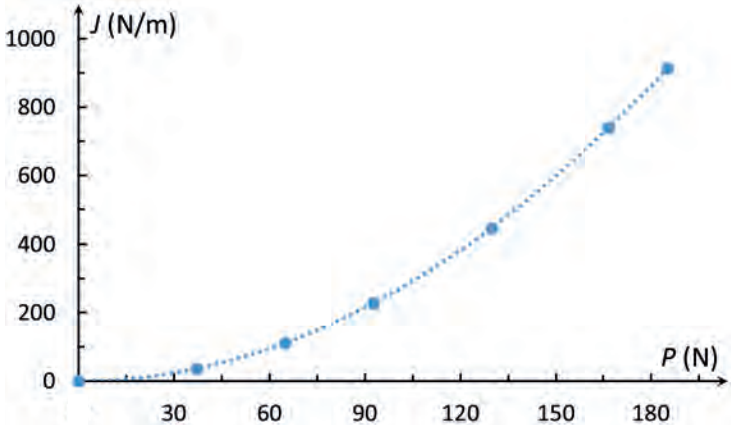

Figure 5.12: Plot of discrete $J = J_{FE}$ values verses the loads $P = \bar{b} \cdot P_{FE}$ obtained from the FEA AC stage of specimen CELS-2-2 for incrementally increased applied displacement values d. The obtained fitting curve relating J and P is also plotted.

calculated as a function of the load P. The resulting fit for specimen CELS-2-2 is shown in Fig. 5.12 with a dotted blue curve. The obtained fitting parameters $A_0^{(i)}$, $A_1^{(i)}$ and $A_2^{(i)}$ in eq. (5.13) are presented for each specimen in Table 5.20.

For each specimen i, three J-integral values, J_{NL}, J_{VIS} and $J_{5\%/max}$, were calculated with eq. (5.13) using P_{NL}, P_{VIS} and $P_{5\%/max}$, respectively, given in Table 5.9. The obtained J values for each specimen, as well as the average and CV values are presented in Table 5.21. Recall that the delamination length of each specimen a_{0AC} in Table 5.9 is accounted for since it is used in the FEAs. It may be noted that since it was difficult to clearly identify P_{VIS} for specimen CELS-2-7, J_{VIS} was not calculated for this specimen. For all specimens, $P_{NL} < P_{VIS} < P_{5\%/max}$ resulting with $J_{NL} < J_{VIS} < J_{5\%/max}$. Moreover, the average J_{NL} value was found to be 23.3% lower than J_{VIS}, whereas the average J_{VIS} value was found to be only 3.5% lower than $J_{5\%/max}$ implying that a damage zone is initiated before the delamination propagates, causing nonlinearities in the load-displacement curve. In addition, pronounced scatter exists for all J values. This scatter is related to the scatter in the measured P_{NL}, P_{VIS} and $P_{5\%/max}$ values. It is interesting

Table 5.20: Fitting parameters for eq. (5.13) relating J from the AC (first) stage FEA to P, for each specimen.

specimen i	$A_0^{(i)}$ ($\times 10^{-4}$ N/m)	$A_1^{(i)}$ ($\times 10^{-6}$ /m)	$A_2^{(i)}$ ($\times 10^{-2}$/(Nm))
CELS-2-2	-0.6	-5.4	3.10
CELS-2-3	-13.9	79.5	3.19
CELS-2-4	-4.7	27.7	2.92
CELS-2-5	-0.0	-3.3	2.84
CELS-2-6	-2.3	14.6	2.97
CELS-2-7	-6.3	50.1	3.07

Table 5.21: Results for the nearly mode II energy release rates $J \approx \mathcal{G}_{IIc}$ calculated by means of the area J-integral in Abaqus (2017) for P_{NL}, P_{VIS} and $P_{5\%/max}$ for all C-ELS AC specimens, as well as the average and CV values.

specimen	J_{NL} (N/m)	J_{VIS} (N/m)	$J_{5\%/max}$ (N/m)
CELS-2-2	604.5	839.4	913.1
CELS-2-3	784.4	1142.9	1180.9
CELS-2-4	750.7	888.6	936.7
CELS-2-5	567.6	716.6	763.7
CELS-2-6	582.7	761.6	855.5
CELS-2-7	711.4	-	759.2
average	666.9	869.8	901.5
CV (%)	5.7	8.6	7.0

to note that scatter of J_{NL} is the lowest, whereas the most scatter was obtained for J_{VIS}. A reason for this may be that P_{NL} and $P_{5\%/max}$ are calculated from the load-displacement curve, whereas P_{VIS} is obtained based on visual interpretation of the delamination length measured from the images. Hence, it is user dependent.

Additional FEAs were performed for the AC (first) test stage with the load $P_{FE} = P_{VIS}/\bar{b}$ applied and P_{VIS} given in Table 5.9. For each specimen, analyses with and without quarter-point elements were performed. Results from the former analyses were used in the DE method, whereas results from the latter were used with the VCCT to determine the in-plane stress intensity factors K_1 and K_2. Note that the DE method was used for verification of the VCCT. The obtained values were normalized by means of eq. (1.26) with $\hat{L} = 100$ μm. Relative differences between the values obtained by means of VCCT verses those determined by means of the DE method were calculated and found to be lower than 5% and 1%, for $\hat{K}_1$ and $\hat{K}_2$, respectively. Note that the ratio $\hat{K}_1/\hat{K}_2$ is approximately 0.13. These differences confirmed the validity of the calculations made by means of VCCT.

In Table 5.22, the resulting $\hat{K}_1$ and $\hat{K}_2$ values obtained for each specimen by means of VCCT, are presented. Values of $\mathcal{G}_{ic} \approx \mathcal{G}_{IIc}$ were obtained by means of eq. (3.17) with $\hat{K}_1$ and $\hat{K}_2$ instead of K_1 and K_2, and $K_{III} = 0$. In the fourth column of Table 5.22, the calculated $\mathcal{G}_{IIc}$ values for each specimen, are shown. Relative differences between J_{VIS} in Table 5.21 and the calculated $\mathcal{G}_{IIc}$ value for the same analysis were determined with eq. (3.31) with (1) representing the former and (2) the latter values. The obtained RDs were found to be less than 0.05% implying that the calculation of $\mathcal{G}_{IIc}$, is valid.

For each specimen, the in-plane phase angle $\hat{\psi}$ was calculated by means of eq. (3.19). The results are presented in the last column of Table 5.22. The average mode mixity for all specimens was found to be $\hat{\psi} = 1.45$ rad. Note that for a case of $K_1 = 0$ for any value of K_2, the in-plane phase angle $\hat{\psi}$ with $\hat{L} = 100$ μm would be calculated to be 1.47 rad. Since the $\hat{\psi}$ values obtained from the analyses of the C-ELS tests are rather close to this

Table 5.22: Stress intensity factors obtained by means of VCCT for P_{VIS} from the AC (first) stage of each test and used to calculate the critical energy release rate $\mathcal{G}_{IIc}$ and in-plane phase angle $\hat{\psi}$ by means of eqs. (3.17) and (3.19), respectively. The average and CV values are also presented.

	$\hat{K}_1$ (MPa$\sqrt{\text{m}}$)	$\hat{K}_2$ (MPa$\sqrt{\text{m}}$)	$\mathcal{G}_{IIc}$ (N/m)	$\hat{\psi}$ (rad)
CELS-2-2	0.323	2.551	839.8	1.44
CELS-2-3	0.377	2.975	1142.4	1.45
CELS-2-4	0.327	2.625	888.8	1.45
CELS-2-5	0.260	2.361	716.9	1.46
CELS-2-6	0.303	2.429	761.6	1.45
CELS-2-7	0.298	2.348	711.4	1.44
average	0.31	2.55	843.5	1.45
CV(%)	5.0	3.8	7.9	0.18

"maximum" $\hat{\psi}$ value, it may be concluded that the assumption that $\mathcal{G}_{ic} \approx \mathcal{G}_{IIc}$ is valid and that, as expected, the contribution of $\hat{K}_1$ to the mode mixity in this problem is negligible.

An attempt was made to obtain the $\mathcal{G}_{IIc}$ values for each specimen from the AC stage of the tests by means of the ECM, presented in Section 5.2. However, since the AC stage is performed in order to create a natural crack with propagation between 2 and 5 mm, only a small number of data points of the delamination length a, the load P and actuator displacement d, were obtained visually to be used in eq. (5.9). It was concluded that ECM is not suitable for C-ELS AC tests.

In order to determine an R-curve for nearly mode II deformation, as described in Section 5.3.1, the energy release rate $\mathcal{G}_{IIR}$ values were obtained as a function of the delamination extension Δa by means of the J-integral of Abaqus (2017), as well as by means of ECM. For each specimen, for both the J-integral, as well as for the ECM, for $\Delta a = 0$, the values of J_{VIS} from Table 5.21, related to the AC (first) stage of the test, were chosen as the initial critical energy release rate $\mathcal{G}_{IIc}$. The reason for choosing these values was that the J and $\mathcal{G}_{IIR}$ values related to the PC stage of the test were calculated based on visually measured values. Hence, in order to be consistent, the initial energy release rate values related to visually measured delamination extension and to the load P_{VIS} were chosen to be used.

With the J-integral, the relation in eq. (5.15) was used to determine J as a function of the load P and delamination length a. The fitting parameters $C_0^{(i)}$, $C_1^{(i)}$ and $C_2^{(i)}$ in eq. (5.15) were determined as described in Section 5.3.1 based on the results from four FEAS for each specimen. The C-ELS model in Fig. 5.10 was used for these FEAs with $a = 50, 60, 70, 80$ mm, $\overline{2h}$ and $\overline{b}$ in Table 5.7, L_{fPC} in Table 5.10 and the spring stiffness K from Table 5.19. The obtained values are presented in Table 5.23. Values of P and a from Tables D.1 through D.6 were substituted into eq. (5.15) to obtain $J(P, a)$. The resulting $J(P, a)$ values are presented in the seventh column of Tables D.1 through D.6 as

Table 5.23: The fitting parameters $C_0^{(i)}$, $C_1^{(i)}$ and $C_2^{(i)}$ in eq. (5.15) for the C-ELS tests.

	$C_0^{(i)}$ $\times 10^{-6}/(\text{Nm})$	$C_1^{(i)}$ $\times 10^{-3}/(\text{Nm}^2)$	$C_2^{(i)}$ $1/(\text{Nm}^3)$
CELS-2-2	58.2	26.7	10.87
CELS-2-3	15.7	27.0	10.20
CELS-2-4	-86.3	30.1	9.96
CELS-2-5	30.4	26.3	10.18
CELS-2-6	6.4	26.7	10.00
CELS-2-7	-12.7	28.2	10.45

$\mathcal{G}_{IIR}$ (J-int), as well as plotted with points for each specimen in Fig. 5.13a as a function of the delamination extension $\Delta a = a - a_0$ where a_0 is the initial delamination length of each specimen, measured from the load-line and presented in Table 5.7.

For the ECM, the values of m in Table 5.12 were substituted into eq. (5.9) to obtain a relation between $\mathcal{G}_{IIR}$, P and a for each specimen. The measured values a and P in Tables D.1 through D.6 were substituted into the equation to obtain values of $\mathcal{G}_{IIR}$ as a function of P and a. The resulting $\mathcal{G}_{IIR}$ values are presented in the eighth column of Tables D.1 through D.6, as well as plotted in Fig. 5.13b as points for each specimen as a function of the delamination extension Δa.

It may be observed for the resulting data from both methods in Figs. 5.13 that as Δa increases, $\mathcal{G}_{IIR}$ increases until reaching a steady state value $\mathcal{G}_{IIss}$ at approximately $\Delta a_{ss} = 15$ mm. A power law of the form in eq. (5.6) between $0 \leq \Delta a \leq 15$ mm was fit to the points obtained by means of the J-integral, as well as the ECM. For $\Delta a \geq 15$ mm, $\mathcal{G}_{IIss}$ is the steady state energy release rate presented for each method in Table 5.24.

The obtained R-curves are shown as the black curves in Figs. 5.13. The fracture toughness $\mathcal{G}_{ic}$, identified as $\mathcal{G}_{IIc}$, was determined in both cases as the average of the six

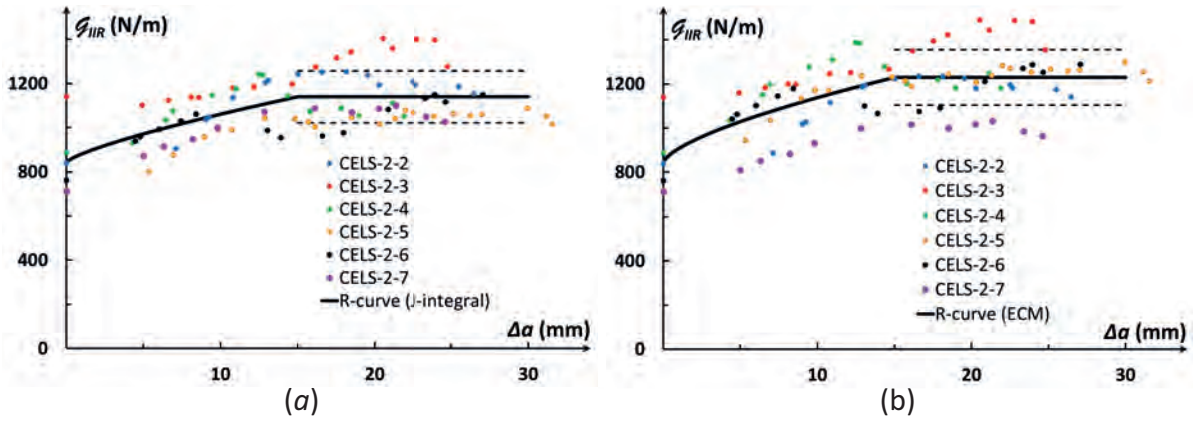

Figure 5.13: Resistance curves: $\mathcal{G}_{IIR}$ versus $\Delta a = a - a_0$ obtained by means of (a) J-integral and eq. (5.15) with the fitting parameters in Table 5.23 and (b) ECM from eq. (5.9) with m from Table 5.12.

Table 5.24: The parameters $\mathcal{G}_{IIc}$ and $\mathcal{G}_{IIss}$, as well as A_1 and B from the power law in eq. (5.6) for the nearly mode II R-curves obtained by means of the J-integral in eq. (5.15) and by means of ECM in eq. (5.9) for the C-ELS specimens. The RMSE are also presented.

method	$\mathcal{G}_{IIc}$ (N/m)	$\mathcal{G}_{IIss}$ (N/m)	A_1 (N/m·mm^B)	B	RMSE (N/m)
J-integral	843.1	1139.8	37.7	0.76	102.0
ECM	843.1	1229.1	63.7	0.66	119.3

J_{VIS} values found for each tested specimen. The obtained average value is presented in Table 5.24. Recall that the initial values applied to the R-curve related to ECM were also obtained by means of the J-integral. Hence, for both methods, the initial values are the same. The fitting parameter A_1 in eq. (5.6) was obtained for each set of data points, related to each method, by means of the nonlinear Generalized Reduced Gradient (GRG) method in Excel (2016). The calculation was performed so that for the linear relation between the individual data points of $\mathcal{G}_{IIR}$ for each specimen, shown in Fig. 5.13, and Δa^B where B is related to A_1, a minimum value, for the root mean square error (RMSE), is obtained. During the fitting process, values of A_1 are incremented, so that the value of the RMSE changes. Once the value of the RMSE ceases to decrease, the solver stops and produces the best fit for A_1. Note that this method produces a local minimum for the RMSE which is not necessarily the global one. Hence, for different initial values of A_1, a different fit may be obtained. The parameter B was expressed in the fitting by means of eq. (5.10) where $\mathcal{G}_{iss} \approx \mathcal{G}_{IIss}$ are given in Table 5.24 for each method. The values of $\mathcal{G}_{IIss}$ were calculated as the average value of all J or $\mathcal{G}_{IIc}$ data points obtained for $\Delta a \geq 15$ mm. The parameters A_1 and B related to the J-integral and to the ECM are also given in this table. The initial value used in the GRG method to obtain these parameters was $A_1 = 100$.

From the two plots in Fig. 5.13 it may be observed that for the ECM larger scatter in the results was found. In Fig. 5.14, the two R-curves obtained by the two methods are plotted and may be compared. It may be clearly observed that the J-integral local approach resulted in more conservative energy release rate values with a more moderate power law increase until steady state. The RD between the $\mathcal{G}_{IIss}$ steady state energy release rate values given in Table 5.24 obtained by means of the two methods was calculated using eq. (3.31) with (1) being the ECM result and (2) the J-integral. The RD was found to be 7.8% which implies that the results obtained from the global and local analyses are rather similar.

In addition to the R-curves, $\hat{K}_m$ $(m = 1, 2)$ values were obtained as a function of the delamination extension Δa, as described in Section 5.3.1. The relation in eq. (5.16) was used to determine $\hat{K}_m$ as a function of the load P and delamination length a. The fitting parameters $B_0^{(i)}$ and $B_1^{(i)}$ which are the intercept and slope of the line, respectively, in eq. (5.16) for each specimen i were determined as described in Section 5.3.1, based on the

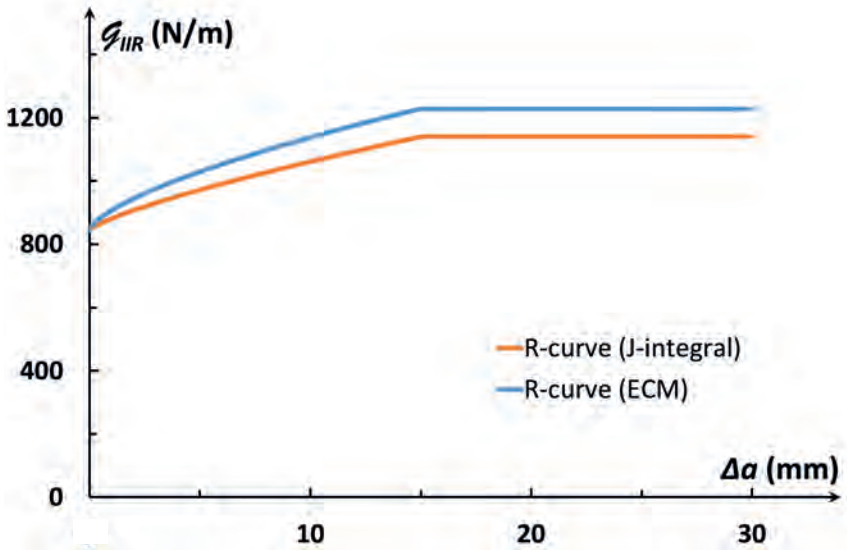

Figure 5.14: Comparison of the nearly mode II resistance curves obtained by means of the J-integral and by means of ECM in eq. (5.9) with m from Table 5.12.

results from the four FEAs with $a = 50, 60, 70, 80$ mm for each specimen, along with the VCCT. The obtained values for $B_0^{(i)}$ and $B_1^{(i)}$ for $m = 1, 2$ are presented in Table 5.25. Values of P and a from Tables D.1 through D.6 were substituted into eq. (5.16) to obtain specific $\hat{K}_m(P, a)$ values.

The resulting $\hat{K}_m(P, a)$ are presented in the fifth and sixth columns of Tables D.1 through D.6, as well as plotted for each specimen as a function of the delamination extension $\Delta a = a - a_0$ where a_0 is the initial delamination length of each specimen, measured from the load-line and presented in Table 5.7. The resulting plots are presented as points in Figs. 5.15a and 5.15b for $m = 1$ and $m = 2$, respectively. Note that the initial $\hat{K}_m$ values at $\Delta a = 0$ were obtained from Table 5.22. From both plots it may be observed that both $\hat{K}_1$ and $\hat{K}_2$ increase slightly as the delamination extends. Note that the scales of the ordinate differ in Figs. 5.15a and 5.15b.

The in-plane phase angle $\hat{\psi}$ was calculated by means of eq. (3.19) using the obtained

Table 5.25: The fitting parameters $B_0^{(i)}$ and $B_1^{(i)}$ in eq. (5.16) for $(m = 1, 2)$ for the C-ELS tests.

	m=1		m=2	
	$B_0^{(i)}$ ($\times 10^2$ m$^{-3/2}$)	$B_1^{(i)}$ ($\times 10^4$ m$^{-5/2}$)	$B_0^{(i)}$ ($\times 10^2$ m$^{-3/2}$)	$B_1^{(i)}$ ($\times 10^5$ m$^{-5/2}$)
CELS-2-2	-3.75	4.49	4.28	2.89
CELS-2-3	-3.78	4.32	4.26	2.80
CELS-2-4	-3.92	4.28	4.29	2.77
CELS-2-5	-3.59	4.29	4.21	2.80
CELS-2-6	-3.71	4.24	4.21	2.77
CELS-2-7	-1.43	3.98	4.23	2.84

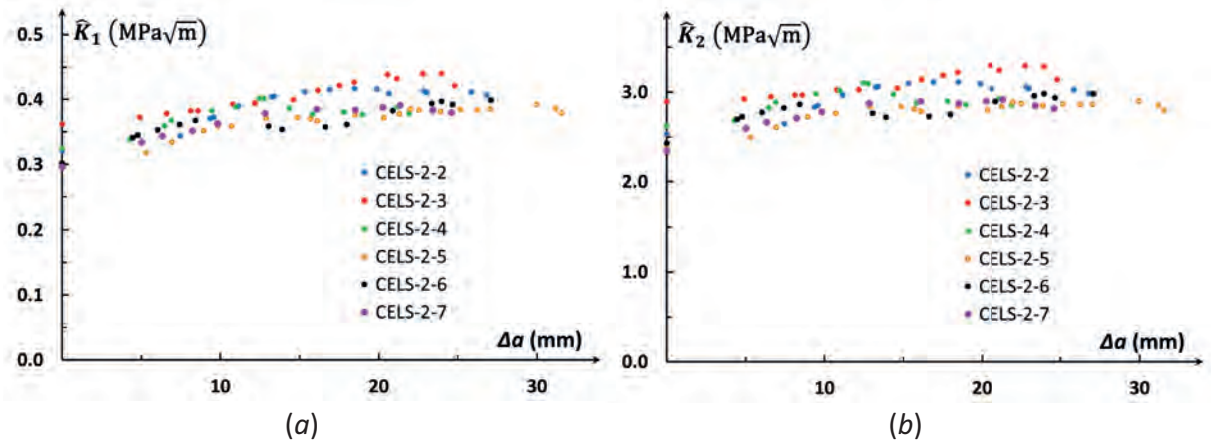

Figure 5.15: Values of $\hat{K}_m$ obtained by means of eq. (5.16) where P and a are shown in Tables D.1 through D.6, as a function of the delamination extension Δa (a) $m = 1$ and (b) $m = 2$.

$\hat{K}_m(P, a)$ $(m = 1, 2)$ values. The resulting $\hat{\psi}$ values are presented in the last column of Tables D.1 through D.6, as well as plotted as a function of the delamination extension Δa, as points, in Fig. 5.16. Note that the scale of the vertical $\hat{\psi}$ axis in this figure is between 1.44 rad and 1.46 rad. From this figure it may be concluded that although a moderate decrease in the $\hat{\psi}$ values was obtained as the delamination extends, the change in the calculated values is very slight and throughout the entire test nearly mode II deformation is dominant.

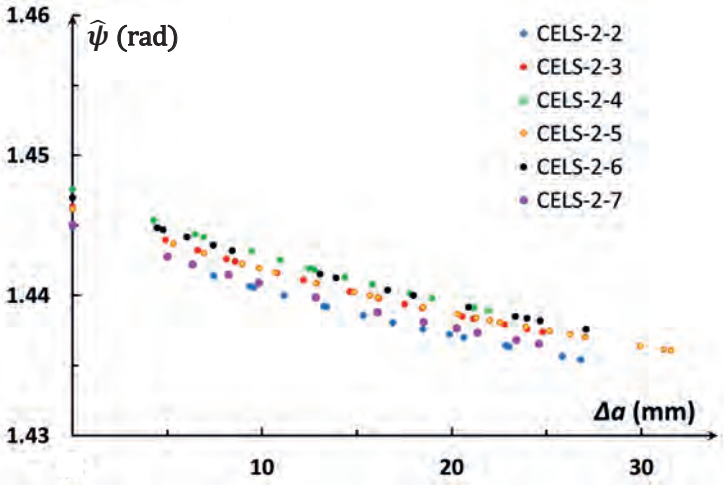

Figure 5.16: Values of $\hat{\psi}$ as a function of the delamination extension Δa; these values were obtained by means of eq. (3.19) with $\hat{K}_m$ $(m = 1, 2)$, shown in Figs. 5.15 and obtained from eq. (5.16) with P and a taken from Tables D.1 through D.6.

5.4 Mixed mode fracture toughness tests - MMELS specimens

Five mixed mode end loaded split (MMELS) specimens were tested quasi-statically with approximately one mixed mode ratio I/II. The test protocol for the MMELS tests is presented in Section 5.4.1. In Section 5.4.2, results from these tests are delineated. Mechanical and thermal three-dimensional FEAs related to the applied load and to the temperature change that the laminate was subjected to during curing were performed for each specimen. These FEAs are described in Section 5.4.3. Also in this section, convergence studies for the mechanical and thermal FEAs are presented. In addition, domain independence was examined for the mechanical and thermal M-integrals.

Stress intensity factors $K_m^{(f)}$ and $K_m^{(r)}$ $(m = 1, 2, III)$ were obtained from the FEAs related to each test by means of the DE method described in Section 3.1, as well as by means of the mechanical and thermal M-integrals presented in Section 3.2. The resulting values were normalized by means of eq. (1.26) with the length scale $\hat{L} = 100$ μm. The normalized values of $\hat{K}_m^{(f)}$ and $\hat{K}_m^{(r)}$ $(m = 1, 2, III)$ were used to determine the mixed mode phase angles $\hat{\psi}$ and ϕ in eqs. (3.19) and (3.20), respectively, through the specimen thickness. By means of these phase angles, the mode mixity of the problem at hand was evaluated. Results from these calculations are presented in Section 5.4.4. Also in this section, the average through the width, along the delamination front, of the critical initiation energy release rate values $\mathcal{G}_{ic}$, as well as the fracture resistance energy values $\mathcal{G}_{iR}$ were obtained and are presented as a function of the delamination extension Δa. These values were determined by means of ECM (ISO-15114:2014(E), 2014), as well as by means of FEA with appropriate post-processors. These calculations, as well as the resulting R-curves determined by means of the two methods are presented and compared in Section 5.4.4.

5.4.1 MMELS test protocol

A test protocol for the MMELS specimen is summarised below based on Blackman et al. (2001). By means of the MMELS test, initiation and propagation resistance energy release rate values from a non-adhesive insert, as well as from a precrack obtained by mixed mode loading, respectively, are to be determined. During the test, the MMELS specimen, shown in Fig. 5.17a, is subjected to mixed mode I/II deformation with a fixed ratio. The ratio for a UD material would be $\mathcal{G}_I/\mathcal{G}_{II} \approx 4/3$. Note that the delamination growth during the test is expected to be stable.

Prior to testing, the MMELS specimen thickness $2h$ and width b illustrated in Fig. 5.17 were measured in the same manner as that described in Section 5.3.1 with higher precision than to the nearest 0.02 mm as recommended by Blackmen et al. (2001). The thickness $2h$

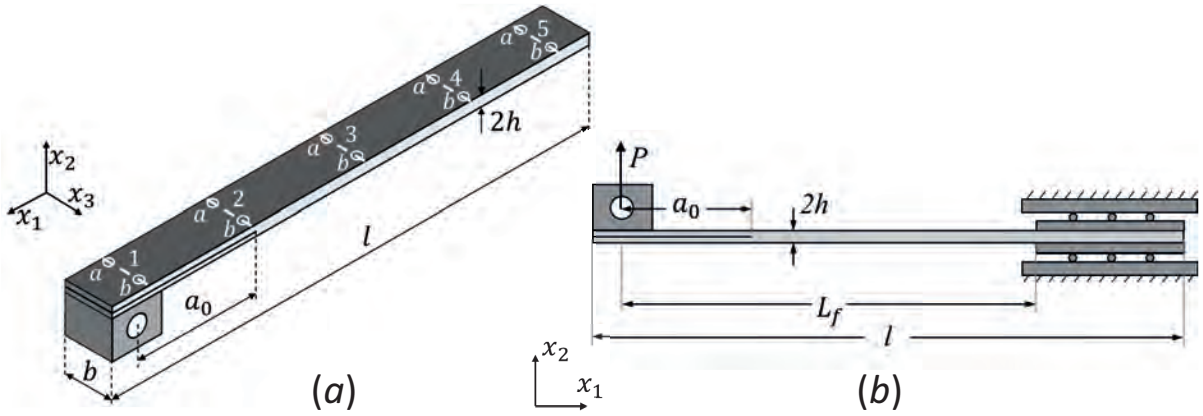

Figure 5.17: Illustration of (a) the MMELS specimen and (b) clamping fixture.

was measured at ten locations and the width b at five locations along the specimen length, as shown in Fig. 5.17a with white circles and white lines, respectively. The thickness $2h$ was measured on each side of the specimen at a distance of approximately 3 mm from the outer specimen edge. It is also recommended in Blackman et al. (2001) that the average values and standard deviations from these measurements would be recorded and not exceed 0.1 mm.

The total length l of the specimens was measured using a ruler to the nearest mm. The recommended specimen total length, shown in Figs. 5.17, is recommended to be $l \geq 170$ mm and $l \geq a_i + 110$ mm (Blackman et al., 2001). The free length L_f illustrated in Fig. 5.17b is typically 100 mm. It may be noted that stability is promoted for $L_f \leq 2.44a$.

With the MMELS specimen, two types of tests are conducted. One is from a PTFE starter film of length a_0, measured from the load-line to the delamination front as shown in Figs. 5.17, the second is a precrack obtained from a mixed mode test. The former stage of the test is referred to here as the artificial crack or AC stage and the latter is the precrack or PC stage. The starter film is 13 μm thick, as recommended. The insert length a_i was measured in the same manner as that described in Section 5.3.1 on the front and back sides of the specimen, a_{if} and a_{ib}, respectively. The length between the load-line and the delamination front a_0, shown in Figs. 5.17 was calculated as the measured a_{if} and a_{ib} values minus half the load block length. The obtained values were averaged to determine the initial insert length a_0 which is also referred to here as a_{0AC}. It is recommended in Blackman et al. (2001) that the differences in length between the two sides a_{if} and a_{ib} would be less than 2 mm. Moreover, it is required that the length between the load-line and the delamination front a_0, shown in Figs. 5.17, would be at least 50 mm implying that $a_i \geq 60$ mm.

After all measurements were completed, in the same manner as performed for the C-ELS specimens and described in Section 5.3.1, both edges of each specimen were coated

with a thin layer of white water based acrylic paint in order to facilitate the detection of delamination growth. After the coating layer was dry, straight vertical lines across the specimen edge were marked every 1 mm for the first 5 mm from the artificial insert tip, then every 5 mm up to 35 mm, and finally, every 1 mm up to 40 mm. For one specimen black spray was applied to the painted surfaces to create speckles to be used for digital image correlation (DIC). One load block with the same width as that of the specimen was attached as illustrated in Fig. 5.17b. It may be noted that the applied displacement is expected to result with $K_2 \geq 0$ for the case of the investigated interface. Note that the UD fabric ply is the upper ply as shown in Fig. 2.1. After all preparations were completed, the same conditioning process as that used for the C-ELS specimens at a temperature of $23^\circ \pm 1^\circ$ C and a relative humidity (RH) of $50\% \pm 3\%$ for at least one week was performed.

In Fig. 5.17b, a schematic illustration of the test apparatus used in the MMELS fracture tests is presented. The same Instron loading machine described in Section 4.3, with a 250 N load cell was used in the tests. Note that for unidirectional (UD) specimens, the load is typically expected to be in the range of 100-200 N (Blackman et al., 2001). The clamping fixture, shown in Fig. 5.17b, is again similar to that in Fig. 5.5b for the C-ELS tests with all relevant descriptions given in Section 5.3.1. The load is applied vertically in displacement control to a pin inserted into the load block as illustrated in Fig. 5.17b. The LaVision system described in Section 4.3, with two cameras, was used. During each test, images of the specimen were acquired from both sides of the specimen, front and back, simultaneously, at a rate of 2 Hz. The synchronized actuator displacement d and load P measured by means of the Instron loading machine were noted on each related image.

The MMELS tests were performed at a temperature of $23^\circ \pm 3^\circ$C and $50\% \pm 10\%$ relative humidity (RH). These conditions are similar to those used for the DCB tests in Chocron and Banks-Sills (2019), as well as in the C-ELS tests described in Section 5.3. It may be noted that in Blackman et al. (2001) it is recommended to perform the tests in accordance with ISO 291 (2008), namely, $23^\circ \pm 2^\circ$C and $50\% \pm 5\%$ RH. Before the AC test stage, the specimen was positioned in the clamping fixture, as shown in Fig. 5.17b so that $L_f = 100$ mm. Quasi-static loading in displacement control was applied to the specimen at a constant cross-head displacement rate of 1 mm/min, until the artificial delamination propagated between 2 and 5 mm. At this point, the test was interrupted and the specimen was unloaded at a displacement rate of 5 mm/min until $P \approx 3$ N. After unloading, the AC (first) stage was complete and the PC (second) stage began. The specimen was reloaded at a displacement rate of 1 mm/min. The precrack initiated and continued to propagate until it arrived within a distance of 10 mm from the clamped end. Then, the specimen was completely unloaded at a constant cross-head rate of 5 mm/min. After the specimen was fully unloaded it was released from the loading machine.

For both stages of the test, load-displacement curves were obtained. In the same manner described in Section 5.3.1, the nonlinear, visual and 5%/max initiation loads at

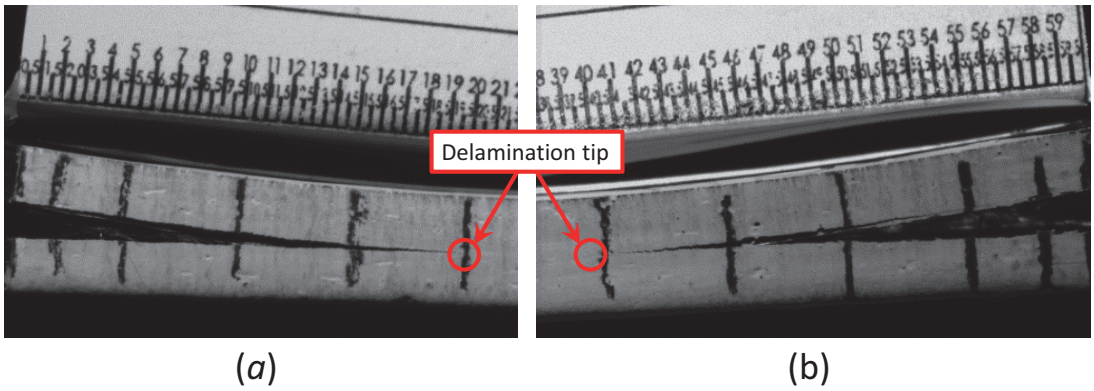

Figure 5.18: An image captured by the LaVision digital camera during the PC (second) stage of the test for specimen MMELS-1-9: (a) front and (b) back sides.

failure, namely, P_{NL}, P_{VIS} and $P_{(5\%/max)}$, were determined for the AC and PC stages of each test.

From the images acquired by means of the LaVision system during the AC (first) stage of the test, the load P_{AC-VIS} and actuator displacement d_{AC-VIS} related to a_{0AC} were determined at initiation. In addition, from this set of images, during the AC stage of the test, just before unloading, the precrack length $a_{0PC-VIS}$ was measured. From the images acquired during the PC (second) stage of the test, the synchronized load P_{PC-VIS} and actuator displacement d_{AC-VIS} related to the measured $a_{0PC-VIS}$, were determined at initiation of the natural precrack. In addition, from the LaVision images captured during the PC stage of the test, just before unloading, a_f which is the final delamination length was measured. Since two cameras were used, the delamination length values were measured on the front (f) and back (b) sides of the specimen. If the difference between these delamination length values was larger than 2 mm for $a_{0PC-VIS}$ or a_f, the tested specimen should be dismissed, as recommended in Blackman et al. (2001).

In addition, from the images acquired by means of the LaVision system during the PC test stage, the delamination length values a, as the delamination extended, were measured and the synchronized load P and actuator displacement d were noted. An example of images captured by the LaVision digital cameras during the PC (second) stage of the test for specimen MMELS-1-9 are presented in Figs. 5.18a and 5.18b from the front and back sides of the specimen, respectively. The delamination extension Δa, defined as

$$\Delta a = a - a_{0AC} \tag{5.19}$$

was measured from such images by means of the ImageJ software (2015) between the right end of the PTFE film and the extended delamination tip, on both specimen sides. In eq. (5.19), a is the total extended delamination length measured from the load-line and a_{0AC} is the initial insert length which was measured before the AC stage by means

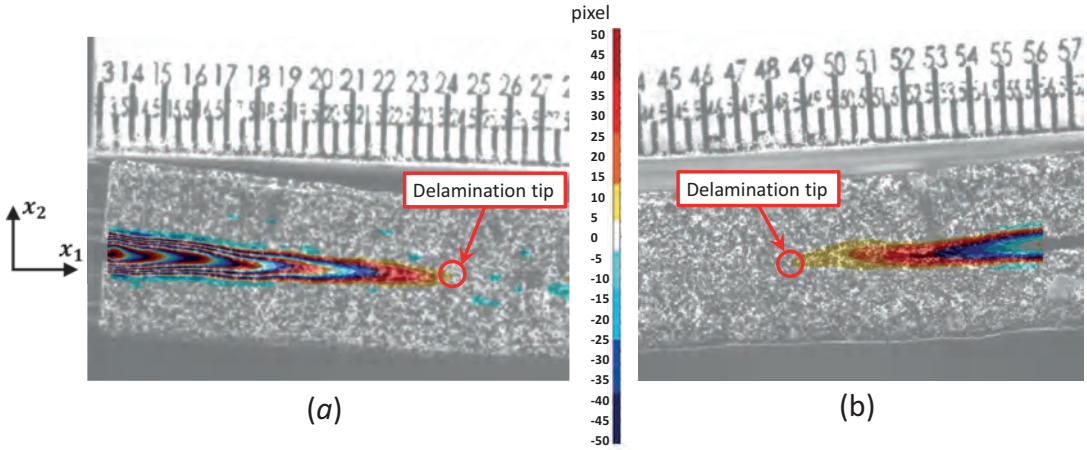

Figure 5.19: Images captured by the LaVision digital camera during the PC (second) stage of the test for specimen MMELS-1-18 with the strain distribution determined with DIC and used to detect the delamination tip: (a) front and (b) back sides of the specimen.

of the confocal microscope. To determine a as the delamination extended, the measured Δa value was added to the initial delamination length a_{0AC}.

In Figs. 5.19a and 5.19b, images of the front and back sides of specimen MMELS-1-18 are shown, respectively. To this specimen, prior to testing, speckles were spread over the front and back sides of the painted surfaces of the specimen. By means of DaVis (2015) software, the digital image correlation (DIC) method was employed to enable detection of the delamination tip from the images of the specimen acquired during the test. Note that the displacement and strain fields obtained by means of DIC were not analyzed quantitatively. It may also be noted that since it was possible to detect the delamination tip from the images without use of DIC, and since it was found that determining the delamination tip using this method takes a longer time but is not necessarily more accurate, DIC was only employed for specimen MMELS-1-18. In Figs. 5.19, the strain field in the x_2- direction, is presented for the front and back sides of the specimen. For this specimen, the delamination length values $a_{0PC-VIS}$ and a, were determined from the images with the DIC results. The values $a_{0PC-VIS}$ and a measured from the front and back sides of the specimen were averaged and used with the related synchronized P_{VIS} and d_{VIS} values to obtain stress intensity factors, phase angles, as well as the critical and resistance energy release rate values as a function of the delamination extension Δa.

Three-dimensional FE mechanical and thermal analyses related to the AC (first) stage of the test were performed for each specimen. For this stage, the load P_{AC-VIS} obtained visually from the related a_{0AC}, was applied in each analysis. Note that the critical initiation values related to the nonlinear and 5%/max loads, P_{NL} and $P_{(5\%/max)}$, respectively, were obtained as will be explained in the sequel. The global response of the load-displacement curve obtained by means of the mechanical FEAs was compared to that measured from the test in order to evaluate the correspondence between the two. The FEA results were

then used to calculate the stress intensity factors $K_1^{(f)}$, $K_2^{(f)}$ and $K_{III}^{(f)}$, resulting from the applied load, as well as $K_1^{(r)}$, $K_2^{(r)}$ and $K_{III}^{(r)}$, resulting from residual stresses which were obtained during the curing process, where the composite was subjected to a thermal change. The mechanical and residual stress intensity factors were determined through the width of each specimen by means of the DE method, described in Section 3.1, as well as by means of the mechanical and thermal M-integrals, described in Section 3.2. Note that the DE method was used for verification of the results obtained by the mechanical and thermal M-integrals. The resulting mechanical and residual stress intensity factors were superposed to obtain the total stress intensity factors $K_1^{(T)}$, $K_2^{(T)}$ and $K_{III}^{(T)}$. These were normalized by means of eq. (1.26) with the length parameter $\hat{L} = 100$ μm to obtain real instead of complex units.

Based on the obtained $\hat{K}_1^{(T)}$, $\hat{K}_2^{(T)}$ and $K_{III}^{(T)}$ values, the phase angles $\hat{\psi}$ and ϕ were calculated through the width of each specimen by means of eqs. (3.19) and (3.20), respectively. These phase angles are related to the in-plane and out-of-plane to in-plane mode mixities. In addition, the initiation critical energy release rate $\mathcal{G}_{ic}$ values at $\Delta a = 0$ for each specimen through the specimen width were determined by means of eq. (3.17). For all calculated parameters, namely, $\hat{K}_m^{(T)}$ ($m = 1, 2$ and III), $\hat{\psi}$, ϕ and $\mathcal{G}_{ic}$, the trend through the specimen width was observed and discussed. In addition, an integrated average for each of these parameters was evaluated.

In order to determine the resistance energy release rate $\mathcal{G}_{iR}$ as a function of the delamination extension Δa, in the same manner described in Section 5.2 for the DCB specimens, two analysis methods were employed. The first, similar to that used in Chocron and Banks-Sills (2019), was based on the M-integral, and the second, was based on ECM (ISO-15114:2014(E), 2014). With the M-integral, for each specimen, six mechanical FEAs and one thermal FEA were performed. In the six mechanical FEAs, a different delamination length was used for each analysis, namely, $a = 40$ mm, 50 mm, 60 mm, 70 mm, 80 mm and 90 mm. For all analyses, the applied load was set to $P = 1$ N. The displacement fields obtained from these analyses were used with the three-dimensional mechanical M-integral described in Section 3.2 to obtain six data sets of $K_m^{(f)}$ ($m = 1, 2, III$), each related to a specific value of a. Each data set is composed of forty $K_m^{(f)}$ values along the delamination front. Hence, for each specimen, data points in the three-dimensional space $(K_m^{(f)}, a, x_3)$ were obtained. Surfaces of the form given in eq. (5.1) were fit through these data sets for $m = 1, 2, III$ and the fitting parameters p_{i0} and p_{j1} ($i = 0, 1, .., 5$ and $j = 0, 1, .., 4$) were obtained. The values of the delamination length a, measured from the test, were substituted into eq. (5.1) to obtain expressions of $K_m^{(f)}$ as a function of x_3.

One thermal analysis was performed for each specimen with an applied temperature $\Delta\vartheta_i$ calculated by means of eq. (5.2). Since the effect of the delamination length on the thermal stress intensity factors was found to be negligible, as was shown in Chocron and Banks-Sills (2019), and will be shown again in the sequel, only one delamination

length $a = 70$ mm was used for all thermal analyses. By means of the thermal M-integral, described in Section 3.2, with the displacement field obtained from each thermal FEA, one set of stress intensity factors $K_m^{(r)}$ $(m = 1, 2, III)$, resulting from residual curing stresses, along the delamination front were obtained. A fourteenth order polynomial curve fit of the form shown in eq. (5.3) was obtained and the fifteen fitting parameters b_i $(i = 0, 1, ..., 14)$ were determined for each specimen.

The expressions obtained from eq. (5.1) for specific measured values of a for $K_m^{(f)}$ as a function of x_3, and the expressions obtained from eq. (5.3) as a function of x_3 were superposed to determine an expression of the form in eq. (5.4). This expression relates the total stress intensity factors $K_m^{(T)}$, for all delamination lengths a, to x_3 where x_3 is a point along the width of the specimen. In eq. (5.4), the load P, associated with each measured delamination length a, was used. For each measured delamination length a, the resistance energy release rate $\mathcal{G}_{iR}$ as a function of x_3 was expressed by means of eq. (3.17) with use of eq. (5.4). Finally, the expression for $\mathcal{G}_{iR}$ was integrated through the width of the specimen, as shown in eq. (5.5), to obtain the average $\overline{\mathcal{G}}_{iR}$ value related to each delamination length a. In addition, the initiation critical energy release rate values $\mathcal{G}_{ic}$, related to the nonlinear, visual and 5%/max initiation loads at failure, P_{NL}, P_{VIS} and $P_{(5\%/max)}$, respectively, of the AC (first) test stage were obtained by means of eq. (5.5) with $a = a_{0AC}$. The $\mathcal{G}_{ic}$ values obtained from eq. (5.5) for P_{VIS} were compared and validated with the values obtained previously from the AC FEAs and the mechanical and thermal M-integrals. This validation gave confidence in the results obtained for all measured delamination length values a.

The ECM method (ISO-15114 standard, 2014, Blackman et al., 2001) described and applied in Section 5.2 for the DCB specimens and applied in Section 5.3 to the C-ELS specimens, was chosen to be used here for the MMELS test results in order compare local and global methods for obtaining a resistance curve for one mixed mode deformation ratio. The load P and actuator displacement d associated with the measured delamination length a were used in eq. (5.12) to calculate the specimen compliance. The resulting values of C, as well as the related measured delamination length values a were substituted into eq. (5.8) to obtain the fitting parameters m and C_0. The obtained value of m, as well as the measured values of a, P and d for each test were then substituted into eq. (5.9) to obtain $\mathcal{G}_{iR}$ values as a function of the delamination extension Δa.

For the values obtained by means of each method, a power law fit of the form given in eq. (5.6) between the initial critical interface energy release rate $\mathcal{G}_{ic}$ and the steady state value $\mathcal{G}_{iss}$ for $\Delta a = \Delta a_{iss}$, was used to determine two R-curves. Note that Δa_{iss} is the initial delamination extension value related to steady state $\mathcal{G}_{iss}$; this latter value was calculated as the average of all J or $\mathcal{G}_{iR}$ values obtained for $\Delta a \geq \Delta a_{iss}$. The fitting parameter A_1 in eq. (5.6) was obtained for each set of data points, related to each method, in the same manner as described in Section 5.3.1. This was performed by means of the

Table 5.26: MMELS specimen measurements: thickness $2h$, width b and artificial delamination length a_0, shown in Fig. 5.17a.

specimen no.	$2h_{1a}$ (mm)	$2h_{1b}$ (mm)	$2h_{2a}$ (mm)	$2h_{2b}$ (mm)	$2h_{3a}$ (mm)	$2h_{3b}$ (mm)	$2h_{4a}$ (mm)	$2h_{4b}$ (mm)	$2h_{5a}$ (mm)	$2h_{5b}$ (mm)	$\overline{2h}$ (mm)	SD (mm)
MMELS-1-9	4.88	4.92	4.84	4.82	4.88	4.82	4.78	4.75	4.60	4.62	4.79	0.108
MMELS-1-11	4.87	4.83	4.68	4.82	4.83	4.75	4.84	4.88	4.64	4.63	4.78	0.093
MMELS-1-12	4.94	4.91	4.80	4.83	4.93	4.85	4.74	4.79	4.67	4.64	4.81	0.105
MMELS-1-17	4.92	4.93	4.73	4.79	4.70	4.76	4.67	4.75	4.67	4.67	4.76	0.098
MMELS-1-18	5.00	4.96	4.81	4.80	4.88	4.75	4.88	4.82	4.64	4.67	4.82	0.116

specimen no.	b_1 (mm)	b_2 (mm)	b_3 (mm)	b_4 (mm)	b_5 (mm)	$\overline{b}$ (mm)	SD
MMELS-1-9	19.87	19.88	19.93	19.72	19.90	19.86	0.071
MMELS-1-11	19.97	19.92	19.90	19.98	19.93	19.94	0.031
MMELS-1-12	19.77	19.91	19.90	19.97	19.82	19.87	0.072
MMELS-1-17	19.85	19.87	19.80	20.10	20.32	19.99	0.196
MMELS-1-18	19.71	19.73	19.71	19.82	19.89	19.77	0.072

specimen no.	a_{0f} (mm)	a_{0b} (mm)	Δa_0 (mm)	a_{0AC} (mm)
MMELS-1-9	52.12	52.27	-0.15	52.20
MMELS-1-11	51.34	51.89	-0.55	51.62
MMELS-1-12	51.66	51.29	0.37	51.47
MMELS-1-17	50.74	50.47	0.27	50.60
MMELS-1-18	50.41	50.53	-0.12	50.47

GRG software of Excel (2016) with the parameter B expressed in the fitting by means of eq. (5.10). For a minimum value of the RMSE, the value of A_1 was determined.

In addition, the phase angle $\hat{\psi}$ as a function of the delamination extension, through the specimen width, was also calculated. The values of $K_m^{(T)}$ from eq. (5.4) for every measured delamination length were normalized by means of eq. (1.26) with $\hat{L} = 100$ μm and substituted into eq. (3.19). From the results, values of $\hat{\psi}$ as a function of the delamination extension Δa were obtained. Note that since the phase angle ϕ was found to be antisymmetric through the specimen width, an integrated average of this parameter results in zero. Hence, the value of the integrated average ϕ as a function of the delamination extension was not examined.

5.4.2 MMELS test results

Five MMELS specimens were tested quasi-statically. The protocol in Section 5.4.1 was used in all tests. Each specimen is denoted as MMELS-R-C where the parameters R and C, shown in Fig. 5.1, denote the row and column location of the specimen in the plate, respectively.

As described in Section 5.4.1, prior to testing, each specimen width b and thickness $2h$ were measured at the locations marked in Fig. 5.17a. Results from these measurements, as well as the average values and standard deviations (SDs) are presented in Table 5.26. Note

Table 5.27: Average temperature ϑ_i and relative humidity (RH) measured during the MMELS tests for specimen i.

specimen no.	ϑ_i °C	RH (%)
MMELS-1-9	24.0	43.2
MMELS-1-11	24.3	41.3
MMELS-1-12	24.6	40.6
MMELS-1-17	22.4	41.6
MMELS-1-18	22.4	49.6

that for all MMELS specimens tested, it may be observed that the maximum difference between the thickness measurements are in the range 0.25 mm to 0.36 mm which may be a result of the wet-layup manufacturing process. These variations are greater than 0.1 mm; hence they do not fulfill the requirements recommended in Blackman (2001) and described in Section 5.4.1. In addition, it may be noted that the variation in the width b is between 0.08 mm and 0.52 mm.

For each specimen, the delamination length values a_{if} and a_{ib} were measured. The measurements were performed as described in Section 5.4.1 between the specimen edge and the delamination front, on both sides of the specimen. In addition, the length of each load block was also measured. Half of the obtained value was subtracted from a_{if} and a_{ib} to obtain a_{0f} and a_{0b}, respectively. The resulting a_{0f} and a_{0b} values are presented in Table 5.26. The difference Δa_0 between a_{0f} and a_{0b}, as well as the average of the two values a_{0AC}, are also presented in this table. It may be observed that the differences between the two sides for all specimens are less than 2 mm which meets the recommendations in Blackman et al. (2001). In addition, the length of the specimens l shown in Fig. 5.17 was measured as 200 mm for all specimens. This value also meets the recommendation in Blackman et al. (2001). For each specimen the temperature ϑ_i and relative humidity (RH) were measured every 5 minutes throughout the test. The measured values were averaged and are presented in Table 5.27. It may be observed that all tests were performed at 23° ± 3°C and 50%±10% relative humidity (RH) which meet the recommendations discussed in Section 5.4.1.

Load-displacement curves for the AC and PC stages of all five MMELS specimens tested are presented in Figs. 5.20a and 5.20b, respectively. In addition, in the sixth and seventh columns in Table 5.28, the stiffnesses K_{AC} and K_{PC} related to the AC and PC stages of each test for each specimen, respectively, are presented. These values were determined as the slope of the loading portion of each curve in Figs. 5.20a and 5.20b. Also in Table 5.28, the average values $\overline{2h}$, $\overline{b}$ and a_{0AC} from Table 5.26 are presented in the second through fourth columns. Values of $a_{0PC-VIS}$ which were measured from the LaVision images, as described in Section 5.4.1, are presented in column five of this table. Note that $\hat{L}_f$ was chosen to be 100 μm in both stages for all tested specimens.

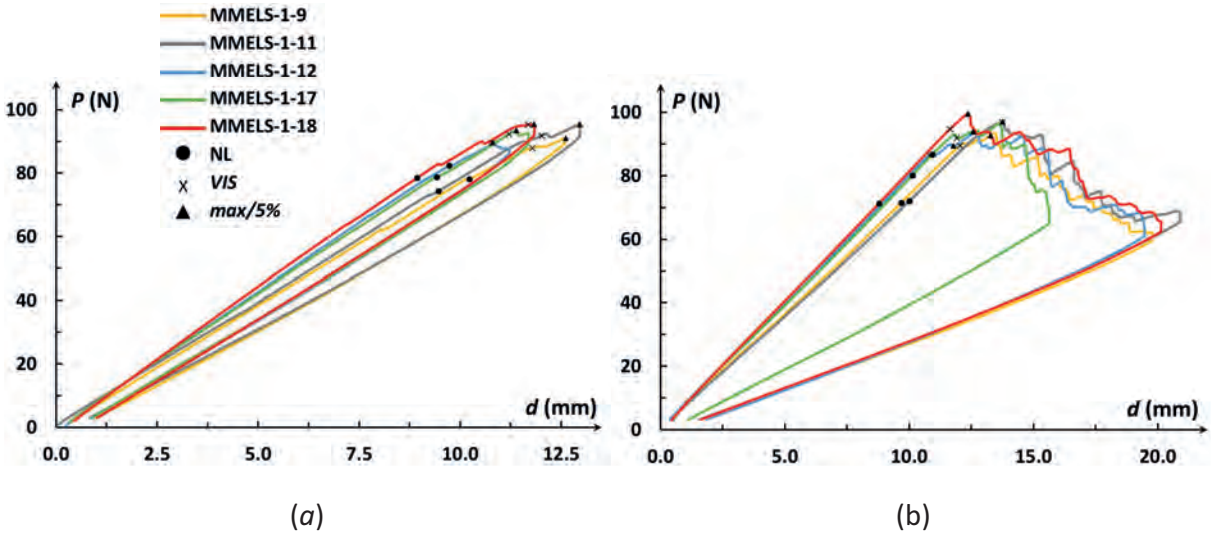

Figure 5.20: Load-displacement curves for the MMELS tests: (a) AC stage and (b) PC stage.

The stiffnesses obtained from both stages of the test was compared. Recall that such a comparison was not possible for the case of the tested C-ELS specimens described in Section 5.3 since there a different value of L_f was chosen for each specimen and test stage. It may be observed that for all specimens the stiffness measured in the PC stage of the test is slightly lower than that observed in the AC stage. This decrease in the measured stiffness is related to the increase of the initial delamination length in the PC stage as compared to that of the AC stage, namely $a_{0PC-VIS} > a_{0AC}$. Also, it may be observed from Figs. 5.20a and 5.20b, as well as from the calculated stiffnesses K_{AC} and K_{PC} in Table 5.28 that specimens MMELS-1-9 and MMELS-1-11 are less stiff than the other specimens in both test stages. A possible reason for these differences may be inhomogeneities of the material which were caused by the wet-layup manufacturing process.

Table 5.28: Measured dimensions of the five MMELS tested specimens including the averaged thickness $\overline{2h}$ and width $\overline{b}$, the delamination length at initiation of the AC (first) and PC (second) stages, a_{0AC} and $a_{0PC-VIS}$, respectively, as well as the stiffness K_{AC} and K_{PC} of the linear loading portion of the load-displacement curves measured from the test and presented in Figs. 5.20.

Specimen no.	$\overline{2h}$ (mm)	$\overline{b}$ (mm)	a_{0AC} (mm)	$a_{0PC-VIS}$ (mm)	K_{AC} (N/mm)	K_{PC} (N/mm)
MMELS-1-9	4.79	19.9	52.2	55.5	7.7	7.3
MMELS-1-11	4.78	19.9	51.6	58.1	7.9	7.2
MMELS-1-12	4.81	19.9	51.5	55.2	8.5	8.0
MMELS-1-17	4.76	20.0	50.6	54.3	8.4	7.9
MMELS-1-18	4.82	19.8	50.5	56.5	8.8	8.1

Table 5.29: Initiation non-linear, visual and 5/%max loads P_{NL}, P_{VIS} and $P_{5\%/max}$, respectively, and the related actuator displacements d_{NL}, d_{VIS} and $d_{5\%/max}$, respectively, obtained from the AC (first) and PC (second) stages of the MMELS tests.

specimen no.	AC test stage						PC test stage					
	P_{NL} (N)	P_{VIS} (N)	$P_{5\%/max}$ (N)	d_{NL} (mm)	d_{VIS} (mm)	$d_{5\%/max}$ (mm)	P_{NL} (N)	P_{VIS} (N)	$P_{5\%/max}$ (N)	d_{NL} (mm)	d_{VIS} (mm)	$d_{5\%/max}$ (mm)
MMELS-1-9	78.2	87.8	91.0	10.2	11.8	12.6	71.5	89.5	92.7	9.7	12.0	13.3
MMELS-1-11	74.3	91.8	95.4	9.5	12.0	13.0	72.1	96.9	97.0	10.0	13.7	13.8
MMELS-1-12	82.4	89.6	89.6	9.7	10.8	10.8	86.8	86.5	89.4	10.9	10.8	11.8
MMELS-1-17	78.8	92.2	93.4	9.4	11.2	11.4	80.1	91.9	93.9	10.1	11.9	12.6
MMELS-1-18	78.4	95.3	95.4	8.9	11.7	11.8	71.3	94.7	99.5	8.8	11.7	12.4
average	78.4	91.4	93.0	9.6	11.5	11.9	76.4	91.9	94.5	9.9	12.0	12.8
SE	1.28	1.27	1.17	0.21	0.22	0.39	3.08	1.84	1.75	0.35	0.48	0.35
CV (%)	1.6%	1.4%	1.3%	2.2%	1.9%	3.3%	4.0%	2.0%	1.9%	3.5%	3.9%	2.7%

Values of P_{NL}, P_{VIS} and $P_{5\%/max}$, as well as the related values of d_{NL}, d_{VIS} and $d_{5\%/max}$ from the AC and PC stages of the MMELS tests are presented for each specimen in Table 5.29. These values are also indicated on each curve in Figs. 5.20a and 5.20b. The average values of all specimens, as well as the standard errors (SEs) and coefficients of variation (CV) are presented at the last three rows in this table.

It may be observed from Figs. 5.20a and 5.20b that the loading portion of the load-displacement curves of the AC stage exhibit a small curvature. This phenomenon does not appear in the corresponding plots of the PC stage of the test. Recall that similar behavior was observed in the load-displacement curves related to the C-ELS tests shown in Fig. 5.9. This behavior may indicate that during the AC (first) loading stage, a process zone was evolving near the insert front. Once the delamination initiated, this process zone was fully evolved. As a result, during the PC (second) loading stage, linearity was obtained. It may be noted that the values of P_{NL}, P_{VIS} and $P_{5\%/max}$ for the AC stage in Table 5.29 are similar to those of the PC stage, resulting with similar average values for both stages. The average values obtained for P_{VIS} and $P_{5\%/max}$ are slightly lower for the AC stage than for the PC stage; whereas, the average P_{NL} value obtained for the AC stage is slightly higher than that for the PC stage. It is interesting to note that opposite behavior was obtained for the initial loads in the AC and PC stages of the C-ELS tests, given in Tables 5.9 and 5.11, respectively, with larger and more pronounced differences. In addition, it may be observed from Table 5.29 that for all parameters presented, namely, P_{NL}, P_{VIS} and $P_{5\%/max}$, as well as d_{NL}, d_{VIS} and $d_{5\%/max}$, the CV values obtained are quite similar and less than 5%.

As the delamination propagated, values of a were measured from the load-line to the delamination tip by means of ImageJ (2015) software, as described in Section 5.4.1, from images captured using the LaVision system during the PC test stage. From each measured image, the related synchronized load P and actuator displacement d were also obtained. In Tables E.1 through E.5, the measured values of a, P and d are presented

Table 5.30: Values of m and C_0 used in eq. (5.8) and (5.9) for each MMELS test based on a linear fit to the data of a^3 verses C in Tables E.1 through E.5.

specimen no.	C_0 ($\times 10^{-2}$ mm/N)	m ($\times 10^{-7}$/(mm^{2}N))
MMELS-1-9	8.47	3.11
MMELS-1-11	8.54	3.04
MMELS-1-12	8.09	2.89
MMELS-1-17	7.43	2.76
MMELS-1-18	7.26	3.08

for each specimen. In addition, for each specimen and for every measured delamination length, the compliance values C were calculated using eq. (5.12). The obtained values of C, related to each measured delamination length are also presented in these tables. Using the data points (C, a^3), the slope and intercept m and C_0, respectively, in eq. (5.8), were obtained for each specimen, as described in Section 5.3.1. The obtained values for each specimen are presented in Table 5.30. In order to capture the delamination extension which was out of the frame, the two cameras on both sides of specimen MMELS-1-18 were shifted during the test. Recall that the delamination length values a were measured for this specimen using DIC, whereas for the rest of the specimens these values were measured by means of ImageJ (2015) software. During the shifting, some data was lost. An attempt was made to measure the delamination length values after the cameras were shifted, but the value of m which was obtained when accounting for these values was high with respect to the value of m measured for the other specimens. In order to avoid inaccuracies resulting from this measurement, only values measured up to $\Delta a = 15.6$ mm, before the cameras were shifted, were used to determine m for this specimen.

5.4.3 MMELS FE model, convergence and domain independence

In this section, mesh convergence for the MMELS mechanical and thermal FEAs is presented. In addition, domain independence for the mechanical and thermal M-integrals is examined. Thermal analyses were performed for three delamination length values to account for the residual curing stresses. This was done to examine the variation of $K_m^{(r)}$ for different delamination lengths.

Three-dimensional FEAs were performed with Abaqus (2017) and convergence of the two different problems, mechanical and thermal, was examined. In the former, a load was applied to the MMELS specimen, and in the latter, a change in temperature was considered. In Figs. 5.21a and 5.21b, three-dimensional and two-dimensional views of the mechanical three-dimensional FE model are presented, respectively. For the mechanical FEA, a load of 91.9 N was applied perpendicular to the delamination, as shown in Fig. 5.21b, and distributed along the specimen width $\overline{b}$. The load was applied to nodes

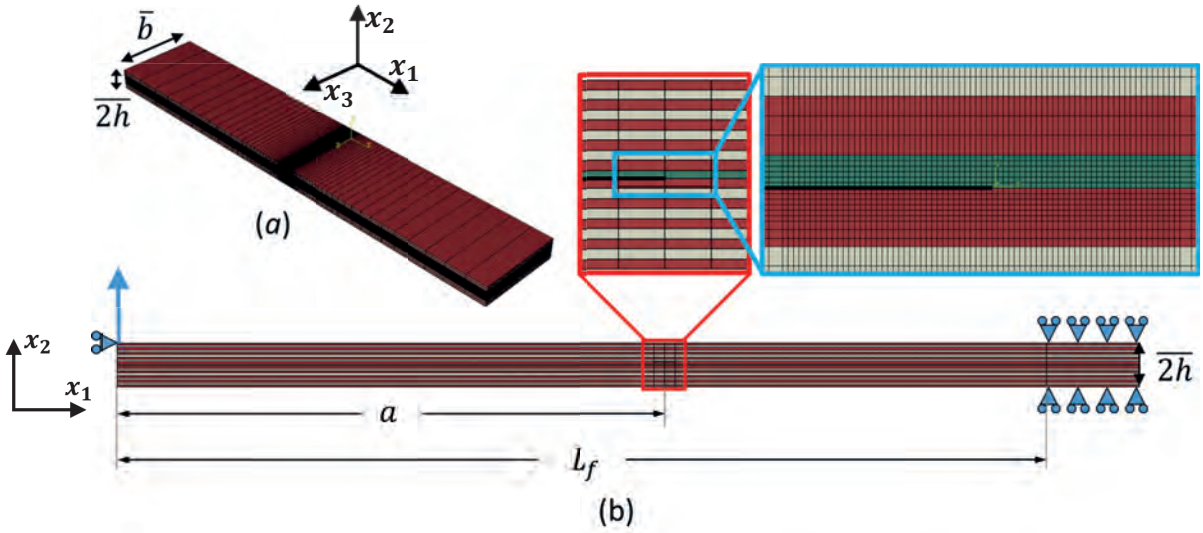

Figure 5.21: (a) Three-dimensional illustration of the MMELS fine FE model and (b) two-dimensional illustration of the MMELS fine FE model including boundary conditions with a focused view of the ply distribution in the red frame and a focused view of the elements near the delamination front in the blue frame.

along the upper surface of the upper arm of the MMELS specimen, deforming them upward at a distance a from the delamination front, as shown in Fig. 5.21b. Note that the free edge of the specimen which is attached to the posterior half of the load block has been removed from the model. In addition, 10 mm of the clamp, shown in Fig. 5.17b, was modeled instead of 50 mm. This was to lower the number of elements used. The degrees of freedom in the region of the clamp in the x_2 and x_3- directions were fixed, and the specimen was free to slide in the x_1-direction, as illustrated in Fig 5.21b. To verify that omission of this part in the model does not affect the results, an additional model with the total clamp length was also analyzed. It was found that the stress and displacement fields obtained in the delamination front region from both analyses are nearly the same. It may be noted that the total length $l = L_f + 10$ mm of the model shown in Fig. 5.21 is not the total measured length l of the specimen in Fig. 5.17, since the posterior half of the load block, as well as part of the clamping fixture were omitted. For the thermal FEAs, a temperature difference was imposed as calculated in eq. (5.2), where $\vartheta_i = 22.5°\text{C}$, which is within the range of values presented in Table 5.27, was used, resulting with $\Delta\vartheta_i = -67.5°\text{C}$.

The dimensions of the model in the mechanical and thermal analyses were the same. The width $\bar{b}$ and thickness $\overline{2h}$ of specimen MMELS-1-17, given in Table 5.28, were used in the model with $a = 59$ mm and $L_f = 100$ mm. Each ply was modeled separately with ten plies above the interface and nine plies below it, as shown in Fig. 5.21b. The effective material properties in Tables 5.3 and 5.4 for the UD fabric and for the $+45°/-45°$ and $0°/90°$ woven fabrics, respectively, were employed. Since the MMELS specimens were manufactured from the same plate used in Chocron and Banks-Sills (2019) for the DCB

Table 5.31: Three meshes which were used in a convergence study of the MMELS specimen.

	no. of elements	no. of nodes	element size near delamination tip (mm^2)
coarse	169,920	718,369	$0.0483 \times 0.0483 \times 0.5$
fine	277,200	1,163,221	$0.02417 \times 0.02417 \times 0.5$
finest	569,520	2,369,797	$0.01208 \times 0.01208 \times 0.5$

specimens, the thickness of the UD ply in the MMELS model was set to $h_0^{(1)} = 0.145$ mm which is the same as that modeled for the DCB specimens in that study. The thickness of each of the remaining eighteen woven plies was calculated as

$$h_{45} = \frac{\overline{2h} - h_0^{(1)}}{18} \quad . \tag{5.20}$$

A focused view of the modeled plies is presented in the red frame in Fig. 5.21b with the UD fabric illustrated in green and the $+45°/-45°$ and $0°/90°$ woven fabrics illustrated in red and white, respectively.

Three different meshes were used in the mechanical and thermal convergence studies, namely, coarse, fine and finest. For all three meshes, along the width $\overline{b}$ of the specimen, in the x_3- direction, the mesh was composed of forty elements. A description of each mesh, including the amount of elements, nodes and smallest element dimensions, is presented in Table 5.31. Both the mechanical and thermal models were composed of twenty-noded, isoparametric, quadratic brick elements of type C3D20. Near the delamination front, quarter-point elements were used, as well as a denser mesh, to model the square-root, oscillatory singularity. In addition, along the delamination front, elements with an in-plane aspect ratio of 1×1 were used for each mesh. In the same manner performed for the C-ELS specimen described in Section 5.3.3, in order to obtain such elements, the woven ply was partitioned into two layers, as shown in the focused view in the blue frame in Fig. 5.21b. The properties of both layers were described by means of the properties for the $+45°/-45°$ woven fabric in Table 5.4. The thickness of the upper layer was chosen to be $h_{45}^{(1)} = h_0^{(1)}$. In this way, the UD ply and the upper layer of the lower woven ply near the delamination have the same thickness and meshed with elements of the same size.

From the mechanical and thermal FEAs, the displacement fields were obtained and used in the mechanical and thermal M-integrals, respectively, described in Section 3.2, to determine stress intensity factors resulting from applied mechanical loads, as well as from residual thermal curing stresses. It may be noted that in the case of the MMELS specimens, the stress intensity factors resulting from residual curing stresses at mid-width of the specimen were found to be significantly lower than those resulting from mechanical applied load, whereas, the differences obtained near the specimen edges were larger. Hence, unlike the case of the C-ELS specimens, here the residual curing stresses were accounted for in the analyses of the test results. Convergence of the obtained mechanical and residual

Table 5.32: Largest relative difference (LRD), in absolute value, between stress intensity factors obtained by means of mechanical and thermal M-integrals along the delamination front with $0.0375 \leq x_3/\bar{b} \leq 0.9625$, for pairs of meshes for mechanical and thermal MMELS FEA results.

	mechanical model LRD (%)						thermal model LRD (%)					
meshes	coarse and fine			fine and finest			coarse and fine			fine and finest		
domain	$K_1^{(f)}$	$K_2^{(f)}$	$K_{III}^{(f)}$	$K_1^{(f)}$	$K_2^{(f)}$	$K_{III}^{(f)}$	$K_1^{(r)}$	$K_2^{(r)}$	$K_{III}^{(r)}$	$K_1^{(r)}$	$K_2^{(r)}$	$K_{III}^{(r)}$
1	2.0%	1.4%	0.4%	1.6%	0.8%	0.2%	4.3%	17.7%	0.3%	3.5%	12.8%	0.2%
2	0.0%	0.2%	0.2%	0.1%	0.1%	0.2%	0.3%	12.1%	0.1%	0.4%	7.6%	0.2%
3	0.0%	0.1%	0.2%	0.0%	0.1%	0.2%	0.3%	7.4%	0.1%	0.1%	3.7%	0.1%
4	-	-	-	0.0%	0.1%	0.1%	-	-	-	0.4%	3.3%	0.1%
5	-	-	-	0.0%	0.1%	0.1%	-	-	-	0.5%	3.2%	0.1%
6	-	-	-	0.0%	0.1%	0.1%	-	-	-	0.6%	3.3%	0.1%

stress intensity factors was examined for the three meshes. Between $x_3/\bar{b} = 0.0375$ and $x_3/\bar{b} = 0.9625$, the relative differences between the stress intensity factors, for each pair of meshes and for each problem type, were calculated by means of eq. (3.31) with (1) being the results for the coarser mesh and (2) for the finer. In Table 5.32, the largest relative differences (LRD), in absolute value, calculated between the stress intensity factors are presented. For both the mechanical and thermal cases, convergence is observed as the meshes become finer. As a result of the singularity, the results obtained for the first domain are less accurate as compared to the other domains. This may be observed in Table 5.32 where a significant decrease in the LRDs is observed for the rest of the domains. It may be observed that for the thermal results, the LRDs, in absolute value, are larger than in the mechanical case. In addition, it is pointed out that even though convergence was reached, since the obtained $K_2^{(r)}$ values are quite small, the calculated relative differences between the fine and finest meshes for this parameter are approximately 3% in domains three through six for thermal case. Based on the convergence results obtained, for both the mechanical and thermal cases, it appears that convergence has been reached for the fine mesh. Hence, it was chosen to be used in the remainder of this investigation. The model shown in Figs. 5.21a and 5.21b was used for all specimens and the data of the mesh is presented in the third line of Table 5.31.

In addition to the convergence study, domain independence was examined for the chosen fine mesh for both the mechanical and thermal M-integrals. In Table 5.33, the largest relative differences (LRD), in absolute value, calculated by means of eq. (3.31) with (1) indicating the stress intensity factors obtained for the smaller domain and (2) the stress intensity factors obtained for the larger one. Since the largest relative differences calculated between domains three through six for the mechanical cases are lower than 0.5%, it may be concluded from this comparison that domain independence was achieved. For the thermal case, it is more difficult to show domain independence since the obtained values are relatively small. However for the in-plane stress intensity factors, differences of

Table 5.33: Largest relative difference (LRD), in absolute value, calculated by means of eq. (3.31) between the stress intensity factors obtained for adjacent domains of the fine mesh by means of mechanical and thermal M-integrals along the delamination front at $0.0375 \leq x_3/\overline{b} \leq 0.9625$.

	mechanical LRD (%)			thermal LRD (%)		
domains	RD($K_1^{(f)}$)	RD($K_2^{(f)}$)	RD($K_{III}^{(f)}$)	RD($K_1^{(r)}$)	RD($K_2^{(r)}$)	RD($K_{III}^{(r)}$)
1 and 2	4.5%	12.8%	5.8%	6.9%	10.8%	5.9%
2 and 3	1.1%	0.3%	0.1%	2.4%	4.0%	0.2%
3 and 4	0.3%	0.1%	0.0%	1.9%	0.6%	0.1%
4 and 5	0.1%	0.0%	0.0%	0.7%	1.1%	0.0%
5 and 6	0.0%	0.0%	0.0%	0.4%	1.0%	0.0%

less than 2% were found, whereas for the out-of-plane stress intensity factor the differences in the results from domains three to six are approximately 0%. From these results it may be concluded that domain independence was also achieved for the thermal case, as well.

After the convergence study and domain independence were completed, three thermal analyses were performed for $a = 40$ mm, 70 mm and 90 mm. The model in Fig. 5.21 with $\overline{b}$ and $\overline{2h}$ of specimen MMELS-1-17, given in Table 5.26 was used in the analyses with the chosen fine mesh, described in the third row in Table 5.31. A temperature difference of $\Delta\vartheta = -67.5°\text{C}$ was employed. By means of the thermal M-integral in Section 3.2, stress intensity factors resulting from residual curing stresses were obtained for each delamination length a. Relative differences (RDs) between the stress intensity factors obtained along the delamination front at $0.0375 \leq x_3/\overline{b} \leq 0.9625$ from the thermal FEAs with $a = 70$ versus $a = 90$, as well as with $a = 40$ versus $a = 90$m were calculated using eq. (3.31) with (1) representing the former delamination length in the comparison and (2) the latter. The LRDs, in absolute value, related to each stress intensity factor are presented in Table 5.34. From the results, it may be concluded that the stress intensity factors resulting from residual curing stresses are approximately the same for all delamination length values. Hence, only one thermal analysis was performed for each specimen with a delamination length of $a = 70$ mm. The results from this analysis were used for

Table 5.34: Largest relative difference (LRD), in absolute value, calculated by means of eq. (3.31) for two cases, namely, $a = 70$ versus $a = 90$ and $a = 40$ versus $a = 90$, with (1) and (2) implying on the stress intensity factors obtained by means of the thermal M-integral along the delamination front at $0.0375 \leq x_3/\overline{b} \leq 0.9625$ based on the thermal FEAs, respectively.

a	$K_1^{(r)}$	$K_2^{(r)}$	$K_{III}^{(r)}$	$\mathcal{G}_i$
70 mm vs 90 mm	0.04%	0.45%	0.01%	0.02%
40 mm vs 90 mm	1.16%	0.29%	0.02%	0.29%

Table 5.35: Comparison between the stiffness obtained from the AC and PC stages of each MMELS test and that obtained from the FEA.

specimen no.	K_{FE-AC} (N/mm)	K_{FE-PC} (N/mm)	RD(K_{AC}) (%)	RD(K_{PC}) (%)
MMELS-1-9	7.8	7.3	1.9	-0.9
MMELS-1-11	7.9	6.9	0.2	-4.4
MMELS-1-12	8.0	7.4	-5.6	-7.3
MMELS-1-17	8.0	7.4	-4.6	-5.8
MMELS-1-18	8.6	7.7	-3.2	-5.7

all measured delamination length values as will be described next.

5.4.4 MMELS test analyses and $\mathcal{G}_{iR}$-curve

In this section, the analyses performed for the MMELS tests will be described and the results will be presented. For each MMELS specimen, mechanical FEAs related to the AC (first) and PC (second) stages of the test, were performed. The accuracy of the global response of the mechanical FEAs related to both stages was evaluated by comparing the stiffness values obtained from the initial loading portion of each test with those obtained from the analyses. In addition, one thermal FEA was performed for each specimen with $a = 70$ mm. Results from these analyses were used to determine the stress intensity factors resulting from applied loads $K_m^{(f)}$, as well as from residual curing stresses $K_m^{(r)}$, through the specimen thickness. These resulting values were normalized, superposed and used to determine the initiation energy release rate $\mathcal{G}_{ic}$ in eq. (3.17), through the specimen width, as well as the phase angles $\hat{\psi}$ and ϕ in eqs. (3.19) and (3.20), respectively. Variations of each parameter through the specimen width are discussed in this section. In addition, an integrated average was calculated for each parameter.

The mechanical FEAs for the initial AC and PC stages of each test were carried out with a_{0AC} and $a_{0PC-VIS}$ from Table 5.28 employed, respectively. The visual loads P_{VIS} related to each test stage and given in Table 5.29 were employed in the models. For each specimen and test stage, the resulting FEA stiffnesses K_{FE-AC} and K_{FE-PC} were calculated. The obtained values are presented in the second and third columns in Table 5.35, respectively. Note that these stiffnesses do not account for the residual curing stresses. Relative differences (RDs) were calculated by means of eq. (3.31) where (1) indicates the stiffness obtained from the FEA and (2) the stiffness calculated from the test and presented in Table 5.28. In the fourth and fifth columns of Table 5.35, the obtained RDs for the AC and PC stages of the test are presented, respectively. It is interesting to note that for specimens MMELS-1-9 and MMELS-1-11 the RDs, in absolute value, are smaller than that for all other specimens. Recall that lower stiffness for both the AC and PC stages of the test were observed for these two specimens in Figs. 5.20a

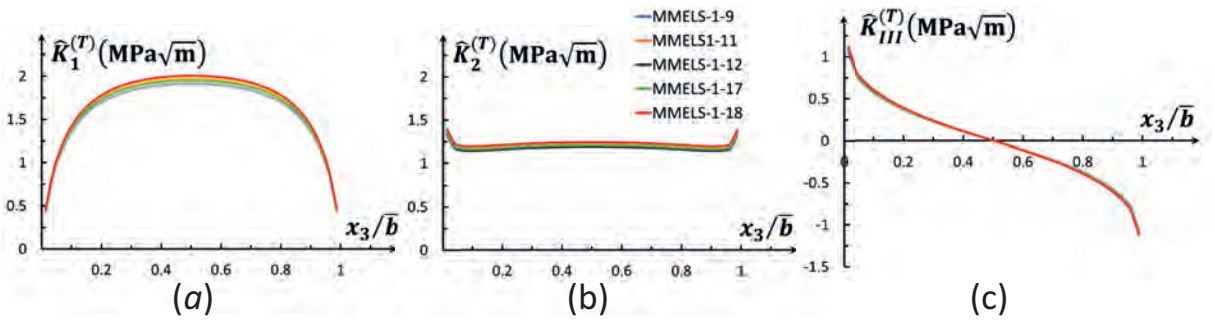

Figure 5.22: Stress intensity factors for the AC (first) stage of the MMELS fracture tests as a function of the normalized specimen width $x_3/\bar{b}$ through the delamination front: (a) $\hat{K}_1^{(T)}$; (b) $\hat{K}_2^{(T)}$ and (c) $K_{III}^{(T)}$.

and 5.20b, as well as in Table 5.28. In addition, it may be observed that except for specimens MMELS-1-9 and MMELS-1-11 in the AC stage, for all specimens, in both test stages, RD ≤ 0 implying that $K_{FE} \leq K_{\text{test}}$. It may be concluded that the stiffness of the specimens is somewhat higher in the tests than that obtained from the FEAs. Since the differences in the calculated stiffness are less than 7.5% in absolute value for all specimens, it may be assumed that the analyses simulate the tests quite well and that the results may be used for further analyses and prediction of the resistance energy release rate required for delamination extension.

Next, using the mechanical analyses related to the AC (first) test stage and described above, as well as one thermal analysis for each specimen, the total stress intensity factors along the delamination front through the specimen width $\bar{b}$ as a function of x_3, were obtained and normalized by means of eq. (1.26) with $\hat{L} = 100$ μm. The values of $K_m^{(T)}$ are calculated by means of eq. (5.4). It may be noted that the in-plane stress intensity factors $\hat{K}_1^{(r)}$ and $\hat{K}_2^{(r)}$, related to the residual curing stresses, were found to be less than 1% of the total stress intensity factors $\hat{K}_1^{(T)}$ and $\hat{K}_2^{(T)}$, respectively, within the range $0.875 \leq x_3/\bar{b} \leq 0.9125$ which is negligible. The out-of-plane $K_{III}^{(r)}$ value was found to be approximately 10% of $K_{III}^{(T)}$. The resulting normalized stress intensity factors $\hat{K}_1^{(T)}$ and $\hat{K}_2^{(T)}$, as well as $K_{III}^{(T)}$ are plotted as a function of the normalized specimen width $x_3/\bar{b}$ in Figs. 5.22a, 5.22b and 5.22c, respectively. It may be observed from these figures that for all MMELS specimens tested the behavior obtained through the specimen width is similar. The obtained in-plane stress intensity factors $\hat{K}_1^{(T)}$ and $\hat{K}_2^{(T)}$ in Figs. 5.22a and 5.22b, respectively, are symmetric with respect to specimen mid-width ($x_3/\bar{b} = 0.5$), whereas the out-of-plane stress intensity factor shown in Fig. 5.22c is anti-symmetric. The change of $\hat{K}_1^{(T)}$ along the specimen width is between approximately 0.4 and 1.9 MPa$\sqrt{\text{m}}$ which is apparent and should be noted. From Fig. 5.22b, it may be observed that except for the value obtained at the outer specimen edges, $\hat{K}_2^{(f)}$ is nearly constant throughout the specimen width for all specimens. A difference of less than 1%, in absolute value, was obtained within the range $0.3125 \leq x_3/\bar{b} \leq 0.6875$ and less than 4%, in absolute

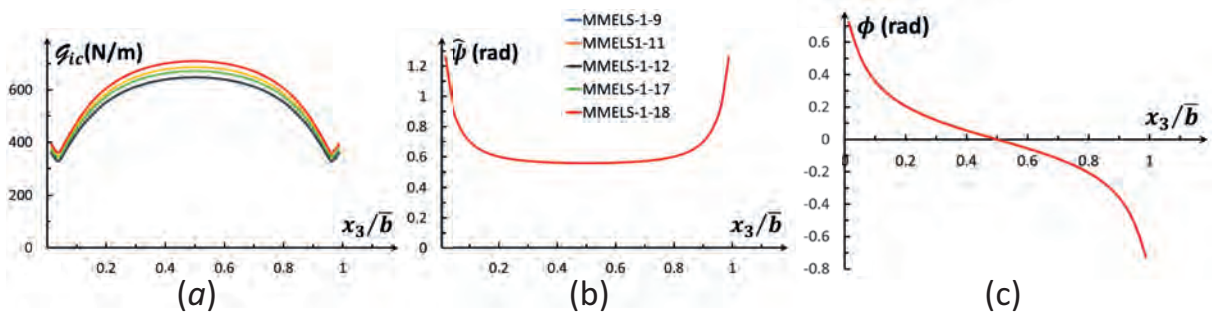

Figure 5.23: Results for the AC (first) stage of the MMELS fracture tests as a function of the normalized specimen width $x_3/\overline{b}$ through the delamination front: (a) critical initiation energy release rate $\mathcal{G}_{ic}$; (b) $\hat{\psi}$ and (c) ϕ.

value, within $0.0375 \leq x_3/\overline{b} \leq 0.9625$. The value of $K_{III}^{(T)}$ ranges between approximately -1.1 MPa$\sqrt{\text{m}} \geq K_{III}^{(f)} \geq 1.1$ MPa$\sqrt{\text{m}}$ throughout each specimen width. Note that except for the outer specimen edges, $K_{III}^{(f)}$ is relatively small compared to the in-plane stress intensity factors.

For the AC test stage, values of $\mathcal{G}_{ic}$, $\hat{\psi}$ and ϕ were calculated through the width of each specimen by means of eqs. (3.17), (3.19) and (3.20), respectively. The results are plotted in Figs. 5.23a, 5.23b and 5.23c, respectively. It may be observed that through the width of the specimen, the critical initial interface energy release $\mathcal{G}_{ic}$ ranges between 328 N/m and 709 N/m for all specimens where the lowest, most conservative energy release rate value, was obtained at the specimen outer edges and increased towards mid-width. From Figs. 5.23b and 5.23c, it may be observed that the obtained $\hat{\psi}$ values are symmetric with respect to specimen mid-width ($x_3/\overline{b} = 0.5$), whereas the obtained ϕ values are anti-symmetric. The obtained $\hat{\psi}$ values range approximately between 0.5 rad at mid-width to approximately 1.3 rad at the specimen outer edges. The values obtained for the out-of-plane to in-plane phase angle ϕ range between approximately -0.7 rad to 0.7 rad.

Numerically integrated average values of $\mathcal{G}_{ic}$ and $\hat{\psi}$ through the width of each specimen were calculated. The resulting values are presented in the second and third columns in Table 5.36. In the last two rows of this table, average values and CVs for each parameter are presented. Note that since ϕ is anti-symmetric through the specimen width, the integrated average is zero, hence, it is not discussed here. It may be observed that the $\hat{\psi}$ value obtained for all specimens is approximately the same for $\hat{L} = 100$ μm with a negligible difference between the different specimens. In addition, the greatest difference in the numerically averaged values of $\mathcal{G}_{ic}$ is about 9.8% with a range between 536.4 N/m and 588.1 N/m.

An attempt was made to obtain the $\mathcal{G}_{ic}$ values for each specimen from the AC stage of the tests by means of the ECM, presented in Section 5.2. However, since the AC stage

Table 5.36: Integrated average values of $\mathcal{G}_{ic}$ and $\hat{\psi}$ obtained from the AC (first) test stage through the width of each MMELS specimen with $P = P_{AC-VIS}$ given in Table 5.29.

specimen no.	$\mathcal{G}_{ic}$ (N/m)	$\hat{\psi}$ (rad)
MMELS-1-9	535.5	0.63
MMELS-1-11	569.3	0.63
MMELS-1-12	536.4	0.62
MMELS-1-17	556.9	0.62
MMELS-1-8	588.1	0.62
average	557.2	0.62
CV (%)	0.80%	0.01%

is performed in order to create a natural crack with propagation between 2 and 5 mm, only a small number of data points of the delamination length a, the load P and actuator displacement d, were obtained visually to be used in eq. (5.9). It was concluded that ECM is not suitable for MMELS AC tests.

In order to determine an R-curve for the specific in-plane mixed mode ratio tested here, as described in Section 5.4.1, the energy release rate $\mathcal{G}_{iR}$ values for the PC (second) test stage were obtained as a function of the delamination extension Δa by means of two methods, namely, based on the mechanical and thermal M-integrals, as well as by means of ECM.

With the M-integral approach for determination of the resistance energy release rate, for each specimen, six mechanical FEAs were performed as described in Section 5.4.1 to obtain six data sets of $K_m^{(f)}$ $(m = 1, 2, III)$, each related to a specific value of a. From the results, for each specimen, data points in the three-dimensional space $(K_m^{(f)}, a, x_3)$ were obtained. An example of such data points obtained from the FEAs and the M-integral for specimen MMELS-1-17 are presented as blue points in Fig. 5.24. Surfaces of the form given in eq. (5.1) were fit through these data sets for $m = 1, 2, III$ and the fitting parameters p_{i0}

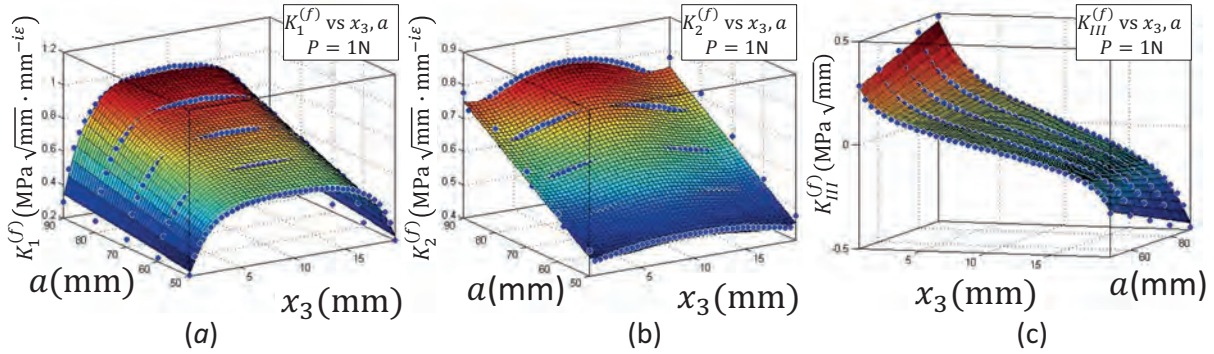

Figure 5.24: The relation between $(K_m^{(f)}, a, x_3)$ in eq. (5.1) with the coefficients p_{ij} in Tables E.6 through E.8 for specimen MMELS-1-17 (a) $m = 1$ (b) $m = 2$ and (c) $m = III$.

and p_{j1} ($i = 0, 1, .., 5$ and $j = 0, 1, .., 4$) were obtained. The resulting fitting parameters for each specimen, related to $K_1^{(f)}$, $K_2^{(f)}$ and $K_{III}^{(f)}$, are given in Tables E.6 through E.8, respectively. In Fig. 5.24, an example of the surfaces presented in eq. (5.1) with the fitting parameters related to specimen MMELS-1-17, are shown. To verify the values of $K_m^{(f)}$ calculated by means of eq. (5.1), the initial delamination length a_{0AC} from Table 5.28 and the visual initiation load P_{VIS} from Table 5.29 were substituted into the equation to obtain $K_m^{(f)}$ values through the specimen width. Relative differences (RDs) between the obtained values and those obtained by means of the mechanical M-integral for the FEAs related to the AC (first) test stage, were calculated. The LRDs, in absolute value, obtained for $K_m^{(f)}$ ($m = 1, 2, III$) were approximately 3.5%, 3% and 3.2%, respectively.

In addition, from the thermal analysis for each specimen with $a = 70$ mm as described earlier, one set of stress intensity factors $K_m^{(r)}$ ($m = 1, 2, III$), resulting from residual curing stresses, along the delamination front were obtained and a fourteenth order polynomial curve fit of the form shown in eq. (5.3) was determined. The fifteen fitting parameters b_i found for each specimen, related to $K_1^{(r)}$, $K_2^{(r)}$ and $K_{III}^{(r)}$ are presented in Tables E.9 through E.11, respectively. Note that since the specimens were tested in a small range of temperatures given in Table 5.27, the resulting fitting coefficients are similar for all specimens for each stress intensity factor. To verify the values of $K_m^{(r)}$ calculated by means of eq. (5.3), relative differences (RDs) between the obtained values and those obtained by means of the thermal M-integral for the FEAs related to the AC (first) test stage were calculated. The LRDs, in absolute value, obtained for $K_m^{(r)}$ ($m = 1, 2, III$) were approximately 0.8%, 0.5% and 0.5%, respectively.

Next, an expression for the in-plane mixed mode phase angle $\hat{\psi}$ as a function of a and x_3 was obtained. The expressions of $K_m^{(T)}$ in eq. (5.4) were normalized by means of eq. (1.26). These expressions were then substituted into eq. (3.19) to determine expressions for $\hat{\psi}$. The delamination length a, synchronized load P and actuator displacement d, presented in the first through third columns in Tables E.1 through E.5, were substituted into the obtained expressions. Then, a single value of $\hat{\psi}$ was determined for each delamination length a, for each specimen by means of numerical integration through the specimen width $\overline{b}$ which was performed using Lobatto–Kronrod segmented quadrature (Shampine, 2008) in a MATLAB (2019) code. The obtained $\hat{\psi}$ values are presented in the last column in Tables E.1 through E.5, as well as plotted as a function of the delamination extension Δa in Fig. 5.25. It may be observed that the in-plane mode mixity remains approximately constant with a slight increase as the delamination extends. It varies between 0.656 rad and 0.668 rad.

Note that in Table 5.36 the values of $\hat{\psi}$ at $\Delta a = 0$ were also calculated from the FEAs related to the AC (first) test stage by means of numerical integration. It may be noted that the values of $\hat{\psi}$ at $\Delta a = 0$ which are shown in Fig. 5.25 and were obtained based on numerical integration in MATLAB (2019) are approximately 5% higher than those in

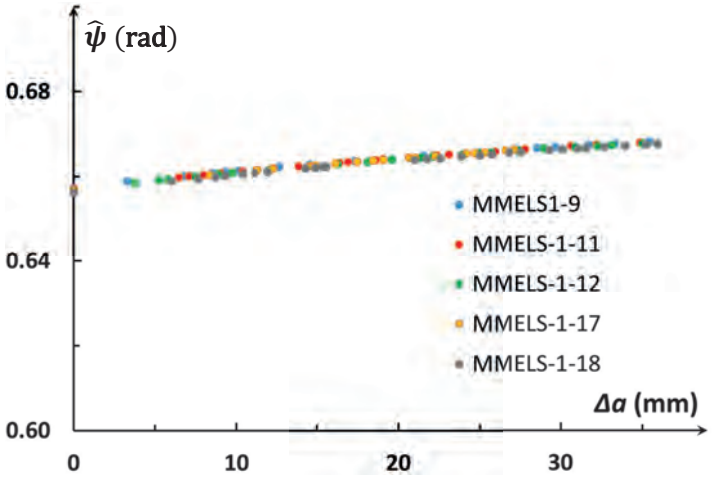

Figure 5.25: Values of $\hat{\psi}$ ($\hat{L} = 100$ μm) as a function of the delamination extension Δa; these values were obtained by means of eq. (3.19) with the expressions in eq. (5.4) normalized by eq. (1.26), integrated through the specimen width $\overline{b}$ with P and a taken from Tables E.1 through E.5, for $\Delta a = 0$, a_{0AC} and P_{VIS} from Tables 5.28 and 5.29.

Table 5.36. This difference is probably a result of the differences in the evaluated $K_m^{(f)}$ and $K_m^{(r)}$ ($m = 1, 2, III$) values from eqs. (5.1) and (5.3) versus those obtained by means of the mechanical and thermal M-integrals, respectively, for the FEAs related to the AC test stage. It was mentioned previously, that these differences could be as much as 3.5%.

Next, the resistance interface energy release rate $\mathcal{G}_{iR}$ as a function of x_3 was expressed for each measured delamination length a by means of eq. (3.17) with use of the expressions in eq. (5.4). These expressions were integrated analytically by MATLAB (2019) with respect to x_3, through the specimen width $\overline{b}$, by means of eq. (5.5), to obtain the average $\overline{\mathcal{G}}_{iR}$ value for each delamination length a. In addition, the critical initiation $\overline{\mathcal{G}}_{ic}$ values related to $\Delta a = 0$ were also determined by means of eq. (5.5) for the initiation loads P_{AC-NL}, P_{AC-VIS} and $P_{AC-max/5\%}$ in Table 5.29. The obtained $\mathcal{G}_{ic-NL}, \mathcal{G}_{ic-VIS}$ and $\mathcal{G}_{ic-5\%/max}$ values, respectively, are presented in columns two through four in Table 5.37. The average values and CVs are presented for each parameter in the last two rows of this table. The $\mathcal{G}_{ic-VIS}$ values, related to P_{VIS} in Table 5.37 were compared with the values of $\mathcal{G}_{ic}$ presented in Table 5.36 which were obtained from the FEAs related to the AC (first) test stage. It was found that the obtained values in Table 5.37 and those in Table 5.36 differ by approximately 1%. This small difference validated the use of eq. (5.4) to approximate the stress intensity factors. The obtained average $\mathcal{G}_{iR}$ values for each delamination length a are presented in the fifth column in Tables E.1 through E.5.

In addition, the resistance energy release rate values were obtained by means of the ECM, as described in Section 5.4.1. For each test, the values of a, P and d in Tables E.1 through E.5, as well as the fitting parameter m from Table 5.30, were substituted into eq. (5.9) to obtain $\mathcal{G}_{iR}$ values as a function of the delamination extension Δa. The obtained

Table 5.37: Initial interface energy release rate $\mathcal{G}_{ic}$ values related to the AC (first) test stage with the NL, visual and 5%/max loads in Table 5.29

specimen no.	$\mathcal{G}_{ic-NL}$ (N/m)	$\mathcal{G}_{ic-VIS}$ (N/m)	$\mathcal{G}_{ic-5\%/max}$ (N/m)
MMELS-1-9	432.3	544.4	583.7
MMELS-1-11	382.2	578.8	626.3
MMELS-1-12	461.5	544.5	545.4
MMELS-1-17	415.5	571.8	581.2
MMELS-1-18	406.8	597.7	598.6
average	419.7	567.4	587.0
CV (%)	3.2	1.8	2.2

$\mathcal{G}_{iR}$ values for each delamination length a are presented in the sixth column in Tables E.1 through E.5.

In Figs. 5.26a and 5.26b, the $\overline{\mathcal{G}}_{iR}$ values obtained based on the M-integral, as well as based on the ECM, respectively, are plotted as points as a function of the delamination extension Δa. Note that the bar indicting the integrated average in eq. (5.5) is omitted. Moreover, for each specimen, for both the M-integral, as well as for the ECM, for $\Delta a = 0$, the values of $\mathcal{G}_{ic}$ from Table 5.36, related to P_{AC-VIS} in Table 5.29 for a_{0AC}, were used. Recall that for specimen MMELS-1-18 the delamination extension Δa was measured up to $\Delta a = 15.6$ mm. Hence, values of $\mathcal{G}_{iR}$ were determined and plotted for this specimen only up to this value.

A power law fit of the form given in eq. (5.6) between the initial critical interface energy release rate $\mathcal{G}_{ic}$ and the steady state value $\mathcal{G}_{iss}$ for $\Delta a = \Delta a_{iss}$, was used to determine two R-curves. The initial interface fracture toughness $\mathcal{G}_{ic}$ in both cases was calculated as the

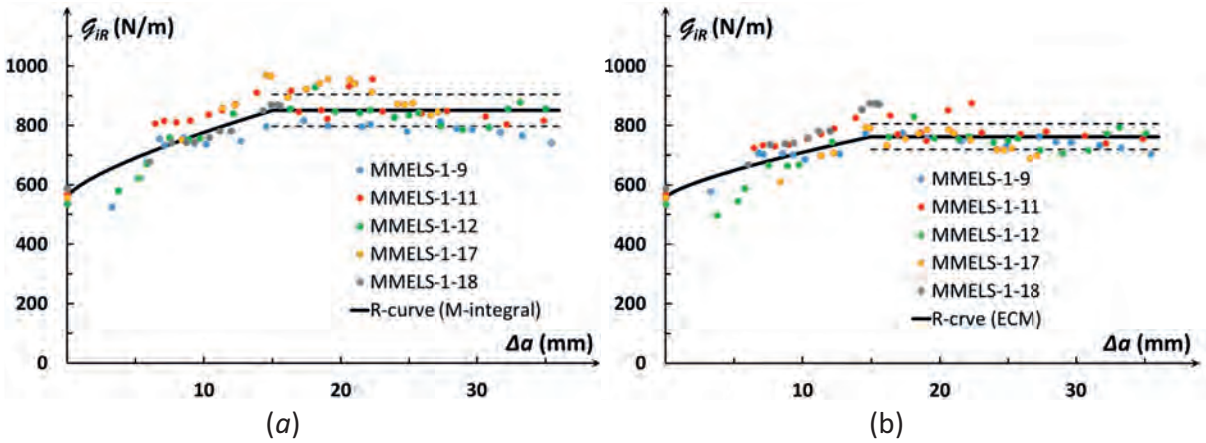

Figure 5.26: Fracture resistance curves: $\mathcal{G}_{iR}$ versus $\Delta a = a - a_0$ obtained by means of (a) M-integral and eq. (5.5) with eq. (5.4) and the fitting parameters in Tables E.6 through E.11 and (b) ECM from eq. (5.9) with m from Table 5.30.

Table 5.38: The parameters $\mathcal{G}_{ic}$ and $\mathcal{G}_{iss}$, as well as A_1 and B from the power law in eq. (5.6) for the mixed mode I/II R-curves obtained by means of the M-integral with eqs. (5.4), (5.5) and the fitting parameters in Tables E.6 through E.11 and by means of the ECM in eq. (5.9) with m from Table 5.30. The RMSE are also presented.

method	$\mathcal{G}_{ic}$ (N/m)	$\mathcal{G}_{iss}$ (N/m)	A_1 (N/m·mm^B)	B	RMSE (N/m)
M-integral	557.2 ±22.4	850.2 ±53.8	42.0	0.72	62.6
ECM	–	762.3 ±42.5	27.8	0.74	60.2

average of the five $\mathcal{G}_{ic}$ values found for each tested specimen by means of the M-integral. This average value and standard deviation are presented the second column in Table 5.38. Recall that the initial values used in the R-curve for ECM were those obtained by means of the M-integral. Hence, for both methods, the initial values are the same. A steady state energy release rate value $\mathcal{G}_{iss}$ was reached at approximately $\Delta a_{iss} = 15$mm, as may be observed in Figs. 5.26. This steady state energy release rate value was calculated as the average of all $\mathcal{G}_{iR}$ values obtained for $\Delta a \geq \Delta a_{iss}$ for each method. The $\mathcal{G}_{iss}$ values obtained for each method are presented in the third column in Table 5.38. The standard deviation of all $\mathcal{G}_{iR}$ values obtained for $\Delta a \geq \Delta a_{iss}$ for each method were added to or subtracted from the average value and presented as dashed black lines in Figs. 5.26 . The obtained values for these standard deviations are given in Table. 5.38. It may be observed that the difference between the two $\mathcal{G}_{iss}$ values is large. The RD between the two $\mathcal{G}_{iss}$ values was calculated using eq. (3.31) with (1) being the ECM result and (2) to the M-integral. The RD was found to be -10.3% which implies that the results obtained from the global and local analyses methods are not as similar as was found in the case

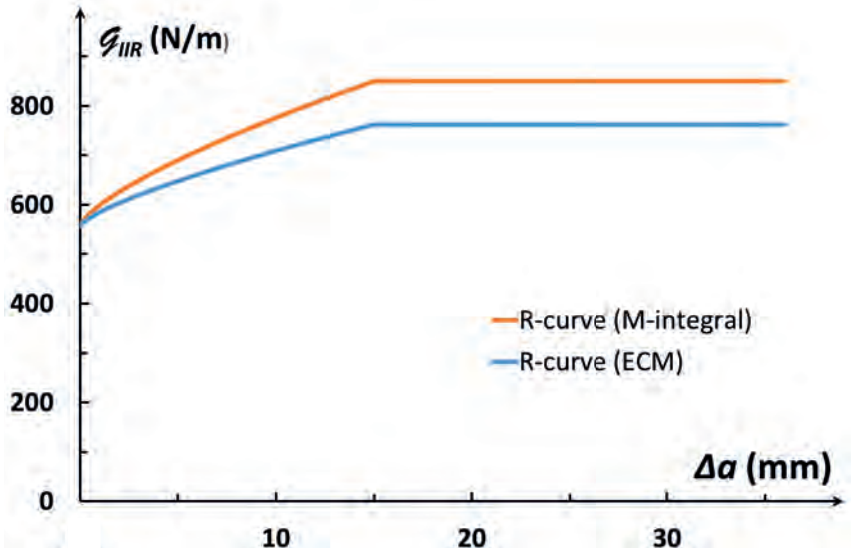

Figure 5.27: Comparison of the mixed mode resistance curves obtained by means of the M-integral with eqs. (5.4), (5.5) and the fitting parameters in Tables E.6 through E.11 and by means of ECM in eq. (5.9) with m from Table 5.30.

of the C-ELS or DCB tests. The fitting parameter A_1 was obtained for each set of data points, related to each method, in the same manner as described in Section 5.3.1. This was determined by means of the GRG software of Excel (2016) with the parameter B expressed by means of eq. (5.10). For a minimum value of the RMSE, the value of A_1 was determined. The obtained R-curves are shown as the black curves in Figs. 5.26.

In Fig. 5.27, the R-curves obtained by means of the two methods are plotted and compared. The difference between the two curves is apparent. It may be clearly observed that the ECM global approach resulted in more conservative energy release rate resistance values than those obtained by means of the M-integral. In addition, a more moderate increase until steady state was obtained from the ECM results. An opposite result was observed for the DCB and C-ELS analyses in Figs. 5.4 and 5.14, respectively, where the M-integral and J-integral, respectively, produced more conservative R-curves.

Chapter 6

Summary, discussion and conclusions

This investigation focused on the fracture behavior of a multi-directional carbon fiber reinforced polymer (CFRP) composite which is commonly used in the aircraft industry. A delamination, illustrated in Fig. 2.1, along an interface between a UD fabric upper ply with fibers mainly oriented in the 0° or x_1-direction and a lower plain balanced woven fabric ply with tows oriented in the $+45°/-45°$ directions, was studied. The CFRP composite considered was manufactured as a wet-layup and composed of an EPR-L20/EPH-960 epoxy matrix with T300 carbon fibers. The UD upper ply also contained a small percentage of glass fibers. The investigation included analytical, numerical and experimental work. A full mixed mode range for failure initiation was studied by testing and analyzing Brazilian disk (BD) specimens. In addition, both initiation and propagation behavior of the delamination using beam type specimens subjected to nearly mode I, nearly mode II and mixed mode deformations was studied.

This section begins with a summary of the work presented in this thesis, followed by the contribution of the work, as well as a discussion, the main conclusions and recommendations for future work. In Chapter 1, an introduction to the subjects in this investigation was presented, beginning with a short introduction to fracture mechanics for a linear elastic, homogeneous and isotropic material and for an interface between two linear elastic, isotropic, homogeneous materials in Section 1.1. Methods for extracting stress intensity factors for such materials were described in Section 1.2. First, in Section 1.2.1, the displacement extrapolation (DE) method was introduced. Then, in Sections 1.2.2.1 and 1.2.2.2, two and three-dimensional mechanical and thermal M-integrals, were presented, respectively.

Chapter 1 continues with a description of several fracture toughness test types from the literature, presented in Section 1.3. This section begins with a review of the structural differences between UD, MD and woven fabric composites presented in Section 1.3.1. Next, modes I and II fracture toughness and resistance energy release rate tests were described in Section 1.3.2. Among these are the mode I and mode II standardized test methods, namely, the ASTM D 5528-13 (2014) standard and the ISO 15024:2001 (2001) standard

for mode I and the ASTM-D7905 (2014) standard and ISO 15114:2014(E) (2014) standard for mode II. All four standardized methods make use of beam type specimens which are subjected to quasi-static loading in displacement control, resulting in stable delamination growth as the displacement increases. It should be noted that all mode I and II standards are limited to UD CFRPs and GFRPs which have a less complex structure than MD composites which may consist of UD or woven fabric plies oriented in various directions.

In Section 1.3.3, several specimens which may be used for mixed mode fracture tests, as well as examples of use of these specimens in the literature, were presented. A focus on two beam type specimens and test configurations was made in Section 1.3.3.1, namely, the MMB (ASTM D6671M-13, 2014) and MMELS specimens. Both the MMB and MMELS specimens are appropriate for determining the mixed mode fracture toughness $\mathcal{G}_c$, as well as the mixed mode fracture resistance energy release rate $\mathcal{G}_R$ as the delamination extends. The MMB test is the only standardized mixed mode fracture test which enables various mixed mode combinations. However, the setup of the test is cumbersome. The MMELS specimen has been proposed for standardization by Technical Committee 4 (TC4) of the European Structural Integrity Society (ESIS). This specimen enables testing of one mixed mode combination with a relatively simple setup. In order to obtain additional mixed mode ratios, the thickness of each arm in the specimen should be varied; thus, a different plate is required for each mode mixity. The MMELS specimen was chosen to be used in this investigation for testing approximately one mixed mode ratio averaged through the specimen width. In Sections 1.3.3.2 and 1.3.3.3, the Arcan and BD specimens which enable a wide range of mixed mode combinations using a simple test setup and only one specimen type and fixture, were described, respectively. The delamination in both specimens propagates in an unstable manner. In the current investigation, the BD specimen was chosen to be used to obtain the initiation interface fracture toughness for a wide range of mode mixities. In Section 1.3.3.3, the methodology and results, which were obtained using this specimen in previous investigations, were summarized.

Chapter 2 begins with a description of the mechanical structure of the investigated material and interface which is presented in Section 2.1. In addition, in this section, the mechanical properties and CTEs of the materials comprising each ply were presented. These properties were used with the High-Fidelity Generalized Method of Cells (HFGMC) (Aboudi, 2004) to determine the effective mechanical properties and CTEs of the UD and plain woven fabrics. In Sections 2.2 and 2.3, the first term of the asymptotic expansion of the displacement and stress fields for the considered interface were derived based on the Stroh (1958) and Lekhnitskii (1963) formalisms, as described by Ting (1996) and summarized in Appendix A. The final expressions for the in-plane and out-of-plane displacement and stress fields are presented in Section 2.3. These are a function of the complex in-plane stress intensity factor $K = K_1 + iK_2$ and the out-of-plane stress intensity factor K_{III}. The complex stress intensity factor is the amplitude of the oscillatory, square-root singularity

and the mode III stress intensity factor is the amplitude of the square-root singular stress components.

The analytical development is continued in Chapter 3 where the displacement extrapolation (DE) method, as well as the conservative mechanical and thermal M-integrals were extended to three dimensions for the current material symmetries. These derivations are presented in Sections 3.1 and 3.2, respectively. Both methods were used to obtain stress intensity factors resulting from applied loads, as well as from residual thermal curing stresses. The numerical part of this investigation included programming the first term of the asymptotic solution for the displacement component for the DE method and the conservative, interaction energy M-integrals for mechanical and thermal loading. In Section 3.3, three benchmark problems were solved in order to check and verify the results of the derivations and software used in the current investigation.

The experimental part of the investigation included three types of fracture toughness and resistance tests which were presented in Chapters 4 and 5. In Chapter 4, the Brazilian disk (BD) specimen was used for mixed mode initiation fracture tests. In this chapter, the test, analyses and obtained results were presented. First, in Section 4.1, the structure and dimensions of the plate which was designed for the BD specimens, was described. Then, the fiber volume fraction in each ply in the manufactured plate was used to determine the properties of that ply based on the methodology in Section 2.1. The obtained mechanical properties and CTEs of each ply were presented in Section 4.2. In Section 4.3, a protocol for the BD tests was presented. The specimen and loading arrangement were illustrated in Figs. 1.19 and 4.10, respectively. During each test, a load P was applied at an angle ω with respect to the artificial delamination located between the investigated plies. Each loading angle created a different mixed mode combination, so that approximately seven different mode mixities were tested. Dimensions and results from the tests were presented in Section 4.4. Both mechanical and thermal FEAs were performed for each tested specimen. In Section 4.5, the FE model used was described. In addition, a convergence study was performed and domain independence was examined. The results from these analyses were used in conjunction with the post-processors for the DE method and M-integrals to separate the stress intensity factors resulting from applied load $K_m^{(f)}$ $(m = 1, 2, III)$, as well as from residual curing thermal stresses $K_m^{(r)}$, respectively. The mechanical and residual stress intensity factors were superposed to obtain the total stress intensity factors $K_m^{(T)}$ and used to calculate the critical initiation interface energy release rates $\mathcal{G}_{ic}$ from eq. (3.17), related to each tested specimen and mode mixity. In addition, the phase angles $\hat{\psi}$ and ϕ were calculated from eqs. (3.19) and (3.20). The results obtained from the analyses were presented in Section 4.6. Employing the experimental and numerical results obtained from the BD fracture tests, two and three-dimensional failure criteria were generated as described in Section 4.7. In order to account for scatter in the results, a statistical analysis with a 10% probability of unexpected failure and a 95% confidence was performed.

Two peer-reviewed articles were published related to this part of the investigation, namely, Mega and Banks-Sills (2019) and Mega et al. (2019). The former included a description of the BD tests, as well as the numerical analyses and obtained results. In the latter article, the results obtained in Mega and Banks-Sills (2019) were compared with BD test results of a different CFRP (Dolev, 2020) with a delamination along an interface between an upper $0°/90°$ and a lower $+45°/-45°$ woven fabric. Two and three-dimensional failure criteria were proposed for both materials based on the BD fracture test results. Also, statistical analyses were performed and presented in the paper.

In Chapter 5, initiation and propagation properties based on nearly mode I, nearly mode II and mixed mode fracture toughness and fracture resistance tests were determined. For mode I, DCB tests were performed and described in Chocron and Banks-Sills (2019). The results from that investigation were reanalyzed here using the experimental compliance method (ECM). For the nearly mode II and mixed mode initiation and resistance properties, C-ELS and MMELS fracture tests were performed, respectively, and analyzed. First, in Section 5.1, a description of the plate which was designed, manufactured and used for the DCB, C-ELS and MMELS tests, as well as the mechanical properties and CTEs which were determined for each ply type, are presented. Next, in Section 5.2, results from Chocron and Banks-Sills (2019) determined from mode I DCB tests were reanalyzed by means of the ECM. The R-curve obtained by means of the global ECM was compared with that obtained in Chocron and Banks-Sills (2019) by means of the M-integral local approach.

Both Sections 5.3 and 5.4 are composed of four subsections. In Sections 5.3.1 and 5.4.1, the protocols which were used in this investigation for the C-ELS and MMELS fracture tests, respectively, were presented. Both specimens and clamping arrangements are illustrated in Figs.5.5 and 5.17, respectively. Both tests were carried out quasi-statically in displacement control to provide stable delamination propagation. The AC (first) and PC (second) test stages, related to the artificial delamination and to the natural precrack, respectively, were described in the protocols. Also, the analysis methods which were used for each test stage were detailed. In Section 5.3.2 results from the calibration test, as well as from the C-ELS fracture tests were presented. Results from the MMELS fracture tests were discussed in Section 5.4.2. Among the results were the specimen dimensions, load-displacement curves, as well as initial loads and displacements before the artificial or precrack delamination propagated. In addition, values of the delamination length and corresponding load and displacement obtained from the images captured during propagation are presented in those sections. Based on the data obtained from the tests, fitting parameters relating the compliance and the delamination length were determined.

Next, mechanical and thermal FEAs were performed. In Sections 5.3.3 and 5.4.3, mesh convergence and domain independence were examined for the two-dimensional mechanical C-ELS FEAs, as well as for the three-dimensional mechanical and thermal MMELS FEAs.

In Section 5.4.3, the results from the thermal analysis as a function of the delamination length were also examined. Finally, in Sections 5.3.4 and 5.4.4, the experimental and numerical results obtained were employed to determine the fracture resistance $\mathcal{G}_{iR}$-curves for nearly mode II and for one mixed mode I/II deformation ratio. The $\mathcal{G}_{iR}$-curves were generated by means of a local M-integral approach, as well as by means of the global ECM and included determination of the initiation $\mathcal{G}_{ic}$ and steady state propagation $\mathcal{G}_{iss}$ values. The $\mathcal{G}_{iR}$-curves obtained using both methods were compared for each tested specimen. In addition, in these sections, the phase angles $\hat{\psi}$ and ϕ were calculated. The integrated through the width in-plane phase angle $\hat{\psi}$ was presented as a function of the delamination extension with minor changes observed as the delamination extended. The R-curves found may be used to account for the fracture resistance energy release rate required for propagation and to assist in improving the design and safety of a structure made of this laminate with this interface. Two peer-review articles are currently in preparation, discussing the foundations of this part of the investigation.

The scientific contribution of this research includes three main aspects. First, since most investigations related to delaminations in composite laminates focus on a delamination along an interface between two UD plies oriented in one or in different directions, the type of interface studied here is not commonly investigated where the two plies are completely different from one another both in structure and properties. Second, use of several experimental methods for different mode mixities was made. The BD specimen enabled various mode mixities, however since propagation is unstable, only critical initiation energy release rate values were obtained as a function of approximately thirteen differen mixed mode ratios. On the other hand, the beam type specimens, namely, the DCB, C-ELS and MMELS specimens are each limited to a specific fracture mode, namely, nearly mode I, nearly mode II and one mixed mode ratio, respectively. However, with these test set-ups, delamination propagation is generally stable. For each of these three fracture modes, an R-curve showing the energy release rate as a function of the delamination extension was obtained. It may be concluded that in order to determine both initiation and propagation behavior under various mode mixities, both BD and beam specimens are required. The third aspect of this work is based on the use and comparison of various local analyses methods, as well as the global ECM to determine critical initiation and propagation energy release rate values as a function of the mode mixity. The local methods used in this investigation were the three-dimensional M-integral, as well as the two-dimensional J-integral and VCCT all verified by means of the DE method.

The analytical and numerical tools developed and used here may be used for additional MD laminate composites with an interface between an upper transversely isotropic and a lower tetragonal ply. In order to determine critical initiation and propagation energy release rate values, three-dimensional analyses were performed for the BD, DCB and MMELS specimens in conjunction with the M-integral and DE method. For the C-ELS specimens, two-dimensional FEAs were performed and use of the J-integral, VCCT and

DE method was made. Both the M-integral and VCCT are known to be more accurate than the DE method. It may be shown that if three-dimensional VCCT was used instead of the M-integral, the differences between the results would have been negligible. For additional material pairs analytical and numerical adaptations are required. However, it should be noted that less analytical development, as well as fewer numerical adaptations are needed for the VCCT (Farkash, 2020). Although the three-dimensional M-integral was employed here to determine the values of the partitioned stress intensity factors, in future investigations use of VCCT for two or three-dimensional FEAs is recommended. Moreover, it should be pointed out that for another material pair, the methodology used here may be applied. Once the analytical developments and numerical tools are prepared, much experimental and numerical work are required. Finally, results obtained by means of the local and global methods are compared and conclusions are made in the sequel.

For an interface between two plies which are the same in structure and properties, the partitioning modes are distinct. However, for a delamination along an interface between two dissimilar plies, as in the case studied here, coupling of the fracture modes occurs and an oscillatory parameter ε is used to describe the oscillations of the displacement and stress fields near the delamination front. Hence, the mode partitioning becomes more complicated. Note that for a smaller oscillatory parameter the effect is less. In this study $\varepsilon = 0.02257$ which is not negligible. Moreover, in order to investigate a delamination between two dissimilar plies, as was done in this investigation, the layup of the upper and lower arms in the beam type specimens is different, resulting in different thicknesses, flexural moduli, as well as effective mechanical properties of each arm. For such a case, the standard data reduction techniques presented in the ASTM D5528-13, ISO 15024:2001(E), ASTM D7905/D7905M-14, ISO 15114:2014(E), and ASTM D6671M-13 standards for DCB, ENF, C-ELS and MMB specimens, respectively, which are used to determine the partitioned critical initiation and propagation energy release rate values, are not applicable.

That being said, in the literature in some studies (Gong et al., 2019; Rzeczkowski, 2020), beam specimens which include MD interfaces were tested using DCB, ENF and MMB specimens under nearly mode I, nearly mode II and mixed mode deformations, and analyzed by means of standard global reduction techniques. It may be interesting to reanalyze the data from those investigations by means of local methods such as the M-integral or VCCT to compare and verify the results. In de Morais et al., 2002, de Morais and Pereira, 2007, Pereira and de Morais, 2008, Gong et al., 2010, the partitioned energy release rate values were determined by means of the standard global methods, as well as with VCCT, and compared. In all cases, good correlation in the results was achieved. However, it shall be noted that in the cases treated, the layup of the specimen arms had the same thickness and flexural modulus. However, in the case studied here, this was not achieved. Moreover, when an MD interface is considered, the partitioned energy release rate values oscillate as a function of the distance from the delamination front. Hence,

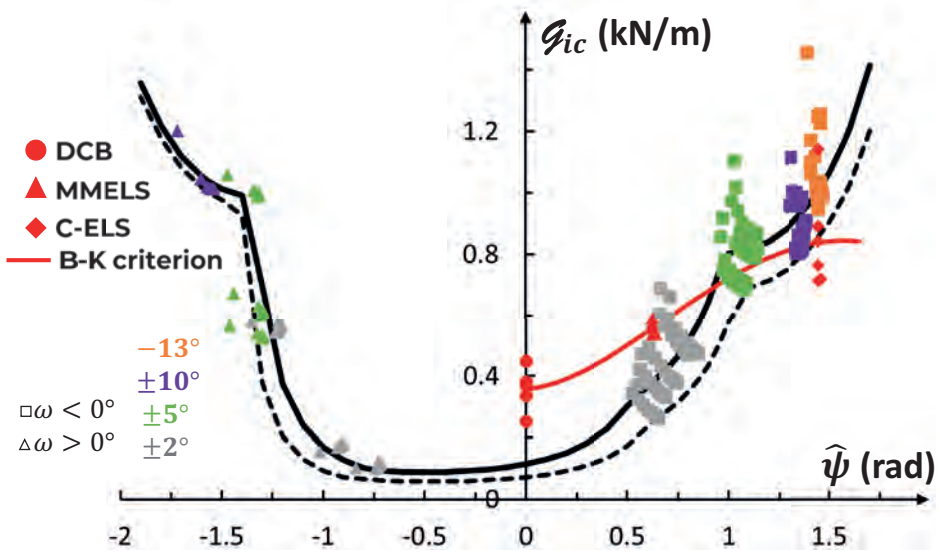

Figure 6.1: Two-dimensional in-plane critical initiation interface energy release rate $\mathcal{G}_{ic}$ values from the BD specimen tests, as well as from the DCB, C-ELS and MMELS tests, obtained based on eq. (3.17) and plotted as a function of $\hat{\psi}$ with $\hat{L} = 100$ μm. The two-dimensional five branch criterion in the $(\mathcal{G}_{ic}, \hat{\psi})$-plane with $\hat{L} = 100$ μm obtained using eq. (4.30) substituted into eq. (4.19) and then into eq. (4.18) based on the data from the BD tests is plotted in black and the statistical curve in dashed black. The B-K failure curve given in eq. (6.2) ($\eta = 0.83$) was generated based on the beam type specimen results and plotted in red.

there is some doubt regarding the results obtained by VCCT, since these may change as a function of the mesh used in the calculation. In the current investigation, instead of obtaining the partitioned energy release rate values, the partitioned stress intensity factors were determined by means of the M-integral or VCCT (Farkash and Banks-Sills, 2017), and used to calculate the phase angles which describe the mode mixity of each tested specimen.

Fracture toughness initiation values obtained using the BD and beam type specimens are compared in Fig. 6.1. This figure is the same as Fig. 4.27b with the two-dimensional five-branch criterion in the $(\mathcal{G}_{ic}, \hat{\psi})$-plane shown as the black curve. Recall that this criterion was generated based on the BD test results using eq. (4.30) substituted into eq. (4.19) and then into eq. (4.18). For eq. (4.30), the parameters $\hat{K}_{2c}^{(N)}$, $\hat{K}_{2c}^{(P)}$, $\beta^{(N)}$, $\beta^{(P)}$, $\hat{K}_{1c}$, I and $\beta^{(S)}$ may be found in Tables 4.22 through 4.24. The dashed black curve in Fig. 6.1 is the statistical two-dimensional five-branch criterion obtained by means of the same equations as the deterministic criterion, but with the parameters for eq. (4.30) in Tables 4.27 through 4.29. Also in Fig. 6.1, the critical initiation interface energy release rate data of $\mathcal{G}_{ic}$ through the delamination front are plotted. These values were obtained for the BD specimens using eq. (3.17) with $K_{III} = 0$.

The critical initiation interface energy release rate values $\mathcal{G}_{ic}$ obtained for the beam type specimens are also plotted in Fig. 6.1 as a function of the mixed mode phase angle

$\hat{\psi}$ with $\hat{L} = 100$ μm. These are shown in red. It may be observed from Fig. 6.1 that the data points $\mathcal{G}_{Ic}$, obtained based on the DCB tests for all specimens, are higher than those obtained from the '5-branch' criterion for $\hat{\psi} = 0$. As mode II becomes dominant, namely as $\hat{\psi}$ increases, the difference between the $\mathcal{G}_{IIc}$ and $\mathcal{G}_{ic}$ values obtained from the C-ELS and MMELS specimens, respectively, versus those from the '5-branch' criterion decreases.

The plotted values for the DCB specimen were obtained in Chocron and Banks-Sills (2019) by means of eq. (5.5), where $\mathcal{G}_{ic}(a, x_3) \approx \mathcal{G}_{Ic}(a_0, x_3)$ was calculated from eq. (3.17) with eq. (5.4) for $\hat{\psi} = 0$. The average $\mathcal{G}_{Ic}$ value was found to be 357.9 N/m. For the BD specimens $\mathcal{G}_{1c} = 114.4$ N/m as found from the '5-branch' criterion using eqs. (4.19) and $(4.30)_2$ with $\hat{\psi} = 0$ and $\hat{L} = 100$ μm. The difference between the fracture toughness obtained by means of the DCB specimens verses those obtained with the BD specimens may be a result of the thickness difference between the two specimens, namely $2h$ in Fig. 1.11 for the DCB specimens verses $H = H_T + H_B$ in Fig. 4.12 for the BD specimens. The thickness is defined here as $2h$ for all specimens. Recall that the composite strip of the BD specimens was composed of 69 plies resulting in a thickness of approximately 17 mm; whereas, the DCB specimens were composed of only 19 plies with a thickness of approximately 5 mm. Some previous experimental results in the literature (Prel et al., 1989; Davies et al., 1992; Hojo and Aoki, 1993) showed that there is no effect of the specimen thickness on the fracture toughness at initiation. Note that these investigations focused on UD CFRPs. In those investigations, the results were obtained by means of the experimental compliance calibration method or using modified beam theory, both described in the ASTM D5528-13 (2014) standard. In more recent publications (Kravchenko et al., 2017; Dolev, 2020), a clear relation between the specimen nominal thickness and the initiation energy release rate values was observed.

In Kravchenko et al. (2019), a clear effect of the DCB specimen thickness on the fracture toughness at initiation was shown. It was observed in that study that higher fracture toughness values are expected for thinner specimens. Tests were performed on UD CFRP DCB specimens with various thicknesses of 2.03 mm, 4.05 mm, 6.1 mm and 8.2 mm with five specimens in each group. The obtained $\mathcal{G}_{Ic}$ values were found to decrease as the thickness increased with a maximum value of $\mathcal{G}_{Ic} = 286$ N/m for the thinnest specimen and a minimum value of 193 N/m for the thickest one. These results were obtained by means of beam theory and are presented in Table 6.1. Note that in the table, the $\mathcal{G}_{Ic}$ value for $2h = 16$ mm was determined from extrapolation of the values obtained in Kravchenko et al. (2019). In Dolev (2020), DCB and BD specimens with a nominal thickness of approximately 5 mm and 16 mm, respectively, were tested. The results are presented in Table 6.1. In addition, in Simon et al (2017), DCB tests were performed for specimens made from the same composite material and interface tested in Dolev (2020) but with a nominal thickness of 3.7 mm. It may be observed from the results in Table 6.1 that as the thickness of the specimens increase the $\mathcal{G}_{Ic}$ values decrease.

Table 6.1: Values of $\mathcal{G}_{Ic}$ as a function of the specimen thicknesses $2h$ as obtained for a UD CFRP from Kravchenko et al. (2019), for a delamination along a $+45°/-45°//0°/90°$ interface from Dolev(2020) and Simon et al. (2017), as well as for a delamination along a $0°//+45°/-45°$ interface investigated here from Chocron and Banks-Sills (2019) and Section 4.

	$2h$ (mm)	$\mathcal{G}_{Ic}$ (N/m)
Kravchenko et al. (2017)	2.0	277
	4.1	233
	6.1	184
	8.2	192
	16.0	61
Chocron and Banks-Sills (2019) Chapter 4	5.0	358
	17.1	114
Simon et al (2017)	3.7	508
Dolev (2020)	5.0	376
	15.6	210

The results in Table 6.1 are also plotted in Fig. 6.2. It may be observed that the behavior of the three material systems examined is rather similar with a trend of decreasing $\mathcal{G}_{Ic}$ values as the specimen thickness increases. A physical explanation for this phenomena is that the thickness of the DCB specimen bounds the process zone, producing a structural constraint. It was shown in Kravchenko et al. (2019) that the K-dominant zone is of the same order of magnitude as the fracture process zone reported in the literature for

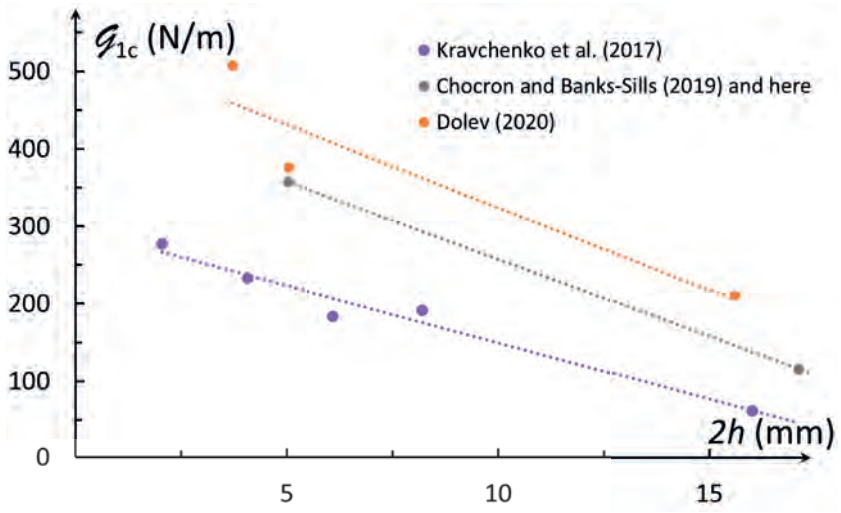

Figure 6.2: Values of $\mathcal{G}_{Ic}$ plotted as a function of the specimen thicknesses $2h$ for three different material systems obtained from Kravchenko et al. (2019) for a UD composite, from Dolev(2020) and Simon et al. (2017) for a woven prepreg, and from Chocron and Banks-Sills (2019) and Section 4 here for the material composite and interface investigated here.

Table 6.2: Nearly mode II energy release rate $\mathcal{G}_{ic} \approx \mathcal{G}_{IIc}$ values obtained for the C-ELS and BD specimens by means of the J-integral (Abaqus, 2017), BT method (Williams, 1988), as well as the statistical and deterministic '5 branch' criteria in eq. $(4.30)_1$ substituted into eq. (4.19) and then into eq. (4.18), for $\hat{\psi} = 1.45$ rad and $\hat{L} = 100$ μm.

method of calculation	specimen type	$\mathcal{G}_{ic}$
J-integral (Abaqus, 2017)	C-ELS	843.1
5 branch statistical criterion	BD	853.7
5 branch deterministic criterion	BD	1063.1
BT (Williams, 1988)	C-ELS	1031.7

brittle thermosets and thermoplastics. Based on the results presented here, as well as those shown in Kravchenko et al. (2019) and Dolev (2020), it may be concluded that for dominant mode I deformation, thick specimens are required to determine failure criteria for the design of thicker structures.

For the C-ELS specimens, the plotted $\mathcal{G}_{ic} \approx \mathcal{G}_{IIc}$ values, as well as the in-plane phase angle $\hat{\psi}$ were obtained based on results from two-dimensional FEAs of the AC (first) test stage with P_{VIS} from Table 5.9. The displacement and stress fields from the FEAs were used with the VCCT (Farkash and Banks-Sills, 2016) to determine stress intensity factors which were substituted into eq. (3.19) to calculate $\hat{\psi}$. In addition, values of $\mathcal{G}_{IIC}$ were obtained by means of the J-integral of Abaqus (2017). The obtained values are plotted in Fig. 6.1 and were given explicitly in Table 5.22. The average values from all C-ELS tests were found to be $\hat{\psi} = 1.45$ rad and $\mathcal{G}_{IIc} = 843.1$ N/m. It may be observed in Fig. 6.1 that most of the obtained $\mathcal{G}_{IIc}$ values for the C-ELS specimens are lower than those obtained for the BD specimens tested with $\omega \approx -13°$.

In the second row of Table 6.2, the average $\mathcal{G}_{IIc}$ value obtained by means of the J-integral of Abaqus (2017) for the C-ELS specimens is presented. In the third and fourth rows of that table, the statistical and deterministic $\mathcal{G}_{ic}$ values, respectively, determined by means of the BD '5-branch' statistical and deterministic criteria in eq. $(4.30)_1$ substituted into eq. (4.19) and then into eq. (4.18), for $\hat{\psi} = 1.45$ rad, are shown. It may be observed that the statistical value related to the BD specimens is close to that obtained with the J-integral for the C-ELS specimens. The difference between the two values is 1.3% with respect the J-integral of Abaqus (2017). Note that the average value obtained by means of the J-integral is a bit lower. Perhaps lower values were obtained for the C-ELS tests since two-dimensional FEAs were performed; hence, the $\mathcal{G}_{IIc}$ values which were obtained by means of the J-integral of Abaqus (2017) produced a lower value for $\mathcal{G}_{ic}$ with $\hat{K}_2$ dominant. Moreover, in the two-dimensional analyses performed for the C-ELS specimens, effective material was used for the alternating $+45°/-45°$ and $0°/90°$ woven plies in the upper and lower parts of the modeled specimen, as shown in Fig. 5.10. It should be noted that use of this effective material in the model results in slightly more conservative J values than would have been obtained for a model with every ply modeled

separately. It might be interesting to reexamine the C-ELS specimens in the future by means of three-dimensional FEAs with all plies modeled and compare the resulting energy release rate values with those obtained by means of the two-dimensional FEAs carried out here.

In Mega and Banks-Sills (2020), the critical initiation energy release rate values related to the C-ELS specimens were analyzed by means of an additional global method based on beam theory (BT), as described in Williams (1988). The solution used takes into account the different thicknesses of the specimen arms, neglecting the differences in the flexural modulus of each arm. Since an interface between two dissimilar materials is studied, it should be noted that the influence of these parameters may not be negligible and may substantially affect the results. However, since a delamination along an interface between two dissimilar plies is considered, the global methods, namely, simple beam theory (SBT) and corrected beam theory using an effective crack length (CBTE), presented in the ISO Standard 15114:2014(E), are not applicable. Moreover, since insufficient data points are obtained from the NPC (first) test stage, it was not possible to determine $\mathcal{G}_{IIc}$ by means of ECM. Hence, calculation was made with the BT method (Williams, 1988) with a possibility of an error as a result of the different flexure moduli which were not accounted for in the calculation.

In the fifth row in Table 6.2, the average $\mathcal{G}_{IIc}$ value obtained by means of the BT method (Williams, 1988) is presented. It may be observed that for the C-ELS specimens the BT method provided a substantially higher $\mathcal{G}_{IIc}$ value with respect to that obtained by means of the J-integral or by means of the statistical BD '5-branch' criterion in eq. $(4.30)_1$ substituted into eq. (4.19) and then into eq. (4.18), for $\hat{\psi} = 1.45$ rad, shown in the second and third rows of Table 6.2. The difference between the results obtained with the J-integral and the BT method is approximately 18% with respect to the BT method. It may also be observed that the $\mathcal{G}_{ic}$ value determined using the deterministic BD '5-branch' criterion in eq. $(4.30)_1$ substituted into eq. (4.19) and then into eq. (4.18), for $\hat{\psi} = 1.45$ rad, was found to be relatively close to the result obtained by means of the BT method, with only 3% difference with respect to the '5-branch' deterministic criterion. It may be noted that it was previously shown in Blackman et al. (2012), for a UD material, that the BT method results in an upper bound for the energy release rate value. The results here may confirm that indeed an upper bound was obtained by means of this global method.

From the comparison shown here for the energy release rate values obtained from the C-ELS specimens versus the data from the BD specimens, as well as the value obtained from the '5-branch' deterministic criterion, it may be observed that for dominant K_2, the thickness of the specimens did not seem to influence $\mathcal{G}_{ic}$. The individual $\mathcal{G}_{ic}$ values which were calculated by means of the J-integral for each C-ELS specimen were found to be generally in the range between the statistical and the deterministic criteria values given in Table 6.2, which are based upon the BD test results.

For the MMELS specimens, the $\mathcal{G}_{ic}$ and $\hat{\psi}$ values, plotted in Fig. 6.1, were determined from an integrated average of the form in eq. (5.5), through the specimen width $\overline{b}$. The integrated expressions for $\mathcal{G}_{ic}(a_{0AC}, x_3)$ and $\hat{\psi}(a_{0AC}, x_3)$ were determined from eqs. (3.17) and (3.19), respectively, with $\hat{K}_m^{(T)}$ $(m = 1, 2, III)$ obtained from eq. (5.4) for a_{0AC} and P_{VIS} in Tables 5.28 and 5.29, respectively. The resulting $\mathcal{G}_{ic}$ values were presented explicitly in Table 5.37 and are plotted in Fig. 6.1 versus the obtained $\hat{\psi}$ values. The values of $\hat{\psi}$ at $\Delta a = 0$ were also plotted in Fig. 5.25. The integrated average $\mathcal{G}_{ic}$ and $\hat{\psi}$ values which were obtained for all MMELS tests were averaged and found to be $\mathcal{G}_{ic} = 567.4$ N/m and $\hat{\psi} = 0.67$ rad. This $\hat{\psi}$ value is approximately equivalent to the average mode mixity through the thickness of the BD specimens tested with $\omega \approx -2°$. The $\mathcal{G}_{ic}$ value obtained from the '5-branch' criterion in in eq. $(4.30)_1$ substituted into eq. (4.19) and then into eq. (4.18), for $\hat{\psi} = 0.67$ rad with $\hat{L} = 100$ μm, was found to be 406.0 N/m which is lower than that obtained by means of the MMELS specimens. In addition, it may be observed that the individual $\mathcal{G}_{ic}$ values determined from the MMELS tests and plotted in Fig. 6.1 are slightly higher than the majority of those obtained from the BD specimens for $\omega \approx -2°$, yet the results are within the scatter of the data. This difference is more apparent since twenty data points through the width of each BD specimen were plotted in Fig. 6.1, whereas for the MMELS tests only the integrated average through the width of the specimen is shown. Recall that the change in $\mathcal{G}_{ic}$ as a function of the specimen width $\overline{b}$, presented in Fig. 5.23a, was substantial. In that figure lower $\mathcal{G}_{ic}$ values were obtained near the outer specimen edges.

Although when averaged through the width $\overline{b}$, $\hat{\psi} \approx 0.67$ rad for all specimens for $\Delta a = 0$, a great change in the value of $\hat{\psi}$ may be observed in Fig. 5.23b near the specimen outer edges. Through the width of each specimen, $\hat{\psi}$ ranges between about 0.5 rad at mid-width to about 1.3 rad at the outer edges. However, between $0.2 \leq x_3/\overline{b} \leq 0.8$, the value of $\hat{\psi}$ changes by less than 6% ranging between 0.56 rad and 0.61 rad. Based on the calculated $\hat{\psi}$ values between $0.2 \leq x_3/\overline{b} \leq 0.8$ it may be concluded that $0.6\hat{K}_1 < \hat{K}_2 < 0.7\hat{K}_1$; hence, $\hat{K}_1$ is slightly larger than $\hat{K}_2$ through most of the specimen width. Since the in-plane mixed mode ratio is found to be mostly $\hat{K}_1$ dominant, perhaps, the explanation for the lower values obtained from the BD specimens versus those obtained from the MMELS tests is similar to that shown in the case of the DCB specimens for nearly mode I tests and related to the specimen thicknesses. Additional factors may be at work, as well. In addition, it may be observed from Fig. 5.23c that the out-of-plane to in-plane deformation, described with the phase angle ϕ, increases when approaching the specimen edges. This increase may be related to Poisson's ratio, as is the case of an interface between two homogeneous materials. Since the increase of both $\hat{\psi}$ and ϕ is most dominant near the specimen edges, it appears that the in-plane shear deformation is influenced by the out-of-plane shear deformation.

An empirical criterion proposed in Benzeggagh and Kenane (1996) and given in eqs. (4.10) and (4.11) was used for the beam type specimens. In eqs. (4.10) and (4.11),

the criterion relates the total critical energy release rate $\mathcal{G}_{Tc}$ to the mode mixity $\mathcal{G}_{II}/\mathcal{G}_T$. In order to plot the criterion as a function of $\hat{\psi}$ instead of $\mathcal{G}_{II}/\mathcal{G}_T$ it is assumed here that

$$\tan^2\hat{\psi} = \frac{\mathcal{G}_{II}}{\mathcal{G}_I} \quad . \tag{6.1}$$

With this relation, the B-K criterion from eq. (4.10) may be written as

$$\mathcal{G}_{ic} = \mathcal{G}_{Ic} + (\mathcal{G}_{IIc} - \mathcal{G}_{Ic}) \left(\frac{\tan^2\hat{\psi}}{1 + \tan^2\hat{\psi}} \right)^{\eta} \tag{6.2}$$

where η is a fitting parameter which is determined empirically based on experimental data. Note that the parameter $\mathcal{G}_{Tc}$ in eq. (4.10) has been replaced with $\mathcal{G}_{ic}$ in eq. (6.2) where i represents interface. The criterion in eq. (6.2) was employed here with the data obtained by means of the beam type specimens. The values $\mathcal{G}_{Ic} = 357.9$ N/m and $\mathcal{G}_{IIc} = 843.1$ N/m were obtained as the average energy release rate values of all DCB and C-ELS specimens tested, respectively. By means of the nonlinear Generalized Reduced Gradient (GRG) method in Excel (2016), the best fit of eq. (6.2) to the data related to the beam type specimens was found using a minimum value for the root mean square error (RMSE). The value for η was determined to be 0.83. The resulting B-K-criterion is plotted as the red curve in Fig. 6.1. It may be observed that for $0 \leq \hat{\psi} \leq 0.93$, the B-K criterion is less conservative than the '5 branch' deterministic criterion related to the BD specimens. For $\hat{\psi} = 0.93$, $\mathcal{G}_{ic} = 692.3$ N/m for both the B-K and the deterministic criterion. From that point, as $\hat{\psi}$ increases, the B-K criterion becomes more conservative, whereas the energy release rate values obtained from the '5 branch' deterministic and statistical criteria increase rapidly.

It may be concluded that the initiation fracture toughness values obtained in the current investigation using the BD specimens, as well as by means of the deterministic '5-branch' criterion are more conservative for $\hat{K}_2 \leq 1.34\hat{K}_1$ obtained for $\hat{\psi} \leq 0.93$ rad. This was observed in Fig. 6.1 for nearly mode I fracture toughness test results obtained using the DCB specimens, as well as for the mixed mode MMELS test results for the specific mode mixity tested. In addition, it was found that the critical interface initiation energy release rate values obtained by means of the C-ELS specimens, as well as the values calculated by means of the B-K criterion for $\hat{\psi} \geq 0.93$, were generally more conservative than those determined using the BD specimens or by means of the deterministic '5 branch' failure criterion. Moreover, it was observed that the critical initiation $\mathcal{G}_{ic}$ value is dependent on specimen thickness for the case of dominant $\hat{K}_1$. It appears that when $\hat{K}_2$ is dominant, this dependence is not apparent.

The resistance energy release rate $\mathcal{G}_{iR}$ values were determined for each tested beam type specimen by means of two methods, the local M or J- integral approach and the global ECM. The data obtained for the DCB, MMELS and C-ELS tested specimens were plotted versus Δa. It was observed that $\mathcal{G}_{iR}$ increased as the delamination extended until

reaching steady state. Since the investigated interface consisted of an upper UD fabric and a lower plain weave, the combination of both plies results in a complex fracture mechanism which includes fiber bridging, matrix cracking, delamination bifurcation, etc. As a result of the combination of these common failure mechanisms, a rise in the $\mathcal{G}_{iR}$ values was obtained as the delamination advanced. A power-law of the form in eq. (5.6) was fit to the rising portion of the data. For the C-ELS and MMELS tests, steady state was reached at approximately $\Delta a = 15$ mm. For the DCB specimens, steady state was obtained at approximately $\Delta a = 30$ mm. As steady state was reached, the energy required for extension remained constant as the delamination propagated.

In Dolev (2020), DCB, C-ELS, MMELS and BD tests were carried out for another material system. In that study, the investigated material tested was manufactured from a prepreg and consisted of a delamination along the interface between an upper $0°/90°$ and a lower $+45°/-45°$ woven fabric. A rising R-curve, similar to that observed here, was also obtained in that study. For the DCB and MMELS specimens, steady state was reached at $\Delta a \approx 13$ mm and for the C-ELS test at $\Delta a \approx 8$ mm. Moreover, in Dolev (2020), the rising portion of the C-ELS tests was found to be approximately linear. In Gong et al. (2017) a linear rise in $\mathcal{G}_{iR}$ was also observed for nearly mode I, nearly mode II and mixed mode tests which were performed using DCB, ENF and MMB specimens for an MD laminate composite with a delamination along a $+45°//-45°$ interface. The rising portion in Gong et al. (2017) reached steady state in the case of the DCB specimen at $\Delta a \approx 25$ mm. For the ENF and MMB tests, data for only 12 mm and 13 mm of propagation was obtained from the tests and steady state was not yet reached.

A comparison of the resulting curves obtained by means of the M or J- integrals and those obtained using the ECM is presented in Figs. 5.4, 5.14 and 5.26 for nearly mode I, nearly mode II and approximately one integrated through the specimen width mixed mode ratio I/II, respectively. It may be observed that the steady state energy release rate value obtained by means of the local M or J-integral approach versus those obtained from the global ECM differ by approximately 7% to 10% in absolute value. Although the analyses made with ECM are simpler and faster to perform, since the local M-integral includes FE models which account for the different stiffness of each specimen arm, as well as modeling of the investigated interface, the results obtained by means of this method appear to be more reliable. From this comparison, it may be observed that for the DCB and C-ELS tests a more conservative curve was determined by means of the local M and J-integral approach with respect to the resulting curve obtained by means of the ECM; whereas for the MMELS tests, the ECM produced more conservative values. This difference may be related to the coupling between the normal and shear forces, as well as the coupling between the bending and twisting moments with respect to the mid-plane of the specimen, as well as to the mid-plane of each specimen arm which are not fully accounted for using the global ECM.

This investigation may be continued and extended in several directions. First, scanning electron microscopy (SEM) micrographs of the fracture surfaces of both the UD and woven plies should be performed for the BD and beam type specimens. Such SEM results may provide additional information regarding the fracture mode and failure mechanisms which occurred during initiation and propagation of each test. In addition, use of X-ray micro-computed tomography, or micro-CT, which is a non-destructive technique (NDT) used to investigate the internal structure of a sample, may be used for the BD and beam type specimens. Such scans may provide highly accurate three-dimensional inspections of fiber architectures, as well as manufacturing defects. These may be examined to better understand the failure mechanisms related to each mode. It would also be interesting to analyze the C-ELS tests in three dimensions with each ply modeled separately and compare the results to those obtained here for two dimensions. Next, criteria of the form used for the BD specimens, given in eq. (4.43), should be employed with the data from the beam type specimens for both initiation and steady state energy release rate values. By doing so, initiation and steady state criteria for thin structures would be determined. It may also be interesting to perform additional DCB, C-ELS and MMELS tests from a new laminate plate with a larger thickness than that tested here. The results may be used to examine the phenomena shown here, as well as in Dolev (2020) and in Kravchenko et al. (2019), that the laminate thickness influences the initiation interface energy release rate under mode I dominant deformations. Moreover, using these results, the influence of laminate thickness on the steady state energy release rate could be examined. Results from such additional tests may also be used to test the B-K criteria which was employed here, as well as additional criteria in the form of the criterion in eq. (4.43). Moreover, by changing the thickness ratio of the MMELS specimen arms or by using the MMB test setup, several mode mixities may be tested. Results from these tests may verify prediction of the mixed mode criteria presented here.

Finally, fatigue delamination propagation tests using the C-ELS and MMELS specimens for nearly pure mode II and mixed mode deformation, respectively, for the material and interface investigated here should be carried out. Recall that such tests were performed for nearly mode I in Chocron and Banks-Sills (2019). The results from these tests may be used to evaluate the delamination growth rate and propagation parameters for the different deformation modes, as well as to generate a master curve for delamination growth rate versus a function of the energy release rate.

Bibliography

[1] Abaqus. Version 6.17. Dassault Systémes Simulia Corp., Johnston, RI, 2017.

[2] Aboudi, J. Mechanics of Composite Materials: A Unified Micromechanical Approach. Elsevier, Amsterdam, 1991.

[3] Aboudi, J. The generalized method of cells and the high-fidelity generalized method of cells micromechanical models–a review. Mech. Adv. Mater. Struct., 11: 329–366, 2004.

[4] Aksoy, A. and Carlsson, L.A. Interlaminar shear fracture of interleaved graphite/epoxy composites. Compos. Sci. Technol., 43: 55–69, 1992.

[5] Akisanya, A.R. and Fleck, N.A. Brittle fracture of adhesive joints. Int. J. Fract., 58: 93–114, 1992.

[6] Arcan, M., Hashin, Z. and Voloshin, A. A method to produce uniform plane-stress states with applications to fiber-reinforced materials. Exp. Mech., 18: 141–146, 1978.

[7] Arcan, L., Arcan, M. and Daniel, I.M. SEM fractography of pure and mixed mode interlaminar fracture in graphite/epoxy composites. In: ASTM-STP 948, Fractography of Modern Engineering Materials: Composites and Metals. Eds. Masters, J.E. and Au, J.J., American Society for Testing and Materials, Philadelphia PA, pp. 41–67, 1987.

[8] ASTM D5229/D5229M-92 (reapproved 2010). Test method for moisture absorption properties and equilibrium conditioning of polymer matrix composites. Space simulation; Aerospace and Aircraft; Composite Materials, Vol. 15.03, ASTM International, West Conshohocken, PA, 2011.

[9] ASTM Standard D5528-13. Standard test method for mode I interlaminar fracture toughness of unidirectional fiber-reinforced polymer matrix composites. Space Simulation; Aerospace and Aircraft; Composite Materials, Vol. 15.03, ASTM International, West Conshohocken, PA, pp. 289–301, 2014.

[10] ASTM Standard D6671M-13. Test method for mixed mode I - mode II interlaminar fracture toughness of unidirectional fiber-reinforced polymer matrix composites. Space Simulation; Aerospace and Aircraft; Composite Materials, Vol. 15.03, ASTM International, West Conshohocken, PA, pp. 429–438, 2014.

[11] ASTM Standard D7905/D7905M-14, Standard test method for determination of the mode II interlaminar fracture toughness of unidirectional fiber-reinforced polymer matrix composites, Space Simulation; Aerospace and Aircraft; Composite Materials, Vol. 15.03, ASTM International, West Conshohocken, PA, pp. 718–735, 2014.

[12] Atkinson, C., Smelser, R. and Sanchez, J. Combined mode fracture via the cracked Brazilian disk test. Int. J. Fract., 18: 279–291, 1982.

[13] Banks-Sills, L., Arcan, M. and Bortman, Y. A mixed mode fracture specimen for mode II dominant deformation. Eng. Fract. Mech., 20: 145–157, 1984.

[14] Banks-Sills, L. Application of the finite element method to linear elastic fracture mechanics. Appl. Mech. Rev., 44: 447–461, 1991.

[15] Banks-Sills, L. Weight functions for interface cracks. Int. J. Fract., 60: 89–95, 1993.

[16] Banks-Sills, L., Travitzky, N., Ashkenazi, D. and Eliasi, R. A methodology for measuring interface fracture properties of composite materials. Int. J. Fract., 99: 143–161, 1999.

[17] Banks-Sills, L. and Ashkenazi, D. A note on fracture criteria for interface fracture. Int. J. Fract., 103: 177–188, 2000.

[18] Banks-Sills, L., Travitzky, N. and Ashkenazi, D. Interface fracture properties of a bimaterial ceramic composite. Mech. Mater., 32: 711–722, 2000.

[19] Banks-Sills, L. and Boniface, V. Fracture mechanics for an interface crack between a special pair of transversely isotropic materials. In: Multiscale Deformation and Fracture in Materials and Structures-the James R. Rice 60th Anniversary Volume. Eds. Chuang, T.J. and Rudnicki, J.W., Kluwer Academic Publishers, The Netherlands, pp. 183–204, 2000.

[20] Banks-Sills, L. and Dolev, O. The conservative M-integral for thermal-elastic problems. Int. J. Fract., 125: 149–170, 2004.

[21] Banks-Sills, L., Hershkovitz, I., Wawrzynek, P.A., Eliasi, R. and Ingraffea, A.R. Methods for calculating stress intensity factors in anisotropic materials: Part I–z=0 is a symmetric plane. Eng. Fract. Mech., 72: 2328–2358, 2005a.

[22] Banks-Sills, L., Boniface, V. and Eliasi, R. Development of a methodology for determination of interface fracture toughness of laminate composites–the $0°/90°$ pair. Int. J. Solids Struct., 42: 663–680, 2005b.

[23] Banks-Sills, L., Freed, Y., Eliasi, R. and Fourman, V. Fracture toughness of the $+45°/-45°$ interface of a laminate composite. Int. J. Fract., 141: 195–210, 2006.

[24] Banks-Sills, L. Update: application of the finite element method to linear elastic fracture mechanics. Appl. Mech. Rev. 63: 020803(1)–020803(17), 2010.

[25] Banks-Sills, L., Konovalov, N. and Fliesher, A. Comparison of two and three-dimensional analyses of interface fracture data obtained from Brazilian disk specimens. Int. J. Struct. Integr., 1: 20–42, 2010.

[26] Banks-Sills, L., Ishbir, C., Fourman, V., Rogel, L. and Eliasi, R. Interface fracture toughness of a multi-directional woven composite. Int. J. Fract., 182: 187-207, 2013.

[27] Banks-Sills, L. Interface fracture mechanics: theory and experiment. Int. J. Fract., 191: 131–146, 2015.

[28] Banks-Sills, L. Interface fracture: failure criteria. J. Appl. Mech., 87: 051007 1–9, 2020.

[29] Barnett, D.M. and Kirchner, H.O.K. A proof of the equivalence of the Stroh and Lekhnitskii sextic equations for plane anisotropic elastostatics. Philos. Mag. A, 76: 231–239, 1997.

[30] Benzeggagh, M.L. and Kenane, M. Measurement of mixed-mode delamination fracture toughness of unidirectional glass/epoxy composites with mixed-mode bending apparatus. Compos. Sci. Technol., 56: 439–449, 1996.

[31] Bhashyan, S. and Davidson, B.D. Evaluation of data reduction methods for the mixed-mode bending test. AIAA J., 35: 546–552, 1997.

[32] Blackman, B.R.K, Brunner, A.J and Davies P. Delamination fracture of continuous fibre composites: mixed-mode fracture. In: Fracture Mechanics Testing Methods for Polymers, Adhesives and Composite, Vol. 28. Eds. Moore, D.R., Williams, J.G. and Pavan, A., ESIS, Oxford, UK, pp. 335–367, 2001.

[33] Blackman, B.R.K, Kinloch, A.J and Paraschi, M. The determination of the mode II adhesive fracture resistance, G_{IIc}, of structural adhesive joints: an effective crack length approach. Eng. Fract. Mech., 72: 877–897, 2005.

[34] Blackman, B.R.K., Brunner, A.J. and Williams, J.G. Mode II fracture testing of composites: a new look at an old problem. Eng. Fract. Mech., 73: 2443–2455, 2006.

[35] Blackman, B.R.K, Conroy, M., Ivankovic, A., Karac, A., Kinloch, A.J. and Williams J.G. Mode-mixity in beam-like geometries: linear elastic cases and local partitioning. In: 15th European Conference on Composite Materials, Venice, Italy, 2012.

[36] Bowles, D.E. and Tompkins, S.S. Prediction of coefficients of thermal expansion for unidirectional composites. J. Compos. Mater., 23: 370–388, 1989.

[37] Carlsson, L.A., Gillespie, J.W. and Pipes, R.B. On the analysis and design of the end notched flexure (ENF) specimen for mode II testing. J. Compos. Mater., 20: 594–604, 1986a.

[38] Carlsson, L.A., Gillespie, J.W. and Trethewey, B.R. Mode II interlaminar fracture of graphite/epoxy and graphite/PEEK. J. Reinf. Plast. Compos., 5: 170–187, 1986b.

[39] Chan, S.K., Tuba, I.S. and Wilson, W.K. On the finite element method in linear fracture mechanics. Eng. Frac. Mech., 2: 1–17, 1970.

[40] Chow, W.T. and Atluri, S.N. Stress intensity factors as the fracture parameters for delamination crack growth in composite laminates. Compos. Part B: Eng., 28: 375–384, 1997.

[41] Chen, F.H.K. and Shield, R.T. Conservation laws in elasticity of the J-integral type. Z. Angew. Math. Phys., 28: 1–22, 1977.

[42] Chocron, T. and Banks-Sills, L. Nearly mode I fracture toughness and fatigue delamination propagation in a multidirectional laminate fabricated by a wet-layup. Phys. Mesomech., 22: 107–140, 2019.

[43] Choi, N.S., Kinloch, A.J. and Williams, J.G. Delamination fracture of multidirectional carbon-fiber/epoxy composites under mode I, mode II and mixed-mode I/II loading. J. Compos. Mater., 33: 73–100, 1999.

[44] Choupani, N. Mixed-mode cohesive fracture of adhesive joints: experimental and numerical studies. Eng. Fract. Mech., 75: 4363–4382, 2008.

[45] Davidson, B.D., Kruger, R. and König, M. Three dimensional analysis and resulting design recommendations for unidirectional and multidirectional end-notched flexure tests. J. Compos. Mater., 29: 2108–2133, 1995.

[46] Davidson, B.D. and Sundararaman, V. A single leg bending test for interfacial fracture toughness determination. Int. J. Fract., 78: 193–210, 1996.

[47] Davies, P., Kausch, H.H., Williams, J.G., Kinloch, A.J., Charalambides, M.N., Pavan, A., Moore, D.R., Prediger, R., Robinson, I., Burgoyne, N., et al. Round-robin interlaminar fracture testing of carbon-fibre-reinforced epoxy and PEEK composites. Compos. Sci. Technol., 43: 129–136, 1992.

[48] Davies, P., Blackman, B.R.K. and Brunner, A.J. Standard test methods for delamination resistance of composite materials: current status. Appl. Compos. Mater., 5: 345–364, 1998.

[49] DaVis Version 8.3. LaVison, Göttingen, Germany, 2015.

[50] Decad, D. Micromechanics-based modeling of woven composite materials. M.Sc. Thesis, Tel Aviv University, Israel, 2008.

[51] Deng, X. General crack-tip fields for stationary and steadily growing interface cracks in anisotropic bimaterials. J. Appl. Mech., 60: 183–189, 1993.

[52] De Morais, A.B., De Moura, M.F., Marques, A.T. and De Castro, P.T. Mode-I interlaminar fracture of carbon/epoxy cross-ply composites. Compos. Sci. Technol., 62: 679–686, 2002.

[53] de Morais, A.B., De Moura, M.F., Gonçalves, J.P.M. and Camanho, P.P. Analysis of crack propagation in double cantilever beam tests of multidirectional laminates. Mech. Mater., 35: 641–652, 2003.

[54] de Morais, A.B. and Pereira, A.B. Interlaminar fracture of multidirectional glass/epoxy laminates under mixed-mode I+II loading. Mech. Compos. Mater., 43: 233–244, 2007.

[55] Dexter, H.B. Development of textile reinforced composites for aircraft structures. In: Fourth International Symposium for Textile Composites, Kyoto Institute of Technology, Kyoto, Japan, pp. D1–D6, 1998.

[56] Dharmawan, F., Simpson, G., Herszberg, I. and John, S. Mixed mode fracture toughness of GFRP composites. Compos. Struct., 75: 328–338, 2006.

[57] Dolev, O. Mixed mode fracture behavior of a multi-directional plain weave composite - an interface delamination between a $0°/90^{circ}$ and a $+45°/-45^{circ}$ weave. Ph.D. Thesis, Tel Aviv University, Israel, Submitted for review, 2020.

[58] Donaldson, S.L. Fracture toughness testing of Graphite/Epoxy and Graphite/PEEK composites. Compos., 16: 103–112, 1985.

[59] Erdogan, F. and Sih, G.C. On the crack extension in plates under plane loading and transverse shear. J. Basic Eng., 85: 519–525, 1963.

[60] Excel Software, Version: 16.0.4266.1001. Microsoft Corporation, 2016.

[61] Farkash, E. and Banks-Sills, L. Virtual crack closure technique for an interface crack between two transversely isotropic materials. Int. J. Fract., 205: 189–202, 2017.

[62] Farkash, E. Extension of the virtual crack closure technique and Clifford formalism. Ph.D. Thesis, Tel Aviv University, Israel, Submitted for review, 2020.

[63] Feret, V., Ghiasi, H. and Hubert, P. Effect of fibre volume fraction on mixed-mode fracture of a fabric carbon/epoxy composite. Appl. Compos. Mater., 20: 415–429, 2013.

[64] Freed, Y. and Banks-Sills, L. A through interface crack between a $\pm 45^{\circ}$ transversely isotropic pair of materials. Int. J. Fract., 133: 1–41, 2005.

[65] Gill, A.F, Robinson, P. and Pinho, S. Effect of variation in fibre volume fraction on modes I and II delamination behaviour of 5HS woven composites manufactured by RTM. Compos. Sci. Technol., 69: 2368–2375, 2009.

[66] Gong, X.J., Hurez, A. and Verchery, G. On the determination of delamination toughness by using multidirectional DCB specimens. Polym. Test., 29: 658–666, 2010.

[67] Gong, Y., Zhao, L., Zhang, J., Wang, Y. and Hu, N. Delamination propagation criterion including the effect of fiber bridging for mixed-mode I/II delamination in CFRP multidirectional laminates. Compos. Sci. Technol., 151: 302–309, 2017.

[68] Gong, Y., Zhang, B., Zhao, L., Zhang, J., Hu, N. and Zhang, C. *R*-curve behaviour of the mixed-mode I/II delamination in carbon/epoxy laminates with unidirectional and multidirectional interfaces. Compos. Struct., 223: 110949-1–8, 2019.

[69] Griffith, A.A. The phenomena of fracture and flow in solids. Philos. Trans. Roy. Soc. A, A221: 163–198, 1920.

[70] Griffith, A.A. The theory of rupture. In: Proceedings of the First International Congress of Applied Mechanics. Eds. Biezeno C.B. and Burgers J.M., Delft, pp. 55–63, 1924.

[71] Hashemi, S., Kinloch, A.J. and Williams, J.G. The analysis of interlaminar fracture in uniaxial fibre-polymer composites. Proc. R. Soc. Lond. A, 427: 173–199, 1990.

[72] Heydari, M.H., Choupani, N. and Shameli, M. Experimental and numerical investigation of mixed-mode interlaminar fracture of carbon-polyester laminated woven composite by using Arcan set-up. Appl. Compos. Mater., 6: 499–511, 2011.

[73] Hojo, M., and Aoki, T. Thickness effect of double cantilever beam specimen on interlaminar fracture toughness of AS4/PEEK and T800/epoxy laminates. In: ASTM-STP 1156, Composite Materials: Fatigue and Fracture, Fourth Volume. Eds. Stinchcomb W., and Ashbaugh N., American Society for Testing and Materials International, West Conshohocken, PA, pp. 281–298, 1993.

[74] Hussain, M.A., Pu, S.L. and Underwood, J. Strain energy release rate for a crack under combined mode I and mode II. In: Fracture Analysis: Proceedings of the 1973 National Symposium on Fracture Mechanics, Part II, ASTM STP 560, Eds. Paris, P.C. and Irwin, G.R., American Society for Testing and Materials. Philadelphia, PA, pp. 2–28, 1974.

[75] ImageJ, Image processing and analysis in Java. Version December 22, 2015. Fiji, Madison, Wisconsin, USA.

[76] Irwin, G.R. Fracture dynamics. In: Proceedings of the ASM Symposium on Fracturing of Metals. Cleveland, OH, pp. 147–166, 1948.

[77] Irwin, G.R and Kies, J.A. Critical energy rate analysis of fracture strength. Weld. J., 137: 193–198, 1954.

[78] Irwin, G.R. Analysis of stresses and strains near the end of a crack traversing a plate. J. Appl. Mech., 24: 361–364, 1957.

[79] Irwin, G.R. Fracture. In: Handbuch Der Physik, Vol. 6. Ed. Flügge, S., Springer, Berlin, pp. 551–590, 1958.

[80] ISO Standard 291. Plastics-standard atmospheres for conditioning and testing. ISO, England, 2008.

[81] ISO Standard 15024:2001(E). Fibre-reinforced plastic composites - determination of mode I interlaminar fracture toughness, G_{IC}, for unidirectionally reinforced materials. ISO, Switzerland, 2011.

[82] ISO Standard 15114:2014(E). Fibre-reinforced plastic composites - determination of the mode II fracture resistance for unidirectionally reinforced materials using the calibrated end-loaded split (C-ELS) test and an effective crack length approach. ISO, Switzerland, 2014.

[83] Jones, R.M. Mechanics of Composite Materials. CRC Press, Philadelphia, PA, 1998.

[84] Kinloch, A.J., Wang, Y., Williams, J.G. and Yayla, P. The mixed-mode delamination of fibre-composite materials. Compos. Sci. Technol., 47: 225–237, 1993.

[85] Kravchenko, O.G., Kravchenko, S.G., and Sun, C.T. Thickness dependence of mode I interlaminar fracture toughness in a carbon fiber thermosetting composite. Compos. Struct., 160: 538–546, 2017.

[86] Kusaka, T., Hojo, M., Mai, Y.W., Kurokawa, T., Nojima, T. and Ochiai, S. Rate dependence of mode I fracture behaviour in carbon-fibre/epoxy composite laminates. Compos. Sci. Technol., 58: 591–602, 1998.

[87] Lai, Y.H., Rakestraw, M.D. and Dillard, D.A. The cracked lap shear specimen revisited-a closed form solution. Int. J. Solids Struct., 33: 1725–1743, 1996.

[88] Lekhnitskii, S.G. Theory of Elasticity of an Anisotropic Body. Holden-Day, San Francisco, 1950, in Russian; translated by P. Fern, 1963, in English.

[89] Li, F.Z., Shih, C.F. and Needleman, A. A comparison of methods for calculating energy release rates. Eng. Frac. Mech., 21: 405–421, 1985.

[90] Luko, S.N. and Neubauer, D.V. Statistical intervals-part 2: the predicition interval. ASTM Stand. News, American Society for Testing and Materials, Sept/Oct: 14-15, 2011.

[91] Mall, S. and Kochhar, N.K. Criterion for mixed mode fracture in composite bonded joints. NASA CR-178112, National Aeronautics and Space Administration, Washington, DC, 1986.

[92] Mallick, P.K. Fiber-Reinforced Composites: Materials, Manufacturing, and Design. CRC Press, New York, NY, 2007.

[93] Malyshev, B.M. and Salganik, R.L. The strength of adhesive joints using the theory of cracks. Int. J. Fract. Mech., 1: 114–128, 1965.

[94] MATLAB version 9.6.0.1072779 (R2019a) Natick, Massachusetts: The Mathworks, Inc., 2019.

[95] Matweb - material property data. http://www.matweb.com/search/Data Sheet.aspx?MatGUID=3dbc779c2f034329b2836b02b9483629, accessed 20 October 2015.

[96] Mega, M. and Banks-Sills, L. Mixed mode interface fracture toughness of a multi-directional composite UD/woven pair. Theor. Appl. Fract. Mech., 104: 102323: 1–13, 2019.

[97] Mega, M. and Banks-Sills, L. Two- and three-dimensional failure criteria for laminate composites. J. Appl. Mech., 87: 021001: 1–11, 2019.

[98] Mega, M. and Banks-Sills, L. Comparison of methods for determination of fracture toughness in a multi-directional CFRP laminate. Procedia Struct. Integr., 28: 917924, 2020.

[99] Miyagawa, H., Sato, C., Mase, T., Drown, E., Drzal, L.T. and Ikegami, K. Transverse elastic modulus of carbon fibers measured by Raman spectroscopy. Mater. Sci. Eng.: A, 412: 88–92, 2005.

[100] Naik, N.K., Reddy, K.S., Meduri, S., Raju, N.B., Prasad, P.D., Azad, S.K.N.M., Ogde, P.A. and Reddy, B.C.K. Interlaminar fracture characterization for plain weave fabric composites. J. Mater. Sci., 37: 2983–2987, 2002.

[101] Naik, N.K. Woven-fibre thermoset composites. In: Fatigue in Composites. Ed. Harris, B., Woodhead Publishing Ltd., Cambridge, England, pp. 296–313, 2003.

[102] Nakamura, T. and Parks, D.M. Antisymmetrical 3-D stress field near the crack front of a thin elastic plate. Int. J. Solids and Struct., 25: 1411–1426, 1989.

[103] Natrella, M.G. Experimental Statistics. National Bureau of Standards Handbook 91. U.S. Government Printing Office, Washington, DC, pp. 2-13–2-15, 1963.

[104] Nikbakht, M. and Choupani, N. Fracture toughness characterization of carbon-epoxy composite using Arcan specimen. Int. J. Aerosp. Mech. Eng., 2: 247–253, 2008.

[105] Nikbakht, M. and Choupani, N. Experimental investigation of mixed-mode fracture behaviour of woven laminated composite. J. Mater. Sci., 44: 3428–3437, 2009.

[106] Ozdil, F., Carlsson, L.A. and Davies, P. Beam analysis of angle-ply laminate end-notched flexure specimens. Compos. Sci. Technol., 58: 1929–1938, 1998.

[107] Ozdil, F. and Carlsson, L.A. Beam analysis of angle-ply laminate mixed-mode bending specimens. Compos. Sci. Technol., 59: 937–945, 1999.

[108] Pereira, A.B. and de Morais, A.B. Mode I interlaminar fracture of carbon/epoxy multidirectional laminates. Compos. Sci. Technol., 64: 2261–2270, 2004.

[109] Pereira, A.B., de Morais, A.B., Marques, A.T. and de Castro, P.T. Mode II interlaminar fracture of carbon/epoxy multidirectional laminates. Compos. Sci. Technol., 64: 1653–1659, 2004.

[110] Pereira, A.B., De Morais, A.B., De Moura, M.F.S.F. and Magalhães, A.G. Mode I interlaminar fracture of woven glass/epoxy multidirectional laminates. Compos. Part A - Appl. Sci. Manuf., 36: 1119–1127, 2005.

[111] Pereira, A.B. and de Morais, A.B. Mixed mode I+II interlaminar fracture of carbon/epoxy laminates. Compos. Part A - Appl. Sci. Manuf., 39: 322–333, 2008.

[112] Pérez-Galmés, M., Renart, J., Sarrado, C., Brunner, A.J. and Rodríguez-Bellido, A. Towards a consensus on mode II adhesive fracture testing: Experimental study. Theor. Appl. Fract. Mech., 98: 210–219, 2018.

[113] Prel, Y., Davies, P., Benzeggagh, M. and Charentenay de F., Mode I and mode II delamination of thermosetting and thermoplastic composites. In: ASTM-STP

1012, Composite Materials: Fatigue and Fracture, Second Volume. Ed. Lagace, P., American Society for Testing and Materials International, West Conshohocken, PA, pp. 251–269, 1989.

[114] Ramkumar, R.L. and Whitcomb, J.D. Characterization of mode I and mixed-mode delamination growth in T300/5208 graphite/epoxy. In: ASTM-STP 876, Delamination and Debonding of Materials. Ed. Johnson, W.S., American Society for Testing and Materials, Philadelphia, PA, pp. 315–335, 1985.

[115] Reeder, J.R. and Crews, J.H. Mixed-mode bending method for delamination testing. AIAA J., 28: 1270–1276, 1990.

[116] Reeder, J.R. A bilinear failure criterion for mixed-mode delamination. In: Composite Materials - Testing and Design (Eleventh Volume), ASTM STP 1206. Ed. Camponeschi, J.R., American Society for Testing and Materials. Philadelphia, PA, pp. 303–322, 1993.

[117] Reeder, J.R. 3-D mixed mode delamination fracture criteria - an experimentalist's perspective. In: Damage in Composites. Eds. Sankar, B.V, Waas, A.M. and Hyer, M.W., Destech Publications. Lancaster, PA, pp. 129 – 146, 2013.

[118] Rice, J.R. A path independent integral and the approximate analysis of strain concentration by notches and cracks. J. Appl. Mech., 35: 379–386, 1968.

[119] Rice, J.R. Elastic fracture mechanics concepts for interfacial cracks. J. Appl. Mech., 55: 98–103, 1988.

[120] Rice, J.R., Suo, Z. and Wang, J.S. Mechanics and thermodynamics of brittle interfacial failure in bimaterial systems. In: Metal Ceramic Interfaces. Eds. Rühle, M., Evans, A.G., Ashby, M.F. and Hirth, J.P., Pergamon Press, Oxford, pp. 269–294, 1990.

[121] Rikards, R. Interlaminar fracture behaviour of laminated composites. Comput. Struct., 76: 11–18, 2000.

[122] Rogel, L. A through interface crack between a transversly isotropic pair of materials: $+30°/-60°$ and $-30°/+60°$. M.Sc. Thesis, Tel Aviv University, Israel, 2009.

[123] Rzeczkowski, J., Samborski, S. and de Moura, M. Experimental investigation of delamination in composite continuous fiber-reinforced plastic laminates with elastic couplings. Mater., 13: 5146-1–17, 2020.

[124] Shampine, L.F. Vectorized adaptive quadrature in MATLAB. J. Comput. Appl. Math., 211: 131-140, 2008.

[125] Shih, C.F., Moran, B. and Nakamura, T. Energy release rate along a three-dimensional crack front in a thermally stressed body Int. J. Fract., 30: 79–102, 1986.

[126] Sih, G.C., Paris, P.C. and Irwin, G.R. On cracks in rectilinearly anisotropic bodies. Int. J. Fract. Mech., 1: 189–203, 1965.

[127] Sih, G.C. Mechanics of Fracture I: Methods of Analysis and Solution of Crack Problems: Recent Developments in Fracture Mechanics, Theory and Methods of Solving Crack Problems Ed. Sih, G.C., Noordhoff International Publishing, Leyden, The Netherlands, 1973.

[128] Simon, I., Banks-Sills, L. and Fourman, V. Mode I delamination propagation and R-ratio effects in woven composite DCB specimens for a multi-directional layup. Int. J. Fatigue, 96: 237–251, 2017.

[129] Stroh, A.N. Dislocations and cracks in anisotropic elasticity. Philos. Mag., 3: 625–646, 1958.

[130] Szekrényes, A. and Uj, J. Beam and finite element analysis of quasi-unidirectional composite SLB and ELS specimens. Compos. Sci. Technol., 64: 2393–2406, 2004.

[131] Tamuzs, V., Tarasovs, S. and Vilks, U. Progressive delamination and fiber bridging modeling in double cantilever beam composite specimens. Eng. Fract. Mech., 68: 513–525, 2001.

[132] Taylor, R.P. Fibre composite aircraft: capability and safety. Australian Government-Australian Transport Safety Bureau, Australia, 2008.

[133] Ting, T.C.T. Anisotropic Elasticity: Theory and Applications. Oxford University Press, New York, NY, 1996.

[134] Torayca T300 Data Sheet, Toray Carbon Fibers America, Inc., http://www.toraycfa.com/pdfs/T300DataSheet.pdf, Accessed 22 November 2015.

[135] Tracy, G.D., Feraboli, P. and Kedward, K.T. A new mixed mode test for carbon/epoxy composite systems. Compos. Part A - Appl. Sci. Manuf., 34: 1125–1131, 2003.

[136] Vision Assistant, Version 8.0, National Instruments Corporation, Austin, TX, USA, 2005.

[137] Wang, J.S. and Suo, Z. Experimental determination of interfacial toughness curves using Brazil-nut-sandwiches. Acta. Metall. Mater., 38: 1279–1290, 1990.

[138] Wang, Y. and Williams, J.G. Corrections for mode II fracture toughness specimens of composites materials. Compos. Sci. Technol., 43: 251–256, 1992.

[139] Wang, C.H. Fracture of interface cracks under combined loading. Eng. Fract. Mech., 56: 77–86, 1997.

[140] Whitmore, G.A. Prediction limits for a univariate normal observation. Am. Stat., 40: 141–143, 1986.

[141] Whittaker, B.N., Singh, R.N. and Sun, G. Rock fracture mechanics: principles, design and applications. Developments in Geotechnical Engineering, Vol. 71. Elsevier, Amsterdam, 1996.

[142] Williams, J.G. On the calculation of energy release rates for cracked laminates. Int. J. Fract., 36: 101–119, 1988.

[143] Williams, J.G. The fracture mechanics of delamination tests. J. Strain Anal. Eng. Des., 24: 207–214, 1989.

[144] Williams, M.L. On the stress distribution at the base of a stationary crack. J. Appl. Mech., 24: 109–114, 1957.

[145] Williams, M.L. The stresses around a fault or crack in dissimilar media. Bull. Seismol. Soc. Am., 49: 199–204, 1959.

[146] Wilson, W.K. and Yu, I.W. The use of the J-integral in thermal stress crack problems. Int. J. Fract., 15: 377–387, 1979.

[147] Wisnom, M.R. The role of delamination in failure of fibre-reinforced composites. Philos. Trans. Roy. Soc. A, 370: 1850–1870, 2012.

[148] Wu, E.M. Application of fracture mechanics to anisotropic plates J. Appl. Mech., 34: 967–974, 1967.

[149] Xiao, F., Hui, C.Y. and Kramer, E.J. Analysis of a mixed mode fracture specimen: the asymmetric double cantilever beam. J. Mater. Sci., 28: 5620–5629, 1993.

[150] Yarema, S.Y. On the contribution of G.R. Irwin to fracture mechanics. Mater. Sci., 31: 617–623, 1996.

[151] Yau, J.F., Wang, S.S., Corten, H.T. A mixed-mode crack analysis of isotropic solids using conservation laws of elasticity. J. App. Mech., 47: 335–341, 1980.

[152] Yau, J.F. and Wang, S.S. An analysis of interface cracks between dissimilar isotropic materials using conservation integrals in elasticity. Eng. Fract. Mech., 20: 423–432, 1984.

[153] Yoon, S.H. and Hong, C.S. Modified end notched flexure specimen for mixed mode interlaminar fracture in laminated composites. Int. J. Fract., 43: R3–R9, 1990a.

[154] Yoon, S.H. and Hong, C.S. Interlaminar fracture toughness of graphite/epoxy composite under mixed-mode deformations. Exp. Mech., 30: 234–239, 1990b.

[155] Zhao, J.M and Wang, H.L. and Liu, B. Two objective and independent fracture parameters for interface cracks, J. Appl. Mech., 84: 041006 1–9, 2017.

Appendix A

The Lekhnitskii and Stroh formalisms

A.1 The Lekhnitskii formalism

Following Ting (1996), the Lekhnitskii (1963) formalism for plane deformation of anisotropic elastic materials is in terms of the reduced elastic compliances. It begins with the assumption that the stresses are independent of x_3, namely

$$\sigma_{ij} = \sigma_{ij}(x_1, x_2). \tag{A.1}$$

With the stresses independent of x_3, the equilibrium equations reduce to

$$\sigma_{i1,1} + \sigma_{i2,2} = 0, \quad i = 1, 2, 3. \tag{A.2}$$

The form of eq. (A.2) in conjunction with stress symmetry, enables the use of the Airy stress functions, χ and ψ, respectively. These functions are related to the stress components by

$$\begin{gathered} \sigma_{11} = \chi_{,22}\,, \quad \sigma_{22} = \chi_{,11}\,, \quad \sigma_{12} = -\chi_{,12}\,, \\ \sigma_{32} = -\psi_{,1}\,, \quad \sigma_{31} = \psi_{,2}\,. \end{gathered} \tag{A.3}$$

When the stress components are represented as in eq. (A.3) in terms of χ and ψ, the equations of equilibrium (A.2) are automatically satisfied.

Following the assumption that the stresses are independent of x_3, the strains also depend on only x_1 and x_2 and the displacements should be linear with respect to x_3. For such a case, the strains may be formulated as

$$\begin{gathered} \varepsilon_{11} = u_{1,1}, \quad \varepsilon_{22} = u_{2,2}, \quad \varepsilon_{33} = Ax_1 + Bx_2 + C, \\ 2\varepsilon_{23} = u_{3,2} + \omega x_1, \quad 2\varepsilon_{13} = u_{3,1} - \omega x_2 \quad 2\varepsilon_{12} = u_{1,2} + u_{2,1}, \end{gathered} \tag{A.4}$$

where u_1, u_2 and u_3 are the displacement components that solely depend on x_1 and x_2; the parameters A, B, C are constants and ω is a constant which represents the deformation

related to torsion about the x_3-axis. It may be noted that A, B, C and ω are taken to be zero so that the displacement field is independent of x_3. The related compatibility equations are given as

$$\varepsilon_{13,2} - \varepsilon_{23,1} = 0,$$
$$\varepsilon_{11,22} + \varepsilon_{22,11} - 2\varepsilon_{12,12} = 0. \tag{A.5}$$

The stress-strain relations in contracted notation are given by

$$\varepsilon_\alpha = S_{\alpha\beta}\sigma_\beta, \quad \alpha, \beta = 1...6, \tag{A.6}$$

where, ε_α and σ_α are the contracted strain and stress components, and $S_{\alpha\beta}$ are the elastic compliance components. The stress-strain relations may be written with reduced elastic compliance components as

$$\varepsilon_\alpha = S'_{\alpha\beta}\sigma_\beta + \frac{S_{\alpha 3}}{S_{33}}\varepsilon_3 \tag{A.7}$$

where

$$S'_{\alpha\beta} = S_{\alpha\beta} - \frac{S_{\alpha 3}\, S_{3\beta}}{S_{33}}\ . \tag{A.8}$$

It is clear that $S'_{\alpha\beta}$ is symmetric and that

$$S'_{\alpha 3} = S'_{3\alpha} = 0 \qquad (\alpha = 1, 2, ..., 6). \tag{A.9}$$

With eq. (A.9), the reduced compliance matrix $\boldsymbol{S'}$ is reduced to a 5×5 matrix.

Substitution of eqs. (A.3) into eq. (A.7) leads to a formulation for the strains in terms of χ and ψ as

$$\varepsilon_\alpha = S'_{\alpha 1}\chi_{,22} + S'_{\alpha 2}\chi_{,11} - S'_{\alpha 4}\psi_{,1} + S'_{\alpha 5}\psi_{,2} - S'_{\alpha 6}\chi_{,12} + \frac{S_{\alpha 3}}{S_{33}}\varepsilon_3. \tag{A.10}$$

Insertion of (A.10) into the compatibility conditions (A.5) produces a set of differential equations (Ting, 1996, p. 121) which may be manipulated to obtain a sixth order differential equation, namely

$$\left(L_2 L_4 - L_3 L_3\right)\chi = 0, \tag{A.11}$$

where the operators L_2, L_3, and L_4 are

$$\begin{aligned} L_2 &= S'_{55}\frac{\partial^2}{\partial x_2^2} - 2S'_{45}\frac{\partial^2}{\partial x_2 \partial x_1} + S'_{44}\frac{\partial^2}{\partial x_1^2}, \\ L_3 &= S'_{15}\frac{\partial^3}{\partial x_2^3} - \left(S'_{14} + S'_{56}\right)\frac{\partial^3}{\partial x_2^2 \partial x_1} + \left(S'_{25} + S'_{46}\right)\frac{\partial^3}{\partial x_2 \partial x_1^2} - S'_{24}\frac{\partial^3}{\partial x_1^3}, \\ L_4 &= S'_{11}\frac{\partial^4}{\partial x_2^4} - 2S'_{16}\frac{\partial^4}{\partial x_2^3 \partial x_1} + \left(2S'_{12} + S'_{66}\right)\frac{\partial^4}{\partial x_2^2 \partial x_1^2} - 2S'_{26}\frac{\partial^4}{\partial x_2 \partial x_1^3} + S'_{22}\frac{\partial^4}{\partial x_1^4}. \end{aligned} \tag{A.12}$$

A general solution of the form

$$\chi(x_1, x_2) = F(z), \tag{A.13}$$

is assumed where

$$z = x_1 + p x_2, \tag{A.14}$$

and p is a complex constant. Substitution of eq. (A.13) into eq. (A.11) leads to a sextic equation in p, namely

$$l_2(p)l_4(p) - l_3(p)l_3(p) = 0, \tag{A.15}$$

where,

$$\begin{aligned} l_2(p) &= S'_{55}p^2 - 2S'_{45}p + S'_{44}, \\ l_3(p) &= S'_{15}p^3 - (S'_{14} + S'_{56})\,p^2 + (S'_{25} + S'_{46})\,p - S'_{24}, \\ l_4(p) &= S'_{11}p^4 - 2S'_{16}p^3 + (2S'_{12} + S'_{66})\,p^2 - 2S'_{26}p + S'_{22}. \end{aligned} \tag{A.16}$$

Solution of eq. (A.15) produces three pairs of complex conjugate roots p_α and $\overline{p}_\alpha$ ($\alpha = 1, 2, 3$) which are the eigenvalues of the elastic constants, given in Section 2.2 in eq. (2.36). A general solution for the stress and displacement fields is obtained by superimposing the six solutions which are associated with the six eigenvalues p_α and $\overline{p}_\alpha$.

A.2 The Stroh formalism

Stroh's (1958) sextic formalism for plane deformation of an anisotropic elastic body is mathematically elegant and technically powerful. With the Stroh formalism, the assumption is made that the displacement components are a function of the coordinates x_1 and x_2, namely,

$$u_i = u_i(x_1, x_2), \quad i = 1, 2, 3. \tag{A.17}$$

The stress-stain laws and equilibrium equations using the stiffness tensor coefficients C_{ijks}, $i, j, k, s = 1, 2, 3$ take the form of

$$\sigma_{ij} = C_{ijks}u_{k,s}, \tag{A.18}$$

and

$$C_{ijks}u_{k,sj} = 0. \tag{A.19}$$

A general solution for u_i is composed of a linear combination of the coordinates x_1 and x_2, so that

$$u_i = a_i f(z). \tag{A.20}$$

In eq. (A.20), $f(z)$ is an arbitrary function of z which is defined in eq. (A.14) and a_i are unknown complex constants to be determined. Differentiation of eq. (A.20) with respect to x_s and x_j and satisfaction of eq. (A.19) leads to

$$\left\{\boldsymbol{Q} + p(\boldsymbol{R} + \boldsymbol{R}^T) + p^2\boldsymbol{T}\right\}\boldsymbol{a} = 0, \tag{A.21}$$

where $\boldsymbol{Q}$, $\boldsymbol{R}$, and $\boldsymbol{T}$ are 3×3 matrices whose components are given by

$$Q_{ik} = C_{i1k1}, \quad R_{ik} = C_{i1k2}, \quad T_{ik} = C_{i2k2}. \tag{A.22}$$

A non-trivial solution for $\boldsymbol{a}$ requires that

$$\left|\boldsymbol{Q} + p(\boldsymbol{R} + \boldsymbol{R}^T) + p^2\boldsymbol{T}\right| = 0. \tag{A.23}$$

From eq. (A.23), three pairs of complex conjugate eigenvalues p are obtained. It was shown by Barnett and Kirchner (1997) that these eigenvalues are the same as those produced by eq. (A.15) in the Lekhnitskii formalism, and presented in eq. (2.36). The associated eigenvectors a_α ($\alpha = 1...6$) are found from eq. (A.21).

Under the assumption that p_α ($\alpha = 1...6$) are distinct, the general solution of the displacement is obtained by superposing the six solutions from eq. (A.20), namely

$$\boldsymbol{u} = \sum_{\alpha=1}^{3} \left\{ \boldsymbol{a}_\alpha f_\alpha(z_\alpha) + \overline{\boldsymbol{a}}_\alpha f_{\alpha+3}(\overline{z}_\alpha) \right\}, \tag{A.24}$$

where f_α ($\alpha = 1...6$) are arbitrary functions of their arguments z_α which are given in eq. (A.14).

Once the displacement field $\boldsymbol{u} = \boldsymbol{u}(x_1, x_2)$ is obtained, the stress components σ_{ij} are found from eq. (A.18), so that they are independent of x_3, as well. The stress components may be written as

$$\sigma_{i1} = -p b_i f'(z), \quad \sigma_{i2} = b_i f'(z), \tag{A.25}$$

where the complex constants b_i are related to a_i by

$$\boldsymbol{b} = \left(\boldsymbol{R}^T + p\boldsymbol{T} \right) \boldsymbol{a} = -\frac{1}{p} \left(\boldsymbol{Q} + p\boldsymbol{R} \right) \boldsymbol{a}. \tag{A.26}$$

A stress function $\boldsymbol{\phi}$ is selected to represent the stress components as

$$\phi_i = b_i f(z). \tag{A.27}$$

The relation between ϕ_i and σ_{ij} is given by

$$\sigma_{i1} = -\phi_{i,2} \quad \sigma_{i2} = \phi_{i,1} \tag{A.28}$$

where $i = 1, 2, 3$.

The general solution for the stress function $\boldsymbol{\phi}$ is obtained by superposing six solutions from eq. (A.27) associated with the six eigenvalues p_α, namely

$$\boldsymbol{\phi} = \sum_{\alpha=1}^{3} \left\{ \boldsymbol{b}_\alpha f_\alpha(z_\alpha) + \overline{\boldsymbol{b}}_\alpha f_{\alpha+3}(\overline{z}_\alpha) \right\}. \tag{A.29}$$

Equations (A.24) and (A.29) comprise the sextic formalism due to Stroh (1958). For both, the functions $f_\alpha(z_\alpha)$ and $f_{\alpha+3}(\overline{z}_\alpha)$ are chosen as

$$f_\alpha(z_\alpha) = f(z_\alpha) q_\alpha, \quad f_{\alpha+3}(\overline{z}_\alpha) = f(\overline{z}_\alpha) \widetilde{q}_\alpha, \quad (\alpha = 1, 2, 3), \tag{A.30}$$

where q_α and $\widetilde{q}_\alpha$ are arbitrary complex vectors. The Stroh eigenvectors $\boldsymbol{a}$ and $\boldsymbol{b}$ are assumed to obey the relations

$$\boldsymbol{a}_{\alpha+3} = \overline{\boldsymbol{a}}_\alpha, \qquad \boldsymbol{b}_{\alpha+3} = \overline{\boldsymbol{b}}_\alpha, \quad (\alpha = 1, 2, 3). \tag{A.31}$$

The Lekhnitskii and Stroh formalisms were presented above. The Lekhnitskii formalism is compliance based and formulates a sextic differential equation using a stress function that satisfies equilibrium in conjunction with the compatibility conditions and is related to the stresses that are independent of x_3. The Stroh formalism is stiffness based and formulates a sextic eigenvalue problem using displacements which are independent of x_3 and satisfy equilibrium in conjunction with the compatibility conditions. Barnett and Kirchner (1997) have shown that the sextic equations from both methods, leading to the field solution, are equivalent despite the differences between the two formalisms.

Appendix B

Tabulated results of benchmark problems

The methods used in this investigation to analyze test results and compute the stress intensity factors were the DE method and the M-integral. Both methods made use of the first term of the asymptotic expansion of the displacement components. In order to examine the accuracy of the asymptotic solution, as well as the software written for these methods, three benchmark problems. The geometry of the cylindrical body analyzed is presented in Fig. 3.2. The body contains an edge delamination between an upper transversely isotropic UD material with fibers oriented in the 0°-direction and a lower tetragonal woven material with fibers oriented in the $+45°/-45°$-directions. The mesh used is shown in Fig. 3.3. For each benchmark problem, displacements were applied to the outer surface of the body. The displacements were obtained from the first term of the asymptotic solution for three specific sets of stress intensity factors. The delamination faces are traction free. The expected results are the same as the applied stress intensity factors for each problem. For the DE method, the exact imposed solutions were obtained for most local stress intensity factors K_1^*, K_2^* and K_{III}^* in eqs. (3.10) and (3.13), respectively. Hence, extrapolation of these results led to the exact stress intensity factors.

The M-integral was carried out in six domains shown in Fig. 1.8. In this section, tabulated results obtained from the M-integral in all six domains are presented. For the first benchmark problem, the applied stress intensity factors were $K_1 = 1$, $K_2 = 0$ and $K_{III} = 0$. The obtained results are presented in Tables B.1 and B.2. In the second benchmark problem, the applied stress intensity factors were $K_1 = 0$, $K_2 = 1$ and $K_{III} = 0$. The obtained results are presented in Tables B.3 and B.4. In the third benchmark problem, the applied stress intensity factors were $K_1 = 0$, $K_2 = 0$ and $K_{III} = 1$. The obtained results are presented in Tables B.5 and B.6.

Table B.1: $K_1^{(f)}$, $K_2^{(f)}$ and $K_{III}^{(f)}$ calculated in domains 1, 2 and 3 for the first benchmark problem: $K_1^{(f)} = 1$, $K_2^{(f)} = 0$, $K_{III}^{(f)} = 0$. The geometry and mesh of the problem are shown in Figs. 3.2 and 3.3, respectively. Note that the units of $K_i^{(f)}$ $(i = 1, 2)$ are $\text{MPa}\sqrt{\text{mm}}(\text{mm})^{-i\varepsilon}$, and that the units of $K_{III}^{(f)}$ are $\text{MPa}\sqrt{\text{mm}}$.

	domain 1			**domain 2**			**domain 3**		
x_3/B	$K_1^{(f)}$	$K_2^{(f)}$	$K_{III}^{(f)}$	$K_1^{(f)}$	$K_2^{(f)}$	$K_{III}^{(f)}$	$K_1^{(f)}$	$K_2^{(f)}$	$K_{III}^{(f)}$
0.025	1.028	0.004	0.001	1.003	0.001	0.002	1.002	-0.001	0.002
0.075	1.006	0.007	0.000	1.001	0.002	0.000	1.001	0.000	0.000
0.125	1.011	0.007	0.000	1.001	0.002	0.000	1.001	0.000	0.000
0.175	1.009	0.007	0.000	1.001	0.002	0.000	1.001	0.000	0.000
0.225	1.010	0.007	0.000	1.001	0.002	0.000	1.000	0.000	0.000
0.275	1.010	0.007	0.000	1.001	0.002	0.000	1.000	0.000	0.000
0.325	1.010	0.007	0.000	1.001	0.002	0.000	1.000	0.000	0.000
0.375	1.010	0.007	0.000	1.001	0.002	0.000	1.000	0.000	0.000
0.425	1.010	0.007	0.000	1.001	0.002	0.000	1.000	0.000	0.000
0.475	1.010	0.007	0.000	1.001	0.002	0.000	1.000	0.000	0.000
0.525	1.010	0.007	0.000	1.001	0.002	0.000	1.000	0.000	0.000
0.575	1.010	0.007	0.000	1.001	0.002	0.000	1.000	0.000	0.000
0.625	1.010	0.007	0.000	1.001	0.002	0.000	1.000	0.000	0.000
0.675	1.010	0.007	0.000	1.001	0.002	0.000	1.000	0.000	0.000
0.725	1.010	0.007	0.000	1.001	0.002	0.000	1.000	0.000	0.000
0.775	1.010	0.007	0.000	1.001	0.002	0.000	1.000	0.000	0.000
0.825	1.009	0.007	0.000	1.001	0.002	0.000	1.001	0.000	0.000
0.875	1.011	0.007	0.000	1.001	0.002	0.000	1.001	0.000	0.000
0.925	1.006	0.007	0.000	1.001	0.002	0.000	1.001	0.000	0.000
0.975	1.028	0.004	-0.001	1.003	0.001	-0.002	1.002	-0.001	-0.002

A thermal problem was also solved. It simulates the temperature change during curing of the composite. A temperature change of $-60°$ C was imposed and the stress intensity factors resulting from the residual stresses were obtained. With the DE method, local stress intensity factors K_1^*, K_2^* and K_{III}^* were calculated. Using extrapolation of three sequential points at a chosen distance from the delamination front, the stress intensity factors $K_1^{(r)}$, $K_2^{(r)}$ and $K_{III}^{(r)}$ were obtained. The obtained values as well as the normalized distance from the delamination front $(r/R)_1$, $(r/R)_2$ and $(r/R)_{III}$, where r is the distance from the delamination front, R is the radius of the model and the subscript $1, 2, III$ are related to the relevant stress intensity factor, are presented in Table B.7. The

Table B.2: $K_1^{(f)}$, $K_2^{(f)}$ and $K_{III}^{(f)}$ calculated in domains 4, 5 and 6 for the first benchmark problem: $K_1^{(f)} = 1$, $K_2^{(f)} = 0$, $K_{III}^{(f)} = 0$. The geometry and mesh of the problem are shown in Figs. 3.2 and 3.3, respectively. Note that the units of $K_i^{(f)}$ $(i = 1, 2)$ are $\text{MPa}\sqrt{\text{mm}}(\text{mm})^{-i\varepsilon}$, and that the units of $K_{III}^{(f)}$ are $\text{MPa}\sqrt{\text{mm}}$.

	domain 4			**domain 5**			**domain 6**		
x_3/B	$K_1^{(f)}$	$K_2^{(f)}$	$K_{III}^{(f)}$	$K_1^{(f)}$	$K_2^{(f)}$	$K_{III}^{(f)}$	$K_1^{(f)}$	$K_2^{(f)}$	$K_{III}^{(f)}$
0.025	1.002	-0.001	0.002	1.002	-0.001	0.002	1.002	-0.001	0.002
0.075	1.000	0.000	0.000	1.000	0.000	0.000	1.000	0.000	0.000
0.125	1.000	0.000	0.000	1.000	0.000	0.000	1.000	0.000	0.000
0.175	1.000	0.000	0.000	1.000	0.000	0.000	1.000	0.000	0.000
0.225	1.000	0.000	0.000	1.000	0.000	0.000	1.000	0.000	0.000
0.275	1.000	0.000	0.000	1.000	0.000	0.000	1.000	0.000	0.000
0.325	1.000	0.000	0.000	1.000	0.000	0.000	1.000	0.000	0.000
0.375	1.000	0.000	0.000	1.000	0.000	0.000	1.000	0.000	0.000
0.425	1.000	0.000	0.000	1.000	0.000	0.000	1.000	0.000	0.000
0.475	1.000	0.000	0.000	1.000	0.000	0.000	1.000	0.000	0.000
0.525	1.000	0.000	0.000	1.000	0.000	0.000	1.000	0.000	0.000
0.575	1.000	0.000	0.000	1.000	0.000	0.000	1.000	0.000	0.000
0.625	1.000	0.000	0.000	1.000	0.000	0.000	1.000	0.000	0.000
0.675	1.000	0.000	0.000	1.000	0.000	0.000	1.000	0.000	0.000
0.725	1.000	0.000	0.000	1.000	0.000	0.000	1.000	0.000	0.000
0.775	1.000	0.000	0.000	1.000	0.000	0.000	1.000	0.000	0.000
0.825	1.000	0.000	0.000	1.000	0.000	0.000	1.000	0.000	0.000
0.875	1.000	0.000	0.000	1.000	0.000	0.000	1.000	0.000	0.000
0.925	1.000	0.000	0.000	1.000	0.000	0.000	1.000	0.000	0.000
0.975	1.002	-0.001	-0.002	1.002	-0.001	-0.002	1.002	-0.001	-0.002

stress intensity factors $K_1^{(r)}$, $K_2^{(r)}$ and $K_{III}^{(r)}$, for the thermal problem, obtained using the thermal M-integral, for six domains, are presented in Table B.8 for domains 1, 2 and 3 and Table B.9 for domains 4, 5 and 6, respectively. In Table B.10, the averaged values of the stress intensity factors $K_1^{(r)}$, $K_2^{(r)}$ and $K_{III}^{(r)}$, obtained using the DE method, for each of two adjacent nodes along the delamination front are presented with the values obtained using the M-integral in the sixth domain. In addition, the differences between the values obtained with the two methods are shown. These differences were calculated using eq. (3.31) where $K_i^{(1)}$, $i = 1, 2, III$, is the averaged value obtained by means of the DE method and $K_i^{(2)}$ is the stress intensity factor obtained from the thermal M-integral.

Table B.3: $K_1^{(f)}$, $K_2^{(f)}$ and $K_{III}^{(f)}$ calculated in domains 1, 2 and 3 for the second benchmark problem: $K_1^{(f)} = 0$, $K_2^{(f)} = 1$, $K_{III}^{(f)} = 0$. The geometry and mesh of the problem are shown in Figs. 3.2 and 3.3, respectively. Note that the units of $K_i^{(f)}$ $(i = 1, 2)$ are $\mathrm{MPa}\sqrt{\mathrm{mm}}(\mathrm{mm})^{-i\varepsilon}$, and that the units of $K_{III}^{(f)}$ are $\mathrm{MPa}\sqrt{\mathrm{mm}}$.

	domain 1			**domain 2**			**domain 3**		
x_3/B	$K_1^{(f)}$	$K_2^{(f)}$	$K_{III}^{(f)}$	$K_1^{(f)}$	$K_2^{(f)}$	$K_{III}^{(f)}$	$K_1^{(f)}$	$K_2^{(f)}$	$K_{III}^{(f)}$
0.025	0.013	0.737	-0.005	-0.001	1.000	-0.007	-0.001	1.002	-0.007
0.075	0.018	0.745	0.000	-0.001	0.993	0.001	0.000	0.996	0.001
0.125	0.017	0.742	0.000	-0.001	0.993	-0.001	0.000	0.996	-0.001
0.175	0.017	0.742	0.000	-0.001	0.992	0.000	0.000	0.995	0.000
0.225	0.017	0.742	0.000	-0.001	0.992	0.000	0.000	0.995	0.000
0.275	0.017	0.742	0.000	-0.001	0.992	0.000	0.000	0.995	0.000
0.325	0.017	0.742	0.000	-0.001	0.992	0.000	0.000	0.995	0.000
0.375	0.017	0.742	0.000	-0.001	0.992	0.000	0.000	0.995	0.000
0.425	0.017	0.742	0.000	-0.001	0.992	0.000	0.000	0.995	0.000
0.475	0.017	0.742	0.000	-0.001	0.992	0.000	0.000	0.995	0.000
0.525	0.017	0.742	0.000	-0.001	0.992	0.000	0.000	0.995	0.000
0.575	0.017	0.742	0.000	-0.001	0.992	0.000	0.000	0.995	0.000
0.625	0.017	0.742	0.000	-0.001	0.992	0.000	0.000	0.995	0.000
0.675	0.017	0.742	0.000	-0.001	0.992	0.000	0.000	0.995	0.000
0.725	0.017	0.742	0.000	-0.001	0.992	0.000	0.000	0.995	0.000
0.775	0.017	0.742	0.000	-0.001	0.992	0.000	0.000	0.995	0.000
0.825	0.017	0.742	0.000	-0.001	0.992	0.000	0.000	0.995	0.000
0.875	0.017	0.742	0.000	-0.001	0.993	0.001	0.000	0.996	0.001
0.925	0.018	0.745	0.000	-0.001	0.993	-0.001	0.000	0.996	-0.001
0.975	0.013	0.737	0.005	-0.001	1.000	0.007	-0.001	1.002	0.007

Table B.4: $K_1^{(f)}$, $K_2^{(f)}$ and $K_{III}^{(f)}$ calculated in domains 4, 5 and 6 for the second benchmark problem: $K_1^{(f)} = 0$, $K_2^{(f)} = 1$, $K_{III}^{(f)} = 0$. The geometry and mesh of the problem are shown in Figs. 3.2 and 3.3, respectively. Note that the units of $K_i^{(f)}$ $(i = 1, 2)$ are $\text{MPa}\sqrt{\text{mm}}(\text{mm})^{-i\varepsilon}$, and that the units of $K_{III}^{(f)}$ are $\text{MPa}\sqrt{\text{mm}}$.

	domain 4			**domain 5**			**domain 6**		
x_3/B	$K_1^{(f)}$	$K_2^{(f)}$	$K_{III}^{(f)}$	$K_1^{(f)}$	$K_2^{(f)}$	$K_{III}^{(f)}$	$K_1^{(f)}$	$K_2^{(f)}$	$K_{III}^{(f)}$
0.025	0.000	1.004	-0.007	0.000	1.005	-0.007	-0.001	1.006	-0.007
0.075	0.000	0.999	0.001	0.000	0.999	0.001	0.000	1.000	0.001
0.125	0.000	0.998	-0.001	0.000	0.999	-0.001	0.000	0.999	-0.001
0.175	0.000	0.998	0.000	0.000	0.999	0.000	0.000	0.999	0.000
0.225	0.000	0.998	0.000	0.000	0.998	0.000	0.000	0.999	0.000
0.275	0.000	0.997	0.000	0.000	0.998	0.000	0.000	0.999	0.000
0.325	0.000	0.997	0.000	0.000	0.998	0.000	0.000	0.999	0.000
0.375	0.000	0.997	0.000	0.000	0.998	0.000	0.000	0.998	0.000
0.425	0.000	0.997	0.000	0.000	0.998	0.000	0.000	0.998	0.000
0.475	0.000	0.997	0.000	0.000	0.998	0.000	0.000	0.998	0.000
0.525	0.000	0.997	0.000	0.000	0.998	0.000	0.000	0.998	0.000
0.575	0.000	0.997	0.000	0.000	0.998	0.000	0.000	0.998	0.000
0.625	0.000	0.997	0.000	0.000	0.998	0.000	0.000	0.998	0.000
0.675	0.000	0.997	0.000	0.000	0.998	0.000	0.000	0.999	0.000
0.725	0.000	0.997	0.000	0.000	0.998	0.000	0.000	0.999	0.000
0.775	0.000	0.998	0.000	0.000	0.998	0.000	0.000	0.999	0.000
0.825	0.000	0.998	0.000	0.000	0.999	0.000	0.000	0.999	0.000
0.875	0.000	0.998	0.001	0.000	0.999	0.001	0.000	0.999	0.001
0.925	0.000	0.999	-0.001	0.000	0.999	-0.001	0.000	1.000	-0.001
0.975	0.000	1.004	0.007	0.000	1.005	0.007	-0.001	1.006	0.007

Table B.5: $K_1^{(f)}$, $K_2^{(f)}$ and $K_{III}^{(f)}$ calculated in domains 1, 2 and 3 for the third benchmark problem: $K_1^{(f)} = 0$, $K_2^{(f)} = 0$, $K_{III}^{(f)} = 1$. The geometry and mesh of the problem are shown in Figs. 3.2 and 3.3, respectively. Note that the units of $K_i^{(f)}$ $(i = 1, 2)$ are $\text{MPa}\sqrt{\text{mm}}(\text{mm})^{-i\varepsilon}$, and that the units of $K_{III}^{(f)}$ are $\text{MPa}\sqrt{\text{mm}}$.

	domain 1			**domain 2**			**domain 3**		
x_3/B	$K_1^{(f)}$	$K_2^{(f)}$	$K_{III}^{(f)}$	$K_1^{(f)}$	$K_2^{(f)}$	$K_{III}^{(f)}$	$K_1^{(f)}$	$K_2^{(f)}$	$K_{III}^{(f)}$
0.025	0.000	-0.003	0.974	0.001	-0.005	1.001	0.001	-0.005	1.002
0.075	0.000	0.001	0.967	0.000	0.001	1.000	0.000	0.001	1.000
0.125	0.000	0.000	0.968	0.000	0.000	0.999	0.000	0.000	1.000
0.175	0.000	0.000	0.968	0.000	0.000	0.999	0.000	0.000	1.000
0.225	0.000	0.000	0.968	0.000	0.000	0.999	0.000	0.000	1.000
0.275	0.000	0.000	0.968	0.000	0.000	0.999	0.000	0.000	1.000
0.325	0.000	0.000	0.968	0.000	0.000	0.999	0.000	0.000	1.000
0.375	0.000	0.000	0.968	0.000	0.000	0.999	0.000	0.000	1.000
0.425	0.000	0.000	0.968	0.000	0.000	0.999	0.000	0.000	1.000
0.475	0.000	0.000	0.968	0.000	0.000	0.999	0.000	0.000	1.000
0.525	0.000	0.000	0.968	0.000	0.000	0.999	0.000	0.000	1.000
0.575	0.000	0.000	0.968	0.000	0.000	0.999	0.000	0.000	1.000
0.625	0.000	0.000	0.968	0.000	0.000	0.999	0.000	0.000	1.000
0.675	0.000	0.000	0.968	0.000	0.000	0.999	0.000	0.000	1.000
0.725	0.000	0.000	0.968	0.000	0.000	0.999	0.000	0.000	1.000
0.775	0.000	0.000	0.968	0.000	0.000	0.999	0.000	0.000	1.000
0.825	0.000	0.000	0.968	0.000	0.000	0.999	0.000	0.000	1.000
0.875	0.000	0.000	0.968	0.000	0.000	0.999	0.000	0.000	1.000
0.925	0.000	-0.001	0.967	0.000	-0.001	1.000	0.000	-0.001	1.000
0.975	0.000	0.003	0.974	-0.001	0.005	1.001	-0.001	0.005	1.002

Table B.6: $K_1^{(f)}$, $K_2^{(f)}$ and $K_{III}^{(f)}$ calculated in domains 4, 5 and 6 for the third benchmark problem: $K_1^{(f)} = 0$, $K_2^{(f)} = 0$, $K_{III}^{(f)} = 1$. The geometry and mesh of the problem are shown in Figs. 3.2 and 3.3, respectively. Note that the units of $K_i^{(f)}$ $(i = 1, 2)$ are $\text{MPa}\sqrt{\text{mm}}(\text{mm})^{-i\varepsilon}$, and that the units of $K_{III}^{(f)}$ are $\text{MPa}\sqrt{\text{mm}}$.

	domain 4			**domain 5**			**domain 6**		
x_3/B	$K_1^{(f)}$	$K_2^{(f)}$	$K_{III}^{(f)}$	$K_1^{(f)}$	$K_2^{(f)}$	$K_{III}^{(f)}$	$K_1^{(f)}$	$K_2^{(f)}$	$K_{III}^{(f)}$
0.025	0.001	-0.005	1.002	0.001	-0.005	1.002	0.001	-0.005	1.002
0.075	0.000	0.001	1.000	0.000	0.001	1.000	0.000	0.001	1.000
0.125	0.000	0.000	1.000	0.000	0.000	1.000	0.000	0.000	1.000
0.175	0.000	0.000	1.000	0.000	0.000	1.000	0.000	0.000	1.000
0.225	0.000	0.000	1.000	0.000	0.000	1.000	0.000	0.000	1.000
0.275	0.000	0.000	1.000	0.000	0.000	1.000	0.000	0.000	1.000
0.325	0.000	0.000	1.000	0.000	0.000	1.000	0.000	0.000	1.000
0.375	0.000	0.000	1.000	0.000	0.000	1.000	0.000	0.000	1.000
0.425	0.000	0.000	1.000	0.000	0.000	1.000	0.000	0.000	1.000
0.475	0.000	0.000	1.000	0.000	0.000	1.000	0.000	0.000	1.000
0.525	0.000	0.000	1.000	0.000	0.000	1.000	0.000	0.000	1.000
0.575	0.000	0.000	1.000	0.000	0.000	1.000	0.000	0.000	1.000
0.625	0.000	0.000	1.000	0.000	0.000	1.000	0.000	0.000	1.000
0.675	0.000	0.000	1.000	0.000	0.000	1.000	0.000	0.000	1.000
0.725	0.000	0.000	1.000	0.000	0.000	1.000	0.000	0.000	1.000
0.775	0.000	0.000	1.000	0.000	0.000	1.000	0.000	0.000	1.000
0.825	0.000	0.000	1.000	0.000	0.000	1.000	0.000	0.000	1.000
0.875	0.000	0.000	1.000	0.000	0.000	1.000	0.000	0.000	1.000
0.925	0.000	-0.001	1.000	0.000	-0.001	1.000	0.000	-0.001	1.000
0.975	-0.001	0.005	1.002	-0.001	0.005	1.002	-0.001	0.005	1.002

Table B.7: $K_1^{(r)}$, $K_2^{(r)}$ and $K_{III}^{(r)}$ calculated with the DE method at the chosen normalized distance from the delamination front $(r/R)_1$, $(r/R)_2$ and $(r/R)_{III}$, respectively, for the thermal problem where r is the distance from the delamination front and R is the radius of the model. The geometry and mesh of the problem are shown in Figs. 3.2 and 3.3, respectively. Note that the units of $K_i^{(r)}$ $(i = 1, 2)$ are MPa$\sqrt{\text{mm}}(\text{mm})^{-i\varepsilon}$, and that the units of $K_{III}^{(r)}$ are MPa$\sqrt{\text{mm}}$.

x_3/B	$K_1^{(r)}$	$(r/R)_1$	$K_2^{(r)}$	$(r/R)_2$	$K_{III}^{(r)}$	$(r/R)_{III}$
0	-	-	-	-	-	-
0.05	-	-	-	-	21.237	0.025
0.1	1.316	0.017	-0.756	0.025	18.749	0.023
0.15	0.951	0.025	-1.696	0.015	16.305	0.025
0.2	0.759	0.025	-2.346	0.020	13.821	0.023
0.25	0.654	0.025	-2.741	0.020	11.419	0.023
0.3	0.594	0.025	-3.009	0.020	9.070	0.023
0.35	0.560	0.025	-3.190	0.020	6.764	0.023
0.4	0.541	0.025	-3.307	0.020	4.491	0.023
0.45	0.532	0.025	-3.373	0.020	2.240	0.023
0.5	0.529	0.025	-3.394	0.020	0.000	0.000
0.55	0.532	0.025	-3.373	0.020	-2.240	0.023
0.6	0.541	0.025	-3.307	0.020	-4.491	0.023
0.65	0.560	0.025	-3.190	0.020	-6.764	0.023
0.7	0.594	0.025	-3.009	0.020	-9.070	0.023
0.75	0.654	0.025	-2.741	0.020	-11.419	0.023
0.8	0.759	0.025	-2.346	0.020	-13.821	0.023
0.85	0.951	0.025	-1.696	0.015	-16.305	0.025
0.9	1.316	0.017	-0.756	0.025	-18.749	0.023
0.95	-	-	-	-	-21.237	0.025
1	-	-	-	-	-	-

Table B.8: $K_1^{(r)}$, $K_2^{(r)}$ and $K_{III}^{(r)}$ calculated in domains 1, 2 and 3 for the thermal problem. The geometry and mesh of the problem are shown in Figs. 3.2 and 3.3, respectively. Note that the units of $K_i^{(r)}$ $(i = 1, 2)$ are MPa$\sqrt{\text{mm}}(\text{mm})^{-i\varepsilon}$, and that the units of $K_{III}^{(r)}$ are MPa$\sqrt{\text{mm}}$.

	domain 1			**domain 2**			**domain 3**		
$x3/B$	$K_1^{(r)}$	$K_2^{(r)}$	$K_{III}^{(r)}$	$K_1^{(r)}$	$K_2^{(r)}$	$K_{III}^{(r)}$	$K_1^{(r)}$	$K_2^{(r)}$	$K_{III}^{(r)}$
0.025	3.572	3.289	21.031	3.399	4.549	21.438	3.400	4.566	21.440
0.075	1.706	0.139	19.341	1.698	0.141	19.954	1.693	0.159	19.979
0.125	1.114	-1.014	17.011	1.134	-1.318	17.523	1.131	-1.315	17.532
0.175	0.823	-1.622	14.601	0.865	-2.130	15.049	0.861	-2.129	15.059
0.225	0.669	-2.007	12.246	0.725	-2.630	12.620	0.720	-2.631	12.628
0.275	0.582	-2.263	9.941	0.646	-2.965	10.245	0.641	-2.967	10.251
0.325	0.532	-2.438	7.682	0.601	-3.192	7.918	0.596	-3.195	7.922
0.375	0.503	-2.553	5.461	0.575	-3.343	5.628	0.570	-3.346	5.632
0.425	0.487	-2.625	3.266	0.562	-3.435	3.366	0.556	-3.439	3.368
0.475	0.480	-2.659	1.087	0.556	-3.479	1.120	0.550	-3.483	1.121
0.525	0.480	-2.659	-1.087	0.556	-3.479	-1.120	0.550	-3.483	-1.121
0.575	0.487	-2.625	-3.266	0.562	-3.435	-3.366	0.556	-3.439	-3.368
0.625	0.503	-2.553	-5.461	0.575	-3.343	-5.628	0.570	-3.346	-5.632
0.675	0.532	-2.438	-7.682	0.601	-3.192	-7.918	0.596	-3.195	-7.922
0.725	0.582	-2.263	-9.941	0.646	-2.965	-10.245	0.641	-2.967	-10.251
0.775	0.669	-2.007	-12.246	0.725	-2.630	-12.621	0.720	-2.631	-12.628
0.825	0.823	-1.622	-14.601	0.865	-2.130	-15.050	0.861	-2.129	-15.060
0.875	1.114	-1.014	-17.011	1.134	-1.318	-17.523	1.131	-1.315	-17.532
0.925	1.706	0.139	-19.341	1.698	0.141	-19.954	1.693	0.159	-19.979
0.975	3.572	3.289	-21.031	3.399	4.549	-21.438	3.400	4.566	-21.440

Table B.9: $K_1^{(r)}$, $K_2^{(r)}$ and $K_{III}^{(r)}$ calculated in domains 4, 5 and 6 for the thermal problem. The geometry and mesh of the problem are shown in Figs. 3.2 and 3.3, respectively. Note that the units of $K_i^{(r)}$ $(i = 1, 2)$ are MPa$\sqrt{\text{mm}}(\text{mm})^{-i\varepsilon}$, and that the units of $K_{III}^{(r)}$ are MPa$\sqrt{\text{mm}}$.

	domain 4			**domain 5**			**domain 6**		
$x3/B$	$K_1^{(r)}$	$K_2^{(r)}$	$K_{III}^{(r)}$	$K_1^{(r)}$	$K_2^{(r)}$	$K_{III}^{(r)}$	$K_1^{(r)}$	$K_2^{(r)}$	$K_{III}^{(r)}$
0.025	3.403	4.569	21.439	3.404	4.568	21.437	3.405	4.567	21.437
0.075	1.694	0.164	19.985	1.694	0.165	19.986	1.695	0.166	19.987
0.125	1.131	-1.318	17.534	1.131	-1.320	17.534	1.132	-1.320	17.534
0.175	0.861	-2.132	15.062	0.861	-2.134	15.062	0.861	-2.135	15.062
0.225	0.720	-2.636	12.630	0.720	-2.638	12.630	0.720	-2.639	12.630
0.275	0.640	-2.972	10.253	0.640	-2.975	10.253	0.641	-2.976	10.253
0.325	0.595	-3.200	7.923	0.595	-3.203	7.924	0.595	-3.204	7.924
0.375	0.569	-3.352	5.632	0.570	-3.354	5.632	0.570	-3.356	5.632
0.425	0.556	-3.445	3.369	0.556	-3.448	3.369	0.556	-3.449	3.369
0.475	0.550	-3.489	1.121	0.550	-3.492	1.121	0.550	-3.493	1.121
0.525	0.550	-3.489	-1.121	0.550	-3.492	-1.121	0.550	-3.493	-1.121
0.575	0.556	-3.445	-3.369	0.556	-3.448	-3.369	0.556	-3.449	-3.369
0.625	0.569	-3.352	-5.632	0.570	-3.354	-5.632	0.570	-3.356	-5.632
0.675	0.595	-3.200	-7.923	0.595	-3.203	-7.924	0.595	-3.204	-7.924
0.725	0.640	-2.972	-10.253	0.640	-2.975	-10.253	0.641	-2.976	-10.253
0.775	0.720	-2.636	-12.630	0.720	-2.638	-12.630	0.720	-2.639	-12.630
0.825	0.861	-2.132	-15.062	0.861	-2.134	-15.062	0.861	-2.135	-15.062
0.875	1.131	-1.318	-17.534	1.131	-1.320	-17.534	1.132	-1.320	-17.534
0.925	1.694	0.164	-19.985	1.694	0.165	-19.986	1.695	0.166	-19.987
0.975	3.403	4.569	-21.439	3.404	4.568	-21.437	3.405	4.567	-21.437

Table B.10: Comparison of $K_1^{(r)}$, $K_2^{(r)}$ and $K_{III}^{(r)}$ calculated for the thermal problem using the DE method and averaged for two adjacent points along the delamination front and using the thermal M-integral in the sixth domain. The geometry and mesh of the problem are shown in Figs. 3.2 and 3.3, respectively. Note that the units of $K_i^{(r)}$ $(i = 1, 2)$ are $\text{MPa}\sqrt{\text{mm}}(\text{mm})^{-i\varepsilon}$, and that the units of $K_{III}^{(r)}$ are $\text{MPa}\sqrt{\text{mm}}$.

	DE average values for comparison			**M-integral domain 6**			**difference**		
x_3/B	$K_1^{(r)}$	$K_2^{(r)}$	$K_{III}^{(r)}$	$K_1^{(r)}$	$K_2^{(r)}$	$K_{III}^{(r)}$			
0.025	-	-	-	3.405	4.567	21.437	-	-	-
0.075	-	-	19.993	1.695	0.166	19.987	-	-	0.0%
0.125	1.134	-1.226	17.527	1.132	-1.320	17.534	0.2%	-7.2%	0.0%
0.175	0.855	-2.021	15.063	0.861	-2.135	15.062	-0.7%	-5.3%	0.0%
0.225	0.707	-2.544	12.620	0.720	-2.639	12.630	-1.9%	-3.6%	-0.1%
0.275	0.624	-2.875	10.244	0.641	-2.976	10.253	-2.6%	-3.4%	-0.1%
0.325	0.577	-3.099	7.917	0.595	-3.204	7.924	-3.1%	-3.3%	-0.1%
0.375	0.551	-3.248	5.627	0.570	-3.356	5.632	-3.3%	-3.2%	-0.1%
0.425	0.536	-3.340	3.366	0.556	-3.449	3.369	-3.5%	-3.2%	-0.1%
0.475	0.530	-3.384	1.120	0.550	-3.493	1.121	-3.6%	-3.1%	-0.1%
0.525	0.530	-3.384	-1.120	0.550	-3.493	-1.121	-3.6%	-3.1%	-0.1%
0.575	0.536	-3.340	-3.366	0.556	-3.449	-3.369	-3.5%	-3.2%	-0.1%
0.625	0.551	-3.248	-5.627	0.570	-3.356	-5.632	-3.3%	-3.2%	-0.1%
0.675	0.577	-3.099	-7.917	0.595	-3.204	-7.924	-3.1%	-3.3%	-0.1%
0.725	0.624	-2.875	-10.244	0.641	-2.976	-10.253	-2.6%	-3.4%	-0.1%
0.775	0.707	-2.544	-12.620	0.720	-2.639	-12.630	-1.9%	-3.6%	-0.1%
0.825	0.855	-2.021	-15.063	0.861	-2.135	-15.062	-0.7%	-5.3%	0.0%
0.875	1.134	-1.226	-17.527	1.132	-1.320	-17.534	0.2%	-7.2%	0.0%
0.925	-	-	-19.993	1.695	0.166	-19.987	-	-	0.0%
0.975	-	-	-	3.405	4.567	-21.437	-	-	-

Appendix C

Tabulated BD tests results from analyses

For each tested BD specimen, results from the analyses are presented in Tables C.1 through C.27. Each parameter is given along the normalized specimen thickness x_3/B. The parameters presented in the second through fourth columns are the averaged total stress intensity factors $K_1^{(T)}$, $K_2^{(T)}$ and $K_{III}^{(T)}$ from the fourth, fifth and sixth domains as were obtained from the FE analyses. Note that the units of $K_{III}^{(T)}$ are MPa$\sqrt{\text{mm}}$. These values were obtained directly from the FEAs where the length unit was in mm. Normalized total stress intensity factors $\hat{K}_1^{(T)}$ and $\hat{K}_2^{(T)}$ calculated for $\hat{L} = 100$ μm are presented in the fifth and sixth columns in these tables. In the seventh column, $K_{III}^{(T)}$ is shown with different units of MPa$\sqrt{\text{m}}$. In the eighth and ninth columns of Tables C.1 through C.27, the phase angles $\hat{\psi}$ and ϕ are shown. Finally, the critical interface energy release rates $\mathcal{G}_{ic}$ are given in the last column of these tables.

Table C.1: Averaged total stress intensity factors $K_1^{(T)}$, $K_2^{(T)}$ and $K_{III}^{(T)}$ from the fourth, fifth and sixth integration domains, normalized total stress intensity factors $\hat{K}_1^{(T)}$, $\hat{K}_2^{(T)}$ and $K_{III}^{(T)}$ calculated for $\hat{L} = 100$ μm, phase angles $\hat{\psi}$ and ϕ, and the critical interface energy release rates $\mathcal{G}_{ic}$ along the specimen thickness for specimen BD1.6.1 with loading angle $\omega = -1.9°$.

x_3/B	$K_1^{(T)}$ $\left(\text{MPa}\sqrt{\text{mm}}\,(\text{mm})^{-i\varepsilon}\right)$	$K_2^{(T)}$	$K_{III}^{(T)}$ (MPa$\sqrt{\text{mm}}$)	$\hat{K}_1^{(T)}$ (MPa$\sqrt{\text{m}}$)	$\hat{K}_2^{(T)}$	$K_{III}^{(T)}$	$\hat{\psi}$ (rad)	ϕ (rad)	$\mathcal{G}_{ic}$ (N/m)
0.025	38.77	26.51	17.43	1.27	0.77	0.55	0.548	0.375	430.1
0.075	37.87	24.71	8.26	1.24	0.72	0.26	0.526	0.191	358.1
0.125	36.02	24.84	4.97	1.18	0.73	0.16	0.552	0.120	327.9
0.175	34.34	25.05	3.24	1.13	0.73	0.10	0.578	0.081	306.9
0.225	32.96	25.24	2.17	1.08	0.74	0.07	0.601	0.055	291.8
0.275	31.89	25.38	1.46	1.05	0.75	0.05	0.620	0.038	280.9
0.325	31.09	25.49	0.97	1.02	0.75	0.03	0.635	0.026	273.0
0.375	30.52	25.57	0.61	1.01	0.76	0.02	0.645	0.016	267.7
0.425	30.16	25.62	0.34	0.99	0.76	0.01	0.652	0.009	264.3
0.475	29.98	25.64	0.11	0.99	0.76	0.00	0.656	0.003	262.7
0.525	29.98	25.64	-0.11	0.99	0.76	0.00	0.656	-0.003	262.7
0.575	30.16	25.62	-0.34	0.99	0.76	-0.01	0.652	-0.009	264.3
0.625	30.52	25.57	-0.61	1.01	0.76	-0.02	0.645	-0.016	267.7
0.675	31.09	25.49	-0.97	1.02	0.75	-0.03	0.635	-0.026	273.0
0.725	31.89	25.38	-1.46	1.05	0.75	-0.05	0.620	-0.038	280.9
0.775	32.96	25.24	-2.17	1.08	0.74	-0.07	0.601	-0.055	291.8
0.825	34.34	25.05	-3.24	1.13	0.73	-0.10	0.578	-0.081	306.9
0.875	36.02	24.84	-4.97	1.18	0.73	-0.16	0.552	-0.120	327.9
0.925	37.87	24.71	-8.26	1.24	0.72	-0.26	0.526	-0.191	358.1
0.975	38.77	26.51	-17.43	1.27	0.77	-0.55	0.548	-0.375	430.1

Table C.2: Averaged total stress intensity factors $K_1^{(T)}$, $K_2^{(T)}$ and $K_{III}^{(T)}$ from the fourth, fifth and sixth integration domains, normalized total stress intensity factors $\hat{K}_1^{(T)}$, $\hat{K}_2^{(T)}$ and $K_{III}^{(T)}$ calculated for $\hat{L} = 100$ μm, phase angles $\hat{\psi}$ and ϕ, and the critical interface energy release rates $\mathcal{G}_{ic}$ along the specimen thickness for specimen BD1.14.2 with loading angle $\omega = -2.0°$.

x_3/B	$K_1^{(T)}$	$K_2^{(T)}$	$K_{III}^{(T)}$	$\hat{K}_1^{(T)}$	$\hat{K}_2^{(T)}$	$K_{III}^{(T)}$	$\hat{\psi}$	ϕ	$\mathcal{G}_{ic}$
	$\left(\text{MPa}\sqrt{\text{mm}}\,(\text{mm})^{-i\varepsilon}\right)$		(MPa$\sqrt{\text{mm}}$)	(MPa$\sqrt{\text{m}}$)			(rad)	(rad)	(N/m)
0.025	43.03	30.85	17.84	1.41	0.90	0.56	0.570	0.343	533.6
0.075	40.83	28.83	8.65	1.34	0.84	0.27	0.563	0.182	435.9
0.125	38.98	28.90	5.27	1.28	0.85	0.17	0.586	0.115	402.7
0.175	37.29	29.14	3.40	1.23	0.86	0.11	0.611	0.076	380.2
0.225	35.87	29.38	2.24	1.18	0.87	0.07	0.634	0.051	363.8
0.275	34.75	29.56	1.47	1.15	0.88	0.05	0.653	0.034	351.8
0.325	33.90	29.71	0.95	1.12	0.88	0.03	0.668	0.022	343.1
0.375	33.28	29.81	0.59	1.10	0.89	0.02	0.679	0.014	337.1
0.425	32.89	29.88	0.32	1.09	0.89	0.01	0.685	0.008	333.3
0.475	32.70	29.91	0.10	1.08	0.89	0.00	0.689	0.002	331.4
0.525	32.70	29.91	-0.10	1.08	0.89	0.00	0.689	-0.002	331.4
0.575	32.89	29.88	-0.32	1.09	0.89	-0.01	0.685	-0.008	333.3
0.625	33.28	29.81	-0.59	1.10	0.89	-0.02	0.679	-0.014	337.1
0.675	33.90	29.71	-0.95	1.12	0.88	-0.03	0.668	-0.022	343.1
0.725	34.75	29.56	-1.47	1.15	0.88	-0.05	0.653	-0.034	351.8
0.775	35.87	29.38	-2.24	1.18	0.87	-0.07	0.634	-0.051	363.8
0.825	37.29	29.14	-3.40	1.23	0.86	-0.11	0.611	-0.076	380.2
0.875	38.98	28.90	-5.27	1.28	0.85	-0.17	0.586	-0.115	402.7
0.925	40.83	28.83	-8.65	1.34	0.84	-0.27	0.563	-0.182	435.9
0.975	43.03	30.85	-17.84	1.41	0.90	-0.56	0.570	-0.343	533.6

Table C.3: Averaged total stress intensity factors $K_1^{(T)}$, $K_2^{(T)}$ and $K_{III}^{(T)}$ from the fourth, fifth and sixth integration domains, normalized total stress intensity factors $\hat{K}_1^{(T)}$, $\hat{K}_2^{(T)}$ and $K_{III}^{(T)}$ calculated for $\hat{L} = 100$ μm, phase angles $\hat{\psi}$ and ϕ, and the critical interface energy release rates $\mathcal{G}_{ic}$ along the specimen thickness for specimen BD1.8.2 with loading angle $\omega = -2.2°$.

x_3/B	$K_1^{(T)}$	$K_2^{(T)}$	$K_{III}^{(T)}$	$\hat{K}_1^{(T)}$	$\hat{K}_2^{(T)}$	$K_{III}^{(T)}$	$\hat{\psi}$	ϕ	$\mathcal{G}_{ic}$
	$\left(\text{MPa}\sqrt{\text{mm}}\,(\text{mm})^{-i\varepsilon}\right)$		(MPa$\sqrt{\text{mm}}$)	(MPa$\sqrt{\text{m}}$)			(rad)	(rad)	(N/m)
0.025	44.77	35.81	22.37	1.47	1.06	0.71	0.623	0.393	649.8
0.075	42.81	33.17	11.45	1.41	0.98	0.36	0.607	0.221	519.9
0.125	40.32	33.08	7.19	1.33	0.98	0.23	0.635	0.145	469.0
0.175	38.25	33.22	4.83	1.26	0.99	0.15	0.663	0.101	437.7
0.225	36.61	33.39	3.33	1.21	0.99	0.11	0.687	0.071	416.5
0.275	35.35	33.53	2.29	1.17	1.00	0.07	0.707	0.050	401.7
0.325	34.41	33.65	1.55	1.14	1.01	0.05	0.722	0.034	391.4
0.375	33.74	33.73	1.00	1.12	1.01	0.03	0.733	0.022	384.4
0.425	33.32	33.79	0.56	1.11	1.01	0.02	0.740	0.012	380.1
0.475	33.11	33.82	0.18	1.10	1.01	0.01	0.744	0.004	378.0
0.525	33.11	33.82	-0.18	1.10	1.01	-0.01	0.744	-0.004	378.0
0.575	33.32	33.79	-0.56	1.11	1.01	-0.02	0.740	-0.012	380.1
0.625	33.74	33.73	-1.00	1.12	1.01	-0.03	0.733	-0.022	384.4
0.675	34.41	33.65	-1.55	1.14	1.01	-0.05	0.722	-0.034	391.4
0.725	35.35	33.53	-2.29	1.17	1.00	-0.07	0.707	-0.050	401.7
0.775	36.61	33.39	-3.33	1.21	0.99	-0.11	0.687	-0.071	416.5
0.825	38.25	33.22	-4.83	1.26	0.99	-0.15	0.663	-0.101	437.7
0.875	40.32	33.08	-7.19	1.33	0.98	-0.23	0.635	-0.145	469.0
0.925	42.81	33.17	-11.45	1.41	0.98	-0.36	0.607	-0.221	519.9
0.975	44.77	35.81	-22.37	1.47	1.06	-0.71	0.623	-0.393	649.8

Table C.4: Averaged total stress intensity factors $K_1^{(T)}$, $K_2^{(T)}$ and $K_{III}^{(T)}$ from the fourth, fifth and sixth integration domains, normalized total stress intensity factors $\hat{K}_1^{(T)}$, $\hat{K}_2^{(T)}$ and $K_{III}^{(T)}$ calculated for $\hat{L} = 100$ μm, phase angles $\hat{\psi}$ and ϕ, and the critical interface energy release rates $\mathcal{G}_{ic}$ along the specimen thickness for specimen BD1.8.1 with loading angle $\omega = -2.5°$.

x_3/B	$K_1^{(T)}$	$K_2^{(T)}$	$K_{III}^{(T)}$	$\hat{K}_1^{(T)}$	$\hat{K}_2^{(T)}$	$K_{III}^{(T)}$	$\hat{\psi}$	ϕ	$\mathcal{G}_{ic}$
	$\left(\text{MPa}\sqrt{\text{mm}}\,(\text{mm})^{-i\varepsilon}\right)$		(MPa$\sqrt{\text{mm}}$)	(MPa$\sqrt{\text{m}}$)			(rad)	(rad)	(N/m)
0.025	48.33	41.78	22.91	1.60	1.24	0.72	0.661	0.363	788.6
0.075	45.38	39.08	11.35	1.50	1.16	0.36	0.659	0.198	629.8
0.125	42.64	39.01	7.02	1.41	1.16	0.22	0.689	0.128	573.2
0.175	40.38	39.18	4.63	1.34	1.17	0.15	0.718	0.087	538.4
0.225	38.59	39.36	3.13	1.28	1.18	0.10	0.743	0.060	514.7
0.275	37.21	39.51	2.12	1.24	1.19	0.07	0.763	0.041	498.0
0.325	36.19	39.61	1.41	1.21	1.19	0.04	0.779	0.028	486.3
0.375	35.46	39.69	0.89	1.18	1.20	0.03	0.790	0.018	478.3
0.425	35.00	39.74	0.49	1.17	1.20	0.02	0.797	0.010	473.4
0.475	34.77	39.76	0.16	1.16	1.20	0.00	0.800	0.003	471.0
0.525	34.77	39.76	-0.16	1.16	1.20	0.00	0.800	-0.003	471.0
0.575	35.00	39.74	-0.49	1.17	1.20	-0.02	0.797	-0.010	473.4
0.625	35.46	39.69	-0.89	1.18	1.20	-0.03	0.790	-0.018	478.3
0.675	36.19	39.61	-1.41	1.21	1.19	-0.04	0.779	-0.028	486.3
0.725	37.21	39.51	-2.12	1.24	1.19	-0.07	0.763	-0.041	498.0
0.775	38.59	39.36	-3.13	1.28	1.18	-0.10	0.743	-0.060	514.7
0.825	40.38	39.18	-4.63	1.34	1.17	-0.15	0.718	-0.087	538.4
0.875	42.64	39.01	-7.02	1.41	1.16	-0.22	0.689	-0.128	573.2
0.925	45.38	39.08	-11.35	1.50	1.16	-0.36	0.659	-0.198	629.8
0.975	48.33	41.78	-22.91	1.60	1.24	-0.72	0.661	-0.363	788.6

Table C.5: Averaged total stress intensity factors $K_1^{(T)}$, $K_2^{(T)}$ and $K_{III}^{(T)}$ from the fourth, fifth and sixth integration domains, normalized total stress intensity factors $\hat{K}_1^{(T)}$, $\hat{K}_2^{(T)}$ and $K_{III}^{(T)}$ calculated for $\hat{L} = 100$ μm, phase angles $\hat{\psi}$ and ϕ, and the critical interface energy release rates $\mathcal{G}_{ic}$ along the specimen thickness for specimen BD1.12.2 with loading angle $\omega = -2.6°$.

x_3/B	$K_1^{(T)}$	$K_2^{(T)}$	$K_{III}^{(T)}$	$\hat{K}_1^{(T)}$	$\hat{K}_2^{(T)}$	$K_{III}^{(T)}$	$\hat{\psi}$	ϕ	$\mathcal{G}_{ic}$
	$\left(\text{MPa}\sqrt{\text{mm}}\,(\text{mm})^{-i\varepsilon}\right)$		(MPa$\sqrt{\text{mm}}$)	(MPa$\sqrt{\text{m}}$)			(rad)	(rad)	(N/m)
0.025	45.40	43.10	24.21	1.50	1.29	0.77	0.707	0.389	772.9
0.075	43.25	40.54	11.64	1.43	1.21	0.37	0.701	0.205	618.9
0.125	40.60	40.67	6.93	1.35	1.22	0.22	0.734	0.127	566.5
0.175	38.33	40.91	4.46	1.28	1.23	0.14	0.766	0.084	534.2
0.225	36.53	41.11	2.94	1.22	1.24	0.09	0.792	0.057	512.2
0.275	35.16	41.26	1.94	1.18	1.25	0.06	0.813	0.038	496.8
0.325	34.16	41.38	1.25	1.15	1.25	0.04	0.829	0.025	486.3
0.375	33.46	41.46	0.77	1.12	1.25	0.02	0.840	0.015	479.2
0.425	33.02	41.51	0.42	1.11	1.26	0.01	0.847	0.008	474.9
0.475	32.81	41.53	0.13	1.10	1.26	0.00	0.850	0.003	472.8
0.525	32.81	41.53	-0.13	1.10	1.26	0.00	0.850	-0.003	472.8
0.575	33.02	41.51	-0.42	1.11	1.26	-0.01	0.847	-0.008	474.9
0.625	33.46	41.46	-0.77	1.12	1.25	-0.02	0.840	-0.015	479.2
0.675	34.16	41.38	-1.25	1.15	1.25	-0.04	0.829	-0.025	486.3
0.725	35.16	41.26	-1.94	1.18	1.25	-0.06	0.813	-0.038	496.8
0.775	36.53	41.11	-2.94	1.22	1.24	-0.09	0.792	-0.057	512.2
0.825	38.33	40.91	-4.46	1.28	1.23	-0.14	0.766	-0.084	534.2
0.875	40.60	40.67	-6.93	1.35	1.22	-0.22	0.734	-0.127	566.5
0.925	43.25	40.54	-11.64	1.43	1.21	-0.37	0.701	-0.205	618.9
0.975	45.40	43.10	-24.21	1.50	1.29	-0.77	0.707	-0.389	772.9

Table C.6: Averaged total stress intensity factors $K_1^{(T)}$, $K_2^{(T)}$ and $K_{III}^{(T)}$ from the fourth, fifth and sixth integration domains, normalized total stress intensity factors $\hat{K}_1^{(T)}$, $\hat{K}_2^{(T)}$ and $K_{III}^{(T)}$ calculated for $\hat{L} = 100$ μm, phase angles $\hat{\psi}$ and ϕ, and the critical interface energy release rates $\mathcal{G}_{ic}$ along the specimen thickness for specimen BD1.2.2 with loading angle $\omega = -4.4°$.

x_3/B	$K_1^{(T)}$	$K_2^{(T)}$	$K_{III}^{(T)}$	$\hat{K}_1^{(T)}$	$\hat{K}_2^{(T)}$	$K_{III}^{(T)}$	$\hat{\psi}$	ϕ	$\mathcal{G}_{ic}$
	$\left(\text{MPa}\sqrt{\text{mm}}\,(\text{mm})^{-i\varepsilon}\right)$		(MPa$\sqrt{\text{mm}}$)	(MPa$\sqrt{\text{m}}$)			(rad)	(rad)	(N/m)
0.025	37.71	60.43	31.77	1.29	1.85	1.00	0.961	0.442	1048.1
0.075	34.73	56.81	17.51	1.19	1.74	0.55	0.970	0.272	806.5
0.125	32.76	56.73	11.59	1.13	1.74	0.37	0.995	0.186	750.0
0.175	31.21	56.93	8.18	1.08	1.75	0.26	1.017	0.133	724.1
0.225	29.98	57.13	5.90	1.04	1.76	0.19	1.036	0.097	709.3
0.275	29.03	57.29	4.25	1.01	1.76	0.13	1.050	0.070	699.8
0.325	28.31	57.42	3.00	0.99	1.77	0.09	1.061	0.050	693.4
0.375	27.80	57.50	1.99	0.97	1.77	0.06	1.068	0.033	689.3
0.425	27.47	57.56	1.14	0.96	1.77	0.04	1.074	0.019	686.8
0.475	27.31	57.58	0.37	0.96	1.77	0.01	1.076	0.006	685.6
0.525	27.31	57.58	-0.37	0.96	1.77	-0.01	1.076	-0.006	685.6
0.575	27.47	57.56	-1.14	0.96	1.77	-0.04	1.074	-0.019	686.8
0.625	27.80	57.50	-1.99	0.97	1.77	-0.06	1.068	-0.033	689.3
0.675	28.31	57.42	-3.00	0.99	1.77	-0.09	1.061	-0.050	693.4
0.725	29.03	57.29	-4.25	1.01	1.76	-0.13	1.050	-0.070	699.8
0.775	29.98	57.13	-5.90	1.04	1.76	-0.19	1.036	-0.097	709.3
0.825	31.21	56.93	-8.18	1.08	1.75	-0.26	1.017	-0.133	724.1
0.875	32.76	56.73	-11.59	1.13	1.74	-0.37	0.995	-0.186	750.0
0.925	34.73	56.81	-17.51	1.19	1.74	-0.55	0.970	-0.272	806.5
0.975	37.71	60.43	-31.77	1.29	1.85	-1.00	0.961	-0.442	1048.1

Table C.7: Averaged total stress intensity factors $K_1^{(T)}$, $K_2^{(T)}$ and $K_{III}^{(T)}$ from the fourth, fifth and sixth integration domains, normalized total stress intensity factors $\hat{K}_1^{(T)}$, $\hat{K}_2^{(T)}$ and $K_{III}^{(T)}$ calculated for $\hat{L} = 100$ μm, phase angles $\hat{\psi}$ and ϕ, and the critical interface energy release rates $\mathcal{G}_{ic}$ along the specimen thickness for specimen BD1.3.1 with loading angle $\omega = -4.7°$.

x_3/B	$K_1^{(T)}$	$K_2^{(T)}$	$K_{III}^{(T)}$	$\hat{K}_1^{(T)}$	$\hat{K}_2^{(T)}$	$K_{III}^{(T)}$	$\hat{\psi}$	ϕ	$\mathcal{G}_{ic}$
	$\left(\text{MPa}\sqrt{\text{mm}}\,(\text{mm})^{-i\varepsilon}\right)$		(MPa$\sqrt{\text{mm}}$)	(MPa$\sqrt{\text{m}}$)			(rad)	(rad)	(N/m)
0.025	36.78	66.38	31.75	1.27	2.04	1.00	1.013	0.418	1163.7
0.075	32.96	62.33	17.68	1.14	1.91	0.56	1.032	0.260	898.4
0.125	31.36	62.12	11.55	1.09	1.91	0.37	1.051	0.174	842.7
0.175	29.95	62.37	7.94	1.05	1.92	0.25	1.071	0.121	819.9
0.225	28.75	62.63	5.56	1.01	1.93	0.18	1.089	0.085	807.6
0.275	27.79	62.85	3.90	0.98	1.94	0.12	1.102	0.060	800.0
0.325	27.05	63.01	2.69	0.96	1.95	0.09	1.113	0.042	795.0
0.375	26.53	63.12	1.75	0.94	1.95	0.06	1.121	0.027	791.8
0.425	26.18	63.19	0.99	0.93	1.95	0.03	1.126	0.015	789.8
0.475	26.02	63.22	0.32	0.93	1.95	0.01	1.128	0.005	788.9
0.525	26.02	63.22	-0.32	0.93	1.95	-0.01	1.128	-0.005	788.9
0.575	26.18	63.19	-0.99	0.93	1.95	-0.03	1.126	-0.015	789.8
0.625	26.53	63.12	-1.75	0.94	1.95	-0.06	1.121	-0.027	791.8
0.675	27.05	63.01	-2.69	0.96	1.95	-0.09	1.113	-0.042	795.0
0.725	27.79	62.85	-3.90	0.98	1.94	-0.12	1.102	-0.060	800.0
0.775	28.75	62.63	-5.56	1.01	1.93	-0.18	1.089	-0.085	807.6
0.825	29.95	62.37	-7.94	1.05	1.92	-0.25	1.071	-0.121	819.9
0.875	31.36	62.12	-11.55	1.09	1.91	-0.37	1.051	-0.174	842.7
0.925	32.96	62.33	-17.68	1.14	1.91	-0.56	1.032	-0.260	898.5
0.975	36.78	66.38	-31.75	1.27	2.04	-1.00	1.013	-0.418	1163.7

Table C.8: Averaged total stress intensity factors $K_1^{(T)}$, $K_2^{(T)}$ and $K_{III}^{(T)}$ from the fourth, fifth and sixth integration domains, normalized total stress intensity factors $\hat{K}_1^{(T)}$, $\hat{K}_2^{(T)}$ and $K_{III}^{(T)}$ calculated for $\hat{L} = 100$ μm, phase angles $\hat{\psi}$ and ϕ, and the critical interface energy release rates $\mathcal{G}_{ic}$ along the specimen thickness for specimen BD1.1.2 with loading angle $\omega = -4.9°$.

x_3/B	$K_1^{(T)}$	$K_2^{(T)}$	$K_{III}^{(T)}$	$\hat{K}_1^{(T)}$	$\hat{K}_2^{(T)}$	$K_{III}^{(T)}$	$\hat{\psi}$	ϕ	$\mathcal{G}_{ic}$
	$\left(\text{MPa}\sqrt{\text{mm}}\,(\text{mm})^{-i\varepsilon}\right)$		(MPa$\sqrt{\text{mm}}$)	(MPa$\sqrt{\text{m}}$)			(rad)	(rad)	(N/m)
0.025	38.50	62.92	33.27	1.32	1.92	1.05	0.970	0.446	1128.6
0.075	34.90	58.51	19.29	1.20	1.79	0.61	0.981	0.292	854.1
0.125	32.86	58.01	13.16	1.13	1.78	0.42	1.003	0.206	783.3
0.175	31.23	58.05	9.43	1.08	1.78	0.30	1.025	0.151	750.3
0.225	29.91	58.20	6.86	1.04	1.79	0.22	1.044	0.111	731.7
0.275	28.87	58.35	4.98	1.01	1.80	0.16	1.059	0.081	720.1
0.325	28.07	58.48	3.52	0.98	1.80	0.11	1.071	0.058	712.6
0.375	27.50	58.57	2.35	0.96	1.80	0.07	1.080	0.038	707.7
0.425	27.13	58.63	1.35	0.95	1.81	0.04	1.085	0.022	704.8
0.475	26.95	58.66	0.44	0.95	1.81	0.01	1.088	0.007	703.4
0.525	26.95	58.66	-0.44	0.95	1.81	-0.01	1.088	-0.007	703.4
0.575	27.13	58.63	-1.35	0.95	1.81	-0.04	1.085	-0.022	704.8
0.625	27.50	58.57	-2.35	0.96	1.80	-0.07	1.080	-0.038	707.7
0.675	28.07	58.48	-3.52	0.98	1.80	-0.11	1.071	-0.058	712.6
0.725	28.86	58.35	-4.98	1.01	1.80	-0.16	1.060	-0.081	720.1
0.775	29.91	58.20	-6.86	1.04	1.79	-0.22	1.044	-0.111	731.7
0.825	31.23	58.05	-9.43	1.08	1.78	-0.30	1.025	-0.151	750.3
0.875	32.86	58.01	-13.16	1.13	1.78	-0.42	1.003	-0.206	783.3
0.925	34.90	58.51	-19.29	1.20	1.79	-0.61	0.981	-0.292	854.0
0.975	38.50	62.92	-33.27	1.32	1.92	-1.05	0.970	-0.446	1128.6

Table C.9: Averaged total stress intensity factors $K_1^{(T)}$, $K_2^{(T)}$ and $K_{III}^{(T)}$ from the fourth, fifth and sixth integration domains, normalized total stress intensity factors $\hat{K}_1^{(T)}$, $\hat{K}_2^{(T)}$ and $K_{III}^{(T)}$ calculated for $\hat{L} = 100$ μm, phase angles $\hat{\psi}$ and ϕ, and the critical interface energy release rates $\mathcal{G}_{ic}$ along the specimen thickness for specimen BD1.2.1 with loading angle $\omega = -5.3°$.

x_3/B	$K_1^{(T)}$	$K_2^{(T)}$	$K_{III}^{(T)}$	$\hat{K}_1^{(T)}$	$\hat{K}_2^{(T)}$	$K_{III}^{(T)}$	$\hat{\psi}$	ϕ	$\mathcal{G}_{ic}$
	$\left(\text{MPa}\sqrt{\text{mm}}\,(\text{mm})^{-i\varepsilon}\right)$		(MPa$\sqrt{\text{mm}}$)	(MPa$\sqrt{\text{m}}$)			(rad)	(rad)	(N/m)
0.025	36.30	68.63	35.66	1.26	2.11	1.13	1.032	0.453	1259.0
0.075	32.19	64.03	20.67	1.12	1.97	0.65	1.053	0.297	948.1
0.125	30.38	63.65	14.05	1.06	1.96	0.44	1.073	0.208	877.1
0.175	29.07	63.79	10.04	1.02	1.97	0.32	1.091	0.151	848.6
0.225	28.02	64.04	7.29	0.99	1.98	0.23	1.106	0.110	834.9
0.275	27.20	64.26	5.28	0.96	1.98	0.17	1.118	0.080	827.2
0.325	26.57	64.43	3.74	0.94	1.99	0.12	1.128	0.057	822.6
0.375	26.12	64.56	2.49	0.93	2.00	0.08	1.134	0.038	819.9
0.425	25.82	64.64	1.43	0.92	2.00	0.05	1.139	0.022	818.2
0.475	25.68	64.68	0.47	0.92	2.00	0.01	1.141	0.007	817.5
0.525	25.68	64.68	-0.46	0.92	2.00	-0.01	1.141	-0.007	817.5
0.575	25.82	64.64	-1.43	0.92	2.00	-0.05	1.139	-0.022	818.2
0.625	26.12	64.56	-2.49	0.93	2.00	-0.08	1.134	-0.038	819.8
0.675	26.57	64.43	-3.74	0.94	1.99	-0.12	1.128	-0.057	822.6
0.725	27.20	64.26	-5.28	0.96	1.98	-0.17	1.118	-0.080	827.2
0.775	28.02	64.04	-7.29	0.99	1.98	-0.23	1.106	-0.110	834.9
0.825	29.07	63.79	-10.04	1.02	1.97	-0.32	1.091	-0.151	848.7
0.875	30.38	63.65	-14.05	1.06	1.96	-0.44	1.073	-0.208	877.1
0.925	32.19	64.03	-20.67	1.12	1.97	-0.65	1.053	-0.297	948.1
0.975	36.30	68.63	-35.66	1.26	2.11	-1.13	1.032	-0.453	1259.0

Table C.10: Averaged total stress intensity factors $K_1^{(T)}$, $K_2^{(T)}$ and $K_{III}^{(T)}$ from the fourth, fifth and sixth integration domains, normalized total stress intensity factors $\hat{K}_1^{(T)}$, $\hat{K}_2^{(T)}$ and $K_{III}^{(T)}$ calculated for $\hat{L} = 100$ μm, phase angles $\hat{\psi}$ and ϕ, and the critical interface energy release rates $\mathcal{G}_{ic}$ along the specimen thickness for specimen BD1.1.1 with loading angle $\omega = -5.3°$.

x_3/B	$K_1^{(T)}$	$K_2^{(T)}$	$K_{III}^{(T)}$	$\hat{K}_1^{(T)}$	$\hat{K}_2^{(T)}$	$K_{III}^{(T)}$	$\hat{\psi}$	ϕ	$\mathcal{G}_{ic}$
	$\left(\text{MPa}\sqrt{\text{mm}}\,(\text{mm})^{-i\varepsilon}\right)$		(MPa$\sqrt{\text{mm}}$)	(MPa$\sqrt{\text{m}}$)			(rad)	(rad)	(N/m)
0.025	38.40	71.25	36.39	1.33	2.19	1.15	1.025	0.445	1357.3
0.075	34.27	66.39	21.22	1.19	2.04	0.67	1.042	0.293	1027.7
0.125	32.28	65.78	14.48	1.13	2.02	0.46	1.063	0.207	946.0
0.175	30.75	65.79	10.37	1.08	2.03	0.33	1.082	0.150	910.7
0.225	29.53	65.95	7.54	1.04	2.03	0.24	1.098	0.110	892.2
0.275	28.58	66.08	5.47	1.01	2.04	0.17	1.111	0.080	880.6
0.325	27.85	66.21	3.87	0.99	2.05	0.12	1.121	0.057	873.8
0.375	27.33	66.29	2.58	0.97	2.05	0.08	1.128	0.038	869.1
0.425	27.00	66.34	1.48	0.96	2.05	0.05	1.132	0.022	866.2
0.475	26.83	66.36	0.48	0.96	2.05	0.02	1.135	0.007	864.8
0.525	26.83	66.36	-0.48	0.96	2.05	-0.02	1.135	-0.007	864.8
0.575	27.00	66.34	-1.48	0.96	2.05	-0.05	1.132	-0.022	866.2
0.625	27.34	66.29	-2.58	0.97	2.05	-0.08	1.128	-0.038	869.1
0.675	27.85	66.20	-3.87	0.99	2.04	-0.12	1.121	-0.057	873.6
0.725	28.58	66.07	-5.47	1.01	2.04	-0.17	1.111	-0.080	880.5
0.775	29.53	65.95	-7.54	1.04	2.03	-0.24	1.098	-0.110	892.1
0.825	30.75	65.78	-10.37	1.08	2.03	-0.33	1.081	-0.150	910.5
0.875	32.27	65.77	-14.48	1.13	2.02	-0.46	1.063	-0.207	945.8
0.925	34.27	66.39	-21.22	1.19	2.04	-0.67	1.042	-0.293	1027.7
0.975	38.41	71.25	-36.39	1.33	2.19	-1.15	1.024	-0.445	1357.6

Table C.11: Averaged total stress intensity factors $K_1^{(T)}$, $K_2^{(T)}$ and $K_{III}^{(T)}$ from the fourth, fifth and sixth integration domains, normalized total stress intensity factors $\hat{K}_1^{(T)}$, $\hat{K}_2^{(T)}$ and $K_{III}^{(T)}$ calculated for $\hat{L} = 100$ μm, phase angles $\hat{\psi}$ and ϕ, and the critical interface energy release rates $\mathcal{G}_{ic}$ along the specimen thickness for specimen BD1.3.2 with loading angle $\omega = -9.9°$.

x_3/B	$K_1^{(T)}$ $\left(\text{MPa}\sqrt{\text{mm}}\,(\text{mm})^{-i\varepsilon}\right)$	$K_2^{(T)}$	$K_{III}^{(T)}$ (MPa$\sqrt{\text{mm}}$)	$\hat{K}_1^{(T)}$ (MPa$\sqrt{\text{m}}$)	$\hat{K}_2^{(T)}$	$K_{III}^{(T)}$	$\hat{\psi}$ (rad)	ϕ (rad)	$\mathcal{G}_{ic}$ (N/m)
0.025	16.54	73.55	38.33	0.64	2.30	1.21	1.298	0.495	1238.4
0.075	12.97	68.41	24.25	0.52	2.14	0.77	1.331	0.354	929.9
0.125	12.29	67.78	17.44	0.50	2.12	0.55	1.340	0.262	858.7
0.175	11.96	67.84	13.00	0.49	2.12	0.41	1.344	0.198	833.1
0.225	11.69	68.06	9.78	0.48	2.13	0.31	1.349	0.149	823.1
0.275	11.46	68.28	7.29	0.47	2.14	0.23	1.353	0.111	819.3
0.325	11.26	68.48	5.27	0.47	2.14	0.17	1.356	0.080	818.3
0.375	11.11	68.63	3.57	0.46	2.15	0.11	1.358	0.054	818.4
0.425	11.01	68.74	2.07	0.46	2.15	0.07	1.360	0.032	818.8
0.475	10.96	68.79	0.68	0.46	2.15	0.02	1.361	0.010	819.0
0.525	10.96	68.79	-0.68	0.46	2.15	-0.02	1.361	-0.010	819.0
0.575	11.01	68.74	-2.07	0.46	2.15	-0.07	1.360	-0.032	818.8
0.625	11.11	68.63	-3.57	0.46	2.15	-0.11	1.358	-0.054	818.4
0.675	11.26	68.48	-5.27	0.47	2.14	-0.17	1.356	-0.080	818.3
0.725	11.46	68.28	-7.29	0.47	2.14	-0.23	1.353	-0.111	819.3
0.775	11.69	68.06	-9.78	0.48	2.13	-0.31	1.349	-0.149	823.0
0.825	11.96	67.84	-13.00	0.49	2.12	-0.41	1.344	-0.198	833.0
0.875	12.29	67.78	-17.44	0.50	2.12	-0.55	1.340	-0.262	858.7
0.925	12.97	68.41	-24.25	0.52	2.14	-0.77	1.331	-0.354	929.9
0.975	16.54	73.55	-38.33	0.64	2.30	-1.21	1.298	-0.495	1238.4

Table C.12: Averaged total stress intensity factors $K_1^{(T)}$, $K_2^{(T)}$ and $K_{III}^{(T)}$ from the fourth, fifth and sixth integration domains, normalized total stress intensity factors $\hat{K}_1^{(T)}$, $\hat{K}_2^{(T)}$ and $K_{III}^{(T)}$ calculated for $\hat{L} = 100$ μm, phase angles $\hat{\psi}$ and ϕ, and the critical interface energy release rates $\mathcal{G}_{ic}$ along the specimen thickness for specimen BD1.4.2 with loading angle $\omega = -10.1°$.

x_3/B	$K_1^{(T)}$ $\left(\text{MPa}\sqrt{\text{mm}}\,(\text{mm})^{-i\varepsilon}\right)$	$K_2^{(T)}$	$K_{III}^{(T)}$ (MPa$\sqrt{\text{mm}}$)	$\hat{K}_1^{(T)}$ (MPa$\sqrt{\text{m}}$)	$\hat{K}_2^{(T)}$	$K_{III}^{(T)}$	$\hat{\psi}$ (rad)	ϕ (rad)	$\mathcal{G}_{ic}$ (N/m)
0.025	17.12	79.41	39.67	0.67	2.48	1.25	1.306	0.478	1413.0
0.075	13.46	74.52	24.50	0.55	2.33	0.77	1.340	0.331	1082.0
0.125	12.90	74.18	17.42	0.53	2.32	0.55	1.347	0.241	1014.5
0.175	12.63	74.40	12.91	0.52	2.33	0.41	1.351	0.180	992.9
0.225	12.40	74.71	9.68	0.51	2.34	0.31	1.354	0.135	985.8
0.275	12.19	74.99	7.20	0.51	2.35	0.23	1.358	0.100	984.0
0.325	12.01	75.21	5.20	0.50	2.36	0.16	1.360	0.072	984.3
0.375	11.87	75.38	3.52	0.50	2.36	0.11	1.363	0.049	985.2
0.425	11.78	75.48	2.04	0.50	2.36	0.06	1.364	0.028	986.0
0.475	11.73	75.54	0.67	0.49	2.37	0.02	1.365	0.009	986.5
0.525	11.73	75.54	-0.67	0.49	2.37	-0.02	1.365	-0.009	986.5
0.575	11.78	75.48	-2.04	0.50	2.36	-0.06	1.364	-0.028	986.0
0.625	11.87	75.38	-3.52	0.50	2.36	-0.11	1.363	-0.049	985.2
0.675	12.01	75.21	-5.20	0.50	2.36	-0.16	1.360	-0.072	984.3
0.725	12.19	74.99	-7.20	0.51	2.35	-0.23	1.358	-0.100	984.0
0.775	12.40	74.71	-9.68	0.51	2.34	-0.31	1.354	-0.135	985.8
0.825	12.63	74.40	-12.91	0.52	2.33	-0.41	1.351	-0.180	992.9
0.875	12.90	74.18	-17.42	0.53	2.32	-0.55	1.347	-0.241	1014.5
0.925	13.46	74.52	-24.50	0.55	2.33	-0.77	1.340	-0.331	1082.0
0.975	17.12	79.41	-39.67	0.67	2.48	-1.25	1.306	-0.478	1413.0

Table C.13: Averaged total stress intensity factors $K_1^{(T)}$, $K_2^{(T)}$ and $K_{III}^{(T)}$ from the fourth, fifth and sixth integration domains, normalized total stress intensity factors $\hat{K}_1^{(T)}$, $\hat{K}_2^{(T)}$ and $K_{III}^{(T)}$ calculated for $\hat{L} = 100$ μm, phase angles $\hat{\psi}$ and ϕ, and the critical interface energy release rates $\mathcal{G}_{ic}$ along the specimen thickness for specimen BD1.6.2 with loading angle $\omega = -10.3°$.

x_3/B	$K_1^{(T)}$	$K_2^{(T)}$	$K_{III}^{(T)}$	$\hat{K}_1^{(T)}$	$\hat{K}_2^{(T)}$	$K_{III}^{(T)}$	$\hat{\psi}$	ϕ	$\mathcal{G}_{ic}$
	$\left(\text{MPa}\sqrt{\text{mm}}\,(\text{mm})^{-i\varepsilon}\right)$		(MPa$\sqrt{\text{mm}}$)	(MPa$\sqrt{\text{m}}$)			(rad)	(rad)	(N/m)
0.025	14.03	75.70	37.88	0.57	2.37	1.20	1.336	0.481	1273.1
0.075	11.00	71.59	23.09	0.46	2.24	0.73	1.366	0.326	986.9
0.125	10.51	71.47	16.34	0.45	2.24	0.52	1.373	0.236	931.7
0.175	10.33	71.72	12.10	0.44	2.25	0.38	1.376	0.175	914.0
0.225	10.18	72.01	9.05	0.44	2.26	0.29	1.378	0.131	908.3
0.275	10.05	72.25	6.72	0.44	2.27	0.21	1.381	0.097	906.8
0.325	9.94	72.45	4.85	0.43	2.27	0.15	1.382	0.070	907.2
0.375	9.85	72.60	3.28	0.43	2.28	0.10	1.384	0.047	908.0
0.425	9.78	72.69	1.90	0.43	2.28	0.06	1.385	0.027	908.8
0.475	9.75	72.74	0.62	0.43	2.28	0.02	1.386	0.009	909.2
0.525	9.75	72.74	-0.62	0.43	2.28	-0.02	1.386	-0.009	909.2
0.575	9.78	72.69	-1.90	0.43	2.28	-0.06	1.385	-0.027	908.8
0.625	9.85	72.60	-3.28	0.43	2.28	-0.10	1.384	-0.047	908.0
0.675	9.94	72.45	-4.85	0.43	2.27	-0.15	1.382	-0.070	907.2
0.725	10.05	72.25	-6.72	0.44	2.27	-0.21	1.381	-0.097	906.8
0.775	10.18	72.01	-9.05	0.44	2.26	-0.29	1.378	-0.131	908.3
0.825	10.33	71.72	-12.10	0.44	2.25	-0.38	1.376	-0.175	914.0
0.875	10.51	71.47	-16.34	0.45	2.24	-0.52	1.373	-0.236	931.7
0.925	11.00	71.59	-23.09	0.46	2.24	-0.73	1.366	-0.326	986.9
0.975	14.03	75.70	-37.88	0.57	2.37	-1.20	1.336	-0.481	1273.1

Table C.14: Averaged total stress intensity factors $K_1^{(T)}$, $K_2^{(T)}$ and $K_{III}^{(T)}$ from the fourth, fifth and sixth integration domains, normalized total stress intensity factors $\hat{K}_1^{(T)}$, $\hat{K}_2^{(T)}$ and $K_{III}^{(T)}$ calculated for $\hat{L} = 100$ μm, phase angles $\hat{\psi}$ and ϕ, and the critical interface energy release rates $\mathcal{G}_{ic}$ along the specimen thickness for specimen BD1.5.1 with loading angle $\omega = -10.3°$.

x_3/B	$K_1^{(T)}$ $\left(\text{MPa}\sqrt{\text{mm}}\,(\text{mm})^{-i\varepsilon}\right)$	$K_2^{(T)}$	$K_{III}^{(T)}$ (MPa$\sqrt{\text{mm}}$)	$\hat{K}_1^{(T)}$ (MPa$\sqrt{\text{m}}$)	$\hat{K}_2^{(T)}$	$K_{III}^{(T)}$	$\hat{\psi}$ (rad)	ϕ (rad)	$\mathcal{G}_{ic}$ (N/m)
0.025	15.82	75.53	38.94	0.62	2.36	1.23	1.312	0.492	1293.3
0.075	12.31	70.37	24.64	0.50	2.20	0.78	1.346	0.351	976.9
0.125	11.60	69.79	17.78	0.48	2.18	0.56	1.354	0.261	904.9
0.175	11.23	69.87	13.32	0.47	2.19	0.42	1.360	0.197	879.0
0.225	10.94	70.10	10.06	0.46	2.20	0.32	1.364	0.149	868.8
0.275	10.70	70.33	7.52	0.45	2.20	0.24	1.368	0.112	864.9
0.325	10.51	70.53	5.46	0.45	2.21	0.17	1.371	0.081	863.9
0.375	10.36	70.68	3.71	0.44	2.22	0.12	1.373	0.055	864.0
0.425	10.26	70.79	2.15	0.44	2.22	0.07	1.375	0.032	864.4
0.475	10.21	70.84	0.71	0.44	2.22	0.02	1.376	0.010	864.7
0.525	10.21	70.84	-0.71	0.44	2.22	-0.02	1.376	-0.010	864.7
0.575	10.26	70.79	-2.15	0.44	2.22	-0.07	1.375	-0.032	864.4
0.625	10.36	70.68	-3.71	0.44	2.22	-0.12	1.373	-0.055	864.0
0.675	10.51	70.53	-5.46	0.45	2.21	-0.17	1.371	-0.081	863.9
0.725	10.70	70.33	-7.52	0.45	2.20	-0.24	1.368	-0.112	864.9
0.775	10.94	70.10	-10.06	0.46	2.20	-0.32	1.364	-0.149	868.8
0.825	11.23	69.87	-13.32	0.47	2.19	-0.42	1.360	-0.197	879.0
0.875	11.60	69.79	-17.78	0.48	2.18	-0.56	1.354	-0.261	904.9
0.925	12.31	70.37	-24.64	0.50	2.20	-0.78	1.346	-0.351	976.9
0.975	15.82	75.53	-38.94	0.62	2.36	-1.23	1.312	-0.492	1293.3

Table C.15: Averaged total stress intensity factors $K_1^{(T)}$, $K_2^{(T)}$ and $K_{III}^{(T)}$ from the fourth, fifth and sixth integration domains, normalized total stress intensity factors $\hat{K}_1^{(T)}$, $\hat{K}_2^{(T)}$ and $K_{III}^{(T)}$ calculated for $\hat{L} = 100$ μm, phase angles $\hat{\psi}$ and ϕ, and the critical interface energy release rates $\mathcal{G}_{ic}$ along the specimen thickness for specimen BD1.4.1 with loading angle $\omega = -10.5°$.

x_3/B	$K_1^{(T)}$	$K_2^{(T)}$	$K_{III}^{(T)}$	$\hat{K}_1^{(T)}$	$\hat{K}_2^{(T)}$	$K_{III}^{(T)}$	$\hat{\psi}$	ϕ	$\mathcal{G}_{ic}$
	$\left(\text{MPa}\sqrt{\text{mm}}\,(\text{mm})^{-i\varepsilon}\right)$		(MPa$\sqrt{\text{mm}}$)	(MPa$\sqrt{\text{m}}$)			(rad)	(rad)	(N/m)
0.025	15.52	73.64	38.15	0.61	2.30	1.21	1.311	0.493	1232.6
0.075	12.20	68.60	24.28	0.50	2.15	0.77	1.343	0.354	931.3
0.125	11.64	68.02	17.65	0.48	2.13	0.56	1.349	0.265	863.1
0.175	11.36	68.08	13.31	0.47	2.13	0.42	1.354	0.202	837.7
0.225	11.12	68.28	10.12	0.46	2.14	0.32	1.357	0.154	827.2
0.275	10.91	68.48	7.61	0.46	2.14	0.24	1.361	0.116	822.8
0.325	10.73	68.66	5.55	0.45	2.15	0.18	1.364	0.085	821.1
0.375	10.60	68.80	3.78	0.45	2.16	0.12	1.366	0.058	820.7
0.425	10.52	68.89	2.20	0.45	2.16	0.07	1.367	0.033	820.7
0.475	10.47	68.94	0.72	0.44	2.16	0.02	1.368	0.011	820.8
0.525	10.47	68.94	-0.72	0.44	2.16	-0.02	1.368	-0.011	820.8
0.575	10.52	68.89	-2.20	0.45	2.16	-0.07	1.367	-0.033	820.7
0.625	10.60	68.80	-3.78	0.45	2.16	-0.12	1.366	-0.058	820.7
0.675	10.73	68.66	-5.55	0.45	2.15	-0.18	1.364	-0.085	821.1
0.725	10.91	68.48	-7.61	0.46	2.14	-0.24	1.361	-0.116	822.8
0.775	11.12	68.28	-10.12	0.46	2.14	-0.32	1.357	-0.154	827.2
0.825	11.36	68.08	-13.31	0.47	2.13	-0.42	1.354	-0.202	837.7
0.875	11.64	68.02	-17.65	0.48	2.13	-0.56	1.349	-0.265	863.1
0.925	12.20	68.60	-24.28	0.50	2.15	-0.77	1.343	-0.354	931.3
0.975	15.52	73.64	-38.15	0.61	2.30	-1.21	1.311	-0.493	1232.6

Table C.16: Averaged total stress intensity factors $K_1^{(T)}$, $K_2^{(T)}$ and $K_{III}^{(T)}$ from the fourth, fifth and sixth integration domains, normalized total stress intensity factors $\hat{K}_1^{(T)}$, $\hat{K}_2^{(T)}$ and $K_{III}^{(T)}$ calculated for $\hat{L} = 100$ μm, phase angles $\hat{\psi}$ and ϕ, and the critical interface energy release rates $\mathcal{G}_{ic}$ along the specimen thickness for specimen BD1.7.1 with loading angle $\omega = -12.7°$.

x_3/B	$K_1^{(T)}$	$K_2^{(T)}$	$K_{III}^{(T)}$	$\hat{K}_1^{(T)}$	$\hat{K}_2^{(T)}$	$K_{III}^{(T)}$	$\hat{\psi}$	ϕ	$\mathcal{G}_{ic}$
	$\left(\text{MPa}\sqrt{\text{mm}}\,(\text{mm})^{-i\varepsilon}\right)$		(MPa$\sqrt{\text{mm}}$)	(MPa$\sqrt{\text{m}}$)			(rad)	(rad)	(N/m)
0.025	7.25	81.05	39.75	0.36	2.55	1.26	1.430	0.478	1417.9
0.075	3.88	76.55	24.60	0.25	2.41	0.78	1.468	0.328	1106.7
0.125	3.98	76.41	17.53	0.25	2.41	0.55	1.467	0.238	1046.6
0.175	4.30	76.75	13.03	0.26	2.42	0.41	1.463	0.178	1029.7
0.225	4.56	77.13	9.79	0.27	2.43	0.31	1.460	0.134	1026.0
0.275	4.73	77.46	7.30	0.28	2.44	0.23	1.458	0.099	1026.7
0.325	4.84	77.72	5.28	0.28	2.45	0.17	1.457	0.072	1028.8
0.375	4.91	77.91	3.58	0.28	2.45	0.11	1.456	0.049	1031.0
0.425	4.95	78.03	2.07	0.28	2.46	0.07	1.455	0.028	1032.7
0.475	4.97	78.09	0.68	0.29	2.46	0.02	1.455	0.009	1033.6
0.525	4.97	78.09	-0.68	0.29	2.46	-0.02	1.455	-0.009	1033.6
0.575	4.95	78.03	-2.07	0.28	2.46	-0.07	1.455	-0.028	1032.7
0.625	4.91	77.91	-3.58	0.28	2.45	-0.11	1.456	-0.049	1031.0
0.675	4.84	77.72	-5.28	0.28	2.45	-0.17	1.457	-0.072	1028.8
0.725	4.73	77.46	-7.30	0.28	2.44	-0.23	1.458	-0.099	1026.7
0.775	4.56	77.13	-9.79	0.27	2.43	-0.31	1.460	-0.134	1026.0
0.825	4.30	76.75	-13.03	0.26	2.42	-0.41	1.463	-0.178	1029.7
0.875	3.98	76.41	-17.53	0.25	2.41	-0.55	1.467	-0.238	1046.6
0.925	3.88	76.55	-24.60	0.25	2.41	-0.78	1.468	-0.328	1106.7
0.975	7.25	81.05	-39.75	0.36	2.55	-1.26	1.430	-0.478	1417.9

Table C.17: Averaged total stress intensity factors $K_1^{(T)}$, $K_2^{(T)}$ and $K_{III}^{(T)}$ from the fourth, fifth and sixth integration domains, normalized total stress intensity factors $\hat{K}_1^{(T)}$, $\hat{K}_2^{(T)}$ and $K_{III}^{(T)}$ calculated for $\hat{L} = 100$ μm, phase angles $\hat{\psi}$ and ϕ, and the critical interface energy release rates $\mathcal{G}_{ic}$ along the specimen thickness for specimen BD1.11.2 with loading angle $\omega = -12.9°$.

x_3/B	$K_1^{(T)}$	$K_2^{(T)}$	$K_{III}^{(T)}$	$\hat{K}_1^{(T)}$	$\hat{K}_2^{(T)}$	$K_{III}^{(T)}$	$\hat{\psi}$	ϕ	$\mathcal{G}_{ic}$
	$\left(\text{MPa}\sqrt{\text{mm}}\,(\text{mm})^{-i\varepsilon}\right)$		(MPa$\sqrt{\text{mm}}$)	(MPa$\sqrt{\text{m}}$)			(rad)	(rad)	(N/m)
0.025	11.96	92.13	48.27	0.53	2.89	1.53	1.390	0.504	1899.7
0.075	6.62	85.79	31.64	0.35	2.70	1.00	1.442	0.372	1439.8
0.125	5.61	85.00	23.38	0.32	2.67	0.74	1.453	0.283	1328.7
0.175	5.35	85.02	17.90	0.31	2.68	0.57	1.456	0.219	1285.8
0.225	5.27	85.26	13.78	0.31	2.68	0.44	1.457	0.169	1267.8
0.275	5.24	85.52	10.48	0.31	2.69	0.33	1.458	0.129	1260.1
0.325	5.23	85.76	7.70	0.31	2.70	0.24	1.458	0.095	1257.3
0.375	5.22	85.94	5.28	0.31	2.71	0.17	1.458	0.065	1256.6
0.425	5.21	86.06	3.09	0.31	2.71	0.10	1.458	0.038	1256.7
0.475	5.21	86.13	1.02	0.31	2.71	0.03	1.458	0.012	1256.9
0.525	5.21	86.13	-1.02	0.31	2.71	-0.03	1.458	-0.012	1256.9
0.575	5.21	86.06	-3.09	0.31	2.71	-0.10	1.458	-0.038	1256.7
0.625	5.22	85.94	-5.28	0.31	2.71	-0.17	1.458	-0.065	1256.6
0.675	5.23	85.76	-7.70	0.31	2.70	-0.24	1.458	-0.095	1257.3
0.725	5.24	85.52	-10.48	0.31	2.69	-0.33	1.458	-0.129	1260.1
0.775	5.27	85.26	-13.78	0.31	2.68	-0.44	1.457	-0.169	1267.8
0.825	5.35	85.02	-17.90	0.31	2.68	-0.57	1.456	-0.219	1285.8
0.875	5.61	85.00	-23.38	0.32	2.67	-0.74	1.453	-0.283	1328.7
0.925	6.62	85.79	-31.64	0.35	2.70	-1.00	1.442	-0.372	1439.8
0.975	11.96	92.13	-48.27	0.53	2.89	-1.53	1.390	-0.504	1899.7

Table C.18: Averaged total stress intensity factors $K_1^{(T)}$, $K_2^{(T)}$ and $K_{III}^{(T)}$ from the fourth, fifth and sixth integration domains, normalized total stress intensity factors $\hat{K}_1^{(T)}$, $\hat{K}_2^{(T)}$ and $K_{III}^{(T)}$ calculated for $\hat{L} = 100$ μm, phase angles $\hat{\psi}$ and ϕ, and the critical interface energy release rates $\mathcal{G}_{ic}$ along the specimen thickness for specimen BD1.7.2 with loading angle $\omega = -12.9°$.

x_3/B	$K_1^{(T)}$ $\left(\text{MPa}\sqrt{\text{mm}}\,(\text{mm})^{-i\varepsilon}\right)$	$K_2^{(T)}$	$K_{III}^{(T)}$ (MPa$\sqrt{\text{mm}}$)	$\hat{K}_1^{(T)}$ (MPa$\sqrt{\text{m}}$)	$\hat{K}_2^{(T)}$	$K_{III}^{(T)}$	$\hat{\psi}$ (rad)	ϕ (rad)	$\mathcal{G}_{ic}$ (N/m)
0.025	8.63	78.79	38.70	0.40	2.47	1.22	1.410	0.478	1345.0
0.075	5.47	74.71	23.99	0.30	2.35	0.76	1.446	0.328	1056.6
0.125	5.38	74.65	17.20	0.29	2.35	0.54	1.447	0.239	1001.7
0.175	5.55	74.96	12.85	0.30	2.36	0.41	1.445	0.179	984.9
0.225	5.70	75.30	9.69	0.30	2.37	0.31	1.443	0.135	980.3
0.275	5.80	75.59	7.24	0.31	2.38	0.23	1.442	0.101	980.0
0.325	5.87	75.82	5.25	0.31	2.38	0.17	1.442	0.073	981.3
0.375	5.91	75.98	3.57	0.31	2.39	0.11	1.441	0.050	982.9
0.425	5.93	76.10	2.07	0.31	2.39	0.07	1.441	0.029	984.2
0.475	5.94	76.15	0.68	0.31	2.40	0.02	1.441	0.009	984.8
0.525	5.94	76.15	-0.68	0.31	2.40	-0.02	1.441	-0.009	984.9
0.575	5.93	76.10	-2.07	0.31	2.39	-0.07	1.441	-0.029	984.2
0.625	5.91	75.98	-3.57	0.31	2.39	-0.11	1.441	-0.050	982.9
0.675	5.87	75.82	-5.25	0.31	2.38	-0.17	1.442	-0.073	981.3
0.725	5.80	75.59	-7.24	0.31	2.38	-0.23	1.442	-0.101	980.0
0.775	5.70	75.30	-9.69	0.30	2.37	-0.31	1.443	-0.135	980.3
0.825	5.55	74.96	-12.85	0.30	2.36	-0.41	1.445	-0.179	984.9
0.875	5.38	74.65	-17.20	0.29	2.35	-0.54	1.447	-0.239	1001.8
0.925	5.47	74.71	-23.99	0.30	2.35	-0.76	1.446	-0.328	1056.6
0.975	8.63	78.79	-38.70	0.40	2.47	-1.22	1.410	-0.478	1345.0

Table C.19: Averaged total stress intensity factors $K_1^{(T)}$, $K_2^{(T)}$ and $K_{III}^{(T)}$ from the fourth, fifth and sixth integration domains, normalized total stress intensity factors $\hat{K}_1^{(T)}$, $\hat{K}_2^{(T)}$ and $K_{III}^{(T)}$ calculated for $\hat{L} = 100$ μm, phase angles $\hat{\psi}$ and ϕ, and the critical interface energy release rates $\mathcal{G}_{ic}$ along the specimen thickness for specimen BD1.13.2 with loading angle $\omega = -12.9°$.

x_3/B	$K_1^{(T)}$ $\left(\text{MPa}\sqrt{\text{mm}}\,(\text{mm})^{-i\varepsilon}\right)$	$K_2^{(T)}$	$K_{III}^{(T)}$ (MPa$\sqrt{\text{mm}}$)	$\hat{K}_1^{(T)}$ (MPa$\sqrt{\text{m}}$)	$\hat{K}_2^{(T)}$	$K_{III}^{(T)}$	$\hat{\psi}$ (rad)	ϕ (rad)	$\mathcal{G}_{ic}$ (N/m)
0.025	9.03	82.79	42.15	0.42	2.60	1.33	1.410	0.493	1508.2
0.075	5.10	77.42	26.94	0.29	2.44	0.85	1.453	0.353	1153.9
0.125	4.87	76.90	19.60	0.28	2.42	0.62	1.456	0.264	1075.1
0.175	5.02	77.05	14.81	0.29	2.43	0.47	1.454	0.201	1047.9
0.225	5.17	77.33	11.27	0.29	2.43	0.36	1.452	0.153	1038.1
0.275	5.27	77.61	8.49	0.29	2.44	0.27	1.451	0.115	1035.0
0.325	5.33	77.84	6.20	0.30	2.45	0.20	1.450	0.084	1034.8
0.375	5.37	78.01	4.23	0.30	2.45	0.13	1.450	0.057	1035.5
0.425	5.39	78.13	2.46	0.30	2.46	0.08	1.450	0.033	1036.3
0.475	5.40	78.18	0.81	0.30	2.46	0.03	1.450	0.011	1036.8
0.525	5.40	78.18	-0.81	0.30	2.46	-0.03	1.450	-0.011	1036.9
0.575	5.39	78.13	-2.46	0.30	2.46	-0.08	1.450	-0.033	1036.3
0.625	5.37	78.01	-4.23	0.30	2.45	-0.13	1.450	-0.057	1035.5
0.675	5.33	77.84	-6.20	0.30	2.45	-0.20	1.450	-0.084	1034.8
0.725	5.27	77.61	-8.49	0.29	2.44	-0.27	1.451	-0.115	1035.0
0.775	5.17	77.33	-11.27	0.29	2.43	-0.36	1.452	-0.153	1038.1
0.825	5.02	77.05	-14.81	0.29	2.43	-0.47	1.454	-0.201	1047.9
0.875	4.87	76.90	-19.60	0.28	2.42	-0.62	1.456	-0.264	1075.1
0.925	5.10	77.42	-26.94	0.29	2.44	-0.85	1.453	-0.353	1153.9
0.975	9.03	82.79	-42.15	0.42	2.60	-1.33	1.410	-0.493	1508.2

Table C.20: Averaged total stress intensity factors $K_1^{(T)}$, $K_2^{(T)}$ and $K_{III}^{(T)}$ from the fourth, fifth and sixth integration domains, normalized total stress intensity factors $\hat{K}_1^{(T)}$, $\hat{K}_2^{(T)}$ and $K_{III}^{(T)}$ calculated for $\hat{L} = 100$ μm, phase angles $\hat{\psi}$ and ϕ, and the critical interface energy release rates $\mathcal{G}_{ic}$ along the specimen thickness for specimen BD1.5.2 with loading angle $\omega = -13.0°$.

x_3/B	$K_1^{(T)}$ $\left(\text{MPa}\sqrt{\text{mm}}\,(\text{mm})^{-i\varepsilon}\right)$	$K_2^{(T)}$	$K_{III}^{(T)}$ (MPa$\sqrt{\text{mm}}$)	$\hat{K}_1^{(T)}$ (MPa$\sqrt{\text{m}}$)	$\hat{K}_2^{(T)}$	$K_{III}^{(T)}$	$\hat{\psi}$ (rad)	ϕ (rad)	$\mathcal{G}_{ic}$ (N/m)
0.025	9.15	80.21	39.79	0.42	2.52	1.26	1.405	0.482	1400.8
0.075	6.06	76.12	24.50	0.32	2.39	0.77	1.439	0.328	1098.4
0.125	5.97	76.13	17.56	0.31	2.39	0.56	1.441	0.239	1042.9
0.175	6.14	76.46	13.18	0.32	2.40	0.42	1.439	0.180	1026.2
0.225	6.29	76.80	9.99	0.32	2.42	0.32	1.437	0.137	1021.3
0.275	6.39	77.09	7.51	0.33	2.42	0.24	1.436	0.103	1020.6
0.325	6.46	77.31	5.47	0.33	2.43	0.17	1.435	0.075	1021.5
0.375	6.49	77.47	3.72	0.33	2.44	0.12	1.435	0.051	1022.7
0.425	6.51	77.57	2.17	0.33	2.44	0.07	1.435	0.030	1023.7
0.475	6.52	77.62	0.71	0.33	2.44	0.02	1.435	0.010	1024.3
0.525	6.52	77.62	-0.71	0.33	2.44	-0.02	1.435	-0.010	1024.3
0.575	6.51	77.57	-2.17	0.33	2.44	-0.07	1.435	-0.030	1023.7
0.625	6.49	77.47	-3.72	0.33	2.44	-0.12	1.435	-0.051	1022.7
0.675	6.46	77.31	-5.47	0.33	2.43	-0.17	1.435	-0.075	1021.5
0.725	6.39	77.09	-7.51	0.33	2.42	-0.24	1.436	-0.103	1020.6
0.775	6.29	76.80	-9.99	0.32	2.42	-0.32	1.437	-0.137	1021.4
0.825	6.14	76.46	-13.18	0.32	2.40	-0.42	1.439	-0.180	1026.2
0.875	5.97	76.13	-17.56	0.31	2.39	-0.56	1.441	-0.239	1042.9
0.925	6.06	76.12	-24.50	0.32	2.39	-0.77	1.439	-0.328	1098.4
0.975	9.15	80.21	-39.79	0.42	2.52	-1.26	1.405	-0.482	1400.8

Table C.21: Averaged total stress intensity factors $K_1^{(T)}$, $K_2^{(T)}$ and $K_{III}^{(T)}$ from the fourth, fifth and sixth integration domains, normalized total stress intensity factors $\hat{K}_1^{(T)}$, $\hat{K}_2^{(T)}$ and $K_{III}^{(T)}$ calculated for $\hat{L} = 100$ μm, phase angles $\hat{\psi}$ and ϕ, and the critical interface energy release rates $\mathcal{G}_{ic}$ along the specimen thickness for specimen BD2.8.1 with loading angle $\omega = 2.0°$.

x_3/B	$K_1^{(T)}$	$K_2^{(T)}$	$K_{III}^{(T)}$	$\hat{K}_1^{(T)}$	$\hat{K}_2^{(T)}$	$K_{III}^{(T)}$	$\hat{\psi}$	ϕ	$\mathcal{G}_{ic}$
	$\left(\text{MPa}\sqrt{\text{mm}}\,(\text{mm})^{-i\varepsilon}\right)$		(MPa$\sqrt{\text{mm}}$)	(MPa$\sqrt{\text{m}}$)			(rad)	(rad)	(N/m)
0.025	17.29	-17.36	-1.64	0.52	-0.58	-0.05	-0.839	-0.071	130.3
0.075	20.76	-16.64	-3.03	0.63	-0.56	-0.10	-0.728	-0.120	135.0
0.125	20.76	-16.23	-2.91	0.63	-0.55	-0.09	-0.716	-0.117	127.5
0.175	20.32	-15.99	-2.53	0.62	-0.54	-0.08	-0.719	-0.103	120.1
0.225	19.87	-15.83	-2.12	0.60	-0.53	-0.07	-0.725	-0.088	114.2
0.275	19.49	-15.70	-1.71	0.59	-0.53	-0.05	-0.730	-0.072	109.7
0.325	19.19	-15.61	-1.32	0.58	-0.52	-0.04	-0.735	-0.056	106.3
0.375	18.98	-15.54	-0.93	0.57	-0.52	-0.03	-0.738	-0.040	104.0
0.425	18.84	-15.50	-0.56	0.57	-0.52	-0.02	-0.740	-0.024	102.4
0.475	18.77	-15.47	-0.18	0.57	-0.52	-0.01	-0.741	-0.008	101.7
0.525	18.77	-15.47	0.18	0.57	-0.52	0.01	-0.741	0.008	101.7
0.575	18.84	-15.50	0.56	0.57	-0.52	0.02	-0.740	0.024	102.4
0.625	18.98	-15.54	0.93	0.57	-0.52	0.03	-0.738	0.040	104.0
0.675	19.19	-15.61	1.32	0.58	-0.52	0.04	-0.735	0.056	106.3
0.725	19.49	-15.70	1.71	0.59	-0.53	0.05	-0.730	0.072	109.7
0.775	19.87	-15.83	2.12	0.60	-0.53	0.07	-0.725	0.088	114.2
0.825	20.32	-15.99	2.53	0.62	-0.54	0.08	-0.719	0.103	120.1
0.875	20.76	-16.23	2.91	0.63	-0.55	0.09	-0.716	0.117	127.5
0.925	20.76	-16.64	3.03	0.63	-0.56	0.10	-0.728	0.120	135.0
0.975	17.29	-17.36	1.64	0.52	-0.58	0.05	-0.839	0.071	130.3

Table C.22: Averaged total stress intensity factors $K_1^{(T)}$, $K_2^{(T)}$ and $K_{III}^{(T)}$ from the fourth, fifth and sixth integration domains, normalized total stress intensity factors $\hat{K}_1^{(T)}$, $\hat{K}_2^{(T)}$ and $K_{III}^{(T)}$ calculated for $\hat{L} = 100$ μm, phase angles $\hat{\psi}$ and ϕ, and the critical interface energy release rates $\mathcal{G}_{ic}$ along the specimen thickness for specimen BD2.7.1 with loading angle $\omega = 2.3°$.

x_3/B	$K_1^{(T)}$	$K_2^{(T)}$	$K_{III}^{(T)}$	$\hat{K}_1^{(T)}$	$\hat{K}_2^{(T)}$	$K_{III}^{(T)}$	$\hat{\psi}$	ϕ	$\mathcal{G}_{ic}$
	$\left(\text{MPa}\sqrt{\text{mm}}\,(\text{mm})^{-i\varepsilon}\right)$		(MPa$\sqrt{\text{mm}}$)	(MPa$\sqrt{\text{m}}$)			(rad)	(rad)	(N/m)
0.025	17.19	-24.74	-1.45	0.50	-0.81	-0.05	-1.016	-0.051	168.4
0.075	21.19	-24.57	-1.35	0.63	-0.81	-0.04	-0.911	-0.044	185.5
0.125	21.64	-24.48	-0.91	0.64	-0.81	-0.03	-0.899	-0.029	185.1
0.175	21.41	-24.43	-0.51	0.64	-0.81	-0.02	-0.903	-0.017	181.4
0.225	21.05	-24.39	-0.25	0.62	-0.80	-0.01	-0.911	-0.008	177.6
0.275	20.71	-24.34	-0.10	0.61	-0.80	0.00	-0.918	-0.003	174.1
0.325	20.43	-24.30	-0.02	0.61	-0.80	0.00	-0.924	-0.001	171.3
0.375	20.21	-24.26	0.02	0.60	-0.80	0.00	-0.928	0.001	169.2
0.425	20.07	-24.23	0.02	0.59	-0.80	0.00	-0.931	0.001	167.9
0.475	20.00	-24.22	0.01	0.59	-0.80	0.00	-0.933	0.000	167.2
0.525	20.00	-24.22	-0.01	0.59	-0.80	0.00	-0.933	0.000	167.2
0.575	20.07	-24.23	-0.02	0.59	-0.80	0.00	-0.931	-0.001	167.9
0.625	20.21	-24.26	-0.02	0.60	-0.80	0.00	-0.928	-0.001	169.2
0.675	20.43	-24.30	0.02	0.61	-0.80	0.00	-0.924	0.001	171.3
0.725	20.71	-24.34	0.10	0.61	-0.80	0.00	-0.918	0.003	174.1
0.775	21.05	-24.39	0.25	0.62	-0.80	0.01	-0.911	0.008	177.6
0.825	21.41	-24.43	0.51	0.64	-0.81	0.02	-0.903	0.017	181.4
0.875	21.64	-24.48	0.91	0.64	-0.81	0.03	-0.899	0.029	185.1
0.925	21.19	-24.57	1.35	0.63	-0.81	0.04	-0.911	0.044	185.5
0.975	17.19	-24.74	1.45	0.50	-0.81	0.05	-1.016	0.051	168.4

Table C.23: Averaged total stress intensity factors $K_1^{(T)}$, $K_2^{(T)}$ and $K_{III}^{(T)}$ from the fourth, fifth and sixth integration domains, normalized total stress intensity factors $\hat{K}_1^{(T)}$, $\hat{K}_2^{(T)}$ and $K_{III}^{(T)}$ calculated for $\hat{L} = 100$ μm, phase angles $\hat{\psi}$ and ϕ, and the critical interface energy release rates $\mathcal{G}_{ic}$ along the specimen thickness for specimen BD2.7.2 with loading angle $\omega = 1.9°$.

x_3/B	$K_1^{(T)}$ $\left(\text{MPa}\sqrt{\text{mm}}\,(\text{mm})^{-i\varepsilon}\right)$	$K_2^{(T)}$	$K_{III}^{(T)}$ (MPa$\sqrt{\text{mm}}$)	$\hat{K}_1^{(T)}$ (MPa$\sqrt{\text{m}}$)	$\hat{K}_2^{(T)}$	$K_{III}^{(T)}$	$\hat{\psi}$ (rad)	ϕ (rad)	$\mathcal{G}_{ic}$ (N/m)
0.025	15.57	-56.42	-16.46	0.40	-1.81	-0.52	-1.353	-0.290	646.0
0.075	22.71	-53.80	-12.44	0.63	-1.74	-0.39	-1.223	-0.222	611.0
0.125	23.42	-53.10	-9.62	0.65	-1.72	-0.30	-1.207	-0.174	589.2
0.175	23.10	-52.82	-7.44	0.64	-1.71	-0.24	-1.211	-0.136	573.2
0.225	22.62	-52.68	-5.72	0.63	-1.70	-0.18	-1.217	-0.106	561.8
0.275	22.17	-52.59	-4.35	0.61	-1.70	-0.14	-1.224	-0.081	553.6
0.325	21.81	-52.52	-3.19	0.60	-1.69	-0.10	-1.229	-0.059	547.6
0.375	21.54	-52.48	-2.19	0.59	-1.69	-0.07	-1.233	-0.041	543.5
0.425	21.36	-52.45	-1.28	0.59	-1.69	-0.04	-1.236	-0.024	540.9
0.475	21.27	-52.43	-0.42	0.59	-1.69	-0.01	-1.237	-0.008	539.6
0.525	21.27	-52.43	0.42	0.59	-1.69	0.01	-1.237	0.008	539.6
0.575	21.36	-52.45	1.28	0.59	-1.69	0.04	-1.236	0.024	540.9
0.625	21.54	-52.48	2.19	0.59	-1.69	0.07	-1.233	0.041	543.5
0.675	21.81	-52.52	3.19	0.60	-1.69	0.10	-1.229	0.059	547.6
0.725	22.17	-52.59	4.34	0.61	-1.70	0.14	-1.224	0.081	553.6
0.775	22.62	-52.68	5.72	0.63	-1.70	0.18	-1.217	0.106	561.8
0.825	23.10	-52.82	7.44	0.64	-1.71	0.24	-1.211	0.136	573.2
0.875	23.42	-53.10	9.62	0.65	-1.72	0.30	-1.207	0.174	589.2
0.925	22.71	-53.80	12.44	0.63	-1.74	0.39	-1.223	0.222	611.0
0.975	15.57	-56.42	16.46	0.40	-1.81	0.52	-1.353	0.290	646.0

Table C.24: Averaged total stress intensity factors $K_1^{(T)}$, $K_2^{(T)}$ and $K_{III}^{(T)}$ from the fourth, fifth and sixth integration domains, normalized total stress intensity factors $\hat{K}_1^{(T)}$, $\hat{K}_2^{(T)}$ and $K_{III}^{(T)}$ calculated for $\hat{L} = 100$ μm, phase angles $\hat{\psi}$ and ϕ, and the critical interface energy release rates $\mathcal{G}_{ic}$ along the specimen thickness for specimen BD1.13.1 with loading angle $\omega = 4.9°$.

x_3/B	$K_1^{(T)}$ $\left(\text{MPa}\sqrt{\text{mm}}\,(\text{mm})^{-i\varepsilon}\right)$	$K_2^{(T)}$	$K_{III}^{(T)}$ (MPa$\sqrt{\text{mm}}$)	$\hat{K}_1^{(T)}$ (MPa$\sqrt{\text{m}}$)	$\hat{K}_2^{(T)}$	$K_{III}^{(T)}$	$\hat{\psi}$ (rad)	ϕ (rad)	$\mathcal{G}_{ic}$ (N/m)
0.025	11.31	-62.12	-22.15	0.26	-1.98	-0.70	-1.443	-0.356	766.2
0.075	18.11	-58.33	-16.35	0.48	-1.87	-0.52	-1.322	-0.277	680.4
0.125	19.20	-57.40	-12.47	0.51	-1.84	-0.39	-1.300	-0.215	647.9
0.175	19.27	-57.06	-9.64	0.51	-1.83	-0.30	-1.297	-0.168	629.9
0.225	19.10	-56.90	-7.47	0.51	-1.83	-0.24	-1.299	-0.131	618.7
0.275	18.88	-56.80	-5.71	0.50	-1.82	-0.18	-1.302	-0.101	610.9
0.325	18.68	-56.73	-4.23	0.50	-1.82	-0.13	-1.305	-0.075	605.4
0.375	18.51	-56.68	-2.91	0.49	-1.82	-0.09	-1.307	-0.052	601.7
0.425	18.40	-56.65	-1.71	0.49	-1.82	-0.05	-1.309	-0.030	599.4
0.475	18.34	-56.63	-0.56	0.49	-1.82	-0.02	-1.310	-0.010	598.3
0.525	18.34	-56.63	0.56	0.49	-1.82	0.02	-1.310	0.010	598.3
0.575	18.40	-56.65	1.71	0.49	-1.82	0.05	-1.309	0.030	599.4
0.625	18.51	-56.68	2.91	0.49	-1.82	0.09	-1.307	0.052	601.7
0.675	18.68	-56.73	4.23	0.50	-1.82	0.13	-1.305	0.075	605.4
0.725	18.88	-56.80	5.71	0.50	-1.82	0.18	-1.302	0.101	610.9
0.775	19.10	-56.90	7.47	0.51	-1.83	0.24	-1.299	0.131	618.7
0.825	19.27	-57.06	9.64	0.51	-1.83	0.30	-1.297	0.168	629.9
0.875	19.20	-57.40	12.47	0.51	-1.84	0.39	-1.300	0.215	647.9
0.925	18.11	-58.33	16.35	0.48	-1.87	0.52	-1.322	0.277	680.4
0.975	11.31	-62.12	22.15	0.26	-1.98	0.70	-1.443	0.356	766.2

Table C.25: Averaged total stress intensity factors $K_1^{(T)}$, $K_2^{(T)}$ and $K_{III}^{(T)}$ from the fourth, fifth and sixth integration domains, normalized total stress intensity factors $\hat{K}_1^{(T)}$, $\hat{K}_2^{(T)}$ and $K_{III}^{(T)}$ calculated for $\hat{L} = 100$ μm, phase angles $\hat{\psi}$ and ϕ, and the critical interface energy release rates $\mathcal{G}_{ic}$ along the specimen thickness for specimen BD2.8.2 with loading angle $\omega = 5.1°$.

x_3/B	$K_1^{(T)}$	$K_2^{(T)}$	$K_{III}^{(T)}$	$\hat{K}_1^{(T)}$	$\hat{K}_2^{(T)}$	$K_{III}^{(T)}$	$\hat{\psi}$	ϕ	$\mathcal{G}_{ic}$
	$\left(\text{MPa}\sqrt{\text{mm}}\,(\text{mm})^{-i\varepsilon}\right)$		(MPa$\sqrt{\text{mm}}$)	(MPa$\sqrt{\text{m}}$)			(rad)	(rad)	(N/m)
0.025	9.39	-57.01	-18.70	0.20	-1.82	-0.59	-1.459	-0.331	641.0
0.075	16.38	-54.01	-13.98	0.43	-1.73	-0.44	-1.328	-0.257	581.1
0.125	17.70	-53.33	-10.86	0.47	-1.71	-0.34	-1.302	-0.202	558.6
0.175	17.94	-53.09	-8.50	0.48	-1.71	-0.27	-1.297	-0.160	545.2
0.225	17.90	-52.98	-6.65	0.48	-1.70	-0.21	-1.297	-0.125	536.5
0.275	17.78	-52.91	-5.12	0.47	-1.70	-0.16	-1.299	-0.097	530.4
0.325	17.65	-52.87	-3.80	0.47	-1.70	-0.12	-1.301	-0.072	526.0
0.375	17.54	-52.84	-2.63	0.47	-1.70	-0.08	-1.302	-0.050	523.0
0.425	17.47	-52.82	-1.54	0.46	-1.70	-0.05	-1.303	-0.029	521.1
0.475	17.43	-52.81	-0.51	0.46	-1.70	-0.02	-1.304	-0.010	520.2
0.525	17.43	-52.81	0.51	0.46	-1.70	0.02	-1.304	0.010	520.2
0.575	17.47	-52.82	1.54	0.46	-1.70	0.05	-1.303	0.029	521.1
0.625	17.54	-52.84	2.63	0.47	-1.70	0.08	-1.302	0.050	523.0
0.675	17.65	-52.87	3.80	0.47	-1.70	0.12	-1.301	0.072	526.0
0.725	17.78	-52.91	5.12	0.47	-1.70	0.16	-1.299	0.097	530.4
0.775	17.90	-52.98	6.65	0.48	-1.70	0.21	-1.297	0.125	536.5
0.825	17.94	-53.09	8.50	0.48	-1.71	0.27	-1.297	0.160	545.2
0.875	17.70	-53.33	10.86	0.47	-1.71	0.34	-1.302	0.202	558.6
0.925	16.38	-54.01	13.98	0.43	-1.73	0.44	-1.328	0.257	581.1
0.975	9.39	-57.01	18.70	0.20	-1.82	0.59	-1.459	0.331	641.0

Table C.26: Averaged total stress intensity factors $K_1^{(T)}$, $K_2^{(T)}$ and $K_{III}^{(T)}$ from the fourth, fifth and sixth integration domains, normalized total stress intensity factors $\hat{K}_1^{(T)}$, $\hat{K}_2^{(T)}$ and $K_{III}^{(T)}$ calculated for $\hat{L} = 100$ μm, phase angles $\hat{\psi}$ and ϕ, and the critical interface energy release rates $\mathcal{G}_{ic}$ along the specimen thickness for specimen BD2.1.1 with loading angle $\omega = 5.4°$.

x_3/B	$K_1^{(T)}$ $\left(\text{MPa}\sqrt{\text{mm}}\,(\text{mm})^{-i\varepsilon}\right)$	$K_2^{(T)}$	$K_{III}^{(T)}$ (MPa$\sqrt{\text{mm}}$)	$\hat{K}_1^{(T)}$ (MPa$\sqrt{\text{m}}$)	$\hat{K}_2^{(T)}$	$K_{III}^{(T)}$	$\hat{\psi}$ (rad)	ϕ (rad)	$\mathcal{G}_{ic}$ (N/m)
0.025	11.79	-78.21	-26.42	0.24	-2.49	-0.84	-1.473	-0.341	1188.5
0.075	21.14	-74.30	-18.94	0.55	-2.38	-0.60	-1.346	-0.255	1075.4
0.125	22.83	-73.54	-14.42	0.60	-2.36	-0.46	-1.322	-0.196	1040.3
0.175	23.07	-73.31	-11.15	0.61	-2.35	-0.35	-1.318	-0.153	1020.7
0.225	22.93	-73.24	-8.62	0.60	-2.35	-0.27	-1.319	-0.119	1008.4
0.275	22.70	-73.21	-6.58	0.60	-2.35	-0.21	-1.322	-0.091	999.8
0.325	22.46	-73.19	-4.86	0.59	-2.35	-0.15	-1.325	-0.067	993.8
0.375	22.26	-73.18	-3.34	0.58	-2.35	-0.11	-1.327	-0.046	989.7
0.425	22.13	-73.17	-1.96	0.58	-2.35	-0.06	-1.329	-0.027	987.1
0.475	22.05	-73.17	-0.64	0.58	-2.35	-0.02	-1.330	-0.009	985.8
0.525	22.05	-73.17	0.64	0.58	-2.35	0.02	-1.330	0.009	985.8
0.575	22.13	-73.17	1.96	0.58	-2.35	0.06	-1.329	0.027	987.1
0.625	22.26	-73.18	3.34	0.58	-2.35	0.11	-1.327	0.046	989.6
0.675	22.46	-73.19	4.86	0.59	-2.35	0.15	-1.325	0.067	993.8
0.725	22.70	-73.21	6.58	0.60	-2.35	0.21	-1.322	0.091	999.8
0.775	22.93	-73.24	8.62	0.60	-2.35	0.27	-1.319	0.119	1008.4
0.825	23.07	-73.31	11.15	0.61	-2.35	0.35	-1.318	0.153	1020.7
0.875	22.83	-73.54	14.42	0.60	-2.36	0.46	-1.322	0.196	1040.3
0.925	21.14	-74.30	18.94	0.55	-2.38	0.60	-1.346	0.255	1075.4
0.975	11.79	-78.21	26.42	0.24	-2.49	0.84	-1.473	0.341	1188.5

Table C.27: Averaged total stress intensity factors $K_1^{(T)}$, $K_2^{(T)}$ and $K_{III}^{(T)}$ from the fourth, fifth and sixth integration domains, normalized total stress intensity factors $\hat{K}_1^{(T)}$, $\hat{K}_2^{(T)}$ and $K_{III}^{(T)}$ calculated for $\hat{L} = 100$ μm, phase angles $\hat{\psi}$ and ϕ, and the critical interface energy release rates $\mathcal{G}_{ic}$ along the specimen thickness for specimen BD2.4.2 with loading angle $\omega = 9.5°$.

x_3/B	$K_1^{(T)}$	$K_2^{(T)}$	$K_{III}^{(T)}$	$\hat{K}_1^{(T)}$	$\hat{K}_2^{(T)}$	$K_{III}^{(T)}$	$\hat{\psi}$	ϕ	$\mathcal{G}_{ic}$
	$\left(\text{MPa}\sqrt{\text{mm}}\,(\text{mm})^{-i\varepsilon}\right)$		(MPa$\sqrt{\text{mm}}$)	(MPa$\sqrt{\text{m}}$)			(rad)	(rad)	(N/m)
0.025	-8.27	-83.93	-32.82	-0.40	-2.64	-1.04	-1.721	-0.392	1405.3
0.075	1.43	-78.67	-23.91	-0.08	-2.49	-0.76	-1.605	-0.312	1153.6
0.125	3.94	-77.64	-18.65	0.00	-2.46	-0.59	-1.572	-0.249	1086.1
0.175	4.97	-77.34	-14.73	0.03	-2.45	-0.47	-1.559	-0.199	1055.0
0.225	5.51	-77.26	-11.59	0.05	-2.45	-0.37	-1.552	-0.157	1038.2
0.275	5.81	-77.24	-8.96	0.06	-2.45	-0.28	-1.548	-0.122	1027.9
0.325	5.99	-77.23	-6.67	0.06	-2.45	-0.21	-1.545	-0.091	1021.4
0.375	6.10	-77.24	-4.62	0.07	-2.45	-0.15	-1.544	-0.063	1017.4
0.425	6.16	-77.24	-2.71	0.07	-2.45	-0.09	-1.543	-0.037	1015.0
0.475	6.18	-77.25	-0.90	0.07	-2.45	-0.03	-1.543	-0.012	1013.8
0.525	6.18	-77.25	0.90	0.07	-2.45	0.03	-1.543	0.012	1013.8
0.575	6.16	-77.24	2.71	0.07	-2.45	0.09	-1.543	0.037	1015.0
0.625	6.10	-77.24	4.62	0.07	-2.45	0.15	-1.544	0.063	1017.4
0.675	5.99	-77.23	6.67	0.06	-2.45	0.21	-1.545	0.091	1021.4
0.725	5.81	-77.24	8.96	0.06	-2.45	0.28	-1.548	0.122	1027.9
0.775	5.51	-77.26	11.59	0.05	-2.45	0.37	-1.552	0.157	1038.2
0.825	4.97	-77.34	14.73	0.03	-2.45	0.47	-1.559	0.199	1055.1
0.875	3.94	-77.64	18.65	0.00	-2.46	0.59	-1.572	0.249	1086.1
0.925	1.43	-78.67	23.91	-0.08	-2.49	0.76	-1.605	0.312	1153.6
0.975	-8.27	-83.93	32.82	-0.40	-2.64	1.04	-1.721	0.392	1405.3

Appendix D

Tabulated results measured from the C-ELS tests

As described in Section 5.3, six C-ELS specimens were tested quasi-statically. For each C-ELS specimen, values of the delamination length a between the load-line and the delamination tip were measured by the ImageJ (2015) software from images obtained during the PC (second) stage of the test. These values, as well as the synchronized values of the load P and actuator displacement d are presented in the first through third columns of Tables D.1 through D.6. Values of the compliance C were calculated for each delamination length using eq. (5.12) and the results are presented in the fourth column of these tables. In addition, the stress intensity factors resulting from applied loads were calculated based on FEA results by means of VCCT (Farkash and Banks-Sills, 2016). For each measured delamination length a, the obtained K_m $(m = 1, 2)$ values were normalized by means of eq. (1.26) with $\hat{L} = 100$ μm. The results are presented for each delamination length in columns five and six of Tables D.1 through D.6.

To obtain $\mathcal{G}_{IIR}$ as a function of the delamination extension Δa two methods were used, namely, the J-integral and the ECM; both methods are described in Sections 5.3.1 and 5.2, respectively. The resulting $\mathcal{G}_{IIR}$ values which were calculated by means of the J-integral with eq. (5.15) are presented in the seventh column of Tables D.1 through D.6. In the eighth column of these tables, the resulting $\mathcal{G}_{IIR}$ values calculated with ECM using eq. (5.9) and the fitting parameter m from Table 5.12, are shown. Finally, in the last column of Tables D.1 through D.6, the values of $\hat{\psi}$ which were obtained from eq. (3.19) using $\hat{K}_1$ and $\hat{K}_2$ in columns five and six of Tables D.1 through D.6 for each delamination length, are shown. Note that the in-plane mode mixity obtained for each specimen remains approximately constant for all delamination length values for all specimens.

Table D.1: Dimensions from the test, as well as analysis results for specimen CELS-2-2.

a (mm)	P (N)	d (mm)	C (mm/N)	$\hat{K}_1$ (MPa$\sqrt{\text{m}}$)	$\hat{K}_2$ (MPa$\sqrt{\text{m}}$)	$\mathcal{G}_{IIR}$ (J-int) (N/m)	$\mathcal{G}_{IIR}$ (ECM) (N/m)	$\hat{\psi}$ (rad)
51.8	164.6	10.5	0.070	0.32	2.53	841.0	841.0	1.445
59.2	150.8	15.7	0.106	0.34	2.65	904.9	870.9	1.441
61.1	156.5	16.7	0.108	0.37	2.83	1036.5	998.8	1.441
61.4	156.8	16.8	0.108	0.37	2.85	1048.4	1010.4	1.441
62.9	159.2	17.5	0.111	0.39	2.96	1136.2	1096.1	1.440
65.0	158.8	17.9	0.113	0.40	3.05	1205.4	1164.4	1.439
65.2	159.0	18.1	0.114	0.41	3.06	1214.0	1172.8	1.439
67.1	156.3	18.4	0.118	0.41	3.10	1243.0	1202.2	1.439
68.7	153.4	18.6	0.121	0.42	3.11	1252.1	1212.1	1.438
70.3	150.1	18.7	0.124	0.42	3.11	1252.6	1213.5	1.438
71.7	146.4	18.9	0.127	0.42	3.10	1239.2	1201.4	1.437
72.4	142.3	19.0	0.131	0.41	3.04	1194.9	1158.9	1.437
74.6	138.9	19.1	0.135	0.41	3.06	1208.8	1173.5	1.436
74.8	137.8	19.2	0.136	0.41	3.04	1194.1	1159.3	1.436
77.6	132.4	19.3	0.142	0.41	3.03	1185.1	1152.1	1.436
78.6	129.0	19.3	0.145	0.41	2.99	1153.3	1121.5	1.435

Table D.2: Dimensions from the test, as well as analysis results for specimen CELS-2-3.

a (mm)	P (N)	d (mm)	C (mm/N)	$\hat{K}_1$ (MPa$\sqrt{\text{m}}$)	$\hat{K}_2$ (MPa$\sqrt{\text{m}}$)	$\mathcal{G}_{IIR}$ (J-int) (N/m)	$\mathcal{G}_{IIR}$ (ECM) (N/m)	$\hat{\psi}$ (rad)
53.1	189.4	11.1	0.063	0.36	2.90	1082.4	1082.4	1.446
58.0	175.3	16.5	0.096	0.37	2.92	1103.0	1159.0	1.444
59.7	172.1	16.9	0.100	0.38	2.95	1124.7	1183.2	1.443
61.2	169.0	16.9	0.102	0.38	2.97	1138.5	1199.0	1.443
61.7	167.7	17.0	0.103	0.38	2.97	1137.4	1198.3	1.442
63.9	165.0	17.0	0.105	0.39	3.02	1180.2	1245.1	1.442
65.2	161.9	17.1	0.107	0.39	3.03	1184.4	1250.7	1.441
67.7	157.0	17.6	0.113	0.40	3.04	1197.9	1266.7	1.440
69.2	158.5	18.4	0.117	0.41	3.14	1275.4	1349.8	1.440
70.6	158.0	18.8	0.119	0.42	3.19	1316.6	1394.4	1.439
71.5	157.5	19.2	0.122	0.43	3.22	1342.8	1422.9	1.439
73.6	156.6	19.6	0.125	0.44	3.30	1404.5	1489.7	1.439
74.2	152.8	19.8	0.129	0.43	3.24	1359.6	1442.5	1.438
75.9	151.8	19.9	0.130	0.44	3.29	1400.9	1487.6	1.438
77.0	149.3	19.9	0.132	0.44	3.29	1396.3	1483.4	1.438
77.9	141.3	20.3	0.142	0.42	3.14	1276.1	1356.2	1.437

Table D.3: Dimensions from the test, as well as analysis results for specimen CELS-2-4.

a (mm)	P (N)	d (mm)	C (mm/N)	$\hat{K}_1$ (MPa$\sqrt{\text{m}}$)	$\hat{K}_2$ (MPa$\sqrt{\text{m}}$)	$\mathcal{G}_{IIR}$ (J-int) (N/m)	$\mathcal{G}_{IIR}$ (ECM) (N/m)	$\hat{\psi}$ (rad)
52.7	189.4	11.8	0.068	0.32	2.62	888.9	888.9	1.448
57.0	165.5	15.3	0.095	0.34	2.69	930.8	1033.4	1.445
59.2	168.2	15.9	0.096	0.36	2.83	1034.1	1150.1	1.444
59.6	170.4	16.4	0.098	0.37	2.89	1077.1	1198.3	1.444
62.1	168.8	16.8	0.101	0.38	2.98	1147.2	1278.6	1.443
63.7	166.9	17.3	0.104	0.39	3.02	1175.3	1311.2	1.443
65.2	167.8	17.7	0.105	0.40	3.10	1243.1	1388.1	1.442
65.5	166.7	17.8	0.107	0.40	3.10	1238.6	1383.4	1.442
67.0	156.5	17.9	0.113	0.39	2.98	1144.0	1279.0	1.441
68.5	148.5	17.9	0.118	0.38	2.88	1074.3	1202.0	1.441
70.5	145.2	17.9	0.120	0.38	2.90	1087.6	1218.3	1.440
71.6	140.9	18.0	0.124	0.38	2.86	1055.9	1183.5	1.440
73.8	140.3	18.0	0.124	0.39	2.93	1111.6	1247.3	1.439
74.6	135.2	18.0	0.128	0.38	2.85	1052.6	1181.6	1.439

Table D.4: Dimensions from the test, as well as analysis results for specimen CELS-2-5.

a (mm)	P (N)	d (mm)	C (mm/N)	$\hat{K}_1$ (MPa$\sqrt{\text{m}}$)	$\hat{K}_2$ (MPa$\sqrt{\text{m}}$)	$\mathcal{G}_{IIR}$ (J-int) (N/m)	$\mathcal{G}_{IIR}$ (ECM) (N/m)	$\hat{\psi}$ (rad)
52.8	158.8	12.7	0.086	0.30	2.41	716.8	716.8	1.446
58.1	149.4	16.6	0.114	0.32	2.49	801.6	944.9	1.444
59.7	152.1	17.2	0.116	0.33	2.61	877.0	1035.0	1.443
61.7	154.0	17.6	0.117	0.35	2.72	958.9	1133.2	1.442
62.6	154.3	17.8	0.119	0.36	2.77	990.7	1171.6	1.442
63.5	152.1	18.1	0.121	0.36	2.77	988.9	1170.1	1.442
65.7	151.2	18.2	0.123	0.37	2.84	1044.0	1236.9	1.441
67.6	146.6	18.7	0.130	0.37	2.84	1038.9	1232.3	1.440
68.5	143.8	18.8	0.132	0.37	2.82	1024.8	1216.2	1.440
68.9	141.4	18.8	0.135	0.37	2.79	1003.5	1191.0	1.440
71.3	139.7	18.9	0.136	0.38	2.85	1046.9	1244.2	1.439
73.1	134.3	19.1	0.143	0.37	2.80	1016.0	1208.5	1.439
74.1	134.1	19.3	0.144	0.38	2.84	1041.1	1238.9	1.438
74.8	135.3	19.8	0.147	0.39	2.89	1079.0	1284.5	1.438
75.3	133.7	20.2	0.151	0.38	2.87	1067.8	1271.4	1.438
76.7	130.3	20.5	0.157	0.38	2.85	1051.5	1252.8	1.438
77.9	129.0	20.6	0.159	0.38	2.87	1063.8	1268.2	1.437
79.0	126.8	20.8	0.162	0.38	2.86	1056.5	1260.0	1.437
79.8	125.8	21.1	0.166	0.39	2.86	1060.0	1264.6	1.437
82.7	123.0	21.4	0.171	0.39	2.90	1088.1	1299.6	1.436
83.9	119.2	21.4	0.176	0.39	2.85	1051.9	1256.9	1.436
84.3	116.6	21.4	0.180	0.38	2.80	1015.1	1213.1	1.436

Table D.5: Dimensions from the test, as well as analysis results for specimen CELS-2-6.

a (mm)	P (N)	d (mm)	C (mm/N)	$\hat{K}_1$ (MPa$\sqrt{\text{m}}$)	$\hat{K}_2$ (MPa$\sqrt{\text{m}}$)	$\mathcal{G}_{IIR}$ (J-int) (N/m)	$\mathcal{G}_{IIR}$ (ECM) (N/m)	$\hat{\psi}$ (rad)
52.8	158.8	12.7	0.086	0.30	2.43	761.7	761.7	1.447
57.7	164.5	16.0	0.097	0.34	2.70	939.9	1042.0	1.445
58.0	165.3	16.4	0.098	0.35	2.73	959.1	1063.6	1.445
59.2	164.8	16.5	0.099	0.35	2.77	993.6	1102.9	1.444
60.6	164.1	16.6	0.100	0.36	2.83	1031.0	1145.5	1.444
61.6	163.8	16.9	0.102	0.37	2.87	1060.4	1179.1	1.443
66.2	147.2	17.3	0.115	0.36	2.76	987.3	1101.0	1.442
67.1	143.0	17.3	0.119	0.35	2.72	955.3	1065.9	1.441
69.8	138.0	17.4	0.123	0.36	2.73	961.8	1074.7	1.440
71.2	136.5	17.4	0.124	0.36	2.75	976.7	1092.2	1.440
74.1	138.2	18.8	0.132	0.38	2.89	1082.5	1212.2	1.439
76.5	136.9	19.3	0.137	0.39	2.96	1133.5	1270.7	1.439
77.1	136.7	19.3	0.137	0.40	2.98	1148.3	1287.7	1.438
77.8	133.6	19.6	0.142	0.39	2.94	1116.5	1252.4	1.438
80.3	131.5	19.7	0.144	0.40	2.98	1148.5	1289.6	1.438

Table D.6: Dimensions from the test, as well as analysis results for specimen CELS-2-7.

a (mm)	P (N)	d (mm)	C (mm/N)	$\hat{K}_1$ (MPa$\sqrt{\text{m}}$)	$\hat{K}_2$ (MPa$\sqrt{\text{m}}$)	$\mathcal{G}_{IIR}$ (J-int) (N/m)	$\mathcal{G}_{IIR}$ (ECM) (N/m)	$\hat{\psi}$ (rad)
52.9	146.9	9.7	0.066	0.30	2.35	711.6	711.6	1.445
57.9	154.5	16.5	0.107	0.33	2.60	872.8	809.6	1.443
59.2	154.9	16.7	0.108	0.34	2.66	916.6	851.1	1.442
61.1	152.8	17.1	0.112	0.35	2.71	949.0	882.4	1.442
62.7	153.0	17.3	0.113	0.36	2.78	1000.5	931.2	1.441
65.7	151.1	18.1	0.119	0.38	2.88	1071.5	999.2	1.440
68.9	145.3	18.4	0.125	0.39	2.90	1088.4	1016.8	1.439
71.4	139.3	18.5	0.130	0.38	2.88	1070.3	1001.2	1.438
73.1	137.1	18.5	0.132	0.39	2.90	1087.1	1017.7	1.438
74.2	135.9	18.5	0.133	0.39	2.92	1101.1	1031.4	1.437
76.2	129.3	18.6	0.140	0.38	2.85	1050.5	984.9	1.437
77.4	125.9	19.0	0.146	0.38	2.82	1027.5	963.8	1.437

Appendix E

Tabulated results measured from the MMELS tests

Five MMELS specimens were tested, as described in Section 5.4. In Section E.1, values measured and obtained from the PC (second) test stage are given. In addition, values obtained from the analyses of the results such as the energy release rate and phase angles, integrated through the width of each specimen, are presented. The fitting parameters used to determine $K_m^{(f)}$ and $K_m^{(r)}$ $(m = 1, 2, III)$ for each specimen by means of eqs. (5.1) and (5.3), respectively, are presented in Section E.2.

E.1 Specimen dimensions and analysis results

For each MMELS specimen, values of the delamination length a between the load-line and the delamination tip were measured by the ImageJ (2015) software from the images obtained during the PC stage of the test. These values, as well as the synchronized load P and actuator displacement d are presented in the first through third columns of Tables E.1 through E.5. Values of the compliance C were calculated for each delamination length using eq. (5.12) and the results are presented in the fourth column of these tables. In addition, the expressions for the stress intensity factors resulting from the applied load, as well as those resulting from residual curing stresses in eqs. (5.1) and (5.3), respectively, with the fitting parameters in Tables E.6 through E.11 were superposed in eq. (5.4). The energy release rate values through the specimen width were then determined by means of eq. (3.17). The obtained result was then integrated through the width of the specimen with eq. (5.5) to obtain values of $\mathcal{G}_{iR}$ as a function of the delamination extension Δa, as described in Sections 5.4.1. The resulting $\mathcal{G}_{iR}$ values are presented in the fifth column of Tables E.1 through E.5. Values of $\mathcal{G}_{iR}$ were also determined by means of the ECM, as described in 5.2. In the sixth column of these tables, the resulting $\mathcal{G}_{iR}$ values calculated with ECM using eq. (5.9) and the fitting parameter m from Table 5.30, are shown. Finally, in the last column of Tables E.1 through E.5, values of $\hat{\psi}$ for each delamination length a,

Table E.1: Data from the test, as well as analysis results for specimen MMELS-1-9.

a (mm)	P (N)	d (mm)	C (mm/N)	$\mathcal{G}_{iR}$ (M-int) (N/m)	$\mathcal{G}_{iR}$ (ECM) (N/m)	$\hat{\psi}$ (rad)
55.5	89.4	12.0	0.139	525.4	576.4	0.659
58.9	93.3	13.5	0.148	756.6	708.4	0.660
59.3	92.4	13.5	0.150	733.1	704.0	0.660
60.7	90.4	13.6	0.153	759.6	706.1	0.661
61.5	89.0	13.7	0.157	740.7	702.9	0.661
62.3	86.8	13.7	0.161	737.0	687.3	0.661
64.9	84.5	14.1	0.170	748.2	704.7	0.662
66.7	86.0	15.2	0.179	797.2	772.3	0.663
69.5	82.8	15.2	0.186	816.7	776.5	0.664
71.3	79.7	15.5	0.196	799.9	755.7	0.664
73.7	76.5	16.1	0.210	797.6	747.0	0.665
74.4	76.2	16.1	0.212	804.3	752.4	0.665
77.0	72.4	16.5	0.227	780.1	728.5	0.666
79.5	71.7	17.2	0.238	813.2	762.8	0.666
80.7	69.8	17.4	0.247	789.8	744.5	0.667
81.8	68.8	17.8	0.255	787.8	743.3	0.667
83.9	66.7	18.2	0.269	777.1	734.1	0.667
85.5	65.0	18.5	0.280	765.5	724.6	0.668
87.6	62.6	18.9	0.295	741.5	705.2	0.668

Table E.2: Data from the test, as well as analysis results for specimen MMELS-1-11.

a (mm)	P (N)	d (mm)	C (mm/N)	$\mathcal{G}_{iR}$ (M-int) (N/m)	$\mathcal{G}_{iR}$ (ECM) (N/m)	$\hat{\psi}$ (rad)
58.1	96.9	13.7	0.146	807.1	724.8	0.660
58.7	96.5	13.8	0.147	815.5	733.2	0.660
59.6	94.8	13.9	0.150	811.0	730.0	0.660
60.6	93.6	14.0	0.154	817.2	736.6	0.661
61.9	92.8	14.4	0.159	837.2	756.2	0.661
62.9	92.2	14.6	0.162	852.3	770.9	0.662
63.9	92.0	14.9	0.165	872.4	790.1	0.662
65.5	91.8	15.4	0.170	910.9	826.8	0.663
68.0	88.8	15.4	0.176	916.7	834.3	0.663
68.5	84.7	15.5	0.185	846.1	769.9	0.664
70.2	83.0	15.6	0.190	851.9	776.9	0.664
70.6	81.0	15.7	0.195	821.8	749.1	0.664
72.2	84.5	16.6	0.198	932.3	852.2	0.665
73.9	83.7	16.6	0.200	956.7	876.1	0.665
74.7	78.0	16.7	0.214	847.4	775.7	0.665
77.5	75.0	17.0	0.227	841.4	771.9	0.666
79.4	73.6	17.7	0.240	849.7	780.7	0.666
82.2	70.3	18.1	0.255	831.3	765.2	0.667
83.8	67.9	18.3	0.266	803.4	740.0	0.667
86.5	66.4	19.1	0.282	817.2	754.2	0.668

are presented. These values were determined from expressions for $\hat{\psi}$ which were obtained using eq. (3.19) with the expressions in eqs. (5.4), for each specimen, and integrated through the width. Note that the in-plane mode mixity obtained for each specimen remains approximately constant for all delamination length values.

Table E.3: Data from the test, as well as analysis results for specimen MMELS-1-12.

a (mm)	P (N)	d (mm)	C (mm/N)	$\mathcal{G}_{iR}$ (M-int) (N/m)	$\mathcal{G}_{iR}$ (ECM) (N/m)	$\hat{\psi}$ (rad)
55.2	86.5	10.8	0.129	581.3	497.6	0.659
56.8	87.3	11.2	0.133	622.6	545.1	0.659
57.3	89.8	11.7	0.134	671.0	588.3	0.659
59.0	93.0	12.7	0.140	758.5	667.5	0.660
60.4	90.6	12.8	0.144	753.7	664.5	0.661
61.2	89.6	12.9	0.147	757.2	668.3	0.661
63.6	91.1	13.9	0.155	840.9	745.3	0.662
67.8	86.4	14.7	0.171	855.9	762.3	0.663
69.6	87.8	15.5	0.177	929.0	829.5	0.664
71.1	82.2	15.6	0.190	848.4	758.0	0.664
72.9	80.1	15.7	0.195	844.0	755.2	0.665
73.6	79.7	15.7	0.196	852.3	763.2	0.665
75.4	76.7	15.8	0.203	828.7	742.9	0.665
76.5	76.0	16.2	0.211	835.6	750.0	0.666
77.2	75.7	16.3	0.212	843.1	757.2	0.666
78.9	72.1	16.4	0.223	798.4	717.6	0.666
80.5	70.2	16.7	0.233	786.8	708.0	0.667
82.4	68.9	17.3	0.245	793.5	715.0	0.667
83.7	70.5	18.1	0.250	856.8	773.4	0.667
84.6	70.7	18.4	0.253	878.8	793.9	0.667
86.5	68.3	18.7	0.265	856.8	774.8	0.668

Table E.4: Data from the test, as well as analysis results for specimen MMELS-1-17.

a (mm)	P (N)	d (mm)	C (mm/N)	$\mathcal{G}_{iR}$ (M-int) (N/m)	$\mathcal{G}_{iR}$ (ECM) (N/m)	$\hat{\psi}$ (rad)
59.0	91.9	11.9	0.135	751.8	608.6	0.660
61.9	93.8	12.8	0.141	859.7	699.6	0.662
62.9	93.0	12.8	0.143	869.5	708.4	0.662
65.1	95.1	13.7	0.149	971.2	794.2	0.663
65.5	94.4	13.7	0.150	966.8	790.8	0.663
66.7	89.2	13.8	0.158	896.3	733.6	0.663
68.1	88.8	13.8	0.159	922.7	756.6	0.664
69.0	88.5	14.1	0.163	942.0	773.4	0.664
69.6	88.4	14.2	0.165	956.5	785.5	0.664
71.2	86.5	14.7	0.174	955.6	786.3	0.664
71.6	85.4	14.8	0.176	940.9	774.2	0.665
72.8	82.7	14.8	0.182	913.4	752.3	0.665
74.7	78.9	14.8	0.190	872.6	719.7	0.666
75.2	78.3	14.9	0.193	870.9	718.6	0.666
75.8	77.9	14.9	0.194	876.3	723.3	0.666
77.2	74.8	15.1	0.204	834.6	689.4	0.666
77.7	74.8	15.1	0.204	846.6	699.8	0.666

Table E.5: Data from the test, as well as analysis results for specimen MMELS-1-18.

a (mm)	P (N)	d (mm)	C (mm/N)	$\mathcal{G}_{iR}$ (M-int) (N/m)	$\mathcal{G}_{iR}$ (ECM) (N/m)	$\hat{\psi}$ (rad)
56.5	94.7	11.7	0.128	676.4	729.4	0.659
58.1	96.6	12.5	0.134	742.1	803.0	0.660
59.2	95.0	12.6	0.136	743.0	805.5	0.660
59.8	94.2	12.7	0.139	745.0	804.6	0.660
60.9	93.6	13.0	0.142	760.9	808.4	0.661
61.6	93.7	13.2	0.145	780.9	809.8	0.661
62.5	92.6	13.3	0.147	781.9	827.2	0.661
64.8	93.3	14.3	0.156	851.2	849.9	0.662
65.4	93.6	14.5	0.158	870.7	850.1	0.662
65.9	92.9	14.6	0.160	870.3	852.2	0.662
66.1	92.4	14.6	0.162	865.7	849.5	0.662
71.5	88.1	15.6	0.180	916.5	930.9	0.664
72.2	88.2	16.3	0.187	936.3	953.2	0.664
73.0	87.9	16.5	0.190	949.8	953.4	0.664
74.3	82.6	16.6	0.203	867.3	948.5	0.665
75.5	82.0	16.7	0.206	881.4	932.9	0.665
76.2	79.8	16.8	0.213	848.9	954.6	0.665
77.4	78.1	17.0	0.219	837.5	1011.2	0.666
78.1	76.5	17.0	0.224	817.0	1011.0	0.666
79.8	72.7	17.4	0.239	771.8	1023.6	0.666
80.6	73.6	18.0	0.245	805.6	1033.9	0.666
81.5	73.2	18.2	0.248	814.6	1049.4	0.667
82.0	72.7	18.3	0.251	812.8	1054.1	0.667
83.2	71.0	18.5	0.260	796.2	1049.8	0.667
84.4	71.1	18.9	0.266	821.8	951.2	0.667
85.7	70.1	19.1	0.272	822.7	959.7	0.667
86.4	68.2	19.4	0.282	791.2	976.5	0.668

Table E.6: Constants p_{i0}, $(i = 0, 1, .., 5)$, and p_{j1}, $(j = 0, 1, .., 4)$, of eq. 5.1 for $K_1^{(f)}$ for the MMELS specimens.

	MMELS-1-9	MMELS-1-11	MMELS-1-12	MMELS-1-17	MMELS-1-18
p_{00} ($\text{mm}^{-3/2}\text{mm}^{-i\varepsilon}$)	8.07 $\times 10^{-2}$	8.09 $\times 10^{-2}$	8.03 $\times 10^{-2}$	8.12 $\times 10^{-2}$	8.02$\times 10^{-2}$
p_{10} ($\text{mm}^{-5/2}\text{mm}^{-i\varepsilon}$)	-1.65 $\times 10^{-2}$	-1.65 $\times 10^{-2}$	-1.64$\times 10^{-2}$	-1.67$\times 10^{-2}$	-1.63$\times 10^{-2}$
p_{20} ($\text{mm}^{-7/2}\text{mm}^{-i\varepsilon}$)	1.71 $\times 10^{-3}$	1.70 $\times 10^{-3}$	1.69 $\times 10^{-3}$	1.71 $\times 10^{-3}$	1.67$\times 10^{-3}$
p_{30} ($\text{mm}^{-9/2}\text{mm}^{-i\varepsilon}$)	-8.80 $\times 10^{-5}$	-8.76 $\times 10^{-5}$	-8.71$\times 10^{-5}$	-8.79$\times 10^{-5}$	-8.61$\times 10^{-5}$
p_{40} ($\text{mm}^{-11/2}\text{mm}^{-i\varepsilon}$)	2.22 $\times 10^{-6}$	2.20 $\times 10^{-6}$	2.19 $\times 10^{-6}$	2.20 $\times 10^{-6}$	2.17$\times 10^{-6}$
p_{50} ($\text{mm}^{-13/2}\text{mm}^{-i\varepsilon}$)	1.16 $\times 10^{-11}$	-6.15 $\times 10^{-12}$	3.92 $\times 10^{-11}$	-2.46$\times 10^{-12}$	2.02$\times 10^{-11}$
p_{01} ($\text{mm}^{-5/2}\text{mm}^{-i\varepsilon}$)	7.12 $\times 10^{-4}$	6.95 $\times 10^{-4}$	7.13 $\times 10^{-4}$	6.80 $\times 10^{-4}$	7.35$\times 10^{-4}$
p_{11} ($\text{mm}^{-7/2}\text{mm}^{-i\varepsilon}$)	4.43 $\times 10^{-3}$	4.42 $\times 10^{-3}$	4.40 $\times 10^{-3}$	4.43 $\times 10^{-3}$	4.40$\times 10^{-3}$
p_{21} ($\text{mm}^{-9/2}\text{mm}^{-i\varepsilon}$)	-6.80 $\times 10^{-4}$	-6.76 $\times 10^{-4}$	-6.75$\times 10^{-4}$	-6.76$\times 10^{-4}$	-6.74$\times 10^{-4}$
p_{31} ($\text{mm}^{-11/2}\text{mm}^{-i\varepsilon}$)	4.60 $\times 10^{-5}$	4.56 $\times 10^{-5}$	4.56 $\times 10^{-5}$	4.55 $\times 10^{-5}$	4.55$\times 10^{-5}$
p_{41} ($\text{mm}^{-13/2}\text{mm}^{-i\varepsilon}$)	-1.16 $\times 10^{-6}$	-1.14 $\times 10^{-6}$	-1.15$\times 10^{-6}$	-1.14$\times 10^{-6}$	-1.15$\times 10^{-6}$

E.2 Fitting parameters related to the mechanical and residual stress intensity factors

As described in Section 5.4.4, mechanical and thermal FEAs were performed for the five MMELS specimens tested. Stress intensity factors resulting from applied loads, as well as from thermal residual curing stresses were obtained for each analysis by means of the mechanical and thermal M-integrals, described in Section 3.2. For the mechanical problem (f), surfaces were fitted through the finite element results to obtain a relation between $K_m^{(f)}$ $(m = 1, 2, III)$, the delamination length a and position along the delamination front x_3. In eq. (5.1), the expression for these surfaces is presented. The values of p_{i0} and p_{j1} $(i = 0, 1, .., 5$ and $j = 0, 1, .., 4)$ in this equation are given in Tables E.6 through E.8 for $m = 1, 2$ and III, respectively. For the thermal problem (r), curves were fitted through the finite element results to obtain a relation between $K_m^{(r)}$ $(m = 1, 2, III)$ and position along the delamination front x_3. In eq. (5.3), the expression for this curve is presented. The values of $b_i (i = 0, 1, .., 14)$ in this equation are given in Tables E.9 through E.11 for $m = 1, 2$ and III, respectively.

Table E.7: Constants p_{i0}, $(i = 0, 1, .., 5)$, and p_{j1}, $(j = 0, 1, .., 4)$, of eq. 5.1 for $K_2^{(f)}$ for the MMELS specimens.

	MMELS-1-9	MMELS-1-11	MMELS-1-12	MMELS-1-17	MMELS-1-18
p_{00} $(\text{mm}^{-3/2}\text{mm}^{-i\varepsilon})$	5.77 $\times 10^{-2}$	5.83 $\times 10^{-2}$	5.72 $\times 10^{-2}$	5.92 $\times 10^{-2}$	5.64 $\times 10^{-2}$
p_{10} $(\text{mm}^{-5/2}\text{mm}^{-i\varepsilon})$	-5.24 $\times 10^{-3}$	-5.43 $\times 10^{-3}$	-5.13 $\times 10^{-3}$	-5.65 $\times 10^{-3}$	-4.89 $\times 10^{-3}$
p_{20} $(\text{mm}^{-7/2}\text{mm}^{-i\varepsilon})$	-1.55 $\times 10^{-3}$	-1.53 $\times 10^{-3}$	-1.55 $\times 10^{-3}$	-1.51 $\times 10^{-3}$	-1.56 $\times 10^{-3}$
p_{30} $(\text{mm}^{-9/2}\text{mm}^{-i\varepsilon})$	1.83 $\times 10^{-4}$	1.81 $\times 10^{-4}$	1.82 $\times 10^{-4}$	1.80 $\times 10^{-4}$	1.82 $\times 10^{-4}$
p_{40} $(\text{mm}^{-11/2}\text{mm}^{-i\varepsilon})$	-4.60 $\times 10^{-6}$	-4.53 $\times 10^{-6}$	-4.57 $\times 10^{-6}$	-4.50 $\times 10^{-6}$	-4.57 $\times 10^{-6}$
p_{50} $(\text{mm}^{-13/2}\text{mm}^{-i\varepsilon})$	5.05 $\times 10^{-12}$	5.34 $\times 10^{-12}$	-8.88 $\times 10^{-12}$	-9.90 $\times 10^{-12}$	-2.99 $\times 10^{-12}$
p_{01} $(\text{mm}^{-5/2}\text{mm}^{-i\varepsilon})$	7.97 $\times 10^{-3}$	7.94 $\times 10^{-3}$	7.93 $\times 10^{-3}$	7.94 $\times 10^{-3}$	7.97 $\times 10^{-3}$
p_{11} $(\text{mm}^{-7/2}\text{mm}^{-i\varepsilon})$	-5.80 $\times 10^{-5}$	-5.10 $\times 10^{-5}$	-6.19 $\times 10^{-5}$	-4.28 $\times 10^{-5}$	-6.98 $\times 10^{-5}$
p_{21} $(\text{mm}^{-9/2}\text{mm}^{-i\varepsilon})$	8.87 $\times 10^{-5}$	8.71 $\times 10^{-5}$	8.87 $\times 10^{-5}$	8.60 $\times 10^{-5}$	8.97 $\times 10^{-5}$
p_{31} $(\text{mm}^{-11/2}\text{mm}^{-i\varepsilon})$	-8.63 $\times 10^{-6}$	-8.48 $\times 10^{-6}$	-8.61 $\times 10^{-6}$	-8.38 $\times 10^{-6}$	-8.67 $\times 10^{-6}$
p_{41} $(\text{mm}^{-13/2}\text{mm}^{-i\varepsilon})$	2.17 $\times 10^{-7}$	2.13 $\times 10^{-7}$	2.17 $\times 10^{-7}$	2.10 $\times 10^{-7}$	2.18 $\times 10^{-7}$

Table E.8: Constants p_{i0}, $(i = 0, 1, .., 5)$, and p_{j1}, $(j = 0, 1, .., 4)$, of eq. 5.1 for $K_{III}^{(f)}$ for the MMELS specimens.

	MMELS-1-9	MMELS-1-11	MMELS-1-12	MMELS-1-17	MMELS-1-18
p_{00} $(\text{mm}^{-3/2}\text{mm}^{-i\varepsilon})$	3.31 $\times 10^{-2}$	3.32 $\times 10^{-2}$	3.30 $\times 10^{-2}$	3.33 $\times 10^{-2}$	3.29 $\times 10^{-2}$
p_{10} $(\text{mm}^{-5/2}\text{mm}^{-i\varepsilon})$	-4.83 $\times 10^{-2}$	-4.80 $\times 10^{-2}$	-4.82 $\times 10^{-2}$	-4.78 $\times 10^{-2}$	-4.84 $\times 10^{-2}$
p_{20} $(\text{mm}^{-7/2}\text{mm}^{-i\varepsilon})$	1.65 $\times 10^{-2}$	1.63 $\times 10^{-2}$	1.65 $\times 10^{-2}$	1.63 $\times 10^{-2}$	1.65 $\times 10^{-2}$
p_{30} $(\text{mm}^{-9/2}\text{mm}^{-i\varepsilon})$	-2.19 $\times 10^{-3}$	-2.16 $\times 10^{-3}$	-2.18 $\times 10^{-3}$	-2.14 $\times 10^{-3}$	-2.19 $\times 10^{-3}$
p_{40} $(\text{mm}^{-11/2}\text{mm}^{-i\varepsilon})$	1.23 $\times 10^{-4}$	1.21 $\times 10^{-4}$	1.23 $\times 10^{-4}$	1.20 $\times 10^{-4}$	1.23 $\times 10^{-4}$
p_{50} $(\text{mm}^{-13/2}\text{mm}^{-i\varepsilon})$	-2.49 $\times 10^{-6}$	-2.43 $\times 10^{-6}$	-2.47 $\times 10^{-6}$	-2.40 $\times 10^{-6}$	-2.48 $\times 10^{-6}$
p_{01} $(\text{mm}^{-5/2}\text{mm}^{-i\varepsilon})$	5.92 $\times 10^{-3}$	5.91 $\times 10^{-3}$	5.89 $\times 10^{-3}$	5.92 $\times 10^{-3}$	5.91 $\times 10^{-3}$
p_{11} $(\text{mm}^{-7/2}\text{mm}^{-i\varepsilon})$	-1.22 $\times 10^{-3}$	-1.21 $\times 10^{-3}$	-1.21 $\times 10^{-3}$	-1.21 $\times 10^{-3}$	-1.21 $\times 10^{-3}$
p_{21} $(\text{mm}^{-9/2}\text{mm}^{-i\varepsilon})$	9.37 $\times 10^{-5}$	9.30 $\times 10^{-5}$	9.30 $\times 10^{-5}$	9.30 $\times 10^{-5}$	9.30 $\times 10^{-5}$
p_{31} $(\text{mm}^{-11/2}\text{mm}^{-i\varepsilon})$	-3.15 $\times 10^{-6}$	-3.11 $\times 10^{-6}$	-3.12 $\times 10^{-6}$	-3.10 $\times 10^{-6}$	-3.12 $\times 10^{-6}$
p_{41} $(\text{mm}^{-13/2}\text{mm}^{-i\varepsilon})$	4.62 $\times 10^{-13}$	1.62 $\times 10^{-13}$	-7.23 $\times 10^{-13}$	-8.87 $\times 10^{-14}$	-4.66 $\times 10^{-13}$

Table E.9: Constants b_i, $(i = 0, 1, 2, ..., 14)$, of eq. (5.3) for $K_1^{(r)}$ for the MMELS specimens

	MMELS-1-9	MMELS-1-11	MMELS-1-12	MMELS-1-17	MMELS-1-18
b_0 $(\text{MPa mm}^{1/2}(\text{mm})^{-i\varepsilon})$	-5.39	-5.36	-5.33	-5.53	-5.53
b_1 $(\text{MPa mm}^{-1/2}(\text{mm})^{-i\varepsilon})$	12.5	12.4	12.4	12.7	12.8
b_2 $(\text{MPa mm}^{-3/2}(\text{mm})^{-i\varepsilon})$	-15.2	-14.9	-15.0	-15.3	-15.4
b_3 $(\text{MPa mm}^{-5/2}(\text{mm})^{-i\varepsilon})$	11.0	10.8	10.9	11.0	11.2
b_4 $(\text{MPa mm}^{-7/2}(\text{mm})^{-i\varepsilon})$	-5.09	-4.97	-5.03	-5.07	-5.18
b_5 $(\text{MPa mm}^{-9/2}(\text{mm})^{-i\varepsilon})$	1.58	1.54	1.56	1.57	1.61
b_6 $(\text{MPa mm}^{-11/2}(\text{mm})^{-i\varepsilon})$	-0.343	-0.332	-0.339	-0.337	-0.349
b_7 $(\text{MPa mm}^{-13/2}(\text{mm})^{-i\varepsilon})$	5.32 $\times 10^{-2}$	5.13 $\times 10^{-2}$	5.25 $\times 10^{-2}$	5.19 $\times 10^{-2}$	5.41 $\times 10^{-2}$
b_8 $(\text{MPa mm}^{-15/2}(\text{mm})^{-i\varepsilon})$	-5.96 $\times 10^{-3}$	-5.73 $\times 10^{-3}$	-5.88 $\times 10^{-3}$	-5.78 $\times 10^{-3}$	-6.06 $\times 10^{-3}$
b_9 $(\text{MPa mm}^{-17/2}(\text{mm})^{-i\varepsilon})$	4.83 $\times 10^{-4}$	4.63 $\times 10^{-4}$	4.77 $\times 10^{-4}$	4.66 $\times 10^{-4}$	4.91 $\times 10^{-4}$
b_{10} $(\text{MPa mm}^{-19/2}(\text{mm})^{-i\varepsilon})$	-2.81 $\times 10^{-5}$	-2.68 $\times 10^{-5}$	-2.77 $\times 10^{-5}$	-2.69 $\times 10^{-5}$	-2.85 $\times 10^{-5}$
b_{11} $(\text{MPa mm}^{-21/2}(\text{mm})^{-i\varepsilon})$	1.14 $\times 10^{-6}$	1.08 $\times 10^{-6}$	1.12 $\times 10^{-6}$	1.08 $\times 10^{-6}$	1.16 $\times 10^{-6}$
b_{12} $(\text{MPa mm}^{-23/2}(\text{mm})^{-i\varepsilon})$	-3.06 $\times 10^{-8}$	-2.89 $\times 10^{-8}$	-3.01 $\times 10^{-8}$	-2.89 $\times 10^{-8}$	-3.10 $\times 10^{-8}$
b_{13} $(\text{MPa mm}^{-25/2}(\text{mm})^{-i\varepsilon})$	4.89 $\times 10^{-10}$	4.61 $\times 10^{-10}$	4.81 $\times 10^{-10}$	4.59 $\times 10^{-10}$	4.96 $\times 10^{-10}$
b_{14} $(\text{MPa mm}^{-27/2}(\text{mm})^{-i\varepsilon})$	-3.52 $\times 10^{-12}$	-3.30 $\times 10^{-12}$	-3.46 $\times 10^{-12}$	-3.28 $\times 10^{-12}$	-3.56 $\times 10^{-12}$

Table E.10: Constants b_i, $(i = 0, 1, 2, ..., 14)$, of eq. (5.3) for $K_2^{(r)}$ for the MMELS specimens

	MMELS-1-9	MMELS-1-11	MMELS-1-12	MMELS-1-17	MMELS-1-18
b_0 (MPa mm$^{1/2}$(mm)$^{-i\varepsilon}$)	0.374	0.370	0.372	0.379	0.378
b_1 (MPa mm$^{-1/2}$(mm)$^{-i\varepsilon}$)	-2.43	-2.40	-2.40	-2.47	-2.48
b_2 (MPa mm$^{-3/2}$(mm)$^{-i\varepsilon}$)	3.46	3.41	3.42	3.50	3.54
b_3 (MPa mm$^{-5/2}$(mm)$^{-i\varepsilon}$)	-2.60	-2.55	-2.57	-2.61	-2.65
b_4 (MPa mm$^{-7/2}$(mm)$^{-i\varepsilon}$)	1.22	1.19	1.21	1.22	1.24
b_5 (MPa mm$^{-9/2}$(mm)$^{-i\varepsilon}$)	-0.384	-0.373	-0.379	-0.380	-0.391
b_6 (MPa mm$^{-11/2}$(mm)$^{-i\varepsilon}$)	0.0841	0.0815	0.0830	0.0827	0.0856
b_7 (MPa mm$^{-13/2}$(mm)$^{-i\varepsilon}$)	-1.31 $\times 10^{-2}$	-1.27 $\times 10^{-2}$	-1.30 $\times 10^{-2}$	-1.28 $\times 10^{-2}$	-1.34 $\times 10^{-2}$
b_8 (MPa mm$^{-15/2}$(mm)$^{-i\varepsilon}$)	1.48 $\times 10^{-3}$	1.42 $\times 10^{-3}$	1.46 $\times 10^{-3}$	1.44 $\times 10^{-3}$	1.51 $\times 10^{-3}$
b_9 (MPa mm$^{-17/2}$(mm)$^{-i\varepsilon}$)	-1.21 $\times 10^{-4}$	-1.15 $\times 10^{-4}$	-1.19 $\times 10^{-4}$	-1.16 $\times 10^{-4}$	-1.23 $\times 10^{-4}$
b_{10} (MPa mm$^{-19/2}$(mm)$^{-i\varepsilon}$)	7.04 $\times 10^{-6}$	6.71 $\times 10^{-6}$	6.93 $\times 10^{-6}$	6.74 $\times 10^{-6}$	7.14 $\times 10^{-6}$
b_{11} (MPa mm$^{-21/2}$(mm)$^{-i\varepsilon}$)	-2.86 $\times 10^{-7}$	-2.71 $\times 10^{-7}$	-2.82 $\times 10^{-7}$	-2.72 $\times 10^{-7}$	-2.90 $\times 10^{-7}$
b_{12} (MPa mm$^{-23/2}$(mm)$^{-i\varepsilon}$)	7.69 $\times 10^{-9}$	7.27 $\times 10^{-9}$	7.57 $\times 10^{-9}$	7.27 $\times 10^{-9}$	7.80 $\times 10^{-9}$
b_{13} (MPa mm$^{-25/2}$(mm)$^{-i\varepsilon}$)	-1.23 $\times 10^{-10}$	-1.16 $\times 10^{-10}$	-1.21 $\times 10^{-10}$	-1.15 $\times 10^{-10}$	-1.25 $\times 10^{-10}$
b_{14} (MPa mm$^{-27/2}$(mm)$^{-i\varepsilon}$)	8.84 $\times 10^{-13}$	8.29 $\times 10^{-13}$	8.70 $\times 10^{-13}$	8.25 $\times 10^{-13}$	8.96 $\times 10^{-13}$

Table E.11: Constants b_i, $(i = 0, 1, 2, ..., 14)$, of eq. (5.3) for $K_{III}^{(r)}$ for the MMELS specimens

	MMELS-1-9	MMELS-1-11	MMELS-1-12	MMELS-1-17	MMELS-1-18
b_0 (MPa mm$^{1/2}$)	8.82	8.77	8.74	9.04	9.03
b_1 (MPa mm$^{-1/2}$)	-16.7	-16.5	-16.5	-17.0	-17.0
b_2 (MPa mm$^{-3/2}$)	18.5	18.3	18.3	18.7	18.9
b_3 (MPa mm$^{-5/2}$)	-11.9	-11.7	-11.8	-12.0	-12.2
b_4 (MPa mm$^{-7/2}$)	4.83	4.73	4.78	4.83	4.95
b_5 (MPa mm$^{-9/2}$)	-1.31	-1.27	-1.29	-1.30	-1.34
b_6 (MPa mm$^{-11/2}$)	0.243	0.236	0.240	0.240	0.248
b_7 (MPa mm$^{-13/2}$)	-3.18 $\times 10^{-2}$	-3.08 $\times 10^{-2}$	-3.14 $\times 10^{-2}$	-3.12 $\times 10^{-2}$	-3.25 $\times 10^{-2}$
b_8 (MPa mm$^{-15/2}$)	2.96 $\times 10^{-3}$	2.85 $\times 10^{-3}$	2.92 $\times 10^{-3}$	2.88 $\times 10^{-3}$	3.02 $\times 10^{-3}$
b_9 (MPa mm$^{-17/2}$)	-1.93 $\times 10^{-4}$	-1.86 $\times 10^{-4}$	-1.91 $\times 10^{-4}$	-1.87 $\times 10^{-4}$	-1.97 $\times 10^{-4}$
b_{10} (MPa mm$^{-19/2}$)	8.69 $\times 10^{-6}$	8.31 $\times 10^{-6}$	8.57 $\times 10^{-6}$	8.36 $\times 10^{-6}$	8.87 $\times 10^{-6}$
b_{11} (MPa mm$^{-21/2}$)	-2.56 $\times 10^{-7}$	-2.44 $\times 10^{-7}$	-2.52 $\times 10^{-7}$	-2.45 $\times 10^{-7}$	-2.61 $\times 10^{-7}$
b_{12} (MPa mm$^{-23/2}$)	4.44 $\times 10^{-9}$	4.21 $\times 10^{-9}$	4.37 $\times 10^{-9}$	4.22 $\times 10^{-9}$	4.53 $\times 10^{-9}$
b_{13} (MPa mm$^{-25/2}$)	-3.44 $\times 10^{-11}$	-3.25 $\times 10^{-11}$	-3.39 $\times 10^{-11}$	-3.25 $\times 10^{-11}$	-3.51 $\times 10^{-11}$
b_{14} (MPa mm$^{-27/2}$)	1.33 $\times 10^{-19}$	1.31 $\times 10^{-19}$	-2.46 $\times 10^{-19}$	1.58 $\times 10^{-19}$	-1.40 $\times 10^{-21}$

זניח. כמו כן, על סמך התוצאות שהתקבלו הוצג קשר בין קצב שחרור האנרגיה ואורך הדלמינציה. אנרגיית ההתנגדות להתקדמות הדלמינציה $\mathcal{G}_{iR}$ חושבה כפונקציה של אורך הדלמינציה והוצגו עקומות התנגדות מסוג R-curves.

בנוסף, באמצעות שיטה גלובלית מסוג experimental compliance method (ECM), קצב שחרור אנרגית האתחול של הדלמינציה וקצב שחרור אנרגית ההתנגדות חושבו. ניתוח התוצאות באמצעות שיטה זו בוצע עבור תוצאות הניסויים בדגמי C-ELS ו MMELS . בנוסף, בוצעה אנליזה חוזרת באמצעות ECM עבור דגמים מסוג double cantilever beam (DCB) אשר שימשו לניסויים קוואזי סטטיים במחקר שבוצע ב 2017 על ידי תומר שוקרון ולסלי בנקס-סילס עבור החומר והממשק אשר נחקרים כאן. מתוך כלל התוצאות בוצעה השוואה בין עקומות ההתנגדות שנמצאו על סמך השיטה הלוקאלית המוצגת במחקר זה וכוללת הפרדת מודים לעומת העקומות שהתקבלו באמצעות שיטת ECM.

על סמך עקומות ההתנגדות והחסינות לשבר שנמצאו במחקר זה ניתן לשפר את תכנון המבנים המכילים את החומר והממשק הנחקר. התחשבות בממצאים המגבילים את קצב שחרור האנרגיה הדרושה לאתחול או קידום דלמינציה בממשק יאפשרו שיפור בתכנון ובבטיחות של מבנים אלו תוך חיסכון תקציבי מובהק.

תקציר

פולימרים מחוזקים בסיבי פחמן משמשים לשיפור ביצועים ולהוזלת עלויות תפעול של מבנים בתעשיות שונות ובמיוחד בתעשייה האווירית. עם זאת, חוסר ידע על התנהגות השבר של חומרים מרוכבים אלה עלול לגרום לאסונות קטסטרופליים. הבנת אתחול והתקדמות דלמינציה בלמינט מרוכב מסוג פולימר מחוזק בסיבי פחמן עשוי לסייע במניעת כשלים שכאלה במבנים כגון מטוסים. כלים הנדסיים מדויקים עשויים להוביל לתכנון בטוח יותר, לשיפור ביצועים, ולהוזלת עלויות תפעול של מבנים הבנויים מחומרים מרוכבים מסוג זה.

המחקר מתמקד בממשק בין שתי שכבות מרוכבות מחוזקות בסיבים בכיוונים שונים. השכבה העליונה היא אריג חד כיווני עם סיבי פחמן בכיוון $0°$ והשכבה התחתונה הינה אריג פשוט מאוזן עם סיבים ארוגים בכיוון $+45°/-45°$. החומר יוצר בתהליך ידני אשר מכונה הספגה רטובה.

עשרים ושבע ניסויי חסינות לשבר בוצעו במודים מעורבים שונים באמצעות דגמים מסוג דיסקה ברזילאית על מנת לקבוע את מאפייני החסינות לשבר של החומר המרוכב והממשק הספציפיים. במהלך כל בדיקה הופעל עומס P על הדגם בזווית ω ביחס לדלמינציה המלאכותית ההתחלית אשר מוקמה בממשק בין שתי השכבות הנחקרות. שבע זוויות העמסה שונות שימשו ליצירת מודים מעורבים שונים. בהתבסס על התוצאות, תוך שימוש בשיטת אלמנטים סופיים בשילוב עם אינטגרל תלת מימדי משמר מבוסס אנרגייה אשר מכונה אינטגרל M, כמו גם שימוש בשיטת אקסטרפולצית הזזות, חושבו מקדמי עוצמת המאמץ עבור המודים השונים. באמצעות ניתוח הבעיה המכאנית חושבו מקדמי עוצמת המאמץ אשר נובעים מעומסים מכניים. בנוסף, על ידי ניתוח בעיה תרמית אשר קשורה בהיווצרות מאמצים שיוריים כתוצאה מהפרשי הטמפרטורות שהדגמים היו נתונים להם במהלך הייצור חושבו מקדמי עוצמת המאמץ התרמיים.

סופרפוזיציה של מקדמי עוצמת המאמץ המכאניים והתרמיים, הניבו את מקדמי עוצמת המאמץ הכלליים הרלוונטיים לכל דגם אשר שימשו לחישוב קצב שחרור האנרגייה הקריטי להתקדמות הדלמינציה $\mathcal{G}_{ic}$. היחידות המרוכבות של מקדמי עוצמת המאמץ נורמלו והתוצאות שימשו לחישוב זוויות הפאזה $\hat{\psi}$ ו ϕ אשר מתארות את יחס המודים המעורבים בתוך המישור ואת יחס המודים מחוץ למישור לאלו בתוך המישור, בהתאמה. לבסוף הוצעו קריטריוני כשל דו-ממדיים ותלת מימדיים לחומר ולממשק הנחקרים ובוצע ניתוח סטטיסטי עם הסתברות של 10% לכישלון בלתי צפוי באזור הבטוח עם ביטחון של 95%. עקומות ומשטחי הכשל שהוצגו עשויים לאפשר חיזוי כשל קטסטרופלי עבור החומר והממשק הנחקרים. כמו כן, הממצאים מאפשרים הבנה טובה יותר בהקשר של התקדמות דלמינציה בממשק בין שכבתי בלמינט מרוכב.

בנוסף, בוצעו שישה ניסויים קוואזי - סטטיים במוד II כמעט טהור בדגמים מסוג calibrated end loaded split (C-ELS) וחמישה ניסויים קוואזי - סטטיים בדגמים מסוג mixed mode end loaded split (MMELS). כל אחד מהניסויים כלל שני שלבים, שלב אתחול (AC) ושלב התקדמות (PC). בשלב הראשון הדלמינציה המלאכותית מתקדמת ונוצרת דלמינציה טבעית בממשק. בשלב השני נבחנה התקדמות יציבה של הדלמיצנציה הטבעית.

עבור כל דגם שעבר ניסוי נבנה מודל ובוצעה אנליזת אלמנט סופי מכאנית ותרמתי. מקדמי עוצמת המאמץ אשר נובעים כתוצאה מעומסים מכאניים ותרמיים שיוריים חושבו מתוך תוצאות האנליזות תוך שימוש בשיטת אקסטרפולציית ההזזות, באמצעות אינטגרלים משמרים תלת מימדיים מכאניים ותרמיים מסוג M, ועל ידי שימוש ב virtual closure technique (VCCT). על סמך התוצאות, מקדמי עוצמת המאמץ הכוללים חושבו כסופרפוזיציה של המקדמים המכאניים והתרמיים. בנוסף, קצב שחרור האנרגיה $\mathcal{G}_i$, כמו גם זוויות הפאזה $\hat{\psi}$ ו ϕ חושבו עבור כל ניסוי באמצעות קשרים שונים. זוויות הפאזה הוצגו כפונקציה של התקדמות הדלמינציה. לפי הממצאים נראה שהשינוי ביחס המודים כפונקציה של התקדמות הדלמינציה

אוניברסיטת תל – אביב

הפקולטה להנדסה ע"ש איבי ואלדר פליישמן

בית הספר לתארים מתקדמים ע"ש זנדמן סליינר מודל ללימודי הנדסה

עבודה זו נעשתה בהנחיית:

מנחה המחקר: לזלי בנקס-סילס

פרופ' לזלי בנקס-סילס

אוניברסיטת תל – אביב

הפקולטה להנדסה ע"ש איבי ואלדר פליישמן

בית הספר לתארים מתקדמים ע"ש זנדמן סליינר מודל ללימודי הנדסה

דלמינציה בחומר מרוכב בין שכבה חד כיוונית לבין אריג : חקר התנהגות שבר במודים מעורבים

מור מגה

חיבור לשם קבלת התואר "דוקטור לפילוסופיה "

הוגש לסנאט של אוניברסיטת תל-אביב

עבודה זו נעשתה באוניברסיטת ת"א בפקולטה להנדסה בהנחיית פרופ' לסלי בנקס-סילס

ספטמבר 2020

אוניברסיטת תל – אביב

הפקולטה להנדסה ע"ש איבי ואלדר פליישמן

בית הספר לתארים מתקדמים ע"ש זנדמן סליינר מודל ללימודי הנדסה

דלמינציה בחומר מרוכב בין שכבה חד כיוונית לבין אריג : חקר התנהגות שבר במודים מעורבים

חיבור לשם קבלת התואר "דוקטור לפילוסופיה"

מור מגה

הוגש לסנאט של אוניברסיטת תל-אביב

ספטמבר 2020